University of Rochester
Laboratory for Laser Energetics

DOE/SF/19460-380
January 2001

LLE 2000 Annual Report

October 1999 – September 2000

UR LLE

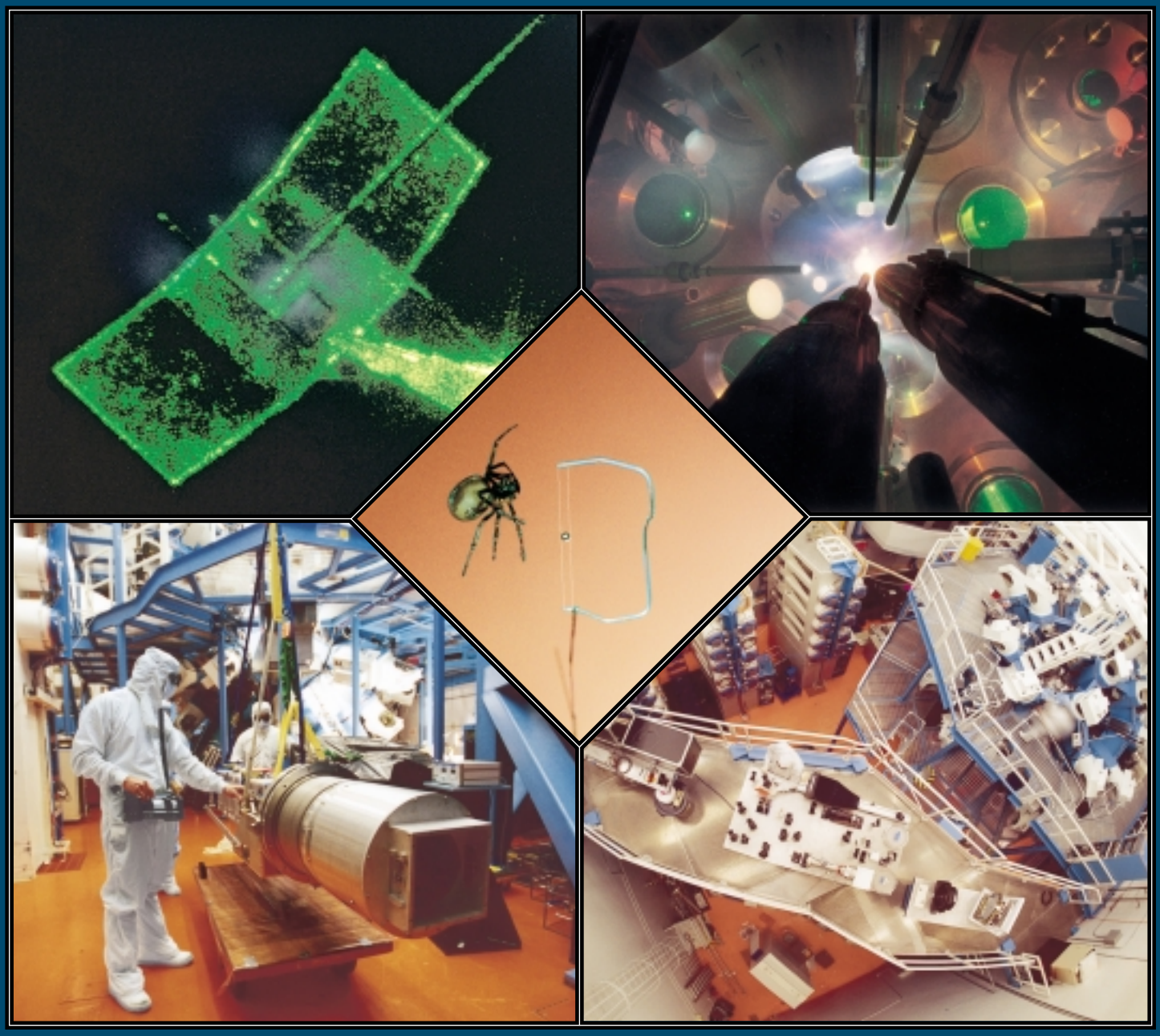

Cover Photos

Upper Left: A variety of targets were fielded on the OMEGA laser system in FY00. The photograph shows one of the target shots during an NLUF laboratory astrophysics campaign to produce and diagnose a radiative precursor shock. The experiment, led by the University of Michigan, was a collaboration of 22 co-principal investigators from 11 institutions.

Lower Left: Mark Romanofsky, senior manufacturing engineer, Thomas Lewis, senior technical associate, and Frederick Rister, senior manufacturing engineer, install a new ten-inch manipulator (TIM). The TIM is a diagnostic shuttle system that is used to position a variety of diagnostics in the OMEGA target chamber. There are six TIM's on OMEGA.

Upper Right: This photograph was taken during the first cryogenic capsule implosion using the new OMEGA Cryogenic Target Handling System (CTHS). The primary purpose of this shot was to test the integrated CTHS subsystems using a deuterium-filled capsule.

Center: To minimize the support structure mass and provide a relatively stiff support for cryogenic targets, the capsule is suspended by three 0.5-μm-thick spider silk strands in the "C"-shaped mount shown in this photograph.

Lower Right: Charles Kellogg, senior laboratory engineer, adjusts the alignment of the new beam diagnostics station installed in the OMEGA Target Bay.

Prepared for
U.S. Department of Energy
San Francisco Operations Office
DOE/SF/19460-332

Distribution Category UC712
October 1999–September 2000

Printed in the United States of America
Available from
National Technical Information Services
U.S. Department of Commerce
5285 Port Royal Road
Springfield, VA 22161

Price codes: Printed Copy A11
Microfiche A01

The work described in this volume includes current research at the Laboratory for Laser Energetics, which is supported by New York State Energy Research and Development Authority, the University of Rochester, the U.S. Department of Energy Office of Inertial Confinement Fusion under Cooperative Agreement No. DE-FC03-92SF19460, and other agencies.

For questions or comments, contact Laboratory for Laser Energetics, 250 East River Road, Rochester, NY 14623-1299, (716) 275-5286.
Worldwide-Web Home Page: http://www.lle.rochester.edu/

University of Rochester
Laboratory for Laser Energetics

DOE/SF/19460-380
January 2001

LLE 2000 Annual Report

UR LLE

October 1999 – September 2000

Inertial Fusion Program and National Laser Users' Facility Program

Contents

Executive Summary

The fiscal year ending September 2000 (FY00) concluded the third year of the cooperative agreement (DE-FC03-92SF19460) five-year renewal with the U. S. Department of Energy (DOE). This report summarizes research at the Laboratory for Laser Energetics (LLE), the operation of the National Laser Users' Facility (NLUF), and programs involving education of high school, undergraduate, and graduate students during the year.

Progress in Laser Fusion

A major goal of the Laboratory for Laser Energetics is to develop the direct-drive approach to inertial fusion for an ignition and gain demonstration on the National Ignition Facility (NIF) currently under construction at the Lawrence Livermore National Laboratory (LLNL). This challenging goal requires precision laser diagnostics and controls, a cryogenic target handling system, sophisticated experimental diagnostics, robust theoretical and computational modeling, and the development of new laser and optical technologies.

At LLE the stability of direct-drive NIF capsules has been studied, and the conditions under which direct-drive NIF capsules ignite are being examined. A numerical study (pp. 1–5) uses two-dimensional hydrodynamic simulations in conjunction with a model that includes the various mechanisms that can influence target performance. Laser nonuniformities and the inner-surface roughness of the DT ice in direct-drive cryogenic capsules have been identified as the principal seeds of the instabilities that can potentially quench ignition. We believe that a target gain greater than 10 can be achieved for a realistic inner-surface ice roughness when beam smoothing with 2-D smoothing by spectral dispersion (SSD) and a bandwidth greater than 0.5 THz is used. Another set of two-dimensional calculations (pp. 181–190) demonstrates how various contributors to implosion disruption (laser imprinting, power imbalance, and target roughness) affect target performance and final gain for NIF target designs.

Two-dimensional hydrodynamic simulations in conjunction with a stability analysis model to study the performance of OMEGA cryogenic capsules show that these targets are energy scaled from the NIF ignition designs and have similar 1-D behavior and stability properties. This similarity will facilitate the extrapolation of cryogenic target studies on OMEGA to ignition targets on the NIF.

A novel technique for laser-imprint reduction in OMEGA cryogenic capsules (pp. 56–62) shows considerable promise. Laser nonuniformities can imprint a target with a "seed" that can cause debilitating hydrodynamic instabilities. Using the two-dimensional hydrodynamics code *ORCHID*, investigations show that an initial spike in the laser pulse can reduce laser imprint by about a factor of 2 for typical target configurations and especially for the nonuniformity modes considered most dangerous for target performance. Further, this modification to the laser pulse need not significantly degrade target performance and is accompanied by only a modest decrease in the one-dimensional neutron yield.

A judicious choice of materials and target dimensions allows one to infer the amount of fast-electron preheat due to laser irradiation on OMEGA. Significant fast-electron preheat can substantially decrease the effectiveness of a direct-drive implosion. Beginning on p. 63, we report on an experiment in planar geometry. The results from this measurement will be used as a reference point to determine fast-electron preheat in ignition-relevant direct-drive spherical targets.

Experimental measurements of target irradiation nonuniformity in the absence of SSD have indicated lower-than-expected levels of nonuniformity. Shots without SSD are baseline measurements for OMEGA; consequently, modeling these shots provides a more complete understanding of the target irradiation nonuniformity. Beginning on p. 78, we report on comparisons of numerical simulations of laser smoothing with measurements. The intensity-dependent phase accumulations by the OMEGA laser (*B*-integral) is identified as the mechanism for the observed smoothing. We found that we can successfully model these *B*-integral-related smoothing mechanisms and find them to be relatively minor compared to the dominant smoothing effect of SSD.

Measurements (pp. 173–180) of the effect of beam smoothing and pulse shape on imprinting show reduced levels of imprint with the higher beam smoothing afforded by 1-THz SSD.

An investigation of the laser prepulse levels on OMEGA (pp. 30–36) has helped to establish a contrast criterion for direct-drive implosions. Control of laser prepulses can be critical since high-intensity prepulses can potentially compromise the aluminum layer and cause unwanted laser damage to direct-drive targets. While OMEGA intermittently produces measurable prepulses, the prepulse level is not expected to significantly degrade target performance.

We report on the results of a series of direct-drive implosions of gas-fusion-fuel–filled plastic shells performed on the OMEGA laser system. The experiments include those performed with 1-THz SSD and high-quality power balance (pp. 191–198).

OMEGA time-integrated x-ray diagnostics have been converted to electronic readout using direct-detection x-ray cameras [charge-injection devices (CID's)]. Pinhole and x-ray microscope images are shown along with inferred calibration measurements of the CID cameras (pp. 119–123). Currently, the same cameras are being used to obtain x-ray spectra in a TIM-based spectrometer, extending their use to all time-integrated imaging and spectroscopic x-ray instruments used on OMEGA.

The spatial structure of the temperature and density of target-shell plasmas at peak compression (stagnation) has been investigated experimentally (pp. 124–129). This is accomplished by examining the energy dependence of the x-ray emission using narrow-band x-ray filters and the known absorption properties of the shell dopant (Ti). A technique to measure the positional dependence of x-ray self-absorption with filtered x-ray framing cameras (pp. 204–213) shows how compressed shell nonuniformities can be measured by carefully modeling the imaging system.

The physics and instrumentation used to obtain and interpret secondary D-^{3}He proton spectra from current gas-filled-target experiments and future cryogenic-target experiments (pp. 130–141) is presented in some detail. Through a novel extension of existing charged-particle detection techniques with track detectors, we now have the ability to obtain secondary proton spectra with increased sensitivity. We have also found that we can measure the secondary neutron yield (DT neutron yield from D_2-filled targets) using current-mode detectors (pp. 199–203). The current-mode detectors can be configured to survey a much larger dynamic range than single-event neutron counters.

Collaborative experiments on OMEGA have continued between LLE and Los Alamos National Laboratory (LANL) on indirect-drive capsule implosions in tetrahedral hohlraums. These hohlraums are particularly well suited to the OMEGA target chamber geometry and have been shown to provide an extremely uniform radiation drive. A principal tool used in this investigation is a three-dimensional (3-D) view-factor code including a time-dependent radiation-transport model in the hohlraum wall and a perturbation treatment of a near-spherically symmetric hydrodynamic implosion of the capsule (pp. 90–106). Simulations of x-ray images of the imploded core with a 3-D x-ray postprocessor show close agreement with experiment on several quantities including radiation drive temperatures, fusion yields, and core deformation.

Cryogenic Target Technology

This year we measured the initial performance of the high-pressure deuterium- and tritium-filling portion of the Cryogenic Target Handling System (pp. 6–11). Thick-walled plastic targets have been successfully pressurized with deuterium to the required levels by this high-pressure filling system. Adequate control of the various factors influencing the filling process has been demonstrated, indicating that even thin-walled plastic targets (such as those required by the cryogenic target designs for OMEGA) can be successfully filled to the required high pressure.

The target detection and shroud pull-sequencing aspects of cryogenic target operations on OMEGA are detailed beginning on p. 21. The newly designed Cryogenic Target Detection System is based on existing elements of OMEGA controls and provides the necessary sequencing, safety features, and flexibility to allow for the evolution of cryogenic target operations.

A numerical study of the principal sources of target nonuniformities for a cryogenic target when placed in the layering sphere is summarized beginning on p. 12. Deviations from idealized symmetry in the capsule-wall thickness, the displacement of the capsule relative to the center of the layering sphere, and the existence of temperature gradients on the layering sphere's inner surface can result in temperature gradients across the cryogenic target. This in turn affects the

uniformity of the cryogenic fuel layer. Calculations of the temperature profile in these targets will be used to guide target fabrication and layering.

Lasers and Optical Materials Technology

Dyes for a liquid crystal–based interferometer to be used on OMEGA for more-accurate wavefront characterization (pp. 37–47) have been identified. Using state-of-the-art computational chemistry tools we have demonstrated the effectiveness of modeling in guiding experimental searches for new dye compounds. The work also has potential for other liquid crystal devices used in optical communications and sensor protection. In other work on interferometry, we have compared the utility of a novel liquid crystal–based, point-diffraction interferometer (LCPDI) with the commercial standard phase-shifting interferometer and conclude that the LCPDI is a viable low-cost alternative (pp. 142–156).

Ongoing experimental and theoretical work relating to holographic grating design and fabrication has resulted in high-diffraction-efficiency, high-wavefront-quality gratings used on the OMEGA laser primarily for laser-beam smoothing and spectroscopy (pp. 71–77). For the high-optical-quality gratings required on OMEGA, it is critical to control environmental factors including humidity, thermal gradients, and air turbulence during grating fabrication. Future work will involve improved modeling of these gratings and further experimental investigations.

Knowledge of the hardness of abrasive particles is a key to understanding the mechanisms of material removal in polishing optical glass. Measurements of the nanohardness of magnetic and nonmagnetic particles used in the magnetorheological finishing (MRF) process are discussed beginning on p. 107. The nanoindentation technique allows for the characterization of mechanical properties of small abrasive particles, which is not possible through traditional microhardness measurement methods. With abrasive particle characterization now possible, subsequent experiments with different combinations of abrasive particles can provide information regarding removal mechanisms in MRF. Additional details about the mechanisms of glass polishing using the MRF technique currently being studied in the Center for Optics Manufacturing (COM) begin on p. 157. Material-removal experiments show that the nanohardness of carbonyl iron (CI) is important in MRF with nonaqueous MR fluids with no nonmagnetic abrasives, but is relatively unimportant in aqueous MR fluids and/or when nonmagnetic abrasives are present.

Laser Facility Report

OMEGA operations during FY00 (p. 216) yielded a total of 1153 target shots, including 284 shots for LLNL, 131 for LANL, 11 for Sandia National Laboratory (SNL), 11 for the French Commissariat à l'Énergie Atomique (CEA), and 124 for the National Laser Users' Facility (NLUF). The principal achievements include activation and testing of the full suite of cryogenic target handling system equipment, improvements to the single-beam uniformity using 1-THz SSD, and significant improvements in the beam-to-beam power fluctuations. This progress required the installation of 60 distributed polarization rotators, a modification to the harmonic conversion cells to accommodate increased bandwidth, and improvements to the SSD equipment.

National Laser Users' Facility

During FY00, external use of OMEGA increased by 12% over the prior fiscal year, accounting for 50% of the total target shots. The seven NLUF experimental campaigns are summarized beginning on p. 217. Shots conducted during the year for the National Laboratories, nuclear weapons effects testing, and the CEA programs are summarized beginning on p. 222. LLNL usage included measurements of x-ray conversion efficiency, experiments on "cocktail" hohlraums, NIF laser beam "foot" symmetry measurements, high-convergence implosions, shock timing, ablator burnthrough, convergent ablator burnthrough, planar Rayleigh–Taylor experiments, experiments on pushered shells, hydrodynamic experiments, and other radiation drive experiments. The LANL campaigns examined the behavior of double-shell targets, direct-drive cylindrical experiments, backlighter studies, high-convergence implosions, Rayleigh–Taylor instability studies, and high-yield shots for neutron diagnostics. LANL also supported additional campaigns at OMEGA: SNL WBS3 ablator characterization, NLUF laser–plasma instability research, jet experiments in collaboration with the United Kingdom's Atomic Weapons Establishment, and transient x-ray diffraction materials work. The French CEA activities included time-resolved broadband x-ray spectroscopic studies, x-ray conversion experiments, and neutron imaging of an imploding DT target.

Education at LLE

As the only major university participant in the National ICF Program, education continues to be an important mission for the Laboratory. Graduate students are using the world's most powerful ultraviolet laser for fusion research on OMEGA, making significant contributions to LLE's research activities. Fourteen faculty from five departments collaborate with LLE's

scientists and engineers. Presently 55 graduate students are pursuing Ph.D. degrees at the Laboratory. The research includes theoretical and experimental plasma physics, high-energy-density plasma physics, x-ray and atomic physics, nuclear fusion, ultrafast optoelectronics, high-power-laser development and applications, nonlinear optics, optical materials and optical fabrications technology, and target fabrication. Technological developments from ongoing Ph.D. research will continue to play an important role on OMEGA.

One hundred forty-one University of Rochester students have earned Ph.D. degrees at LLE since its founding. An additional 70 graduate students and 21 postdoctoral positions from other universities were funded by NLUF grants. The most recent University of Rochester Ph.D. graduates and their thesis titles are

Brian J. Buerke	*Accurate Measurement of Tunneling Ionization Rates of Atoms in a High-Intensity Laser Field*
Jan L. Chaloupka	*Observation of Electron Trapping in an Intense Laser Beam*
Selena Chan	*Porous Silicon Multilayer Structures: From Interference Filters to Light-Emitting Devices to Biosensors*
Faiz Dahmani	*Laser-Driven Mechanical Fracture in Fused Silica*
Andres C. Gaeris	*The Stimulated Brillouin Scattering During the Interaction of Picosecond Laser Pulses with Moderate-Scale-Length Plasmas*
Kenton A. Green	*Characterization of Time- and Frequency-Varying Optoelectronic Microwave Silicon Switches*
Karl D. Hirschman	*Fabrication, Characterization, and Integration of Oxide Passivated Nano-crystalline Silicon Light-Emitting Devices*
Oleg A. Konoplev	*Generation and Measurement of High-Contrast, Ultrashort Intense Laser Pulses*
John M. Larkin	*Optical and Photodynamic Properties of the Higher-Lying States of Rose Bengal*
Stuart J. McNaught	*Precise Measurements of Electron Initial Conditions for Tunneling Ionization in an Intense, Elliptically Polarized Laser Field*
Han Pu	*Properties of Multiple-Component Bose-Einstein Condensate*
James P. Shaffer	*Heteronuclear and Homonuclear Ultracold Optical Collisions Involving Na and Cs: Parts I and II*
Aric B. Shorey	*Mechanisms of Material Removal in Magnetorheological Finishing (MRF) of Glass*
Leon J. Waxer	*Quantum State Measurement for Molecules*

Approximately 55 University of Rochester undergraduate students participated in work or research projects at LLE this past year. Student projects include operational maintenance of the OMEGA laser system, work in the materials and optical-thin-film coating laboratories, programming, image processing, and diagnostic development. This is a unique opportunity for students, many of whom will go on to pursue a higher degree in the area in which they gained experience at the Laboratory.

LLE continues to run a Summer High School Student Research Program (pp. 214–215), where this year 13 high school juniors spent eight weeks performing individual research projects. Each student is individually supervised by a staff scientist or an engineer. At the conclusion of the program, the students make final oral and written presentations on their work. The reports are published as an LLE report.

In 2000, LLE presented its fourth William D. Ryan Inspirational Teacher Award to Mr. James Shannon of Pittsford–Mendon High School. Alumni of our Summer High School Student Research Program were asked to nominate teachers who had a major role in sparking their interest in science, mathematics, and/or technology. This award, which includes a $1000 cash prize, was presented at the High School Student Summer Research Symposium. Mr. Shannon, a chemistry teacher, was nominated by three alumni of the Research Program: Mr. Chen-Lin Lee (1994 participant), Mr. Steven Costello (1998 participant), and Ms. Leslie Lai (1998 participant).

Robert L. McCrory
Director

Stability Analysis of Directly Driven NIF Capsules

Introduction

In inertial confinement fusion (ICF), a spherical shell filled with a DT-gas mixture is compressed to high densities and temperatures to achieve ignition conditions.[1] Degradation from spherical symmetry during the implosion, however, limits the achievable compression ratios and could quench the ignition of the target. The main source of such asymmetry is hydrodynamic instabilities [such as Rayleigh–Taylor (RT)[2] and Bell–Plesset (BP)[3] instabilities] seeded by both irradiation nonuniformities and target-fabrication imperfections. We have developed an analytical model to study stability of the direct-drive cryogenic NIF targets. The drive pulse for such targets consists of two distinct temporal regions (stages): the low-intensity (a few 10^{13} W/cm^2) "foot" and the main drive (up to more than 10^{15} W/cm^2). During the first stage, the laser energy is absorbed by the outermost layer of the target, heating up the shell material and launching a heat wave toward the pellet center. Material behind the heat front expands outwardly, creating an ablation pressure that induces the first shock wave propagating through the shell. Since the laser intensity in the first stage is constant in time and the equilibrium pressure behind the shock is uniform, the ablation front travels at constant velocity. In the absence of acceleration, the perturbations at the ablation front could grow due to the velocity and acceleration perturbations imposed by the laser-intensity modulations ("laser imprint") and surface roughness [Richtmyer–Meshkov (RM)[4] instability]. When the first shock breakout occurs at the rear surface of the DT ice, the pulse ramps up to the drive region (second or acceleration stage), launching the second shock. At this time, the ablation front starts to accelerate, creating conditions for the RT instability that magnify the perturbations seeded during the first stage. If the perturbation amplitude becomes too large during the shell acceleration, the shell breaks up and fails to reach ignition conditions. The shell integrity can be quantified by the "integrity factor" defined as $\Upsilon = A_{\mathrm{mix}}/\Delta R$, where $A_{\mathrm{mix}} \simeq \sqrt{2}\sigma$ is the mix amplitude (bubble amplitude), ΔR is the shell thickness, and σ is the rms sum of the modes. The shell remains intact during the implosion if the integrity factor is less than unity for all time. At the end of the laser pulse, the shell starts to coast inward with a constant velocity until the pressure of the DT-gas mixture becomes high enough to slow down the shell compression (beginning of the deceleration phase). During the deceleration phase the inner DT-ice surface is RT unstable. The growth due to this instability limits the compression ratios and increases the thermal conduction losses, reducing the total energy gain. Results from 2-D *ORCHID*[5] simulations show that the gain reduction depends on the mode spectrum at the end of the acceleration stage. In this article we estimate the integrity factor during the acceleration phase and calculate the spectral distribution of the modes by using the results of the developed model and 2-D *ORCHID* simulations.

Seeding of RT Instability: Laser Imprint, Ablative RM Instability, and "Feedout"

As mentioned earlier, at the beginning of implosion, the ablation pressure launches a shock wave toward the target center. The surface roughness (due to the target fabrication imperfections) and also modulations in the laser intensity deform the shock front and generate perturbed velocity and acceleration fields inside the compressed region. During the shock transit time, the ablation front travels with a constant velocity, and the front perturbations could grow due to imposed velocity and acceleration perturbations.

1. Laser Imprint

Nonuniformities in the laser intensity cause different parts of the beam to ablate shell material at different rates, generating an ablation-pressure modulation along the ablation front. Since the shock speed scales as a square root of the shock strength, stronger shocks launched at the peak of ablation pressure propagate faster than shocks launched at the pressure valleys. The difference in the shock speeds distorts the shock front and creates a perturbed velocity field inside the compressed region. A velocity perturbation at the ablation front, in turn, leads to a linear-in-time front distortion growth $\eta \sim t$. Then, a rippled shock generates a lateral mass flow that leads to a pressure deficiency in the convex part (which protrudes the most into the uncompressed shell) and a pressure excess in the concave part of the shock front. This creates a pressure gradient that accel-

erates fluid elements, leading to an additional growth $\eta \sim t^2$. In ICF, however, several physical processes significantly reduce the imprint growth. First, as the heat front propagates into the cold portion of the target, material heats up and expands outwardly, creating a hot plasma corona. Thus, a finite zone (conduction zone) of hot plasma exists between the energy absorption region and the ablation front. Any pressure perturbations inside such a zone are reduced by the thermal conduction. The simplest theory[6] ("cloudy day effect") predicts that the pressure perturbations decay exponentially away from the critical surface $\tilde{p} \sim e^{-kx}$; thus, nonuniformities in the ablation pressure are reduced by a factor of e^{-kD_c}, where D_c is a distance between the absorption region and the ablation front, and k is the wave number corresponding to a specific mode of nonuniformity. An additional reduction in the imprint growth is due to the mass ablation. The main stabilizing mechanism produced by ablation is the dynamic overpressure or "rocket effect."[7,8] As a result, the imprint amplitude η_{imp}, which is defined as the amplitude of the ablation-front ripple calculated at the shock breakout time, takes the following form:[9]

$$\frac{\eta_{\text{imp}}}{\Delta R\left(\delta I_l / I_0\right)} \simeq 0.4 \frac{A}{l} \hat{\eta}\left(e^{-\Delta_c} - e^{-2\Delta_a} \cos\Delta_{\text{bl}}\right)$$

$$+ \frac{e^{-2\Delta_a}}{\Delta_{\text{bl}}}\left(0.9 + 0.8 \frac{V_c}{c_s}\,\hat{\eta}\right) \sin\Delta_{\text{bl}} + \eta_v^{\text{imp}}, \quad (1)$$

where δI_l is the intensity modulation, I_0 is the average intensity,

$$\hat{\eta} = c_s^2 \big/ \left(V_a V_{\text{bl}} + V_c^2\right),$$

$$\Delta_a = 2\left(l/A\right) V_a / c_s,$$

$$\Delta_{\text{bl}} = 2\left(l/A\right) \sqrt{V_a V_{\text{bl}}}\,/ c_s,$$

A is the shell's in-flight aspect ratio, V_a and V_{bl} are the ablation and blow-off velocities, respectively, V_c is the velocity of the critical surface with respect to the ablation front, and c_s is the sound speed of the compressed material. The term η_v^{imp} is due to the vorticity convection from the shock front.

Using the analytical model of the RT instability (described later in the **Acceleration Phase** section), it is found that laser imprint alone can break up the shell during target acceleration and this can quench ignition; thus, an additional reduction in imprint amplitude is critical for a successful implosion. A significant improvement in the beam uniformity has been made in recent years by introducing smoothing by spectral dispersion (SSD)[10] and induced spatial incoherence (ISI)[11] smoothing techniques. To account for the intensity variation in a realistic laser pulse, SSD is modeled using the 2-D hydrocode *ORCHID*, where the intensity nonuniformities have been reduced by the factor $\sqrt{t_c/\left(t_c + 4t\right)}$. This gives on average a reduction in rms of laser nonuniformity $\sigma = \sqrt{t_c / t_{\text{avg}}}\,\sigma_0$, where the coherence time is taken to be

$$t_c = \left[\Delta\nu \sin\left(k\delta/2\right)\right]^{-1},$$

$\Delta\nu$ is the bandwidth, t_{avg} is the averaging time, and δ is the speckle size. The result of 2-D *ORCHID* simulations (mode spectrum due to imprint (thin solid line) at the beginning of the acceleration phase) of the "all-DT" NIF target design[12] is plotted in Fig. 81.1. This result will be used later as an initial condition for the RT model.

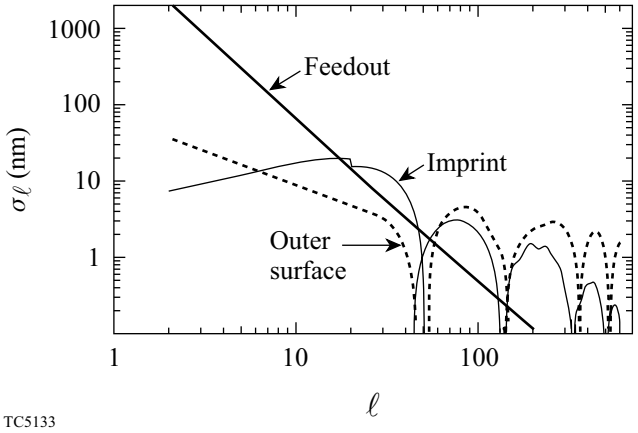

Figure 81.1
Mode spectrum at the beginning of the acceleration phase.

2. Outer-Surface Roughness

When the outer surface of the target is distorted, the ablation pressure launches a ripple shock at the beginning of implosion. The ripple shock, as discussed in the previous subsection, generates a lateral flow that leads to a perturbed pressure gradient and the perturbation growth. The theory describing the perturbation evolution at the corrugated ablation front driven by uniform laser irradiation has been described in Ref. 7. The theory shows that in the presence of ablation, the front perturbations oscillate in time with a damped amplitude. The main stabilizing mechanisms are the rocket effect and the vorticity

convection from the ablation front. Calculations[7] show that the perturbation amplitude at the beginning of the acceleration phase normalized to the initial amplitude $\eta_0(l)$ can be written as

$$\frac{\eta^s}{\eta_0(l)} \simeq \eta_v\left(\frac{2\Delta R}{c_s}\right)$$

$$+\left\{\frac{0.8c_s}{\sqrt{V_a V_{\rm bl}}}\sin\Delta_{\rm bl} - \left[0.1+\eta_v(0)\right]\cos\Delta_{\rm bl}\right\}e^{-2\Delta_a}, \qquad (2)$$

where the vorticity term $\eta_v(t)$ is defined in Ref. 7. Using Eq. (2) and taking the initial spectrum $\eta_0(l)$ from Ref. 12 (assuming surface finish of 840 Å), the mode spectrum due to a finite outer-surface finish is plotted in Fig. 81.1 (dashed line).

3. Inner-Surface Roughness (Feedout)

An additional seed of the RT instability is due to the rear-surface roughness that feeds out by the rarefaction wave generated at the first shock breakout time.[13] The shock front first reaches the perturbation valleys, generating a rarefaction wave that starts to propagate toward the ablation front with the sound speed. By the time the shock reaches the perturbation peaks, the rarefaction wave originated at the perturbation valley has moved a finite distance, distorting the rarefaction wavefront. The peaks and valleys of the rarefaction wave travel at the sound speed, keeping the ripple amplitude constant. As the rarefaction wave breaks out of the shell, the ablation front starts to accelerate. Since the rarefaction front is distorted, however, there is a delay in accelerating the ablation front at the peaks and valleys. Because of such a delay, a finite velocity perturbation imprints at the ablation front, generating a seed for the RT instability. An additional seed (perturbation acceleration field) is created by the mass difference under the perturbation valleys and peaks. According to calculations,[13] the feedout amplitude, $\eta^{\rm f.o.}$, takes the following form:

$$\frac{\eta^{\rm f.o.}}{\Delta_l} = \frac{0.06A}{l} + 0.15\sqrt{\frac{A}{l}}, \qquad (3)$$

where Δ_l is the initial rear-surface spectrum. Figure 81.1 shows mode spectrum due to feedout at the beginning of acceleration phase (thick solid line), assuming $\Delta_l \sim l^{-2}$ (Ref. 14) and initial total rms of the rear-surface modes $\sigma_r = 3\ \mu$m.

Acceleration Phase

During the shell acceleration, the pressure and density gradients at the ablation front have opposite directions, creating a condition for the RT instability. In addition, because of the spherical convergence, the inner surface is subject to the BP instability. The RT and BP instabilities amplify the perturbations seeded during the first stage of the implosion.

Since the implosion of spherical shells is intrinsically unsteady (shell density, ablation velocity, and acceleration change in time), steady-equilibrium models cannot be used to study perturbation evolution, and a model for unsteady equilibria must be developed. The full system of conservation equations, however, is too difficult to be solved analytically. One of the simplifications that make the problem analytically tractable is an idealization of the ablation front as a surface of discontinuity ["sharp-boundary model" (SBM)]. The accuracy of such a model is compromised only when the mode wavelength is shorter than the ablation-front thickness L_0. For ablators with small Froude numbers, such as CH or Be [the Froude number is defined as $V_a^2/(gL_0)$, where g is acceleration], $L_0 \simeq 0.1$ to 1 μm; hence, for modes with the largest growth factors (the most damaging modes: $80 < l < 300$), the condition $kL_0 < 1$ is satisfied during the acceleration stage (assuming the minimum shell radius is 500 μm). The density-gradient stabilization, nevertheless, can be included in simplified fashion by reducing the ablation-front acceleration by a factor $(1 + lL_m/R)^{-1}$, where L_m is the minimum density-gradient scale length and R is the shell radius. For ablation fronts with large Froude numbers, such as cryogenic DT, the unstable spectrum consists of only long-wavelength modes; thus, the SBM is valid in this case for all unstable modes. The model yields coupled differential equations describing the evolution of the outer and inner surfaces. The coefficients of these equations are functions of the ablation and the inner DT-ice interface trajectories and the ablation velocity that can be calculated using 1-D numerical simulations. To account for the nonlinear saturation, 3-D Haan's model[15] is applied after the mode amplitude reaches the saturation level $S(l) = 2R/l^2$. The accuracy of the developed RT model has been tested against 2-D *ORCHID* and FCI2[16] simulations. For the most damaging modes, the prediction of the model is in good agreement with the numerical results.

The model shows that the shell remains intact during the implosion (the integrity factor is less than unity) if the laser nonuniformities are smoothed by 2-D SSD with the laser bandwidth larger than 0.3 THz, the outer-surface finish not exceeding 0.1 μm, and the inner-surface finish $\sigma_r < 8\ \mu$m (assuming $\Delta_l \sim l^{-2}$). As shown in the next section, however,

the restriction on the minimum target gain imposes more stringent requirements for the irradiation uniformity and the surface finish.

Target Gain

As the shell accelerates inward, ablation-front perturbations grow due to the RT instability and feed through the shell approximately as $\eta_i(l) \approx \eta_a(l)\left(r_i/r_a\right)^l$, where $\eta_i(l)$ and $\eta_a(l)$ are the l– components of the inner- and ablation-surface amplitudes, respectively, and r_i and r_a are the inner- and ablation-surface radii. During the coasting and deceleration stages, the "feedthrough" grows, reducing the target compression ratio and limiting the ignition gain. To study the gain-reduction dependence on the mode spectrum, a series of 2-D *ORCHID* multimode simulations have been performed for an α = 3 cryogenic NIF target design[12] with the distorted inner DT-ice interface. The initial power spectrum is taken in the form $\sigma_l = \sigma_0 / l^\beta$ (Ref. 14), where σ_0 and β are the normalization constants. Since the spectrum of the inner-surface perturbations at the end of acceleration phase is heavily weighted toward the low mode numbers, the simulations have been performed for modes $2 < l < 50$ with the range of β and total rms 0 to 1.5 and 0.5 to 12 μm, respectively. The target gain is found to be a function of

$$\overline{\sigma} = \sqrt{0.06\,\sigma_{<10}^2 + \sigma_{\geq 10}^2},$$

where $\sigma_{<10}^2$ and $\sigma_{\geq 10}^2$ are rms nonuniformity of the modes below and higher than $l = 10$. $\overline{\sigma}$ is calculated by using the inner-surface spectrum at the end of the acceleration phase. The simulation results are summarized in Fig. 81.2, where target gain is plotted versus $\overline{\sigma}$. Next, to take into account the laser imprint and surface roughness, the model described in the **Acceleration Phase** section is applied to the $\alpha = 3$ cryogenic NIF target design using the initial conditions derived in the **Seeding of RT Instability** section. Then, using both the derived mode spectrum and the result of Fig. 81.2, the target gain is plotted in Fig. 81.3 as a function of rear-DT-ice-surface finish and the laser bandwidth, assuming the initial outer-surface rms of 840 Å. Figure 81.3 shows that the yield reduction is less than 50% with respect to 1-D calculations if the inner-surface finish does not exceed 1.5 μm and the laser nonuniformities are smoothed by 1-THz, 2-D SSD.

Summary

An analytical model has been presented to study perturbation evolution at the ablation and inner surfaces of the imploding shell. The model describes the ablative Rayleigh–Taylor and Bell–Plesset instabilities. The initial conditions for the model are determined by using existing theories of laser imprint, ablative Richtmyer–Meshkov instability, and feedout, and by performing a series of 2-D *ORCHID* simulations. The model and simulations showed that the direct-drive cryogenic $\alpha = 3$ NIF capsules remain intact during the implosion and the target gain is expected to be larger than 10 if laser nonuniformities are smoothed by 2-D SSD with the bandwidth $\Delta\nu > 0.5$ THz and inner-surface rms <1.5 μm.

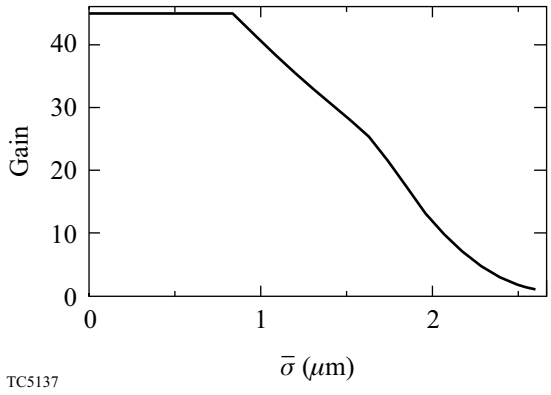

Figure 81.2
Plot of target gain G versus $\overline{\sigma}$.

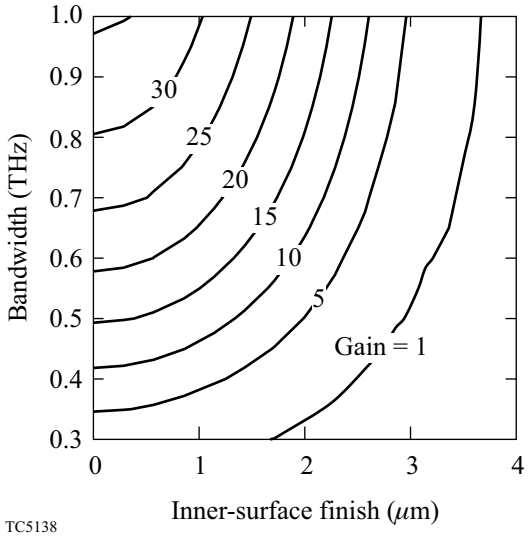

Figure 81.3
Plot of target gain versus initial rear-surface finish and laser bandwidth.

ACKNOWLEDGMENT

This work was supported by the U.S. Department of Energy Office of Inertial Confinement Fusion under Cooperative Agreement No. DE-FC03-92SF19460, the University of Rochester, and the New York State Energy Research and Development Authority. The support of DOE does not constitute an endorsement by DOE of the views expressed in this article.

REFERENCES

1. J. D. Lindl, *Inertial Confinement Fusion: The Quest for Ignition and Energy Gain Using Indirect Drive* (Springer-Verlag, New York, 1998).
2. Lord Rayleigh, in *Scientific Papers* (Cambridge University Press, Cambridge, 1900), Vol. II, p. 200.
3. M. S. Plesset, J. Appl. Phys. **25**, 96 (1954); G. I. Bell, Los Alamos National Laboratory, Report No. LA-1321 (1951).
4. R. D. Richtmyer, Commun. Pure. Appl. Math. **XIII**, 297 (1960).
5. R. L. McCrory and C. P. Verdon, in *Computer Applications in Plasma Science and Engineering*, edited by A. T. Drobot (Springer-Verlag, New York, 1991), pp. 291–325.
6. S. E. Bodner, J. Fusion Energy **1**, 221 (1981).
7. V. N. Goncharov *et al*., Phys. Rev. Lett. **82**, 2091 (1999).
8. A. R. Piriz, J. Sanz, and L. F. Ibanez, Phys. Plasmas **4**, 1117 (1997).
9. V. N. Goncharov, S. Skupsky, P. W. McKenty, R. P. J. Town, T. R. Boehly, D. D. Meyerhofer, and O. V. Gotchev, "A Model of Laser Imprinting," accepted for publication in Physics of Plasmas.
10. S. Skupsky, R. W. Short, T. Kessler, R. S. Craxton, S. Letzring, and J. M. Soures, J. Appl. Phys. **66**, 3456 (1989).
11. R. H. Lehmberg, A. J. Schmitt, and S. E. Bodner, J. Appl. Phys. **62**, 2680 (1987).
12. S. V. Weber, S. G. Glendinning, D. H. Kalantar, M. H. Key, B. A. Remington, J. E. Rothenberg, E. Wolfrum, C. P. Verdon, and J. P. Knauer, Phys. Plasmas **4**, 1978 (1997); Laboratory for Laser Energetics LLE Review **79**, 121, NTIS document No. DOE/SF/19460-317 (1999). Copies may be obtained from the National Technical Information Service, Springfield, VA 22161.
13. R. Betti, V. Lobatchev, and R. L. McCrory, Phys. Rev. Lett. **81**, 5560 (1998).
14. Laboratory for Laser Energetics LLE Review **79**, 131, NTIS document No. DOE/SF/19460-317 (1999). Copies may be obtained from the National Technical Information Service, Springfield, VA 22161.
15. S. W. Haan, Phys. Rev. A **39**, 5812 (1989).
16. E. Buresi *et al.*, Laser Part. Beams **4**, 531 (1986).

Initial Performance of the High-Pressure DT-Filling Portion of the Cryogenic Target Handling System

Cryogenic targets for the OMEGA laser are polymer shells of ~1-mm diameter and 1- to 5-μm wall thickness that require internal D_2 or DT solid layers of ~100-μm thickness. Targets containing D_2 may also be doped with gaseous He^3 to aid in diagnosing the implosion using the charged-particle spectrometer. To achieve the required inner ice layer, shells are first permeated to a pressure of ~1000 atm at room temperature and then cooled to ~25°K. A slow, controlled pressure ramp to avoid buckling of the target and a slow, controlled temperature ramp to 25°K are required to successfully fill targets. The thinnest-walled shells, which are of the greatest interest, have buckling pressures ≤0.1 atm, which imposes a requirement of considerable precision in controlling the pressure differential across the shell wall during the pressurization and cooldown. LLE has constructed a system that successfully fills thick-walled targets and demonstrates the capabilities necessary to fill thin-walled targets.

System Description

The pressurization portion of the Cryogenic Target Handling System achieves compression in two stages (as seen in Fig. 81.4): (1) by slowly heating the cryogenically concentrated D_2 or DT and (2) by using a diaphragm compressor. The process begins with valves V1, V3, and V6 open, all other valves closed, and the targets evacuated. The condensation tube (volume 12.0 cm^3) is cooled to ~10°K, and the contents (~0.3 mole) of the D_2 or DT vessel are condensed into it; then valves V4 and V5 are opened, providing a path for gas to reach the permeation cell, which contains four targets at room temperature. Next, valve V1 is closed and V2 is opened, allowing a small quantity of He^3 to flow to the targets. A pressure of ~0.03 atm of He^3 added at this point will produce a 5% concentration of He^3 in the gaseous D_2 in the center of a target at the triple point, 18.7°K. To start the first stage of compression, valve V3 is closed, and the condensation tube is slowly heated

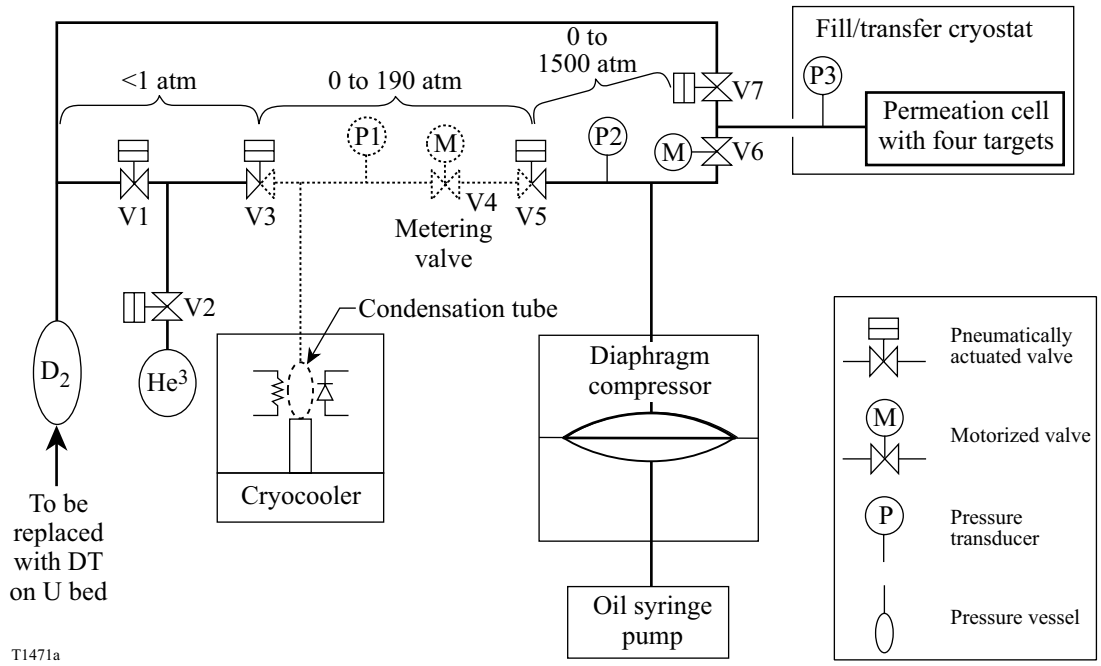

Figure 81.4
Abbreviated diagram of the pressurization portion of the system. The parts omitted include burst discs, limit switches, solenoid valves, and controllers.

until the pressure in the targets reaches ~150 atm (190 atm maximum). The second stage of compression is achieved by closing valve V5 and slowly driving the diaphragm compressor to the final pressure, typically 1000 atm (1500 atm maximum). This compressor has a flexible metal diaphragm with up to 30.9 cm^3 of gas on one side and hydraulic oil on the other. The oil is compressed by a syringe pump, which uses a piston (area = 1.60 cm^2, stroke = 24.3 cm) linked by a gear train (126 turns/cm) to a stepper motor (1000 steps per turn). Although pressure transducers are located in both stages and on the permeation cell, system control depends primarily on the transducer P2—a highly accurate ($\pm$0.14 atm) Bourdon tube—in the second stage.

After the targets have reached the maximum pressure, they are slowly cooled to <25°K before the D_2 or DT external to the targets is pumped out of the permeation cell. For thick-walled targets, the cooling is done with valve V6 closed. Cooling must be done slowly enough that the cooled portion of the pressurization system remains isothermal, avoiding temperature gradients that could produce a pressure differential across the target wall, causing the target to burst or buckle. Thin-walled targets, because they are weaker, require an alternative cooling strategy:* Valve V6 is left open, and the compression equipment is run in reverse to lower the pressure as the targets are cooled, keeping the measured external pressure very close to the calculated internal pressure. Once the targets are cooled to <25°K, the vapor pressure of D_2 or DT is <2 atm, and the gas external to the targets can be pumped out of the permeation cell without risk of bursting the targets. This pumping is done with valve V7 open; it continues (possibly for several hours) until the residual quantity of gas in the permeation cell will be manageable when the cell is unsealed and this residual gas is released into the cryostat.

*If valve V6 could be located inside the cryostat and cooled along with the permeation cell so that all portions of the pressurized volume remained isothermal, the pressures internal and external to the target would be nearly equal throughout the cooling process. (A small excess pressure would still arise internal to the target because the thermal contraction of a polymer shell exceeds that of the metal permeation cell.) Such a cryogenically compatible valve is not available. If valve V6 is closed prior to the cooldown, the small volume in the room-temperature plumbing (~0.3 cm^3, compared to 5.0 cm^3 of cooled volume) generates a pressure external to the target. This is because gas in the room-temperature portion is less dense than the cooled gas. The external pressure generated by this density difference is sufficient to cause thin-walled targets (wall thickness <5 μm) to buckle. Success in cooling thin-walled targets with valve V6 open and the compression equipment running in reverse requires accurate determination of the target temperature and calculation of the corresponding internal pressure. Since thin-walled targets are much stronger against bursting than against buckling, the best strategy is to keep the external pressure slightly below the calculated internal pressure.

The system is controlled by a programmable logic controller (PLC), which is linked to a workstation with a graphical user interface (GUI). All valves and motors in the system are controlled by the PLC, which also monitors all pressures, temperatures, and the status of limit switches. The pressurization ramp is managed by control loops that include the high-accuracy pressure transducer, the condensation tube thermometer and heater, and the motor driving the oil syringe pump. These loops are executed and maintained by "C" programs residing in the PLC. The GUI software allows the user to monitor, log, and view data from the target-fill process in real-time. It also allows modification of the fill rate and parameters of the control loops. There are several hard-wired safeguards, such as limit switches that prevent excess piston travel in the syringe pump.

All system parts that will contain ≥1 atm of DT have been provided with secondary vacuum containment, with a glovebox providing tertiary containment. This secondary containment is divided into four chambers. Helium gas at ~0.5 atm will be circulated through three of these chambers with a circulation pump, while the fourth chamber is kept evacuated to insulate the condensation tube. The divisions of the secondary containment system are shown in Fig. 81.5. A modified ion gauge will detect tritium leakage with a resolution of ~10 mCi/m^3 at 1 atm and ~150 mCi/m^3 at <1 Torr. If a low-level tritium leak is detected, the tritium-contaminated helium will be pumped to the tritium recovery system, evacuating the contaminated chamber. High-level leakage will be routed with the circulation pump to a local uranium bed, which will absorb the DT. Volumes in the secondary containment chambers are sufficient to contain the entire DT inventory of 0.34 mole (10^4 Ci) below 1 atm at room temperature.

Target Filling

Four targets are filled simultaneously. Each target is supported by three submicron strands of spider silk[1] as shown in Fig. 81.6. The spider silk is stretched across a beryllium wire frame, which is formed into a shape that avoids the OMEGA laser beams, and coated with a uniform, conformal layer of 0.1 μm of parylene, which fastens the silk to the shell. The Be frame is attached to a boron fiber, which is in turn attached to an Al base. This mounting method is highly robust at cryogenic temperatures. The four targets are placed in a contoured copper holder, as shown in Fig. 81.6. The copper holder acts to improve the temperature uniformity inside the permeation cell and also provides a space filler to minimize the volume. With this holder inside the sealed permeation cell, the cooled volume is 5.0 cm^3. Reducing the gap between the copper holder and the

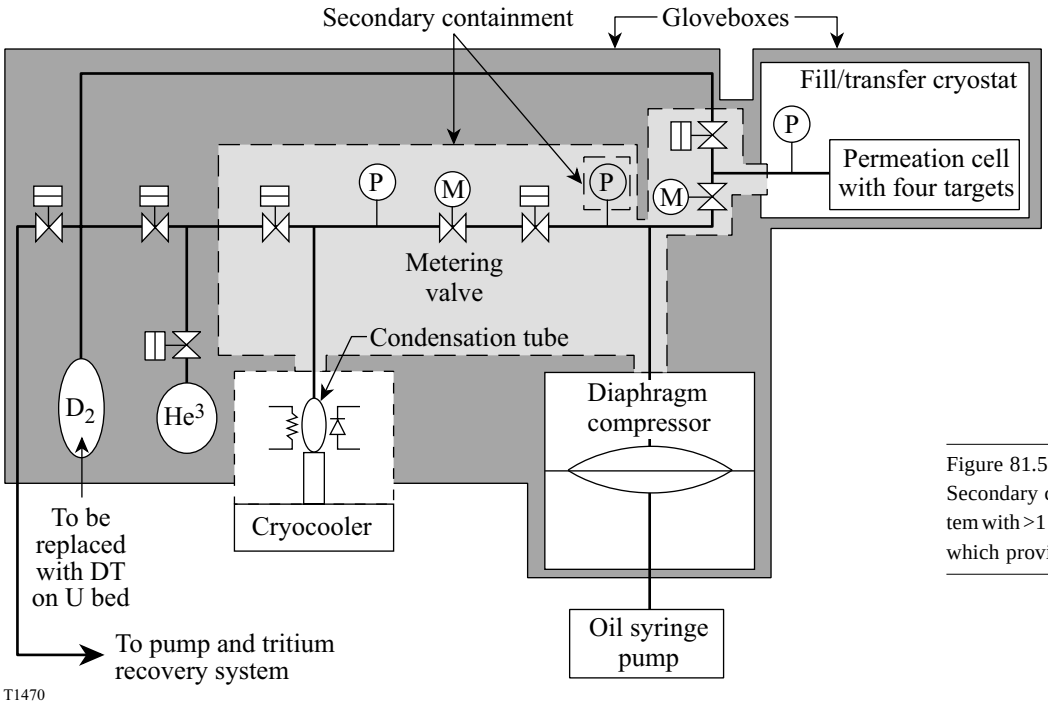

Figure 81.5
Secondary containment for all parts of the system with >1 atm of DT, and the outer gloveboxes, which provide tertiary containment.

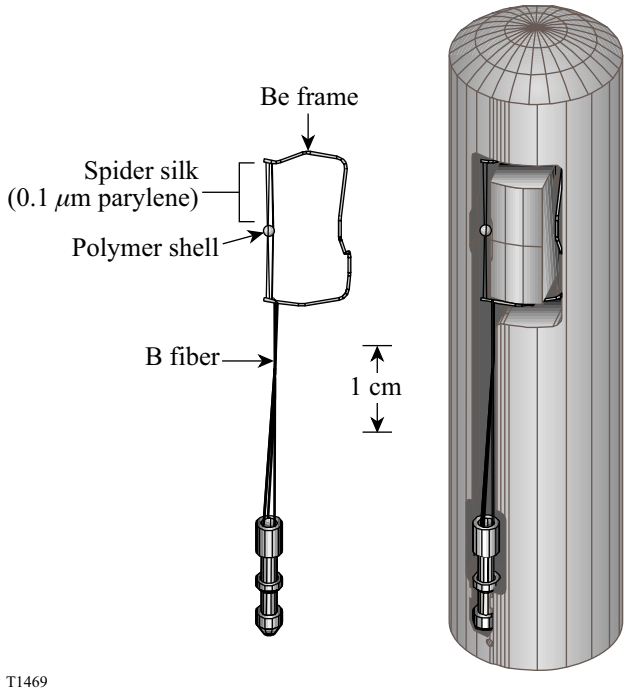

Figure 81.6
Cryogenic target supported with spider silk, and a holder for four targets (only one of the four cavities is shown); also see p. 21, Fig. 81.21, this issue.

target support elements could reduce this volume, which would reduce the percentage of the DT inventory required to fill a set of targets (currently 82%). The tighter tolerances, however, would increase the difficulty of removing targets for transport, and a higher target attrition rate might be expected.

Filling thin-walled targets will take from 8 to 60 h, depending on the specifications of the targets. To fill them as quickly as possible, the pressure is increased at a uniform rate such that the external pressure exceeds the internal pressure by an amount ΔP, which is less than the buckling pressure:[2]

$$\Delta P < \frac{8E}{\left[3\left(1-\mu^2\right)\right]^{1/2}}\left(\frac{w}{D}\right)^2, \qquad (1)$$

where w = wall thickness, D = diameter, E = Young's modulus, and μ = Poisson's ratio. For plasma polymer shells,[3] this formula was confirmed experimentally at LLE by pressurizing shells of various wall thicknesses in the 1- to 10-μm range and measuring their buckling pressures. To compare the data to Eq. (1), the value of E used was 2.1 GPa, obtained by measuring the expansion of several plasma polymer shells due to internal pressure. The value of μ used was 0.35 (the value for polystyrene, a glassy polymer with somewhat similar properties to plasma polymer). The permeation time constant for an ideal gas is given by

$$\tau = \frac{wD}{6pRT}, \tag{2}$$

where p = permeability, R = gas constant, and T = absolute temperature. Since D_2 at high pressure is less dense than an ideal gas (62% of the ideal gas density for 1000 atm at 294°K), a larger time constant is expected at high pressure, suggesting that a cautious rate of pressure rise should be used. For a uniform rate of pressure rise, the pressure differential across the shell wall is proportional to the permeation time constant after a time $t >> \tau$:

$$\Delta P = \tau \frac{dP}{dt}. \tag{3}$$

Combining Eqs. (1), (2), and (3), the maximum pressurization rate is proportional to wall thickness/(diameter)^3:

$$\frac{dP}{dt} = \frac{\Delta P}{\tau} < \frac{48EpRT}{\left[3\left(1-\mu^2\right)\right]^{1/2}} \frac{w}{D^3}. \tag{4}$$

For a plasma polymer shell with $w = 1$ μm and $D = 1$ mm, the buckling pressure is 0.1 atm, $\tau = 10$ s, and filling to 1000 atm at room temperature requires more than 30 h. The filling time may be reduced by filling at an elevated temperature.

System Performance

Several thick-walled targets have survived filling with D_2 to a pressure of 1000 atm. In the first test, two mounted targets with 1-mm diameter and wall thicknesses of 10 μm and 20 μm were filled to 1000 atm over an 8-h period, left under pressure for 3 days, and then depressurized over an 8-h period. After removing the targets from the permeation cell, microscopic examination indicated no damage to the targets or the mounts. In the second test a similar pair of plasma polymer targets along with a polyimide target were pressurized and then slowly cooled to 20°K. The permeation cell was then unsealed, and the targets were viewed at 20°K through a fiber-optic borescope. The targets were seen to be intact. One of the targets was picked up with the robot arm and deposited on the tip of the moving cryostat, where the target was warmed. A sudden spike in pressure of the expected magnitude indicated that it had exploded, as expected, and that it had retained all the D_2 from the filling process.

The performance of the two compression stages is studied by comparing experimental data to the D_2 equation of state. This comparison requires knowledge of the volume of each part of the system. The volume of each part is determined by connecting to a known volume and observing the pressure change when gas flows to or from the volume being measured. A 24-term equation developed by NIST[4] gives pressure as a function of density for D_2 above the critical point (38.3°K), using terms up to the seventh power of density and sixth power of temperature. At temperatures below the critical point, saturated vapor pressures[5] are used. It is difficult to predict pressure and density accurately in the region of the critical point (and down to the point where the liquid phase begins), and it is planned to rely on data taken with the pressurization apparatus itself.

Performance of the condensation tube for pressure generation is shown in Fig. 81.7. The data are taken by condensing 0.123 moles of D_2 (determined by measuring the change in pressure in the D_2 supply reservoir and converting to moles with the equation of state), and then raising the temperature of the condensation tube slowly enough to assure isothermal conditions in the tube (the tube, made of stainless steel, is in good contact on all sides with copper of high thermal conductivity). The 0.123 moles are distributed between the 12.0-cm^3 cooled volume and the 5.32-cm^3 volume (tubing, burst disc, and valves) at room temperature. A good match is obtained between measured data points and the expected pressure, calculated with the NIST equation of state.

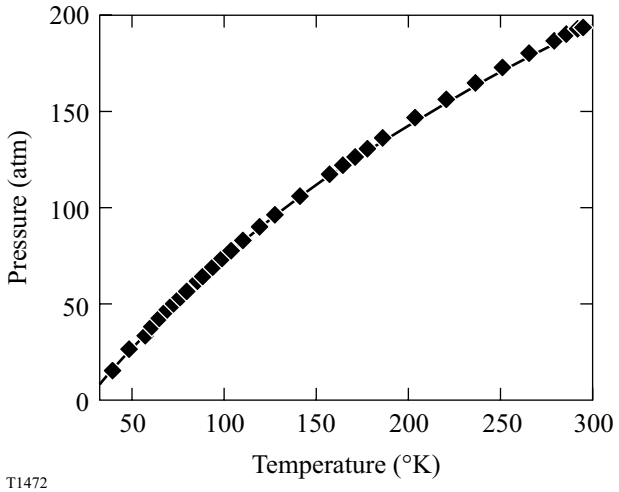

Figure 81.7
The pressure in the condensation tube (measured points) is accurately characterized by the D_2 equation of state above 38°K (used to compute the solid line).

Analyzing the performance of the diaphragm compressor requires knowledge of the oil compressibility. The manufacturer of the compressor[6] supplies compressibility data for the oil,[7] which are fit by the equation

$$C(P) = b_1\left(P/1\text{ atm}\right) - b_2\left(P/1\text{ atm}\right)^2, \tag{5}$$

where $b_1 = 5.30 \times 10^{-5}$, $b_2 = 6.4 \times 10^{-9}$, and $C(P)$ is defined as the fractional reduction in oil volume from its uncompressed value at pressure P. The expected pressure is obtained by first computing the D_2 molar density,

$$\rho = \frac{M}{V_0 - \left[A \cdot z - V_{\text{oil}} \cdot C(P)\right]}, \tag{6}$$

where M is the number of moles, V_0 is the initial volume, A is the area of the piston, z is the distance of piston travel, and V_{oil} is the uncompressed volume of oil. The pressure values entered in this equation are obtained by expressing the experimentally measured pressure data as a continuous function of z. The NIST equation of state is then used to convert density to pressure. Figure 81.8 shows good agreement between measured and calculated pressure. The fitting parameter adjusted to obtain agreement between measured and calculated pressures is $V_{\text{oil}} = 113.5\text{ cm}^3$, which cannot easily be measured. In addition, $b_2 = 4.2 \times 10^{-9}$ provided a much better fit at high pressures than the manufacturer's data. For this analysis, it has been assumed that the oil pressure and gas pressure are the same, and that the extra component of oil pressure required to deform the diaphragm is negligible.

To pressurize targets, a temperature versus time profile is calculated for the condensation tube, using vapor pressure data, and the equation of state. This calculated profile is used to program a temperature controller, which uses a PID loop to control the temperature. An example of a successful temperature profile and the resulting uniform rate of pressure rise is shown in Fig. 81.9. The difference in pressure between the first and second stages is due to the metering valve, fully open in this case. The ramp that was obtained would be suitable for a shell with a 3-μm-thick wall and a 1-mm diameter, but the method should work equally well to generate a pressure ramp suitable for a shell with a 1-μm wall. Hidden in these data are small departures from a constant rate of pressure rise, which should be correctable by adjusting the temperature profile with measured data near the critical point. This procedure's success in generating a constant rate of pressure rise offers an opportunity to eliminate the metering valve. There is strong incentive to eliminate this valve because of stem-seal leakage. Leakage through this valve stem was detected by pressurizing the system with He and was not eliminated by replacing the O-ring. The stem is sealed by a single O-ring, which appears not to be sufficiently constrained. Even if constraints on the O-ring were improved, leakage would be expected when the valve stem is moved.

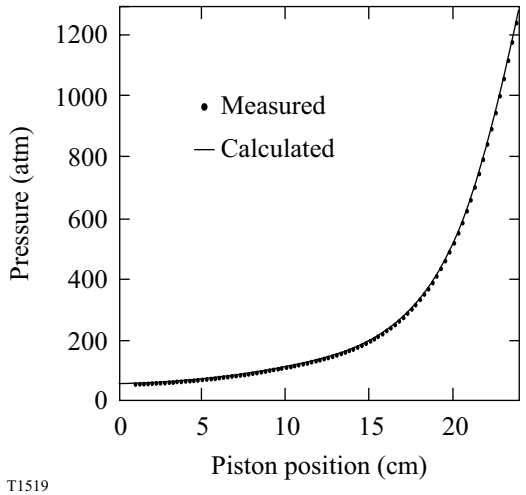

Figure 81.8
Pressure versus piston position is accurately characterized by the D_2 equation of state and oil compressibility data. Error bars for the measured points are too small to see. The maximum difference between measured and computed pressures is 8 atm for the whole data set, 2 atm at pressures <500 atm, and 0.1 atm at pressures <160 atm.

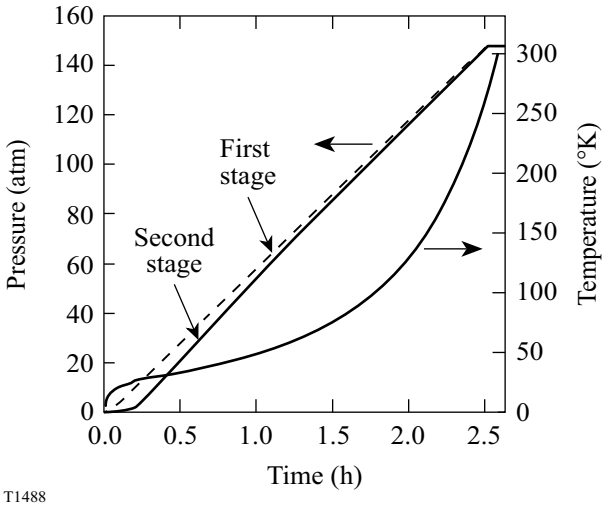

Figure 81.9
A uniform rate of pressure rise is produced by applying a calculated temperature profile to the condensation tube.

To generate the high-pressure portion of the pressure ramp, a valve is closed to isolate the diaphragm compressor from the condensation tube. The piston of the syringe pump is then given an initial velocity, and a simple algorithm is applied to the resulting rate of pressure rise to adjust the piston velocity to match the desired rate of pressure rise. The result is shown in Fig. 81.10, which shows a pressure ramp suitable for a shell with a 5-μm wall thickness. Upon magnification of the pressure versus time data in Fig. 81.10, the pressure is found to be increasing smoothly at all times, with small variations in slope due to the control algorithm. No obstacle is found to the use of a much slower rate of pressure rise, which would be suitable for filling shells with 1-μm wall thickness.

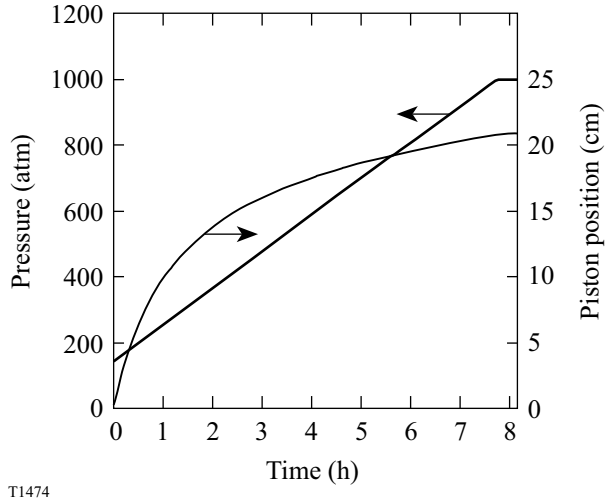

Figure 81.10
A constant rate of pressure rise is produced by controlling the piston position with a simple algorithm.

The pressurization system has proven robust, with all indications that it will be able to fill shells with the thinnest walls. Three additional observations contribute to this conclusion. The smallest motion increment of the motor driving the oil syringe pump corresponds to 0.002 atm at a pressure of 1000 atm, and less at lower pressures, much less than the 0.1-atm buckling pressure of shells with 1-μm wall thickness. When the motor direction is reversed, as will be necessary when cooling thin-walled shells, there is one turn of backlash in the mechanical system, but no observable pressure drop that could threaten shell survival. Finally, it appears that the low rate of temperature rise required for the condensation tube (~0.1°K/min at 40°K) is achievable by applying a slowly increasing power level ~12 W. To demonstrate the capacity to fill thin-walled shells, a series of increasingly slower pressure ramps will be used to fill successively thinner walled shells, followed by depressurization ramps and examination of the shells. The final and most difficult step will be to again fill such targets and reduce the external pressure while cooling the targets by running the pressurization apparatus in reverse.

ACKNOWLEDGMENT

The pressurization portion of the CTHS is based on a conceptual design by General Atomics. The use of spider silk to support targets was pioneered by S. G. Noyes of LLE, who also developed the present attachment method. This work was supported by the U.S. Department of Energy Office of Inertial Confinement Fusion under Cooperative Agreement No. DE-FC03-92SF19460, the University of Rochester, and the New York State Energy Research and Development Authority. The support of DOE does not constitute an endorsement by DOE of the views expressed in this article.

REFERENCES

1. B. A. Brinker, J. M. Cavese, J. R. Miller, S. G. Noyes, S. Sheble, and L. T. Whitaker, J. Vac. Sci. Technol. A **1**, 941 (1983).

2. W. C. Young, in *Roark's Formulas for Stress & Strain*, 6th ed. (McGraw-Hill, New York, 1989), p. 691.

3. S. A. Letts, D. W. Myers, and L. A. Witt, J. Vac. Sci. Technol. **19**, 739 (1981); S. A. Letts *et al.*, Fusion Technol. **28**, 1797 (1995); B. W. McQuillan *et al.*, Fusion Technol. **31**, 381 (1997).

4. R. Prydz, K. D. Timmerhaus, and R. B. Stewart, in *Advances in Cryogenic Engineering*, edited by K. D. Timmerhaus (Plenum Press, New York, 1968), Vol. 13, pp. 384–396.

5. P. C. Souers, *Hydrogen Properties for Fusion Energy* (University of California Press, Berkeley, 1986), p. 52.

6. Fluitron, Inc., Ivyland, PA.

7. This type of oil is "Tellus 10" made by Shell Oil Company, Houston, TX.

Modeling the Temperature and Ice-Thickness Profiles Within OMEGA Cryogenic Targets

Introduction

Cryogenic targets for direct-drive experiments on OMEGA require a 100-μm-thick layer of solid hydrogen isotopes (DT or D_2) uniformly distributed around the inside of a thin-walled (1 μm), 1-mm-diam polymer capsule. This uniformity is achieved by maintaining the capsule in a uniform and stable thermal environment where the inner and outer ice surfaces are each positioned along a single isotherm. The hydrogen fuel is layered[1–3] in the following sequence: the capsule is permeation-filled with gaseous DT or D_2; the gas is cooled to the liquid phase, then gradually cooled through the triple point; polycrystalline DT or D_2 solid expands from a single nucleation site. Heat provided during cooling through the triple point is needed to sublime the hydrogen ice from regions where the ice is thickest and redeposit it where ice is thinnest to form a uniformly thick layer. For solid DT this energy is provided by the radioactive decay of a triton atom, which produces an electron with a mean energy of 4.6 keV and provides 12 μW of uniform bulk heating in an OMEGA target. D_2 layers require an external source of heat, which is provided by an IR light source operating at the strongest vibrational–rotational absorption frequency of the D_2 lattice (3.2 cm^{-1}).

The allowed deviation of the inner ice layer from a completely smooth symmetrical geometry is less than 1-μm rms for all spherical Legendre modes $\ell < 50$.[4] This demanding specification requires a diagnostic technique that is capable of measuring how accurately the capsule is positioned along the isotherms within the layering sphere. The only available technique with the requisite sensitivity is the interferometric technique used to measure the smoothness of the ice layer.[5] The uniformity and smoothness of the ice are the best measures of the thermal environment in the layering sphere. Since the interferometric technique is also in development, additional information is needed to understand the thermal environment present in the layering sphere to allow us to iterate the layering and characterizing development process. This information can be obtained only by numerical simulation and is needed to define the initial layering conditions. As experimental data becomes available, the theoretical model can be refined.

This work is an initial endeavor to develop a numerical model of the thermal conditions of a cryogenic target inside the layering sphere. The layering sphere is a spherical cavity containing two sets of orthogonal windows for viewing and a hole for inserting and removing the target. The temperature gradients within the ice are calculated for specific conditions and nonuniformities inside the layering sphere. This allows the pressure inside the capsule and the ice thickness to be calculated from the measurable temperature on the layering sphere. The numerical simulations are validated against analytic solutions where possible. The sensitivity of the ice layer's uniformity to the effects of three principal nonuniformities are calculated: (1) misalignment of the capsule from the center of the layering sphere; (2) variability in the uniformity of the capsule wall thickness; and (3) temperature gradients on the internal surface of the layering sphere. Knowing the magnitude of these effects will guide our target fabrication and cryo-engineering research priorities.

A commercially available computational fluid dynamics (CFD) code *FLUENT*[6] is used to model the cryogenic target in the layering sphere. This code employs an advanced variable-size mesh generation mechanism that provides maximum computational resolution where it is most needed. *FLUENT* also possesses two properties that are required for more sophisticated modeling: (1) it allows mass transport to be calculated concurrently with thermal calculations, and (2) it has the provision to model condensation, an integral component of the layering process.

Two-dimensional (2-D) axisymmetric models of the environment, which included the layering sphere, exchange gas, target capsule, and DT-ice layer, were used for the calculations. The models were created with *GAMBIT* (Fluent, Inc.) geometry/mesh generation software, the companion program to *FLUENT*. For these initial calculations, the target mount, layering sphere windows, and target-extraction hole were not included in the models. The geometry of the environment, along with the meshing scheme, is shown in Figs. 81.11 and 81.12. A finer mesh was used in the ice and capsule, where

greater temperature resolution was required, while a gradually coarser mesh was used in the exchange gas extending to the layering sphere's inside surface. The cell size in the ice was 10×10 μm^2, and the complete environment totaled over 15,000 cells.

The layering sphere had an inside diameter of 25.4 mm. The capsule, which was centered in the layering sphere (unless decentered for modeling purposes), had an outside diameter of 950 μm and a wall thickness of 2 μm. The DT ice was a 100-μm-thick layer on the inside of the capsule. The geometry was considered symmetric about the vertical axis; therefore, only half the overall geometry was modeled. A 50-mTorr helium exchange gas was placed in the layering sphere to allow heat conduction between the target and the layering sphere.

With this model the dimensions (thickness) of the capsule and ice could be readily changed, simulating capsule non-uniformities and DT layering, respectively. Also, the target's position within the layering sphere could be changed easily. This flexibility allowed many situations to be modeled, and the steady-state ice-thickness profile was calculated iteratively.

The temperature-dependent properties of the materials in the model were used at 18.5 to 20 K whenever possible. The properties of the capsule material—polyimide (Kapton)—were taken from literature and product specifications supplied from DuPont. These are listed in Table 81.I.

To first order, a uniform and stable thermal environment will produce a uniform hydrogen fuel layer if a perfectly spherical capsule with a uniformly thick wall is positioned at the center of an isothermal layering sphere. In actual operation, deviations from ideality exist, which will affect the uniformity of the ice. The following three models were generated to calculate the magnitude of these deviations from ideality on the steady-state temperature and ice-thickness profiles.

Case 1: Misalignment of the Target from the Center of the Layering Sphere.

The target can be moved within the layering sphere using a four-axis motion controller (x, y, z, θ) with an absolute encoder defining its position. The primary goal is to make fine adjustments to position the target at the center of the target chamber for the implosion. Generically, it is known that centering the

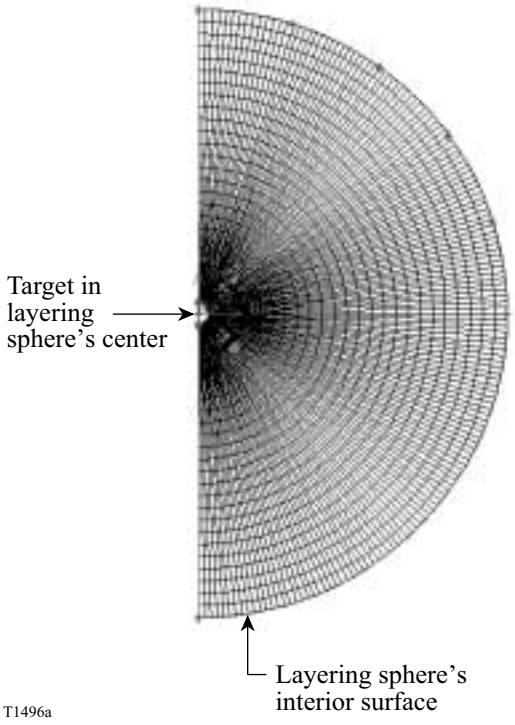

Figure 81.11
Axisymmetric 2-D geometry/mesh of the target capsule, DT ice, helium exchange gas, and layering sphere's interior surface used in the CFD simulation. The inside diameter of the layering sphere is 25.4 mm, and the outside diameter of the capsule is 950 μm.

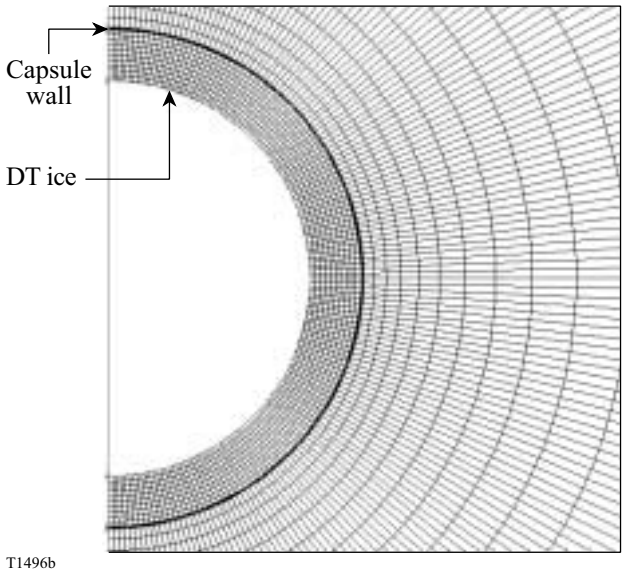

Figure 81.12
Close-up view of the geometry/mesh of the capsule and DT ice used in the CFD simulation. The DT ice is 100 μm thick, and the capsule is 2 μm thick.

Table 81.I: Properties of the materials used in the CFD simulation.

	Solid DT[7]	Polyimide (Kapton)[8,9]	Helium at 50 mTorr[10]
Thermal conductivity k (W/m K)	0.35	0.05	0.0227
Heat capacity C_p (J/kg K)	2720	130	5600
Density ρ (kg/m^3)	257.6	1500	0.0002
Heat-generation rate Q (W/m^3)	51000	0	0

uniform target in the layering sphere is critical to achieve a uniform ice layer; however, the sensitivity of the target's position in the uniformity layering sphere to the ice is not known. When the center of the target does not coincide with the center of the layering sphere, the side of the capsule farthest from the layering sphere's surface will be warmer than the side closest to the layering sphere. (The cooler walls of the layering sphere act as a heat sink for the heat-generating target.) This results in a nonisothermal inner-ice-surface temperature and a consequent thinning of the ice from the warmer side. At steady-state conditions an ice-thickness nonuniformity is created.

Case 2: Capsule-Wall-Thickness Nonuniformities.

Direct-drive target capsules have been produced with a high degree of uniformity in dimension and thickness.[11] The current method of measuring the variability in the wall thickness is white-light interferometry and has an accuracy of one interferometric fringe ~0.3 μm. This case studies the effect of a capsule nonuniformity, which is too small to be measured, on the ice thickness. (If it is found to be significant, a more accurate method will have to be used to select quality capsules.) These nonuniformities in the capsule wall can lead to thermal gradients in the ice as thinner areas in the wall offer less thermal resistance to heat loss to the exchange gas than do thick ones. As research continues on engineering precise uniform capsules, the effects that nonuniformly thick capsules have on cryogenic layers must be calculated.

Case 3: Temperature Gradients on the Inner Surface of the Layering Sphere.

During calculations for Cases 1 and 2, it was assumed that the layering sphere was isothermal; that premise will be investigated here. In this case, the effects that a temperature nonuniformity over 12% of the layering sphere's inner surface will produce in the target at the center of the layering sphere were calculated. The source of the heat load could be (1) a localized, small thermal short to an adjacent shroud along an instrumentation sensor or the optical fiber used for IR layering and/or (2) heating on the windows during IR layering and target viewing, and from external radiation. Depending on the magnitude of the temperature nonuniformity, polar and azimuthal temperature gradients may develop in the ice. The effects of these heat sources must be identified by calculations so they can be minimized by engineering.

The most obvious initial concern—heating caused by room-temperature radiation—is not expected to be a significant contributing factor: radiation will be absorbed in the windows (BK glass) of the first stage of the cryocooler, which are at 45 K. Less than 0.4% of the light is transmitted by these 1-mm-thick glass windows. (Re-radiation from these windows at 45 K through the layering sphere's sapphire windows was calculated to heat the target by less than 20 nW, which is negligible.)

The Target Viewing System (TVS) is used to illuminate and view the target when it is positioned in the center of the target chamber. Absorption of this radiation in the sapphire windows is a contributor to a nonuniform layering-sphere temperature. The source is filtered to 532 nm with a bandwidth of 40 nm, and the heat load is localized around the windows. Because of the excellent thermal conductivity of the copper layering sphere, that area is expected to have a temperature nonuniformity of the order of 1 mK. (If the illumination source is unfiltered, the heat absorbed in the sapphire window is ~40 mW.)

A nonisothermal layering-sphere surface will transmit its effects into the surrounding helium exchange gas, which will produce an uneven heat load on the capsule. The nonuniform capsule environment will result in a shift in the target isotherms to create a nonuniform cryogenic-fuel layer.

Solution Procedure

Separate models were developed to determine the sensitivity of the smoothness of the DT ice to deviations from ideal boundary conditions that may be expected in actual operations. This was done to identify those parameters that most affected

the layer's smoothness. Only heat transfer via conduction was modeled: the pressure of the helium exchange gas (50 mTorr) is too low for convection to contribute to heat flow, and the small temperature gradients between the capsule and the layering sphere preclude a significant radiation effect. (A more complicated refinement to be added later will incorporate mass transfer and the presence of helium inside the capsule into the model. This will allow the dynamics and time dependency of the layering process to be determined. These capabilities will be needed to complement the experimental observations.)

An iterative procedure was used to calculate the final ice profile. Initially, the ice was defined as a uniformly thick layer inside the capsule to calculate the heat generation and the temperature gradient over the ice thickness. Next, a new boundary condition was established to introduce a perturbation of interest, and the resultant temperature profile in the ice was calculated. The ice's void was offset, with the void remaining spherical, to alter the ice thickness and to simulate the layering process. (The solid, which has a temperature-dependent vapor pressure, sublimes and diffuses from the warmer surfaces to the colder surfaces, where it condenses). The simulation was repeated with the adjusted ice geometry, and new temperature profiles were calculated. The process was repeated until the temperature difference on the internal surface of the ice was minimized. At this approximately uniform ice temperature the net transfer of DT would be approximately zero. This convergent configuration was the best approximation of the steady-state ice profile that can be achieved with a spherical void for the prescribed boundary condition.

Results and Discussion

1. Analytical Solutions

An initial, idealized model was created to determine the temperature profile of a uniform spherical ice layer. This model was used for two reasons: (1) to determine the thermal parameter space expected inside the target layering sphere, and (2) to compare the numerical solution to the analytical result to ensure the model was functioning correctly. The model consisted of a uniform 100-μm DT-ice layer inside a 2-μm-thick polyimide capsule with the temperature of the outer layer of the ice constant at 19.5 K (the defined boundary condition). The DT was self-heated with a volumetric heating rate of 51,000 W/m^3 (about 12 μW per target). The numerical simulation calculated the steady-state inner ice temperature to be 19.50065 K. Thus, a radial temperature difference of 650 μK existed between the inner and outer ice surfaces. The temperature profile is shown in Fig. 81.13. This result compared well with the following analytical result.

The steady-state governing equation[12] of a spherical shell with heat generation is

$$\frac{1}{r}\frac{d^2}{dr^2}(rT)+\frac{Q}{k}=0, \tag{1}$$

where r is the radius, T is the temperature, Q is the heat generation, and k is the thermal conductivity. The boundary conditions are (1) the inner surface, $r = R_i$, is at T_i and the outer surface, $r = R_o$ is at T_o; (2) no heat transfers from the solid to the gas (assuming negligible thermal conductivity and heat generation in the gas). The solution is given by

$$T_i - T_o = \frac{1}{6}\frac{Q}{k}\left[R_o^2 - R_i^2 - 2R_i^3\left(\frac{1}{R_i}-\frac{1}{R_o}\right)\right]. \tag{2}$$

This calculation assumes spherical symmetry, i.e., uniform ice thickness and heat transfer solely in the radial direction. Using the dimensions of the ice, $R_o = 473$ μm and $R_i = 373$ μm, and the thermal conductivity k = 0.35 W/m K, the temperature difference between the inner and outer surfaces ($T_i - T_o$) was 630 μK. This result agrees within 3% of the numerical solution, validating the mesh resolution and sensitivity of the numerical approach.

A second model was created to determine the temperature profiles from pole to pole along the outside surface of a nonuniformly thick DT-ice layer. If the ice is uniform, there is no pole-to-pole temperature difference because the heat load is

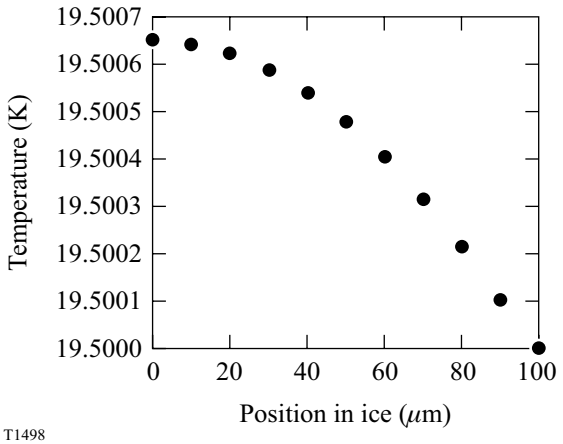

Figure 81.13
Radial temperature profile of a uniformly 100-μm-thick DT-ice layer inside an OMEGA cryo target. The outside ice surface was fixed at 19.5 K. The volumetric heating rate of DT was 51,000 W/m^3.

symmetric. When thickness variations exist, heat can flow in the tangential direction, leading to a nonisothermal inner ice surface. To model nonuniformities, a 100-μm-thick ice layer was constructed with a 2.0-μm $\ell = 1$ nonuniformity. The model with dimensions is shown in Fig. 81.14. The isothermal boundary condition on the inner surface of the ice was 19.5 K, with all other thermal and material properties of DT the same as the previous model. The CFD simulation predicted a temperature difference ($\Delta T_o = 12$ μK) along the outer surface of the ice.

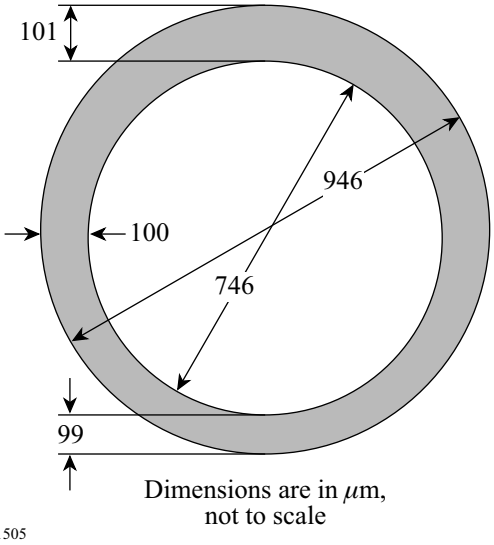

Figure 81.14
A nominal 100-μm-thick ice layer with 2-μm $\ell = 1$ nonuniformity used in the CFD simulation to determine the pole-to-pole temperature difference in nonuniformly thick DT ice.

For the analytical solution, Eq. (2) was rearranged and two calculations were performed. Each calculation gave the temperature of the outer ice surface for a given thickness. The equations were solved by using the inner-surface boundary condition:

$$T_i = \frac{1}{6}\frac{Q}{k}\left[R_o^2 - R_{i1}^2 - 2R_{i1}^3\left(\frac{1}{R_{i1}} - \frac{1}{R_o}\right)\right] + T_{o1}$$

$$= \frac{1}{6}\frac{Q}{k}\left[R_o^2 - R_{i2}^2 - 2R_{i2}^3\left(\frac{1}{R_{i2}} - \frac{1}{R_o}\right)\right] + T_{o2}\,, \qquad (3)$$

where the indices "1" and "2" on the radii and temperatures indicate two different locations. By solving the equations with real radii and properties (shown in Fig. 81.14) and allowing the indices 1 and 2 to refer to the north and south poles, respectively, the temperature difference along the outer ice surface ($\Delta T_o = T_{o1} - T_{o2}$) was 14 μK. This result agrees within 17% of the numerical solution above.

2. Numerical Simulations

The two models above determined the thermal parameter space and compared well with the analytical solutions. The next task was to calculate the effects of realistic perturbations to the system on the DT-ice temperature and thickness profiles. For these more complicated situations, no simple analytical solution existed against which to compare; instead, the numerical models were used to predict the profiles.

Case 1: Misalignment of the target from the center of the layering sphere.

In this model the target was shifted from the center of the layering sphere as shown in Fig. 81.15. The figure depicts the centers of the target and layering sphere offset by 1 mm, about one target diameter. The interior surface of the layering sphere is isothermal at 19.2 K (the prescribed boundary condition). The capsule and DT ice were initially uniform 2 μm and 100 μm thick, respectively. The calculated temperature profiles in the DT ice and vapor space prior to layering are shown in Fig. 81.16. Since the bottom of the target was farthest away from the colder layering sphere, it had the relatively warmer inner ice surface. The pole-to-pole temperature difference along the inner ice surface caused by the target misalignment of 1 mm was 85.5 μK.

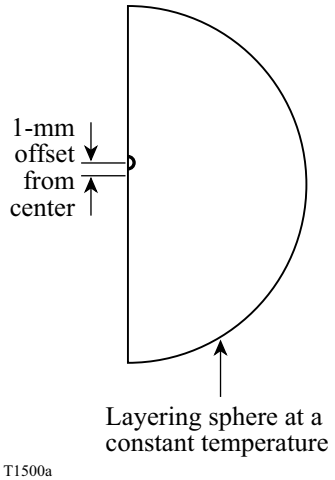

Figure 81.15
Axisymmetric model of a target offset from the center of the layering sphere.

The next step of the simulation was to determine the expected shift in ice thickness caused by the temperature difference on the inner surface. Since the bottom part of the target was warmer, the temperature-dependent vapor pressure of DT above the ice was greater than where the ice was colder. The resulting pressure gradient would create a net mass transfer of DT to the colder, upper half of the target where it condenses on the ice surface. This reduces the ice thickness at the bottom of the capsule and increases it at the top. The semi-circle that represented the inner ice surface was shifted downward to represent the thinning of the lower layer and thickening of the upper layer of DT. Following the iterative solution procedure described previously, the ice's void was manually varied to simulate layering, and the simulation was repeated until the pole-to-pole temperature difference along the ice surface was approximately zero. This occurred when the total ice $\ell = 1$ nonuniformity was 1.1 μm. (The ice thicknesses at the north and south poles were 100.55 μm and 99.45 μm, respectively.)

The simulation was repeated for different values of the misalignment of the target from the layering sphere's center. The inner ice pole-to-pole temperature differences before redistribution caused by different target offsets are listed in Table 81.II. The corresponding $\ell = 1$ nonuniformities in the DT layer resulting from the offsets are displayed in Fig. 81.17. Using the $\ell = 1$ mode for these analyses is a reasonable compromise as it is the dominant contribution to the total rms roughness[4] and makes the calculation tractable. Clearly, in actual operation the change in ice thickness would be observed in additional modes of the power spectrum ($\ell > 1$); however, at present, modeling these additional modes is beyond the scope of this article.

Case 2: Capsule $\ell = 1$ nonuniformities.

The capsule itself can produce temperature nonuniformities in the ice if the wall is not uniformly thick because the capsule's thermal conductivity is much less than that of the ice. The effects of these small perturbations required an adaption to the model. To model the sensitivity of nonuniformities of the order of tenths of microns, the scale of the area under investigation was reduced to include only the target capsule and the DT ice and vapor space. This removed the exchange gas and layering sphere from the calculations. Instead, an isothermal boundary condition on the outer capsule surface at a temperature of 19.5 K was used in all simulations.

Table 81.II: Pole-to-pole temperature difference on the inner DT-ice layer before redistribution for various offsets of the target from the center of the layering sphere.

Offset from center (μm)	Temperature difference in ice (μK)
0	0.0
500	–52.0
1000	–85.5
1500	–190.0

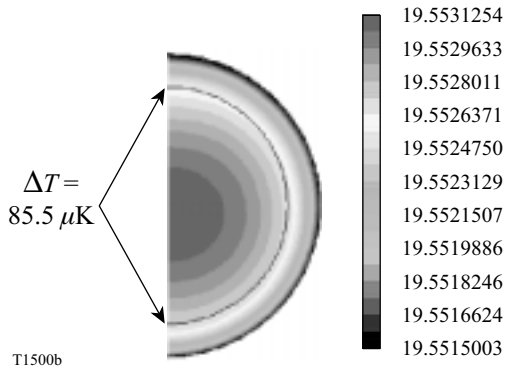

Figure 81.16
Temperature profiles in the DT ice and vapor space for a target offset from the center of the layering sphere by 1 mm. The pole-to-pole temperature difference on the inner ice surface was 85.5 μK.

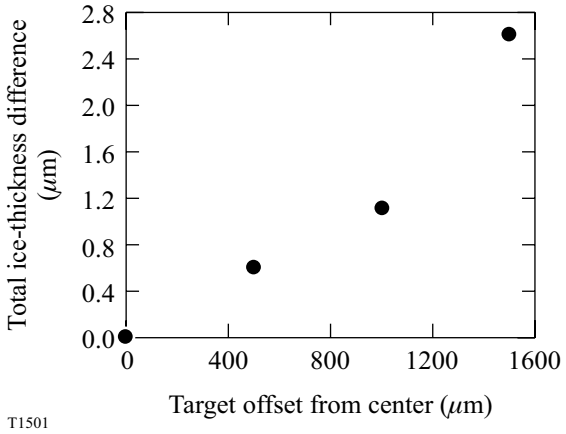

Figure 81.17
Total ice $\ell = 1$ nonuniformity in a nominal 100-μm-thick ice layer for various offsets of the target from the center of the layering sphere.

An example case is shown in Figs. 81.18–81.20. The capsule (nominal thickness 2 μm) was modeled to be nonuniform by shifting the semicircle representing the outer shell surface upward by 0.15 μm to create a total $\ell = 1$ nonuniformity of 0.3 μm. A uniform 100-μm DT-ice layer was placed inside the nonuniform capsule; the complete geometry is shown in Fig. 81.18. Since there was a greater thermal resistance at the north pole than the south pole due to the thicker capsule wall, the ice was relatively warmer at the north pole. The calculated pole-to-pole temperature variation (~25 μK) along the inner ice surface is shown in Fig. 81.19. Using the iterative solution procedure, the ice thickness was shifted to simulate layering (by moving the ice's free surface) until the temperature gradient between the poles reached zero. This result is shown in Fig. 81.20, where a total 1.86-μm ice $\ell = 1$ nonuniformity was calculated. (The ice thicknesses at the north and south poles were 99.07 μm and 100.93 μm, respectively.) The results of simulation recreating other capsule $\ell = 1$ nonuniformities are listed in Table 81.III.

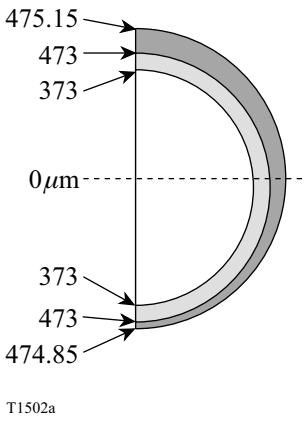

Figure 81.18
A 0.3-μm nonuniformity ($\ell = 1$) in the target-capsule thickness. The ice was 100 μm thick. Figures are not to scale.

Case 3: Temperature gradients on the inner surface of the layering sphere.

In the model for this investigation, the temperature was raised by a fixed amount on an area covering 12% of the layering sphere. The remainder of the layering sphere was held at 19.2 K. This simulated the effect that a localized heat load on the layering sphere has on a target. The capsule and DT ice were initially uniform 2 μm and 100 μm thick, respectively. The resultant effects on the ice temperature and distribution were calculated for a target centered in the layering sphere.

The presence of helium exchange gas allowed temperature perturbations on the layering sphere to transmit to the target and create an uneven heat load. Naturally, the side of the capsule closer to the heat source was warmer than the opposite side. The DT ice thinned from the warmer side and redistributed on the cooler side, until the free DT surface was isothermal. The

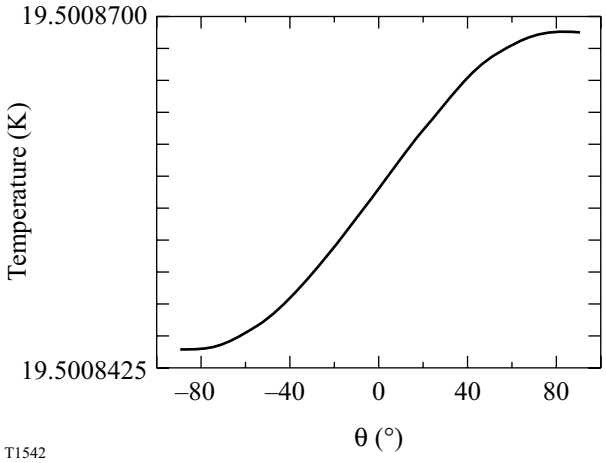

Figure 81.19
Temperature distribution along the inner surface of the ice (0° at target equator, 90° at north pole, –90° at south pole). A pole-to-pole temperature difference occurs as a result of the $\ell = 1$ nonuniformity (capsule thickness nonuniformity).

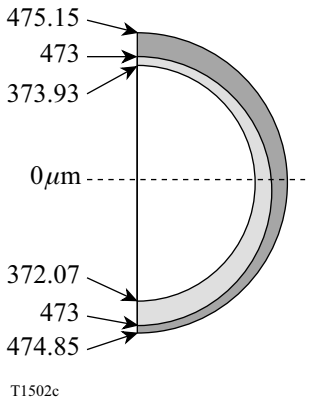

Figure 81.20
The ice's void was shifted until zero temperature difference occurred between the poles. This was considered to be the final ice-thickness profile. Figures are not to scale.

results are listed in Table 81.IV. A 10-mK nonuniformity over 12% of the layering sphere caused a ~0.5-μm ice $\ell = 1$ nonuniformity. A temperature gradient along the layering sphere greater than 10 mK must be present to change the ice thickness by a significant amount.

Summary

The temperature field within the cryogenic target is influenced by many factors, including the presence of exchange gases, target alignment within the layering sphere, target capsule thickness uniformity, temperature gradients on the layering sphere, *in-situ* target characterization methods, and external radiation. This temperature field determines the thickness uniformity of the DT-ice layer.

The temperature profile and ice $\ell = 1$ nonuniformity of the target within the OMEGA cryogenic target positioner were calculated using a thermal model in CFD simulations. The work isolated the effect of discrete factors that affect the uniformity of the ice thickness and determined a first-order sensitivity of the ice smoothness to the effect: (1) variations in target alignment in the layering sphere, (2) capsule-thickness uniformity, and (3) temperature uniformity on the layering sphere. The resultant ice-thickness profiles were calculated for these various boundary and initial conditions.

For a target misalignment from the center of the layering sphere by 1 mm, the expected ice $\ell = 1$ nonuniformity is ~1.0 μm. For a capsule $\ell = 1$ nonuniformity of 0.1 μm in a nominal 2-μm-thick shell, the expected ice $\ell = 1$ nonuniformity is 0.6 μm. A temperature gradient along the inner surface of the layering sphere greater than 10 mK must be present to change the ice thickness more than 0.5 μm. Results from this study determine which variables have the greatest effect on the ice smoothness to guide target fabrication, layering, and cryo-engineering priorities.

Table 81.III: Pole-to-pole temperature difference before redistribution and resultant $\ell = 1$ nonuniformity for different capsule $\ell = 1$ nonuniformities.

Capsule-wall nonuniformity ($\ell = 1$) (μm)	Pole-to-pole temperature difference in ice before redistribution (μK)	Resultant ice-thickness nonuniformity ($\ell = 1$) (μm)
0.1 (1.95 to 2.05)	9.5	0.6 (99.7 to 100.3)
0.3 (1.85 to 2.15)	24.5	1.86 (99.07 to 100.93)
0.6 (1.7 to 2.3)	52.5	3.72 (98.14 to 101.86)

For an OMEGA cryo target (2-μm capsule wall, 950-μm OD, 100-μm ice layer)

Table 81.IV: Pole-to-pole temperature difference before redistribution and resultant ice $\ell = 1$ nonuniformity for temperature gradients over 12% of the area of the layering sphere.

Temperature gradient over 12% of layer sphere area (mK)	Pole-to-pole temperature gradient in ice before redistribution (μK)	Resultant ice-thickness nonuniformity ($\ell = 1$) (μm)
5	15.4	0.34
10	28.7	0.54

ACKNOWLEDGMENT

This work was supported by the U.S. Department of Energy Office of Inertial Confinement Fusion under Cooperative Agreement No. DE-FC03-92SF19460, the University of Rochester, and the New York State Energy Research and Development Authority. The support of DOE does not constitute an endorsement by DOE of the views expressed in this article.

REFERENCES

1. J. K. Hoffer and L. R. Foreman, Phys. Rev. Lett. **60**, 1310 (1988).
2. A. J. Martin, R. J. Simms, and R. B. Jacobs, J. Vac. Sci. Technol. A **6**, 1885 (1988).
3. J. K. Hoffer and L. R. Foreman, J. Vac. Sci. Technol. A **7**, 1161 (1989).
4. T. R. Dittrich *et al.*, Phys. Plasmas **5**, 3708 (1998).
5. Laboratory for Laser Energetics LLE Review **79**, 131, NTIS document No. DOE/SF/19460-317 (1999). Copies may be obtained from the National Technical Information Service, Springfield, VA 22161.
6. Version 5.0, Fluent, Inc., Lebanon, NH.
7. P. C. Souers, *Hydrogen Properties for Fusion Energy* (University of California Press, Berkeley, 1986).
8. H. Yokoyama, Cryogenics **35**, 799 (1995).
9. Kapton product literature, DuPont® High Performance Polymers, Circleville, OH.
10. "NIST-Thermophysical Properties of Pure Fluids," computer code, NIST Std. Ref. Database 12 (1992).
11. F. Y. Tsai, E. L. Alfonso, S.-H. Chen, and D. R. Harding, "Mechanical Properties and Gas Permeability of Polyimide Shells Fabricated by the Vapor Deposition Method," to be published in Fusion Technology.
12. J. R. Welty, C. E. Wicks, and R. E. Wilson, *Fundamentals of Momentum, Heat, and Mass Transfer*, 3rd ed. (Wiley, New York, 1984), p. 247.

Target Detection and Shroud Pull Sequencing for Cryogenic-Target Operations on the OMEGA System

Introduction

The long-term plan for the upgraded OMEGA laser system includes continued improvements in beam quality, beam-to-beam energy and power balance, and the incremental addition of several beam-smoothing techniques. Incorporating the capability to shoot "cryogenic" targets is also part of the plan. Integration and activation of the Cryogenic Target Handling System is in progress as of this writing. This article introduces the elements of cryogenic-target operations and details the technique that will ensure correct and safe sequencing of cryogenic shots.

1. Cryogenic Operations

A cryogenic target is a ~1-mm-diameter spherical shell that is processed at very low temperatures and delivered to the target chamber with the fuel frozen as a layer of "ice" approximately 100 μm thick on the inside surface of the shell. These targets can contain significantly more fuel than the normal, room-temperature, gas-filled targets. Figure 81.21 illustrates how cryogenic targets are suspended by spider's silk from a beryllium "C" mount (see description in the **Target Filling** section, p. 7, this issue).

Figure 81.22 shows the equipment installed in the OMEGA target area to allow cryogenic targets to be positioned and shot. The lower pylon, supported by the target chamber (TC), extends downward from the center of the TC and through the Target Bay floor; this lower pylon is basically a cylindrical vacuum vessel fitted with a kinematic dock inside its upper end and an isolation valve and flange at its lower end. The upper pylon extends from above the center of the TC, through a bellows joint at the top of the TC; it is supported by the bridge structure that spans the Target Bay. The linear induction motor and shroud retractor, which are housed within the upper pylon, are used to remove a thermal shroud that protects the target until shot time.

Figure 81.23 shows the elements at the center of the TC in more detail. The target is housed in a moving cryostat (MC) that is placed at the center of the TC by the lower pylon equipment. The position of the target can be checked and adjusted using the standard OMEGA Target Viewing System and the positioner built into the MC. The OMEGA system may then be charged and sequenced to shoot the target. The charging and countdown take approximately 3 min. In the last second, the shroud retractor is commanded to pull the upper shroud upward, away from the target, so that it is clear of the beams before the laser pulse arrives.

Cryogenic targets are produced by permeating deuterium or deuterium/tritium fuel into the shell at pressures of up to 2000 atm and then cooling the assembly to below 20°K. The

G3970

Figure 81.21
Cryogenic targets utilize a "C" mount configuration that minimizes the mass in the vicinity of the target and does not obscure any of the 60 OMEGA beams.

MC maintains a cold environment around the target while it is moved from the permeation site, completes its preparation cycle, and is moved to the center of the target chamber. Figure 81.24(a) shows the base of the MC; Fig. 81.24(b) shows the components that make up the upper shroud. The inner, middle, and outer shrouds are joined to form a single upper-shroud assembly that can move in a vertical direction over the target and mate with the lower shrouds on the base. In this configuration, the target is centered in the "layering sphere," which is a metal cylinder with an internal spherical cavity that is controlled to provide the low-temperature, spatially uniform radiation environment that promotes formation of a smooth, concentric ice layer. Windows in the layering sphere, the middle shroud, and the outer shroud allow the target to be viewed along two axes by the Target Viewing System (TVS), which is used to position objects in the OMEGA target chamber.

The MC transport cart mounts all of the cooling, vacuum, and control equipment required to maintain the MC at the required low-temperature, high-vacuum condition. A major feature of the transport cart is an evacuated umbilical spool that manages the electrical and fluid lines that connect the MC to the equipment on the cart. Figure 81.25 shows the transport cart. In this view, the cryostat is located below the large gate valve near the top of the cylindrical vacuum vessel (left of center). The entire transport cart is mounted on a pneumatic bearing system that allows operators to push it from place to place within the facility. A total of five transport carts are planned.

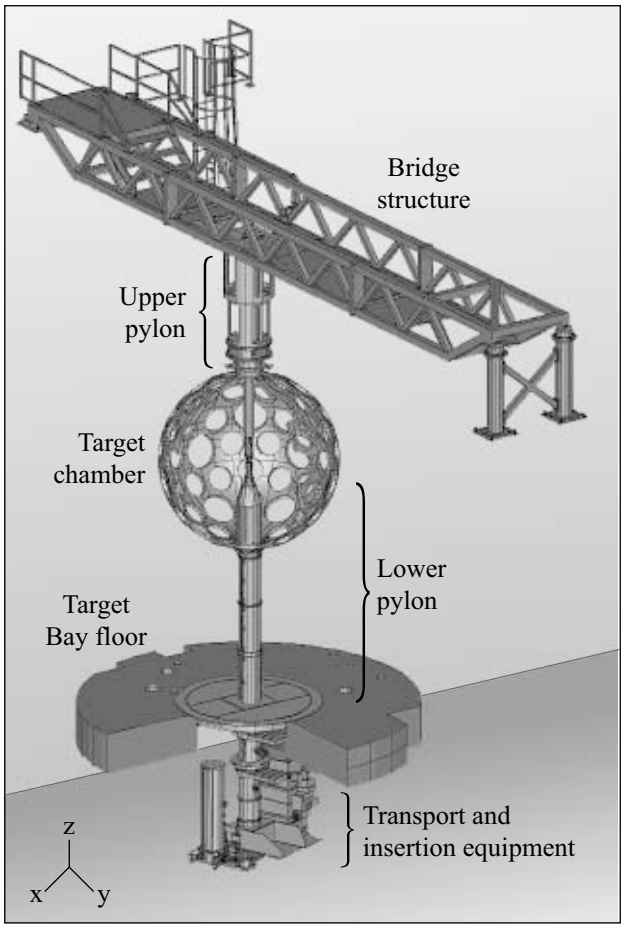

Figure 81.22
The major equipment items recently installed in the OMEGA target area to facilitate cryogenic target shots include transport and insertion equipment beneath the target chamber, upper and lower pylons, and a structural bridge.

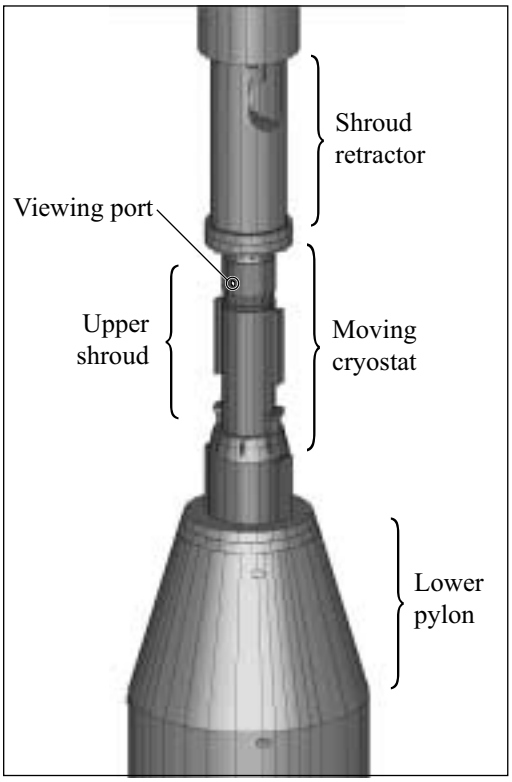

Figure 81.23
The cryogenic target is housed in a moving cryostat (MC) that is placed at the center of the target chamber. The MC includes thermal shrouds that isolate the target from the room-temperature target chamber environment. The shroud retractor removes the upper shroud just prior to the shot.

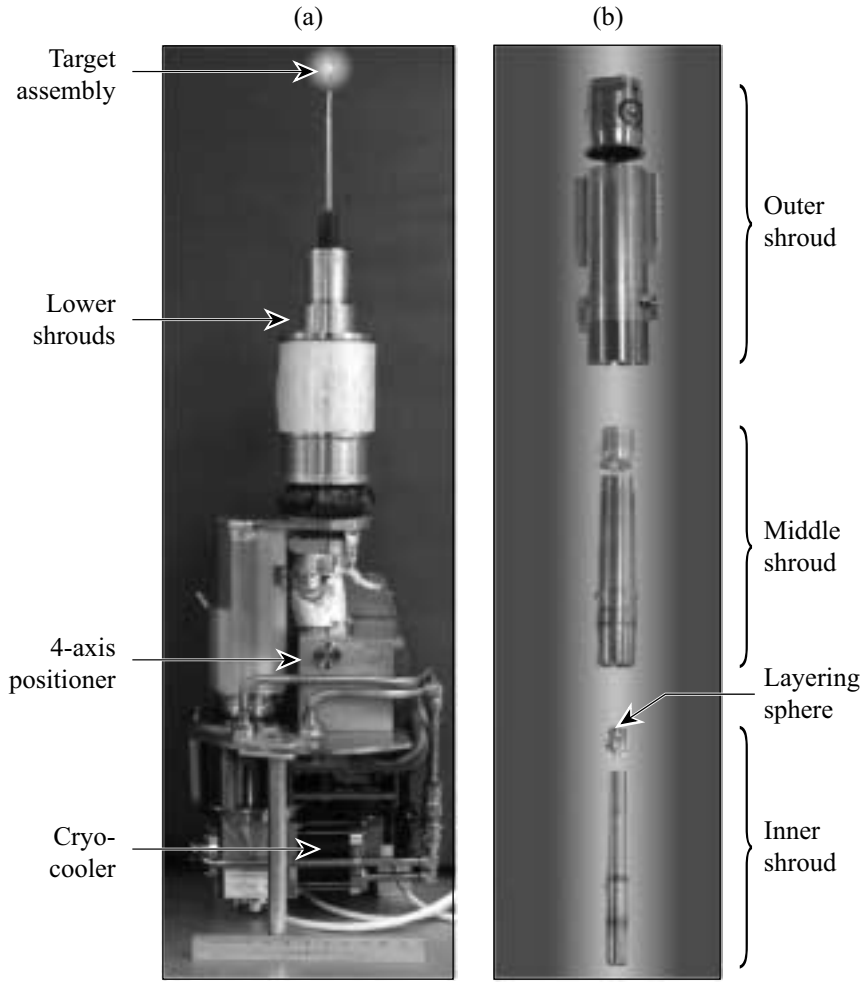

Figure 81.24
Parts of the moving cryostat: (a) The base includes a target positioner, a cooler, and the lower protective shrouds; (b) the upper shroud is a three-layer assembly. The layering-sphere element that immediately surrounds the target provides a spatially uniform radiation environment that determines the properties of the ice.

Figure 81.25
The moving cryostat transport cart carries the moving cryostat and its cooling, vacuum, and control equipment. It is moved around the facility on a pneumatic bearing system.

Figure 81.26 shows the lower pylon, in the room below the target chamber, with the transport cart docked to it. The vertical cylinder in the foreground is an evacuated "chain locker." When the system is ready, the isolation gate valves are opened, and the MC is driven to the center of the target chamber by the action of the chain being driven out of the locker and along guide rails inside the transport cart and lower pylon vacuum vessels. When it arrives at the center of the target chamber, the MC mates with the kinematic dock built into the lower surface of the top of the lower pylon and is clamped into place. This places the layering sphere and target within approximately 100 μm at the convergence of the laser beams.

The linear induction motor (LIM) in the upper pylon can then be operated to lower the shroud retractor from above to engage the upper shroud and prepare it for removal (this configuration is shown in Fig. 81.23). The shooting sequence includes commanding the removal of the upper shroud so that it is clear of the beams before the pulse arrives, assuring that the target is intact and in place, and preventing the laser pulse from propagating if a problem is detected. The details of this final sequencing, detection, and shot authorization process are performed by the cryogenic target detection equipment described in this article.

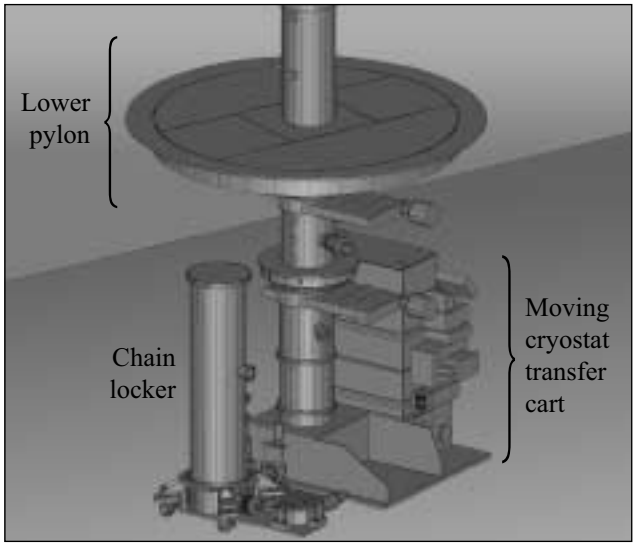

G4943

Figure 81.26
For an OMEGA shot, the transport cart is positioned under the lower pylon and connected to it. A compression chain system is used to drive the moving cryostat upward into the target chamber.

2. Cryogenic Target Detector

Because the beam ports on OMEGA's target chamber are arranged in opposing pairs, energy propagated forward in one beamline can pass through the chamber and propagate in the backward direction on the opposing beam train. This feature is exploited routinely in alignment procedures that use low-energy laser beams. High-value optics can be seriously damaged, however, if even a fraction of the high-energy shot pulse is allowed to pass the target and enter the opposing focus lens. "Target existence detectors" have been put into place to help prevent this from happening. The automatic imaging target existence detector (AITED)—a system used on noncryogenic target shots—protects against the situation where a properly aligned target moves or falls out of position late in the shot cycle. The cryogenic target detector (CTD) performs the same functions in the altered circumstances dictated by cryogenic-target operations. (The Target Viewing System cannot be used for target detection in either case because its lenses extend well into the target chamber and are protected from flash and debris by rugged shutters. Because these shutters require approximately 10 s to close, they are closed and verified prior to charging the laser system.)

AITED is designed to deal with targets of any shape (planar or spherical) positioned at any location near the target chamber's center. It features a single video camera to view a backlighted image of the target using an arrangement of lenses mounted outside the target chamber. Since it functions by processing video frames at 30 Hz, AITED is useful until about 30 ms prior to the shot. After the last pre-shot frame has been acquired, a fast shutter closes to protect the camera from the flash of the target event. The presence of the shroud and the sub-frame-rate timing of events prevent the use of AITED for cryogenic shots.

The CTD uses a pair of apertured photodiodes to analyze the intensity of signals provided by dedicated laser illuminators. This technique can provide detection arbitrarily close to the shot, but it is limited to spherical targets positioned at the center of the target chamber. As the design concept for the CTD developed, it was extended to include the precision timing of the shroud-retraction (or pulling) event.

Both target detectors prevent the high-energy pulse from propagating by interrupting the 5-Hz signal that triggers the power conditioning units for the regenerative amplifiers at the beginning of the laser system. The pulse that then propagates to the power amplifier stages is too low in energy to be amplified to normal levels in the remainder of the system. As a result, essentially no energy reaches the target, and damage

due to energy passing through the center of the target chamber is prevented.

Discussion

The Cryogenic Target Detection (CTD) System has been designed to meet the following requirements:

a. Synchronize the pulling of the shroud to the laser shot.
   - Ensure that the shroud is clear of all the beams before the energy arrives at the center of the target chamber.
   - Minimize the time that the target is exposed to the target chamber's thermal radiation environment (goal: 50 ms, max).
   - Ensure that the shot occurs before the vibration caused by stopping the shroud at the top of its travel can disturb the target.

b. Prevent propagation of the high-energy pulse if the target is not in place at the center of the target chamber.
   - Initiate detection when the shroud has cleared the target.
   - Continue to monitor as close as possible to shot time.

c. Prevent propagation of the high-energy pulse if the target is displaced or if shroud retraction deviates from nominal.
   - Accommodate 700- to 1100-μm-diam spherical targets at the center of the target chamber.
   - Detect displacement of the target from the center of the target chamber.
   - Detect early or late exposure of the target.
   - Detect failure of the shroud to clear the beams.

d. Provide operability and testability features compatible with OMEGA operations.
   - Provide consistent user interface look and feel.
   - Allow operator input of setup parameters.
   - Detect and display errors.
   - Implement correct responses to shot-cycle system states including "stand-down" and "abort."
   - Include test modes and signal outputs to facilitate installation, readiness checks, and trouble shooting.
   - Provide reduced functionality with one axis inoperative.

e. Fail to the "safe" triggers-are-interrupted mode.

The major elements of the CTD include a set of detectors installed on the target chamber; a rate interrupt module (RIM), which is located in the Driver Electronics Room (DER) below the Laser Bay; and user interface software, which creates a display in the Control Room. These are shown schematically in Fig. 81.27. The CTD uses two orthogonal optical detectors that are similar to the TVS. These elements are co-located with the corresponding TVS equipment on the target chamber but view along slightly different axes and operate independently. Because the CTD viewing axes are blocked by the edge of the viewing port in the outer shroud of the MC, target detection is not possible until the shroud has been pulled clear of the target late in the shot sequence.

The RIM is a package of electronics that is mounted in the same rack as the primary driver-timing equipment. A dedicated RS-485 serial link relays signals between the detector packages and the rate interrupt module (RIM). In addition to those associated with the detectors and illuminators these include the three shown connecting to the upper pylon controls in Fig. 81.27. The RIM also receives the T–10 and T–0 timing marks and the three 5-Hz rates that it controls from the Hardware Timing System equipment in the DER. The RIM communicates, via a standard RS-232 serial link, with a Sun workstation that contains the video frame grabber used by AITED. CTD operator interface software running on that computer provides the Graphical User Interface that is displayed on the laser drivers workstation in the Control Room.

1. CTD Illuminators

Each CTD illuminator consists of a small diode laser with a collimating optical system and a fast-acting shutter. The lasers are turned on and off by a general-purpose control software item that allows the lasers to be operated manually, as needed for checkout, and automatically cued by shot-cycle software messages. The fast shutter is controlled (like the AITED camera shutter) by the hardware timing system and a dedicated controller. It closes 1 to 5 ms before every shot to prevent the flash from damaging the illuminator laser optics and re-opens automatically after the shot. A photodiode mounted in the illuminator optics provides a signal to the RIM to indicate when the laser is on, regardless of the position of the shutter.

2. Detector Packages

The CTD optics focus the illuminator laser beam into the detector package, through a manually adjustable aperture, and onto a photodiode mounted within the TVS enclosure on the opposite side of the target chamber. This system is set up so that three distinct levels of illumination can be detected:

(a) No light means that the illuminator is either not on or is shuttered or that the MC shroud is blocking the line of sight.

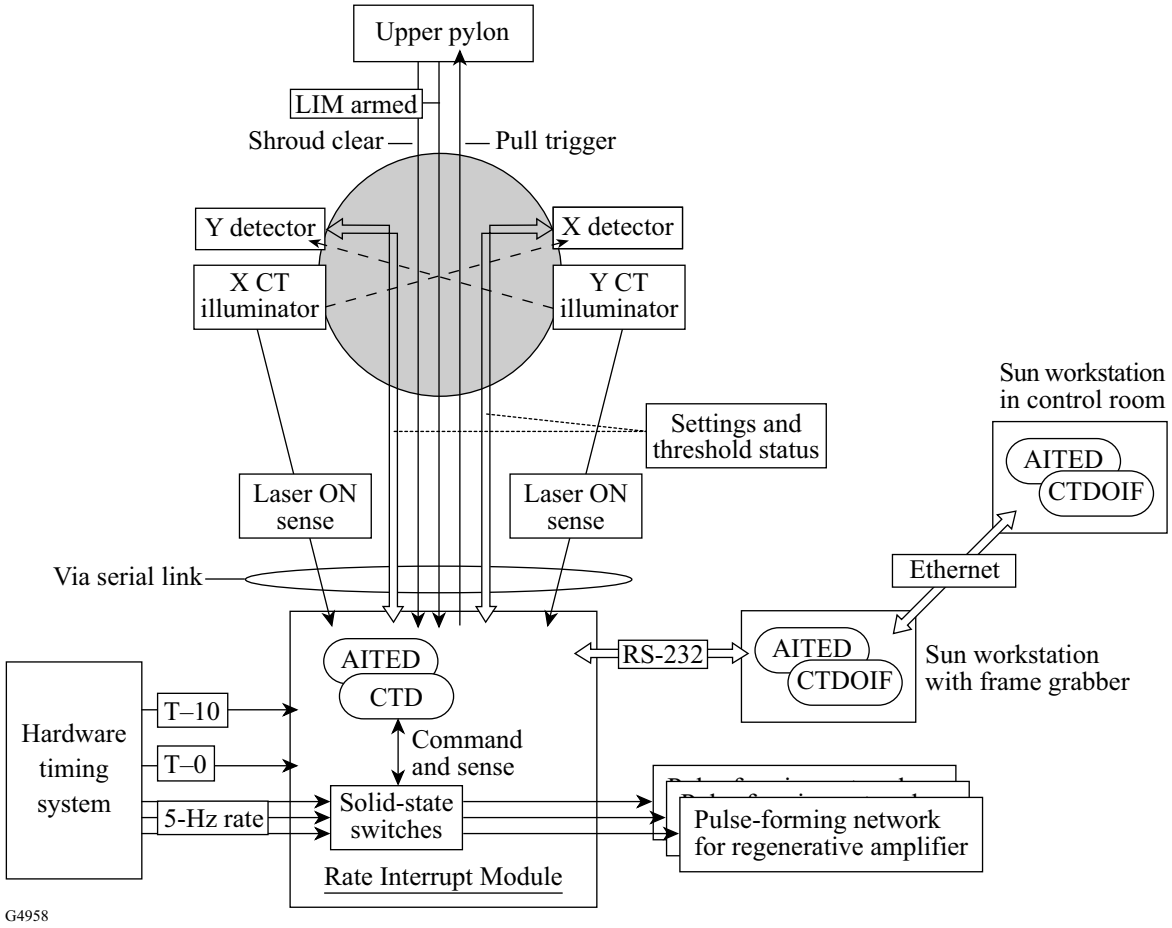

Figure 81.27
The rate interrupt module (RIM) is the heart of the Cryogenic Target Detection (CTD) System. It receives signals from detectors in the target chamber, controls the triggers to the driver preamplifiers, and communicates with the Control Room operators.

(b) A medium level means that the shroud is clear of the target and the target is in place.

(c) A higher level means that the shroud is clear but the target is out of place.

The "low" and "high" threshold settings that make this discrimination are set by the operator and passed to the detectors for implementation. Each detector uses a Microchip PICMicro 8-bit RISC microcontroller running at 16 MHz. This microcontroller includes on-board 8-bit analog-to-digital converters that transduce the photodiode signal. I/O bits on the PICMicro's are used to sense the illuminator status and handle the signals to and from the upper pylon. The detector packages also include RS-485 transceivers. The RS-485 standard uses differential signals that allow greater noise immunity, higher speed, and greater cable lengths than the RS-232 standard wire.

3. Rate Interrupt Module (RIM)

The RIM developed for cryogenic operations replaces the unit that was installed for AITED and is also built around the PICMicro microcontroller. The firmware running on this chip has separate AITED and CTD operating modes. The mode is determined by whether the AITED or the CTD software is running on the Sun computer. In the AITED mode, the RIM functions the same as previous versions of the RIM. In the CTD mode, the RIM implements the cryogenic target requirements. In both modes the code coordinates the activities of the RIM, including communication with the Sun, and control of the 5-Hz flashlamp triggers. Final control of the flashlamp triggers is provided by opto-isolators rather than the relays used in the previous versions of the RIM. This approach provides improved reliability and switching speed. The closed-to-open signal switching time of the rate interrupt opto-isolators has been measured as approximately 500 ns.

The overall shroud-retraction sequence must be repeatable within ±1 ms. This allocation includes the "pull trigger" signal that originates in the RIM and is relayed over the RS-485 to the Y detector package, where it is output as a voltage level to the LIM controller in the upper pylon. The performance of the CTD elements was assessed in LLE's Electronics Shop using the actual components connected by cables of representative lengths. The result of 20 trials is that the "pull trigger" can be timed and generated in the RIM, transmitted to the detector package, and output with an average latency of 128.8 μs and a rms ("jitter") of 2.6 μs—well within the required limits.

4. CTD Operator Interface (CTDOIF)

The CTD operator interface software was developed using X/Motif Designer 5 and is designed to run under Solaris on the AITED Sun workstation to make use of the dedicated serial link to the RIM. The Graphical User Interface is displayed on the laser drivers workstation in the Control Room. Figure 81.28 illustrates the windows that are presented to the operator. The main window provides the functions for normal shot-to-shot operation of the CTD, which includes monitoring the status of the RIM and arming the system for a shot. In particular, the status of the illuminators and the resulting signal levels at the detectors are portrayed. The setup window allows the operator to review and change the selection of axes that will be armed and the values of the RIM parameters. When revised values are applied to the RIM, they are automatically saved to the OMEGA database. The selection of one axis or both will depend on the status of the CTD hardware. Variations in target size or opacity may necessitate adjustment of the threshold values. The timing parameters will be a function of the acceleration profile that the LIM/shroud puller is commanded to follow. It is expected that once the correct set-up values have been established, they will seldom be changed.

(a) Main window (b) Setup window

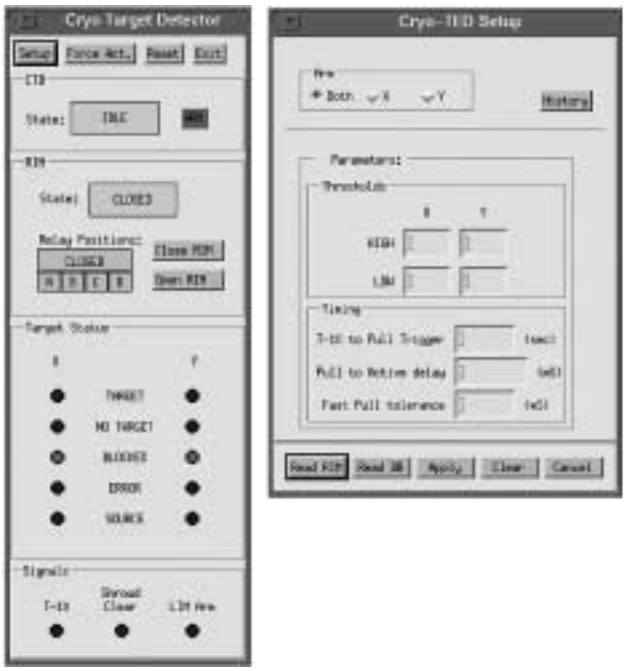

G4957

Figure 81.28
The CTD operator interface windows (a) arm the system, enable/disable the solid-state relays, and monitor status; (b) choose axes to be armed and set detection thresholds and timing values.

The communication link between the Rate Interrupt Module and the Operator Interface is monitored by both elements. If communication is lost after the system has been armed for a shot, the RIM will interrupt the driver triggers. It will also abort the shroud pull if it is not too late. The OIF supports the executive-level intercommunication protocol that is used to coordinate shots. This ensures that the CTD is operated when necessary and that the operators are aware of any problems. It also allows the CTD to participate correctly in system-wide aborts or stand-downs.

5. Operating Sequence

Figure 81.29 illustrates the events in the cryogenic shot sequence. After the MC has been inserted and the target has been positioned and verified by the Experimental System operator using the Target Viewing System, the laser driver operator will verify that the CTD is set up correctly and "arm" it for the shot. In the armed state, the CTD will act in response to the events it can sense. When the CTD is not armed, the information is simply displayed to the operator.

When the entire OMEGA system is ready, the power amplifiers are charged over a period of about 2.5 min. After charging is complete, the precision timing sequence starts at T–20 s. At about T–10 s (exact timing to be determined during system activation), the pylon controller element of the Cryogenic Target Handling System initiates a "pre-pull" activity that prepares the shroud for removal. The RIM receives the "LIM armed" signal when this is complete. Meanwhile, at exactly T–10 s, the RIM computer starts a "pull timer" that counts down to the time at which the pull trigger signal must be output. Since the shroud takes about 470 ms to clear the target after it is triggered, the pull timer will run for about 9.5 s. When the pull timer expires, the RIM logic checks to ensure that it is prudent to initiate the retraction sequence. As is indicated in Fig. 81.29,

the pull trigger will not be output if a system-wide abort is underway or if the pre-pull did not complete successfully (as indicated by "LIM armed") or if the CTD illuminator(s) for the axes that are armed is(are) not on at this point. (The separate function that controls the illuminators is cued by the executive-level intercommunication protocol.) In addition to inhibiting the pull trigger, these contingencies will cause the opto-isolators to be disabled, interrupting the driver pulse.

After the pull trigger has been output, the RIM logic waits until the shroud should be clear (this is timed by the "activation timer"). Figure 81.30 is a plot of the shroud trajectory that has been the baseline for the system design. The actual optimum trajectory is currently being developed on the basis of the operating performance of the LIM and its controls. The baseline features an initial constant-velocity pull that separates the upper shroud from the lower shroud. This is followed by acceleration at 2.5 g until after the time of the shot. The LIM will then decelerate the shroud to a stop at the upper end of its travel (this part of the trajectory is not shown in the plot). In Fig. 81.30, note that the shot must occur in the 4-ms window between the shroud clearing the beams (at 0.484 s) and the end of the 50-ms exposure limit (at 0.488 s). These timing values depicted in Fig. 81.30 are also reflected in Fig. 81.29. (The critical timing parameters used by the CTD can be easily adjusted to accommodate any retraction trajectory that can be executed by the LIM.)

The shroud will clear the CTD lines of sight at the point on the trajectory marked "Target is exposed…". This will allow the light from the illuminators to reach the detectors and will cause the lower thresholds to be exceeded. The activation timer will be set for the latest time that this can occur and still have a successful shot. If this "slow pull" limit is exceeded, the RIM will disable the opto-isolators to abort the driver pulse. This prevents shooting with the shroud in a position where it will intercept some of the high-energy laser beams. The "fast pull tolerance" [see Fig. 81.28(b)] will be set to represent the earliest time at which the shroud can clear the target and still allow a successful shot. If the illuminators are detected before the activation timer is below the fast pull tolerance, the driver pulse will be interrupted because the target could be exposed long enough to explode before the shot (the 50-ms exposure limit). In an extreme fast pull case, vibrations resulting from the shroud puller deceleration could reach the target and disturb it prior to the shot.

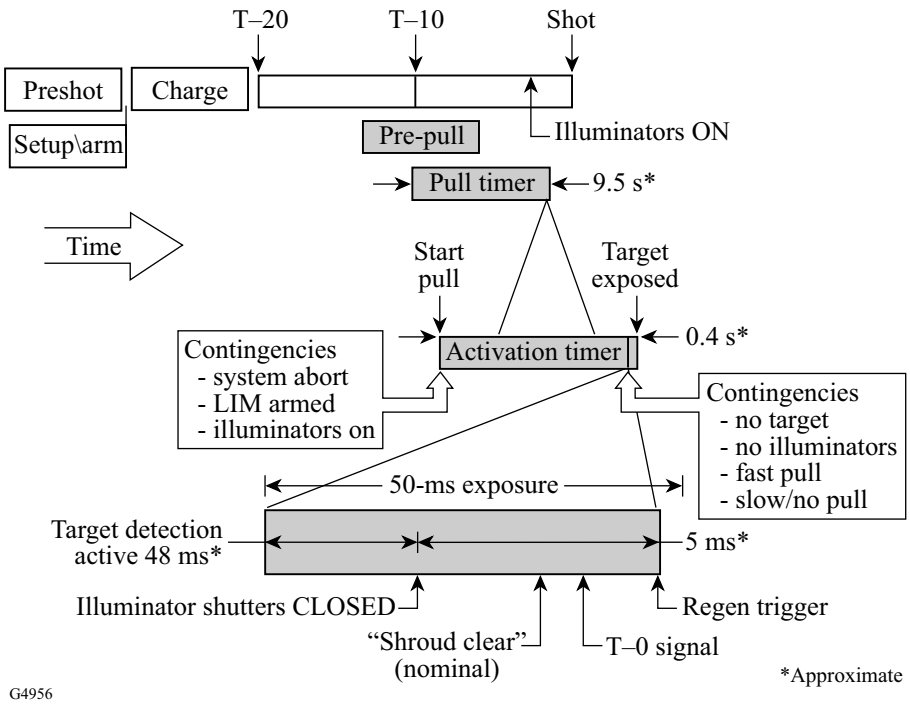

Figure 81.29
The nominal timeline for a cryogenic-target shot illustrates the increasingly precise timing of events orchestrated by the CTD system.

If the target is in place when the shroud clears the CTD lines of sight, the detector signals will be above the lower thresholds but will not exceed the upper thresholds. This is the "TARGET" situation on the operator displays and within the CTD logic. If the armed axes are in this condition, the shot and monitoring can continue until the illuminator fast shutters close a few milliseconds before T = 0. At that point, the signals will drop back below the lower threshold. The detection logic is then disabled. While the detection logic is active, the driver pulse will be aborted if the detector signals indicate that the target is not present or that the illuminators have failed.

The "shroud clear" signal is derived from a photosensor attached to the LIM structure. It indicates that the shroud is near the point at which it is out of the beam paths. This signal is monitored by the CTD to deal with the contingency that the shroud retractor slows down or stops after a successful initial retraction. A T–0 signal is provided to the RIM primarily as a means for disarming the target detector after the shot (so that an abort is not initiated when the target disappears due to the shot). This T–0 signal will be delayed by the timing system so that it occurs as close as possible prior to the arrival of the driver PFN triggers. If the "shroud clear" signal is received before the T–0 signal, the shot can continue. If "shroud clear" has not been received when T–0 arrives, the opto-isolators will be disabled.

The RIM will count the time interval between the "shroud clear" and T–0 and report it to the OIF for review by the operator. These values will also be logged to the database as an indication of the shroud puller's performance.

Conclusion

Cryogenic target detection (CTD) is a critical part of the functional integration of the Cryogenic Target Handling System into OMEGA. The newly designed CTD is based on existing elements of the OMEGA controls and will provide the necessary sequencing and safety features. The CTD setup features sufficient flexibility for the evolution of the details of cryogenic operations and target physics research.

ACKNOWLEDGMENT

This work was supported by the U.S. Department of Energy Office of Inertial Confinement Fusion under Cooperative Agreement No. DE-FC03-92SF19460, the University of Rochester, and the New York State Energy Research and Development Authority. The support of DOE does not constitute an endorsement by DOE of the views expressed in this article.

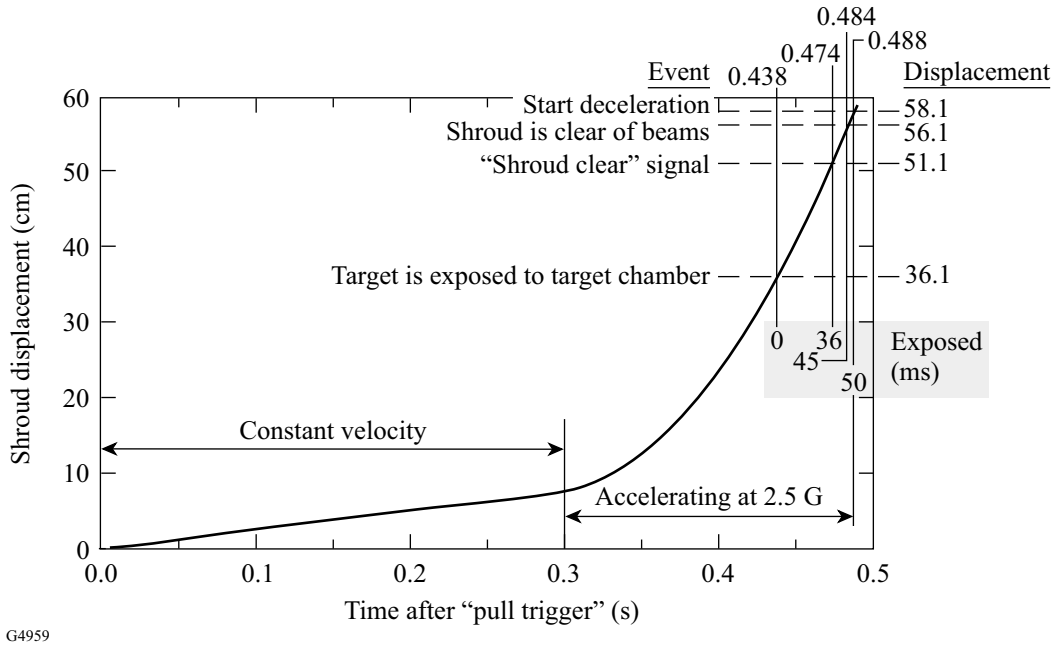

Figure 81.30
The baseline shroud-removal trajectory features constant velocity separation of the shrouds followed by constant acceleration until after the shot.

The Effect of Optical Prepulse on Direct-Drive Inertial Confinement Fusion Target Performance

Introduction

In direct-drive inertial confinement fusion (ICF), laser light directly irradiates a capsule with a pulse of less than 10-ns duration. Laser ablation of material from the capsule surface produces extreme pressure that drives the implosion of the thermonuclear fuel. Ignition target designs[1–3] require a temporal pulse shape tailored to produce two or more converging shocks that coalesce in the imploding core. Ideally, the implosion occurs without premature heating of the shell or the fuel contained within because preheat reduces the implosion efficiency. Since ICF targets are inherently Rayleigh–Taylor (RT) unstable, it is particularly important to direct-drive ICF that the target perturbations produced by irradiation nonuniformities[3] are minimized. Another method to ameliorate the effects of this instability is to enhance ablative stabilization[3] by judiciously preheating the shell with shocks produced by the rise of the drive pulse. Successful ICF implosions therefore require precise control of the temporal shape of the drive intensity and minimal perturbations of the shell by that drive.

Typically drive pulses start with a low-intensity (~2%) "foot," several nanoseconds before the peak drive occurs. This foot is essential for producing the correct isentrope of the imploding target, i.e., one with sufficient heating to help stabilize the target but not high enough to greatly reduce its hydrodynamic efficiency. The simulations typically assume perfect optical contrast (i.e., no prepulses before the drive pulse begins). ICF lasers have high gain and experience significant saturation around the peak of the pulse; thus, low-level noise in the driver can readily produce prepulses. Since hydrodynamic target simulations generally cannot correctly model the effects of prepulses at less than 10^{-5} of the peak power, the specifications for optical contrast must be determined experimentally using target performance.

Implosion experiments[4,5] and theoretical calculations[6] carried out using 1054-nm lasers generally found that prepulse levels had to be kept eight to nine orders of magnitude below the peak power to obtain maximum performance (neutron yield). Corresponding optical measurement techniques[7,8] were also developed at that time. Since then ICF lasers and targets have changed significantly, but no new reliable experimental data exists on the effect of prepulses on target performance. Today, direct-drive targets are usually coated with a thin ($\leq$1000-Å) Al layer that retains the hydrogen isotopes in the gaseous fuel and prevents target damage caused by filamentation of laser light inside the target shell prior to plasma formation.[9,10] This layer can be compromised easily by low-energy optical prepulses. Most modern ICF lasers are frequency-tripled (351-nm) Nd:glass lasers that benefit greatly from the prepulse suppression afforded by the frequency conversion. Recently Elton *et al.*[11] suggested that prepulses on the OMEGA laser system[12] might be higher than expected, prompting the implementation of a contrast-monitoring system on OMEGA. This work presents the measured prepulse levels on OMEGA and a contrast criterion for OMEGA direct-drive implosions. Similar contrast criteria will apply to direct-drive experiments on the National Ignition Facility (NIF).[13]

In this article several techniques for characterizing prepulses on OMEGA and their effect on target performance (i.e., neutron yield) are presented. The results indicate that the upper limit for the allowable prepulse on target is ~0.1 J/cm^2 at peak intensities of $\leq 10^8$ W/cm^2. This translates to an intensity contrast of ~10^7 between the allowable prepulse and the peak of the main laser pulse. This limit is most relevant for Al-coated targets. The allowable prepulse may be higher for uncoated targets if such targets should prove viable in the future.

Optical Diagnostics and Their Interpretation

Optical contrast on OMEGA is measured at two places: (1) a UV contrast station located after the frequency converters and just ahead of the target chamber, and (2) an IR contrast station at the input to the amplifier chain, ahead of the first beam splitter on OMEGA. In both cases, the full beam aperture is sampled. The contrast is measured using fast vacuum photodiodes (Hamamatsu, R1328U-01-S-1 and R1328U-02-S-20) and high-speed oscilloscopes (TEK7250 or IN7101). A schematic layout of the UV contrast station is shown in Fig. 81.31. An air breakdown region is included in the design to protect the

diodes against damaging fluences during the main pulse. The prepulse monitors are calibrated with removable filters. These filters allow the main laser pulse to be fully measured on calibration shots that are typically performed daily. Removing these filters accesses the low-intensity prepulse region within 20 ns before the main laser pulse. The calibration filters have an optical density (OD) of 5.3 in the UV (2.9 in the IR), and, when removed, the detection threshold is typically around 8 orders of magnitude below the peak UV power (~5 to 6 orders of magnitude below the IR peak power). Extensive precautions have been taken to block stray light from affecting the measurements, including the spatial-filter aperture shown in Fig. 81.31. The temporal resolution of this system is better than 200 ps.

Typical prepulse records for a full-power OMEGA laser pulse are shown as the lower two curves in Fig. 81.32. The respective calibration curves with filters inserted are shown in the upper portion of this figure. (Note that their peaks are normalized to 1.) An IR prepulse (or prepulses) can be seen rising to ~10^{-4} of the peak IR power within ~1 ns of the arrival of the main pulse (the steep rise at $t = 0$). The corresponding UV power is <10^{-7} of the peak UV power. The difference in contrast level between the IR and UV pulses results from both the unsaturated gain in the IR system and the nonlinear frequency conversion. [Low-power prepulses experience small-signal conversion $\left(I_{UV} \propto I_{IR}^{3}\right)$, whereas the conversion is almost linear with the intensity near the peak of the pulse.] From simulations and experiments we have found that the prepulse contrast ratio obeys a heuristic relationship of $C_{UV} \propto (C_{IR})^2$, where $C = P_{peak}/P_{prepulse}$ (the subscripts refer to the peak and prepulse powers). This relationship is born out in the results shown in Fig. 81.32, where the UV prepulse level is mostly below the noise limit, i.e., flat portions of the trace. (The flat lines for $t > 0$ are the saturated diode signals.) The UV prepulse ($P_{prepulse} < 10^{-7}\ P_{peak}$) within the last nanosecond before the onset of the main pulse is very close to the detection threshold.

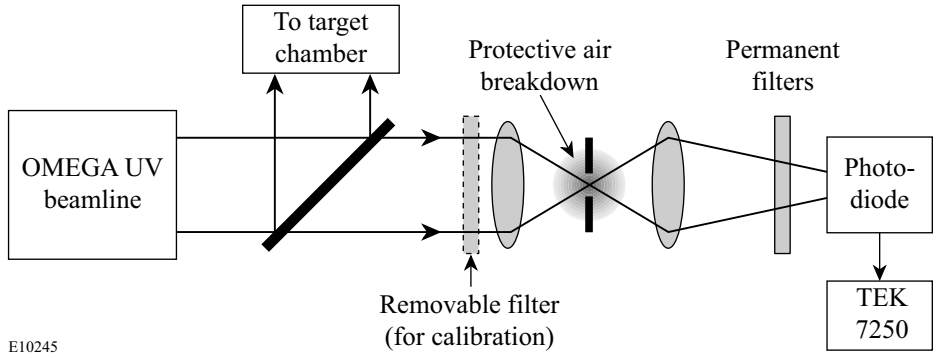

Figure 81.31
Schematic layout of the UV contrast monitor station. To protect the photodiode the confocal lens pair breaks down the air when the high-intensity laser pulse arrives. The removable filter pack is inserted for calibration of the prepulse monitor.

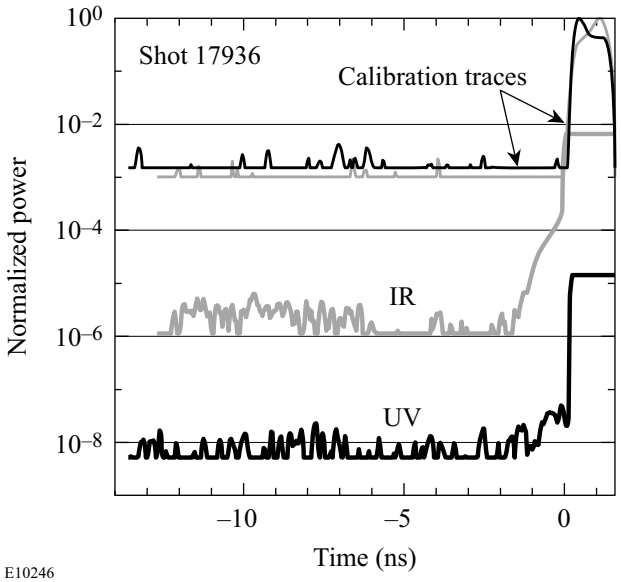

Figure 81.32
Contrast monitor traces for the UV at the output and the IR at the input to OMEGA. The thin traces on top show the calibration traces with the main pulses on scale and normalized. The thick lower traces are taken without the calibration filter (see Fig. 81.31) and permit prepulse monitoring to a contrast of 10^{-8} from the peak in the UV (10^{-6} from the peak in the IR). No prepulses are seen above the noise for times $t < -2$ ns.

The prepulse within 1 ns of the main pulse originates in either the regenerative amplifier (regen) or the pulse-shaping system before the regen. Such prepulses are only marginally affected by the Pockels cells following the regen. The general shape and position of these prepulses are reproducible although the intensity fluctuates, particularly in the UV. These observations rule out regen amplified stimulated emission (ASE), leaving spurious intracavity reflections within the regen or imperfections in the laser pulse injected into the regen as likely sources. The exact prepulse source is still under investigation.

A large number of OMEGA shots have been examined for UV prepulses; it was found that none had a prepulse in excess of 10^{-8} of the peak pulse within the time window of −17 ns and −1 ns prior to the main pulse. Within the last nanosecond the contrast degrades but the prepulse level typically does not exceed 10^{-6} of the main pulse (the corresponding cumulative time-integral of the intensity or the fluence is about 0.2 J/cm^2 in the prepulse) and in most cases remains at or below 10^{-7}.

Apart from UV prepulses, additional prepulses on target could be due to IR and green laser light left over from the frequency-conversion process. In each of OMEGA's 60 beams, the frequency converters are followed by two dielectric multilayer mirrors, each with nearly 100% reflectivity at 351 nm and average reflectivities of ~6% in the IR and ~10% in the green. The residual green energy is always much smaller (1%–5%) than either the UV or IR energies and can therefore be neglected. The IR intensity on target is reduced by a factor of ~280 because of the IR transmission of the UV mirrors. The chromatic shift of the OMEGA lenses produces IR spots of ~15-mm diameter in the target plane. Since the random phase plates[14] produce a UV focal spot with a FWHM of 0.5 mm and do not measurably affect the IR spot size, the IR on-target intensity is reduced by an additional factor of 900 because of this chromatic defocusing. Since there is no IR prepulse monitor at the laser output, we must estimate the IR output prepulse from the measured UV prepulse. Assuming small-signal, third-harmonic conversion efficiency for the IR prepulse [$P_{IR,out} \approx (P_{UV,out})^{1/3}$], we find that the IR on-target prepulse contrast is approximately $C_{IR,on\text{-}target} = \sim 900 \times 280 \times (C_{UV})^{1/3}$, which is $\sim 8 \times 10^7$, when the UV contrast is $\sim 3 \times 10^7$ as obtained from Fig. 81.32. Making the pessimistic assumption of 50% third-harmonic conversion efficiency for the main pulse, we find that the IR energy prepulse on target is ~1/3 of the UV prepulse energy.

An independent estimate of the IR on-target prepulse level (or contrast) can be obtained from the IR input prepulse monitor, the ten-fold deterioration of the IR contrast due to the gain saturation in the amplifiers, and the small-signal UV conversion efficiency. Since the IR output energy can be as high as the UV energy (depending on pulse shape and duration), one can obtain an upper limit for the IR prepulse intensity on target as $I_{IR,on\text{-}target,prepulse} < [10/(900 \times 280 \times C_{IR,input})] \times I_{UV,peak\ on\text{-}target} \approx (4 \times 10^{-5}/C_{IR}) \times I_{UV,peak\ on\text{-}target}$. For $C_{IR,input} \approx 1.5 \times 10^4$ (Fig. 81.32) the upper estimate for the IR prepulse is $I_{IR,on\text{-}target,prepulse} < 10^{-8}\ I_{UV,peak\ on\text{-}target}$, which is still well below the corresponding measured UV prepulse level $\approx 5 \times 10^{-8}$ in Fig. 81.32. The two estimates of the on-target IR prepulse level (shot 17936, Fig. 81.32) lie within a factor of ~4, consistent with the accuracy of these estimates.

Threshold Experiments

The thin Al coatings (0.1 μm) applied to all imploding targets on OMEGA are particularly susceptible to damage due to prepulses. To determine if prepulses had any effect on these layers, their integrity (reflectivity) was optically probed from $t \simeq 15$ ns up to the arrival of the main pulse ($t = 0$). The experimental configuration for those measurements is shown schematically in Fig. 81.33. An Al-coated flat CH target was irradiated with one or six beams symmetrically arranged around the target and at ~20° with respect to the target normal (see Fig. 81.33). The Al coating was also used as one mirror of an interferometer whose fringes were temporally resolved with a streak camera.* The interferometer was illuminated with a 10-ns, second-harmonic pulse (532 nm) of a Nd:YAG laser.

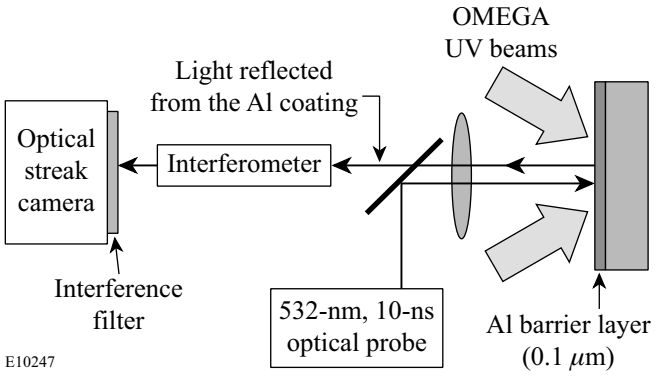

Figure 81.33
Schematic experimental setup for measuring the integrity of thin Al surface layers prior to irradiation with one or six OMEGA laser beams. The Al layer on the target acts as one end mirror for the interferometer. The target and the fringes are imaged onto a streak camera to monitor the integrity (reflectivity) of the Al. An interference filter, which protects the streak camera against excessive stray light, is required for high fringe contrast.

*This instrument [the active shock breakout (ASBO) instrument] was developed and installed on OMEGA by the Lawrence Livermore National Laboratory.

Figure 81.34 shows streaked interferometer images for two shots with Al-coated (0.1 μm) plastic targets (20 μm) irradiated with 1-ns square-top UV pulses containing 90 J (top image) and 2.7 kJ (lower image). The OMEGA beams were outfitted with phase plates[14] that produce a spot size (FWHM) of 0.5 mm. Smoothing by spectral dispersion (SSD) was not used; OMEGA was operated with narrow bandwidth. The probe beam for the interferometer was timed primarily to determine if early prepulses ($t \leq -10$ ns) were present, as suggested by Elton *et al.*[11] The beam energies for shot 16882 produced an intensity of 8×10^{14} W/cm^2 on target, which is similar to that used for spherical implosion shots. (These intensities are averaged over the envelope of the beam; the actual peak intensities in the speckles can be 4 to 5 times higher.[15]) Shot 16881 (Fig. 81.34, top image) was a low-energy shot to test the instrument under conditions where any prepulses (if present) were expected to be below the damage threshold for the Al coating; no change in reflectivity was observed. (Note that the streak camera trigger was adjusted between the two shots in Fig. 81.34, explaining the lack of early data for shot 16881. Furthermore, the interferometer illumination beam came ~1 ns earlier in shot 16882 compared to shot 16881.)

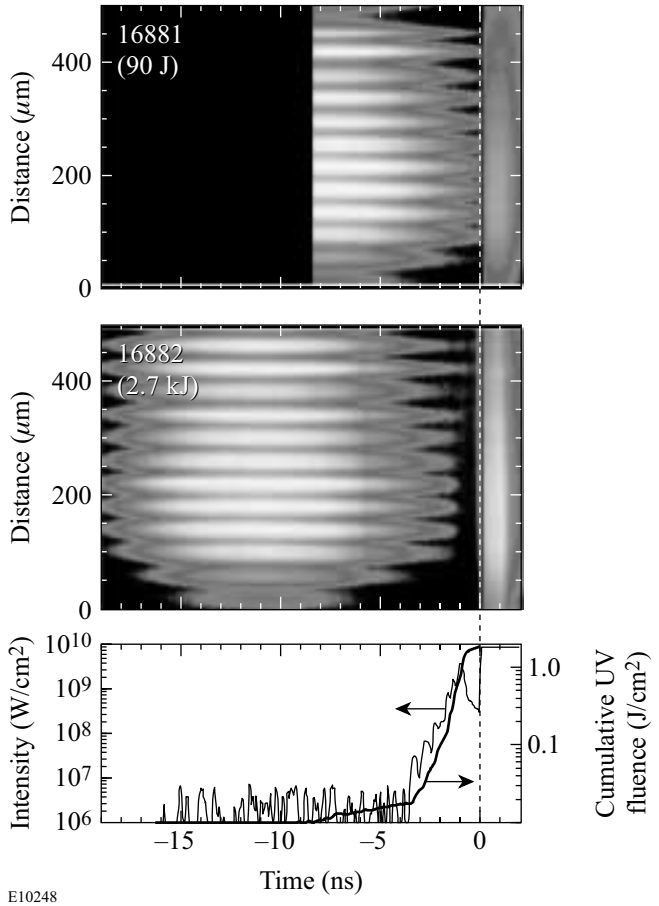

Figure 81.34
Streaked interferometer fringes for two different irradiation conditions. Upper image: A low-energy shot shows interference fringes leading right up to the start of the main laser pulse. The signal to the right of $t = 0$ is due to plasma self-emission. Lower image: A high-energy shot under OMEGA implosion conditions ($I \sim 10^{15}$ W/cm^2). The two traces are the measured UV prepulse intensity on target and the cumulative fluence on target for shot 16882. The absence of fringes in the lower part of the lower image indicates complete disruption of the Al layer at fluences ≥1 J/cm^2.

As seen in Fig. 81.34, the streaked interferometer image of shot 16882 shows no evidence of an early (-16 ns $< t < -2$ ns) prepulse affecting the Al surface. There is also no evidence of a prepulse in the corresponding UV diode trace for that shot. The latter, which was normalized to the peak UV intensity on target, is plotted in the graph directly below the image. The cumulative time integral (i.e., fluence) is shown in the bottom trace. This level of prepulse is higher than typical OMEGA performance but is useful because it allowed the measurement of the effects a prepulse has on the Al layer. The interferometer fringes completely disappear once the cumulative prepulse fluence reaches ~1 J/cm^2 ($t \approx -1$ ns in Fig. 81.34), corresponding to a prepulse intensity of $\sim 2 \times 10^9$ W/cm^2. Figure 81.34 also shows that the fringe contrast degrades well before the fringes disappear completely. It is likely that the disruption of the Al surface is not spatially uniform, and one expects a gradual decrease in fringe visibility as the Al layer is destroyed. Unfortunately the images in Fig. 81.34 do not allow a precise evaluation of the prepulse fluence or the intensity at which the disruption of the Al layer begins. These measurements are therefore supplemented with others to determine the effect prepulses have on target damage and target performance (see below).

Aluminum-Barrier-Layer Damage Threshold

Measurements of the UV breakdown threshold[16] of thin barrier layers coated on plastic targets were carried out on LLE's tabletop terawatt laser system.[17] To provide relevant interaction conditions, the output from the 1-μm-wavelength, Nd:glass laser system was frequency tripled to 351 nm and focused onto the targets with a 60-cm-focal-length lens (f number ~9) after passing through a binary distributed phase plate.[14] In these experiments, the first minimum in the Airy pattern had a 380-μm diameter, and the characteristic speckle size was ~3 μm. The experiments were carried out with 1.4-ps and 40-ps Gaussian laser pulses.

The target disruption (surface breakdown) was measured by a change in transmission through the target as a function of laser fluence. An example of the results is shown in Fig. 81.35, where the transmission as a function of laser fluence is shown for a 15-μm-thick parylene target coated with 0.02 μm of Al. The transmission was normalized to the transmission of the optical system in the absence of a target. The data show that the transmission begins to decrease when the fluence exceeds ~0.1 J/cm^2 (defined as the damage fluence). The transmission data for both the 1.4- and 40-ps pulses were found to be indistinguishable, confirming that laser fluence, rather than intensity (factor of ~30 difference), determines the breakdown threshold. Other metal coatings show similar behavior.

Microscopic inspection of targets exposed to single shots showed damage to the plastic (CH) substrate at twice the threshold for observable changes in transmission.

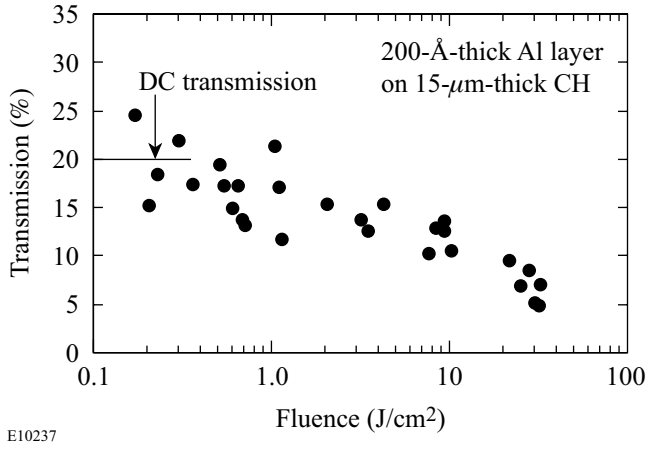

Figure 81.35
The UV transmission as a function of laser fluence for a 15-μm-thick parylene target coated with 0.02 μm of Al. The transmission begins to decay at fluence levels above 0.1 J/cm^2.

Target Performance

The effect of prepulses on capsule implosions was investigated with a series of 17 OMEGA implosions. The imploding capsules were of nearly identical diameter (896 to 908 μm) and wall thickness (19.6 to 20.5 μm) and were filled with 10 atm of D_2. Their shells consisted of an outside CH layer ranging in thickness from 14 to 19.6 μm with an inner CH layer doped with 1% Si with a thickness ranging from 0 to 8.8 μm. All capsules were coated with 0.1 μm of Al. Two pulse shapes of 3-ns overall duration were used in these shots; one had a foot of 1 ns at the half peak intensity while the other had a similar foot at 1/8 of the peak. SSD beam smoothing was used on all shots. The on-target UV energy ranged from 17 to 19.5 kJ for these experiments.

The prepulse monitor was used to characterize the prepulse power on these shots. The fluence was determined from the cumulative integral of that power. A scintillator-photomultiplier detector at a distance of 3 m from target center measured the DD neutron yield on these shots.

To characterize the neutron yield performance for these experiments the yields for each pulse shape and target combination were normalized to the highest neutron yield shot with that combination. In Fig. 81.36 these normalized neutron yields are plotted as a function of the measured prepulse fluence. In general, target shots with lower prepulse levels outperform those with higher prepulse levels. From this limited set of data it appears that prepulse fluence levels in excess of 0.2 J/cm^2 cause a reduction of the neutron yield by a factor of 2 compared to shots with lower prepulse levels.

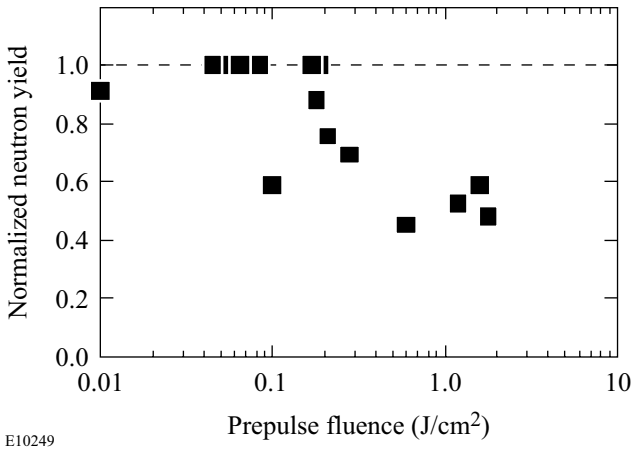

Figure 81.36
Normalized neutron yield as a function of prepulse fluence level (J/cm^2) indicates degraded target performance for prepulse fluences above 0.2 J/cm^2.

Discussion

This work quantifies the on-target irradiation contrast of the OMEGA laser and establishes an acceptable prepulse fluence criterion for high-performance ICF implosions. Of primary concern was the assertion[11] that, 5 to 10 ns prior to the main laser pulse, OMEGA produces prepulses that lead to plasmas with electron temperatures exceeding 100 eV. A prepulse monitor subsequently installed on OMEGA indicates that no prepulses have been observed between 20 ns and ~2 ns before the arrival of the main pulse; however, in the final 1 to 2 ns

before the main laser pulse, OMEGA occasionally produces a prepulse that can affect target performance.

The photodiodes that monitor the prepulse contrast in both the initial IR and final UV portions of the system are cross calibrated to the main laser pulse. The corresponding prepulse sensitivities are 10^{-6} and 10^{-8} below the main pulse intensity. Experiments that optically probe the integrity of thin Al coatings using interferometry demonstrate that the 0.1-μm Al layers are completely destroyed by prepulse fluences in excess of 1 J/cm^2. Independent transmission measurements on plastic targets with 0.02-μm Al layers (Fig. 81.35) indicate that the transmission through these Al layers is altered when the incident fluence exceeds 0.1 to 0.2 J/cm^2. Damage to the plastic substrate was typically observed, however, at two times higher fluences.

The neutron yields of imploding targets (Fig. 81.36) indicate that prepulse fluences of $\geq$0.2 J/cm^2 measurably affect and decrease target performance. This prepulse "threshold" fluence is consistent with that necessary to change the transmission through thin Al layers (Fig. 81.35). This threshold fluence is significantly lower than that required to completely destroy the fringe contrast of the interferometer experiments testing the integrity of the Al layer (Fig. 81.34). The interferometer experiments show decreased contrast, however, well before the fringe visibility disappears completely. Thus the transmission experiments and the interferometer experiments support each other and are consistent with the target performance data. We conjecture that the small-scale perturbations in the Al surface layer likely serve as seed for the RT instability during the ablation phase of the implosion. These perturbations are thus amplified to levels that affect the symmetry of the implosion and thus reduce the neutron yield.

Conclusions

The contrast monitors for the OMEGA laser system are capable of sensing UV prepulses that are $\geq 10^{-8}$ of the main laser pulse. Our observations indicate that the prepulse level is below the detection threshold of 10^{-8} of the main pulse for all shots up to ~2 ns before the onset of the main pulse. During the last 1 or 2 ns before the main pulse, OMEGA intermittently produces prepulses up to 10^{-6} of the main-pulse intensity (with a fluence ~0.2 J/cm^2). The source of this problem is under investigation.

Optical probe experiments using interferometry show that the thin Al layers on the target surface maintain measurable fringe visibility until the prepulse fluence reaches ~1 J/cm^2, which is attained when the prepulse reaches $\sim 2 \times 10^{-6}$ of the peak laser power. These findings are consistent with independent transmission measurements on thin (0.02-μm) Al layers that exhibit decreased transmission at fluences exceeding 0.1 or 0.2 J/cm^2. Imploding targets also have decreased neutron yields for prepulse fluences exceeding 0.1 or 0.2 J/cm^2. This is believed to be the result of small-scale perturbations created by laser damage in the target surface.

From the experiments reported here we conclude that precision ICF experiments on OMEGA require that the cumulative prepulse fluences be kept below 0.2 J/cm^2 corresponding to an optical intensity contrast $\geq 10^7$ on OMEGA. Prepulse requirements for NIF direct-drive targets are expected to be similar to these requirements if Al barrier layers are necessary.

ACKNOWLEDGMENT

This work was supported by the U.S. Department of Energy Office of Inertial Confinement Fusion under Cooperative Agreement No. DE-FC03-92SF19460, the University of Rochester, and the New York State Energy Research and Development Authority. The support of DOE does not constitute an endorsement by DOE of the views expressed in this article.

REFERENCES

1. R. L. McCrory, R. E. Bahr, T. R. Boehly, T. J. B. Collins, R. S. Craxton, J. A. Delettrez, W. R. Donaldson, R. Epstein, V. N. Goncharov, R. Q. Gram, D. R. Harding, P. A. Jaanimagi, R. L. Keck, J. P. Knauer, S. J. Loucks, F. J. Marshall, P. W. McKenty, D. D. Meyerhofer, S. F. B. Morse, O. V. Gotchev, P. B. Radha, S. P. Regan, W. Seka, S. Skupsky, V. A. Smalyuk, J. M. Soures, C. Stoeckl, R. P. J. Town, M. D. Wittman, B. Yaakobi, J. D. Zuegel, R. D. Petrasso, D. G. Hicks, and C. K. Li, "OMEGA Experiments and Preparation for Direct-Drive Ignition on the National Ignition Facility," to be published in *Inertial Fusion Sciences and Applications 1999*, Bordeaux, France, 12–17 September 1999.

2. S. V. Weber *et al.*, *ICF Quarterly Report* **7**, 43, Lawrence Livermore National Laboratory, Livermore, CA, UCRL-LR-105821-97-2 (1997).

3. S. E. Bodner, D. G. Colombant, J. H. Gardner, R. H. Lehmberg, S. P. Obenschain, L. Phillips, A. J. Schmitt, J. D. Sethian, R. L. McCrory, W. Seka, C. P. Verdon, J. P. Knauer, B. B. Afeyan, and H. T. Powell, Phys. Plasmas **5**, 1901 (1998).

4. E. B. Goldman *et al.*, J. Appl. Phys. **45**, 1158 (1974).

5. J. M. Soures, T. C. Bristow, H. Deckman, J. Delettrez, A. Entenberg, W. Friedman, J. Forsyth, Y. Gazit, G. Halpern, F. Kalk, S. Letzring, R. McCrory, D. Peiffer, J. Rizzo, W. Seka, S. Skupsky, E. Thorsos, B. Yaakobi, and T. Yamanaka, in *Laser Interaction and Related Plasma Phenomena*, edited by H. J. Schwarz (Plenum Press, New York, 1981), Vol. 5, pp. 463–481.

6. Yu. V. Afanas'ev and O. N. Krokhin, Sov. Phys.-JETP **25**, 639 (1967).

7. J. Bunkenburg, J. Boles, D. C. Brown, J. Eastman, J. Hoose, R. Hopkins, L. Iwan, S. D. Jacobs, J. H. Kelly, S. Kumpan, S. Letzring,

D. Lonobile, L. D. Lund, G. Mourou, S. Refermat, W. Seka, J. M. Soures, and K. Walsh, IEEE J. Quantum Electron. **QE-17**, 1620 (1981).

8. G. Mourou, J. Bunkenburg, and W. Seka, Opt. Commun. **34**, 252 (1980).

9. J. E. Balmer, T. P. Donaldson, W. Seka, and J. A. Zimmermann, Opt. Commun. **24**, 109 (1978).

10. D. K. Bradley, T. Boehly, D. L. Brown, J. Delettrez, W. Seka, and D. Smith, in *Laser Interaction and Related Plasma Phenomena*, edited by H. Hora and G. Miley (Plenum Press, New York, 1991), Vol. 9, pp. 323–334.

11. R. C. Elton, H. R. Griem, and E. J. Iglesias, Bull. Am. Phys. Soc. **44**, 38 (1999).

12. T. R. Boehly, R. S. Craxton, T. H. Hinterman, P. A. Jaanimagi, R. L. Keck, J. H. Kelly, T. J. Kessler, R. L. Kremens, S. A. Kumpan, S. A. Letzring, R. L. McCrory, S. F. B. Morse, W. Seka, S. Skupsky, J. M. Soures, and C. P. Verdon, in *Proceedings of the IAEA Technical Committee Meeting on Drivers for Inertial Confinement Fusion*, edited by J. Coutant (IAEA, Vienna, 1995), pp. 79–86.

13. J. R. Murray, in *Third Annual International Conference on Solid State Lasers for Application to Inertial Confinement Fusion*, Supplement to *Proceedings of SPIE, Volume 3492* (SPIE, Bellingham, WA, 1998), pp. 1–10.

14. T. J. Kessler, Y. Lin, J. J. Armstrong, and B. Velazquez, in *Laser Coherence Control: Technology and Applications*, edited by H. T. Powell and T. J. Kessler (SPIE, Bellingham, WA, 1993), Vol. 1870, pp. 95–104.

15. H. A. Rose and D. F. DuBois, Phys. Fluids B **5**, 590 (1993).

16. Y. Fisher, T. R. Boehly, D. K. Bradley, D. R. Harding, D. D. Meyerhofer, and M. D. Wittman, Bull. Am. Phys. Soc. **43**, 1784 (1998).

17. Y.-H. Chuang, D. D. Meyerhofer, S. Augst, H. Chen, J. Peatross, and S. Uchida, J. Opt. Soc. Am. B **8**, 1226 (1991).

Design and Synthesis of Near-Infrared Absorbing Dyes for the Liquid Crystal Point-Diffraction Interferometer (LCPDI)

Introduction

Although considerable progress in achieving the goals of ICF has been made in recent years, considerable work still remains in improving direct-drive laser systems to the point where fuel ignition can occur. Because of difficulties in manufacturing large-aperture optical elements such as those used in OMEGA, these optics can add aberrations to each laser beam that can result in wavefront errors in the incident beams. Such wavefront errors can manifest themselves in unequal illumination of the target, which in turn reduces the uniformity of the energy being delivered by the laser. Although numerous diagnostic instruments are used on OMEGA to analyze beam-uniformity problems, a more effective method of measuring wavefront aberrations than is currently available is required. Shearing interferometery is currently used to analyze OMEGA beamlines, but the method suffers from (1) an inability to perform gradient measurements in more than two directions; (2) a low sensitivity to high-order phase errors; and (3) low spatial resolution. One approach taken to avoid these difficulties is to use a point-diffraction interferometric setup that relies on a liquid crystal (LC) electro-optical device as the primary modulation element. The fundamental design of this liquid crystal point-diffraction interferometer (LCPDI), as first introduced by Mercer and Creath,[1,2] is similar to that of the general PDI design. In the LCPDI, however, an LC layer replaces the semitransparent filter of the conventional design, and the point used for diffraction (i.e., creation of the reference beam) is a microsphere embedded in the liquid crystal layer (Fig. 81.37). The incident beam is focused on the area of the cell that contains the microsphere, and optical interference occurs between the portions of the beam that pass through the glass microsphere and the liquid crystal fluid.

Phase shifting is accomplished by applying a voltage to the LC device, which undergoes a change in birefringence with applied voltage. A distinct advantage of the LCPDI is its common-path nature, i.e., both object and reference beams follow the same path as opposed to two different paths as in interferometers such as the Mach–Zehnder. This attribute makes the LCPDI less sensitive to environmental disturbances such as mechanical vibration, temperature fluctuations, and air turbulence. It is also inherently phase shifting, allowing higher spatial sampling and generally more accurate wavefront characterization than other interferometric techniques. The single-path design also requires fewer optical elements than the Mach–Zehnder, thereby reducing size and cost of the instrument. Mercer, Rashidnia, and Creath[3] have shown that for operation in the visible region the LCPDI is significantly more robust when compared with a phase-shifting Mach–Zehnder interferometer.[3]

Because the imaged area of the LCPDI device is substantially larger than the cross-sectional area of the microsphere, the portion of the beam that passes through the LC fluid must be attenuated to obtain sufficient contrast to analyze output images. In practice, this attenuation has been accomplished by adding a "guest" dye to the LC fluid "host" material used in the device. The LC host material is a commercial nematic LC

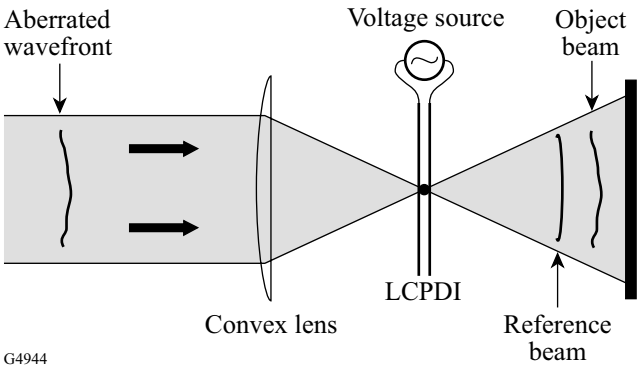

Figure 81.37
Schematic diagram of the liquid crystal point-diffraction interferometer (LCPDI). The laser beam is focused onto an area of the liquid crystal electro-optic device containing a glass or plastic sphere in the LC fluid gap. The portion of the beam passing through the microsphere functions as the reference arm of the interferometer. Application of an electric field to the birefringent LC material produces controlled molecular reorientation with subsequent generation of interference fringes. (Microsphere not drawn to scale.)

mixture of cyanobiphenyl and cyanoterphenyl components (Merck E7), which possesses a relatively high birefringence and positive dielectric anisotropy (Fig. 81.38).

For successful device operation, the guest dye must meet a number of important criteria:

- a strong absorbance maximum at or near the wavelength of incident laser radiation;
- high solubility in the liquid crystal host to maximize contrast and avoid long-term precipitation;
- excellent chemical and thermal stability; and
- low impact on the long-range molecular ordering in the LC host.

Two additional properties that would be highly desirable in dyes intended for LCPDI devices are (1) a low or nonexistent dichroism of the absorption band of interest so as to assure a constant attenuation with applied electric field, and (2) a liquid crystalline phase to allow larger amounts of the dye to be added without degrading the inherent molecular ordering of the host.

Although hundreds of dyes for visible-region LCPDI devices are commercially available, the selection of available dyes for the near IR is considerably more limited, and only a small subset of these absorb at the required 1054-nm wavelength for operation in OMEGA. A further complication is that nearly all of these commercially available near-IR dyes are ionic or highly polar and, as such, show poor solubility in hydrocarbon-like liquid crystal hosts (0.01 to 0.05 wt%). One such example of this type of dye is shown in Fig. 81.39. The low solubility of these dyes essentially limits them to a maximum blocking extinction, or optical density (OD), in the LC host of <0.1, which is two decades less than required for producing acceptable fringe contrast for diagnostic purposes. The lack of a suitable near-IR dye candidate with sufficient LC host solubility dictated that a new dye or series of dyes be synthesized for the LCPDI device to meet its design goals.

Dye Selection and Design

The dye systems that were chosen for study are based on zerovalent transition metal dithiolene complexes,[4,5] which are known to exhibit strong absorbance bands in the 600- to 1500-nm region of the spectrum and to be soluble in nonpolar organic solvents, depending on the dye's molecular structure. Our investigations focused on compounds using nickel as the central transition element (Fig. 81.40). Nickel dithiolenes are of special interest for this application because of their high solubility (up to 10 wt%) in liquid crystalline hosts[6] and because the dyes themselves can possess liquid crystalline properties if appropriate terminal functional groups are selected.[6,7] The latter is a distinct advantage because it would allow higher concentrations of the dye to be added to the liquid crystalline host without substantially reducing its degree of order.

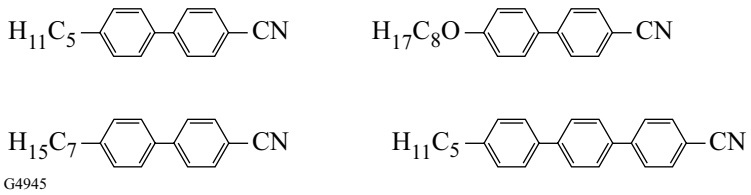

Figure 81.38
Composition of Merck E7, a high-birefringence nematic LC mixture with positive dielectric anisotropy used as the active host medium for the LCPDI device.

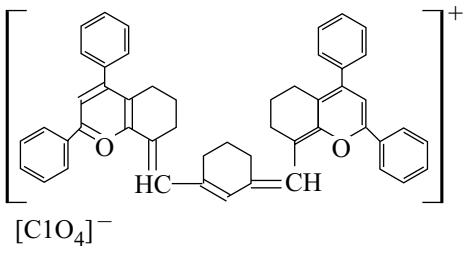

Figure 81.39
Molecular structure of a commercially available laser dye *Q*-switch 5 (Exciton, Inc). Because of their ionic and highly polar nature, nearly all laser dyes exhibit poor solubility in hydrocarbon-like liquid crystal host materials such as E7.

The strong near-infrared absorbance maxima observed in the nickel dithiolenes is a function of both extensive electron delocalization within the dithiolene ring system and interaction of this delocalized system with available d-orbitals on the central metal.[8] This interaction can be depicted both graphically and mathematically by using the linear combination of the atomic orbital–molecular orbital (LCAO–MO) theory. Here the atomic orbitals of the individual atoms are combined to form a series of lower-energy "bonding" and higher-energy "anti-bonding" molecular orbitals. Absorption of photons of sufficient energy results in promotion of electrons from occupied (bonding) molecular orbitals to unoccupied (anti-bonding) molecular orbitals. The lowest-energy transition, and thus the one that occurs at the longest wavelength, occurs between the highest occupied molecular orbital (HOMO) and the lowest unoccupied molecular orbital (LUMO) and is referred to as the bandgap. This HOMO/LUMO transition is responsible for the strong near-IR absorption in the nickel ditholenes.[4,8] Figures 81.41 and 81.42 show ground-state electronic-charge-distribution maps and HOMO/LUMO electron-density-

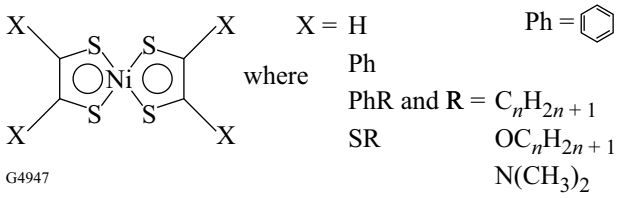

Figure 81.40
The molecular structure of transition metal dithiolenes with nickel as the central metal. The physical properties of the complex are determined by the nature of the terminal functional groups, designated as X, in the figure.

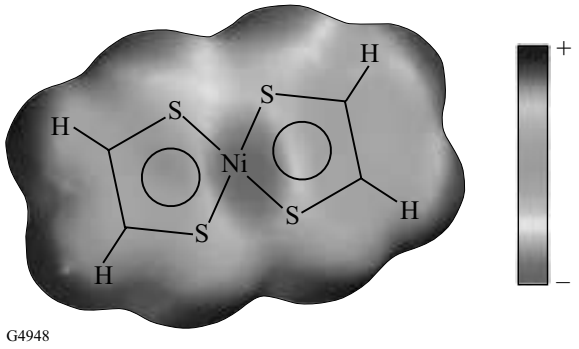

Figure 81.41
Ground-state charge-distribution map of the nickel dithiolene core. The shaded areas indicate electron-rich areas in the molecule.

(a)
Highest Occupied Molecular Orbital (HOMO)

(b)
Lowest Unoccupied Molecular Orbital (LUMO)

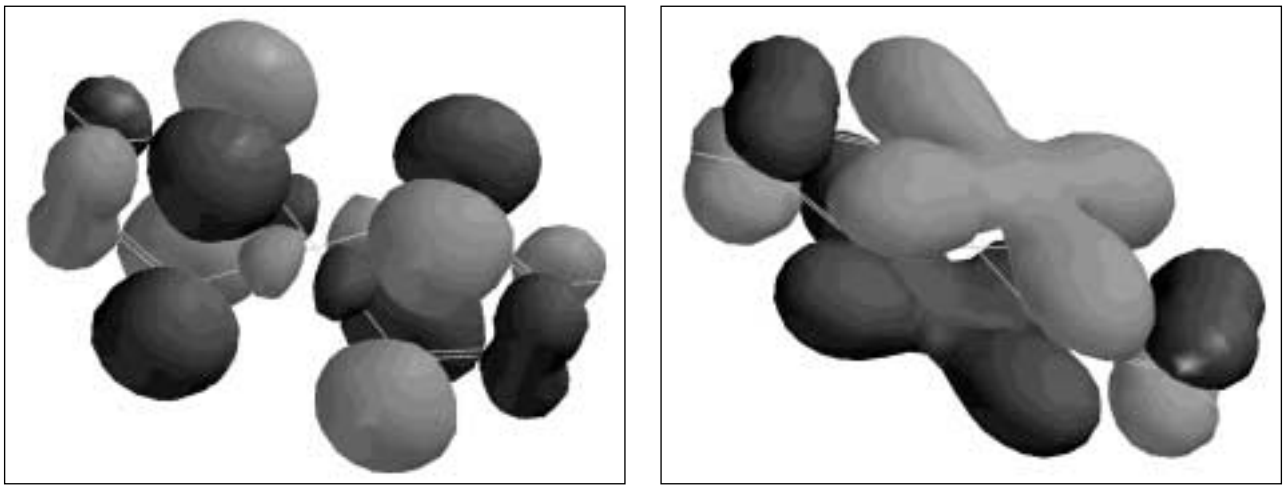

Figure 81.42
Electron-density probability maps of HOMO (left) and the LUMO (right) for the nickel dithiolene core.

probability maps, respectively, over the nickel dithiolene core as generated by Spartan 5.0 computational chemistry software (Wavefunction, Inc.). The energy levels in electron volts for each molecular orbital can also be represented graphically, as shown in Fig. 81.43 for the nickel dithiolene core of Fig. 81.41. The nature of the functional groups attached to the nickel dithiolene core has a large effect on both the position of the electronic absorbance maximum and the solubility of the dye in the host matrix. Figure 81.44 compares the spectroscopic and solubility properties of two *para*-substituted nickel dithiolenes that have been previously studied in liquid crystal host systems.[6]

Because the above two compounds represented nearly the sum total of literature data on the behavior of near-IR dyes in LC hosts, we chose to use these materials as the basis of our design and synthesis efforts. Our goal was to test different combinations of functional groups on the nickel dithiolene core, both empirically and computationally, to observe their effect on both solubility and optical absorbance. To this end, we initiated the synthesis of a series of materials based on compound (a) in Fig. 81.44 with terminal alkyl and alkoxy groups for initial studies of solubility and spectroscopic properties in the E7 LC host. In a parallel effort, we attempted to use computational chemistry methods to aid in predicting the appropriate functional group combinations that would yield materials with the desired solubility and spectroscopic parameters. These calculations were performed using the computational chemistry software packages Spartan 5.0 for molecular geometry optimization and Jaguar 3.5 (Schrödinger, Inc.) for solubility calculations.

Structural energy minimization calculations using semiempirical methods were undertaken using Spartan 5.0 prior to conducting the solubility calculations to ensure that the structural geometry of the compounds under evaluation was in its lowest-energy conformation. We chose the semiempirical approach because it can accurately predict equilibrium geometry using much less computing resources than *ab initio* and density functional methods and, when proper parameters for transition metals are applied, can also take into account contributions from bonding to d-orbitals. All calculations were conducted using a DEC AlphaServer running the Digital UNIX operating system.

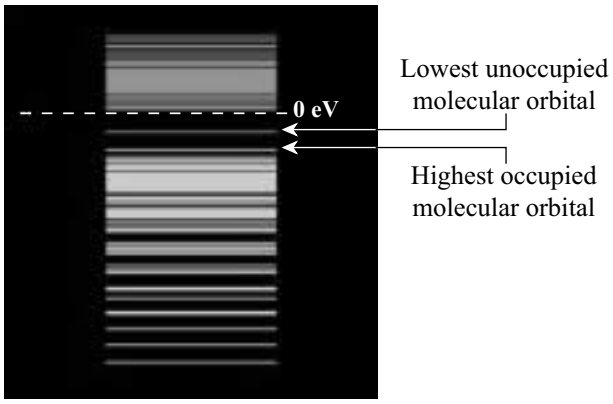

G4950

Figure 81.43
Energy levels for bonding (HOMO) and antibonding (LUMO) molecular orbitals in the nickel dithiolene core shown in Fig. 81.41. The energy difference between the HOMO and LUMO is termed the bandgap and determines the portion of the spectrum (UV, visible, or near IR) where the electronic absorbance bands are observed.

(a)
λ_{max} = 1064 nm
Solubility in Merck E7 = 0.05 wt%

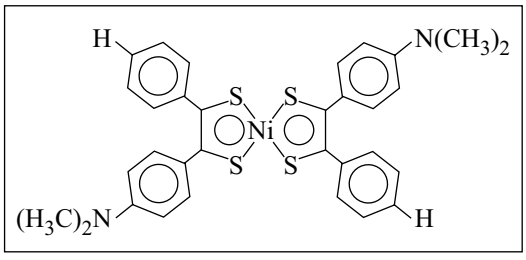

(b)
λ_{max} = 861 nm
Solubility in Merck E7 = 5 to 10 wt%

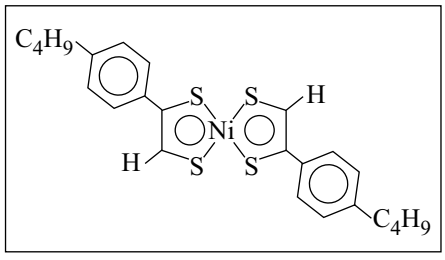

G4951

Figure 81.44
Effect of molecular structure on solubility and spectroscopic properties of two substituted nickel dithiolenes.

The solubility of a given solute in a solvent can be approximated by calculating its solvation energy and comparing this value with the bonding, or "reorganization," energy. The solvation energy ΔG_{solv} is defined in Eq. (1) as[9]

$$\Delta G_{solv} = \Delta G_{elec} + \Delta G_{cav} + \Delta G_{disp} + \Delta G_{vib} + \Delta G_{lib} + \Delta G_{other}, \quad (1)$$

where ΔG_{solv} = solvation energy, ΔG_{elec} = electrostatic solute–solvent interaction, ΔG_{cav} = energy to form a solute shaped cavity, ΔG_{disp} = London and van der Waals interactions, ΔG_{vib} = change in vibrational energy due to damping, ΔG_{lib} = conversion of rotations and translations to librations, and ΔG_{other} = solvent enthalpic and entropic structure (PV term, etc.).

Although Spartan 5.0 has the ability to conduct geometry optimization in solution, it is not capable of dealing with d-orbitals in the solvation calculations. Because the metal d-orbitals play an extremely important role in determining the properties of the nickel dithiolenes, they must be taken into account in these calculations in order to obtain valid results. For these solubility calculations we instead opted to use Jaguar 3.5, a UNIX-based modeling package that does have this capability. Using the dielectric constant, molecular weight, and density of the solvent, Jaguar determines a "probe radius" parameter that is used to calculate the solvation energy.[10]

Solvated molecular systems are treated by Jaguar by means of a self-consistent reaction field method using its own Poisson–Boltzmann solver. The Poisson–Boltzman equation [Eq. (2)][11] sets the sum of the internal and external potentials equal to zero, allowing the program to solve for the elements of the solvation energy according to the three-dimensional grid mapped out by the equation using the finite difference method:

$$\nabla \cdot \varepsilon(r)\, \nabla\phi(r) - \varepsilon\kappa^2 \sinh\left[\phi(r)\right] + 4\pi q \rho^f(r) / kTf(\phi) = 0, \quad (2)$$

where ε = dielectric constant, q = proton charge, k = Boltzman's constant, T = absolute temperature, ρ^f = fixed charge density, $\phi(r)$ = dimensionless electrostatic potential in units of kT/q, r = position vector, and $\kappa^2 = 1/\lambda^2 = 8\pi q^2 I/\varepsilon kT$, where λ = Debye length, and I = ionic strength of the bulk solution.

Because currently available software is incapable of conducting these calculations in solvent systems that are either (1) anisotropic in their physical properties or (2) mixtures of compounds, a direct calculation of dye solubility in the E7 nematic host mixture was not feasible. Our approach was instead to use single-component, *isotropic* solvents with molecular structures similar to that of the components in the E7 host so as to establish qualitative solubility trends with changes in terminal functional groups. Cyclohexane (a common organic solvent) and Merck CB-15 (an isotropic chiral cyanobiphenyl compound structurally similar to the components of E7) were chosen as the solvent host media for the calculations (Fig. 81.45). One difficulty encountered early in the solubility calculations was that the probe radius calculation assumes that the solvent host molecules are rigid and spherical. Although cyclohexane nicely fits this description (Fig. 81.45), CB-15 is a relatively long, cigar-shaped molecule and as such has a substantially larger probe radius value (3.647 Å, as calculated by Jaguar). Unfortunately, current limitations in the Jaguar software package restrict the maximum probe radius for the solvent host to a value of <3.1 Å, and we found it necessary to artificially limit the probe radius value for CB-15 to 2.8 Å in order for the calculations to proceed. The required reduction in probe radius has a minimal impact on the calculation, as the dielectric constant is the parameter that has the greatest influence on the calculated result. Table 81.V shows the calculated solvation energies obtained for compounds containing the nickel dithiolene core with a selected group of terminal functional groups as solutes in cyclohexane and CB-15. The value ΔG_{solv} can be used as a qualitative indicator of general solubility of the dye solutes in the same host, with a larger positive value generally indicating a greater solubility in the solvent host matrix. As shown in Table 81.V, the calculated ΔG_{solv} values imply that sulfur-containing substituents are expected to provide a substantial enhancement in solubility, with the greatest enhancement expected for alkylthio (-SR) terminal groups bonded directly to the nickel dithiolene core.

Dye Synthesis

The synthesis of the nickel dithiolene dyes and their precursors were conducted using literature methods[12–15] with some modifications. The structural identity of synthesized products was verified using UV-visible–near-IR spectrophotometry, Fourier transform infrared (FTIR) spectrometry, and nuclear magnetic resonance (NMR) spectrometry. Product purity was assessed by high-performance liquid chromatography (HPLC) and, for crystalline products, by melting point via hot-stage polarizing microscopy. Phase transitions were

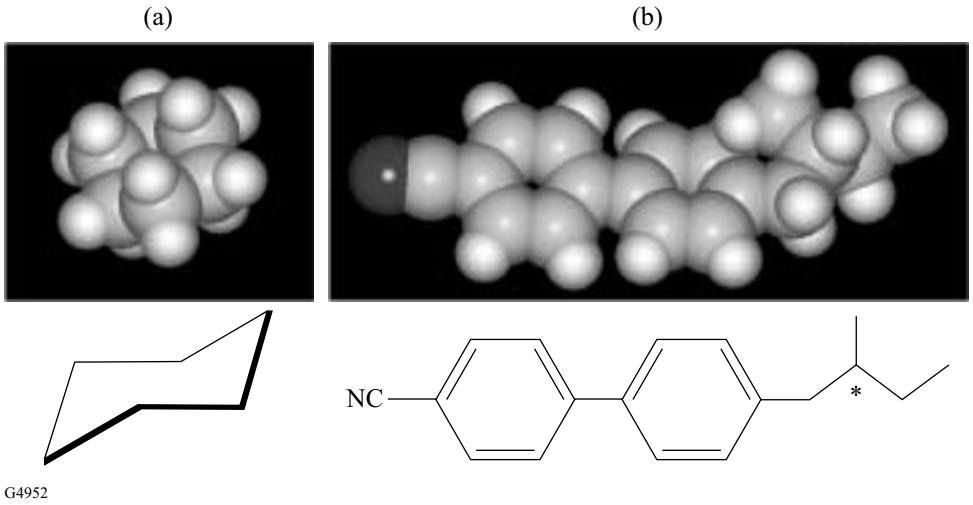

Figure 81.45
The solvent hosts used for the solubility calculations: (a) cyclohexane and (b) Merck CB-15. A space-filling graphical model of each solvent host is shown at the top of the figure, with the chemical structure drawn below. Note that the hydrogen atoms have been omitted in the structural formulas for clarity. The asterisk in the CB-15 structure indicates the presence of an asymmetric (chiral) carbon.

characterized by both differential scanning calorimetry (DSC) and hot-stage polarizing microscopy.

For materials with terminal substituents containing phenyl groups (-PhR and -PhOR), we used the method of Ohta *et al.*,[12] as shown in Fig. 81.46. Compounds with terminal alkylthio substituents (-SR) were synthesized based on methods reported by Wainwright and Underhill,[13] N. Svenstrup *et al.*,[14] and A. Charlton *et al.*,[15] which are shown in Fig. 81.47. Our modifications to the original published procedures afforded substantial improvements in yields of pure product in most cases. Table 81.VI gives the physical properties and yields of dyes synthesized by these two methods.

Table 81.V: Results of solvation energy calculations on nickel dithiolene cores with various terminal functional groups in cyclohexane and CB-15 using Jaguar. A larger positive value indicates a greater solubility in the host matrix.

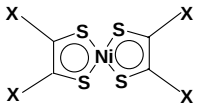	ΔG_{solv} Cyclohexane (kcal/mole)	ΔG_{solv} Merck CB-15 (kcal/mole)
X = SC_8H_{17}	6.9435	–7.6725
X = SC_7H_{15}	6.2764	–7.7164
X = SC_4H_9	3.9248	–7.7190
X = PhC_4H_9	3.2985	–14.4373
X = $PhN(CH_3)_2$	0.0812	–17.4080
X = $PhOC_9H_{19}$	5.2212	–21.6724
X = $PhOC_4H_9$	0.9780	–21.6950

Solubility Studies

Prior to generation of a suitable mixture for use in the LCPDI device, the solubility limits of selected nickel dithiolene dyes in three host systems (cyclohexane, Merck CB-15, and Merck E7) were determined by means of a time-based sedimentation experiment. Samples of each dye chosen for study were prepared in the three host materials at select concentrations between 0.3 wt% to 1 wt%. Each dye was dissolved into 2 ml of each host by heating the host/dye mixture to an elevated temperature (40°C for cyclohexane and 100°C for CB-15 and E7) and stirring for several hours. Upon cooling, each sample was filtered through a 0.45-μm Teflon membrane filter to remove any insoluble material. All samples were checked periodically, both visually and by microscopic inspection at 100× magnification, for evidence of dye precipitation. For samples that showed precipitation at 0.3%, new mixtures at lower concentrations were prepared until a stable dye concentration was achieved. The results are shown in Table 81.VII, along with the ΔG_{solv} values previously calculated from Table 81.VI. Because such a large number of mixtures were required in the sedimentation experiment and only limited quantities of each dye were available, we were unable to determine an absolute upper solubility limit for each dye mixture combination. Experiments are currently underway to

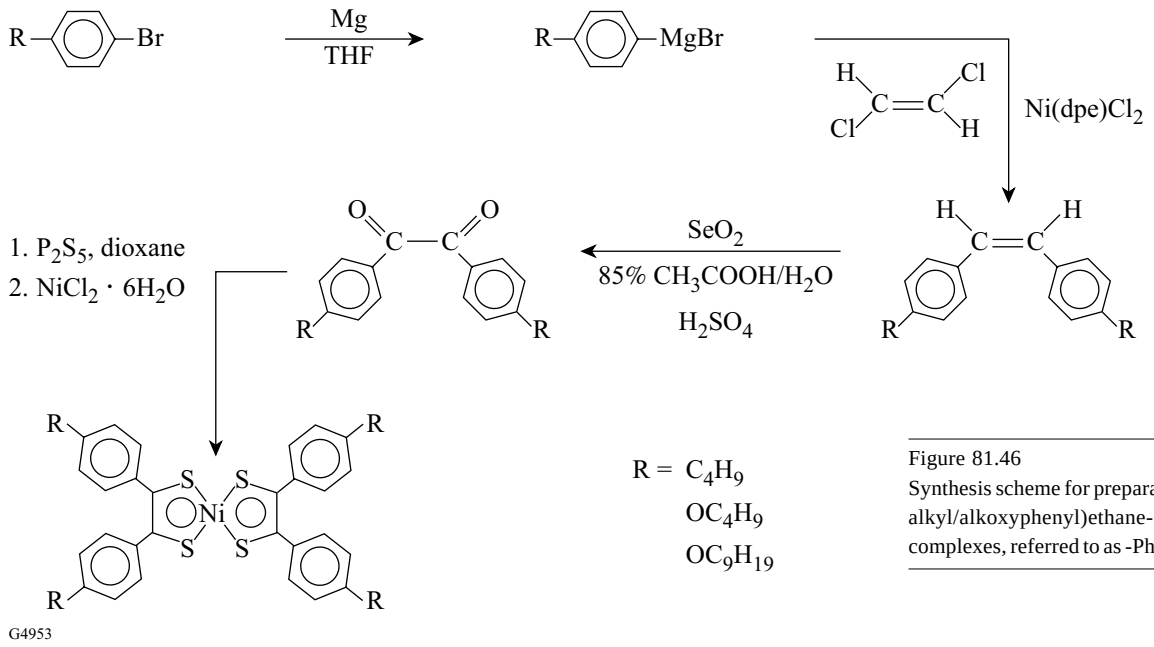

Figure 81.46
Synthesis scheme for preparation of bis-[1,2-di-(4-n-alkyl/alkoxyphenyl)ethane-1,2-dithione]nickel (0) complexes, referred to as -PhR and -PhOR in the text.

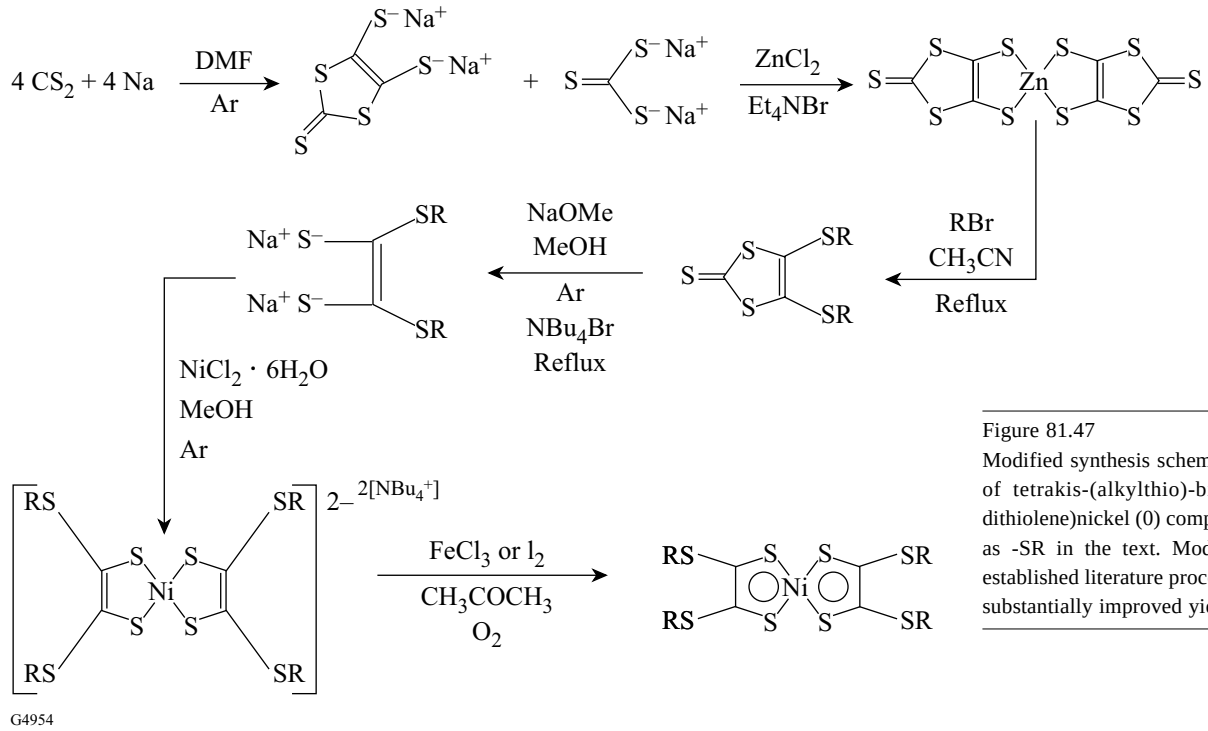

Figure 81.47
Modified synthesis scheme for preparation of tetrakis-(alkylthio)-bis-(ethylene-1,2-dithiolene)nickel (0) complexes, referred to as -SR in the text. Modifications to the established literature procedures resulted in substantially improved yields of product.

more accurately determine the absolute solubility limit using only one supersaturated mixture for each dye/host pair by employing near-IR spectroscopic techniques.

A review of Tables 81.VI and 81.VII shows that there are substantial differences not only in the solubility of each dye in the different hosts but also in the position of its λ_{max} as the host matrix is changed. In general, a 20- to 47-nm bathochromic (red) shift is observed for these dyes in the anisotropic, ordered LC host as compared to an isotropic host such as acetone or cyclohexane.[6] With regard to solubility, the experimental solubility data for the nickel dithiolenes in cyclohexane and CB-15 shows a substantial improvement in solubility when terminal -PhOR substituents are replaced with -SR groups, as was predicted by the computational modeling. This trend is also observed, but to a somewhat lesser degree, in the anisotropic

Table 81.VI: Properties of the substituted nickel dithiolenes synthesized for study as dye "guest" dopants for the LCPDI.

Terminal Group	Yield (%)		Melting point (°C)	λ_{max}, acetone (nm)	Purity %
	Observed	Literature			
$-PhC_4H_9$	51	N.R.	228.3–230.6	870	99.4
$-PhOC_4H_9$	60	59	246.3–248.7	910	94.0
$-PhOC_9H_{19}$	53	57	184.3–189.1	912	90.0
$-SC_4H_9$	68	15	101	1002	99.3
$-SC_5H_{11}$	64	15	95–98	1002	98.8
$-SC_6H_{13}$	27	20	68.5–71.1	1002	98.1
$-SC_7H_{15}$	41	27	81.5	1002	99.2
$-SC_8H_{17}$	56	31	73	1002	99.3
$-SC_9H_{19}$	29	30	80.4–81.2	1002	98.9
$-SC_{10}H_{21}$	11	25	69.4–70.3	1002	96.5

N.R. = not reported

Table 81.VII: Comparison of calculated solvation energies and experimentally determined solubility limits of nickel dithiolene dyes in three host systems. For some dye mixture combinations, an absolute upper solubility limit has not been determined due to limited dye quantities.

Terminal (X) group	λ_{max} in E7 (nm)	Cyclohexane		CB-15		Merck E7
		Solubility limit (wt%)	ΔG_{solv} (kcal/mole)	Solubility limit (wt%)	ΔG_{solv} (kcal/mole)	Solubility limit (wt%)
$-SC_8H_{17}$	1020	≥0.5%	6.9435	≥1.0%	−7.6725	≤0.5%
$-SC_7H_{15}$	1020	≥0.5%	6.2764	≤1.0%	−7.7164	≤0.5%
$-SC_4H_9$	1020	≤0.5%	3.9248	≤1.0%	−7.7190	≤0.5%
$-PhC_4H_9$	910	≤0.05%	3.2985	≤0.5%	−14.4373	≥0.3%
$-PhN(CH_3)_2$	1056	<0.5%	0.0812	≤0.5%	−17.4080	<0.1%
$-PhOC_9H_{19}$	970	≤0.025%	5.2212	≤0.3%	−21.6724	<0.3%
$-PhOC_4H_9$	970	<0.001%	0.9780	≤0.3%	−21.6950	≤0.3%

< = substantial precipitation at indicated value

≤ = marginal precipitation at indicated value

≥ = no precipitation at indicated value; actual upper solubility limit not determined

E7 LC host mixture intended for use in the LCPDI. The -SR materials will provide a larger blocking extinction at the same solution concentration than will their -PhOR counterparts since the λ_{max} of the -SR compounds in E7 is 70 to 110 nm closer to the 1054-nm operational wavelength of OMEGA than is the λ_{max} of the -PhOR substituted materials. The commercial dye with -PhN$(CH_3)_2$ substituents, although its λ_{max} is closest to 1054 nm and is nearly as soluble as the other dyes in cyclohexane and CB-15, displays the lowest solubility of the group in the E7 host.

Because no single dye has sufficient solubility in the E7 host to achieve the required OD of 1.8 to 2, it became necessary to use a mixture of several dyes to increase the total dye concentration past the general solubility limit of 0.3%–0.5% for each dye component.

LCPDI Guest–Host Mixtures

Multicomponent mixtures of various dyes from Table 81.VII were formulated and evaluated for their performance characteristics with regard to optical absorbance capability and stability in the E7 host LC fluid. Table 81.VIII gives the composition of these mixtures. The dye mixtures were prepared in the same manner as described earlier in the solubility experiments. LCPDI test cells were assembled from glass substrates bearing a 500-Å, transparent, conductive indium tin oxide (ITO) coating. The ITO surfaces were spin coated with a polyimide alignment coating, which, after baking and buffing, served as an alignment layer for the guest–host LC mixture. Glass spheres (25-μm diam) were deposited onto the coated, buffed surface of one substrate, and a second coated, buffed substrate was placed on top of the spheres with its rub direction anti-parallel to the bottom substrate to define a 25-μm gap. The substrates were bonded together using Master Bond UV15-7TK1A UV curable epoxy, and the cells were filled with the LCPDI guest–host mixture by capillary action. Absorbance spectra of the devices were determined using a Perkin-Elmer Lambda 9 UV-VIS-NIR spectrophotometer with the incident beam polarized parallel to the cell alignment axis. Figure 81.48 compares the optical properties of the three mixtures. As is evident from Fig. 81.48, the mixture containing six -SR substituted dyes and one commercial -PhN$(CH_3)_2$ dye achieves the desired OD requirements for the LCPDI.

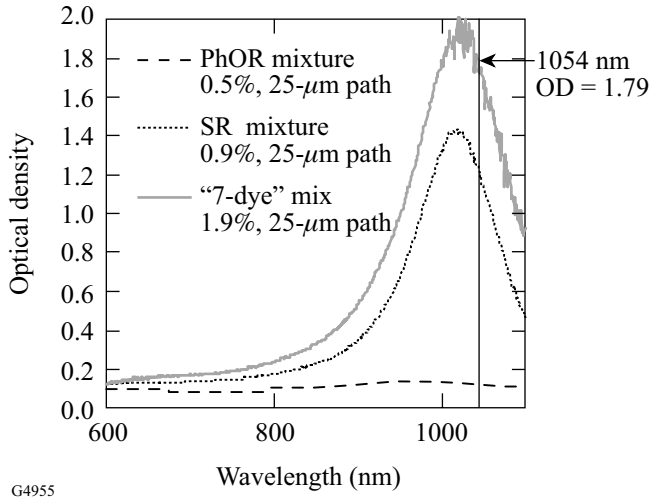

Figure 81.48
Optical-density data on three guest-host dye mixtures for the LCPDI. The measurements were made with the cell alignment axis parallel to the polarized incident beam of the spectrophotometer.

Table 81.VIII: Composition of three dye mixtures formulated for optical density (OD) evaluation in LCPDI test cells.

-PhOR mix		-SR mix		"7-dye" mix	
-PhOC_4H_9	0.25%	-SC_4H_9	0.3%	-SC_4H_9	0.3%
-PhOC_9H_{19}	0.25%	-SC_7H_{15}	0.3%	-SC_5H_{11}	0.3%
Total	0.5%	-SC_8H_{17}	0.3%	-SC_7H_{15}	0.3%
		Total	0.9%	-SC_8H_{17}	0.3%
				-SC_9H_{19}	0.3%
				-S$C_{10}H_{21}$	0.3%
				-PhN$(CH_3)_2$	0.1%
				Total	1.9%

To date, there has been no evidence of crystallization or phase separation of dye components in this mixture after storage periods of several months, either in the bulk mixtures or in fabricated devices. In most-recent developments, a dye mixture containing a new nickel dithiolene compound that is a *liquid* at room temperature as an eighth dye component is being evaluated in an LCPDI device for its performance in the near IR. Devices containing this new mixture have displayed OD values of 2.77 and 1.85 for a 25-μm and 15-μm path length, respectively. The substantial improvement in OD afforded by this new compound now opens the possibility of fabricating thinner LCPDI devices that will exhibit improved contrast, reduced scattering losses, and faster electro-optic temporal response over previous-generation, near-IR devices.

Summary

The LCPDI device has exceptional potential for use in OMEGA due to a number of important attributes. Its inherently phase-shifting nature allows higher spatial sampling and generally more-accurate wavefront characterization than other interferometric techniques, while the single-path design requires fewer optical elements than other types of interferometers, thereby reducing size and cost requirements. The compact and "solid-state" nature of the device provides additional benefits in the form of reduced sensitivity to environmental disturbances such as mechanical vibration, temperature fluctuations, and air turbulence. The largest single obstacle to deployment of the LCPDI in OMEGA has been the availability of a near-IR dye with sufficient LC host solubility; chemical, thermal, and optical stability; and electronic absorbance properties to produce devices capable of sufficient contrast for output image analysis. Here, we have shown that, through selection of appropriate functional groups, zerovalent transition metal dithiolenes can be designed and synthesized that will allow the LCPDI to realize its design goals for deployment in OMEGA.

Although present computational chemistry methods and software are somewhat limited in scope for organometallic compounds, they can still provide useful qualitative guidance in the design and development of new dye compounds with solubility and optical absorbance requirements tailored to a specific host material. Using this approach, we demonstrated both theoretically and experimentally that sulfur-containing alkyl terminal groups are superior to alkoxy, alkylphenyl, and alkoxyphenyl substituents both in enhancing the solubility of the nickel dithiolene core in the host medium and in optimizing the location of the dye λ_{max} for maximum absorbance efficiency. Employing a mixture of dyes rather than just a single-dye substance was shown to have two benefits: (1) a larger overall host dye concentration allows construction of thinner LCPDI devices with better performance characteristics, and (2) thermodynamic stability of the guest–host mixture is substantially enhanced since the relatively low concentration of each dye component reduces the risk of long-term dye precipitation from the host.

In addition to the pending evaluation of the capabilities of current near-IR LCPDI devices, experiments are also underway to more accurately determine the solubility limit of the dyes by spectroscopic techniques and to further refine the dye mixture composition so as to achieve additional gains in OD without sacrificing mixture stability. Our recent modeling efforts have generated a library of over 40 new transition metal dithiolene compounds that await further synthesis efforts to evaluate their potential as dye candidates for the LCPDI as well as for other near-IR LC device applications in optical communications and sensor protection.

ACKNOWLEDGMENT

The authors gratefully acknowledge the contributions of the following individuals and organizations: Dr. Julie R. Wright (Schroedinger, Inc.); Dr. W. Thomas Pollard (Schrodinger, Inc.); Dr. Wayne Huang (Wavefunction, Inc.); and Dr. Ansgar W. Schmid (LLE) for guidance and helpful discussions regarding computational chemistry methods and applications; Prof. Ulrich Muller-Westerhoff (Department of Chemistry, University of Connecticut) and Prof. Alan E. Underhill (Department of Chemistry, University of Wales) for helpful discussions on transition metal dithiolene syntheses; Irene Lippa (LLE) for determination of dye solubilities in host systems; Malia Moore, Awista Ayub, Scott Kinsella, and Kendra Bussey (LLE) for assistance in synthesis of metal complexes and precursors; and Tanya Kosc, Nathan Bickel, Ryan Brecker, and Markar Naradikian (LLE) for construction and characterization of the LCPDI devices. This work was supported by the U.S. Department of Energy Office of Inertial Confinement Fusion under Cooperative Agreement No. DE-FC03-92SF19460, the University of Rochester, and the New York State Energy Research and Development Authority. The support of DOE does not constitute an endorsement by DOE of the views expressed in this article.

REFERENCES

1. C. R. Mercer and K. Creath, Opt. Lett. **19**, 916 (1994).
2. C. R. Mercer and K. Creath, Appl. Opt. **35**, 1633 (1996).
3. C. R. Mercer, N. Rashidnia, and K. Creath, Exp. Fluids **21**, 11 (1996).
4. U. T. Mueller-Westerhoff, B. Vance, and D. I. Yoon, Tetrahedron **47**, 909 (1991).
5. P. Espinet *et al.*, Coord. Chem. Rev. **117**, 215 (1992).
6. K. L. Marshall and S. D. Jacobs, Mol. Cryst. Liq. Cryst. **159**, 181 (1988).
7. U. T. Mueller-Westerhoff *et al.*, Mol. Cryst. Liq. Cryst. Lett. **56**, 249 (1980).
8. U. T. Mueller-Westerhoff and B. Vance, in *Comprehensive Coordination Chemistry: The Synthesis, Reactions, Properties, and Applications of Coordination Compounds*, 1st ed. (Pergamon Press, Oxford, England, 1987), Vol. 2, pp. 595–631.
9. M. Colvin, "Continuum Models of Solvation," Lawrence Livermore National Laboratory (2000), available on the Internet at http://gutenberg.llnl.gov/~colvin/solvation/solv.html.
10. B. Lee and F. M. Richards, J. Mol. Biol. **55**, 379 (1971).
11. B. Honig, K. Sharp, and A. S. Yang, J. Phys. Chem. **97**, 1101 (1993).
12. K. Ohta *et al.*, Mol. Cryst. Liq. Cryst. **147**, 15 (1987).
13. C. E. A. Wainwright and A. E. Underhill, Mol. Cryst. Liq. Cryst. **234**, 193 (1993).
14. N. Svenstrup *et al.*, Synthesis **8**, 809 (1994).
15. A. Charlton *et al.*, J. Mater. Chem. **4**, 1861 (1994).

OMEGA Cryogenic Target Designs

The achievement of high-density implosions using ignition-relevant pulse shapes and cryogenic targets on OMEGA is an important milestone on the path to attaining direct-drive ignition at the National Ignition Facility (NIF). The OMEGA Cryogenic Target Handling System is undergoing final tests and will soon be commissioned for D_2 implosion experiments. Cryogenic targets have also been designed for this system with the primary criterion of being *hydrodynamically equivalent* to the ignition capsule designs. In this context, the constraints placed on OMEGA cryogenic target designs include similar peak shell velocities, hot-spot convergence, in-flight aspect ratio, and stability properties as the NIF designs. NIF designs have been discussed previously in Ref 1. In this article, we report on the cryogenic OMEGA target design and compare its physical behavior with the $\alpha = 3$ ignition NIF design.

The basis for the OMEGA designs is the NIF direct-drive $\alpha = 3$ ignition design, which consists of a 340-μm DT-ice layer encased in a thin (<3-μm) plastic capsule of 1.69-mm outer radius. One-dimensional hydrodynamic scaling arguments[2] can then be used to guide the design of OMEGA cryogenic targets. The laser energy (E) required to contribute to a given plasma thermal energy scales roughly as the radius of the capsule (R) according to $E \sim R^3$. The NIF is designed to provide 1.5 MJ of energy; OMEGA is capable of delivering 30 kJ. Thus, the radius of an OMEGA capsule will be approximately 0.3 times the NIF design (see Fig. 82.1).

Figure 82.2 shows the power history for the NIF and OMEGA pulses. The NIF laser pulse irradiating the ignition design is a 9.25-ns shaped pulse consisting of a 10-TW, 4.25-ns foot rising to a 450-TW pulse for 2.5 ns. The corresponding laser pulse for the OMEGA design is determined by noting that the time (t) or duration of the laser pulse scales as the confinement time and is roughly proportional to the radius of the target; therefore[2] $t \sim R$. The scaling of the peak power (P) in the laser pulse can be obtained from the energy and time scaling; therefore,[2] $P \sim R^2$. Consequently, the length of the laser pulse shrinks from 9.25 ns in the $\alpha = 3$ ignition target design to 2.5 ns for the OMEGA cryogenic target design. The peak power using $P \sim R^2$ then scales to 32 TW. Processes other than hydrodynamics, such as radiation, thermal transport, and thermonuclear burn, do not scale in a simple manner between the ignition designs and the OMEGA cryogenic designs. We will show, however, that these energy-scaled targets possess similar 1-D behavior and instability growth as the ignition designs, thus meeting the requirement of hydrodynamic equivalence.

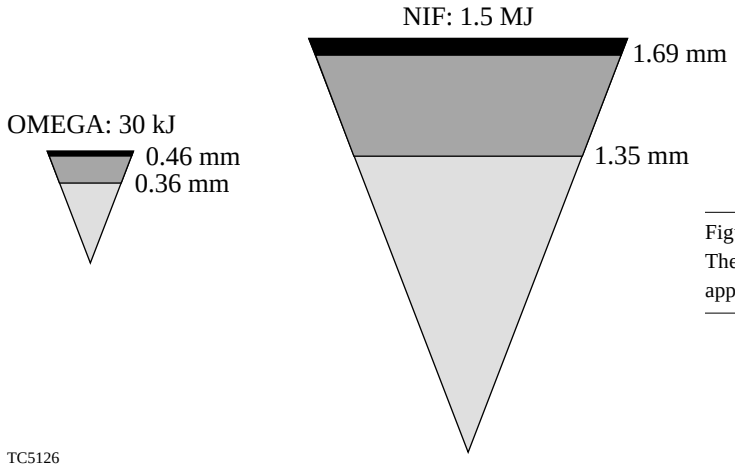

Figure 82.1
The NIF and OMEGA capsule designs. The radius of the OMEGA design is approximately 0.3 times that of the NIF design.

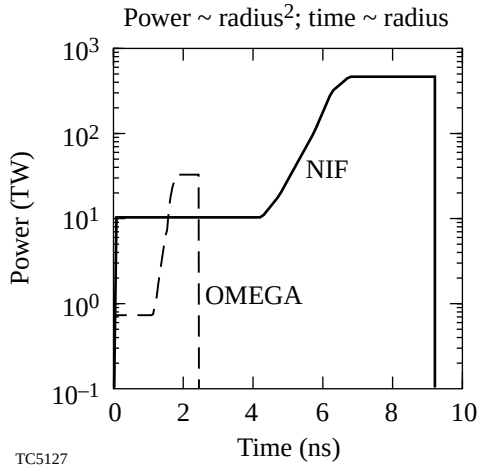

Figure 82.2
The NIF and OMEGA pulse shapes.

The timing of *two* shocks is critical to determining the overall performance of the direct-drive ignition target design. The two distinct shocks in this design are launched into the target at the start of the laser pulse and during its rise to the main drive intensity. The position of the shocks in the target can be calculated from the radial logarithmic derivative of the pressure. Figure 82.3 is a contour map of this quantity $[d(\ln P)/dr]$ as a function of the Lagrangian coordinate and time for the ignition and the OMEGA design. Time has been normalized to the incident laser energy, with $t = 1.0$ corresponding to the end of the laser pulse. This normalization will allow us to compare the two designs at the same stage of the implosion. The darker, more-intense regions represent a larger gradient in pressure and thus capture the position of the shocks. The OMEGA design shows similar shock-timing behavior as that of the ignition design for the first shock. The second shock, however, arrives slightly later in the OMEGA design than in the ignition design in normalized time units. This is a consequence of lower laser-energy absorption in the OMEGA design. Absorption in direct-drive designs is primarily via inverse bremsstrahlung, which depends on the density scale length. The NIF designs typically have scale lengths that are 2 to 3 times longer than OMEGA, which leads to an absorption fraction for the ignition design of 60% on the NIF and 40% on OMEGA.

At the time the first shock breaks out of the rear of the ice surface, a rarefaction wave travels back through the ice layer in the outward direction. This rarefaction wave results in a decreasing density gradient in the inward radial direction. The second shock, which is caused by the rise of the main pulse, then travels through this decreasing density gradient. This serves to increase the adiabat (α) of the ice layer. Since the second shock in the OMEGA design arrives later (in normalized time units) than in the NIF design, the rear ice surface decompresses more than in the ignition design. Consequently, the OMEGA design has a slightly higher adiabat ($\alpha = 3.2$) than the ignition design ($\alpha = 3$).

The adiabat of the implosion is defined as the ratio of the pressure of the cold fuel to the Fermi degenerate pressure and is an important figure of merit for the overall performance of target designs. Lower adiabat implosions have higher one-dimensional performance since less laser energy is needed to

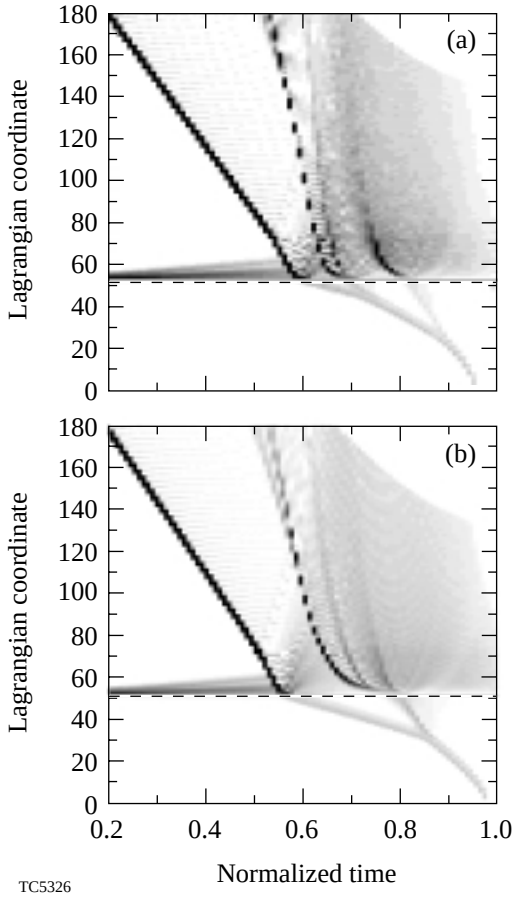

Figure 82.3
Shock propagation as shown by a contour map of the logarithmic derivative of the pressure as a function of normalized time and Lagrangian coordinate for (a) the NIF and (b) the OMEGA designs. Time has been normalized to the incident laser energy, with $t = 1.0$ corresponding to the end of the laser pulse. This allows the two designs to be compared at the same stage of the implosion. The darker shading indicates a larger pressure gradient and thus captures the position of the shocks. The OMEGA design shows similar timing for the first shock but a delayed second shock compared to the NIF design.

compress a cold fuel than a warm fuel. The ablation velocity, however, depends directly on the adiabat ($\sim\alpha^{3/5}$); thus, the Rayleigh–Taylor (RT) growth rates decrease with the adiabat. Higher adiabat implosions, therefore, are more stable to the acceleration-phase RT instability. To ensure similar performance between the NIF and OMEGA cryogenic capsules, the cold fuel layer should have similar adiabats. Plotting the pressure-density trajectory of the Lagrangian cells used in the simulation will show the adiabatic history of target designs. Figure 82.4 is such a plot for both the NIF design and the OMEGA design; also shown is the $\alpha = 3$ adiabat line (dashed). The NIF design obviously accesses a larger portion of phase space than the OMEGA design. Only the extremely compressed and high-density region is inaccessible by the OMEGA design. Table 82.I, which lists other key one-dimensional parameters, indicates that the OMEGA and NIF designs have similar peak shell velocities, hot-spot convergence ratios, and in-flight aspect ratios. To compare an igniting and non-igniting target, we have defined the hot spot as the ratio of the initial outer radius to the radius that contains 90% of the yield at the time of peak neutron production when propagating burn has been switched off.

Implosion efficiency can be quantified in two ways: The *hydrodynamic efficiency* is defined as the ratio of the kinetic energy of the imploding target to the absorbed energy. The *coupling efficiency* is defined as the ratio of the kinetic energy of the imploding target to the incident energy. Although OMEGA has a similar hydrodynamic efficiency to the NIF, the reduced absorption fraction leads to a lower coupling efficiency.

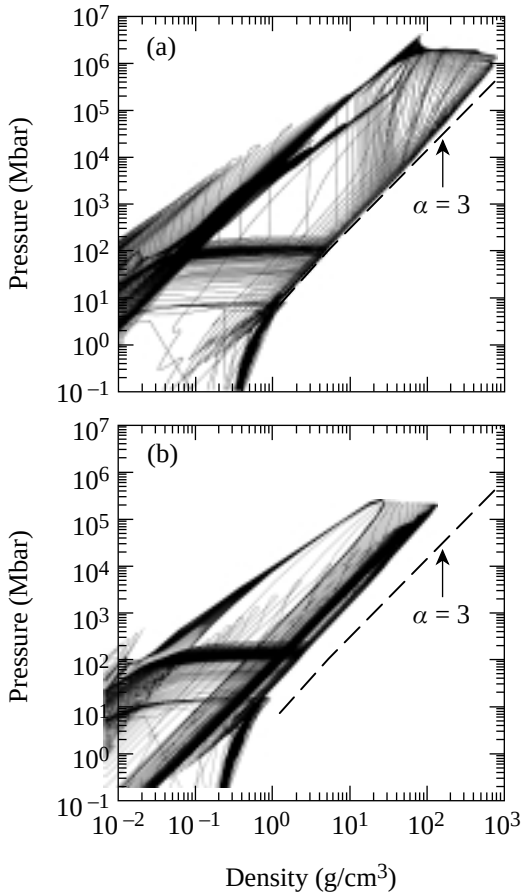

Figure 82.4
The density-pressure trajectories for each Lagrangian cell used in the simulations of (a) NIF and (b) OMEGA designs. Also shown (dashed line) is the $\alpha = 3$ adiabat line.

Table 82.I: Comparison of one-dimensional parameters between the NIF and OMEGA cryogenic target designs.

	NIF	OMEGA
Absorption fraction	60%	40%
Hydrodynamic efficiency	11.0%	11.5%
Coupling efficiency	7%	4.5%
Peak shell velocity (cm/s)	4.0×10^7	3.7×10^7
Hot-spot convergence ratio	28	20
In-flight aspect ratio	60	50
Peak areal density (mg/cm^2)	1200	300
Neutron-averaged ion temperature (keV)	30	4
Neutron yield	2.5×10^{19}	1.8×10^{14}

The NIF design is expected to have different plasma physics issues compared to the OMEGA design. The density and velocity scale lengths at the tenth- and quarter-critical surfaces primarily determine the intensity threshold for plasma instabilities such as stimulated Raman scattering (SRS), stimulated Brillouin scattering (SBS), and two-plasmon decay (TPD). These instabilities in the ablating plasma can significantly influence laser absorption, the occurrence of hot electrons, and therefore the performance of the target. By comparing the actual intensity to the plasma instability thresholds, the susceptibility of the designs to plasma instabilities can be assessed. The quarter- and tenth-critical surfaces have similar intensities in both cases, which is not surprising since the laser power was scaled with the square of the radius of the pellet; the peak intensity as a result of overlapped beams at the quarter-critical surface is 1.0×10^{15} W/cm^2 and 6.0×10^{14} W/cm^2 at the tenth-critical surface for both designs. For the NIF the total overlapped intensity is well above the SBS threshold after about 6 ns; while the single-cluster intensity is comparable to the threshold. The intensity is always below the SRS threshold. As mentioned, OMEGA has shorter scale lengths than the NIF designs. During the rise to the peak of the laser pulse the scale length at the tenth-critical surface in the NIF design rapidly increases to approximately 800 μm^{-1} and is typically three times larger than the OMEGA design. Therefore, we would expect the OMEGA design to be less susceptible to SRS and SBS than the NIF design. However, both designs are well above threshold for the TPD instability. The NIF design also has a larger volume than OMEGA for the nonlinearly saturated state of the TPD instability to generate hot electrons. Separate experiments have been conducted at LLE to study these plasma physics issues. In these experiments, NIF-scale-length plasmas have been generated using a laser pulse similar in intensity to the NIF pulse. Results to date[3] of the high-intensity drive portion of the NIF pulse show little evidence of SRS, suggesting that this instability will have an insignificant effect on the performance of the ignition design.

Hydrodynamic instabilities are the second source of deviations from one-dimensional hydrodynamic simulations. The RT instability can degrade target performance by breaking the spherical symmetry of the implosion. The RT instability occurs twice during the implosion: at the outer ablation surface as the shell accelerates inward and at the hot spot–main fuel layer interface as the capsule decelerates at the end of the implosion. Four sources of nonuniformity primarily seed the RT instability: (1) laser imprinting, (2) outside capsule finish, (3) drive asymmetry, and (4) inner-DT-ice roughness. An important component of the OMEGA campaign will be to experimentally determine the maximum allowable levels of these sources of nonuniformities for the NIF laser and direct-drive ignition targets. OMEGA cryogenic targets must, therefore, have similar stability properties to the NIF designs to ensure that the extrapolation of these results to NIF targets will be valid.

Imprint levels are expected to be smaller on OMEGA than on the NIF. The level of laser imprint in both the NIF and OMEGA direct-drive targets can be quantified in terms of the imprint efficiency, which is defined as the ratio of the amplitude of the ablation surface nonuniformity to the percent of laser nonuniformity. We determine this quantity using two-dimensional (2-D) *ORCHID* simulations, each with a single-mode laser nonuniformity, for NIF and OMEGA designs. These *ORCHID* simulations included the following laser-smoothing techniques: (1) a phase-plate spectrum appropriate to the spot size, (2) a polarization-smoothing wedge, and (3) 2-D smoothing by spectral dispersion (SSD) at two UV bandwidths (0.5 THz$_{UV}$ and 1 THz$_{UV}$). We find good agreement between the imprint efficiency calculated from *ORCHID* and that obtained from the analytic theory of Goncharov.[4] Using this analytic theory and *ORCHID* simulations, the mode spectrum due to imprint for the NIF and OMEGA designs at the start of the acceleration phase is shown in Fig. 82.5. In the NIF design, the laser has imprinted a surface nonuniformity equal to σ_{rms} = 480 Å (in modes ℓ < 1000). OMEGA has a corresponding imprinted nonuniformity of σ_{rms} = 290 Å. The cusps observed in the mode spectrum are a consequence of dynamic overpressure[4] that causes the imprinted mode to oscillate with a period proportional to the wavelength of the mode. The acceleration phase begins when the rarefaction wave from the rear surface reaches the ablation surface; therefore, the time

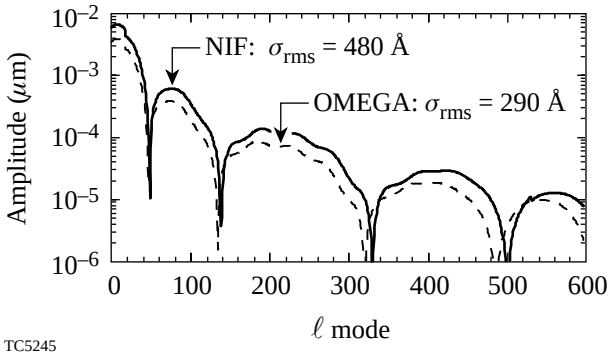

Figure 82.5
Modal spectrum of the surface amplitude due to imprint from a 1-THz$_{UV}$ 2-D SSD smoothed laser for the NIF and OMEGA designs at the start of the acceleration phase.

when this phase begins is roughly proportional to the shell thickness. The cusps in the imprint spectrum will consequently occur for wavelengths that are at a minimum when the acceleration phase begins. For the NIF design, the period of oscillation is three times that of the OMEGA design; however, the acceleration phase begins approximately three times later than the OMEGA design, so the cusps occur at the same part of the ℓ-mode spectrum for both designs. Scaling arguments can be invoked to determine the relation between imprint levels on OMEGA and NIF targets. Since the laser energy deposited at the critical surface is thermally conducted to the ablation surface, significant reductions in the level of imprint-induced nonuniformities can be obtained by thermal smoothing over this *stand-off* distance. Dimensional considerations suggest that imprint levels should vary as kD_c (where k is the perturbation wave number and D_c is the distance between the energy absorption region and the ablation surface). Imprint essentially ends when the laser decouples from the target, i.e., when $kD_c \sim 1$; therefore, a longer wavelength should imprint less than a shorter wavelength. A given ℓ mode on OMEGA has a wavelength that is approximately one-third of the same ℓ mode on the NIF direct-drive target. Thus a single beam on OMEGA will imprint one-third as much as on the NIF for the same ℓ mode. However, since NIF has approximately four times the number of overlapped beams, imprint for OMEGA design will be two-thirds that of the NIF design.

Next, we study the evolution of the shell during the acceleration phase of the implosion. The OMEGA designs have an overdense shell thickness that is approximately one-third the NIF-shell thickness, where the shell thickness is defined as the distance between the 1/e points of the maximum density. If the two designs have the same initial seed and RT e-foldings during the acceleration phase, the OMEGA design's mix-width region will be a greater percentage of the overdense shell. Figure 82.6 shows the results of an instability post-processor to 1-D hydrocode *LILAC* simulations. This post-processor uses a self-consistent model[5] to study the evolution of perturbations at the ablation front and the back surface of an accelerated spherical shell. The model includes the ablative Richtmyer–Meshkov (RM),[6] RT, and Bell–Plesset (BP) instabilities, and 3-D Haan saturation.[7] The model consists of two differential equations (describing the ablation- and inner-surface perturbations) obtained by solving the linearized conservation equations in the DT gas, the shell, and the blowoff plasma regions. The seeds for the nonuniformity processor were (1) the imprint caused by 1-THz$_{UV}$, 2-D SSD; (2) an outer capsule roughness of 840 Å (in an ℓ-mode spectrum taken from Weber[8]); and (3) an inner-ice-surface roughness of 2 μm [with a spectrum of the form $\sigma \sim \ell^{-1.5}$ (Ref. 9)]. Figure 82.6 shows the overdense shell thickness and the mix width for the NIF and OMEGA designs. Both designs survive the acceleration phase, i.e., the mix width is less than the shell width; however, the NIF mix width is approximately 30% of the overdense shell, whereas the OMEGA design's mix width is almost 90% of the shell thickness. Thus the OMEGA design has a lower safety factor for survival through the acceleration phase than the $\alpha = 3$ NIF design for a given level of laser and target nonuniformity.

During the implosion the outer-surface perturbation *feeds through* to the inner surface, which can then grow via the RT instability during the deceleration phase. The feedthrough for a given ℓ mode scales approximately as kD_o, where D_o is the overdense shell thickness. Since the increase in shell thickness for the NIF target is compensated for by the smaller wavelength for the same ℓ mode, the NIF and OMEGA designs are predicted to have similar amounts of feedthrough. Figure 82.7 shows the mode spectrum at the inner surface of the DT ice for both designs at the onset of the deceleration phase. The mode spectrum is heavily weighted toward the low ℓ mode of the spectrum, with most of the power contained below $\ell \sim 20$. The higher level of imprint in the NIF design compared to OMEGA

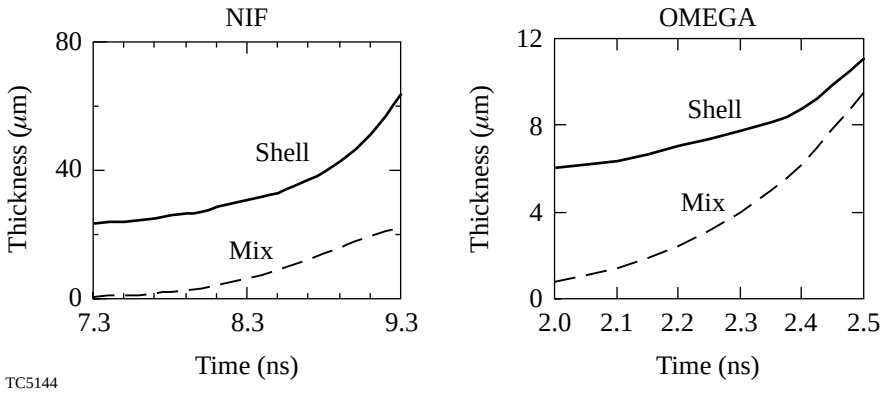

Figure 82.6
The overdense shell thickness and mix width for the NIF design and the OMEGA design during the acceleration phase. In both cases the overdense shell thickness is larger than the mix width, which implies that both designs will survive the acceleration phase.

has led to a higher amount of feedthrough in the range at which imprint dominates ($10 < \ell < 100$). For low ℓ modes ($\ell < 10$), where the effect of the inner ice surface is dominant, the mode amplitudes are comparable in both cases. The instability postprocessor cannot self-consistently determine the degradation in target yield for a given initial nonuniformity level. We therefore use a limited number of *ORCHID* simulations to determine the effect of these levels of inner-ice distortions at the start of the deceleration phase (predicted by the instability postprocessor) on the overall target performance.

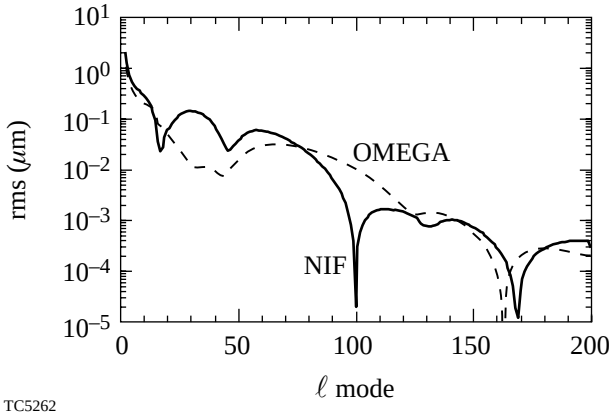

Figure 82.7
The mode spectrum of the NIF (solid line) and OMEGA (dashed line) designs at the onset of the deceleration phase.

The *ORCHID* simulations are initialized at the start of the laser pulse with perturbations on the rear inner ice surface only (the outer surface and laser are assumed to be perfect). As we have seen above, most of the power on the rear surface at the onset of deceleration is concentrated in the low-ℓ-mode part of the spectrum, so the *ORCHID* calculations contain only modes up to $\ell = 50$ (in contrast, the postprocessor calculations take into account modes up to $\ell = 1000$). Various initial spectra of the form $\sigma \sim \ell^{-\beta}$ were simulated to take into account the four seed terms.[9] The *ORCHID* calculations simulate the implosion through peak compression and burn. The spectra at the start of the deceleration phase obtained from the *ORCHID* simulations are compared to the spectra obtained from the instability postprocessor. This comparison is used to relate the postprocessor analysis to the full 2-D *ORCHID* simulations and obtain the yield for a given level of laser and target nonuniformity. It has been shown previously[9] that the $\alpha = 3$ NIF target gain can be written as a function of $\bar{\sigma}$, where

$$\bar{\sigma}^2 = 0.06\,\sigma^2_{\ell<10} + \sigma^2_{\ell\geq 10};$$

$\sigma^2_{\ell<10}$ and $\sigma^2_{\ell\geq 10}$ are the rms nonuniformity of modes below and above 10, respectively. The instability postprocessor gives $\bar{\sigma}$ at the onset of the deceleration phase for different initial conditions (laser imprint and surface roughness.) By comparing the amplitude and mode spectrum it is possible to relate the reduction in target performance for a given initial nonuniformity. For the $\alpha = 3$ NIF design the instability analysis with an initial 1 μm of inner ice nonuniformity, 840-Å outer surface roughness, and 1-THz$_{UV}$, 2-D SSD illumination, the resulting $\bar{\sigma}$ is 1.3 μm. As we have already seen, the OMEGA design imprints less that the NIF design. Power balance and inner-ice-surface roughness are likely to be similar for both laser configurations. We use the same characterization of the nonuniformity in the deceleration phase for the non-igniting OMEGA target to obtain the neutron yield as a function of $\bar{\sigma}$. For the OMEGA design the instability analysis with the same initial conditions as the NIF capsule leads to a $\bar{\sigma}$ of 0.9 μm. Figure 82.8 shows the normalized (to 1-D) yield as a function of the deceleration nonuniformity parameter $\bar{\sigma}$. The OMEGA design has a larger reduction in yield for a given level of $\bar{\sigma}$ than the NIF design. This can be attributed to the OMEGA design's smaller hot-spot radius compared to that of the NIF design, which makes the OMEGA hot spot more easily disrupted by the penetration of cold spikes from the main fuel layer. For the same initial conditions, however, the value of $\bar{\sigma}$ is different between the

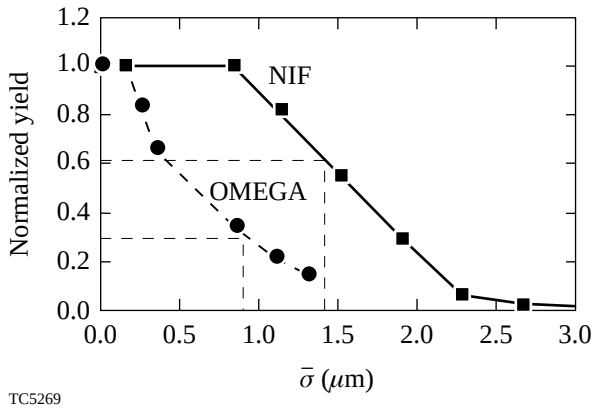

Figure 82.8
The yield, normalized to the 1-D result, as a function of $\bar{\sigma}$, the total nonuniformity at the start of the deceleration phase.

two designs. For the case outlined above, the NIF has a $\bar{\sigma}$ of 1.3 μm, which leads to a reduction to 60% of 1-D yield (giving a gain of 28), whereas the OMEGA design has a $\bar{\sigma}$ of 0.9 μm for the same conditions, which leads to a yield of 30% of 1-D.

This article has described the current target designs for the soon-to-be-commissioned OMEGA Cryogenic Target Handling System. These designs are energy scaled from the direct-drive ignition designs for the NIF with a major goal of experimentally studying the various sources of nonuniformity and their influence on target performance. The OMEGA and the NIF designs have been shown to have similar 1-D behavior and stability properties, which will facilitate the extrapolation of the cryogenic target studies on OMEGA to NIF targets. The smaller hot spot in the OMEGA design implies, however, that OMEGA cryogenic targets will be more sensitive to instability growth than the NIF direct-drive ignition targets. Our stability analyses are consistent with this observation and predict that with 1-THz$_{UV}$, 2-D SSD, and 1 μm of inner-ice-surface roughness we should obtain approximately 30% of the 1-D yield from the OMEGA cryogenic targets. Using the same analysis tools and similar target and laser uniformity levels, we predict that the $\alpha = 3$ direct-drive ignition design will give a gain of 28 on the NIF, a reduction to 60% of the 1-D yield.

ACKNOWLEDGMENT

This work was supported by the U.S. Department of Energy Office of Inertial Confinement Fusion under Cooperative Agreement No. DE-FC03-92SF19460, the University of Rochester, and the New York State Energy Research and Development Authority. The support of DOE does not constitute an endorsement by DOE of the views expressed in this article.

REFERENCES

1. Laboratory for Laser Energetics LLE Review **79**, 121, NTIS document No. DOE/SF/19460-317 (1999). Copies may be obtained from the National Technical Information Service, Springfield, VA 22161.

2. K. A. Brueckner and S. Jorna, Rev. Mod. Phys. **46**, 325 (1974).

3. S. P. Regan, D. K. Bradley, A. V. Chirokikh, R. S. Craxton, D. D. Meyerhofer, W. Seka, R. W. Short, A. Simon, R. P. J. Town, B. Yaakobi, J. J. Caroll III, and R. P. Drake, Phys. Plasmas **6**, 2072 (1999).

4. V. N. Goncharov, S. Skupsky, T. R. Boehly, J. P. Knauer, P. McKenty, V. A. Smalyuk, R. P. J. Town, O. V. Gotchev, R. Betti, and D. D. Meyerhofer, Phys. Plasmas **7**, 2062 (2000).

5. V. N. Goncharov, "Self-Consistent Stability Analysis of Ablation Fronts in Inertial Confinement Fusion," Ph.D thesis, University of Rochester, 1998.

6. V. N. Goncharov, Phys. Rev. Lett. **82**, 2091 (1999).

7. S. W. Haan, Phys. Rev. A **39**, 5812 (1989).

8. S. V. Weber, S. G. Glendinning, D. H. Kalantar, M. H. Key, B. A. Remington, J. E. Rothenberg, E. Wolfrum, C. P. Verdon, and J. P. Knauer, Phys. Plasmas **4**, 1978 (1997).

9. V. N. Goncharov, S. Skupsky, P. W. McKenty, J. A. Delettrez, R. P. J. Town, and C. Cherfils-Clerouin, "Stability Analysis of Directly Driven OMEGA and NIF Capsules," to be published in the *Proceedings of the 1999 Inertial Fusion Sciences and Applications Conference*, Bordeaux, France, 12–17 September 1999; also Laboratory for Laser Energetics LLE Review **81**, 1, NTIS document No. DOE/SF/19460-335 (1999). Copies of the LLE Review may be obtained from the National Technical Information Service, Springfield, VA 22161.

Imprint Reduction Using an Intensity Spike in OMEGA Cryogenic Targets

The primary obstacle to the successful implosion of an inertial confinement fusion target is hydrodynamic instability, which can cause the target to disintegrate and prevent it from reaching the high densities and temperatures required for ignition. The imploding target is primarily subject to the Rayleigh–Taylor (RT) instability, seeded by surface nonuniformity and by laser illumination nonuniformity, which can imprint itself on the target surface. Efforts to reduce laser imprint have employed primarily smoothing mechanisms such as smoothing by spectral dispersion (SSD),[1] distributed polarization rotators (DPR's),[2] and distributed phase plates (DPP's).[3] We present here a novel technique to further reduce imprint in OMEGA cryogenic (cryo) targets by a relatively simple modification to the standard pulse shape.

As reported elsewhere in this volume (p. 49), the base-line OMEGA cryogenic targets consist of a shell of deuterium–tritium (DT) ice surrounding a DT vapor region. For target fabrication, the DT ice must be surrounded by a thin (1–4 μm) layer of plastic (CH) or polyimide. This layer increases, however, the amount of imprint by introducing an additional period of RT growth near the start of the laser pulse.[4] Figure 82.9 shows the growth of laser imprint (i.e., the amplitude η of the outer-surface modulation) for a DT shell coated with 3 μm of CH, compared with the imprint that would result from a pure-DT shell. For this example, the target was illuminated with a 5% laser nonuniformity and a 50-μm nonuniformity wavelength. (To isolate the effect of laser nonuniformity, an initially smooth target surface was used in these simulations.) The qualitative features of the imprint are the same for both cases shown in Fig. 82.9. Initially, the imprint growth, which is roughly linear in time, results from the nonuniform shock, which is launched at the onset of laser irradiation. The imprint amplitude reaches a peak, representing the first quarter-cycle of the oscillations caused by dynamic overpressure.[4] (For some wavelengths of nonuniformity, half the period of oscillation is less than the foot-pulse duration, and the outer-surface amplitude reverses phase.) The amplitude grows exponentially, after about 1.5 ns, as the whole shell begins to accelerate and RT growth sets in. During the drive pulse, the target with the 3-μm CH shell has an imprint amplitude about twice that of the pure-DT shell. The increase in amplitude is initiated very early in the imprint process (within the first few hundred picoseconds for OMEGA targets), when a jump in the amplitude is produced by a brief acceleration of the CH shell, with resulting RT growth. The novel technique presented here significantly reduces this jump in amplitude and thereby reduces the imprint for the CH shell to approximately the level of the pure-DT shell.

The mechanism that produces the early, brief acceleration of the CH shell is illustrated in Fig. 82.10 by three plots of the density as a function of radius, at successive times early in the simulation. The onset of irradiation sends a shock into the CH layer. When the shock reaches the interface between the DT and the CH, a faster shock is sent into the less-dense DT, and a rarefaction wave (RW) returns to the outer surface through the CH layer. The RW accelerates the CH, while decreasing its pressure and density. While the outer surface is accelerated by the RW, it is subject to the RT instability.

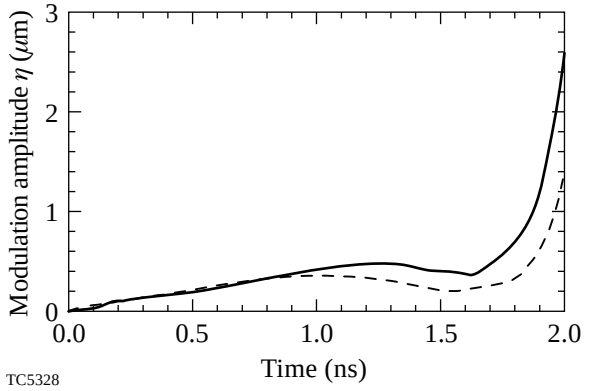

Figure 82.9
The amplitude of outer-surface modulations due to imprint, for an initially smooth target, driven by illumination with a 5%, 50-μm nonuniformity. The solid curve represents a target with a 3-μm CH layer surrounding a 72-μm DT ice shell, while the dashed curve represents 84 μm of DT, which gives the same total shell mass.

As the RW moves through the CH, it lowers the pressure from the post-shock CH pressure to the post-shock DT pressure; however, the laser irradiation imposes a pressure at the outer surface given by the ablation pressure. As a result, after the RW has crossed the outer surface, a weak *adjustment* shock is sent back into the target, which increases its pressure to the ablation pressure. This second shock is launched first at the trough of the surface perturbation, then later at the peak. This discrepancy in the time for the shock to be launched causes a decrease in the rate of amplitude growth $\dot{\eta}$.

The early-time growth due to the RW acceleration has the standard RT scaling and is greater for shorter wavelengths. For a given spherical harmonic with mode number ℓ, the corresponding wavelength for an OMEGA target is approximately three times smaller than for a NIF target, and as a result, the early-time growth is greater.

We have found a relatively simple way to reduce the increased imprint caused by the CH overcoat: By introducing a brief, high-intensity spike at the start of the foot pulse (see Fig. 82.11), the effects of the early-time acceleration of the CH shell can be drastically reduced. Figure 82.12 shows the degree of imprint (given by the outer-surface modulation amplitude) for identical targets, which have pulses with and without this intensity spike, for a 50-μm illumination perturbation. The spike, which is 50 ps in duration and has an intensity ratio with the foot of 6:1, reduces the imprint by ~2 at this wavelength. As seen, targets irradiated with an initial intensity spike experience a shorter period of early RT growth, which begins earlier in time, than those irradiated by the standard pulse. As a result, the RT growth starts with a lower amplitude and terminates earlier.

The intensity spike launches a stronger shock than the canonical foot-pulse shock. This results in a larger shock velocity, a greater amount of compression, and a thinner post-shock CH layer. Thus, the shock reaches the CH–DT interface earlier, and the rarefaction wave returns more quickly because of the thinner post-shock CH layer. (A stronger shock also leads to a greater post-shock temperature and higher sound speed, so that the RW travels more quickly.) This decreases not only the arrival time of the rarefaction wave but also its extent since the width of the RW grows linearly in time. As shown in Appendix A, the duration of the RT growth due to the RW is proportional to $d/(\xi c_s)$, where d is the width of the CH layer, ξ is the amount of shock compression, and c_s is the post-shock sound speed. As this dependence suggests, both of these factors lead to less early-time RT growth and less imprint.

For OMEGA cryo targets, the most-unstable modes are commonly taken to have spherical-harmonic mode numbers in the range $20 \lesssim \ell \lesssim 75$ (corresponding to illumination nonuniformity wavelengths of 40 μm $\lesssim \lambda \lesssim$ 140 μm). RT

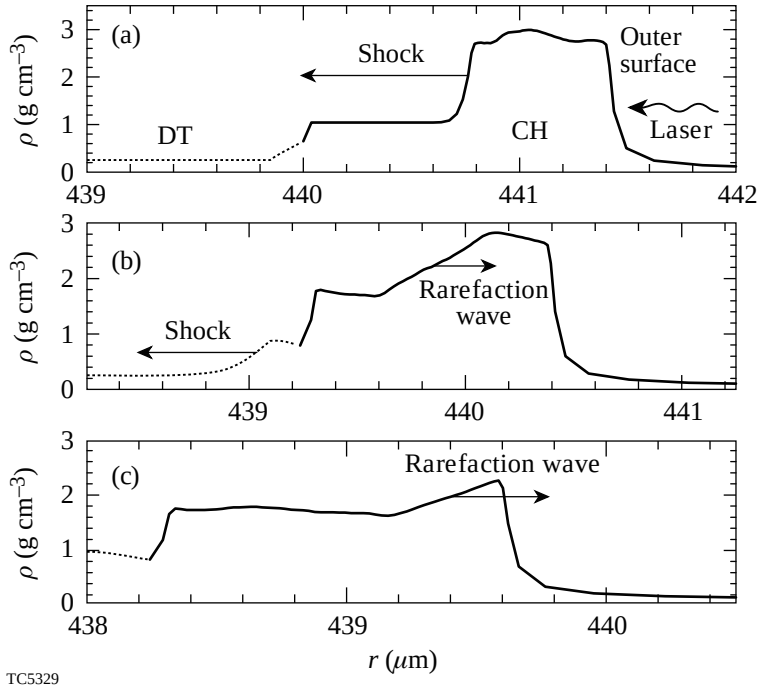

Figure 82.10
The density profile at the outer edge of the target shell is shown at three consecutive times early in the implosion. Panel (a) shows the propagation of the foot-pulse shock through the thin outer CH layer. Panel (b) shows the return of the rarefaction wave from the CH/DT interface through the shocked CH to the outer surface of the target. Panel (c) shows the density while the rarefaction wave is accelerating the outer surface to the post-shock speed of the shocked DT. The CH layer is shown with a solid line, and the DT ice is represented by a dotted line.

growth is greater for shorter wavelengths. Figure 82.13 shows pairs of simulations, with (solid) and without (dashed) the intensity spike, for two wavelengths, demonstrating this wavelength dependence.

A direct measure of the magnitude of imprint was suggested in Ref. 5 by Weber *et al*. They evaluate the degree of imprint by calculating, for a given illumination nonuniformity of wave number k, the *equivalent surface finish* $\varepsilon(k)$, defined as the magnitude of initial surface nonuniformity $\eta_{\text{surface}}(k,t = 0)$ necessary, in the absence of illumination nonuniformity, to produce the same outer-surface modulation amplitude $\eta_{\text{surface}}(k,t)$ during the drive pulse:

$$\varepsilon(k) \equiv \frac{\eta_{\text{imprint}}(k,t)}{\eta_{\text{surface}}(k,t)}\,\eta_{\text{surface}}(k,t=0). \qquad (1)$$

Figure 82.14 shows the equivalent surface finish as a function of mode number ℓ for simulations with and without the intensity spike, compared with that of an all-DT target with the standard pulse. In all cases (except for the short-wavelength, all-DT simulations, not shown in the figure), the spike reduces imprint. The equivalent surface finish was computed using the growth formula of Betti *et al*.,[6] where the ablation velocity, density scale length, and acceleration were taken from the all-DT, no-spike simulation, with coefficients $\alpha = 0.94$ and $\beta = 2.6$ during DT ablation and $\alpha = 1.0$ and $\beta = 1.7$ during CH ablation. We have also found that the thicker the outer CH layer, the greater the imprint reduction. The reduction in equivalent surface finish is large enough that even a target with a 3-μm outer CH layer has the same equivalent surface finish as an all-DT target. This is also shown in Table 82.II, which lists the equivalent surface finish, averaged over mode number ℓ, for a range of CH-layer thicknesses.

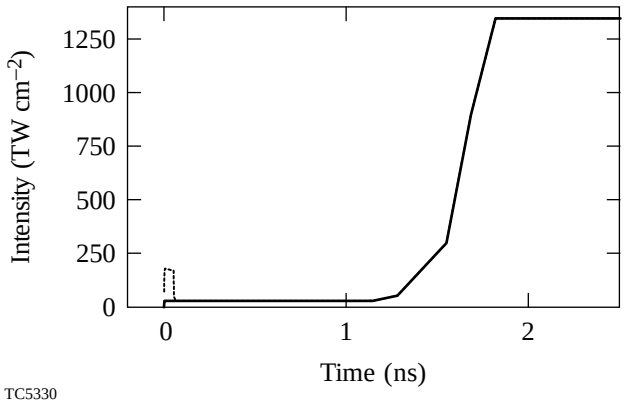

Figure 82.11
The pulse shape of an OMEGA cryogenic target, with (dotted) and without (solid) the initial intensity spike.

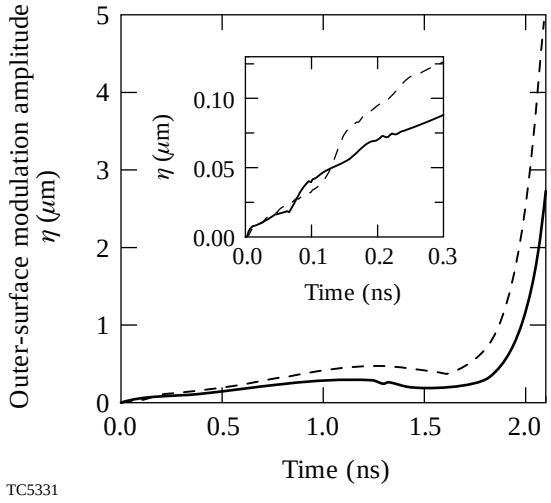

Figure 82.12
The amplitude η of the outer-surface modulation is shown for a 50-μm-wavelength illumination perturbation, for targets using a 3-μm overcoat layer of CH. The simulation using the standard cryo laser pulse is shown by a dashed line, while the simulation that used an initial intensity spike is shown by a solid line. The spike reduces the imprint by a factor of ~2 at this wavelength. The early-time behavior is shown in the inset.

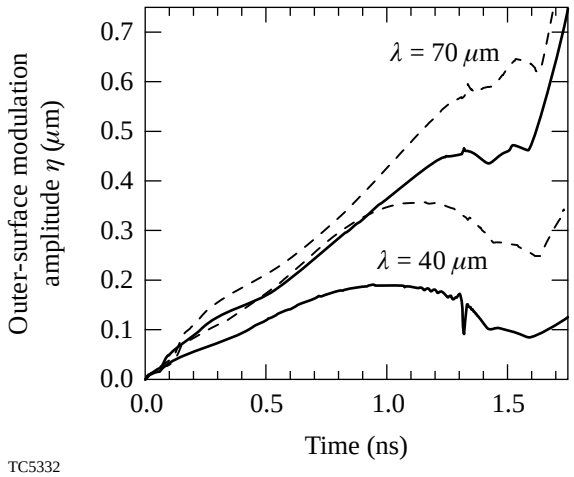

Figure 82.13
The outer-surface modulation amplitude η, for an initially smooth target, for a range of illumination nonuniformity wavelengths λ. Simulations are of targets with a 3-μm outer layer of CH. Pulses with (without) the intensity spike are shown with solid (dashed) lines.

The initial intensity spike reduces imprint primarily by reducing the early-time RT growth resulting from the CH layer that overcoats the DT shell. Even for a single-layer target, however, the period of increased intensity further reduces imprint by increasing the size of the plasma atmosphere around the target. The laser energy is deposited primarily outside the critical surface in the target's corona, where the plasma frequency equals the laser light's frequency. This energy is conducted thermally to the ablation surface. Modeling the conduction zone has shown that the pressure perturbation decreases exponentially with distance from the critical surface,[7] so

$$\tilde{p}_a / p_a \sim \left(\tilde{I}/I\right) \exp\left(-f k D_c\right),$$

where D_c is the distance between the critical and ablation surfaces, or *smoothing distance*, p_a is the ablation pressure, $\tilde{p}_a$ is its modulation amplitude, I is the laser intensity, $\tilde{I}$ its modulation amplitude, and f is of order unity. The smoothing distance increases linearly in time, so $D_c \sim V_c t$, where V_c is the velocity of the critical surface with respect to the ablation surface. Greater laser intensity results in a more rapid growth of the conduction zone and a larger V_c. Analytical modeling of the conduction zone[8] shows a scaling of $D_c \sim I^{4/3}$. Once $kD_c \sim 1$, at the *decoupling time*, the laser nonuniformities are decoupled from the target surface, and the ablation pressure is essentially uniform.

Because the degree of thermal smoothing is greater for higher laser intensities, the initial intensity spike also reduces imprint by increasing the smoothing distance. A series of simulations were performed for different wavelengths, with and without an intensity spike, of a target consisting of a shell of 84 μm of DT ice. This shell width was chosen so the total shell mass would be comparable to that of the simulations with

Table 82.II: The approximate reduction factor in equivalent surface finish, averaged over mode number ℓ, $\langle \varepsilon/\varepsilon_{\text{spike}} \rangle_\ell$, is shown for various thicknesses d (in μm) of the outer CH layer. Also shown is $\langle \varepsilon_{\text{spike}}/\varepsilon_{\text{DT}} \rangle_\ell$, the approximate average over mode number of the ratio of equivalent surface finish for a simulation with an intensity spike and d microns of CH, to that of an all-DT target, without the intensity spike.

d (μm)	$\langle \varepsilon/\varepsilon_{\text{spike}} \rangle_\ell$	$\langle \varepsilon_{\text{spike}}/\varepsilon_{\text{DT}} \rangle_\ell$
0	1.2	2.40
1	1.7	0.80
2	1.9	1.00
3	2.7	0.76

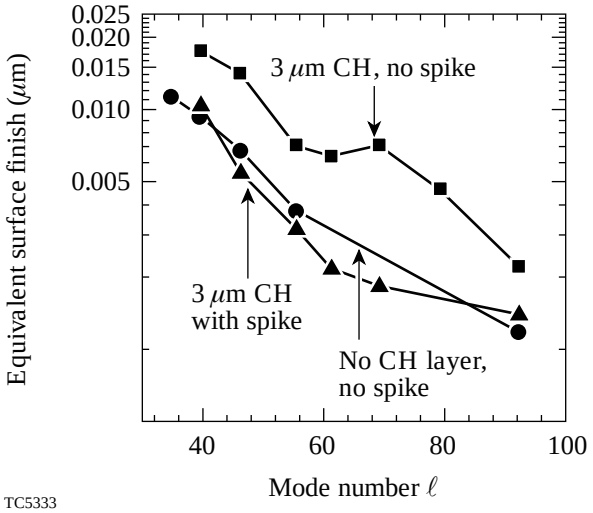

Figure 82.14
The equivalent surface finish for a series of mode numbers ℓ, for simulations with a 3-μm outer CH layer, with and without an initial intensity spike, and for a pure-DT target without an intensity spike.

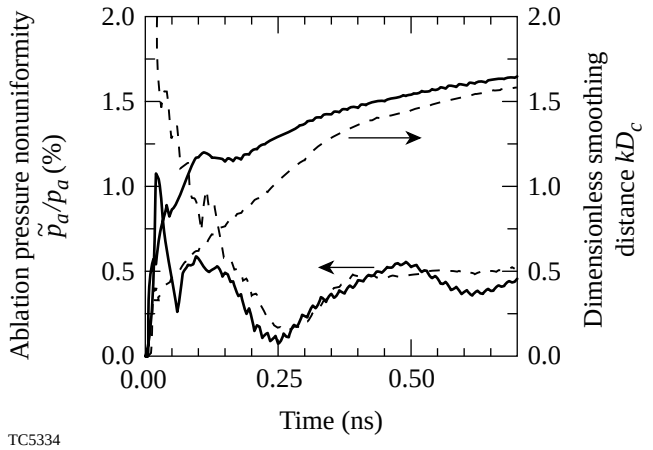

Figure 82.15
The ablation pressure nonuniformity $\tilde{p}_a/p_a$ and dimensionless smoothing distance kD_c for simulations with (solid) and without (dashed) an initial intensity spike. For these simulations, $\lambda = 50$ μm. The smoothing distance is taken to be the distance from the ablation surface to the critical surface. The curves showing $\tilde{p}_a/p_a$ have been smoothed numerically to reduce the noise due to finite simulation resolution.

a 3-μm CH layer, which have 72 μm of DT. Consider first the simulation with $\lambda = 50$ μm: From the slope of $\eta(t)$ in Fig. 82.15, which shows the ablation pressure nonuniformity $\tilde{p}_a/p_a$ and dimensionless smoothing distance kD_c for simulations with (solid) and without (dashed) an initial intensity spike, we see that for the standard pulse shape, $V_c \sim 35$ μm ns^{-1} (ignoring the zero-time offset). This means that the decoupling time $t_c \sim 230$ ps. Figure 82.15 also shows that, for $t \gtrsim t_c$, the ablation pressure nonuniformity $\tilde{p}_a/p_a$ has decreased to its asymptotic foot-pulse value of ~0.4%. By contrast, the simulation (represented by the solid line) with the spike has a decoupling velocity, during the first 100 ps, of $V_c \approx 90$ μm ns^{-1}, and a correspondingly smaller decoupling time and ablation-pressure nonuniformity. In this case, the decoupling speed V_c decreases at $t \sim 100$ ps because of the decrease in the laser intensity. The outer-surface modulation amplitude is shown in Fig. 82.16 (solid curves for pulse shapes including the intensity spike). As described above, η initially grows linearly. For example, the 50-μm simulation without the spike has a perturbed shock speed of $\tilde{v}_s \approx 0.7$ μm ns^{-1}, which produces a linear growth rate of $\dot{\eta} = 0.52$ μm ns^{-1} (see Appendix A). This is comparable to the growth rate shown in Fig. 82.16.

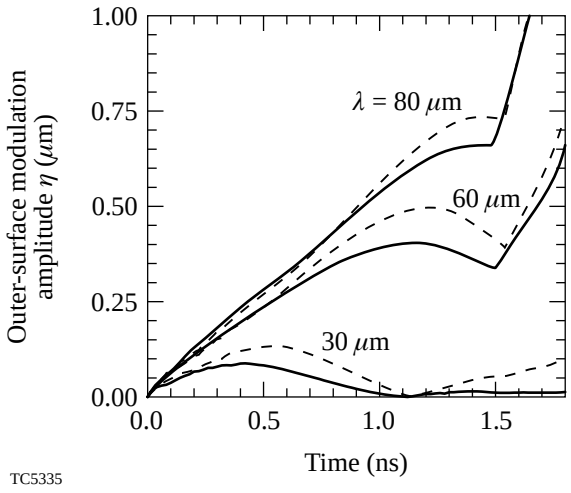

Figure 82.16
The amplitude of the outer-surface modulation for various illumination nonuniformity wavelengths, for targets without a CH overcoat. Dashed curves represent the standard OMEGA cryogenic pulse shape, while the solid curves represent pulses with an initial intensity spike.

To facilitate modeling, an intensity spike with a sharp rise and fall was used for the simulations described above. A realistic pulse will have a finite rise and fall time. Replacing the square spike profile with a Gaussian profile preserves the essential features and imprint reduction described above: For λ = 50 μm, and a 5% laser nonuniformity amplitude, the equivalent surface finish for a 50-ps, 180-TW cm^{-2} spike is 0.0032 μm, while for a 50-ps FWHM Gaussian spike with a peak intensity of 200 TW cm^{-2} (which delivers roughly the same energy), it is 0.003 μm. (This is to be compared with an equivalent surface finish of 0.007 μm without the intensity spike.) For a longer, less-intense spike of 100 ps and 120 TW cm^{-2}, the equivalent surface finish is 0.00055 μm, while for a 100-ps FWHM Gaussian spike with a peak intensity of 140 TW cm^{-2}, it is 0.001 μm.

The performance of an OMEGA target is reflected by the neutron yield Y that it produces. For an OMEGA cryo target, the drive-pulse shock must be launched sufficiently after the weaker foot-pulse shock so that they break out of the main fuel layer at about the same time. A change in the initial intensity changes the shock speed, potentially altering the shock timing. The fractional neutron yield (relative to the yield with no spike) for a range of intensity spike durations (dt) and intensities (I) is shown in Fig. 82.17. As this figure shows, the greater the I or dt, the lower the yield. However, because the foot pulse does not maintain the intensity used in the spike, the shock is unsupported and, after the duration of the spike, evolves into a decaying N-wave.[9] The true measure of the disruption caused by the spike is the energy it delivers to the target, $I\,dt$, as shown by the contours of constant Y in Fig. 82.17. Based on the 1-D

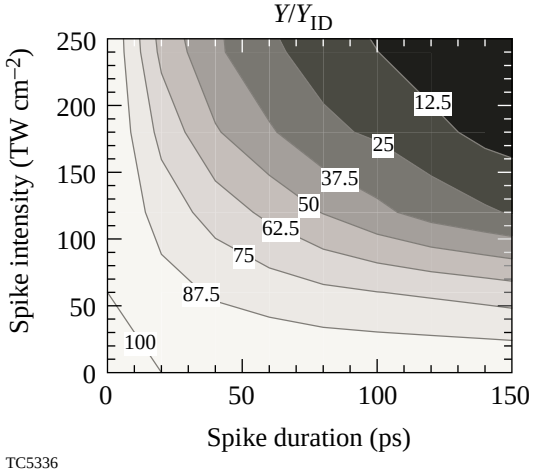

Figure 82.17
Neutron yield as a fraction of the yield with no intensity spike, plotted in terms of the spike duration dt and intensity I. A spike intensity of less than the foot-pulse intensity, or duration of zero, indicates that the spike is absent. Operating on the 80% contour line will reduce imprint by about a factor of 2. Much of the reduction in yield can be recovered by shortening the foot pulse. Yields were calculated with *LILAC*.

simulations, the yield $Y(I, dt)$ is of the same order as that of the canonical cryo target for a wide range of spike intensities and durations. In addition, because $I\,dt << I_{\text{foot}}\,dt_{\text{foot}}$, the fuel adiabat α and the RT growth factor are not significantly changed by the spike. The main effect of the intensity spike is to alter the shock timing. For the example of a 100-ps spike with twice the foot-pulse intensity (i.e., 60 TW cm^{-2}), the imprint reduction is approximately a factor of 2 and the decrease in 1-D yield is only 20%. Much of the reduction in yield shown in Fig. 82.17 may be recovered by slightly shortening the duration of the foot pulse.

In summary, the presence of an initial intensity spike at the start of the foot pulse in an OMEGA cryogenic target reduces imprint by about a factor of 2 for typical target configurations. This imprint reduction comes at the cost of only a modest decrease in yield, most of which can be recovered by a small reduction in pulse length. Furthermore, this reduction in imprint occurs for those wavelengths of illumination nonuniformity considered to be the most dangerous for target performance.

ACKNOWLEDGMENT

One of the authors (TJBC) would like to thank V. Goncharov and P. B. Radha for many useful discussions. This work was supported by the U.S. Department of Energy Office of Inertial Confinement Fusion under Cooperative Agreement No. DE-FC03-92SF19460, the University of Rochester, and the New York State Energy Research and Development Authority. The support of DOE does not constitute an endorsement by DOE of the views expressed in this article.

Appendix A: Rarefaction-Wave Rayleigh–Taylor Growth

The RT growth due to the early-time RW acceleration was first discussed in the context of feedout by Betti *et al.*[10] A simple estimate of the early-time RT growth for NIF targets was performed by Goncharov *et al.*[11] using scaling laws. In this appendix we approximate the period of RT growth due to the RW return from the DT/CH interface in OMEGA cryo targets. As discussed above, when the foot shock reaches the interface between the CH and the DT ice, it behaves as if it has reached a contact discontinuity. At this point it proceeds as a stronger shock into the DT and sends a rarefaction wave outward toward the outer surface, communicating the new post-shock conditions. When the RW crosses the outer surface, it is accelerated to the post-shock speed of the DT.

This process is shown in Fig. 82.18, an r–t diagram for a simulation with a 72-μm shell of DT ice, surrounded by 3 μm of CH, and the standard OMEGA cryo pulse shape (see Fig. 82.11). (This DT-shell width was chosen so the shell would have the same total mass as that of the all-DT simulations.) The duration of the RT growth may be estimated as follows: the RW is launched from the point (r_0, t_0), where $r_0 = R_0 - d$ (d = 3 μm being the width of the CH layer) and $t_0 = r_0/v_s$ (v_s being the shock speed). The outer edge of the RW travels at the post-CH-shock sound speed, while the inner edge travels with a velocity of v_{RW}, given in Ref. 9 as

$$v_{\text{RW}} = -c_s + \frac{1}{2}\left[(\gamma+1)V - (\gamma-1)u\right]. \tag{A1}$$

Here V is the post-DT-shock speed, γ is the ratio of specific heats, and $u = (1-\xi^{-1})\,v_s$ is the post-shock speed, where ξ is the degree of shock compression and a strong shock is assumed. The intersection (r_1, t_1) of the ablation front, which travels at speed u, and the outer edge of the RW wave is given by

$$r_1 = R_0 - d\left(1-\xi^{-1}\right)\left(1+\xi^{-1}M_{\text{CH}}\right), \tag{A2}$$

$$t_1 = \frac{d}{v_s}\left(1+\xi^{-1}M_{\text{CH}}\right), \tag{A3}$$

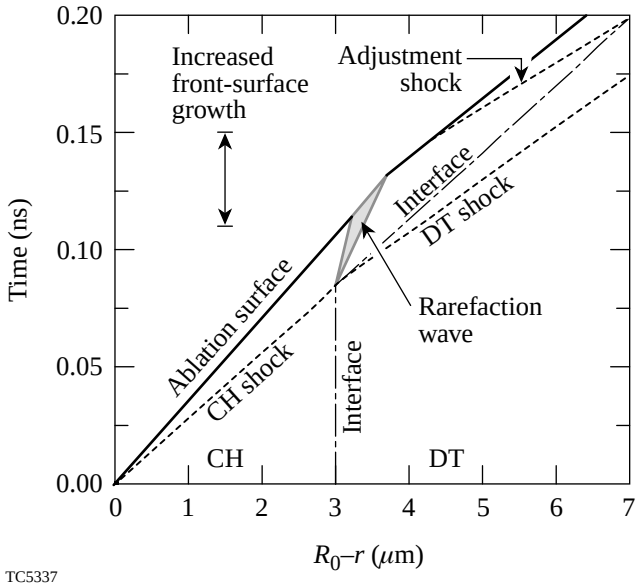

Figure 82.18
An r–t diagram for an OMEGA cryo simulation with a 50-μm illumination perturbation, and a target shell composed of 72 μm of DT ice and 3 μm of CH. Shock and interface trajectories are shown as functions of the time t and the distance R_0–r from the initial outer radius R_0. Note that, when the foot-pulse shock reaches the DT/CH interface, the shock speed increases and a forward-swept rarefaction wave (shaded region) is launched. Because the post-DT-shock pressure is not equal to the ablation pressure, a second adjustment shock is sent into the shell. Shocks are represented by dashed lines, and the CH/DT interface by a dashed–dotted line.

where M_{CH} is the Mach number of the foot-pulse shock traveling through the CH. If we approximate the speed of the ablation front during its passage through the RW by the average between its speeds before and after, $(u + V)/2$, the duration Δt of the RW acceleration is given by

$$\Delta t \approx \frac{(\gamma+1)\left[\xi M_{DT} - (\xi-1) M_{CH}\right]}{\left\{2\xi - \gamma\left[\xi M_{DT} - (\xi-1) M_{CH}\right]\right\}} \times \frac{d}{\xi c_s}, \qquad \text{(A4)}$$

where $M_{DT} \equiv V/c_s$. During this period, the ablation surface is subject to the RT instability. In addition, because the RW reaches the "trough" of the outer-surface perturbation first, the period of acceleration is extended by a period of approximately $\Delta t' = 2|\eta(t_1)|/c_s$. For uniform laser illumination, the outer radius of the target is given, during the foot pulse (and before foot-pulse shock breakout), by $R(t) = R(0) - ut = R(0) - (1-\xi^{-1})v_s t$, where t is the time since the start of the laser pulse and u is the post-shock speed. Perturbing this equation for $R(t)$, we find that an initially smooth target will develop a surface modulation given by

$$\eta(t) = \left(1-\xi^{-1}\right)\tilde{v}_s t, \qquad \text{(A5)}$$

where $\tilde{v}_s$ is the modulation amplitude of the shock speed, assuming a strong shock. Inserting Eq. (A5) into the expression for $\Delta t'$ yields

$$\Delta t' \approx 2\frac{d}{c_s}\left(1-\xi^{-1}\right)\left(1+M_{CH}\,\xi^{-1}\right)\frac{\tilde{M}_{CH}}{M_{CH}}, \qquad \text{(A6)}$$

where $\tilde{M}_{CH} \equiv \tilde{v}_s/c_s$. The RT growth factor due to the RW is given approximately by

$$G_{RW} \approx e^{\sqrt{(V-u)k(\Delta t+\Delta t')}}. \qquad \text{(A7)}$$

After the early period of growth, the outer-surface modulation continues to grow at a constant rate. As the RW propagates, it lowers the pressure and density of the shocked CH; however, as mentioned above, the laser imposes a pressure equal to the ablation pressure at the outer surface. Thus when the RW reaches the outer surface, a second, *adjustment* shock is launched into the CH to increase the pressure in the shell. As this shock is launched, $\dot{\eta}$ is decreased to approximately the value it had before the RW return. The inset in Fig. 82.12 shows the period of initial linear growth, followed by the early-time RT growth. There is a subsequent decrease in the linear growth rate because the adjustment shock is launched from the trough of the surface perturbation before the peak. The outer surface undergoes slightly more than one quarter of a period of an oscillation before the drive pulse begins, followed by RT growth.

REFERENCES

1. S. Skupsky, R. W. Short, T. Kessler, R. S. Craxton, S. Letzring, and J. M. Soures, J. Appl. Phys. **66**, 3456 (1989).
2. T. R. Boehly, V. A. Smalyuk, D. D. Meyerhofer, J. P. Knauer, D. K. Bradley, C. P. Verdon, and D. Kalantar, in *Laser Interaction and Related Plasma Phenomena*, edited by G. H. Miley and E. M. Campbell (American Institute of Physics, New York, 1997), Vol. 406, pp. 122–129.
3. Y. Lin, T. J. Kessler, and G. N. Lawrence, Opt. Lett. **20**, 764 (1995).
4. Laboratory for Laser Energetics LLE Review **80**, 185, NTIS document No. DOE/SF/19460-321 (1999). Copies may be obtained from the National Technical Information Service, Springfield, VA 22161.
5. S. V. Weber, S. G. Glendinning, D. H. Kalantar, M. H. Key, B. A. Remington, J. E. Rothenberg, E. Wolfrum, C. P. Verdon, and J. P. Knauer, Phys. Plasmas **4**, 1978 (1997).
6. R. Betti, V. N. Goncharov, R. L. McCrory, P. Sorotokin, and C. P. Verdon, Phys. Plasmas **3**, 2122 (1996).
7. K. A. Brueckner and S. Jorna, Rev. Mod. Phys. **46**, 325 (1974).
8. W. M. Manheimer, D. G. Colombant, and J. H. Gardner, Phys. Fluids **25**, 1644 (1982).
9. G. B. Whitham, *Linear and Nonlinear Waves*, Pure and Applied Mathematics (Wiley, New York, 1974).
10. R. Betti, V. Lobatchev, and R. L. McCrory, Phys. Rev. Lett. **81**, 5560 (1998).
11. V. N. Goncharov, S. Skupsky, T. R. Boehly, J. P. Knauer, P. McKenty, V. A. Smalyuk, R. P. J. Town, O. V. Gotchev, R. Betti, and D. D. Meyerhofer, Phys. Plasmas **7**, 2062 (2000).

Measurement of Preheat due to Fast Electrons in Laser Implosions

Introduction

Fast electrons due to the two-plasmon-decay (2PD) instability have been measured in previous laser-interaction experiments.[1,2] The main impact of these electrons in laser-fusion experiments is the possible preheat that can reduce the implosion's effectiveness. The preheat caused by these electrons is studied by measuring the Kα line emission from high-Z layers in a flat-target geometry on the OMEGA[3] laser system. The Kα emission is directly related to the preheat level;[4,5] for sufficiently high fast-electron temperatures (T_{fast}) the relationship between the Kα intensity and the preheat level is independent of T_{fast}. The preheat due to fast electrons in UV laser irradiation is relatively small and is usually masked by the preheat due to radiation. To overcome this problem, a target containing titanium (Ti) and vanadium (V) layers was designed so that when irradiated from the Ti side, most of the Ti-Kα is excited by radiation, whereas most of the V-Kα is excited by the fast electrons. As seen below, the thick Ti and V layers required for the Kα measurement precluded conducting this experiment in spherical geometry. We show, however, that such measurements can be used as a reference point for hard x-ray continuum detectors, which can then be used to determine the preheat in undoped spherical targets. The Kα measurements can conveniently be used as a reference point because in the case of x-ray continuum measurements T_{fast} must be known to determine the preheat level even at high temperatures.

Flat-Target Experimental Configuration

The configuration for the flat-target experiment is shown in Fig. 82.19. Ten OMEGA beams of 1-ns square pulse duration and 4.85-kJ total energy are overlapped to yield a target irradiance of 1.5×10^{15} W/cm^2. This value exceeds the irradiance in spherical implosion experiments on OMEGA, thus providing an upper limit on preheat in future experiments. The target consists of two main layers: 5-μm-thick titanium and 40-μm-thick vanadium. The 20-μm-thick CH overcoat precludes any direct laser irradiation or heating of either metal, thus restricting laser interaction with the metals to preheat only. Indeed, the only lines seen in the measured spectra are the Ti- and V-Kα lines. Two time-integrating x-ray spectrometers observe the spectrum emitted from the front side and the back side of the target. The purpose of the two-layer target is to ensure that most of the V-Kα line is excited by fast electrons, not radiation. The Ti layer is thick enough to strongly absorb radiation above the Ti-K edge, thus minimizing the radiative excitation of Kα in the vanadium. To further increase the emission of the V-Kα line due to fast electrons, the V-layer thickness should be made about equal to the range of fast electrons. Analysis of the Kα line intensities indicates, as seen below, a fast-electron temperature exceeding ~50 keV. The range in vanadium can be well approximated[6] by the relation $R(\text{g/cm}^2) = 9.4 \times 10^{-6}\, E^{5/3}$, where E is the electron energy in keV. Thus the range of the fast electrons in vanadium is a few tens of microns. The (1/e) attenuation length of the V-Kα line

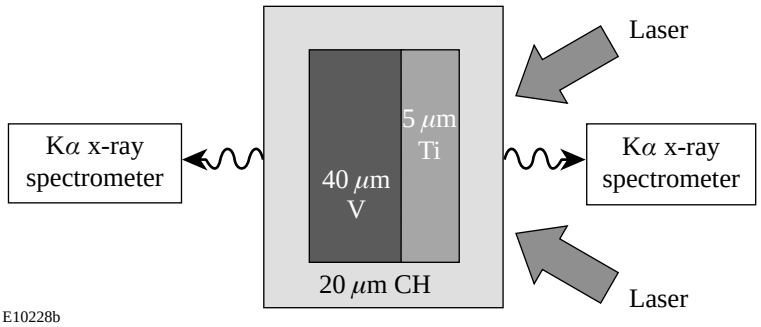

Figure 82.19
Experimental configuration for measuring fast-electron preheat. Ten incident laser beams are absorbed in the CH layer. Radiation excites the Ti-Kα line, but most of it is absorbed before reaching the vanadium layer. On the other hand, fast electrons can penetrate the vanadium layer and excite the V-Kα line.

in vanadium, however, is ~18 μm; thus the vanadium layer should not be significantly thicker than ~18 μm, hence the choice of ~40 μm. Vanadium was chosen because the Kα lines of Ti and V are close enough to be simultaneously observed in the spectrum. Also, the back-layer material should have the higher Z of the two; otherwise, radiation of energy between the Ti-K edge (4.96 keV) and the V-K edge (5.46 keV) will be transmitted through the front layer and will strongly contribute to Kα emission in the back layer, contrary to the main goal of the experiment. Two crystal spectrometers viewed the emitted spectrum from the front and back of the target. The crystal in the front spectrometer was Ge(1,1,1); the one in the back was ADP(1,0,1).

Figure 82.20 shows the observed spectra from the front side and the back side of the target for shot 18167. Kα lines of Ti and V are seen, as well as the continuum emitted from the interaction region in the CH coating. The absolute energy in the Kα lines, which is required to determine preheat, is based on the following calibrations: (a) for the Ge crystal, a calibration performed at LLE[7] that agrees very well with the Darwin–Prins model,[8] (b) for the ADP crystal, two consistent calibrations,[9,10] and (c) for the DEF film, published calibration,[11] for which the film processing procedure was closely followed here. It should be further noted that both crystal calibrations change very little over the energy range of primary interest here, ~4.5 to 5 keV. The target is viewed through a 25-μm-wide slit, which provides a one-dimensional image of the target at each wavelength, from which the space-integrated emission is computed. The space-integrated emission is larger than the measured emission by approximately the factor $d/\left[d\left(1+M^{-1}\right)\right]$, where D is the FWHM of the emission region, d is the slit width, and M is the magnification. The following three sections deal with the analysis of the flat-target experimental results.

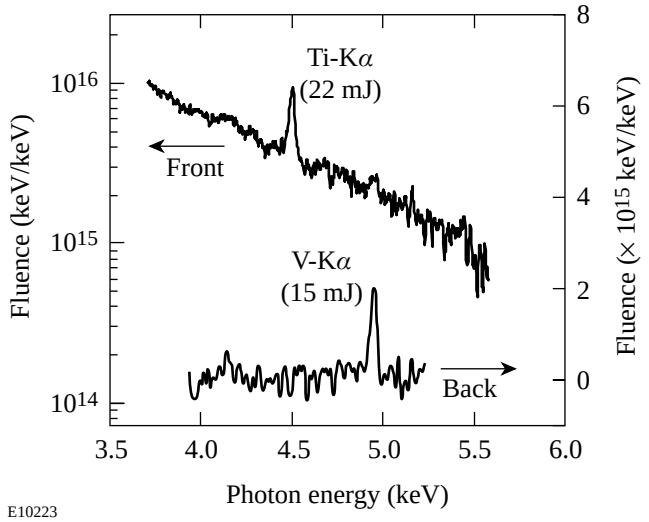

Figure 82.20
Time-integrated spectra emitted from the front and back of the target shown in Fig. 82.19. The measured line-intensity ratios are used to prove that the intensity of the V-Kα line (observed from the back) is mostly due to fast electrons.

Analysis of Kα Emission

To analyze the measured Kα lines we first calculate their excitation due to radiation alone. We use the measured continuum intensity (Fig. 82.20) that is emitted by the laser-interaction region in the CH and transport it through the Ti and V layers (absorption in the CH is negligibly small). Only radiation above the Ti-K edge (4.96 keV) must be included to calculate the excitation of either Kα line. Using the known opacity of cold Ti or V per unit areal density, $\tau(E)$, we solve the radiation transport equation for the spectral intensity $I(x,E)$ into 2π solid angle:

$$dI(x,E)/dx = -\tau(E)\rho I(x,E), \tag{1}$$

from which the local emission of Ti-Kα is calculated according to

$$I(\mathrm{Ti-K}\alpha) = E(\mathrm{K}\alpha)\omega_K(\mathrm{Ti}) \int_{E_K}^{\infty} I(x,E)\left\{1-\exp\left[-\tau(\mathrm{Ti})\rho\Delta x\right]\right\} dE/E, \tag{2}$$

and likewise for the V layer. Here ω_K = 0.22 is the fluorescence yield[12] of Ti, and E(Kα) = 4.508 keV is the photon energy of the Ti-Kα line; for V, ω_K = 0.25 and E(Kα) = 4.952 keV. Using the normal density of the metal (ρ) is justified since in plane geometry the areal density $\rho\Delta x$ does not change when compression or expansion takes place. Also, shock arrival for most of the vanadium occurs after the laser pulse; thus, the preheating has been completed. The cold-metal opacity can be used since, as shown below, the degree of ionization due to the preheat is small (on average, two electrons per atom). Also, when removing the outer (M-shell) electrons, the K edge shifts very slightly to higher energies, but the absorption cross section at a given photon energy changes insignificantly.[13] The resulting spatial profiles of Kα emission, plotted in Fig. 82.21, show that some radiation survives

absorption in the titanium and excites V-Kα near the V–Ti interface. The contribution of the observed Kα lines is finally obtained by performing a radiation transport calculation of the Kα line in both directions (exiting the target on the Ti side and on the V side, respectively). We now show that the results of these calculations disagree with the experiment, indicating that radiation alone cannot explain the measured intensity ratios, without the inclusion of fast-electron excitation of Kα. For these considerations we use only line-intensity ratios, so the conclusion is independent of the accuracy in absolute calibration. Table 82.III compares the measured Kα line-intensity ratios with the prediction of the radiative model, where front designates observation on the Ti (or laser side) and back designates observation on the V side of the target. The first measured ratio, V (back)/Ti (front), is much higher than predicted by the radiative model because fast electrons increase the V-Kα intensity more than that of the Ti-Kα intensity (because of the larger thickness of the former). Also, fast electrons excite V-Kα throughout the vanadium layer rather than only near the V–Ti interface, thus reducing its attenuation when exiting on the V side. The same combination of effects explains the disagreement of the second ratio, V (back)/Ti (back). The third ratio, V (back)/V (front), is sensitive only to the spatial distribution of V-Kα emission rather than to its origin. The disagreement in this case indicates that the V-Kα line is emitted deeper into the vanadium and thus is attenuated less toward the back side, indicating again the contribution from long-range fast electrons.

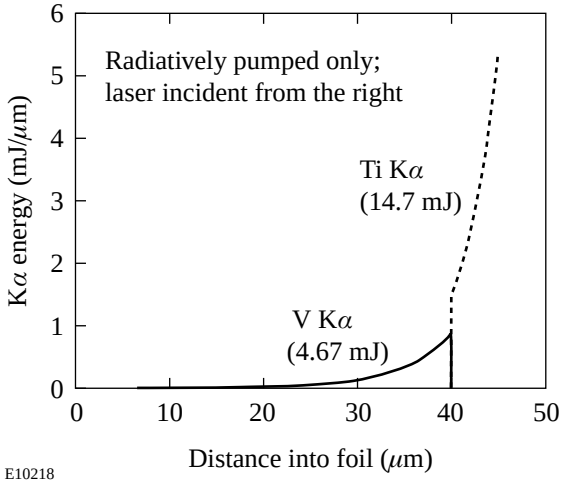

Figure 82.21
Calculated spatial profiles of Kα line emissions due only to radiation in the target of Fig. 82.19. The measured radiation from the interaction region (Fig. 82.20) was used as input.

Table 82.III: Comparison of radiative-model predictions and measurements.

Kα-Line-Intensity Ratios	Radiative-Model Predictions	Measurements (Shot 18167)
V (back)/Ti (front)	0.05	~0.7
V (back)/Ti (back)	0.37	>>1
V (back)/V (front)	0.25	~5

We next analyze quantitatively the contribution of fast electrons to the Kα line emission and show that the V-Kα line viewed from the back is indeed excited mostly by fast electrons. We assume that the energies of fast electrons have a Maxwellian distribution (this assumption is based on 2-D simulations of the two-plasmon-decay instability[14]); the temperature and total energy of the fast electrons are considered free parameters in the calculation. A multigroup transport simulation of the electrons streaming through the Ti and V layers is performed, using the Bethe–Bloch slowing-down formula[15]

$$\left(-dE/dx\right)_{\text{coll}} = \left(2\pi e^4 N_a\, Z/E_0\right) \ln\left(1.16\; E_0/\langle E_i\rangle\right), \quad (3)$$

where N_a is the atomic density, E_0 the energy of the projectile electron, and $\langle E_i\rangle$ the effective ionization energy. $\langle E_i\rangle$ is determined by fitting Eq. (3) to experiments[16] using beam interaction with foil targets. For Ti, $\langle E_i\rangle \sim 215$ eV, and for V, $\langle E_i\rangle \sim 220$ eV. The validity of using this formula is discussed in Appendix A. The production of Kα is calculated by the rate

$$dE(\text{K}\alpha)/dx = \sigma_K(E_v)(\rho/M_a)\omega_K(\text{Ti})E_K\,, \quad (4)$$

where the cross section is given by[17]

$$\sigma_K = \left(\pi e^4/E_v E_K\right) Z_K b_K \ln\left(c_K E_v/E_K\right), \quad (5)$$

where E_v is the photon energy, ρ is the mass density, M_a is the atomic mass, Z_K is the number of electrons in the K shell, and b_K and c_K are constants that change slowly with Z. By fitting Eq. (5) to detailed calculations, b_K and c_K have been determined for a wide range of elements. Even though Eq. (5) is nonrelativistic, the fitting was done for electron energies up to ~30 times the K-edge energy, or ~160 keV. Having determined thus the spatial distribution of Kα line emission due to electrons, we transport the line intensity in both directions (as above) to calculate the contribution to the observed Kα lines.

We finally add up the contributions from radiation and fast electrons and compare the calculated and measured Kα lines. As noted above, the calculated contribution of electrons depends on two free parameters (their temperature and total energy), whereas the contribution of radiation is calculated directly from the observed spectrum.

Figure 82.22 shows the results of the calculations for the ratio V (back)/Ti (front) as a function of the assumed electron temperature. The parameter for each curve is related to the assumed total energy in fast electrons. It is expressed as the fractional contribution of fast electrons to the V-Kα (back) emission intensity. The experimental value of the V-Kα (back)/Ti-Kα (front) ratio, 0.7±0.1, is shown as a gray band in Fig. 82.22. The line marked 0.0 corresponds to removing the fast-electron component, whereas the curve marked 1.0 corresponds to removing the radiation component. In the limit of very high fast-electron temperatures (where the production of Kα lines by fast electrons is uniform over the target volume) the latter curve approaches the value ~2.3. This is smaller than the ratio 8 of V and Ti thicknesses because of the larger attenuation of the back-emergent V-Kα line as compared with the front-emergent Ti-Kα line. At low temperatures the electrons barely penetrate the Ti layer, and the V-Kα line drops sharply. Comparing the curves in Fig. 82.22 with the experimental value indicates that *the electron temperature is higher than ~50 keV*. For lower electron temperatures the V-Kα line cannot be excited appreciably, and any excitation will be close to the Ti–V interface and be severely attenuated toward the back. Additional determinations of the fast-electron temperature will be described in the following sections. The primary conclusion from Fig. 82.22 is that *almost all of the intensity of the V-Kα line (viewed from the back) is due to electron excitation.* This observable will now be used to estimate the preheat due to fast electrons.

Determination of Electron Preheat from Kα Measurements

In this section we discuss the determination of preheat level by fast electrons, using the Kα emission from the vanadium layer; preheat level as determined by hard x-ray emission will be the subject of the subsequent section. By dividing Eq. (3) by Eq. (4) we obtain the ratio of preheat to electron production of Kα lines. The result for V is shown as the curve marked *analytic* in Fig. 82.23. This curve tacitly assumes that the fast electrons are mono-energetic and the target is much thinner than the attenuation length. To remove these assumptions, we used the multigroup transport simulation described above to calculate the attenuation and Kα production of a Maxwellian distribution of electrons moving through the actual target used in this experiment. This calculation accounts for the distortion of the original Maxwellian distribution during transport

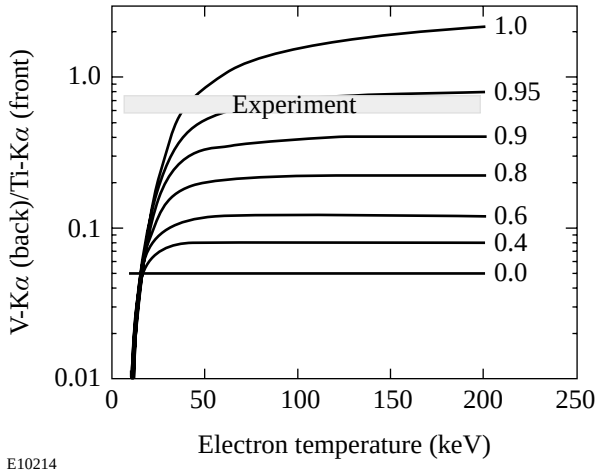

Figure 82.22
Calculated and measured ratio of V-Kα observed from the back to Ti-Kα observed from the front of the target due to both radiation and fast electrons. The parameter for each curve is the fraction of the V-Kα line that is excited by electrons. Comparison with the experimental value of this ratio shows that (a) the V-Kα line is excited almost exclusively by fast electrons, and (b) the temperature of fast electrons is ≳50 keV.

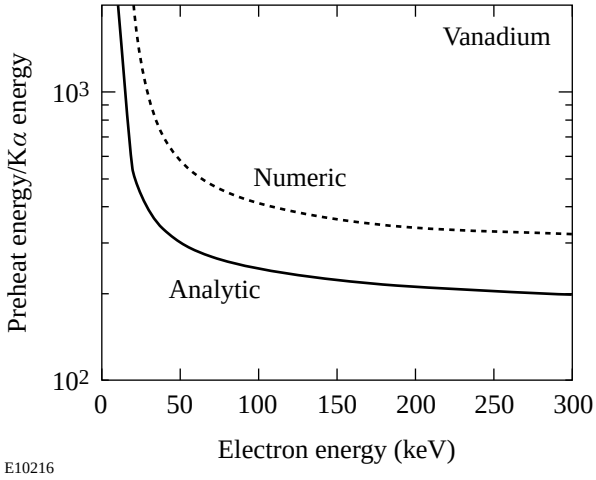

Figure 82.23
Determination of preheat from the measured V-Kα intensity (after correction for transport, using Fig. 82.24). The analytic curve is the ratio of the relevant rates per cm propagation, while the numeric curve is the result of multigroup calculation for an initially Maxwellian distribution transported through the target of Fig. 82.19; for the latter case the abscissa values refer to the temperature of the fast electrons.

through the foil. The ratio of the space-integrated preheat and Kα production is shown by the curve marked *numeric* in Fig. 82.23; the abscissa for this curve is now the temperature rather than the energy of the fast electrons. The numeric curve is higher than the analytic curve because the slowing-down gradually brings the electrons to energies where the preheat is more effective. Finally, by multiplying the measured Kα energy (in absolute magnitude) by the appropriate value of the numeric curve, the preheat energy deposited in the target can be determined. As seen in Fig. 82.23, T_{fast} *need not be known accurately to determine the preheat, as long as it is higher than ~50 keV*; Fig. 82.22 indicates that this was indeed the case here. It should be noted that the Kα intensity for this curve refers to the total local emission of Kα, which must be deduced from the observed Kα. The relation between the two depends on the spatial distribution of Kα, which in turn depends on T_{fast}. Also, the Kα intensity for this curve refers to the fraction of Kα that is excited solely by electrons.

Starting with the 15-mJ observed energy of V-Kα (back), we estimate the total local V-Kα emission. In Fig. 82.24 we show the relationship between the two as a function of T_{fast}. For T_{fast} higher than ~50 keV the ratio is ~0.35, yielding 39 mJ for the total emission of V-Kα. From Fig. 82.23 this corresponds to a preheat in the V of ~12 J. For the total Ti–V target the preheat is ~14 J (an increase of approximately the ratio of thicknesses 45 μm/40 μm); thus the preheat energy is about 0.3% of the incident laser energy.

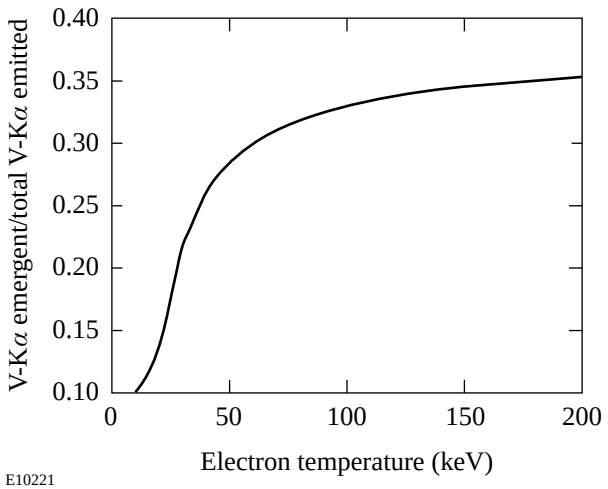

Figure 82.24
Calculated ratio of V-Kα energy emergent from the back of the target to the total volume emission of V-Kα. The former quantity is the one measured, whereas the latter is used to derive the preheat.

Determination of Electron Preheat from Hard X-Ray Measurements

In undoped targets, with no emission of Kα lines, preheat levels can be determined by measuring the spectrum of hard x-ray continuum. We show here that the spectrum-integrated x-ray continuum is directly related to the preheat deposited in the target, with no need to know the trajectories of the fast electrons in and around the target or the energy lost to the acceleration of ions. The loss rate due to bremsstrahlung is given by the Heitler relativistic formula[18]

$$\left(-dE/dx\right)_{\text{rad}} = N_a Z^2 \alpha \left(e^2/mc^2\right)^2 \left(E_0 + mc^2\right)$$

$$\times \left\{4 \ln\left[2\left(E_0 + mc^2\right)/mc^2\right] - 4/3\right\}, \quad (6)$$

where N_a is the atomic density, α is the fine-structure constant, and E_0 is the energy of the projectile electron. It should be noted that, unlike for the collision loss rate, the relativistic formula yields considerably higher values than the classical formula (by a factor of ~2 at 100 keV). Dividing Eq. (3) by Eq. (6) gives the ratio of preheat energy to radiation energy, shown by the curve marked *analytic* in Fig. 82.25. As in the equivalent case of Kα energy (Fig. 82.23) we use a multigroup electron transport calculation applied to the target in

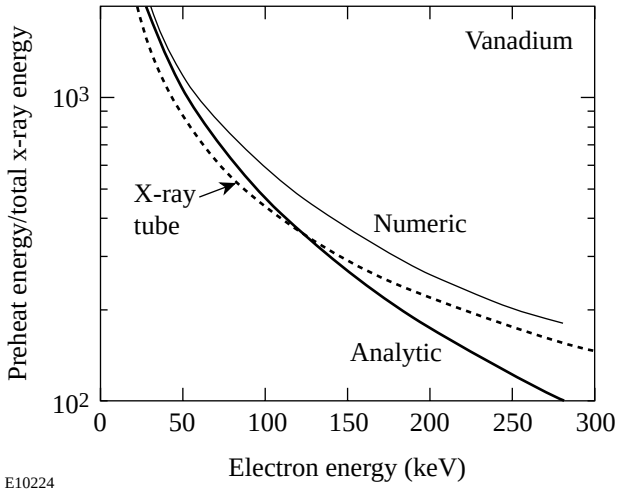

Figure 82.25
Determination of preheat from the spectrum-integrated hard x-ray emission. The analytic curve is the ratio of the relevant rates per cm propagation, while the numeric curve is the result of multigroup calculation for an initially Maxwellian distribution transported through the target of Fig. 82.19; for the latter case the abscissa values refer to the temperature of the fast electrons. The curve marked *x-ray tube* is the inverse of the empirical x-ray efficiency of a vanadium x-ray tube of an applied voltage *E*.

Fig. 82.19. The electrons are assumed to have a Maxwellian distribution of energies (rather than the same energy); the attenuation and distortion of the distribution during transport through the thick target are accounted for, and the ratio of space-integrated preheat and radiation is calculated. The result is marked *numeric* in Fig. 82.25, and for this curve the abscissa designates the temperature rather than the energy of the fast electrons. As in Fig. 82.23, the numeric curve is higher than the analytic curve; this is simply due to the rise of the curves in Fig. 82.25 for lower energies.

We can gain additional confidence in the curves in Fig. 82.25 by comparing them with the efficiency data of an x-ray tube with a vanadium anode. The input power that accelerates the electrons in the tube is converted mainly to heating the anode (equivalent to preheat in our case), with a fraction converted to x rays, mostly continuum. The power of x-ray continuum emission is given by[19] $P = K(Z) \times Z \times I \times V^2$, where V and I are the accelerating voltage and the tube current, respectively, and K depends weakly on Z. Thus, the ratio of preheat to radiation is $\varepsilon = \left[Z \times V \times K(Z)\right]^{-1}$. For vanadium, the empirical value[19] of K is $\sim 1.1 \times 10^{-6}\,\mathrm{keV}^{-1}$, resulting in the curve marked *x-ray tube* in Fig. 82.25 (V is the electron energy). Good agreement with the theoretical curves is seen.

ACKNOWLEDGMENT

Useful discussions with R. W. Short are gratefully acknowledged. This work was supported by the U.S. Department of Energy Office of Inertial Confinement Fusion under Cooperative Agreement No. DE-FC03-92SF19460, the University of Rochester, and the New York State Energy Research and Development Authority. The support of DOE does not constitute an endorsement by DOE of the views expressed in this article.

Appendix A: Slowing-Down Formulas for Partly Ionized Vanadium

The Bethe–Bloch slowing-down equation [Eq. (3)] applies to charged particles interacting with a cold, un-ionized target. In our case the vanadium layer is heated by fast electrons (and also by a shock wave) and is partly ionized. We examine here the required modifications to Eq. (3). We start by estimating the degree of ionization in the vanadium, based on the total target preheat energy estimated above. The total preheat derived from the Kα lines was 14 J. Dividing this energy by the preheated volume (given by the product of the focal-spot area and the target thickness), we derive a preheat per atom of E_a ~100 eV. We estimate the temperature and average ionization consistent with E_a by solving the Saha equations of vanadium charge states and calculating E_a and $\langle Z \rangle$ from

$$E_a = (3/2)\left[\langle Z \rangle + 1\right] kT_e + \Sigma_Z\, N_Z E_i(Z), \qquad \langle Z \rangle = \Sigma_Z\, Z\, N_z\,, \tag{A1}$$

where N_Z is the relative population and $E_i(Z)$ is the ionization energy of charge state Z. For any chosen value of the mass density ρ we find the N_e and T_e values that satisfy two conditions: (a) the calculated value of E_a from Eq. (A1) equals 100 eV and (b) the value of $\langle Z \rangle$ calculated from Eq. (A1) agrees with $N_e M_a / \rho$ (M_a is the atom mass). There is a unique solution consistent with both ρ and E_a. For mass densities in the range of 0.1 to 10 times the solid density of V, the resulting temperature varies from 18 to 43 eV and $\langle Z \rangle$ varies from 1.4 to 2.6; therefore, only about 10% of the V and Ti electrons are ionized, whereas the rest remain bound. In calculating the slowing-down of the projectile electrons we must add the contributions of the bound electrons and the plasma (as shown below, the two are not totally independent). In justifying the approximations adopted below, we shall assume as typical parameter values an electron projectile energy of 50 keV moving through a solid-density vanadium plasma of temperature T_e = 30 eV. Equation (3) plus the equations in this Appendix are valid for electrons that are fast but not highly relativistic. This means that the projectile electron velocity v must be much higher than a typical electron velocity in the medium but the relativistic quantity γ should not be much greater than 1. For a 50-keV-projectile electron, the velocity $v_0 = 0.98 \times 10^{10}$ cm/s and $\gamma \sim 1.1$. For our case, the fully relativistic formula [Eq. (3) in Ref. 15] differs very little from Eq. (3) above; even at an electron projectile of 250 keV the two differ by only 1.5%. On the other hand, v_0 is much larger than the thermal electron velocity in the medium (~4×10^8 cm/s) and larger than the Fermi velocity

$$\left(3\pi^2 N_e\right)^{1/3} \Big/ \left(\hbar / m\right) \sim 2 \times 10^8\ \mathrm{cm/s}.$$

The slowing-down of electrons due to a plasma can be divided into two contributions: binary collisions and collective collisions (i.e., excitation of plasma waves). In the kinetic formulations of the problem the division between the two regimes is marked by an impact parameter that is smaller or larger than the Debye length L_D. In the continuum (or dielectric) formulations of the problem the division is marked by a density-modulation wave number k that is larger or smaller than $k_D = 1/L_D$. The effect of plasma ions is negligible for the

high projectile velocities considered here.[20] The addition of the two electron collision terms for high projectile velocities yields[20]

$$\left(-dE/dx\right)_{\text{free}} = \left(2\pi e^4\, N_{e,\text{free}}/E_0\right) \ln\left(1.52\, E_0/\hbar\omega_p\right), \quad \text{(A2)}$$

where $\omega_p^2 = 4\pi e^2 N_{e,\text{free}}/m$. It should be noted that the Debye length has cancelled out. This is because the argument of the logarithm in the binary-collision term is $(L_D/1.47\, b_{\min})$, where b is the impact parameter, whereas in the collective-collision term it is $(1.123\, v_0/\omega_p L_D)$, where v_0 is the projectile velocity; thus, by adding the two terms, the Debye length cancels out. This is an indication that the result is independent of the degree of degeneracy, which was also shown directly by Maynard and Deutsch.[21] For small degeneracy and high projectile velocity ($v_0 >> v_F$) the logarithm in Eq. (A2) is the first term in a series expansion where the second term is given by

$$\left(kT_e/E_F\right)\left[I_{3/2}(\alpha)/I_{1/2}(\alpha)\right]\left(v_F/v_0\right)^2, \quad \text{(A3)}$$

$I_{3/2}(\alpha)$ and $I_{1/2}(\alpha)$ being the Fermi integrals. For our case $\left(kT_e/E_F\right)\left[I_{3/2}(\alpha)/I_{1/2}(\alpha)\right] \sim 1$, but $(v_F/v_0)^2 \sim 1.5\times 10^{-3}$, making the correction negligible. Likewise Yan *et al.*[22] have shown that when calculating the slowing-down for $v_0/v_F >> 1$, the following effects can be neglected: electron degeneracy, strongly coupled plasma [in which case the random phase approximation implied in Eq. (A2) is invalid], and projectile collisions. In the derivation of Eq. (A3) the substitution $b_{\min} = \hbar/mv_0$ was made. This is the quantum limit (derived from the uncertainty principle) and is the relevant one for our case since it is a factor of ~58 larger than the classical limit given by $b_{\min} = e^2/mv_0^2$.

Before adding the relative contributions of free and bound electrons to the projectile slowing-down we modify Eq. (3) because of the Coulomb screening of the bound electrons by the free electrons.[23] In the derivation of Eq. (3) the maximum impact parameter is given by $b_{\max} \sim \hbar v_0/\langle E_i \rangle$, where $\langle E_i \rangle$ is the average ionization energy; however, for our typical values $b_{\max}$ ~2.5 Å, whereas the Debye length (calculated using N_{free}) is ~1.5 Å. Therefore, we have to replace $b_{\max}$ by L_D, and Eq. (3) then becomes

$$\left(-dE/dx\right)_{\text{bound}} = \left(2\pi e^4\, N_a\, Z/E_0\right) \times \ln\left[\left(2E_0\, KT_e\right)^{1/2}/\hbar\omega_p\right]. \quad \text{(A4)}$$

Here ω_p is given again in terms of the density of free electrons. It should be noted that the polarization of the vanadium ions by the projectile electrons and its effect on the slowing-down are significant only for $\gamma >> 1$ and can be ignored here.[20] The total slowing-down is given by the sum of Eqs. (A2) and (A4). For the typical conditions considered here the logarithm in Eq. (A2) equals ~8.2, and the logarithm in Eq. (A4) equals ~4.5. Since only ~10% of the V electrons are free, the former must be multiplied by 0.1, yielding ~0.8. Finally, the sum 4.5 + 0.8 = 5.3 should be compared with the value of the logarithm in Eq. (3), which was used above to calculate the preheat, namely ~5.4. Therefore, the modified slowing-down formulation yields results that are essentially the same as those of Eq. (3), so the modifications to Eq. (3) can be neglected.

REFERENCES

1. N. A. Ebrahim *et al.*, Phys. Rev. Lett. **45**, 1179 (1980); D. M. Villeneuve, R. L. Keck, B. B. Afeyan, W. Seka, and E. A. Williams, Phys. Fluids **27**, 721 (1984).
2. H. Figueroa *et al.*, Phys. Fluids **27**, 1887 (1984); T. A. Peyser *et al.*, Phys. Fluids B **3**, 1479 (1991).
3. T. R. Boehly, R. S. Craxton, T. H. Hinterman, J. H. Kelly, T. J. Kessler, S. A. Kumpan, S. A. Letzring, R. L. McCrory, S. F. B. Morse, W. Seka, S. Skupsky, J. M. Soures, and C. P. Verdon, Rev. Sci. Instrum. **66**, 508 (1995).
4. B. Yaakobi, I. Pelah, and J. Hoose, Phys. Rev. Lett. **37**, 836 (1976); J. D. Hares *et al.*, Phys. Rev. Lett. **42**, 1216 (1979).
5. A. Hauer, W. Priedhorsky, and D. van Hulsteyn, Appl. Opt. **20**, 3477 (1981).
6. M. J. Berger and S. M. Seltzer, Tables of Energy Losses and Ranges of Electrons and Positrons, NASA Document SP-3012, Washington, DC (1964).
7. See National Technical Information Service No. DE83015439 (A. J. Burek and B. Yaakobi, Final Report to the National Bureau of Standards Contract NB81NAHA2032, Appendix A, 1983). Copies may be ordered from the National Technical Information Service, Springfield, VA 22161.
8. B. L. Henke, E. M. Gullikson, and J. C. Davis, At. Data Nucl. Data Tables **54**, 181 (1993).
9. J. V. Gilfrich, D. B. Brown, and P. G. Burkhalter, Appl. Spectrosc. **29**, 322 (1975).
10. P. G. Burkhalter *et al.*, in *X-Ray Calibration: Techniques, Sources, and Detectors*, edited by P. Lee and P. D. Rockett (SPIE, Bellingham, WA, 1986), Vol. 689, pp. 121–127.
11. B. L. Henke *et al.*, J. Opt. Soc. Am. B **3**, 1540 (1986).
12. W. Bambynek *et al.*, Rev. Mod. Phys. **44**, 716 (1972).

13. D. J. Botto, J. McEnnan, and R. H. Pratt, Phys. Rev. A **18**, 580 (1978).

14. A. B. Langdon, B. F. Lasinski, and W. L. Kruer, Phys. Rev. Lett. **43**, 133 (1979).

15. G. Knop and W. Paul, in *Alpha-, Beta- and Gamma-Ray Spectroscopy*, 1st ed., edited by K. Siegbahn (North-Holland, Amsterdam, 1965), Chap. 1, Vol. 1, p. 12.

16. C. J. Bakker and E. Sergrè, Phys. Rev. **81**, 489 (1951); H. H. Andersen and J. F. Ziegler, *Hydrogen Stopping Powers and Ranges in All Elements*, The Stopping and Ranges of Ions in Matter, Vol. 3 (Pergamon Press, New York, 1977).

17. C. J. Powell, Rev. Mod. Phys. **48**, 33 (1976).

18. W. Heitler, *The Quantum Theory of Radiation*, 2nd ed., The International Series of Monographs on Physics (Oxford University Press, London, 1947).

19. N. A. Dyson, *X-Rays in Atomic and Nuclear Physics*, 2nd ed. (Cambridge University Press, Cambridge, England, 1990), p. 47.

20. J. D. Jackson, *Classical Electrodynamics*, 2nd ed. (Wiley, New York, 1962), Chap. 13.6.

21. G. Maynard and C. Deutsch, Phys. Rev. A **26**, 665 (1982).

22. X.-Z. Yan *et al.*, Phys. Rev. A **32**, 1785 (1985).

23. T. A. Mehlhorn, J. Appl. Phys. **52**, 6522 (1981).

Holographic Transmission Gratings for Spectral Dispersion

Introduction

Over the last 12 years, holographic transmission diffraction gratings have been employed within solid-state laser systems to provide angular spectral dispersion (ASD) for laser beam smoothing. The dispersive property of diffraction gratings provides a versatile means to control the spatial and temporal characteristics of high-bandwidth laser light. Recent research has shown that holographic transmission gratings can possess not only high diffraction efficiency and high damage threshold but also high wavefront quality.

In general, spatial or temporal information that is encoded onto a propagating laser beam can be transferred between time and space by means of the lateral time delay associated with a grating's ASD. At LLE, the ASD from a grating is used to carry out laser beam smoothing involving broadband laser operation.[1] At other laser-fusion facilities, holographic diffraction gratings are being developed for broadband frequency conversion to achieve ultra-uniform levels of irradiation uniformity on solid-state laser systems. In addition, several novel pulse compression, pulse expansion, and pulse shaping schemes, involving highly dispersive holographic gratings, have been extensively developed at many laboratories, including LLE.

This article reviews the latest results from our experimental research in holographic-grating fabrication. The performance of recently fabricated holographic gratings is described in terms of diffraction efficiency and wavefront quality. In addition, several important applications of the holographic transmission grating, such as laser beam smoothing on the OMEGA laser system, are reviewed.

Theoretical Modeling

A periodic thickness variation, or surface relief, formed along one dimension of a photosensitive material, such as photoresist, can deflect an incident laser beam by way of diffraction, as shown in Fig. 82.26. A periodic refractive-index variation within a flat film of material can also act as a diffraction grating. Photorefractive polymers have recently been modulated to form efficient gratings; however, this will be the subject of a future article. The type of holographic transmission grating that is based on surface relief of a transparent material diffracts light according to the same diffraction-grating equation as pertains to the volume holograms, reflection gratings, and conventionally ruled gratings. The grating equation

$$d\left[\sin\left(\theta_d\right)-\sin\left(\theta_i\right)\right]=m\lambda \tag{1}$$

is used to calculate the angle of diffraction (θ_d) for a wavelength λ when the angle of incidence (θ_i) of the laser beam and the groove spacing d of the grating are given. This calculation can be performed for any order of diffraction m; however, only the first order of diffraction is important for the majority of applications.

The ASD of the grating is defined as the rate of change of the diffraction angle with respect to change in wavelength. The ASD is a measure of the angular spreading of the spectral components of light and is calculated using Eq. (2):

$$\Gamma = m/d\cdot\cos\left(\theta_d\right). \tag{2}$$

When used in the symmetric-angle configuration, the angle of the incident laser beam is equal to the angle of the primary diffracted beam, i.e., $(\theta_d)=-(\theta_i)$, where the angles are defined with respect to the plane of the photoresist layer. For this symmetric case, where the lateral magnification between the input beam and the output beam is unity, and m represents the first order of diffraction, the expressions for the grating equation and angular dispersion become

$$2d\cdot\sin\left(\theta\right)=\lambda \tag{3}$$

and

$$\Gamma = 2\cdot\tan\left(\theta\right)/\lambda, \tag{4}$$

respectively. These fundamental grating equations are used to design optical systems with a desired amount of ASD.

An optimum grating design couples as much light as possible to the diffracted laser beam. Figure 82.26 also shows the various paths that can be taken by an incident laser beam. The energy coupled to all additional beam paths is minimized to obtain the highest possible diffraction efficiency, defined as the ratio of the powers of the primary diffracted beam to the incident laser beam. However, even small amounts of energy recirculating within the substrate can cause undesirable temporal modulation. In practice, the grating substrate contains a wedge between the first and second surfaces to prevent secondary beams from propagating coincident with the primary diffracted laser beam.

The diffraction characteristics of the gratings, shown in Fig. 82.26, have been the subject of much research. Several rigorous electromagnetic theories,[2] each based on Maxwell's equations with appropriate boundary conditions, are available to calculate the performance of a diffraction grating. Numerical solutions have been obtained for gratings of arbitrary profiles by the integral-equation and differential-equation methods. The integral method[3] is capable of treating both metallic and dielectric gratings and is often used to benchmark further progress in grating modeling. It has been used with limited success, however, in modeling deep multilayered gratings that approach a height-to-width ratio near 2 to 1.

Previously, the differential method involved either an orthogonal-mode expansion or a coupled-wave expansion, each containing a large system of equations that were difficult to manage computationally. An improved differential method, however, involving a nonorthogonal coordinate system, was shown to accurately model deep, multilayered, metal and/or dielectric gratings.[4] Most recently, major enhancements were made to this method to allow transmitted orders as well as reflected orders.[5]

The modeling results shown in this article were obtained with a code based on the integral method. Since our experimental results have sometimes exceeded the predicted values for diffraction efficiency from this code, as will be addressed later in this article, an alternate code based on the more recent differential method will be examined in the near future.

Grating Fabrication

The fabrication of holographic diffraction gratings involves an interferometric exposure of a photosensitive material called photoresist.[6] The holographic interferometer, shown in Fig. 82.27, consists of a laser source, beam-conditioning optics, and two beamlines that intersect at the final recording

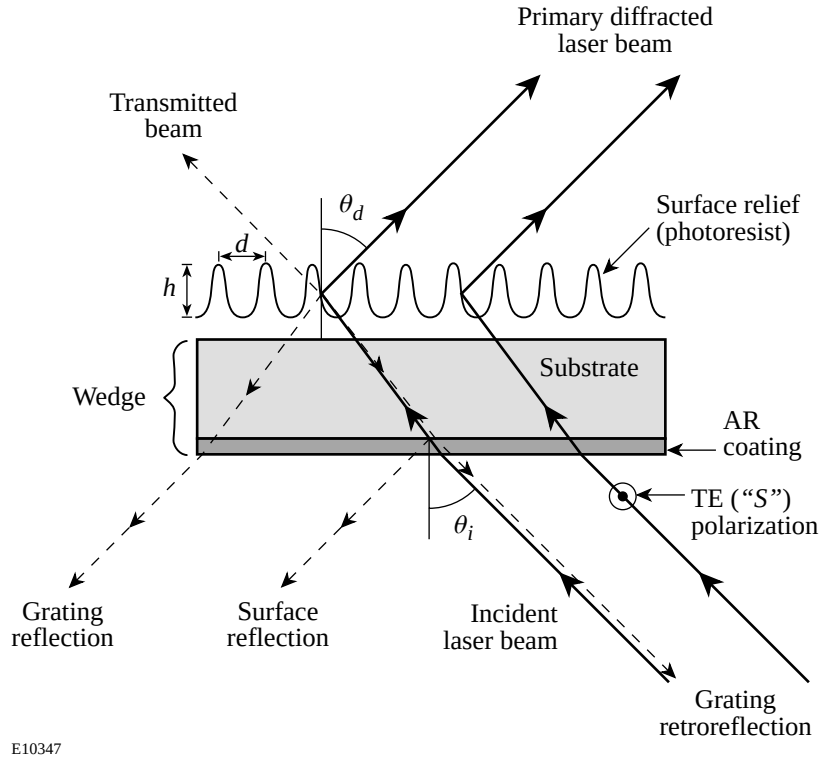

Figure 82.26
A holographic transmission grating, patterned in photoresist, consists of a periodic thickness variation, or surface relief, along one dimension of a material. When used in the symmetric-angle configuration, the angle of the incident laser beam is equal to the angle of the primary diffracted beam, with respect to the plane of the photoresist layer. The energy coupled to all additional beam paths is minimized to obtain the highest-possible diffraction efficiency, defined as the ratio of the powers of the primary diffracted beam to the incident laser beam.

plane. It is used to produce highly visible and stable interference fringes. The laser source is a Spectra-Physics argon-ion laser equipped with an intracavity etalon, narrow-band cavity mirrors, and electronic feedback control to maintain beam power, beam centering, and a single longitudinal mode at the $\lambda = 364$-nm spectral line. Prior to being split into two separate beam paths, the laser beam is raster scanned over the entrance pupils of the two arms of the interferometer. As shown in Fig. 82.28, rotation of a glass cylinder causes a displacement of an incident laser beam without a corresponding change to the laser beam propagation direction. The irradiance at every point within the clear aperture is the superposition of an array of supergaussian beams, resulting in two-dimensional uniformity. This displacement scanning technique increases the exposure uniformity far beyond that of the laser beam itself.[7] With careful chemical processing, fringe exposure results in deep grooves over the entire clear aperture of the grating.

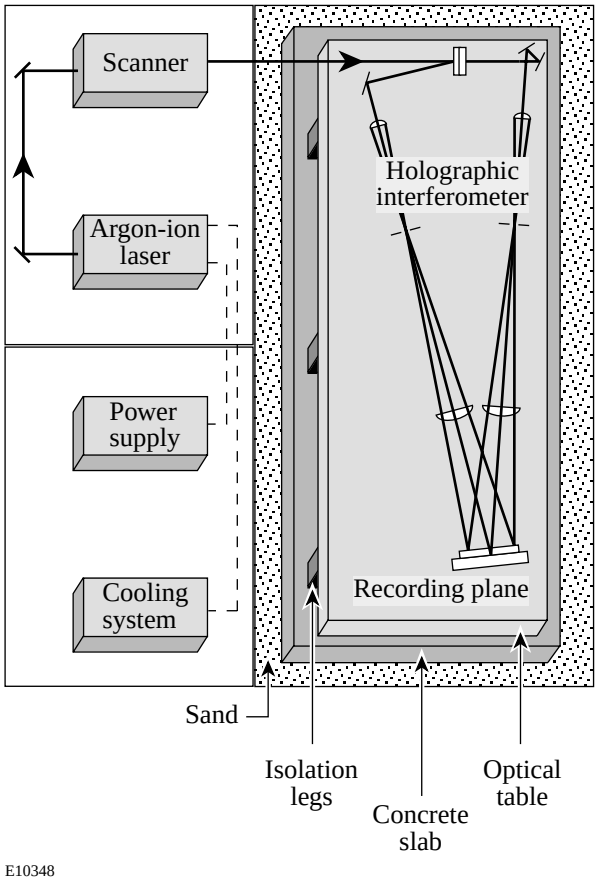

Figure 82.27
The holographic system consists of a laser source, a laser scanner, and an interferometer with two beamlines that intersect at the final recording plane. It produces high-contrast interference fringes. Fringe stability is achieved through a vibration isolation system containing a 2-ft-thick, 8-ft × 16-ft optical table, pneumatically floating on six legs and supported by a 2-ft-thick concrete slab, all resting on a foundation of dry sand. The laser power supply and cooling system, the laser resonator and scanner, and the holographic interferometer are located in three separate rooms to minimize the transfer of vibrations, heat, and atmospheric turbulence.

After exiting the laser scanner, the laser beam is split so that the two arms of the interferometer impose equal amounts of increased path length to an incident beam when the beam is angularly deviated prior to the split. This is the same criterion that was established for the Michelson interferometer,[8] which used an incoherent white-light source. This principle is extended to coherent laser light to achieve stable interference fringes during two-dimensional scanning of the laser beam. To further ensure fringe stability, a 2-ft × 8-ft × 16-ft optical table is pneumatically isolated from building vibrations by six pressurized support legs located on a 2-ft-thick concrete slab. This support system rests on a 3-ft mound of dry sand. To isolate the system from sources of acoustic energy, thermal energy, and air turbulence, the interferometer is located in a "room within a room" environment. Furthermore, the laser power supply and cooling system, the laser resonator and scanner, and the holographic interferometer are located in three separate rooms to minimize the transfer of vibrations, heat, and air turbulence.

In practice, however, it has been found that the holographic system performs optimally only after the room air conditioning has been shut down for between 5 to 20 h, depending on the time of the year. The exact time interval appears to depend on the relationship between the temperature of the ground and the temperature of the air supplied by the building's air-conditioning system. Fringe visibility is continuously monitored prior to a series of holographic exposures. The fringe contrast must remain stable for a period of time exceeding the actual duration of the scan. Otherwise, changes in contrast will map directly to low-efficiency regions of the diffraction grating. Extensive testing has revealed that the success or failure of holographic-grating fabrication does not generally depend on the extent of nearby building or ground activity.

A scanning electron microscope (SEM) is used to characterize the surface relief of the holographic gratings. The size and shape of the grooves are shown in Fig. 82.29. In Fig. 82.29(a), close-up examination of the photoresist surface-relief grating shows a groove shape corresponding to 80% diffraction efficiency, where efficiency is defined as the ratio of the diffracted to incident laser power. Although the surface-

relief profile is not strictly sinusoidal, the etched volume is only slightly larger than the remaining photoresist volume. The SEM in Fig. 82.29(b) shows that the etched volume is much wider than the remaining photoresist volume for a diffraction grating exhibiting over 95% efficiency. The crests of the grooves are straight and rigid when fabricated in controlled laboratory conditions. The SEM in Fig. 82.29(c) reveals the problem associated with uncontrolled humidity in the vicinity of grating fabrication. In the presence of an excessively humid environment, thin walls of photoresist are deformed by capillary attraction from water accumulated within the grooves. It has been observed that groove deformation is accompanied by an increased amount of scatter when probed by a beam of laser light. This is because a distribution of groove deformations acts as a diffuser, scattering light over a broad angular spectrum. Although the mechanical fragility of photoresist structures has long been known, this represents the first time that a specific groove deformation has been associated with the onset

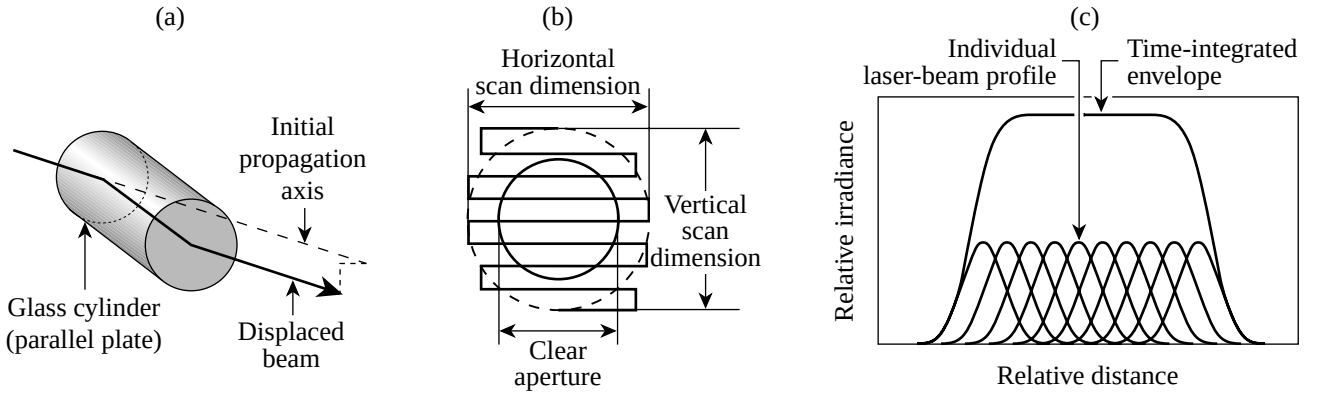

Figure 82.28
Laser-beam scanning is used to increase the time-integrated irradiation uniformity at the recording plane. (a) A tilted glass cylinder displaces an incident laser beam without angular deflection. (b) The laser beam is raster scanned over the entrance pupils of the two arms of the interferometer. (c) The recording-plane irradiance is the superposition of an array of supergaussian beams. The resulting irradiance is substantially more uniform than the laser beam itself.

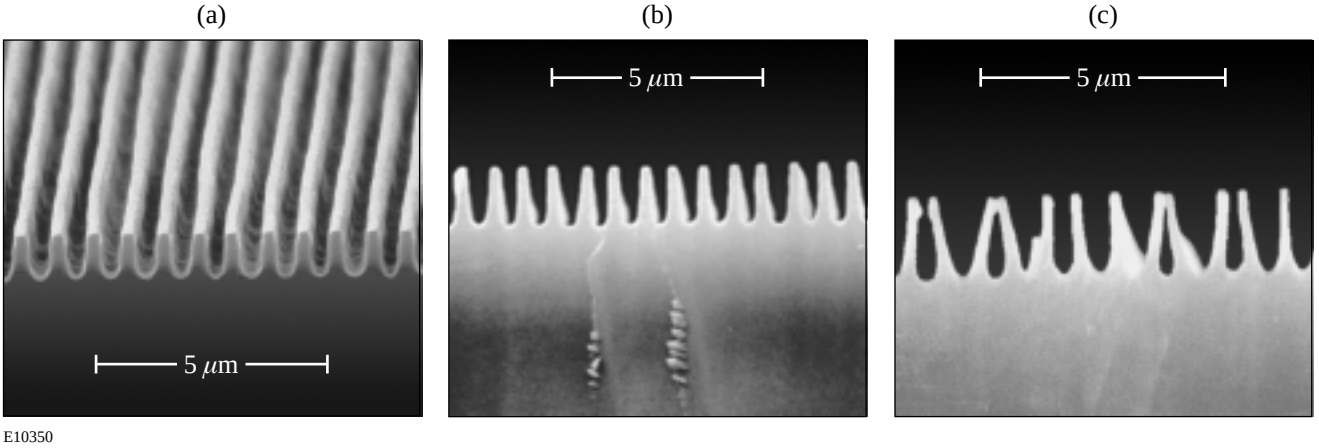

Figure 82.29
The scanning electron microscope (SEM) provides close-up examination of photoresist gratings. Figure 82.29(a) shows the groove profile corresponding to 80% diffraction efficiency, where efficiency is defined as the ratio of the diffracted to incident laser power. Figure 82.29(b) shows that the etched volume is much wider than the remaining photoresist volume for a diffraction grating exhibiting over 95% efficiency. The crests of the grooves are straight and rigid when fabricated in controlled laboratory conditions. The SEM of Fig. 82.29(c) reveals the problem associated with uncontrolled humidity in the vicinity of grating fabrication. Thin walls of photoresist are deformed by capillary attraction from water accumulated within the grooves. Groove deformation is accompanied by an increased amount of laser light scatter.

of scatter loss. As a result of this understanding, careful washing and drying procedures are used to fabricate super-sinusoidal groove shapes.

Grating Performance

Holographic transmission gratings possess deep grooves that, when properly shaped, result in near-unity diffraction efficiency for a wide range of groove spacing. Within the holography laboratory at LLE, transmission gratings have been designed and fabricated for use at three different symmetric angles. At the symmetric angle, the incident and diffracted beams have equal angles with respect to the normal to the grating. Theoretical calculations of the diffraction efficiency, shown in Fig. 82.30, predict that performance decreases for gratings with larger groove spacing, i.e., a smaller symmetric angle. Experimental results for these three different symmetric angles indicate, however, that diffraction efficiency can be maintained at a level higher than the integral-equation method predicts. Experimental results for symmetric angles (groove spacings) of 31.7° (1.00 μm), 46° (0.73 μm), and 49.5° (0.69 μm) show that high diffraction efficiency is possible over this entire range of angles.

Theoretical and experimental results show that a super-sinusoidal phase grating can exhibit high efficiency. As shown in Fig. 82.31, the diffraction efficiency of a super-sinusoidal phase grating decreases slowly and monotonically as it is detuned in angle. This curve represents a grating designed for a symmetric angle of 46°; however, similar performance is obtained for a wide range of angles. As shown in Fig. 82.32, it has been observed that holographic gratings with larger groove spacing, such as the 31.7° grating, exhibit an efficiency profile that drops rapidly at several specific angles when detuned from

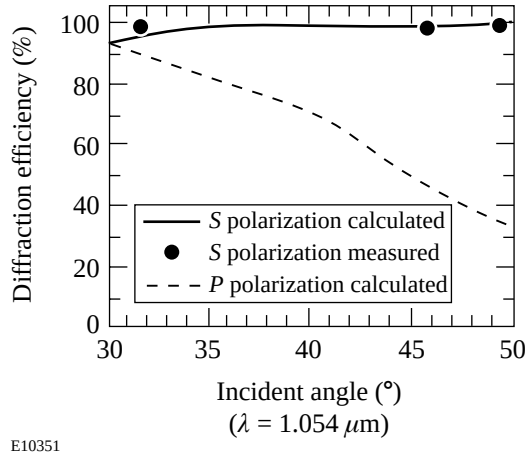

Figure 82.30
Holographic transmission gratings possess deep grooves that, when properly shaped, result in near-unity diffraction efficiency for a wide range of groove spacing. Theoretical calculations of the diffraction efficiency predict that performance decreases for gratings with a symmetric angle decreasing toward 30°. Experimental results for symmetric angles (groove spacings) of 31.7° (1.00 μm), 46° (0.73 μm), and 49.5° (0.69 μm) show that diffraction efficiency can be maintained over this whole range of angles.

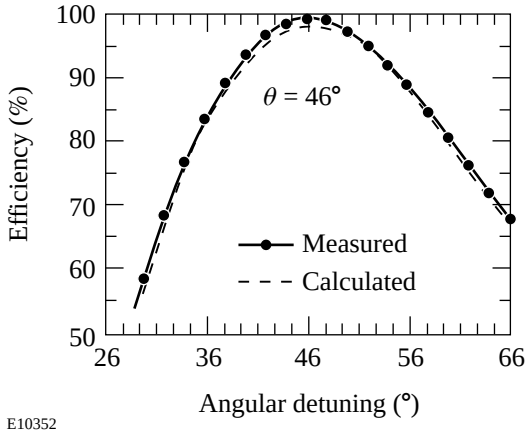

Figure 82.31
Theoretical and experimental results show that the diffraction efficiency of a typical surface-relief transmission grating decreases slowly and monotonically as it is detuned in angle about the peak efficiency, where the incident and diffracted angles are equal. The curves represent a grating designed for a symmetric angle equaling 46°; however, similar performance is obtained for a wide range of angles.

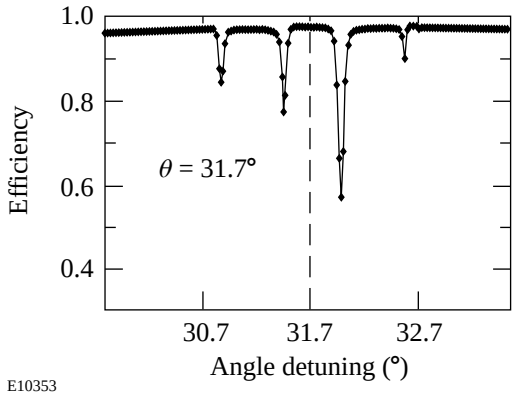

Figure 82.32
Holographic gratings with larger groove spacing, such as the 31.7° grating, exhibit an efficiency profile that rapidly drops at several specific angles when detuned from the symmetric angle. Except for these narrow regions in angle, the measured diffraction efficiency exceeds theoretical predictions. It is observed that the thickness of the photoresist affects the extent to which laser light travels within the photoresist waveguide before being coupled out along the $m = -1$ diffraction order.

the symmetric angle. Except for these narrow regions in angle, the measured efficiency exceeds theoretical predictions. A preliminary investigation of this effect revealed that the thickness of the photoresist affects the extent to which laser light propagates down the photoresist waveguide before being coupled out along the first diffraction order. This waveguide-coupling phenomenon has been correlated to the rapid efficiency drop at specific angles. Additional experimental investigation is needed to determine the maximum photoresist thickness allowed before waveguide modes can exist. It has been experimentally determined that efficient use of the 31.7° grating within the OMEGA laser system requires that an alignment error of less than 10 min of arc be maintained between the laser beam and the grating.

Gratings used within the OMEGA laser *must* possess high optical quality, including both high phase-front quality and minimum phase noise. Holographic phase-front errors, due to optical aberrations within the interferometer, can be measured by analyzing interferograms from both the diffracted beam (minus one order) and the transmitted beam (zero order), individually. The wavefront quality of the diffracted beam, however, is what is important for most applications. Better than one-tenth wave performance is achieved over the clear aperture of a grating used for the OMEGA laser system, as shown in Fig. 82.33(a). Cross sections of the wavefront error are shown in Fig. 82.33(b). This error originates from the two telescopes within the interferometer. The difference in curvature between the two cross sections indicates the presence of astigmatism, the aberration which causes the tangential (horizontal) and sagittal (vertical) planes to focus at different planes. In practice, interferometer alignment is repeated until the measured wavefront error is minimized. In addition, small-scale imperfections are reduced by using high-quality optics and coatings within the interferometer, and by carrying out the photoresist deposition in a well-maintained clean-room laboratory.

Laser Applications

The primary applications of holographic diffraction gratings at LLE involve laser-beam smoothing and spectroscopy. Several sets of gratings, with angular dispersions of between 120 to 220 μrad per angstrom, are now available for one of OMEGA's driver lines for the purpose of laser beam smoothing. Also, high-resolution spectrometers, composed of one or more holographic gratings, are used to characterize the modulation index of phase modulators for broadband beam smoothing. In addition, it is possible that two large-aperture gratings, used in series with a focusing lens, can provide sufficient ASD to fully resolve the individual line structure from a sinusoidally driven modulator. It is important to note that by having holographic gratings incorporated into the driver line of OMEGA, each of the OMEGA beamlines is a potential spectrometer for diagnosis of the laser bandwidth.

A wide variety of additional applications exist for high-efficiency, high-damage-threshold, holographic diffraction gratings. For example, holographic gratings can be used to carry out broadband frequency conversion to achieve ultra-uniform levels of irradiation uniformity on solid-state laser

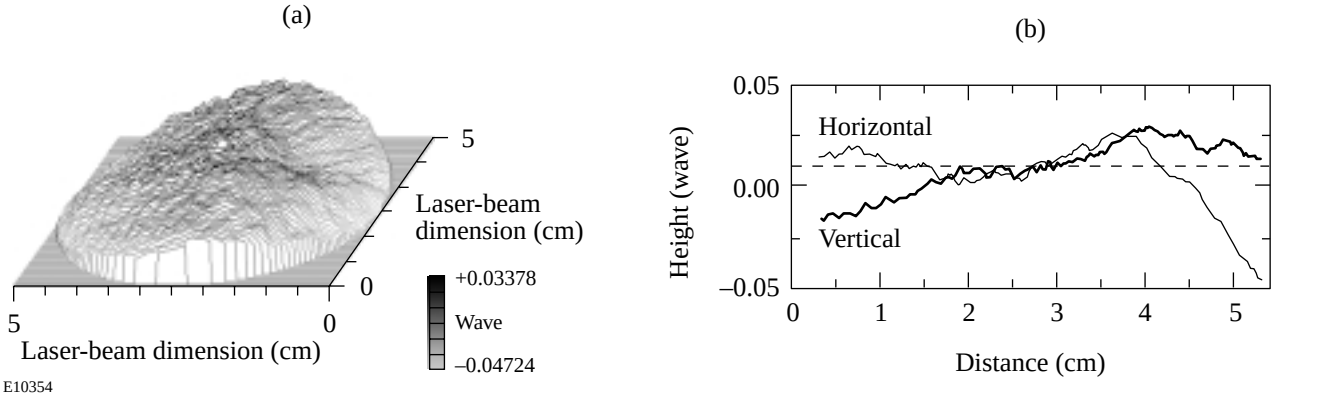

Figure 82.33
(a) Better than one-tenth wave performance is achieved over the clear aperture of a 31.7° grating used in the OMEGA laser system. (b) Cross sections of the wavefront indicate that the largest low-frequency aberration is astigmatism. This error originates from the two telescopes within the interferometer. High-quality optics and mounts can provide similar wavefront quality for large-aperture gratings.

systems. In addition, several novel pulse-compression and pulse-expansion schemes include holographic gratings in their optical design. Advanced pulse-shaping schemes also involve highly dispersive holographic gratings, which provide compactness, high damage threshold, and high diffraction efficiency. Holographic transmission gratings are used within compact spectrometers, fiber-optic couplers, laser scanners, and various semiconductor lasers. Additional applications of high-power, high-dispersion transmission gratings involve their function as a spectral filter. These gratings provide excellent Fourier-blocking capability for small-signal-gain detection and for the suppression of amplified stimulated emission in amplifier chains. It is anticipated that many new applications will be found for holographic transmission gratings when the gratings become more widely available.

Conclusion

Holographic transmission gratings that possess high diffraction efficiency, high wavefront quality, and high damage threshold have been designed, fabricated, and characterized for use within high-power, solid-state laser systems. Holography research has resulted in diffraction gratings that exhibit near-unity efficiency over a wide range of groove spacing. A novel interferometric technique that incorporates laser beam scanning is now routinely used to obtain uniform grating irradiation while maintaining stable, high-contrast, interference fringes. Over 100 gratings, covering a wide range of groove spacing, have been manufactured with this interferometric exposure technique. Several sets of gratings, with different amounts of angular dispersion, are available for one of the driver lines of the OMEGA laser. Numerous applications exist for these high-efficiency, high-damage-threshold holographic gratings. Laser beam smoothing and spectroscopic techniques, many of which have been invented and developed at LLE, incorporate these gratings. High-efficiency and high-wavefront-quality gratings are now in use within the beam-smoothing driver line of the OMEGA laser system. The current research thrust involves an experimental and theoretical investigation of the gratings that exhibit diffraction efficiency that exceeds code predictions and also exhibit waveguide coupling of laser light.

ACKNOWLEDGMENT

This work was supported by the U.S. Department of Energy Office of Inertial Confinement Fusion under Cooperative Agreement No. DE-FC03-92SF19460, the University of Rochester, and the New York State Energy Research and Development Authority. The support of DOE does not constitute an endorsement by DOE of the views expressed in this article.

REFERENCES:

1. Laboratory for Laser Energetics LLE Review **37**, 40, NTIS document No. DOE/DP/40200-83 (1988). Copies may be obtained from the National Technical Information Service, Springfield, VA 22161.
2. R. Petit, ed. *A Tutorial Introduction*, Electromagnetic Theory of Gratings (Springer-Verlag, Berlin, 1980).
3. D. Maystre, J. Opt. Soc. Am. **68**, 490 (1978).
4. J. Chandezon *et al.*, J. Opt. Soc. Am. **72**, 839 (1982).
5. L. Li, "DELTA: A Computer Program for Multilayer-Coated Gratings in Conical Mountings," computer manual (1999).
6. Laboratory for Laser Energetics LLE Review **50**, 61, NTIS document No. DOE/DP/40200-197 (1992). Copies may be obtained from the National Technical Information Service, Springfield, VA 22161.
7. J. J. Armstrong and T. J. Kessler, in *Laser Coherence Control: Technology and Applications*, edited by H. T. Powell and T. J. Kessler (SPIE, Bellingham, WA, 1993), Vol. 1870, pp. 47–52.
8. A. A. Michelson, Am. J. Sci. **22**, 120 (1881).

Laser Beam Smoothing Caused by the Small-Spatial-Scale *B*-Integral

Introduction

Target irradiation uniformity is an important aspect of the direct-drive approach to inertial confinement fusion (ICF),[1,2] where the capsule is directly irradiated by a symmetrically arranged cluster of high-intensity, ultraviolet (UV) laser beams. Nonuniformity in laser irradiation seeds the Rayleigh–Taylor hydrodynamic instability, which consequently degrades target performance.[3,4] Various techniques are employed on the OMEGA[5] laser to improve the on-target irradiation uniformity to reduce laser imprint: two-dimensional smoothing by spectral dispersion (2-D SSD),[6–8] distributed phase plates (DPP's),[9,10] polarization smoothing (DPR's),[5,11,12] and multiple-beam overlap. A complete understanding of the laser focal-spot dynamics is essential to ICF performance, and it provides valuable feedback as a laser diagnostic tool. In Ref. 13, the smoothing rate of 2-D SSD on OMEGA was investigated both experimentally and numerically. Excellent agreement between the experimental results and the corresponding simulations was found for all 2-D SSD cases and for low-energy shots without applied frequency modulation (FM) (i.e., without SSD). Laser beam smoothing of high-power glass lasers caused by small-spatial-scale and whole-beam *B*-integral effects with DPP's and no applied FM is examined in this article.

In the absence of externally applied FM, the beam can acquire bandwidth because of the time-dependent *B*-integral (Ref. 14, p. 385) acquired in the laser chain. The phase difference between a wave traveling in a vacuum and a wave propagating a distance L in a nonlinear medium in the z direction can be expressed as

$$\Delta\varphi = \frac{2\pi\left(n_0 - 1\right)L}{\lambda_0} + \phi_B(z),$$

where λ_0 is the vacuum wavelength, n_0 is the linear index of refraction, and B is the intensity dependent phase given by

$$\phi_B(z) = \frac{2\pi}{\lambda}\int_0^L \gamma\, I(z)\, dz,$$

where γ is the nonlinear constant of the medium and $I(z)$ is the intensity (compare Ref. 15). In the event that the *B*-integral is nonuniform in space and time, it will cause the speckle pattern produced by the DPP to move in the target plane, similar to the effect of SSD. In the absence of a smoothing mechanism such as SSD, the nonuniformity of the measured far fields with DPP's is expected to have an rms value of 100%, reflecting the high contrast of the speckle pattern produced by the presumed coherent illumination of the DPP. Experimental far-field measurements, however, acquired on OMEGA with the ultraviolet-equivalent-target-plane (UVETP) diagnostic of high-energy shots without applied FM yielded smoothed far fields with overall nonuniformity ranging from 62% to 88%.[13] The nonuniformity decreases approximately linearly with increasing average intensity. The amount of smoothing provided by *B*-integral effects alone is not sufficient for direct-drive ICF.[7] However, shots without applied FM are base-line measurements for the high-intensity SSD shots and are therefore studied in this article.

The dominant smoothing mechanism in pulses without externally applied FM is attributed to the small-spatial-scale *B*-integral variation, which possesses sufficient temporal bandwidth and beam divergence to affect OMEGA target spherical-harmonic modes as small as $\ell \sim 40$ or wavelengths as long as $\lambda_{\text{mode}} \sim 80\ \mu$m ($\ell$ modes are related to wavelength by $\ell \equiv 2\pi r/\lambda_{\text{mode}}$, where $r = 0.5$ mm is the target radius). The small-spatial-scale *B*-integral results from intensity nonuniformities as the laser beam propagates through a nonlinear medium, such as amplifier glass, and produces amplitude and phase modulations in the beam (see Ref. 14, p. 381). This effect introduces time-dependent phase variations across the beam, which results in some smoothing of the speckle structure when the beam, without externally applied FM, passes through a DPP and is focused onto the target. The whole-beam *B*-integral affects smoothing to a smaller degree and is produced as the whole beam self-focuses (see Ref. 14, p. 380). The *RAINBOW* code (compare Ref. 15, p. 229) calculates the whole-beam *B*-integral for the pulse shapes used on OMEGA as a function of radius and time. It is shown later in the **Laser Beam**

Smoothing section that the whole-beam *B*-integral produces only a small portion of the observed smoothing because of its small temporal bandwidth coupled to the fact that its imposed laser divergence does not change substantially over time. As a result, the spatiotemporal evolution of the whole-beam *B*-integral is not sufficient to cause rapid movement of the speckle pattern in the far field. The whole-beam *B*-integral changes the on-target focal-spot diameter and shape by a small amount.

The transverse spatial-intensity profile of the near field evolves slowly in time from a center-peaked beam to an edge-peaked beam as a result of gain saturation effects. The highest far-field spatial frequencies produced by coherent illumination of the DPP are caused by the interference from the outer edges of the beam. Consequently, as the effective beam radius increases in time, the energy in the highest spatial frequencies increases. The effective radius of the fluence accurately yields the overall high-frequency cutoff.

The code *Waasikwa'** was developed to simulate the planar, time-integrated far fields produced by the OMEGA laser, which allows a direct comparison of the calculations to the images acquired by the UVETP diagnostic. *Waasikwa'* is a general-purpose simulation program that has the capability to model far fields under a variety of near-field conditions: arbitrary spatial envelopes that possess an arbitrary temporal envelope at any transverse point; whole-beam and small-spatial-scale *B*-integral near-field phase; 2-D SSD; arbitrary static phase aberrations; DPR's; the inherent bandpass characteristic of frequency conversion; and multiple-beam overlap. *Waasikwa'* utilizes the continuous DPP employed on OMEGA. In addition, it can be configured to run within a shared-memory model as a multiprocessing task on a parallel machine such as the SGI Origin 2000.[16]

The following sections describe far-field simulation and analysis, experimental results, simulation results, and conclusions.

Far-Field Simulation and Analysis

Waasikwa' calculates the far-field fluence using

$$F\left(x_{\mathrm{ff}}, y_{\mathrm{ff}}\right) \equiv \int_{\substack{\text{pulse}\\ \text{duration}}} I_{\mathrm{ff}}\left(x_{\mathrm{ff}}, y_{\mathrm{ff}}, t\right) dt, \qquad (1)$$

where I_{ff} (x_{ff}, y_{ff}, t) represents the instantaneous far-field intensity. The evolution of the far-field intensity is calculated by taking the modulus squared of a two-dimensional spatial Fourier transform of the UV near field (compare Goodman, Ref. 17, p. 83),

$$I_{\mathrm{ff}}\left(x_{\mathrm{ff}}, y_{\mathrm{ff}}, t\right) \equiv \left| \iint_{\forall \text{space}} E(x,y,t)\, e^{-i\frac{2\pi}{\lambda_{\mathrm{UV}} f_{\Omega}}\left(x_{\mathrm{ff}} x + y_{\mathrm{ff}} y\right)} dx\, dy \right|^2, \qquad (2)$$

where $E(x,y,t)$ represents the complex-valued UV electric field strength in the near field and (x,y) and $(x_{\mathrm{ff}}, y_{\mathrm{ff}})$ are the near- and far-field coordinate systems, respectively; $\lambda_{\mathrm{UV}} = 351$ nm is the UV vacuum wavelength; and $f_{\Omega} = 180$ cm is the focal length of the OMEGA focusing lens. The spatiotemporal evolution of the complex-valued UV electric field can be expressed as

$$E(x,y,t) \equiv E_0(x,y,t) e^{i\phi_B(x,y,t)} e^{i\phi_{\mathrm{DPP}}(x,y)}, \qquad (3)$$

where $E_0(x,y,t)$ defines the electric field envelope of the pulsed beam; $\phi_B(x,y,t)$ represents the combined phase contributions of the whole-beam and small-spatial-scale intensity-dependent *B*-integral; and $\phi_{\mathrm{DPP}}(x,y)$ is the static DPP phase-plate contribution whose mapping to the far field depends on its design. During OMEGA laser shots, the near fields of the 1- to 3-ns square pulses evolve from a center-peaked to an edge-peaked spatial-intensity profile. The near field of a 100-ps pulse, however, remains center peaked for the duration of the pulse. The spatiotemporal evolutions of both the Gaussian and square pulses are calculated with *RAINBOW* and are used as inputs to the *Waasikwa'* simulations. The equivalent near-field radius and pulse width are useful for calculating the average intensity and are defined as (see discussion of equivalent widths in Ref. 18, p. 148)

$$r_{\mathrm{eq}} \equiv \frac{1}{F_{\mathrm{nf}}(0)} \int_0^{\infty} F_{\mathrm{nf}}(r)\, dr \qquad (4)$$

and

$$t_{\mathrm{eq}} \equiv \frac{1}{P\left(t_c\right)} \int_{-\infty}^{\infty} P(t)\, dt, \qquad (5)$$

*An Anishinaabe word meaning "polishes it" as in smoothing a rough surface. Resource: J. Nichols and E. Nyholm, eds. *Ojibwewi-ikidowinan and Ojibwe Word Resource Book*, Occasional Publications in Minnesota Anthropology, No. 7 (Minnesota Archaelogical Society, St. Paul, MN, 1979).

respectively, where the near-field fluence is defined by

$$F_{\mathrm{nf}}(r) \equiv \int_{\forall t} \left| E_0(r,t) \right|^2 dt,$$

the near-field power is defined by

$$P(t) \equiv 2\pi \int_0^{\infty} r \left| E_0(r,t) \right|^2 dr,$$

and the pulse centroid is given by

$$t_c = \frac{\int_{-\infty}^{\infty} tP(t)\,dt}{\int_{-\infty}^{\infty} P(t)\,dt}.$$

It has been assumed that, for these calculations, the beam profile is azimuthally symmetric so that the spatial energy centroid is always located at $r = 0$. The equivalent widths permit a comparison of the shorter, 100-ps pulses (which have a center-peaked beam profile and a Gaussian pulse shape) to the longer pulses (which are, on the average, nearly square in space and time).

The 2-D power spectral density (2-D power spectrum or simply the 2-D psd) is derived from either the measured or simulated far-field fluences by taking the modulus squared of the 2-D spatial Fourier transform, namely,

$$\mathrm{PSD}\left(k_{x_{\mathrm{ff}}}, k_{y_{\mathrm{ff}}}\right) \equiv \left| \iint_{\forall \text{ far field}} F\left(x_{\mathrm{ff}}, y_{\mathrm{ff}}\right) e^{-i\left(k_{x_{\mathrm{ff}}} x_{\mathrm{ff}} + k_{y_{\mathrm{ff}}} y_{\mathrm{ff}}\right)} dx_{\mathrm{ff}}\, dy_{\mathrm{ff}} \right|^2, \quad (6)$$

where $F(x_{\mathrm{ff}}, y_{\mathrm{ff}})$ represents the far-field fluence as defined by Eq. (1), $(x_{\mathrm{ff}}, y_{\mathrm{ff}})$ is the far-field coordinate system, and $\left(k_{x_{\mathrm{ff}}}, k_{y_{\mathrm{ff}}}\right)$ is the far field's spatial-frequency coordinate system. The azimuthal sum at each radial wave number of the 2-D power spectrum defines the 1-D power spectral density (1-D power spectrum or simply the 1-D psd) and is given by

$$\mathrm{psd}\left(k_{\mathrm{ff}}\right) \equiv \oint \mathrm{PSD}\left(k_{x_{\mathrm{ff}}}, k_{y_{\mathrm{ff}}}\right) k_{\mathrm{ff}}\, d\theta, \quad (7)$$

where the transformation into polar coordinates is defined as $k_{\mathrm{ff}} \equiv \sqrt{{k_{x_{\mathrm{ff}}}}^2 + {k_{y_{\mathrm{ff}}}}^2}$ and $\tan\theta \equiv k_{y_{\mathrm{ff}}} / k_{x_{\mathrm{ff}}}$. The single-beam irradiation nonuniformity σ_{rms} is defined as the square root of the ratio of the speckle power [e.g., the high frequencies $k_{\mathrm{ff}} \geq 0.04$ (rad/μm) at the OMEGA target plane or ℓ modes with $\ell \geq 20$] to the envelope power of the far-field spot [i.e., the low frequencies $k_{\mathrm{ff}} < 0.04$ (rad/μm)]. The envelope/speckle dividing-line wave number of 0.04 (rad/μm) represents the lowest spatial frequency that is smoothed by 2-D SSD, as discussed in Ref. 13. A finite entrance pupil imposes a limitation on the spatial-frequency bandwidth of an optical system (compare the intensity-impulse response or point-spread function of a diffraction-limited system with a circular exit-pupil function in Ref. 17, p. 110). On OMEGA, the highest spatial frequency of the laser speckle (or interference pattern) is limited by the finite diameter of the serrated apodizer, regardless of the beam profile. The OMEGA entrance pupil is defined by the diameter of the serrated aperture, which is located near the end of the laser driver section on OMEGA. The entrance pupil is imaged to the end of OMEGA and sets the final exit pupil to a full-system diameter $D_\Omega = 27.5$ cm. Consequently, the power spectrum possesses an absolute cutoff wave number that corresponds to the *f*-number limited spatial frequency

$$k_{\mathrm{cut}_{\mathrm{ff}}} = \frac{2\pi}{1.22} \frac{D_\Omega}{\lambda_{\mathrm{UV}} f_\Omega} = 2.24 \left[\frac{\mathrm{rad}}{\mu\mathrm{m}}\right]$$

and corresponds to $\lambda_{\mathrm{mode}_{\mathrm{cut}}} = 280\,\mu$m.

Experimental constraints restrict the analysis to the central portion of the laser beam. Consequently, data windowing must be employed to accurately analyze the PSD of the data. Otherwise, when the 2-D PSD is calculated, the result contains Fourier artifacts of the cropping function convolved with the desired underlying power spectrum of the far field. A 2-D generalization of the common Hamming (the Hamming function does not go to zero like the similar Hanning function)[19] windowing function is employed:

$$\mathrm{SQHamming}\left(x_{\mathrm{ff}}, y_{\mathrm{ff}}\right) \equiv \mathrm{Hamming}\left(x_{\mathrm{ff}}\right) \cdot \mathrm{Hamming}\left(y_{\mathrm{ff}}\right). \quad (8)$$

Experimental Results

A full description of the CCD-based UVETP diagnostic can be found in Ref. 13. An example of an acquired image of a 300-J, 3.5-ns shot with no applied FM is presented in

Fig. 82.34, where a lineout through the center of the beam is overplotted to show the highly modulated intensity. The laser-beam focus is centered nominally on the photodetector, and a 584-μm central portion of the whole 950-μm far-field spot (defined as the 95% enclosed energy contour) is captured on a 1024×1024-pixel grid. However, experimental variances of the far-field centroid require that the image be cropped to guarantee a consistent area for all shot data; a 720×720-pixel portion around the far-field centroid yields a 411×411-μm^2 area of the original image for analysis.

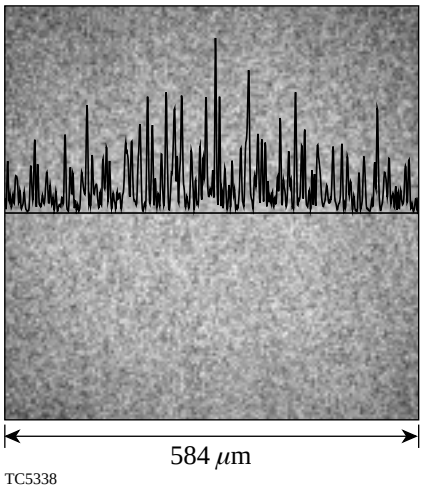

Figure 82.34
UVETP sampled far-field spot demonstrating the 46×, high-magnification setup. The image represents a 300-J, 3.5-ns square laser pulse without applied FM. As demonstrated with the single-pixel lineout through the center of the beam, the spot possesses a highly modulated intensity profile. The laser beam focus is centered nominally on the photodetector, and a 584-μm central portion of the whole 950-μm far-field spot (defined as the 95% enclosed energy contour) is captured on a 1024×1024-pixel grid.

Waasikwa' simulations use a different scale that samples the majority of the far-field spot to avoid aliasing effects from the Fourier transforms in Eq. (2). The far-field spot is calculated over a 1024×1024-pixel grid that spans a 993×993-μm^2 area. The speckle structure is resolved by surrounding the DPP data (defined as a 512×512-pixel grid covering 32.6×32.6-cm^2 area) with a zero buffer of 256 pixels on each side, forming a total near-field grid of 1024×1024 pixels. For a direct comparison of power spectra, the simulated far fields are cropped to match the area of the cropped UVETP images so that they span 424×424 pixels or a 411×411-μm^2 area. Consequently, the power spectrum frequency spacing for either the measurement or simulation is equivalent, i.e., $dk_{\mathrm{ff}} = 0.0153$ (rad/μm), because the total sampled area of the far field dictates the discrete Fourier domain spacing of the power spectrum.

The aforementioned configurations are used for all of the UVETP images and *Waasikwa'* simulations presented in this article. A 1-D power spectrum is calculated for each measured UVETP image and *Waasikwa'* simulation using the square Hamming window. The analysis results for all of the measured and simulated far fields discussed here are compiled in Table 82.IV.

The measured nonuniformity for the high- and low-energy shots without applied FM decreases approximately linearly with increasing average near-field intensity. This trend is illustrated in Fig. 82.35, where the average near-field intensity is given by

$$I_{\mathrm{avg}} \equiv \frac{U_{\mathrm{shot}}}{t_{\mathrm{eq}} \cdot \pi \cdot r_{\mathrm{eq}}^2}, \tag{9}$$

where U_{shot} is the measured shot energy, the equivalent radius r_{eq} was defined in Eq. (4), and the equivalent pulse width t_{eq} was defined in Eq. (5). These values are tabulated in Table 82.IV for different pulse widths and energies. When the average near-field intensity is increased, both the small-spatial-scale and whole-beam *B*-integrals grow (since the small-

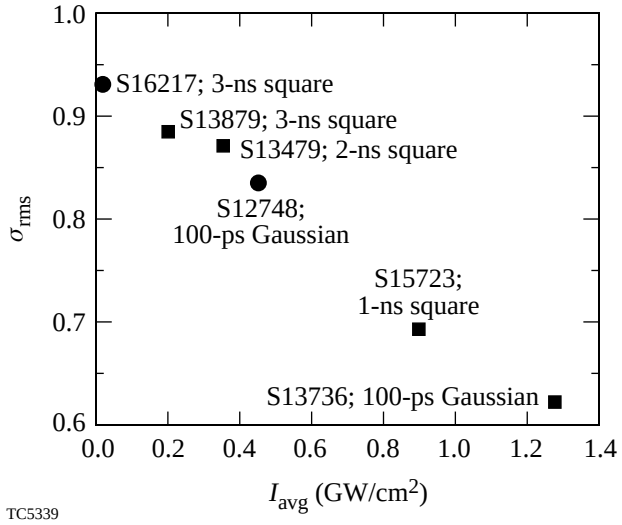

Figure 82.35
The nonuniformity as a function of average intensity for low- and high-energy versions of the pulse shapes. This figure illustrates the trend in the nonuniformity of UVETP images as a function of various pulse shapes and energies. The squares (■) represent the high-energy shots, and the circles (●) correspond to the low-energy counterparts. The points are labeled with the OMEGA shot numbers. Note the suppressed zero.

spatial-scale *B*-integral scales with the whole-beam *B*-integral), which in turn results in a lower measured value of σ_{rms}. For example, the peak whole-beam *B*-integral calculated for the 12.5-J, 100-ps Gaussian pulse increased from 4.64 rad to 9.99 rad (see Table 82.IV) when the energy of the 100-ps pulse was increased by a factor of 3, and the measured σ_{rms} decreased from 83.4% to 62.3%.

Power spectra of measured UVETP images are overplotted in Fig. 82.36 for three types of OMEGA shots without applied FM: a low-energy, 3-ns square pulse is overplotted with a high-energy, 100-ps Gaussian pulse in Fig. 82.36(a) and the same low-energy pulse is overplotted with a high-energy, 1-ns square pulse in Fig. 82.36(b). These spectra represent the three distinct types measured for no-FM pulses. The low-energy, 3-ns

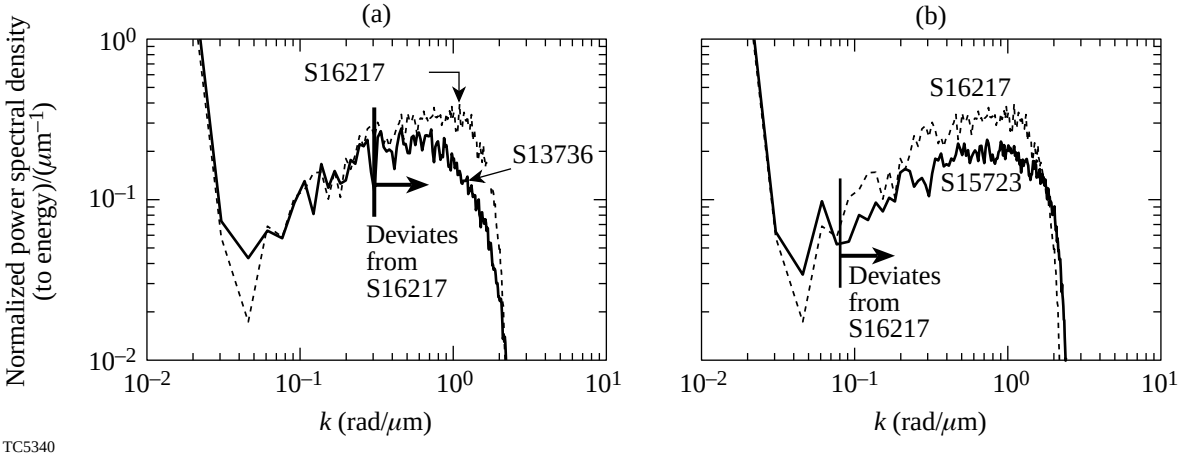

Figure 82.36
The 1-D power spectrum of UVETP images for (a) low-energy, 3-ns square (shot 16217; dashed line) and 100-ps Gaussian (shot 13736; solid black line) shots and (b) low-energy, 3-ns square (shot 16217; dashed line) and high-energy 1-ns square (shot 15723; solid black line). The low-energy shot was 5 J and represents the expected spectrum for shots without applied FM. The high-energy shots were 508 J and 40 J, respectively, and illustrate the smoothing effects of whole-beam and small-spatial-scale *B*-integrals in the regions indicated where the spectral power has been reduced relative to the low-energy shot.

Table 82.IV: Far-field analysis results from typical UVETP images and the *Waasikwa*' simulations that match the near-field conditions for a variety of pulse shapes and energies. A square-Hamming window shape was used. The UVETP image was cropped to span 720 × 720 pixels and covers 0.411 × 0.411 mm. The *Waasikwa*' simulation was cropped to match the area of the UVETP image so that it spans 424 × 424 pixels. Note that this yields identical speckle-frequency spacing of $dk_{ff} = 0.0153$ (rad/μm) for the measurement and simulation.

Shot Number	Nominal Pulse Width	Output-Pulse Shape	UV Beam Energy (J)	*RAINBOW* Calculated r_{eq} (cm)	*RAINBOW* Calculated t_{eq} (ns)	*RAINBOW* Peak Whole-Beam *B*-Integral (radians)	UVETP σ_{rms} (%)	*Waasikwa*' σ_{rms} (%) Whole-Beam *B*-Integral	*Waasikwa*' σ_{rms} (%) Whole-Beam and Small-Spatial-Scale *B*-Integrals
S12748	100 ps	Gaussian	12.5	7.76	0.126	4.64	83±0.5	96.3	94.1
S13736	100 ps	Gaussian	40	8.53	0.116	9.99	62±3	86.2	67.0
S15723	1 ns	square	508	12.6	0.964	20.0	69±5	95.2	69.9
S13479	2 ns	square	370	12.4	1.86	11.1	87±3	96.4	86.5
S16217	3 ns	square	6.6	7.09	2.98	0.970	93±1	98.0	98.9
S13879	3 ns	square	331	12.4	2.880	7.58	88±1	97.7	88.6

square shot without applied FM has a measured nonuniformity σ_{rms} = 93% near the 100% modulation expected for a DPP without *B*-integral effects. The high-energy shots exhibit nonuniformity values σ_{rms} from 62% to 88%. The 1-D power spectra of the 100-ps Gaussian high-energy shot deviate from the theoretical low-energy case over the spatial-frequency range $k_{ff} > 0.3$(rad/μm), as seen in Fig. 82.36(a), which corresponds to $\ell > 150$ and a full-angle near-field laser divergence of about 12 μrad. This pulse has insufficient time to smooth lower spatial frequencies. Conversely, the 1-D power spectra of the high-energy, 1-ns square shot deviates over a larger spatial-frequency range $k_{ff} > 0.08$(rad/μm) ($\ell > 40$), as seen in Fig. 82.36(b), even though this pulse has a lower average intensity and higher nonuniformity. For both cases, the deviation from the low-energy spectrum becomes significant, i.e., a ratio greater than about $\sqrt{2}$ for $k_{ff} > 0.7$ (rad/μm) ($\ell > 350$), which corresponds to a full-angle, near-field laser divergence of about 4 μrad. The other two high-energy square pulses, given in Table 82.IV, exhibit power spectra characteristics similar to the 1-ns case except that the power spectra show less deviation from the low-energy spectrum.

A comparison of the power spectra for the experimental measurements and the simulations demonstrates the smoothing effect of the small-spatial-scale and whole-beam *B*-integrals. The details of the *B*-integral modeling are given in the **Laser Beam Smoothing** section. The power spectra of the UVETP images are shown in Fig. 82.37 through Fig. 82.40 (as solid gray lines) for the 100-ps, 1-ns, 2-ns, and 3-ns pulses with no FM, respectively. The figures include the resultant 1-D power spectra from corresponding *Waasikwa* simulations that include only whole-beam *B*-integral and both small-spatial-scale and whole-beam *B*-integral effects. Each power spectrum is normalized to the spectral energy of the 1-D power spectrum. The measured σ_{rms} is the lowest for the 100-ps pulse at 62.3% and increases with increasing pulse length up to 88.4% for the 3-ns pulse. The values of the nonuniformity σ_{rms} for all the UVETP images are summarized in Table 82.IV. The UVETP diagnostic was configured with a Gaussian-like DPP, which is fabricated to produce a far-field spot with an $N = 2.5$ super-Gaussian spatial-intensity envelope, for all of the shots except the 3-ns pulse. A higher-order DPP, which is fabricated to produce a far-field spot with an $N = 6.5$ super-Gaussian spatial-intensity envelope, was installed for the 3-ns pulse. The spatial-intensity envelope of the far field determines the low-wave-number power spectrum but does not significantly affect the large-wave-number power spectrum. The data windowing occludes the low-wave-number power spectra differences between the two DPP designs.

Simulations of the power spectra demonstrate that temporally varying local phase distortions in the beam caused by small-spatial-scale and whole-beam *B*-integral effects in the laser decrease the nonuniformity to levels that match the experimental results in pulses with no applied FM. The theoretical predictions of the models that include both of the

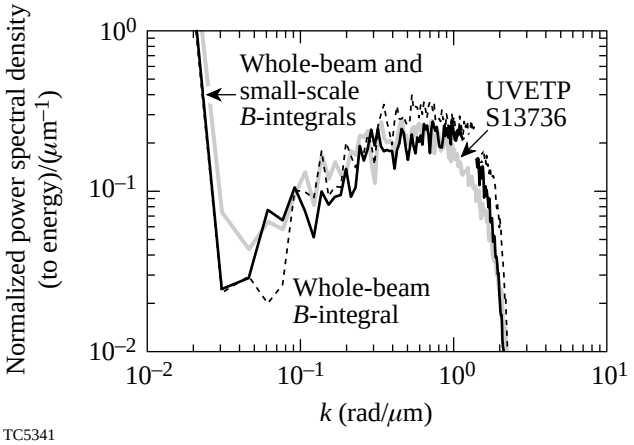

Figure 82.37
The 1-D power spectrum of a UVETP image of a 100-ps Gaussian pulse (shot 13736; solid gray line) and the corresponding *Waasikwa'* simulation including only whole-beam *B*-integral effects (dashed line) and both small-spatial-scale and whole-beam *B*-integral effects (solid black line).

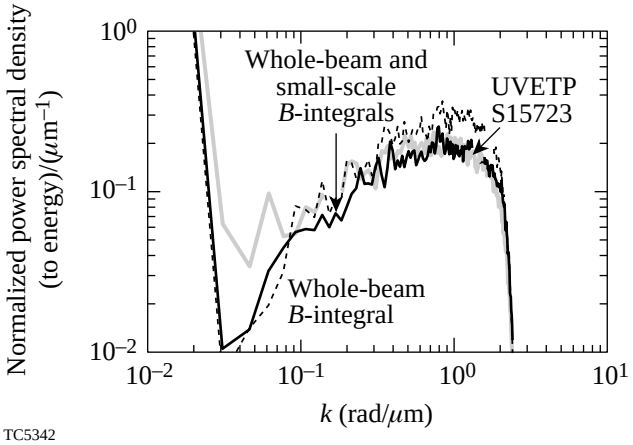

Figure 82.38
The 1-D power spectrum of a UVETP image of a 1-ns square pulse (shot 15723; solid gray line) and the corresponding *Waasikwa'* simulation including only whole-beam *B*-integral effects (dashed line) and both small-spatial-scale and whole-beam *B*-integral effects (solid black line).

B-integral effects are in excellent agreement with the measured power spectra for the 1-ns, 2-ns, and 3-ns square pulses over the range of $k_{ff} > 0.1$ rad/μm. There is a slight discrepancy for the combined *B*-integral model due to excess smoothing over the range of $0.1 < k_{ff} < 0.3$ rad/μm. The 100-ps Gaussian simulations are limited by the near-field measurements as described in the next section. The impact of the small-spatial-scale *B*-integral effects (solid black line) on the power spectrum is evident in Figs. 82.37–82.40, where the simulations (dashed line) that model the whole-beam *B*-integral effects but neglect the small-spatial-scale *B*-integral effects are shown. The effects of the whole-beam *B*-integral reduce the σ_{rms} to a level of 86.2% and 95.2% for the 100-ps and 1-ns high-energy pulses, respectively, which does not match the experimental results with $\sigma_{rms} = 62\%$ for the 100-ps pulse and $\sigma_{rms} = 69.3\%$ for the 1-ns pulse. The combined effects of the whole-beam and small-spatial-scale *B*-integrals, however, reduce the σ_{rms} to a level of 67.0% and 69.9% for the 100-ps and 1-ns high-energy pulses, respectively, which is comparable to the experimental values. The values of the nonuniformity σ_{rms} for all the *Waasikwa'* simulations are summarized in Table 82.IV.

Laser Beam Smoothing

Smoothing in the far field occurs when the state of the transverse phase front of the near field, given by $\phi(x,y,t)$, changes as a function of time such that the spatial coherence is altered. For a particular instant in time, a state $\phi(x,y,t)$ will produce a unique speckle pattern in accordance with the statistics of the DPP. If the state of $\phi(x,y,t)$ changes in time over an interval $\tau \equiv t_2 - t_1$ (where τ is of the order of the coherence time for the pulse) such that a change in state $\Delta\phi(x,y,\tau) \equiv \phi(x,y,t_2) - \phi(x,y,t_1)$ is nonconstant over the near field, the instantaneous far-field speckle pattern will change, resulting in time-integrated smoothing. Alternately, if the quantity $\Delta\phi(x,y,\tau)$ is constant over the near field, during the time interval τ, then no change in the far-field speckle pattern occurs regardless of how rapidly the state $\phi(x,y,t)$ varies in space or time. For example, a nondispersed phase-modulated pulse can be represented by $\phi(x,y,t) = \phi_1(x,y) + \phi_2(t)$.

Time-integrated smoothing in the far field can be understood as a movement of the speckle structure or as a distinct change of the speckle structure as a function of time. If the change in state $\Delta\phi(x,y,\tau)$ has a linear form, i.e.,

$$\Delta\phi(x,y,\tau) \equiv x(\partial\phi/\partial x) + y(\partial\phi/\partial y),$$

then the speckle pattern will appear to laterally shift in the far field by the amounts given by $\Delta x_{ff} = f_\Omega(\partial\phi/\partial x)$ and $\Delta y_{ff} = f_\Omega(\partial\phi/\partial y)$. In the more general case, the phase-state $\phi(x,y,t)$ can be Fourier decomposed into a set of modes as

$$\phi(x,y,t) \equiv \frac{1}{4\pi^2} \iint\limits_{\substack{\forall \text{spatial} \\ \text{frequencies}}} \tilde{\phi}(k_x,k_y,t) e^{+i(k_x x + k_y y)} dk_x dk_y, \quad (10)$$

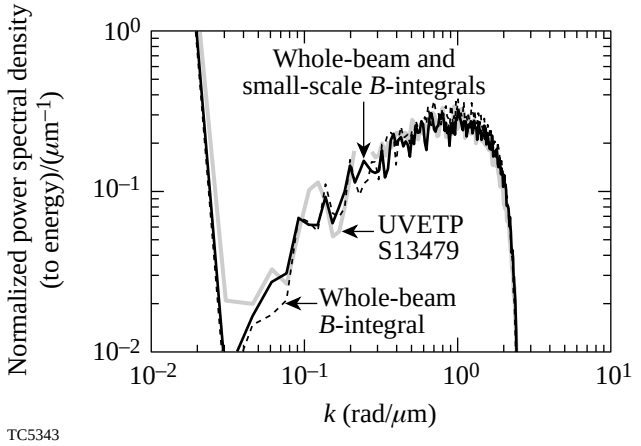

Figure 82.39
The 1-D power spectrum of a UVETP image of a 2-ns square pulse (shot 13479; solid gray line) and the corresponding *Waasikwa'* simulation including only whole-beam *B*-integral effects (dashed line) and both small-spatial-scale and whole-beam *B*-integral effects (solid black line).

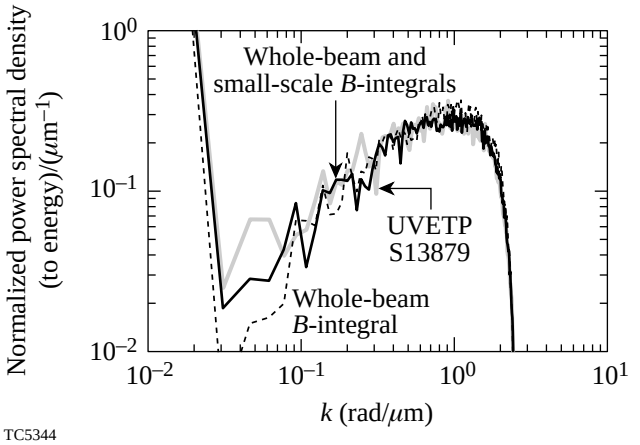

Figure 82.40
The 1-D power spectrum of a UVETP image of a 3-ns square pulse (shot 13879; solid gray line) and the corresponding *Waasikwa'* simulation including only whole-beam *B*-integral effects (dashed line) and both small-spatial-scale and whole-beam *B*-integral effects (solid black line).

where $\tilde{\phi}(k_x,k_y,t)$ represents the complex spectral amplitudes of the Fourier kernel $e^{+i(k_x x+k_y y)}$. At each instant in time $\phi(x,y,t)\in\mathbb{R}$, which implies that the integral in Eq. (10) may be reduced to two times the real part of the integral over the upper half-plane that excludes the negative axis owing to the symmetry properties of the Fourier transform of real functions [i.e., the transform is Hermitian $\tilde{\phi}(k_x,k_y,t)=\phi^*(-k_x,-k_y,t)$ (Ref. 18, p. 14)].

The smoothing effectiveness of an evolving phase state $\phi(x,y,t)$ can be understood by examining the contribution of the term $e^{i\phi(x,y,t)}$ to the far-field distribution. The instantaneous far-field speckle pattern is calculated by Eq. (2). The convolution theorem dictates that the result can be written as

$$I_{\mathrm{ff}}(x_{\mathrm{ff}},y_{\mathrm{ff}},t)=\left|E_{\mathrm{DPP}}(x_{\mathrm{ff}},y_{\mathrm{ff}},t)*E_{\phi}(x_{\mathrm{ff}},y_{\mathrm{ff}},t)\right|^2, \quad (11)$$

where the quantity E_{DPP} (x_{ff}, y_{ff}, t) represents the complex field of the speckle pattern caused by the combined effect of the current beam cross section and the DPP; the quantity $E_{\phi}(x_{\mathrm{ff}}, y_{\mathrm{ff}}, t)$ represents the instantaneous complex far-field pattern caused by the phase state $\phi(x,y,t)$; and the symbol * denotes the convolution operation. The extent of the far-field pattern $E_{\phi}(x_{\mathrm{ff}}, y_{\mathrm{ff}}, t)$ determines the wavelengths that can be smoothed: the greater the area covered, the longer the wavelengths that the phase state $\phi(x,y,t)$ can smooth. The far-field pattern $E_{\phi}(x_{\mathrm{ff}},y_{\mathrm{ff}},t)$ must change over time to affect smoothing. Further, the pulse must be long enough to cover many coherence times: the longer the wavelength, the more smoothing time required.

$$\phi(x,y,t) = 2\left|\tilde{\phi}(k_x,k_y,t)\right|\sin\left(\measuredangle\left\{\tilde{\phi}(k_x,k_y,t)\right\}+k_x x+k_y y\right), \quad (12)$$

where the term $\left|\tilde{\phi}(k_x,k_y,t)\right|$ represents the magnitude of the Fourier component and the term $\measuredangle\left\{\tilde{\phi}(k_x,k_y,t)\right\}$ represents the phase [where the operator $\measuredangle\{e^{i\theta}\}=\theta$]. The term $\left|\tilde{\phi}(k_x,k_y,t)\right|$ determines the amount of laser divergence, given approximately by

$$\Delta\theta\cong 2\left[\left|\tilde{\phi}(k_x,k_y,t)\right|+1\right]\sqrt{k_x^2+k_y^2}\,.$$

If the quantity $\left|\tilde{\phi}(k_x,k_y,t)\right|=\delta_m$, where δ_m is constant and $\measuredangle\left\{\tilde{\phi}(k_x,k_y,t)\right\}=\omega_m t$, then Eq. (12) is functionally identical to 1-D SSD.[20] In this scenario, the spectral components of $E_{\phi}(x_{\mathrm{ff}}, y_{\mathrm{ff}},t)$ in the far field have fixed amplitudes and a fixed spacing (given by the well-known Bessel function expansion; see Ref. 20) but a varying relative phase. If the magnitude of the phase varies in time as $\left|\tilde{\phi}(k_x,k_y,t)\right|=\delta_m(t)$ and if the phase term $\measuredangle\left\{\tilde{\phi}(k_x,k_y,t)\right\}$ is constant, the spectral components of $E_{\phi}(x_{\mathrm{ff}}, y_{\mathrm{ff}}, t)$ in the far field have a fixed spacing analogous to the SSD-like case but with a varying amplitude and a fixed relative phase. As the magnitude $\delta_m(t)$ increases, the number of the spectral components increases and spreads out into the far field (this situation is directly analogous to what happens when the whole-beam *B*-integral modifies the phase magnitude where the Fourier component's wavelength is twice the beam diameter). A general case is constructed when both the magnitude and phase terms in Eq. (12) are allowed to vary with time. A stochastic model may also be employed where the magnitude and relative phase terms change in time of the order of the coherence time and obey a probability density function.

If more than one spectral mode is considered, a variety of complex smoothing mechanisms can be constructed. However, an arbitrary phase state that alters the spatial coherence over time and, in addition, is consistent with the observations cannot be selected. When considering a small number of Fourier components, the member with the greatest laser divergence can be assumed to dominate the remaining members since its laser divergence will be the strongest (see Ref. 21, p. 241 regarding transmission bandwidth). Otherwise, the total divergence of each member must be considered in terms of their combined effect as they convolve together in the far field and produce a greater spread and smooth longer wavelengths. To this end, the dominant mode will contribute a full-angle divergence of $\Delta\theta\cong 2[\delta_m(t)+1]\sqrt{k_x^2+k_y^2}$ and a temporal bandwidth $\Delta\omega\cong[\delta_m(t)+1]\omega_m$, and the other modes will contribute significantly only if their respective spatial or temporal bandwidths are comparable to the dominant mode. The maximum far-field wavelength that can be smoothed is given by $S_{\max}=f_{\Omega}\Delta\theta$. The situation is analogous to the small-spatial-scale *B*-integral when the Fourier components have a fixed phase relationship (i.e., they do not move across the near field) and the modulation depth (of each spectral component) changes as the pulse evolves.

1. Whole-Beam *B*-Integral Modeling

The electric field and phase calculated by *RAINBOW* for a pulsed beam are in cylindrical coordinates, viz. (r,t). Conversely, *Waasikwa'* models both transverse dimensions and time in rectangular cartesian coordinates, viz. (x,y,t). Accordingly, a two-dimensional spline fit is performed at each time step to resample *RAINBOW* data into cartesian coordinates. The complex-valued electric field with no applied FM or DPP

that describes the UV near field is expressed in terms of the converted *RAINBOW* data as

$$E(x,y,t) \equiv E_{0_{\text{rb}}}(x,y,t)e^{i\phi_{B_{\text{rb}}}(x,y,t)}. \quad (13)$$

The phase term $\phi_{B_{\text{rb}}}(x,y,t)$ calculated by *RAINBOW* represents the whole-beam *B*-integral that is an intensity-dependent phase accumulated during propagation within a nonlinear medium.

The phase state calculated by *RAINBOW* is roughly separable, i.e., $\phi_{B_{\text{rb}}}(x,y,t) \cong \delta_{B_{\text{rb}}}(t)\phi_{B_{\text{rb}}}(x,y)$. The quantity $\phi_{B_{\text{rb}}}(x,y)$ represents the initial beam shape that is injected into the laser chain, and the term $\delta_{B_{\text{rb}}}(t)$ represents the initial pulse shape. This occurs because of self-phase modulation in the laser chain that is more severe in the first amplifiers where the local intensity is higher and prior to significant gain saturation that causes the intensity beam profile to change over time. In other words, even though the intensity envelope is altered after the whole laser chain, the phase modulation retains a shape very similar to that of the injected beam. (The form of the phase state is analogous to that discussed in the previous section, where the spatial portion of a mode is fixed and the modulation depth changes over time.) Therefore, the laser divergence causes the far field to expand as a function of time. This effect for a 100-ps Gaussian pulse is illustrated in Fig. 82.41, where the laser divergence is plotted against time. Based on the calculated laser divergence one would expect that the whole-beam *B*-integral would smooth down to the far-field spatial frequency,

$$k_{\text{ff}} = \frac{2\pi}{f_{\Omega}\Delta\theta} \approx 0.35\frac{\text{rad}}{\mu\text{m}},$$

from the calculated full-angle divergence of $\Delta\theta \approx 10\ \mu$rad (see Fig. 82.41). As shown in the **Experimental Results** section the nonuniformity calculated with this model, however, falls short of the measured smoothing. Additionally, the power spectrum (dashed line in Fig. 82.37) is almost identical to the low-energy pulse (dashed line in Fig. 82.36). The primary reason is that although there is sufficient laser divergence, the temporal bandwidth for this method is insufficient to produce a short coherence time because the peak *B*-integral is limited. This model also fails to predict the measured nonuniformity and power spectra for the square pulses for the same reasons.

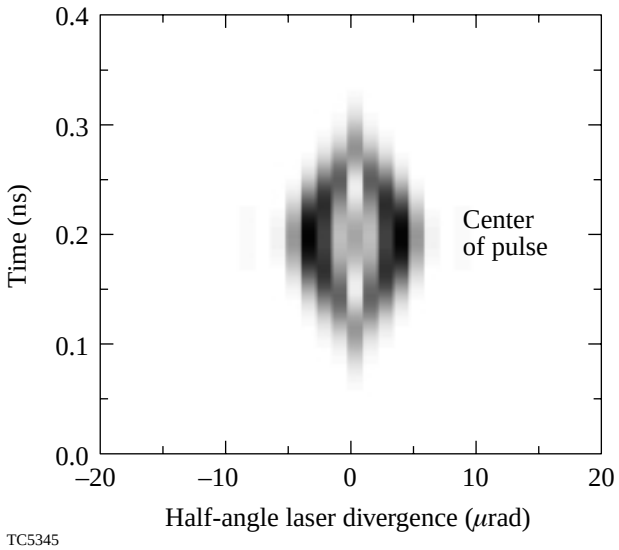

Figure 82.41
The calculated laser divergence due to the whole-beam *B*-integral as a function of time for a 40-J, 100-ps Gaussian pulse.

2. Modeling of Small-Spatial-Scale and Whole-Beam *B*-Integrals

Near-field images of high-energy shots were obtained in the UV section of the OMEGA system (measured after the final amplifiers and after the FCC's). Two pulse lengths—a 100-ps Gaussian [Fig. 82.42(a)] and a 1-ns square [Fig. 82.42(b)]—were captured to compare the fluence of the early times to that at later times. The 100-ps Gaussian near field was representative of a center-peaked beam; the 1-ns square pulse was representative of an edge-peaked beam. These images revealed evidence of small-spatial-scale intensity ripple across the beam, which was more severe for the shorter pulse than the longer pulse because of gain-saturation effects. This evidence has led to speculation that the small-spatial-scale *B*-integral caused the observed smoothing; the depth of the fluence ripple corresponds to the laser divergence required to affect the smoothing in the range $k_{\text{ff}} > 0.1$ (rad/μm), and the growth of the ripple provides the required temporal bandwidth.

The small-spatial-scale and whole-beam *B*-integral phases both result from self-phase modulation, which is proportional to the local accumulated intensity of the beam as it propagates through a nonlinear medium. The combined phase effects of the small-spatial-scale and whole-beam *B*-integrals can be inferred from the fluence measured by the near-field images. The time evolution of the small-spatial-scale *B*-integral can be approximated to follow the spatiotemporal evolution of the whole-beam *B*-integral that is calculated by *RAINBOW*. This is

only valid, however, over a small energy range neighboring the measured near field because the ripple across the beam becomes less pronounced as saturation becomes important. For long, high-energy (fluence) pulses, the beam experiences significant gain saturation in the system amplifiers. The beam profile is smoothed at later times in the pulse because the amount of gain saturation at any spatial location in the beam is proportional to the beam's fluence at that location; initially "hotter" regions of the beam experience reduced gain. This effect is modeled by temporally blending different measured near fields.

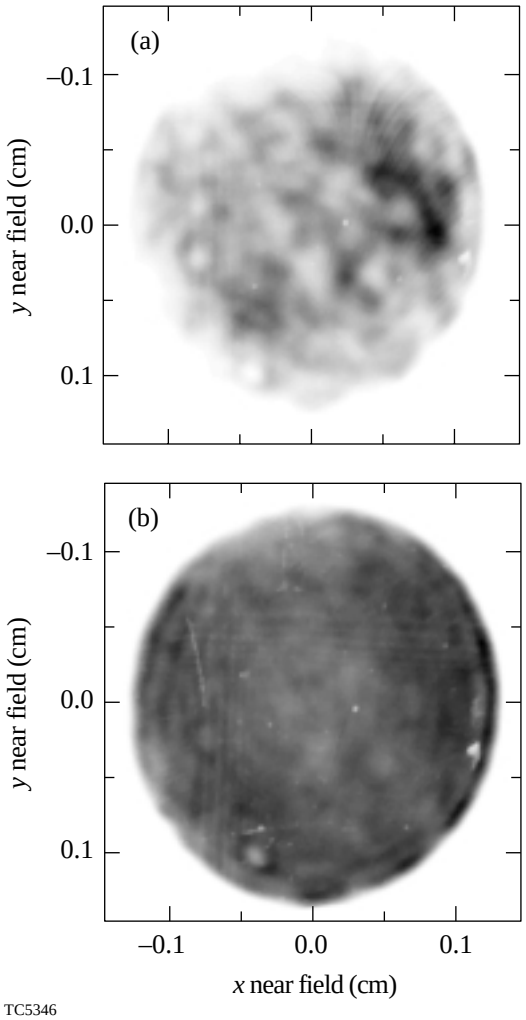

Figure 82.42
Two near-field fluence measurements, taken after the FCC's, represent the early- and late-time evolution of a long pulse. (a) The first image (shot 14233) is a 100-ps Gaussian pulse representative of the early-time evolution. (b) The second image (shot 14234) is a 1-ns square pulse representative of the late-time evolution.

A model of combined *B*-integral effects is constructed by perturbing both the intensity and phase calculated by *RAINBOW* simulations. The electric field of the near field is expressed as [compare Eq. (3)]

$$E_{\text{sim}}(x,y,t) \equiv E_{0_{\text{sim}}}(x,y,t)\, e^{i\phi_{B_{\text{sim}}}(x,y,t)}, \tag{14}$$

where the perturbed magnitude of the electric field is defined by

$$E_{0_{\text{sim}}}(x,y,t) \equiv E_{0_{\text{rb}}}(x,y,t)\sqrt{\Gamma(x,y)}, \tag{15}$$

and the perturbed phase contribution due to both small-spatial-scale and whole-beam *B*-integral effects is given by

$$\phi_{B_{\text{sim}}}(x,y,t) \equiv \phi_{B_{\text{rb}}}(x,y,t)\Gamma(x,y). \tag{16}$$

The unperturbed magnitude and phase of the electric field calculated by *RAINBOW* simulations are given in Eqs. (15) and (16) by $E_{0_{\text{rb}}}(x,y,t)$ and $\phi_{B_{\text{rb}}}(x,y,t)$, respectively. The perturbation function $\Gamma(x,y)$ represents the scaled ratio of a UV near-field fluence measurement to the fluence calculated from a *RAINBOW* simulation, namely

$$\Gamma(x,y) \equiv \alpha \frac{F_{\text{UVnf}}(x,y)}{F_{\text{rb}}(x,y)}, \tag{17}$$

where the subscript UVnf indicates the UV near-field measurement, the subscript rb indicates the *RAINBOW* simulation, and α is the proportionality constant and is defined by

$$\alpha \equiv \frac{W_{\text{rb}}}{W_{\text{UVnf}}}, \tag{18}$$

where W_{rb} is the *RAINBOW* simulation energy and W_{UVnf} is the UV near-field energy.

The two UV near-field measurements are blended temporally to construct a model for longer, higher-energy pulses. The UV near-field measurements are used to divide the longer pulse into segments based on the energy within each measured UV near field. The techniques described previously are employed to evaluate the perturbation function within each temporal segment. The blending function is defined as a dimensionless and smooth step function:

$$b\left(\tau_{\text{on}},\tau_{\text{off}},r,t\right)$$

$$\equiv \frac{1}{2}\left\{\tanh\left[r\left(t-\tau_{\text{on}}\right)\right]-\tanh\left[r\left(t-\tau_{\text{off}}\right)\right]\right\}, \qquad (19)$$

where τ_{on} and τ_{off} are the turn-on and turn-off times and r is the rate at which the blending function mixes the UV near fields. The dividing time of the segments is defined when the *RAINBOW* simulation has equivalent energy to a UV near-field measurement:

$$W_{\text{UVnf}_n} \equiv \int_0^{\tau_n} \iint_{\substack{\text{near}\\ \text{field}}} I_{\text{rb}}(x,y,t)\,dx\,dy\,dt, \qquad (20)$$

where the subscript n refers to a particular near field, e.g., $n = 1$ for the first UV near field. The times τ_n define the turn-on and turn-off times for the blending function; one blending function turns off as the next one turns on, e.g., the first blending function is $b(-\infty,\tau_1,r,t)$ and the second is $b(\tau_1,\tau_2,r,t)$. The final blending function mixes into unperturbed *RAINBOW* data with $b(\tau_2,\infty,r,t)$. Energy conservation requires that

$$\sum_{n=1}^{3} b\left(\tau_{\text{on}_n},\tau_{\text{off}_n},r,t\right)=1;\ \forall t. \qquad (21)$$

The time difference between τ_1 and τ_2 will change according to the modeled pulse. As the differential $\Delta\tau = \tau_2 - \tau_1$ decreases, the mixing rate r increases, which effectively describes how the small-spatial-scale perturbations change more rapidly. The decreased $\Delta\tau$ occurs physically because the saturation fluence is reached earlier for the higher-intensity pulses. The mixing rate is adjusted to eliminate any step that may be introduced in the nonuniformity as a function of time. The switching times and mixing rates for the different modeled pulses are given in Table 82.V.

The calculated laser divergence for this model as a function of time is illustrated in Fig. 82.43 for a 1-ns square pulse at full-system energy. This modeling scheme works well for the longer square pulses but does not adequately describe the smoothing observed for the shorter, 100-ps pulses. This is attributed to the fact that the early time evolution of the small-scale *B*-integral is not captured on either measured near field, and consequently, only a single UV near field is used.

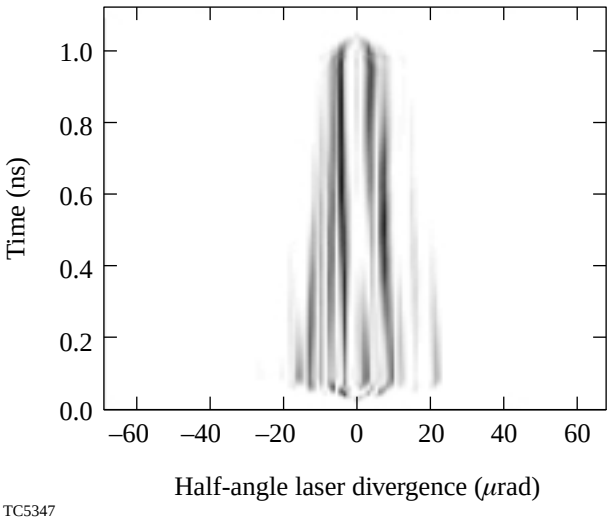

Figure 82.43
The calculated laser divergence due to the whole-beam and small-spatial-scale *B*-integrals as a function of time for a 1-ns square pulse at full system energy.

Table 82.V: Summary of the model parameters for 1-ns, 2-ns, and 3-ns square pulses. The parameters τ_1 and τ_2 define when the *RAINBOW* simulation has energy equivalent to the first and second UV near field, respectively. The energy of the first UV near field is 100 J; the energy of the second UV near field is 290 J.

Shot Number	Nominal Pulse Width (ns)	Measured Energy (J)	τ_1 for 100 J (ns)	τ_2 for 290 J (ns)	r (1/ns)
S15723	1	508	0.225	0.555	1.92
S13479	2	370	0.645	1.57	1.12
S13879	3	331	1.18	2.99	0.775

Conclusion

The observed smoothing on high-energy OMEGA shots without applied FM has been successfully modeled using a combination of small-spatial-scale and whole-beam *B*-integral effects. The smoothing affects mainly the spatial wave numbers $k_{\text{ff}} > 0.1(\text{rad}/\mu\text{m})$ and can reduce the nonuniformity to levels of 62%. The nonuniformity decreases approximately linearly with increasing average intensity of the pulsed beam. The amount of smoothing due to small-spatial-scale *B*-integral effects is insufficient for direct-drive ICF. Reference 13 shows that smoothing by spectral dispersion overwhelms this effect in the mid-range spatial frequencies where these modes are considered the most dangerous spatial frequencies for ICF implosions.[7] Hence, it is not expected that the *B*-integral effects mitigate hydrodynamic instabilities due to their minor influence.

ACKNOWLEDGMENT

This work was partially supported by the U.S. Department of Energy Office of Inertial Confinement Fusion under Cooperative Agreement No. DE-FC03-92SF19460, the University of Rochester, and the New York State Energy Research and Development Authority. The support of DOE does not constitute an endorsement by DOE of the views expressed in this article.

REFERENCES

1. C. P. Verdon, Bull. Am. Phys. Soc. **38**, 2010 (1993).

2. S. E. Bodner, D. G. Colombant, J. H. Gardner, R. H. Lehmberg, S. P. Obenschain, L. Phillips, A. J. Schmitt, J. D. Sethian, R. L. McCrory, W. Seka, C. P. Verdon, J. P. Knauer, B. B. Afeyan, and H. T. Powell, Phys. Plasmas **5**, 1901 (1998).

3. D. K. Bradley, J. A. Delettrez, and C. P. Verdon, Phys. Rev. Lett. **68**, 2774 (1992); J. Delettrez, D. K. Bradley, and C. P. Verdon, Phys. Plasmas **1**, 2342 (1994); J. D. Kilkenny, S. G. Glendinning, S. W. Haan, B. A. Hammel, J. D. Lindl, D. Munro, B. A. Remington, S. V. Weber, J. P. Knauer, and C. P. Verdon, Phys. Plasmas **1**, 1379 (1994); R. Epstein, J. Appl. Phys. **82**, 2123 (1997); V. A. Smalyuk, T. R. Boehly, D. K. Bradley, V. N. Goncharov, J. A. Delettrez, J. P. Knauer, D. D. Meyerhofer, D. Oron, and D. Shvarts, Phys. Rev. Lett. **81**, 5342 (1998).

4. F. J. Marshall and G. R. Bennett, Rev. Sci. Instrum. **70**, 617 (1999); F. J. Marshall, J. A. Delettrez, V. Yu. Glebov, R. P. J. Town, B. Yaakobi, R. L. Kremens, and M. Cable, Phys. Plasmas **7**, 1006 (2000).

5. T. R. Boehly, D. L. Brown, R. S. Craxton, R. L. Keck, J. P. Knauer, J. H. Kelly, T. J. Kessler, S. A. Kumpan, S. J. Loucks, S. A. Letzring, F. J. Marshall, R. L. McCrory, S. F. B. Morse, W. Seka, J. M. Soures, and C. P. Verdon, Opt. Commun. **133**, 495 (1997).

6. S. Skupsky, R. W. Short, T. Kessler, R. S. Craxton, S. Letzring, and J. M. Soures, J. Appl. Phys. **66**, 3456 (1989).

7. Laboratory for Laser Energetics LLE Review **69**, 1, NTIS document No. DOE/SF/19460-152 (1996) (Copies may be obtained from the National Technical Information Service, Springfield, VA 22161); S. Skupsky and R. S. Craxton, Phys. Plasmas **6**, 2157 (1999).

8. J. E. Rothenberg, J. Opt. Soc. Am. B **14**, 1664 (1997).

9. T. J. Kessler, Y. Lin, J. J. Armstrong, and B. Velazquez, in *Laser Coherence Control: Technology and Applications*, edited by H. T. Powell and T. J. Kessler (SPIE, Bellingham, WA, 1993), Vol. 1870, pp. 95–104.

10. Y. Lin, T. J. Kessler, and G. N. Lawrence, Opt. Lett. **21**, 1703 (1996).

11. Y. Kato, unpublished notes (1984); K. Tsubakimoto *et al.*, Opt. Commun. **91**, 9 (1992); K. Tsubakimoto *et al.*, Opt. Commun. **103**, 185 (1993).

12. Laboratory for Laser Energetics LLE Review **45**, 1, NTIS document No. DOE/DP40200-149 (1990) (Copies may be obtained from the National Technical Information Service, Springfield, VA 22161); T. E. Gunderman, J.-C. Lee, T. J. Kessler, S. D. Jacobs, D. J. Smith, and S. Skupsky, in *Conference on Lasers and Electro-Optics*, Vol. 7, 1990 OSA Technical Digest Series (Optical Society of America, Washington, DC, 1990), p. 354.

13. S. P. Regan, J. A. Marozas, J. H. Kelly, T. R. Boehly, W. R. Donaldson, P. A. Jaanimagi, R. L. Keck, T. J. Kessler, D. D. Meyerhofer, W. Seka, S. Skupsky, and V. A. Smalyuk, "Experimental Investigation of Smoothing by Spectral Dispersion," to be published in the Journal of the Optical Society of America B.

14. A. E. Siegman, *Lasers* (University Science Books, Mill Valley, CA, 1986).

15. D. C. Brown, in *High-Peak-Power Nd:Glass Laser Systems*, edited by D. L. MacAdam, Springer Series in Optical Sciences (Springer-Verlag, Berlin, 1981), Vol. 25.

16. D. Cortesi, *Topics in IRIX® Programming*, Document Number 007-2478-007, Silicon Graphics, Inc., Mountain View, CA, 1999.

17. J. W. Goodman, *Introduction to Fourier Optics* (McGraw-Hill, New York, 1968).

18. R. N. Bracewell, *The Fourier Transform and Its Applications*, 2nd ed., rev., McGraw-Hill Series in Electrical Engineering. Circuits and Systems (McGraw-Hill, New York, 1986).

19. J. G. Proakis and D. G. Manolakis, *Introduction to Digital Signal Processing* (Macmillan, New York, 1988).

20. Laboratory for Laser Energetics LLE Review **78**, 62, NTIS document No. DOE/SF/19460-295 (1999). Copies may be obtained from the National Technical Information Service, Springfield, VA 22161.

21. A. B. Carlson, *Communication Systems: An Introduction to Signals and Noise in Electrical Communication*, McGraw-Hill Electrical and Electronic Engineering Series (McGraw-Hill, New York, 1968), p. 154.

Three-Dimensional Modeling of Capsule Implosions in OMEGA Tetrahedral Hohlraums

Introduction

To achieve ignition and gain in inertial confinement fusion (ICF), a spherical target must be compressed with a highly uniform drive mechanism.[1–3] Perturbations in the drive can lead to a distorted fuel core as well as hydrodynamic instabilities, which cause the colder ablator material to mix with the fuel in the central hot spot, effectively quenching the nuclear burn.[4–6] The direct-drive approach to achieving this uniform implosion uses an intense laser pulse to ablate a glass or plastic shell and compress the fuel inside like a spherical rocket.[7] The nonuniformities inherent in the laser beam tend to imprint the target with a "seed" that can cause debilitating hydrodynamic instabilities. To avoid these high-spatial-frequency perturbations, the lasers can alternatively be pointed at the inside of a high-*Z* cavity called a *hohlraum*, which converts the laser energy into a smooth x-ray radiation field that then compresses a similar capsule, again through a rocket-type ablation.[2]

Traditionally, hohlraums have utilized a cylindrical geometry with two laser entrance holes (LEH's) and azimuthal symmetry. Recently, an alternative hohlraum geometry with four LEH's in a spherical case has been proposed as a means for producing an extremely uniform radiation drive.[8,9] These "tetrahedral hohlraums" are particularly well suited for experiments on the University of Rochester's OMEGA laser facility[10] since the soccer-ball geometry of the target chamber possesses multiple beam configurations with perfect tetrahedral symmetry. Accordingly, an extensive series of tetrahedral hohlraum experiments have been carried out on OMEGA under the leadership of the Los Alamos National Laboratory,[11] in a multilaboratory collaboration.

This article reports on the three-dimensional (3-D) view-factor code *BUTTERCUP*, which has been used to model these experiments. Since the code was first reported in Ref. 9, it has been expanded to model the time-dependent radiation transport in the hohlraum and the hydrodynamic implosion of the capsule. Additionally, a 3-D postprocessor has been written to simulate x-ray images of the imploded core. Despite *BUTTERCUP*'s relative simplicity, its predictions for radiation drive temperatures, fusion yields, and core deformation show close agreement with experiment.

The tetrahedral hohlraum experiments on OMEGA[11] have investigated the basic symmetry properties and uniformity of capsule implosions, the radiation drive temperatures, and the effect of high convergence on neutron-yield degradation. Most of these experiments have used thin-walled gold hohlraums with standard Nova implosion capsules filled with DD gas. The best results have been obtained from hohlraums with an inner diameter of 2800 μm, LEH diameter of 700 μm, and typical capsule outer diameter of 550 μm (see Fig. 82.44). The 60 OMEGA beams enter the hohlraum in four groups with 15 beams through each LEH. These 15 beams form three rings with various angles of incidence, namely 23.2° (6 beams), 47.8° (6 beams), and 58.8° (3 beams). As with cylindrical hohlraums, the beam pointing is constrained by minimum clearance requirements to avoid absorption and/or refraction through the plasma ablating off the capsule or the hohlraum

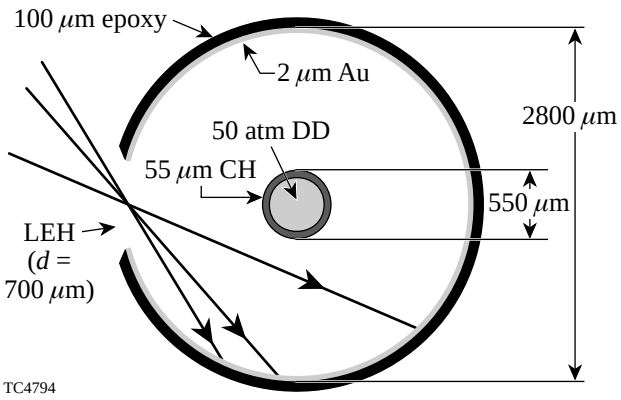

Figure 82.44
Schematic of a thin-walled tetrahedral hohlraum used for OMEGA implosion experiments. One of four laser entrance holes (LEH's) is shown with beams entering at three different angles (23.2°, 47.8°, and 58.8°). The standard Nova capsule has a 550-μm outer diameter and a 55-μm-thick CH shell and is filled with 50 atm of DD gas.

wall. Tetrahedral hohlraums have an additional pointing constraint, that of clearing an opposing LEH to avoid forming plasma blowoff that would interfere with incoming beams. Unlike cylindrical hohlraums, however, the spherical geometry of the tetrahedral design eliminates the possibility of "glint" (irradiation of the capsule by laser light specularly reflected off the hohlraum wall at early times).[12]

The OMEGA soccer-ball geometry has numerous group rotational symmetries, including that of each Platonic solid. The tetrahedral symmetry group is itself embedded in a larger, dodecahedral group where the 60 beams can be divided into 12 sets of 5 independent beams; therefore, pointing coordinates must be calculated for only 5 different beams, and the rest are determined by rotations in the dodecahedral symmetry group. This property provides some inherent symmetry advantages for the tetrahedral hohlraum, causing all l = 1, 2, and 5 spherical-harmonic components of the radiation drive to be identically zero.[8] For the specific hohlraum designs used in this article, the x-ray drive nonuniformity on the capsule ($\sigma_{\rm rms}$) is almost entirely dominated by the Y_{32} spherical-harmonic mode[9,13] and, in the optimal designs, is less than 1% during most of the laser pulse. This highly uniform drive has been confirmed by x-ray images of imploded cores that are essentially round to within the resolution of the instrument.[11]

Despite the remarkable symmetry properties of tetrahedral hohlraums, the cylindrical design has been traditionally dominant in the ICF field, largely because of its azimuthal symmetry. Thus, cylindrical hohlraums can be modeled accurately in a two-dimensional (2-D) geometry, while the tetrahedral hohlraum is inherently a three-dimensional (3-D) problem. Considering the complexity of even a 2-D radiation hydrodynamics code,[14] it is understandable that there has not been significant interest in the 3-D tetrahedral hohlraums until only recently. With the recent progress in developing detailed 3-D codes,[5] however, tetrahedral hohlraums offer an ideal test-bed for theoretical and experimental comparisons. As part of this effort, we have written a 3-D view-factor code called *BUTTERCUP*, which includes radiation transport in the hohlraum and a hydrodynamic treatment of the capsule implosion. Because of the highly uniform nature of these implosions, basic 3-D effects can be accurately modeled as perturbations on a one-dimensional (1-D) model. We will explain this pseudo-3D modeling technique in greater detail below.

Although *BUTTERCUP* does not model laser–plasma interactions in the hohlraum or the motion of the gold wall, its simplicity is perhaps its most powerful trait, allowing for repeated calculations over a wide range of input parameters and thus making it ideal for target design. For example, the dimensions and pointing parameters for the hohlraums described in Ref. 11 were largely based on results of *BUTTERCUP* calculations. Further, by using a simple energy diffusion model, *BUTTERCUP* can predict the time-varying radiation drive temperature $T_r(t)$ in the hohlraum. This agrees closely with experimental measurements as well as with more sophisticated hydrodynamic code calculations. Neutron yields have also been calculated by 1-D and pseudo-3D models and agree well with initial experimental results. Additionally, a postprocessor has been written to simulate x-ray images of the imploded capsule's self-emission. Comparisons with the theoretical core shapes and experimental images provide valuable new insight into the relationship between a 3-D fuel core and its 2-D image and show in particular how a 3-D distortion may be emphasized or smoothed out.

Ultimately, the success of tetrahedral hohlraum experiments on OMEGA will help to determine the feasibility of a tetrahedral ignition design for the National Ignition Facility (NIF). While the NIF laser's port geometry lacks true tetrahedral symmetry, the addition of equatorial direct-drive ports allows for a possible design that can focus 44 of the 48 quads (four beams) into a tetrahedral hohlraum and still provide excellent drive uniformity.[9]

In describing *BUTTERCUP* and its results, we will follow a course of increasing complexity, starting in the next section with an explanation of a static view-factor model that assumes a single albedo over the hohlraum wall. This includes a zero-dimensional implosion model, enabling the time-dependent uniformity on the capsule to be predicted for different tetrahedral hohlraum designs on OMEGA, given the albedo as a function of time. In a subsequent section we introduce a time-dependent model for the laser deposition and radiation transport into the wall of the hohlraum, which allows the time-dependent uniformity and radiation temperature $T_r(t)$ to be calculated directly without reference to the albedo. We then discuss in detail a pseudo-3D radiation-hydrodynamic model for the capsule implosion that predicts convergence ratios, low-order core distortions, and fusion yields. We also describe a 3-D radiation postprocessor that allows direct comparison between theoretical and experimental results.

This work shows that a relatively simple code can make reasonably accurate predictions of hohlraum temperatures, radiation drive uniformity, and the effects of core distortion and high convergence ratio on neutron yield degradation.

BUTTERCUP proves to be immediately useful not only in experimental planning and interpretation, but also as an important tool for aiding in the development of more-sophisticated 3-D ICF codes.

Fundamental Features of the Code *BUTTERCUP*

The most basic features of *BUTTERCUP* include the ability to trace rays from multiple laser beams in a three-dimensional hohlraum and a view-factor algorithm to calculate the resulting radiation uniformity on the surface of the fuel capsule.[9] Both cylindrical and tetrahedral hohlraums can be modeled in a fully 3-D geometry. In the tetrahedral geometry, the four LEH's are located at the angular coordinates (θ,ϕ) = [(54.7°, 0°), (54.7°, 180°), (125.3°, 90°), and (125.3°, 270°)], while in the cylindrical geometry, the axis of the hohlraum is taken to be along $\theta = 0°$. The methods described below apply equally well for either geometry, but we will be concerned primarily with the tetrahedral orientation.

First, each laser beam is divided into a large number of individual rays, each with an equal fraction of the total drive power. The OMEGA beams are treated as circular cones with an *f*/6 focus. For hohlraum experiments on OMEGA, the direct-drive phase plates are removed, giving a laser spot size of about 50-μm diameter at best focus. Once the beam is divided, each individual ray is traced from an initial position and direction through the hohlraum, allowing multiple geometric reflections with a small amount of random scattering until all the energy in the ray has been absorbed (usually no more than two bounces). When the ray hits the hohlraum wall, it deposits a fraction $A(\theta_i)$ of its total energy, given by

$$A(\theta_i) = 1 - \exp\left(-b\cos^r \theta_i\right), \tag{1}$$

where the parameter b determines the absorption at normal incidence and the parameter r gives the angular dependence. In the absence of an accurate experimental determination of $A(\theta_i)$ in a hohlraum, we take $r = 1$ and $b = 3$. These parameters give an absorption of 90% for $\theta_i = 40°$ (thus 99% after two bounces), consistent with Nova data.[15] Of the laser energy absorbed by the wall, typically 60% to 70% is re-emitted as x-ray radiation; the rest is lost to hydrodynamic motion and heating of the hohlraum wall. In this static model, no laser energy is deposited along the beam path and the time evolution of the gold plasma is not simulated. The effect of wall motion on the irradiation uniformity can be modeled by repeating the ray-trace calculation with the same laser pointing but using different hohlraum dimensions, such as might be obtained from 1-D hydrodynamic calculations of a tetrahedral hohlraum or 2-D calculations of a cylindrical hohlraum. For the results reported in this article, however, wall motion was not taken into account.

Despite these simplifications, we can still estimate a single background radiation temperature T_r by assuming an equilibrium Planckian radiation field in the hohlraum cavity. Following Ref. 9, the temperature T_r is calculated with a basic energy equation[16–18] that balances the power entering the radiation field from the laser source and the power lost from the radiation field through the LEH's and absorption by the walls and capsule:

$$P_{\rm las}\,\eta_l = \sigma T_r^4\left(NA_h + \beta_w A_w + \beta_c A_c\right), \tag{2}$$

where $P_{\rm las}$ is the total laser power absorbed by the case, η_l is the conversion efficiency from the laser to x rays in the radiation field, σ is the Stefan–Boltzmann constant, and the term $\left(NA_h + \beta_w A_w + \beta_c A_c\right)$ may be thought of as the effective area of the hohlraum. The quantities A_h, A_w, and A_c are the areas of an LEH, the wall, and the capsule, respectively, in a hohlraum with N holes. The quantity β_w is defined as $1-\alpha_w$, where α_w is the wall albedo, the fraction of the x-ray energy incident on the hohlraum wall that is reradiated into the hohlraum cavity; β_c (= $1-\alpha_c$, where α_c is the capsule albedo) is similarly defined. The wall albedo α_w increases with time and, at the peak of the laser pulse, is typically 0.8 for OMEGA and 0.9 for the NIF. The capsule albedo α_c is taken here to be small (0.1). The x-ray conversion efficiency η_l generally depends on irradiation conditions and is taken to be 0.65 here. The wall albedo may be calculated as a function of time and location on the hohlraum wall (see the next section); however, it is often useful to assume a single, spatially invariant albedo that characterizes the average hohlraum conditions at a given time. We make this single-albedo assumption in this section.

For a given albedo, *BUTTERCUP* calculates the blackbody emission from each point $\mathbf{r}$ on the hohlraum wall by combining a spatially uniform background radiation source σT_r^4 with the absorbed laser intensity $I_l(\mathbf{r})$ at that point. The actual emitted flux $I_e(\mathbf{r})$ depends on the wall albedo and the x-ray conversion efficiency:[9]

$$I_e(\mathbf{r}) = \alpha_w \sigma T_r^4 + \eta_l I_l(\mathbf{r}), \tag{3a}$$

where the spatial dependence of $I_e(\mathbf{r})$ and $I_l(\mathbf{r})$ has been explicitly retained. In this model the wall treats the x-ray and laser sources independently: i.e., a fraction α_w of the radiation flux σT_r^4 incident upon the wall from the cavity and a fraction

η_l of the laser flux $I_l(\mathbf{r})$ absorbed in the wall are emitted into the cavity. The quantity η_l as defined here includes the combined effects of the conversion of the absorbed laser energy to x rays and reradiation from the wall.

To illustrate this, suppose that the laser were converted to x rays in the plasma with efficiency η_l' and the reasonable assumption were made that half were emitted outward from the wall and half were directed inward to be re-emitted with an albedo α_w'. (The use of a different α_w' allows for the x-ray energy fraction reradiated from the laser source to differ from that reradiated from the cavity radiation source.) Equation (3a) would then become

$$I_e(\mathbf{r}) = \alpha_w \sigma T_r^4 + \frac{1}{2}\left(1+\alpha_w'\right)\eta_l' I_l(\mathbf{r}), \tag{3b}$$

giving

$$\eta_l = \frac{1}{2}\left(1+\alpha_w'\right)\eta_l'. \tag{3c}$$

It is also worth noting that Eq. (3a), when integrated over the wall, provides two source terms for the radiation field in the cavity, $\alpha_w \sigma T_r^4 A_w$ and $\eta_l P_{\text{las}}$, consistent with Eq. (2), confirming that the same value of η_l must be used in both equations.

Assuming a Lambertian source, Eq. (3a) permits a brightness (spectrally integrated power/unit area/unit solid angle) $B_e(\mathbf{r}) = I_e(\mathbf{r})/\pi$ that is independent of direction to be defined at all points on the hohlraum wall. *BUTTERCUP* then uses a 3-D view-factor algorithm[9,19–23] to calculate the radiation drive uniformity on the capsule. For each point on the surface of the capsule, the total incident radiation-drive intensity $I(\theta,\phi)$ is determined by integrating the brightness $B_e(\mathbf{r})$ of the wall over all solid angles, as seen by the capsule, for the entire visible hemisphere. The radiation drive as a function of time can be determined by using time-varying input values for the laser pulse shape $P_{\text{las}}(t)$ and the albedo $\alpha_w(t)$; the latter can be inferred from experimental measurements, calculated directly as in the next section, or imported from a calculation by a hydrocode. For a given pulse shape, the albedo is only weakly dependent on the hohlraum irradiation geometry. Theoretical and experimental Nova results can thus be applied to OMEGA hohlraums with a fair level of accuracy.

Since the radiation uniformity on the capsule depends largely on the ratio of the hohlraum radius to the capsule radius,[2,8,20] the changing size of the imploding capsule must be considered when calculating the time-dependent drive uniformity. To do this, a zero-dimensional (0-D) "rocket model" is employed, treating the capsule as a thin shell with a time-varying radius $r_{\text{shell}}(t)$ and mass $m(t)$. Following Lindl,[2] we use scaling laws that relate the ablation pressure P_a (dyn/cm^2) and the mass ablation rate $\dot{m}\left(\text{g/cm}^2/\text{s}\right)$ to powers of $T_r(t)$ (as measured in hundreds of eV):

$$\begin{aligned} P_a(t) &= 5.1\times 10^{12}\, T_r^{3.5}(t), \\ \dot{m}(t) &= 5.9\times 10^{5}\, T_r^{3}(t), \\ P_{\text{gas}}(t) &= 7.7\times 10^{2}\, r_{\text{shell}}^{-5}, \\ m(t)\ddot{r}_{\text{shell}}(t) &= -4\pi r_{\text{shell}}^2\left[P_a(t) - P_{\text{gas}}(t)\right], \end{aligned} \tag{4}$$

where P_{gas} is the internal gas pressure of the capsule, assuming adiabatic heating of the fuel. The radius of the shell r_{shell} is measured in centimeters and the time t in seconds. This simple model has been found to predict remarkably accurate implosion trajectories, giving a stagnation time of 3 ns for PS22 in close agreement with experiment. Coupling the view-factor vacuum radiation transport with the time-varying capsule radius then gives a prediction for the time-dependent radiation-drive uniformity on the capsule.

Figure 82.45 shows the spatial uniformity of the x-ray drive incident on the capsule as a function of time for two different tetrahedral designs. The dashed curves are the result of the radiation source as determined from Eqs. (2) and (3) coupled to the 0-D rocket model. The time-dependent albedo used in Eqs. (2) and (3) was obtained from the wall-diffusion model described in the next section. The results of this diffusion model are shown as the solid curves. Since the nonuniformity is typically dominated (>90%) by the Y_{32} spherical-harmonic mode, we show only the contribution from σ_{32}, where the total σ_{rms} is defined as in Ref. 22:

$$\sigma_{\text{rms}}^2 \equiv \sum_{l,m} \sigma_{lm}^2. \tag{5}$$

For both designs, Fig. 82.45 shows a noticeable improvement in drive uniformity later in time, which is primarily a consequence of the converging capsule radius. Note that the simple energy-balance calculation agrees quite well with the more-detailed wall-diffusion calculation throughout most of the

laser pulse. At early times, the single-albedo assumption of the energy-balance model breaks down since the energy that should be confined to a few small laser-heated spots is spread over the entire hohlraum wall, predicting a more uniform drive. The effect of this early nonuniformity on target performance is not expected to be significant, however, since little energy irradiates the capsule at these times. Also, Eq. (2) implies that, after the laser turns off, the radiation temperature (and thus the drive nonuniformity) immediately goes to zero, while in reality the hohlraum wall acts as a heat reservoir, radiating stored energy well after the end of the laser pulse. This is important for the targets discussed below, where peak compression and neutron production occur several hundred picoseconds after the end of the laser pulse.

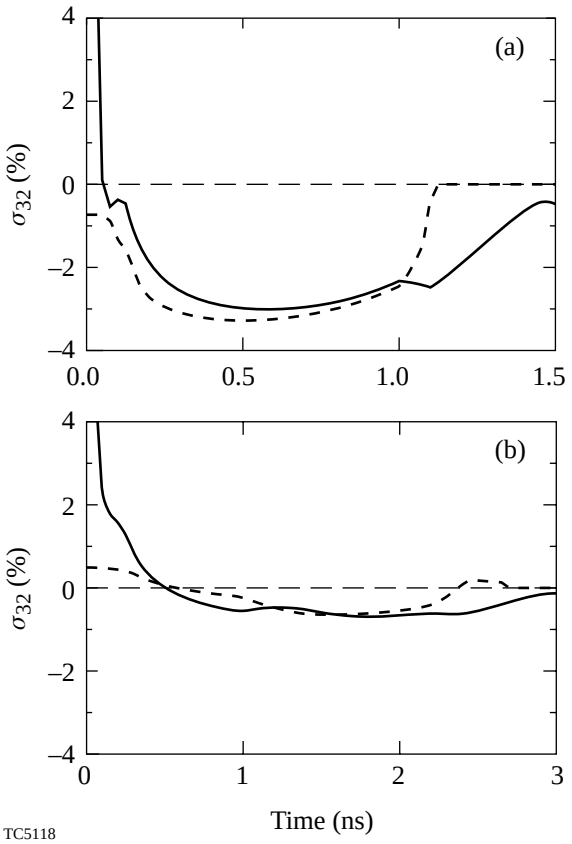

Figure 82.45
Predicted drive uniformity on the capsule in a tetrahedral hohlraum. The σ_{rms} present in the dominant spherical-harmonic mode Y_{32} is plotted versus time for (a) the initial scale-1 design for a 1-ns square pulse and (b) the optimized scale-1.2 PS22 design. The amplitude of σ_{32} gives the rms nonuniformity when all other modes are absent. The dashed curves were produced by the energy-balance model described in the **Fundamental Features of the Code *BUTTERCUP*** section, and the solid curves were calculated by the wall-diffusion model described in the **Radiation Transport and Diffusion** section.

The first experimental tetrahedral hohlraums (shot on OMEGA in March 1997) were designed to have the same surface area and total LEH area as a standard cylindrical Nova hohlraum, thus giving comparable drive temperatures for the same laser pulse. This "scale-1" tetrahedral hohlraum had $R_{case} = 1150\ \mu$m and $R_{LEH} = 450\ \mu$m. The predicted radiation-drive uniformity of 2% to 3% for a 1-ns flat-top pulse was certainly good by most ICF standards,[24,25] but the tetrahedral geometry on OMEGA was capable of much better uniformity. With the help of *BUTTERCUP*, the tetrahedral hohlraum was redesigned to give the best-possible drive uniformity while still maintaining reasonable radiation temperatures and sufficient clearance for the laser beams.[26] The optimized design, known as a scale-1.2 hohlraum, had $R_{case} = 1400\ \mu$m, $R_{LEH} = 350\ \mu$m, and different laser pointing parameters. The optimized design had a total LEH area of 1.54 mm^2, a little less than the 2.26 mm^2 of a standard Nova hohlraum. Additionally, the shaped laser pulse PS22 was used to achieve more-efficient implosions and reduce laser–plasma instabilities in the hohlraum. Figures 82.45(a) and 82.45(b) correspond to the initial and optimized designs, respectively.

The difference between a peak drive uniformity of 3% and one of 1% is apparent when comparing experimental images of the imploded cores, as shown in Fig. 82.46. The initial design, with $\sigma_{32} \sim 3\%$ at the peak of the drive, results in a core with a clear triangular shape [Fig. 82.46(a)], corresponding to weaker

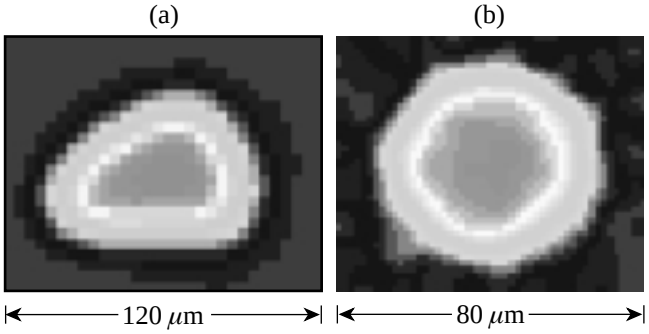

Figure 82.46
Experimental x-ray images[11] of imploded capsule cores for the drive conditions of Fig. 82.45, viewed through an LEH. The initial design (a) has a predicted average drive uniformity of $\sigma_{32} \sim 2\%$ to 3%, causing a characteristic triangular core, while the optimized design (b) produced a nearly round core with a drive uniformity of $\sigma_{32} < 1\%$. The three points in the triangular image are oriented toward the other three LEH's. Image (a) was taken with a time-integrating pinhole camera and image (b) with an x-ray framing camera.

drive pressure at the points on the capsule that directly face the LEH's. The resulting 3-D tetrahedron-shaped core looks like a triangle when viewed along the axis of one of its vertices (through a LEH). With the optimized design, the imploded core is almost perfectly round [Fig. 82.46(b)], representing one of the most-uniform indirect-drive implosions recorded to date.

The optimized design for OMEGA benefits from a favorable ratio of the case radius to the capsule radius. The tradeoff is a lower coupling efficiency due to the ~40% extra wall area. The tetrahedral geometry on OMEGA has the advantage, however, that all 60 beams can be used, compared with a maximum of 40 for cylindrical hohlraums. On the NIF, the tradeoff between uniformity and efficiency will be a key issue, especially for capsules with the larger convergence ratios that will be required.

Radiation Transport and Diffusion

The simple zero-dimensional model described in the previous section works well for designing hohlraum targets and estimating the radiation-drive uniformity, but it has some significant shortcomings. For one, the assumption of a single, spatially independent albedo tends to break down early in the laser pulse, when the cold, unirradiated sections of the wall typically have a much lower albedo than the laser-heated spots.[27,28] The energy-balance model also fails at later times, after the end of the laser pulse, giving a radiation temperature of zero. Additionally, the dependence on an external calculation or experimental measurement of the time-varying albedo limits *BUTTERCUP*'s ability to scan through a wide variety of pulse shapes and hohlraum designs. Finally, while the predicted time-dependent drive uniformity agrees qualitatively with experimental data, it unfortunately provides no means for quantitative comparison.

To address these limitations, *BUTTERCUP* has been expanded to model the gold wall as a 2-D grid of mass elements, each with a different temperature profile and radiation brightness. Each point on this 2-D grid is treated as a separate problem in 1-D planar geometry, with the radiation transport into the wall modeled by solving an energy diffusion equation. The boundary zone of each 1-D section is driven by a radiation source from other portions of the hohlraum wall and, for the directly irradiated sections, a laser source. The deposited energy then propagates into the wall (along x) according to the diffusion equation, assuming a single radiation and matter temperature $T_w(x,t)$ at each point in the wall. This treatment is similar to that of Tsakiris,[27] except that he used 1-D self-similar solutions rather than individual 1-D calculations.

Following Rosen[29,30] we use the diffusion equation

$$\frac{\partial}{\partial t}(\rho\varepsilon) = \frac{\partial}{\partial x}\left[\frac{c}{3}\lambda_R \cdot \frac{\partial}{\partial x}\left(aT_w^4\right)\right] \tag{6a}$$

in the interior of the wall, and apply

$$\frac{\partial}{\partial t}(\rho\varepsilon\Delta x) = \underbrace{\frac{c}{3}\lambda_R \cdot \frac{\partial}{\partial x}\left(aT_w^4\right)}_{\text{diffusion}} \underbrace{-\sigma T_w^4}_{\substack{\text{loss to}\\ \text{hohlraum}\\ \text{cavity}}} + \underbrace{\eta_l I_l}_{\substack{\text{laser}\\ \text{source}}}$$

$$+ \underbrace{\frac{1}{\pi}\int \sigma T_w^4(\mathrm{r})\cos\theta\, d\Omega}_{\substack{\text{radiation}\\ \text{source}}} \tag{6b}$$

to the boundary zone. Here $\rho\varepsilon$ is the energy density of the wall material (ergs/cm^3), which scales as $T_w^{1.5}$, the diffusion coefficient is 1/3 $c\lambda_R$, and $aT_w^4\left[a = 4\sigma/c\right]$ is the radiant energy density. The Rosseland mean free path λ_R is given as a function of temperature and density.[29] The last term in Eq. (6b) is the radiation flux seen by the point on the wall, integrated over all solid angles (i.e., over all other boundary zones on the hohlraum wall). This term couples together all the individual 1-D diffusion calculations: each boundary zone emits into the hohlraum cavity a flux $\sigma T_w^4(\mathbf{r})$ [brightness $\sigma T_w^4(\mathbf{r})/\pi$], of which a large fraction provides a source for other boundary zones and a smaller fraction is lost to the capsule and LEH's.

In Eq. (6b), Δx is the thickness of the boundary zone, where the energy from the laser and radiation source terms is deposited. In the limit of $\Delta x \to 0$ the left-hand side of Eq. (6b) tends to zero (i.e., the boundary cell has negligible heat capacity), and Eq. (6b) then acts as a boundary condition on $\partial T_w^4/\partial x$ for the diffusion equation. It is for this reason that the numerical solutions of Eq. (6) are convergent (i.e., independent of Δx) as $\Delta x \to 0$. In this limit, the laser source and the incident radiation from the other zones on the hohlraum wall balance the radiative loss into the hohlraum cavity and the diffusive loss into the hohlraum wall.

The term $\int \sigma T_w^4(\mathbf{r})\cos\theta\, d\Omega$ is calculated in a way very similar to the view-factor integration used to determine the radiation incident on the capsule. Figure 82.47 shows a schematic representation of this algorithm, where the incident radiation intensity at a given point P on the hohlraum wall is determined by tracing rays over all solid angles and summing the relative brightness detected from each direction. Of course, the LEH's do not contribute anything to the incoming radia-

tion, and the low-albedo capsule acts effectively as a shield, blocking the radiation transfer between opposite sections of the hohlraum wall. If no capsule were present, the spherical geometry would provide perfect radiation uniformity incident on every point of the wall not directly heated by a laser source, regardless of the spatial emission distribution or the size of the LEH's, as long as the spectral brightness is independent of angle (i.e., Lambertian) as is the case for blackbody radiation.[27] This makes tetrahedral hohlraums particularly well suited for nonimplosion experiments that require a uniform x-ray source for driving foils or other packages mounted on the hohlraum wall.

Here, as in the previous section, the emitted wall brightness is taken to be $\sigma T_w^4(\mathbf{r})/\pi$ independent of angle. This is probably a good assumption except at very early times when the steep gradient of T_w within the wall (see Fig. 82.48 below) results in different angles viewing different values of T_w at about one optical depth into the wall. An angle-dependent brightness could be added to the model.

It is instructive to compare Eq. (6b) with Eq. (3a), obtained for the simpler model of the previous section. The radiation source term of Eq. (6b) may be written as $\sigma T_R^4(\mathbf{r})$, defining an effective hohlraum temperature $T_R(\mathbf{r})$ as seen by a point $\mathbf{r}$ on the wall that is analogous to T_r of the previous section. Generally the spatial dependence of $T_R(\mathbf{r})$ is weak: as stated previously, $T_R(\mathbf{r})$ would be independent of $\mathbf{r}$ for a spherical hohlraum in the absence of a capsule. This provides justification for the use of a single T_r in the previous section to describe the radiation field in the cavity. It is also possible to define a local albedo $\alpha_2(\mathbf{r}) \equiv 1 - \beta_2(\mathbf{r})$ by requiring $\beta_2(\mathbf{r})\sigma T_R^4(\mathbf{r})$ to equal (–1) times the first term on the right-hand side of Eq. (6b), i.e., the diffusive loss into the wall. With these definitions, the flux of x rays emitted into the hohlraum cavity becomes

$$\sigma T_w^4 = \alpha_2(\mathbf{r})\sigma T_R^4(\mathbf{r}) + \eta_l I_l(\mathbf{r}), \tag{7}$$

which compares closely with the right-hand side of Eq. (3a). The first model can thus be expected to best match the second model if α_w is taken to be the average of $\alpha_2(\mathbf{r})$ over the hohlraum wall.

An example of the nonlinear heat wave (Marshak wave[31]) described by Eq. (6) is shown in Fig. 82.48, for an unirradiated section of the gold wall. Here the wave is plotted at 100-ps intervals for an illustrative calculation in which a hohlraum is driven by a 1-ns square pulse. The penetration rate is commonly approximated as being proportional to $\sqrt{t}$,[29,31,32]

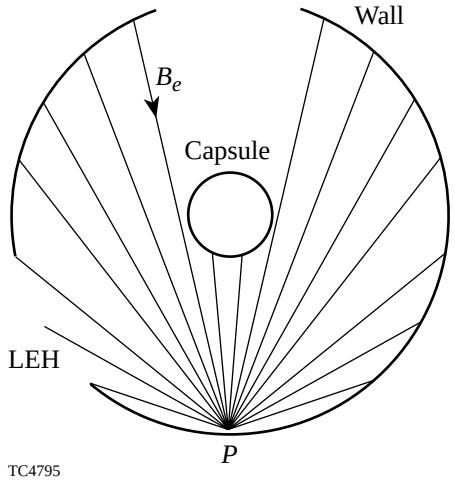

Figure 82.47
Schematic of the view-factor algorithm used by the code *BUTTERCUP* to calculate radiation transfer within the hohlraum. The x-ray flux incident at each point P on the wall is determined by integrating the visible brightness B_e over a hemisphere of solid angle. The low-albedo capsule acts effectively as a shield, blocking the radiation transfer between opposite sections of the hohlraum wall.

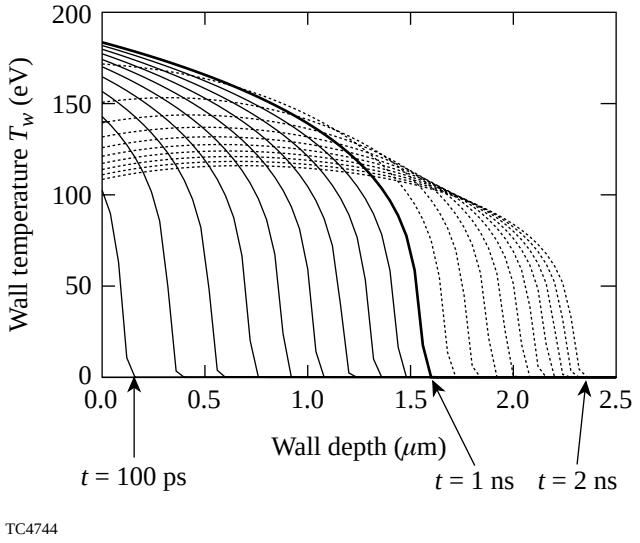

Figure 82.48
Wall temperature T_w as a function of distance into the gold wall, plotted at 100-ps intervals throughout a 1-ns square-pulse drive shot. For the duration of the laser pulse, the temperature at the boundary rises as the Marshak radiation wave propagates into the hohlraum wall; it then decreases as the wall cools after the laser is turned off.

although this approximation breaks down when blowoff and other effects are included.[16,29] Even after the laser is turned off, the radiation continues to diffuse into the wall; however, much of the energy in the radiation field within the hohlraum cavity leaks out through the LEH's, lowering the temperature at the boundary surface. Note that it is not necessary to calculate the albedo explicitly in this model: the radiation emitted into the hohlraum from each boundary cell is given directly from the T_w there as σT_w^4.

With the temperature T_w defined at each point on the hohlraum wall, it is straightforward to predict what the experimentally measured radiation temperature T_r will be as a function of time. For the tetrahedral hohlraum experiments on OMEGA, $T_r(t)$ was measured with the multichannel soft x-ray diagnostic Dante.[33] This looked directly through one of the LEH's, viewing a combination of laser spots and unirradiated wall, representative of what the capsule should see, and thus eliminating the need for "albedo corrections."[34] For a 22.0-kJ PS22 drive shot (i.e., a shot without a capsule), the theoretical and experimental temperatures were in close agreement, as shown in Fig. 82.49.[11] The data are from a scale-1.2 tetrahedral hohlraum with 500-μm-radius LEH's (larger than the 350-μm LEH's used for the optimized implosions). For the *BUTTERCUP* calculation, the experimentally measured SBS backscatter fraction of 6% was taken out of the input laser energy. The close agreement with experiment indicates that the basic hohlraum energetics can be accurately modeled with *BUTTERCUP*'s relatively simple combination of diffusion and view-factor calculations.

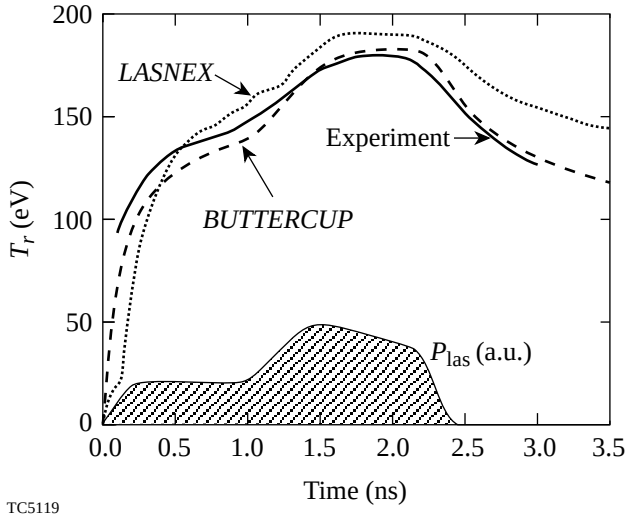

Figure 82.49
Hohlraum radiation temperature T_r as a function of time for a 22.0-kJ PS22 drive experiment with 500-μm-radius LEH's. The *LASNEX* predictions (dotted curve) and the experimental data (solid curve) measured by the Dante multichannel, soft x-ray diagnostic are taken from Ref. 11. The dashed curve is the *BUTTERCUP* calculation, with the input laser power P_{las} adjusted for the experimental SBS backscatter fraction of 6%.

By this method of performing multiple 1-D diffusion calculations on a 2-D grid covering the hohlraum wall, and coupling them together through view-factor radiation transport, *BUTTERCUP* provides a 3-D description of the time-dependent radiation uniformity on the capsule. This approach allows remarkably rapid simulations without sacrificing physical accuracy. Since fully 3-D radiation-hydrodynamics codes typically take hundreds of CPU hours to do a single simulation on even the fastest supercomputers, pseudo-3D calculations like those presented here will be increasingly valuable. The speed of *BUTTERCUP* also provides the ability to perform multiple simulations with different hohlraum parameters, making the code an ideal tool for developing new target designs.

The evaluation of the effects on uniformity of pointing errors and beam imbalance provides a good example of the type of problem for which *BUTTERCUP* is ideally suited.[35] With each point on the hohlraum wall being modeled independently, the computational overhead associated with changing the beam pointings and energies is very small, even though the tetrahedral symmetry is lost.

One limitation of the model is the assumption of an idealized blackbody radiation spectrum. For example, it would not be correct to treat M-band radiation from multi-keV laser-heated plasma with Eq. (6), which emits blackbody radiation into the hohlraum with the temperature of the dense wall plasma. Here, following Eq. (3c), it would be reasonable to assume that half of this radiation is emitted into the hohlraum and half is lost in the wall (with $\alpha'_w = 0$). The flux and uniformity of M-band radiation on the capsule could nevertheless be calculated with the model of the previous section using $\alpha'_w = 0$ and taking η'_l to give the observed emission of M-band radiation from the hohlraum wall.

We conclude this section by demonstrating that the simple energy-balance model described in the previous section provides a remarkably accurate description of the radiation temperature $T_r(t)$ when given a single, spatially averaged albedo as a function of time. This may be seen from Fig. 82.50, which plots $T_r(t)$ for (a) the initial design (1-ns square pulse) and (b) the optimized design (PS22 shaped pulse). The solid curves correspond to the more accurate wall-diffusion model and the

dashed curves to the energy-balance model. Here we use the spatially averaged albedo (dotted curves) calculated by the wall-diffusion model as input for the energy-balance model. For both cases the albedo rises rapidly to about 0.8. For the duration of the laser pulse, the two models agree very closely, suggesting a close equilibrium between the incident laser power and the radiation field. After the laser pulse ends, the albedo becomes greater than unity since the cooling wall emits more energy than it absorbs. This is also the point at which the energy-balance model breaks down completely, as the β_w in Eq. (2) becomes negative, the left-hand side of Eq. (2) becomes zero, and the wall acts like a radiation source rather than a sink.

Capsule Implosions

Given the 3-D, time-dependent radiation field incident on the capsule, *BUTTERCUP* also provides a pseudo-3D model of the actual hydrodynamic capsule implosion within a tetrahedral (or cylindrical) hohlraum. For a given x-ray drive intensity $I_r(\theta,\phi,t)$ on the surface of the capsule, the incident radiation is treated as a blackbody spectrum and deposited into the plastic shell in multiple energy and angular groups. Like the pseudo-3D treatment of the gold wall, the capsule is modeled as a collection of 1-D calculations, each with its own radiation source term. Unlike the treatment of the gold wall (where just the Rosseland opacity is used), however, the radiation transport within the capsule plasma is modeled in greater detail using multigroup opacities.[36]

Each angular wedge of the capsule is modeled as a spherically symmetric problem with 1-D Lagrangian hydrodynamics. About 100 material zones are typically used in the radial direction, with roughly half in the shell and half in the fuel. The radiation energy from the hohlraum wall is deposited in the CH plasma using an S_N algorithm, which divides the incident radiation into different angular groups,[37] as is represented by Fig. 82.51. The x rays that are nearly normal to the surface penetrate deeper into the shell, while the higher-angle x rays deposit the majority of their energy closer to the outside of the capsule. Since opacities are often quite sensitive to photon energy, the Planckian spectrum from the hohlraum wall is divided into multiple frequency groups, each containing a fraction of the blackbody radiation flux σT_r^4 and each penetrating the plastic shell to a different depth.

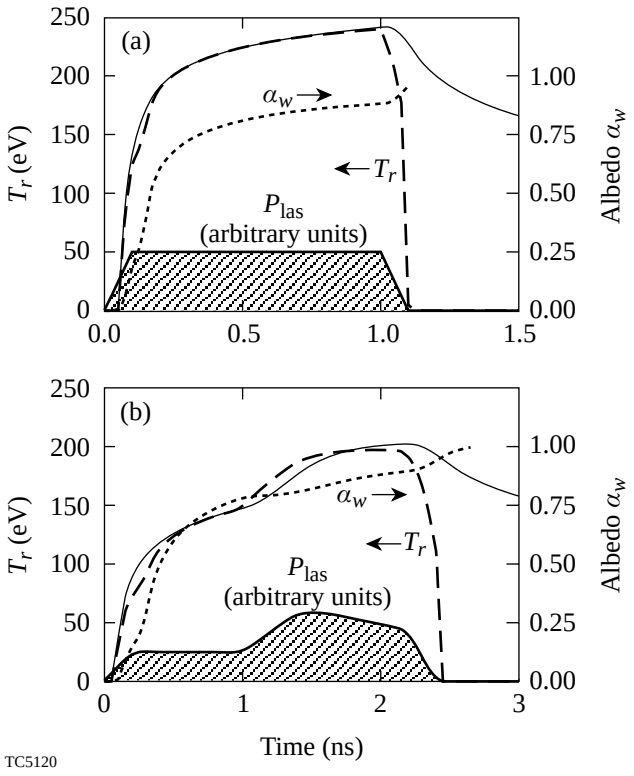

Figure 82.50
Hohlraum radiation temperature T_r as a function of time for two implosion experiments: (a) scale-1 hohlraum with a 30-kJ, 1-ns square pulse (initial design); (b) scale-1.2 hohlraum with a 24.6-kJ, PS22 shaped pulse (optimized design). The wall-diffusion model produced the solid curves and a time-dependent, spatially averaged albedo, defined here as the total power radiated from the hohlraum wall divided by the total radiative power incident on the wall (dotted curve); this albedo was then used as input in the energy-balance model to give the dashed curves.

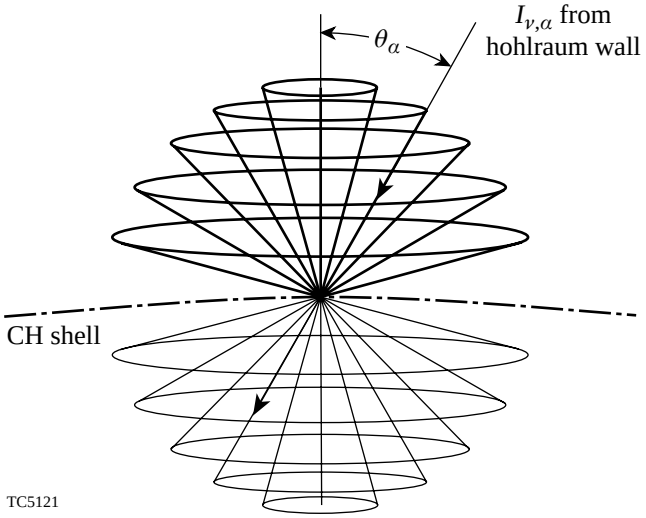

Figure 82.51
Multiple angular groups used to model radiation absorption in the capsule shell. X rays with small angles of incidence θ_α penetrate deeper into the ablating plasma, while higher-angle groups deposit their energy closer to the outside of the capsule.

BUTTERCUP models the capsule implosion by solving the 1-D spherical Lagrangian hydrodynamic equations, including electron thermal diffusion and multigroup radiation diffusion within the capsule. The basic hydrodynamic equations in a spherically symmetric geometry are[37]

$$\frac{\partial r}{\partial t} = v,$$

$$\frac{\partial v}{\partial t} = -4\pi r^2 \frac{\partial}{\partial m}(P+Q), \tag{8}$$

$$\frac{\partial \varepsilon}{\partial t} = -4\pi \frac{\partial}{\partial m}\left(r^2 v\right)(P+Q),$$

where P is the hydrodynamic fluid pressure, Q is the "artificial viscous stress," r and v are the position and velocity of Lagrangian zone markers, and ∂m is the differential mass element. For each step of the calculation, P and the specific energy ε (ergs/g) are determined from the *SESAME* equation-of-state tables.[38] The electron thermal diffusion is calculated using

$$\frac{\partial}{\partial t}(\rho\varepsilon) = -\nabla\cdot Q_e = \nabla\cdot\left(\kappa_0 \nabla T_e\right), \tag{9}$$

where T_e is the electron temperature, here assumed to be the same as the ion temperature T_i; κ_0 is the thermal diffusion coefficient, a function of the temperature, density, and ionization of the plasma.

The multigroup radiation transport is modeled in two steps: first by angular S_N absorption from the hohlraum wall and then with a mean-free-path diffusion approximation within the capsule. The absorption is determined[39] by the opacity κ'_ν corrected for stimulated emission $\left[\kappa'_\nu = \kappa_\nu\left(1-e^{-h\nu/kT}\right)\right]$ and the incident intensity I_ν for each frequency group:

$$\frac{dI_\nu}{ds} = -\kappa'_\nu I_\nu, \tag{10}$$

where s measures distance in the appropriate direction. Thus, in a region of constant opacity, I_ν falls off exponentially. The internal diffusion equation, including emission and reabsorption, is

$$\frac{\partial U_\nu}{\partial t} - \nabla\cdot\left(D_\nu \nabla U_\nu\right) = c\kappa'_\nu\left(U_{\nu p} - U_\nu\right), \tag{11}$$

where U_ν is the spectral radiation energy density (ergs/cm^3/unit frequency), $U_{\nu p}$ is the Planckian radiation energy density for a given temperature, D_ν is the frequency-dependent diffusion constant $\left(= c/3\kappa'_\nu\right)$, and c is the speed of light.

BUTTERCUP uses opacity data from the Los Alamos Astrophysical Tables,[36] which include opacities for values of $h\nu/kT$ between 0.00125 and 30000. For the small number of points outside this regime, the data are interpolated between the cold opacity and the closest-known tabular opacity. As shown in Fig. 82.52(a), the peak x-ray power absorption during the laser pulse occurs in the shell near the steepest density

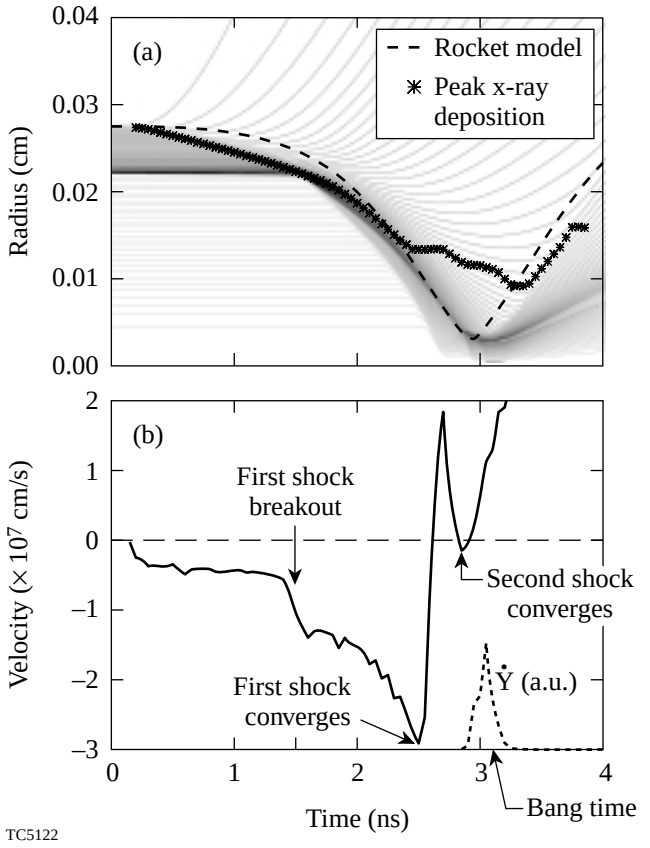

Figure 82.52
(a) Evolution of 1-D Lagrangian interface markers during a PS22 implosion with 50 atm of DD fuel inside a standard Nova capsule. The region of peak x-ray power absorption closely follows the steepest density gradient in the ablating shell for the duration of the laser pulse. The dashed curve shows the trajectory of a thin shell predicted by the 0-D rocket model. (b) Velocity of the shock front propagating through the capsule as a function of time. The first shock breaks out from the shell into the DD fuel at 1.5 ns and converges on the origin at 2.6 ns, followed by the second shock convergence at 2.9 ns. Stagnation and bang time, the time at which the neutron production rate $\dot{Y}$ peaks, occur at $t \sim 3$ ns.

gradient, unlike direct-drive implosions where the laser energy is deposited in the plasma corona and must be transported inward toward the ablation front. Even after the laser pulse ends, the hohlraum still provides significant radiation drive, penetrating deep into the ablating shell.

Indirect-drive capsule implosions involve both radiative and shock heating in addition to the adiabatic heating and cooling of the plasma.[40] The velocity of the shock front, defined as the point of maximum artificial viscous pressure, is shown as a function of time in Fig. 82.52(b), a negative value indicating convergence inward. The first shock is driven by the ~150-eV radiation temperature produced during the foot portion of the laser pulse. When it breaks out on the inside of the plastic shell, it experiences "velocity multiplication," a general phenomenon that occurs whenever a shock wave crosses a boundary from a denser material to a lighter material. Figure 82.52(b) shows that the shock speed jumps from 6×10^6 cm/s to 1.2×10^7 cm/s around $t = 1.4$ ns. Then, as the radiation drive from the hohlraum increases near the peak of the laser pulse, the shell and fuel accelerate inward until 2.6 ns, when the first spherical shock wave converges at the origin and sends a reverse shock outward through the fuel. At 2.75 ns, this reflected shock meets the imploding plastic shell, which continues to converge until stagnation around 3.0 ns.

The point of stagnation closely corresponds to the peak core temperature and also to the time of peak neutron production, referred to as the "bang time." The density and temperature profiles of the core at bang time are shown in Fig. 82.53, plotted as functions of distance from the capsule center. The results shown are from a standard PS22 capsule implosion at t = 3.0 ns, with the DD fuel assembled in a hot, central region surrounded by the cold, dense plastic shell. The radius of the fuel–pusher interface is $R_f = 23\ \mu$m, giving a convergence ratio of $C_R \sim 10$.

BUTTERCUP calculates the neutron yield from the D(D,n)^{3}He reaction using Hively's formulas for Maxwellian distributions.[41] Since this reaction is so strongly dependent on temperature,[42] almost the entire yield occurs during a short (~200-ps) time when the fuel reaches its maximum temperature and density. Figure 82.54 shows this nuclear burn profile as a function of time for a standard PS22 implosion with a bang time of 3.0 ns. The "foot" of the neutron pulse corresponds to the second spherical shock converging at the origin, as shown in Fig. 82.52(b), which raises the average fuel temperature to 0.7 keV. This is followed by the peak compression and stagnation, when most of the neutrons are produced. After bang time, the core rapidly cools by thermal and radiative diffusion into the surrounding cold material, as well as through adiabatic expansion.

The spherical uniformity of capsule implosions is frequently assessed by comparing the experimental fusion yields to those predicted by a purely one-dimensional calculation. Usually referred to as "yield over clean" (YOC), this ratio provides an indication of how the capsule's 3-D distortion affects the neutron yield and thus the success of the implosion.[43,44] The cause of core distortion may be understood on

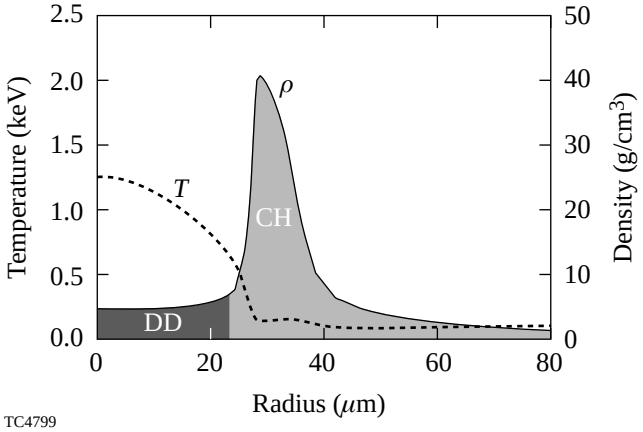

Figure 82.53
Temperature and density profiles for the DD fuel and surrounding CH ablator in the capsule core at bang time (3.0 ns), which closely corresponds to hydrodynamic stagnation. The fuel is assembled in a small, hot region of low-density gas surrounded by the colder, dense plastic pusher. The convergence ratio (R_i /R_f for the CH–DD interface) for this PS22 implosion is about 10.

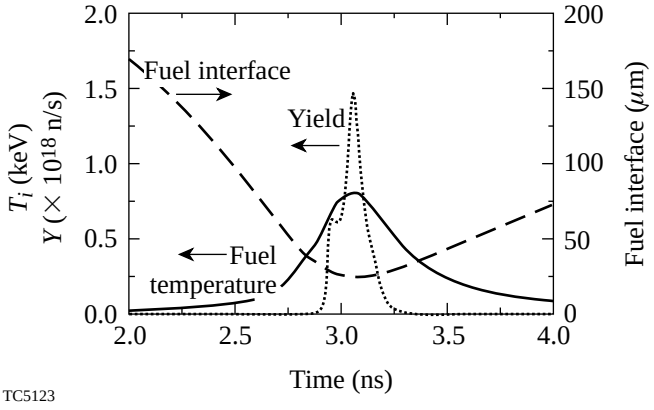

Figure 82.54
D(D,n)^{3}He fusion yield as a function of time for a standard implosion driven with PS22. Also shown are the average fuel temperature and the radius of the fuel–pusher interface. The very strong temperature dependence of the fusion rate results in almost all neutron production occurring within about 200 ps.

a very simple level. Following Wallace,[45] the implosion velocity scales as

$$V_{\text{imp}} \propto T_r^{1.5} \propto I_r^{3/8}, \tag{12}$$

so for a peak-to-valley variation in drive uniformity of 10% (typical for $\sigma_{\text{rms}} = 2.5\%$), there should be a peak-to-valley difference of about 4% for the implosion velocity. For a convergence ratio of 10, this means that at the point of maximum compression, the core distortion—as measured by a/b, the ratio of major to minor axes—will be 1.56. For a peak-to-valley difference of 2% in drive uniformity, however, the resulting core distortion will be only 1.07, or nearly round. For a high-convergence capsule with the same drive uniformity and $C_r = 30$, $a/b = 1.28$. While this model is conceptually helpful to understanding the relation between drive uniformity, convergence, and core distortion, we find that it generally overpredicts the values for a/b. This is probably because it omits the deceleration and stagnation caused by the gas pressure of the compressed fuel, as well as 3-D hydrodynamic smoothing effects that take place during the implosion, causing the relation in Eq. (12) to break down.

BUTTERCUP uses a pseudo-3D algorithm to model more accurately the effects of nonuniform drive on a capsule implosion and thus predict the core deformation as well as the neutron yield degradation. Just as the hohlraum wall is modeled in pseudo-3D by coupling a large number of 1-D calculations, the capsule is modeled by performing many 1-D spherical implosion calculations at the same time and coupling them together. As with earlier work that investigated deviations from uniform spherical implosions using a spherical-harmonic expansion,[46] this approach is best suited to implosions that are close to spherically symmetric.

To divide the capsule into multiple 1-D wedges of equal solid angle, we take advantage of the unique dodecahedral symmetry of the OMEGA target chamber. As mentioned previously, the 60 laser beams can be divided into 12 groups of five independent beams. Only these 5 beams need to be explicitly modeled in the hohlraum; the other 11 groups can be added by rotating the original group, greatly simplifying the 3-D problem. Similarly, the spherical capsule can be divided into 12 pentagonal wedges, all interchangeable through transformations in the dodecahedral rotational group. Figure 82.55 shows schematically how the sphere is divided into pentagonal wedges, only one of which is actually modeled. This wedge corresponds to one group of five laser beams and a section of the hohlraum wall including one-third of an LEH.

The pentagonal wedge of the capsule is then divided into triangular slices, each with the same solid angle and all converging at the same origin. For convenient division into symmetric wedges, 10, 30, or 90 triangular slices are typically used. All of these slices are modeled simultaneously with the spherical 1-D Lagrangian hydrodynamic model described previously. Each has a unique radiation-drive input, determined by the dynamic model of the hohlraum wall and the 3-D view-factor radiation transport. For most tetrahedral implosions, the radiation drive can be thought of as nearly uniform, with a small, time-dependent Y_{32} perturbation. This will in turn cause a nearly spherical implosion, with Y_{32} variations in the hydrodynamic variables throughout the capsule. This is very convenient since the spherical harmonic functions are solutions to the angular portion of the diffusion equation in a spherical geometry:[47]

$$\frac{\partial}{\partial t} f(r,\theta,\phi,t) = \nabla \cdot D(r) \nabla f(r,\theta,\phi,t). \tag{13}$$

For short times Δt, over which the diffusion constant $D(r)$ can be treated as static, solutions are eigenfunctions of the form

$$f(r,\theta,\phi,\Delta t) = R(r,\Delta t)\, U_r(\theta,\phi,\Delta t), \tag{14}$$

where

$$U_r(\theta,\phi,\Delta t) = \sum_{l,m} c_{lm}\, Y_{lm}(\theta,\phi) \exp\left[\frac{-l(l=1)}{r^2} D(r)\, \Delta t\right] \tag{15}$$

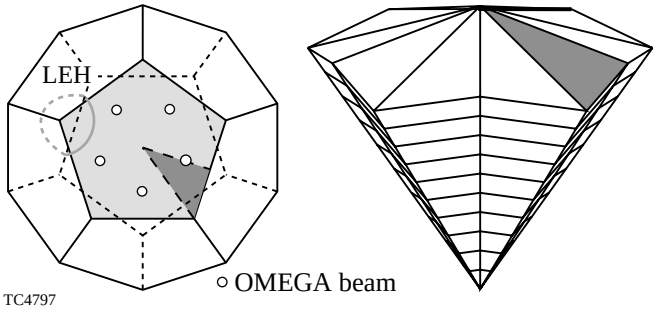

Figure 82.55
Geometry used by *BUTTERCUP* to model a 3-D capsule implosion in a tetrahedral hohlraum on OMEGA. Using the natural dodecahedral symmetry, the spherical target is divided into 12 pentagonal-shaped wedges. Each wedge contains one-third of an LEH and five independent laser beams. This pentagonal wedge of the capsule is in turn divided into multiple triangular wedges of equal solid angle. Each triangular wedge is modeled with a single 1-D hydrodynamic calculation and is then coupled to neighboring wedges.

and $R(r,\Delta t)$ is calculated with the 1-D spherical hydrodynamics of Eqs. (8)–(11). In *BUTTERCUP*, $f(r,\theta,\phi,t)$ represents either the electron temperature or the energy density of a radiation group, and Eq. (15) is used to calculate its evolution over short periods of time Δt. For tetrahedral hohlraums on OMEGA, only the $Y_{lm}(\theta,\phi)$ spherical-harmonic functions with dodecahedral symmetry will have nonzero coefficients in the sum. Just as the Y_{32} moment dominates the radiation incident on the capsule, it is also the primary term in the angular diffusion equation and typically the only term explicitly calculated.

For the angular portion of each 3-D diffusion step, the Lagrangian hydrodynamic variables are projected onto an orthogonal, Eulerian-type grid. This allows *BUTTERCUP* to solve Eq. (15) for each concentric spherical shell of material, as opposed to lateral diffusion between Lagrangian zones with the same radial index that may be located at different physical radii. After the angular diffusion calculation, the new values of the temperature are projected back onto the pseudo-3D Lagrangian grid. This alternates with the separate 1-D hydrodynamic calculations (including diffusion in the r direction) that change the values of $R(r)$ and $D(r)$ for each angular zone, which are then used as input for the next iteration of the 3-D diffusion calculation. In this way, the triangular slices of the capsule are coupled to produce a pseudo-3D implosion simulation.

Since this algorithm does not include lateral mass transport, it cannot model more-complicated 3-D phenomena like shock dispersion and hydrodynamic instabilities. Furthermore, since the converging radiation shock wave is not perfectly spherical, there can be sharp discontinuities in the hydrodynamic variables as the wavefront propagates through the material. At a given radius near the shock front, some material may be cold and uncompressed, while the material in a neighboring zone may have been heated and compressed by the shock. At this point, the assumption of a smooth Y_{32} perturbation in the temperature breaks down; however, for the tetrahedral hohlraum implosions performed on OMEGA, we find that this pseudo-3D model provides reasonable predictions for experimental observations.

Specifically, *BUTTERCUP* was used to model a set of recent experiments on the OMEGA laser that utilized tetrahedral hohlraums to achieve high-convergence implosions.[48,49] Indirect-drive capsules with convergence ratios as high as 20 to 30 have been shot previously on Nova[43] and OMEGA[50] in cylindrical geometry, typically giving YOC measurements of 5% to 25%. By using the improved drive uniformity available with tetrahedral hohlraums, it was hoped to eliminate the effects of low-order nonuniformity on the fusion-yield degradation. For the first series of high-convergence tetrahedral experiments conducted in September 1998 and reported in Refs. 48 and 49, convergence ratios of about 10 to 20 were achieved, with values of YOC similar to earlier results using cylindrical targets with the same convergence. The high-convergence capsules were designed by varying the initial DD fill pressure, with lower-pressure capsules giving higher convergence. The experiment used 550-μm-diam capsules with 55-μm CH shells filled with 50, 25, and 8 atm of DD gas, corresponding to theoretical convergence ratios of 9, 11, and 16, respectively. They were driven with all 60 OMEGA beams with pulse shape PS22, delivering 21 to 25 kJ of UV light into the hohlraum.

Figure 82.56(a) shows how the predicted neutron yields and convergence ratios depend on the DD fill pressure. Low-pressure capsules not only converge to a smaller radius, but they also reach higher core temperatures, leading to higher fusion yields even with significantly less fuel. *BUTTERCUP*'s yield predictions with 3-D effects included are also shown. As expected, for higher-convergence implosions, the predicted 3-D yields are lower with greater degradation from the 1-D prediction. Figure 82.56(b) shows a plot of YOC versus convergence ratio, including both experimental[49] and predicted YOC. A quantitative summary of the predicted results is presented in Table 82.VI.

We believe that the major mechanism for yield degradation in the pseudo-3D model is the thermal transport of energy away from the area of the fuel that is heated earliest in the implosion. As in the 1-D simulation, the fuel temperature increases significantly as the first and second shock waves converge on the origin, but with the 3-D simulation, this occurs at different times for different fuel wedges. As soon as the strongly driven regions of the capsule heat up, they transfer their thermal energy to cooler neighboring zones. Not only does this reduce the yield of the hotter zones, but it also reduces the potential yield of the cooler zones by increasing their adiabat and making an efficient implosion more difficult to achieve. The higher-convergence capsules ($C_R \sim 20$) had the higher 1-D temperature predictions ($T_i = 1650$ eV) but also experienced a greater reduction in core temperature due to 3-D effects (<70% of 1-D temperature), which is clearly reflected in the degraded yield predictions (YOC = 17%).

The preliminary experimental data of Fig. 82.56(b) seem to exhibit a more rapid falloff with convergence ratio than the *BUTTERCUP* calculations, although a larger data set is needed

to quantify this. It appears that *BUTTERCUP* can explain only some of the YOC reduction at higher C_R. The comparison suggests that, even with the best drive uniformity, hohlraum capsules are still susceptible to asymmetric shock convergence and other 3-D effects like Rayleigh–Taylor instabilities associated with physical defects caused during target manufacturing. Future experiments will hopefully help to identify the relative importance of irradiation nonuniformity and hydrodynamic instabilities.

X-Ray Postprocessor

One of the traditional ways[11,44,51–53] to assess hohlraum drive uniformity is simply to implode a capsule and look at the shape of the core: round indicates good uniformity and elliptical (in a cylindrical hohlraum) or triangular (in a tetrahedral hohlraum) indicates poor uniformity. Experimentally, this can be done with a time-resolved x-ray-framing camera or with a time-integrated pinhole camera at high magnification. A pinhole camera with filtering chosen to absorb soft x rays automatically selects the bang-time image since the x-ray film detects mainly the high-intensity emission from the hottest part of the capsule. Since the fuel is usually so much hotter than the surrounding plastic shell, the actual shape of the fuel core tends to be well highlighted. In some instances, to improve the x-ray imaging, a small amount of high-Z gas such as argon or neon is added to the fuel, emitting higher-energy x rays at the same temperature. A thin film of beryllium is typically used as a filter on either camera to block out the low-energy radiation ($\lesssim$2 keV) coming from the pusher region.

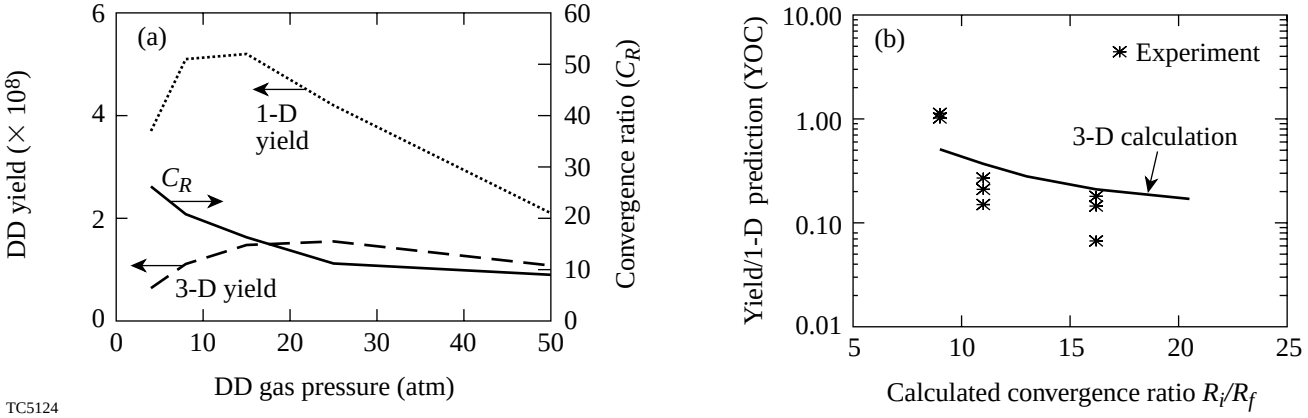

Figure 82.56
(a) Predicted 1-D and pseudo-3D yields and convergence ratio as a function of DD fuel pressure; (b) 3-D yield degradation (solid line) as a function of calculated convergence ratio, along with experimental measurements of these yields.[49] The theoretical yield degradation accounts only for effects caused by drive nonuniformity and not hydrodynamic instabilities. The experimental YOC values were based on experimental yields and 1-D *BUTTERCUP* predictions.

Table 82.VI: Summary of *BUTTERCUP* 1-D and 3-D predictions for the convergence ratio (C_R), neutron yield (Y), peak temperature (T), peak areal density (ρR), core distortion (a/b), and yield-over-clean (YOC) ratio for capsule implosions driven by a PS22 laser pulse. Predictions of C_R and peak ρR are similar for 1-D or 3-D calculations.

DD fill (atm)	C_R	Y (3-D) (10^8)	Y (1-D) (10^8)	Peak T (3-D) (eV)	Peak T (1-D) (eV)	Peak ρR (mg/cm^2)	a/b	YOC (theory)
4	20.5	0.64	3.7	1125	1650	5.8	1.20	17%
8	16.2	1.1	5.1	1150	1525	7.1	1.14	21%
15	13.0	1.5	5.2	1075	1350	8.7	1.12	28%
25	11.0	1.6	4.2	1000	1175	10.0	1.11	37%
50	9.0	1.1	2.1	825	900	12.6	1.06	51%

BUTTERCUP creates an image of the imploded core by analyzing the results of its hydrodynamic calculation with a 3-D radiation postprocessor. The first step is to reconstruct the entire capsule by copying and rotating the single pentagonal wedge modeled by *BUTTERCUP* 11 times, piecing together the 12 sections of a dodecahedron. This produces a complete three-dimensional model of the capsule, which is then rotated to give the correct orientation with respect to the x-ray camera. The complicated 3-D Lagrangian mesh can be projected onto a 2-D image by ray-tracing a grid of parallel lines through the 3-D capsule. Along the path of each ray, *BUTTERCUP* solves the multigroup radiation-transport equation,[39] which is similar to Eq. (10), except now with an additional source term I_{vp}, the blackbody intensity (erg/s/cm^2/unit frequency):

$$\frac{dI_\nu}{ds} = \kappa'_\nu\left(I_{\nu p} - I_\nu\right). \tag{16}$$

Figure 82.57 shows a schematic of this procedure, including the Be filter and the x-ray film. The complicated 3-D mesh portrayed in this figure was constructed by connecting the centers of all adjacent Lagrangian zones, where each individual zone has the shape of a triangular prism. Upon exiting the capsule, each ray on the 2-D grid will have its own x-ray intensity spectrum over the range of relevant frequency groups. This spectrum is in turn filtered by the beryllium (using cold opacities at solid density) and then integrated to give a single intensity point on the x-ray film. The resulting postprocessed image can then be directly compared with experimental data, either time averaged or time resolved.

Figure 82.58 shows the simulated x-ray image of a standard PS22 implosion at bang time. Qualitatively this image is very similar to the experimental image of Fig. 82.46(b): both appear round to within experimental error. It should be noted that the formation of this projected image provides an apparent smoothing of the actual 3-D distortion. For this image the calculated "*a*/*b* ratio," defined as the maximum-to-minimum ratio of the radii of the 50%-intensity contour, is 1.02, while the *a*/*b* ratio of the fuel–pusher interface is 1.06. The reduction from 1.06 to 1.02 could be caused by geometric projection effects or by the nonuniform temperature distribution within the fuel, with the "corners" of the tetrahedral-shaped core being colder and thus not emitting as strongly.

Conclusions

Tetrahedral hohlraums have been proposed as an alternative approach to ignition in indirect-drive ICF. Recent experiments on the OMEGA laser have confirmed the predicted radiation drive uniformity (σ_{rms} < 1%) incident on an imploding capsule. To further understand these implosions, the view-factor code *BUTTERCUP* has been expanded to include a 3-D, time-

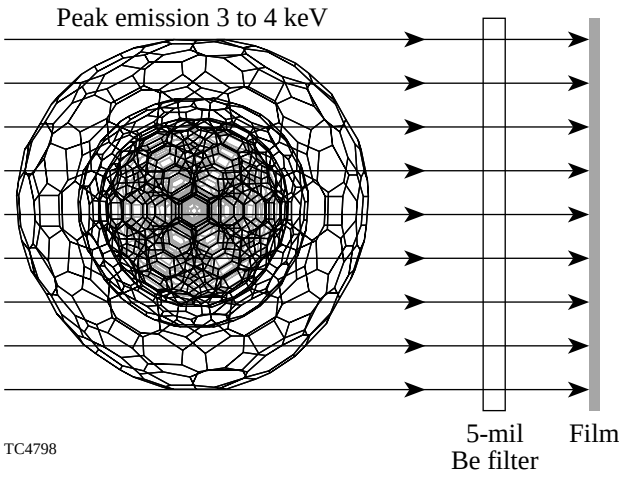

Figure 82.57
Algorithm for simulating experimental x-ray images. A multigroup x-ray postprocessor solves the radiation transport equation along rays traced through the 3-D Lagrangian grid of the capsule. A 5-mil (127-μm) beryllium filter is used to remove low-energy signals coming from the colder plastic shell, giving a view of only the hot central fuel region.

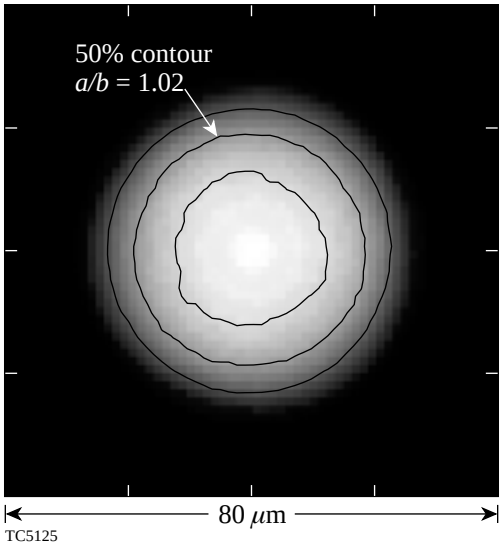

Figure 82.58
A postprocessed simulation of the x-ray image of the imploded core corresponding to Fig. 82.46(b), integrated over a 200-ps window around bang time. The *a*/*b* ratio of major to minor axes (1.02) is measured from the 50% contour of absolute x-ray intensity.

dependent treatment of the radiation diffusion into the gold wall and the radiation transport in the hohlraum. *BUTTERCUP* models the hydrodynamic implosion of the capsule by dividing it into many triangular wedges of equal solid angle, each undergoing a 1-D implosion driven by a different incident radiation source. These individual calculations are coupled together with 3-D thermal and radiation diffusion. Finally, an x-ray postprocessor is used to simulate an image of the imploded core.

The wall-diffusion model predicts a time-dependent radiation-drive temperature that agrees closely with experimental measurements from Dante. Additionally, *BUTTERCUP* is able to calculate a time-dependent albedo, which in turn can be used in a simple energy-balance equation to estimate radiation-drive temperatures. The hydrodynamic implosion calculations have provided valuable insight into the physics of indirect-drive ICF capsule implosions. Given the simplicity of the implosion model, predicted bang times as well as nuclear fusion yields are in reasonable agreement with those seen in the experiments. Pseudo-3D calculations suggest that for high-convergence implosions, one potential cause of yield degradation is the asymmetric shock convergence since the fuel is not heated as efficiently as in a perfectly spherical implosion. The 3-D x-ray postprocessor has shown that experimental images of the imploded capsule underestimate the actual level of core distortion.

These results show that, despite its relative simplicity, *BUTTERCUP* has already provided some critical new understanding of the connection between theory and experiment in hohlraum implosions. Finally, the pseudo-3D methods described here will likely be useful for developing and testing the more-sophisticated, fully three-dimensional codes that are needed to provide detailed modeling of ignition hohlraums on the NIF.

ACKNOWLEDGMENT

The authors gratefully acknowledge many valuable discussions with Dr. S. M. Pollaine and Dr. J. M. Wallace and with the many scientists who have come to LLE to participate in tetrahedral hohlraum experiments. Dr. N. D. Delamater is also thanked for providing the experimental images of Fig. 82.46. This work was supported by the U.S. Department of Energy Office of Inertial Confinement Fusion under Cooperative Agreement No. DE-FC03-92SF19460, the University of Rochester, and New York State Energy Research and Development Authority. The support of DOE does not constitute an endorsement by DOE of the views expressed in this article.

REFERENCES

1. J. Nuckolls *et al.*, Nature **239**, 139 (1972).
2. J. D. Lindl, Phys. Plasmas **2**, 3933 (1995).
3. S. E. Bodner, Comments Plasma Phys. Control. Fusion **16**, 351 (1995).
4. S. W. Haan *et al.*, Phys. Plasmas **2**, 2480 (1995).
5. M. M. Marinak *et al.*, Phys. Plasmas **3**, 2070 (1996).
6. T. R. Dittrich *et al.*, Phys. Plasmas **5**, 3708 (1998).
7. K. A. Brueckner and S. Jorna, Rev. Mod. Phys. **46**, 325 (1974).
8. D. W. Phillion and S. M. Pollaine, Phys. Plasma **1**, 2963 (1994).
9. J. D. Schnittman and R. S. Craxton, Phys. Plasmas **3**, 3786 (1996). See also Laboratory for Laser Energetics LLE Review **68**, 163, NTIS document No. DOE/SF/19460-139 (1996). Copies may be obtained from the National Technical Information Service, Springfield, VA 22161.
10. T. R. Boehly, D. L. Brown, R. S. Craxton, R. L. Keck, J. P. Knauer, J. H. Kelly, T. J. Kessler, S. A. Kumpan, S. J. Loucks, S. A. Letzring, F. J. Marshall, R. L. McCrory, S. F. B. Morse, W. Seka, J. M. Soures, and C. P. Verdon, Opt. Commun. **133**, 495 (1997).
11. J. M. Wallace, T. J. Murphy, N. D. Delamater, K. A. Klare, J. A. Oertel, G. R. Magelssen, E. L. Lindman, A. A. Hauer, P. Gobby, J. D. Schnittman, R. S. Craxton, W. Seka, R. Kremens, D. K. Bradley, S. M. Pollaine, R. E. Turner, O. L. Landen, D. Drake, and J. J. MacFarlane, Phys. Rev. Lett. **82**, 3807 (1999).
12. H. Honda *et al.*, Plasma Phys. Control. Fusion **40**, 1097 (1998).
13. S. M. Pollaine and D. Eimerl, Nucl. Fusion **38**, 1523 (1998).
14. J. A. Harte *et al.*, *ICF Quarterly Report: Special Issue: Computational Advances in ICF*, **6**, 150, Lawrence Livermore National Laboratory, Livermore, CA, UCRL-LR-105821-96-4 (1996).
15. R. L. Kauffman *et al.*, Phys. Rev. Lett. **73**, 2320 (1994).
16. M. D. Rosen, Phys. Plasmas **3**, 1803 (1996).
17. S. H. Glenzer *et al.*, Phys. Rev. Lett. **80**, 2845 (1998).
18. L. J. Suter *et al.*, Phys. Plasmas **3**, 2057 (1996).
19. T. Mochizuki, S. Sakabe, and C. Yamanaka, Jpn. J. Appl. Phys., Part 2, **22**, L124 (1983).
20. A. Caruso and C. Strangio, Jpn. J. Appl. Phys., Part 1, **30**, 1095 (1991).
21. M. Murakami and J. Meyer-ter-Vehn, Nucl. Fusion **31**, 1333 (1991).
22. M. Murakami, Nucl. Fusion **32**, 1715 (1992).

23. K. H. Kang *et al.*, Nucl. Fusion **33**, 17 (1993).

24. P. Amendt *et al.*, Phys. Rev. Lett. **77**, 3815 (1996).

25. P. Amendt, T. J. Murphy, and S. P. Hatchett, Phys. Plasmas **3**, 4166 (1996).

26. The significant contributions of K. A. Klare and D. Drake to the design are acknowledged.

27. G. D. Tsakiris, Phys. Fluids B **4**, 992 (1992).

28. C. Stöckl and G. D. Tsakiris, Phys. Rev. Lett. **70**, 943 (1993).

29. See National Technical Information Service Document No. DE96000344 [M. D. Rosen, Lawrence Livermore National Laboratory, Livermore, CA, UCRL-JC-121585 (1995)]. Copies may be obtained from the National Technical Information Service, Springfield, VA 22161.

30. M. D. Rosen, Phys. Plasmas **6**, 1690 (1999).

31. R. E. Marshak, Phys. Fluids **1**, 24 (1958).

32. R. Sigel *et al.*, Phys. Fluids B **2**, 199 (1990).

33. H. N. Kornblum, R. L. Kauffman, and J. A. Smith, Rev. Sci. Instrum. **57**, 2179 (1986).

34. C. Decker, R. E. Turner, O. L. Landen, L. J. Suter, H. N. Kornblum, B. A. Hammel, T. J. Murphy, J. Wallace, N. D. Delamater, P. Gobby, A. A. Hauer, G. R. Magelssen, J. A. Oertel, J. Knauer, F. J. Marshall, D. Bradley, W. Seka, and J. M. Soures, Phys. Rev. Lett. **79**, 1491 (1997).

35. R. S. Craxton, J. D. Schnittman, and S. M. Pollaine, Bull. Am. Phys. Soc. **41**, 1421 (1996).

36. See National Technical Information Service Document No. LA-6760-M/XAB [W. F. Huebner *et al.*, Los Alamos National Laboratory, Report LA-6760-M (1977)]. Copies may be obtained from the National Technical Information Service, Springfield, VA 22161.

37. R. L. Bowers and J. R. Wilson, *Numerical Modeling in Applied Physics and Astrophysics* (Jones and Bartlett, Boston, 1991).

38. See National Technical Information Service Document No. LA-7130/XAB [B. I. Bennett *et al.*, Los Alamos National Laboratory, Report LA-7130 (1978)]. Copies may be obtained from the National Technical Information Service, Springfield, VA 22161.

39. Ya. B. Zel'dovich and Yu. P. Raizer, in *Physics of Shock Waves and High-Temperature Hydrodynamic Phenomena*, edited by W. D. Hayes and R. F. Probstein (Academic Press, New York, 1966).

40. T. R. Dittrich *et al.*, Phys. Plasmas **6**, 2164 (1999).

41. L. M. Hively, Nucl. Fusion **17**, 873 (1977).

42. B. N. Kozlov, At. Energ. **12**, 247 (1962).

43. M. D. Cable *et al.*, Phys. Rev. Lett. **73**, 2316 (1994).

44. T. J. Murphy, J. M. Wallace, N. D. Delamater, C. W. Barnes, P. Gobby, A. A. Hauer, E. L. Lindman, G. Magelssen, J. B. Moore, J. A. Oertel, R. Watt, O. L. Landen, P. Amendt, M. Cable, C. Decker, B. A. Hammel, J. A. Koch, L. J. Suter, R. E. Turner, R. J. Wallace, F. J. Marshall, D. Bradley, R. S. Craxton, R. Keck, J. P. Knauer, R. Kremens, and J. D. Schnittman, Phys. Plasmas **5**, 1960 (1998).

45. J. M. Wallace, K. A. Klare, T. J. Murphy, N. D. Delamater, E. L. Lindman, G. R. Magelssen, A. A. Hauer, S. M. Pollaine, R. E. Turner, R. S. Craxton, and J. D. Schnittman, Bull. Am. Phys. Soc. **42**, 2009 (1997).

46. R. L. McCrory, R. L. Morse, and K. A. Taggart, Nucl. Sci. Eng. **64**, 163 (1977).

47. G. B. Arfken, *Mathematical Methods for Physicists*, 3rd ed. (Academic Press, Orlando, 1985), p. 450.

48. J. M. Wallace, G. R. Bennett, T. J. Murphy, J. A. Oertel, P. Gobby, A. A. Hauer, W. S. Varnum, D. C. Wilson, R. S. Craxton, J. D. Schnittman, and S. M. Pollaine, Bull. Am. Phys. Soc. **43**, 1737 (1998); J. D. Schnittman, R. S. Craxton, S. M. Pollaine, R. E. Turner, T. J. Murphy, N. D. Delamater, J. A. Oertel, A. A. Hauer, and K. A. Klare, Bull. Am. Phys. Soc. **43**, 1737 (1998).

49. G. R. Bennett, J. M. Wallace, T. J. Murphy, A. A. Hauer, J. A. Oertel, D. C. Wilson, P. L. Gobby, N. D. Delamater, R. E. Chrien, R. S. Craxton, and J. D. Schnittman, Bull. Am. Phys. Soc. **43**, 1737 (1998).

50. P. Amendt, R. E. Turner, O. Landen, S. G. Glendinning, D. Kalantar, M. Cable, J. Colvin, C. Decker, L. Suter, R. Wallace, D. Bradley, S. Morse, G. Pien, W. Seka, and J. M. Soures, Bull. Am. Phys. Soc. **43**, 1739 (1998).

51. A. Hauer *et al.*, Rev. Sci. Instrum. **66**, 672 (1995).

52. A. A. Hauer *et al.*, Phys. Plasmas **2**, 2488 (1995).

53. T. J. Murphy, J. M. Wallace, N. D. Delamater, C. W. Barnes, P. Gobby, A. A. Hauer, E. Lindman, G. Magelssen, J. B. Moore, J. A. Oertel, R. Watt, O. L. Landen, P. Amendt, M. Cable, C. Decker, B. A. Hammel, J. A. Koch, L. J. Suter, R. E. Turner, R. J. Wallace, F. J. Marshall, D. Bradley, R. S. Craxton, R. Keck, J. P. Knauer, R. Kremens, and J. D. Schnittman, Phys. Rev. Lett. **81**, 108 (1998).

Nanoindentation Hardness of Particles Used in Magnetorheological Finishing (MRF)

Introduction

Classical finishing processes of optics employ precisely shaped, viscoelastic pitch or polyurethane foam–faced tools to transfer pressure and velocity through an abrasive slurry to the workpiece. Material is removed by chemical and mechanical interactions among the abrasive (typically micron- to submicron-size cerium oxide or aluminum oxide), the carrier fluid (water), and the workpiece. Magnetorheological finishing (MRF)—a new method of polishing optics—is being studied at the Center for Optics Manufacturing (COM) at the University of Rochester. This method utilizes a suspension consisting of magnetic particles [typically carbonyl iron (CI)], nonmagnetic abrasive particles, water, and stabilizing agents. Figure 82.59 shows an MR polishing machine. Rotation of the bottom wheel takes the fluid from the delivery nozzle and drives it underneath the part, where there is a strong magnetic field. Under the influence of the magnetic field, the fluid behaves like a "plastic" fluid; it is the shear stress caused by the hydrodynamic flow between the part and the rotating wheel that removes the material.[1]

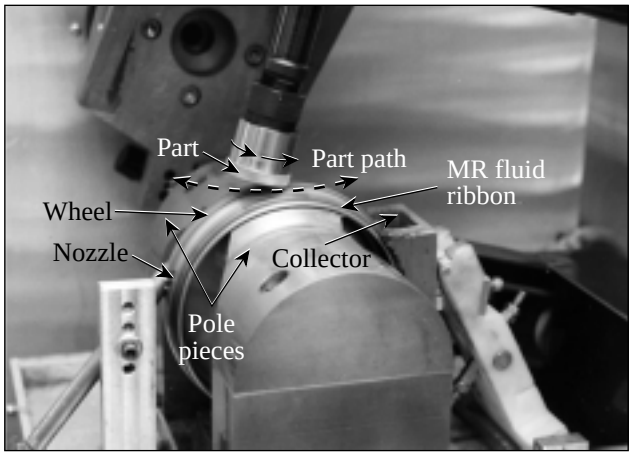

G4973

Figure 82.59
Photograph of the MRF polishing process. The fluid emerges from the nozzle on the left and is carried to the right into the polishing zone under the part surface by the rotation of the wheel. The pole pieces are part of the electromagnet that provides the magnetic field that stiffens the fluid into a ribbon.

Figure 82.60 shows an example of microroughness on the surface of an initially pitch-polished fused-silica part processed without part rotation and with a nonaqueous MR fluid. With all chemistry eliminated, what remains are parallel grooves approximately 16-nm peak-to-valley and 1-nm rms,[2] caused by microscratching along the direction of flow. The water in aqueous MR fluids "turns on" chemistry, and removal rates increase substantially. Removal rates increase further in aqueous-based MR fluids containing nonmagnetic polishing abrasives (e.g., Al_2O_3, CeO_2, and nanodiamonds).[3] The features of the grooves look similar to the ones shown in Fig. 82.60. It is not known whether it is the abrasive action of the magnetic or nonmagnetic particles, or a chemical contribution from water and the presence of the nonmagnetic particles that plays the most important role in enhancing removal. Nanohardness tests described here allow us to begin to understand more fully the role of the various magnetic and nonmagnetic abrasives in the removal process.

Many authors (see Ref. 4 for example) describe a hydrated layer at the glass surface caused by the chemistry of the aqueous slurry. This soft hydrated layer affects polishing since it is easier to remove than the bulk material. An abrasive that is softer than the bulk material could conceivably remove material from a hydrated layer, but a harder particle (under the same load) could penetrate farther into the layer and thus remove more material. Kaller[5] discusses both the importance of finding the unknown hardness of abrasive particles and how the abrasive should actually be softer than the material being polished. An interesting experiment would be to compare removal characteristics of particles of different hardness in the same chemical environments. The variation in groove depth as a function of particle hardness would estimate the extent of the hydrated layer. For this experiment to be of the greatest utility the actual hardness of the particle must be known. The work described above is in progress.[6] To support this work, particle-nanohardness measurements are reported here and compared to some materials important to optics.

The hardness of a material is typically measured by pushing a hard material into a softer one and measuring the area of residual deformation left on the softer material. The hardness is the indenting load divided by the area of the residual deformation. In the past, Steinitz[7] determined particle microhardness through microindentation (material hardness found through microindentation will be referred to as microhardness, and that found through nanoindentation will be referred to as nanohardness). His figures show that the particle areas being indented were of the order of 100 μm in size and that the size of an indent was about 20 μm. Loads from 25 to 300 g (about 0.25 to 3 N) were used. The author points out that relatively large loads were needed for these indents so that the diagonals could be accurately measured for the microhardness calculation. This limited Steinitz to relatively large particles. The particles that we are concerned with have a median diameter of about 5 μm, although it is possible to screen out ≈ 20-μm particles for study. The indent should therefore be significantly smaller than 20 μm for reasons that will be discussed later. These particles are still too small to be tested with a traditional microhardness tester. Small particles could be sintered or pressed together for ease of indentation, but heating or stressing the particles could change their mechanical properties.[7] Using the nanoindentation techniques described below, we are able to make smaller indents on much smaller particles than was done previously with microindentation, without altering the mechanical properties of the particles.

Nanoindenter

Hardness is measured with a commercially available nanoindenter.[8] The indenter is a Berkovich three-sided, pyramidal diamond that accommodates maximum loads up to about 700 mN. Our experiments used maximum loads of 1 and 5 mN. This instrument applies a load by magnetic coil; the displacement of the indenter is continuously measured with a capacitance gauge. The displacement can be measured to within ±0.04 nm and the output voltage from the loading operation to within 4 μV. The loads and displacements for our experiments are such that the measurement error is much less than 1%.

The nanoindenter's computer-automated system allows the user to choose the indentation experiment (loading rate, maximum load, drift correction, etc.) and location of the indent, leaving the instrument unattended as the experiment is performed. A typical experiment takes only about 15 min, but the time depends on the environment where the nanoindenter is located and the number of indents made. The first part of a test requires that the instrument settle to a user-specified critical drift rate. The indenter is kept in an insulated cabinet on a vibration isolation table. If the room containing the instrument has significant vibrations or temperature gradients, it may take some time for the drift rate to settle to the user-selected value. Our tests utilize the default critical drift rate of 0.05 nm/s.

Both nanohardness and the elastic modulus can be calculated via the load-displacement curves.[9] Since the load-displacement curve is of greatest interest, it is important that the particle be constrained from displacing due to the indenter loading from the top. That is, the measured displacement must be due to the motion of the indenter into the particle surface, and not due to the motion of the particle. For this reason,

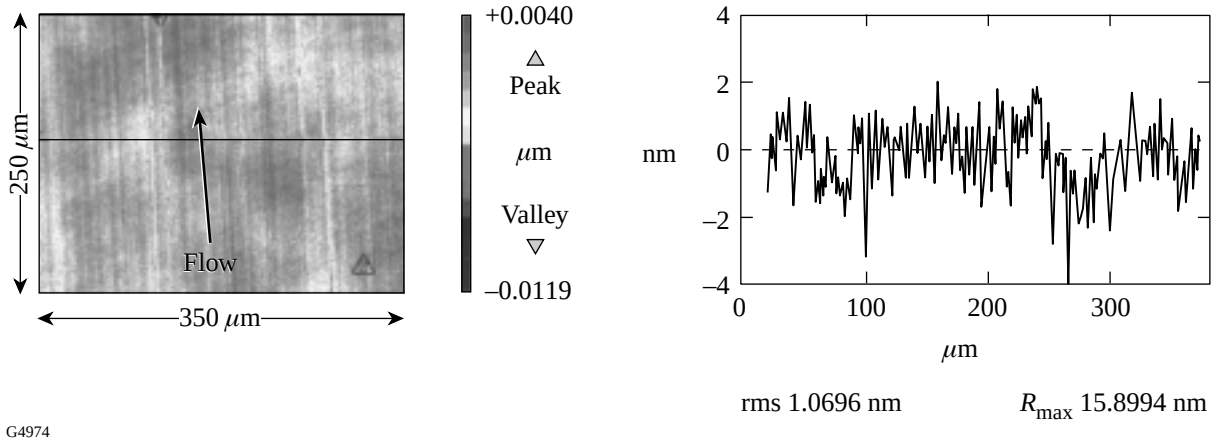

Figure 82.60
Microroughness on the surface of a fused-silica part after MRF without rotation. The MR fluid contains CI and nanodiamonds in a nonaqueous carrier fluid. The grooves are parallel to flow and are a result of particle/glass interaction.

magnetic particles are fixed rigidly to a glass substrate by embedding them in an epoxy matrix, and nonmagnetic particles are cast in a polymer substrate (phenol-formaldehyde or Bakelite). There is evidence in the literature that the substrate affects the measured properties of thin films.[10,11] Initial screening experiments before this study suggested that this problem influenced small-particle indentation as well. Special sample preparation techniques described below were devised to avoid this effect.

One of the strengths of the nanoindenter is that it allows precise positioning of indents. This ability allows us to search for and indent individual particles. Indents can be positioned to within 0.4 μm, but this accuracy is reduced by thermal drift and the accumulation of small errors.[8] Frequent system calibration allows for the precision necessary to indent 5-μm particles, but there are fewer failed tests (i.e., no particles indented) if the indented surface is approximately 20 μm in diameter. The larger particle size reduces the importance of any positioning error caused by the nanoindenter translation stages. For this reason, the particles are suspended in methanol and passed through a sieve[12] to separate out larger particles for testing. A second option, if the particles are relatively small, is to create an array of indents near a particle. For example, a line of indents can be defined so that, while some of the indents will be into the epoxy, the rest will be on the particle. Results reported here are from experiments performed by either method.

Sample Preparation for Magnetic Particles

The magnetic particles (primarily CI) are processed as illustrated in Fig. 82.61. After they are sieved, the particles are placed on a BK7[13] glass substrate, which is set on top of a rare earth permanent magnet.[14] The roughness of the substrate is about 1 μm rms or smoother, and the substrate is flat to within about 1 to 10 μm per cm^2 of surface. These specifications are not critical, but height variations in the substrate surface of the order of tens of microns per centimeter are avoided. Next, a two-part, room-temperature curing epoxy[15] is spread onto a polymer foil,[16] and the foil is placed over the particles, epoxy side down. A microscope slide is placed on top of the back side of the polymer foil (the foil prevents the epoxy from adhering to the slide), and finally a mild iron weight (40 g) is placed over the slide [see Fig. 82.61(a)]. Since the iron weight is attracted to the magnet, the epoxy/particle matrix is forced into a thin layer, and the microscope slide helps to create a more uniform surface on the epoxy. Figure 82.61(b) shows how the epoxy is believed to surround the CI particles to hold them in position during curing.

This fabrication procedure accomplishes two things: First, the particles are attracted downward to the magnet. This pulls the bottom particle layer toward the BK7 surface. Second, when placed in a magnetic field, the magnetic particles tend to align into chain structures.[17] This helps prevent epoxy from getting in between adjacent particles. The perceived advantage is that by having chains of particles resting against the glass substrate, we minimize the possibility of measuring a reduced hardness due to effects of a compliant substrate mentioned above.[10,11] The assembly shown in Fig. 82.61(a) is left to cure in air for 24 h. Once the epoxy has cured, the mild iron weight and microscope slide are removed from the magnet. The polymer foil is stripped away, leaving the BK7 substrate and CI/epoxy matrix. The matrix surface is ground by hand on a serrated, cast iron lap with 9 μm alumina[18] to thin the film and create flat surfaces on the particles. Grinding is performed as described by Parks *et al.*[19] so that work hardening of the particles is minimized. A load of about 35 kPa (about 5 psi)[20] is used with the iron lap rotating at 35 rpm. This step takes no more than a few minutes. The grinding step always results in some wedge being put into the surface, leaving an epoxy/CI

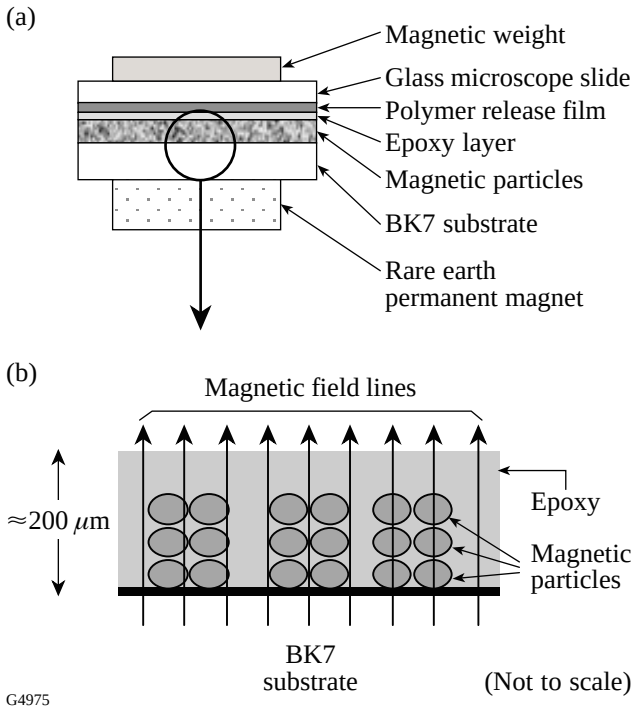

Figure 82.61
(a) Schematic diagram of the method used in sample preparation. The particles and epoxy are sandwiched between two hard, flat surfaces so that a thin layer is formed. (b) Sketch of how the particles are thought to orient in the epoxy layer shown in (a) under the influence of a magnetic field.

film that decreases in height from one side to the other (see Fig. 82.62). The grinding step is complete when the glass substrate starts to become visible. In this way, we know that there is a thin layer of the composite film where indents can be taken very near the glass substrate.

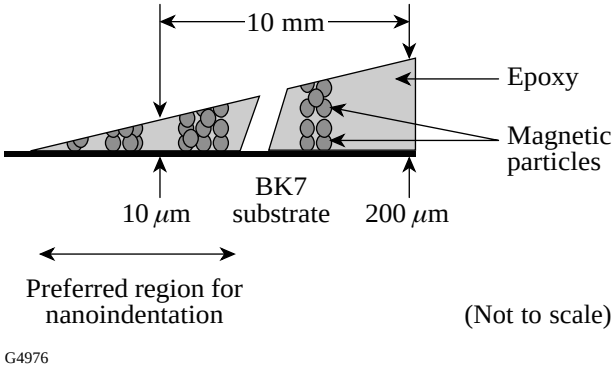

Figure 82.62
Schematic diagram of the sample after the magnet has been removed and the top layer of epoxy has been ground and polished away. The flats on the particles constitute the potential indent sites.

Samples are polished with light pressure on a cerium oxide impregnated felt lap[21] at a rotation speed of 50 rpm. This step is monitored with the help of an optical microscope.[22] The polishing phase is considered complete when few polishing grooves can be seen on the CI surfaces at 1000× magnification. This step is a manual operation that takes approximately 30 min, depending on the skill of the operator.

At the conclusion of sample preparation, the CI/epoxy film thickness varies from about 200 μm down to zero (at the glass surface) over a distance of about 10 mm as measured by mechanical profilometry.[23] Indents are placed where the film is about 25 to 50 μm thick. As shown schematically in Fig. 82.62, the goal of our sample preparation process is to create polished flats on the CI particles.

Sample Preparation for Nonmagnetic Abrasive Particles

The above technique for sample preparation is appropriate only for magnetic particles since we take advantage of the magnetic attraction of the particles to try to minimize the effect of deformation of the embedding medium. The nonmagnetic particles are treated differently. They are mixed with Bakelite pellets in a ratio of about 1 to 5. This mixture is then put into a 1.25-in.-diam cylindrical mold, placed into a press,[24] heated to 150°C, and pressed under 5000-psi pressure. It is assumed that this heat and pressure do not change the particle properties. The heat and pressure allow the Bakelite to form a network around the abrasives so that they are held in place during indentation experiments. The Bakelite sample is then ground and polished as described above until several particles are exposed. We have found that the Bakelite medium has a hardness and elastic modulus of about 0.4 GPa and 7 GPa, respectively. These values are significantly lower than those of the particles being tested, so deformation of the embedding medium is a concern (discussed below).

Validation of Tests

It is important to have a way to verify that indentations are actually being placed on an individual particle. Figures 82.63(a) and 82.63(b) show SEM[25] images of a carbonyl iron particle surface after indentation testing. The programmed maximum load was 5 mN. The test was set up to put an initial indent in the center of the particle and follow it with four more indents spaced 2 μm apart. The five indents are clearly shown in Fig. 82.63(a). Figure 82.63(b) shows a close-up view of two of the indents. The sharpness and repeatability in size of the indents are apparent. Indenter tip radius is 20–80 nm[8].

The sample thickness should be four to ten times larger than the depth of an indent.[10] Also, indents should be more than two times the size of any "stress deformation" that results from indentation. This prevents deformation due to neighboring indents from interacting.[26] Since most indents are approximately 200 nm deep, particles greater than 2 μm in size are sufficiently large for these loads. We choose relatively large particles and avoid the edges of particles so that we meet this criteria. The indents in Fig.82.63 are for illustration only. Quantitative data are obtained mostly by placing a single indent on a single particle. It should be noted, however, that the nanohardness values obtained from the indents shown in Fig. 82.63 were consistent with nanohardness values obtained from other tests performed on the same particle type.

If the particles are particularly small, it might be advantageous to make arrays of indents. In this case, care must be taken to identify valid indents from invalid ones. Figure 82.64 shows the indenter load/displacement curves of three indents from a linear array (similar to Fig. 82.63) on a single CI particle. The maximum load was 5 mN for all three indents, but the vertical displacement of the indenter was about 220 nm for indent 1, about 300 nm for indent 2, and about 550 nm for indent 3. The projected area and calculated nanohardness varied accordingly. The nanohardness was 715 kgf/mm^2 (7.01 GPa) for indent 1, 370 kgf/mm^2 (3.63 GPa) for indent 2, and 86 kgf/mm^2 (0.84 GPa) for indent 3. This wide range in the

measured nanohardness indicates that there is some error in the measurement.

The reason for the variation in the nanohardness for this single particle is evident from the three load/displacement curves in Fig. 82.64. The first indent shows typical loading and unloading behavior[9] for a single, hard material, whereas the second and third indents show a clear slope change in the loading curve (circled in Fig. 82.64). It is believed that this slope change is due to epoxy contamination around the edge of the particle. For the second and third indents, as the load is applied, the indenter first encounters an epoxy film, and the shallow slope of the loading curve is due to the fact that the epoxy is much softer than the CI. The change in slope of the loading curve can be explained by the fact that the thin material under load becomes more stiff (the slope of the curve increases) as the indenter is influenced by the underlying material. That is, we expect the slope of the loading curve to increase due to both elastic and permanent deformation as the indenter moves through the epoxy layer. Hay and Pharr[11] use a similar method to monitor the effects of a thin, hard film on a soft substrate. In their work, the slope of the loading curve becomes shallower as the soft substrate begins to flow under the hard film. As expected, the loading curve becomes steeper in our case since we have a thin film of soft material on a hard substrate. Such an interpretation is also consistent with a quantitative estimate of contact zone width based on the Sneddon solution of a rigid cone indenting an elastic half-space of a material with the properties of epoxy.[27] For these reasons indent 1 would be considered a successful indent, whereas indents 2 and 3 would not.

Krell *et al*.[28] discuss another consideration for indentation experiments. It is possible that a particle could be pushed into the embedding medium under the influence of the indenting load. By creating chains during sample preparation of magnetic particles and indenting particles near the BK7 surface, we minimize the chance of particle motion. The nonmagnetic particles are simply sitting in a relatively soft Bakelite matrix. It is conceivable that a small particle could be pushed into the matrix by the indenting load. To estimate this effect, consider

(a)

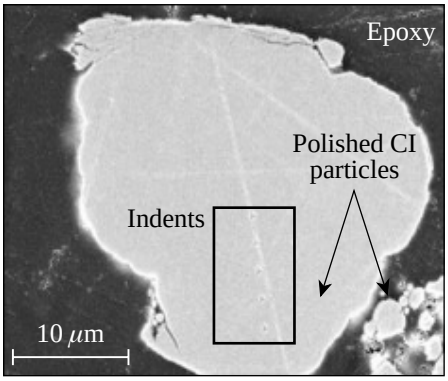

(b)

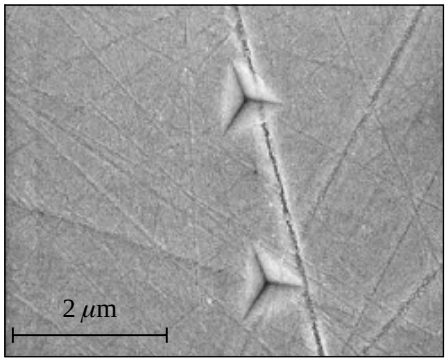

G4977

Figure 82.63
SEM of a large CI particle after a set of five indentations at 5-mN maximum load. The initial indent was placed in the middle of the particle, and the five indents were spaced 2 μm apart. This demonstrates the ability of the nanoindenter to place multiple indents precisely on a 20- to 25-μm-diam particle. Photographs like these are very difficult to obtain because of the difficulty in locating the indentation site after moving the sample from the nanoindenter to the SEM.

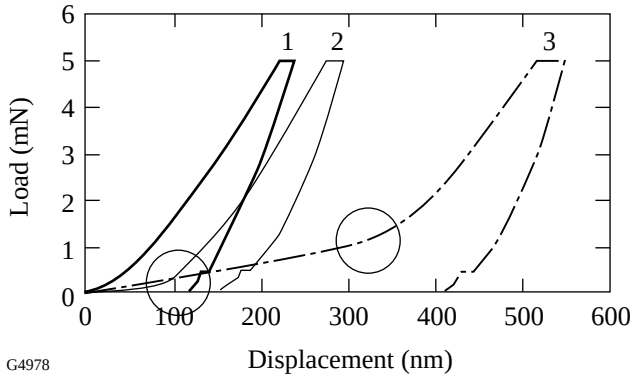

G4978

Figure 82.64
Load/displacement curves of three indents placed in a linear array on a single particle. The continuous behavior of indent 1 suggests a legitimate particle indent, whereas the slope changes in indents 2 and 3 (shown circled) suggest that there may be a region on the edge of the particle contaminated by the epoxy. Indent 2 shows a small region at the beginning of the loading, suggesting a small soft layer between the indenter and the particle. Indent 3 has a much larger region with this shallow slope, suggesting a deeper soft layer. Indents with these distinct changes in slope are not used.

the particle shown in Fig. 82.63(a). The area of this particle is approximately 30 μm × 30 μm (900×10^{-12} m^2) and subject to a 5-mN load. The approximate stress underneath the particle is the force divided by the cross-sectional area or 5.6 MPa in this case. This is two orders of magnitude below the hardness of the Bakelite or epoxy matrix. As the particle size decreases, the applied stress approaches the hardness of the matrix material. For this reason, low indenting loads are used, and particles on the large end of the size distribution are tested.

Finally, a problem that may affect both magnetic and nonmagnetic particles is the indentation-size effect (ISE). Lambropoulos *et al.*[29] and Fang[30] discuss this phenomenon in microindentation tests where the microhardness is a function of the applied load (and therefore size) of the indent. More recently Sangwal *et al.*[31] used an atomic force microscope to study ISE in nanoindentation experiments. Specifically, they report that the nanohardness decreases with an increase in indentation size and that there is a large discrepancy between hardness due to nanoindentation and microindentation of MgO.

Dahmani *et al.*[32] show that the elastic modulus and nanohardness of fused silica measured with nanoindentation agree with published results (the nanohardness was compared with a Vickers microhardness test[33]). This means that the low loads used in nanoindentation are not an immediate cause of ISE. We have also performed experiments at both 1-mN maximum load and 5-mN maximum load. A different nanohardness measured at the two different loads would be a sign that either ISE is a problem and/or the particle was moving relative to the indenter. None of our experiments showed a difference at the two loads, so these effects are not considered significant for our experiments. Sangwal *et al.*[31] perform indents at a load of 10 μN, which is two orders of magnitude below the load that we use. Also, they mention that their indentations fully recover after a sufficiently long time. Our indents do not recover. The fact that we are able to take SEM scans of indents a week after indentation tests is evidence of permanent deformation of the material. It is believed that their low loads and evidence of complete indent recovery put them in a different experimental regime.

Prior Work

Previously obtained hardness data for materials of interest to optics fabrication have typically been measured using either a Moh's test[34] or microindentation techniques on bulk or sintered samples. The Moh's scale is derived from a scratch test that uses ten minerals of increasing hardness. A substrate material is assigned a number on the Moh's scale according to the hardest standard mineral for which there is a visible scratch during a simple abrasion operation.[34] This is a qualitative test, but it gives relative hardness values for different substrate materials against known standards. Microindentation is a more quantitative experimental technique that typically uses a four-sided, pyramidal indenter (usually a Knoop or Vickers diamond) to permanently deform a material under a known load (1 to 1000 gf). The hardness of a material is the applied load divided by a measure of the area of the indent.[26] The Vickers and Knoop microhardness numbers are similar in magnitude.[35] More recently, it has been suggested that the hardness of submicrometer particles may be estimated by associating the hardness to the density of the material.[36] This correlation is unknown and is complicated by internal porosity of the particles. Results reported here for CI show the hardness–density correlation to be invalid.

This is the first work that has utilized nanoindentation to determine the hardness of small abrasive particles. Dahmani *et al.*[32] show that the Berkovich indenter measures a nanohardness similar in value to that from a Vickers microindent. Therefore we validate our results using existing microhardness data from bulk materials to compare with nanohardness results. Moh's data is used for comparison where no microhardness data exist in the literature.

1. Hard and Soft CI

The magnetic particles of interest to us are the "hard" and "soft" carbonyl iron particles that are typically used to prepare aqueous suspensions of MRF. These powders are formed from the decomposition of liquid iron pentacarbonyl. This process is explained elsewhere.[37–39] The high microhardness of the hard CI particles is attributed to the presence of carbon, oxygen, and nitrogen[37] and/or high internal stress in the material,[39] but does not appear to be clearly understood. Pfeil[37] cites a Vickers microhardness (25-g load) of about 850 kgf/mm^2 (8.33 GPa) for the hard carbonyl iron particles. Softening is achieved by annealing in a hydrogen environment to drive out the carbon, oxygen and nitrogen impurities. Boehm[40] discusses this annealing process and claims that, initially, the microhardness rises with heat treatment. Eventually it drops when the temperature is raised above 500°C. Boehm confirms Pfeil's result for the hard CI and gives a minimum microhardness of 280 kgf/mm^2 (2.75 GPa) for the softer, reduced CI. Finally, Ebenhoech[38] cites a Vickers microhardness of 900 kgf/mm^2 (8.82 GPa) for the hard CI and 100 kgf/mm^2 (1 GPa) for the soft CI at the same 25-g load. No details about the tests are given.

2. Nonmagnetic Abrasives

Six nonmagnetic particles have also been chosen for nanohardness tests since they are often used in grinding and polishing. Two types each of alumina and cerium oxide were chosen since they are of particular interest to optics fabrication. The two types of alumina differ in that one is used for grinding and one for polishing. The cerium oxide samples are both refined from a common ore, but with different heat treatments. We also tested silicon carbide and cubic zirconia particles, which were chosen because (1) they, too, are commonly used in optical fabrication and (2) the existing microhardness data in the literature helps to further verify our test results.

Microindentation hardness data for nonmagnetic abrasives exist in the literature. Krell *et al.*[28] test various alumina abrasives and discuss how the particle hardness and fracture toughness can affect the grinding efficiency. They also discuss the importance of knowing the hardness of individual abrasive particles as opposed to bulk values, especially in sintered specimens. Their experiments utilize 0.6-mm-mean-sized samples embedded in an epoxy matrix. They use Vickers indents at 10-N load. They also discuss the effect of the substrate and magnitude of the load on their measurements. Namely, if they use a higher load, the particles are pushed into the matrix. If they use a lower load, then they have difficulty measuring the size of the indent. We discussed the problems associated with using a high load, but we do not have their problem associated with low loads since our hardness is determined from the load/displacement curve. Our loads are four orders of magnitude less than theirs, which allow us to measure smaller particles in more-localized regions. Their results for different types of sintered alumina (at various densities and compositions) show Vickers hardness values of about 15 to 20 GPa. They estimate the actual microhardness values for some of the samples to be as high as 25 GPa, but porosity effects are believed to give lower values. These data are included in Table 82.VII.

Several other references, summarized in Table 82.VII, give bulk microhardness data for materials of interest. Okuyama *et al.*,[41] Nathan,[42] and Brecker *et al.*[43] give hardness data for alumina (Al_2O_3) and silicon carbide (SiC). These references suggest a Moh's hardness of about 9, and an approximate Knoop microhardness of 20±3 GPa for alumina and 27±5 GPa for SiC. Nassau[44] gives the hardness of cubic zirconia between 8.0 and 8.5 on the Moh's scale. Since alumina and SiC have a Moh's hardness of about 9, we can expect cubic zirconia to have a Knoop microhardness similar to, but slightly less than that of Al_2O_3 and SiC. There is, however, no direct relationship between the two hardness scales. No details about these microhardness measurements are given.

Some information on the hardness of cerium oxide is also available in the literature. Izumitani[4] states that cerium oxide has an approximate Moh's hardness of 6 and that most optical glasses range from 5 to 6 on the same hardness scale. Therefore we can expect the hardness of cerium oxide to be of the order of BK7 and FS glasses. While West[45] does not give a number for the hardness of cerium oxide, he does discuss how thermal treatments at elevated temperatures cause cerium oxide to become harder. Izumitani[4] also discusses the heat treatment of cerium oxide and confirms West's result. We will show a similar result with our experiments.

Table 82.VII: Summary of hardness data from the literature for various abrasive materials.

Abrasive	Mohs Hardness(Ref)	Knoop Hardness (Gpa)	Vickers Hardness (Gpa)
Alumina[a,c]	9(41), 9.4(42)	16.58–24.22(41,43)	–
Sintered alumina[b]	–	–	15–25(28)
Zirconia[c]	8.0–8.5(44)	–	–
Cerium oxide[c]	6(4)	–	–
Silicon carbide[a]	9.6(42)	22.15–31.63(41,43)	–

[a]Microhardness tests of bulk material

[b]Microhardness tests of large particles

[c]Moh's tests not well defined

Results

Tables 82.VIII to 82.X show the results from our experiments. Table 82.VIII gives the 11 magnetic particles that were tested with the nanoindenter: ten are carbonyl iron and one is a carbonyl nickel. The types and vendor plus information on the composition and nanohardness of each particle are listed. Table 82.IX lists the nonmagnetic abrasives along with their vendor, crystal structure, and nanohardness information. We also indented two optical glasses (BK7[13] and fused silica, FS[46]), one laser glass (LHG8[47]), and a soft crystal (potassium dihydrogen phosphate, KDP[48]) under identical conditions for comparison. Information on these materials is given in Table 82.X.

Figure 82.65 shows the relative nanohardness values for the different particles compared to the reference glasses. First, consider the CI particles: the hard CI's are as hard (S-1701) or harder (EW, OS 3770, OS 1225, OS 2983, OM) than fused silica. The soft, reduced forms of the CI's are significantly softer than all of the glasses and comparable in hardness to KDP. Two of the OS samples (OS 5942 and OS 9560) have intermediate nanohardness values due to a variation of processing parameters. Some of the nanohardness values measured for hard particles are harder than those cited in the literature, while others are in good agreement with the numbers cited. The soft CI's are much softer, as suggested by the literature. The nickel proved to be an extremely soft particle, in contradiction to our expectations from discussions with the manufacturer.

The differences in nanohardness among the hard CI samples can be analyzed further. The heat treatment process and the presence of impurities play a significant role in determining hardness of the particles. The reduction process softens the particles by removing the impurities in the iron. Conversely, it has been shown that the inclusion of some of these impurities often hardens iron (see, for example, Refs. 58 and 59). It is not known if the impurities are present in atomic or molecular form. It would be expected that impurities strengthen a metal as the square root or cube root of the concentration whether in atomic or molecular form.[60] Specifically, it is expected that the hardness of iron will increase as the square

Table 82.VIII: Summary of the manufacturer information and nanohardness results for the indented magnetic particles, given in rank order from hardest to softest.

ID	Material	Lot Number[Mfr.]	$b_{wt\%}$			Hardness by Nanoindentation (standard deviation) (Gpa)	
			Nitrogen	Carbon	Oxygen		
OS 1225	Carbonyl iron	1225[(49)]	[0.540	0.880	0.580][(52)]	14.4	(0.8)
OS 2983	Carbonyl iron	2983[(49)]	[0.750	0.800	0.590][(52)]	13.1	(0.6)
OM	Carbonyl iron	3999[(49)]	0.800	0.790	0.240	12.4	(1.0)
EW	Carbonyl iron	9970[(49)]	1.000	0.800	0.500	11.7	(0.8)
OS 3770	Carbonyl iron	3770[(49)]	[0.180	1.120	0.650][(52)]	10.5	(1.0)
S-1701	Carbonyl iron	6070111[(50)]	0.850	0.850	0.730	9.7	(0.5)
OS 5942	Carbonyl iron	5942[(49)]	0.060	1.170	0.320	7.3	(1.0)
OS 9560	Carbonyl iron	9560[(49)]	1.180	0.970	0.200	4.9	(1.0)
CM	[a]Carbonyl iron	7829[(49)]	[<0.010	0.009	0.170][(52)]	2.4	(0.5)
R-1521	[a]Carbonyl iron	8052131[(50)]	0.024	0.033	0.240	2.2	(1.0)
Nickel	Carbonyl nickel	101397[(51)]				1.7	(0.6)

[a]Reduced form of particle
[b]Amount of residual nitrogen, oxygen, and carbon in the carbonyl icons is in weight percent, usually per certificate of analysis from the manufacturer.

root or cube root of the concentration of carbon, nitrogen, and oxygen (in this order for the hardening effect).[61] Using the amounts of residual carbon and nitrogen provided by the vendor, nanohardness values are plotted as a function of the total amount of carbon and nitrogen in Fig. 82.66. The OS samples show a relatively large variation in nanohardness; therefore, data for all OS samples have been averaged into a single data point with error bars representing a standard deviation. After discussions with the company, we hypothesize that variations in their internal processing methods, such as annealing, were responsible for this variation in the nanohardness data. The data have been fit with a simple power law curve on a log-log scale, and the equation and correlation coefficient are shown with the plot. Notice that the data fit (correlation better than 0.94) a power law of about 0.38. While the variation due to the OS samples is somewhat large, this trend in the nanohardness as a function of impurity content is in the expected range.

The data for the polishing abrasives reveal some interesting features. The nanohardness values of the #30 grinding alumina, silicon carbide, cubic zirconia, and cerium oxide samples agree with microhardness and Moh's hardness values reported for bulk materials (compare Tables 82.VII and 82.IX), validating our results. The 1-μm alumina has a significantly lower nanohardness than the grinding alumina—a surprising result that can be attributed to proprietary manufacturing methods.[62]

We report for the first time on nanohardness data for cerium oxide abrasives. The two cerium oxides, SRS 372 and SRS 373, differed only in their heat treatments. Specifically, SRS 372 had a higher thermal treatment than did SRS 373.[63] This resulted in SRS 372 having about a 50% higher nanohardness than SRS 373, which agrees with descriptions of heat-treated cerium oxide given by Izumitani[4] and West.[45]

Table 82.IX: Summary of the manufacturer information and nanohardness results for the indented nonmagnetic abrasives, given in rank order from hardest to softest.

ID	Material	Lot Number[Mfr.]	Crystal Structure	Hardness by Nanoindentation (standard deviation) (Gpa)	
SiC	Silicon carbide	[a]N/A(53)	Hexagonal	31.8	(8.0)
#30 Al_2O_3	Grinding alumina	C9043(54)	Hexagonal	29.8	(7.0)
CZ	Cubic zirconia	1502792(55)	Cubic	24.1	(5.0)
1 μm Al_2O_3	Polishing alumina	C602(56)	Not reported	10.0	(4.0)
SRS 372[b]	Cerium oxide	SDH-13-1(57)	Not reported	7.5	(2.0)
SRS 373[c]	Cerium oxide	SDH-13-2(57)	Not reported	5.0	(1.3)

[a]Lot number is not available. Abrasives were received in 8/94.
[b]High thermal treatment
[c]Low thermal treatment

Table 82.X: Summary of the manufacturer information and nanohardness results for the indented bulk optical materials given in rank order from hardest to softest.

ID	Lot Number[Mfr.]	Hardness by Nanoindentation (standard deviation) (Gpa)	
FS	7940(46)	9.8	(0.1)
BK7	N/A(13)	7.7	(0.1)
LHG8	N/A(47)	5.3	(0.1)
KDP	N/A(48)	1.5	(0.4)

The error bars for the magnetic abrasives and optical materials are considerably smaller than those of the polishing abrasives. This is attributed to the more uniform structure of CI and the optical materials versus the multiphase nature and heterogeneity of the polishing abrasives tested. Krell *et al.*[28] also had relatively large errors in their measurements, which they attributed to microstructure. We do not have control of the crystal orientation of the abrasives that we are indenting, which will also affect the measured nanohardness.

Summary

A technique for nanoindentation of small, magnetic and nonmagnetic abrasive particles has been described. Most results are consistent with what has been previously reported, but some results are new. While Krell *et al.*[28] show microhardness differences in various grinding aluminas, it is interesting to see the large differences in nanohardness values of the actual commercial products used in grinding and polishing.

The literature contains only Moh's hardness data for cerium oxide abrasives. We report here, for the first time, an actual nanohardness value for individual cerium oxide abrasives. The tests and procedures described here allow for the characterization of the mechanical properties of small particles that is not possible through microindentation without sintering or using samples much larger than those normally used. This allows for the study of abrasives in forms actually used in polishing, so that full characterization of the mechanical properties of polishing materials is now possible. Furthermore, removal experiments using various combinations of magnetic and nonmagnetic abrasive particles and slurry fluid chemistries should give valuable information in the future regarding the removal mechanisms for MRF.

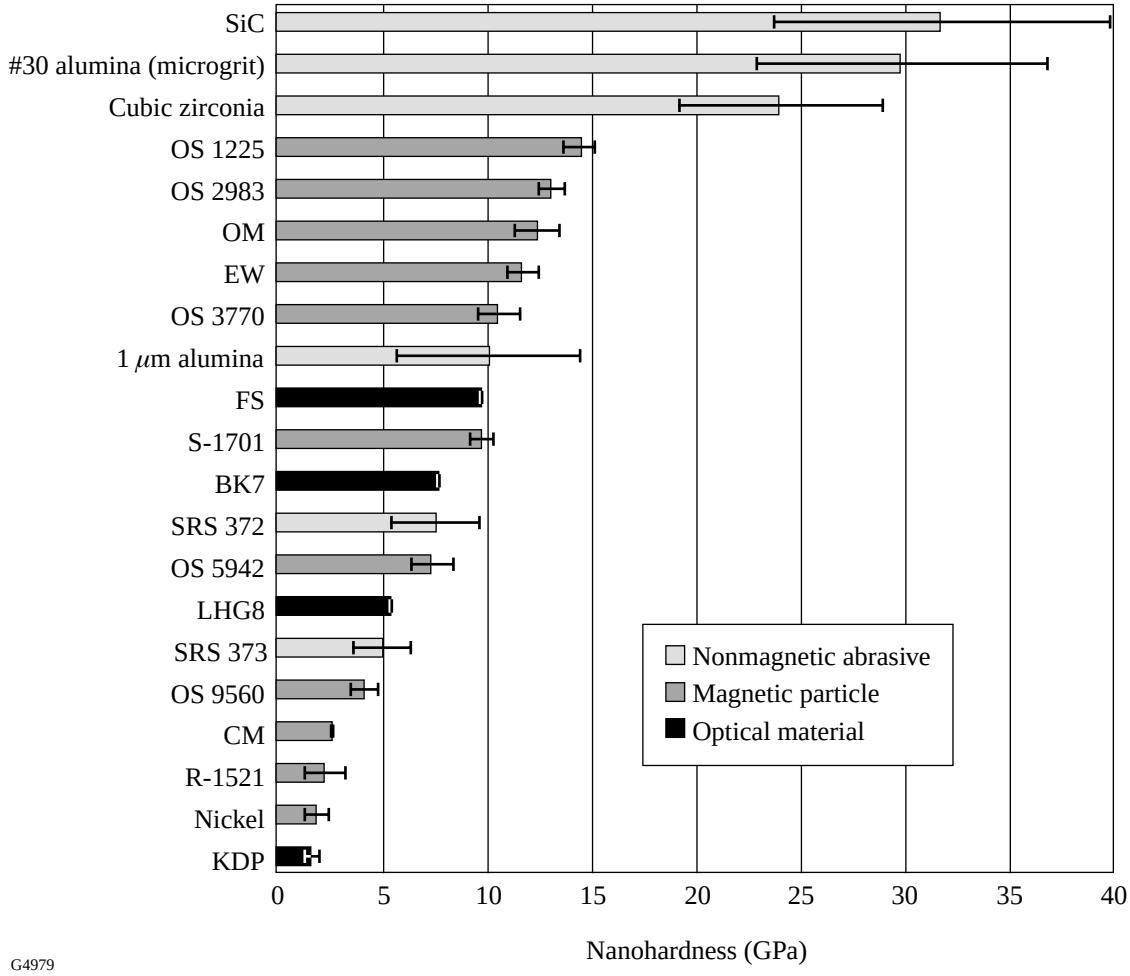

Figure 82.65
The relative nanohardness values of the particles, glasses, and crystal that have been indented (in air) at 5-mN load on the nanoindenter.

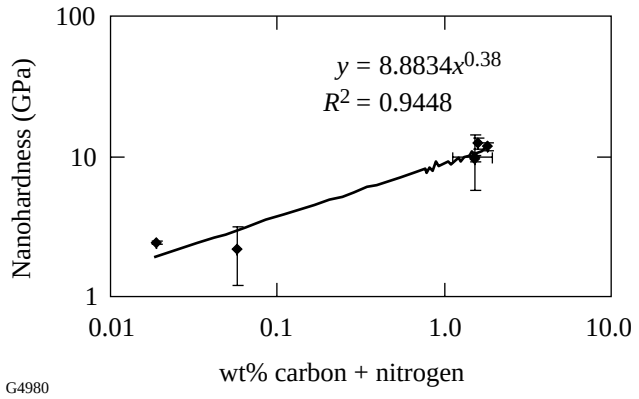

Figure 82.66
Particle nanohardness as a function of the sum of carbon and nitrogen present. An expected power law dependence is seen. Similar results are achieved if only nitrogen or carbon is analyzed.

ACKNOWLEDGMENT

The authors would like to thank Professor John C. Lambropoulos of the Mechanical Engineering Department of the University of Rochester for his assistance. We also acknowledge the contributions of Cindy Barnett and Becky Coppens of the COM and Gail Schlosser and Lisa Cliff of LLE for assistance in preparation of this article; Alexander Maltsev of the LLE and Dennis Van Gee of the COM for assistance in sample preparation, Professor Roger Gans of the Mechanical Engineering Department, Professor James Li of the Materials Science Program at the University of Rochester and Bob Nesin of Micro Abrasives for helpful discussions. Brian McIntyre of the Optics Department at the University of Rochester is acknowledged for his work on the SEM. We would also like to thank Jennifer Murphy, Susan Brandt, Rosa Lee, Caleb Farny, Leslie Gregg, and Dr. Steven Arrasmith for their participation in the project. Dr. Al Friederang of BASF Corporation and Ms. Dana Zagari of Ferro Corporation are thanked for providing many different samples. Support for this work was provided in part by a Department of Education graduate fellowship (GAANN), QED Technologies, LLC, Byelocorp Scientific, Inc, U.S. Army Materiel Command, DARPA (Defense Advanced Research Project Agency), and the National Science Foundation (Grant CMS-9601585).

REFERENCES

1. D. Golini, S. Jacobs, W. Kordonski, and P. Dumas, in *Advanced Materials for Optics and Precision Structures*, edited by M. A. Ealey, R. A. Paquin, and T. B. Parsonage, Critical Reviews of Optical Science and Technology (SPIE, Bellingham, WA, 1997), Vol. CR67, pp. 251–274.

2. Zygo New View™ 100 White-Light Interferometer, 20× Mirau objective, Zygo Corporation, Middlefield, CT 06455.

3. S. D. Jacobs, W. Kordonski, I. V. Prokhorov, D. Golini, G. R. Gorodkin, and T. D. Strafford, U.S. Patent No. 5,795,212 (18 August 1998).

4. T. S. Izumitani, *Optical Glass*, American Institute of Physics Translation Series (American Institute of Physics, New York, 1986), pp. 92–98.

5. A. Kaller, Glass Sci. Technol. **71**, 174 (1998).

6. A. B. Shorey, L. L. Gregg, H. J. Romanofsky, S. R. Arrasmith, I. Kozhinova, J. Hubregsen, and S. D. Jacobs, in *Optical Manufacturing and Testing III*, edited by H. Stahl (SPIE, Bellingham, WA, 1999), Vol. 3782, pp. 101–111.

7. R. Steinitz, Metals & Alloys **17**, 1183 (1943).

8. Nano IIs Nanoindentor and accompanying operating instructions, Version 2.2, p. 7 (1996), Nano Instruments, Oak Ridge, TN 37830.

9. W. C. Oliver and G. M. Pharr, J. Mater. Res. **7**, 1564 (1992).

10. G. M. Pharr and W. C. Oliver, Mater. Res. Bull. **17**, 28 (1992).

11. J. C. Hay and G. M. Pharr, in *Thin-Films—Stresses and Mechanical Properties VII*, edited by R. C. Cammarata *et al.*, Mat. Res. Soc. Symp. Proc. Vol. 505 (Materials Research Society, Warrendale, PA, 1998), pp. 65–70.

12. 16- to 18-μm wire mesh sieve, Newark Wire Cloth Company, Newark, NJ 07104.

13. 2.54 × 1.27 × 0.64-cm samples made from material provided by Schott Glass Technologies, Duryea, PA 18642.

14. Samarium-Cobalt magnets (2.54 × 2.54 × 1.08 cm) purchased from the McMaster-Carr Supply Company, Elmhurst, IL 60126. They supply a field intensity of about 2.5 kG in a direction perpendicular to the surface of the magnet.

15. 2-Ton® Clear Epoxy from ITW Devcon, Danvers, MA 01923.

16. Kapton® is a polyamide film provided by DuPont®. We used type HV300. Teflon® films have also been used.

17. Y. Grasselli, G. Bossis, and E. Lemaire, Prog. Colloid Polym. Sci. **93**, 175 (1993).

18. Microgrit Micro Abrasives Corporation, Westfield, MA 01086-0669.

19. R. E. Parks, R. E. Sumner, and J. T. Appels, Opt. Eng. **16**, 332 (1977).

20. Load was measured by the I-Scan pressure measurement system from Tekscan, Inc., Boston, MA 02127. We used a 5051 pressure film with a maximum allowable load of 345 kPa (50 psi).

21. J. H. Rhodes, # FJ0202, Universal Photonics, Inc., Hicksville, NY 11801-1014.

22. Olympus VANOX-T AH-2 optical microscope, No. 501008, Olympus Optical Co. Ltd., Tokyo, Japan.

23. Measurements were made using the Form Talysurf® mechanical profilometer, Taylor Hobson Ltd., Leicester, LE4 9JQ, UK. The device has a 60-mm stylus arm length and a 2-μm-radius tip.

24. Buehler Ltd., Lake Bluff, IL 60044-1699.

25. LEO 982 field emission SEM (LEO is a Zeiss-Leica company).

26. *Metals Test Methods and Analytical Procedures*, Annual Book of ASTM Standards (American Society for Testing and Materials, West Conshohocken, PA, 1999), Vol. 3.01, p. 393.

27. I. N. Sneddon, *Fourier Transforms*, 1st ed. (McGraw-Hill, New York, 1951), Sec. 52.5.

28. A. Krell, P. Blank, E. Wagner, and G. Bartels, J. Am. Ceram. Soc. **79**, 763 (1996).

29. J. C. Lambropoulos, T. Fang, P. D. Funkenbusch, S. D. Jacobs, M. J. Cumbo, and D. Golini, Appl. Opt. **35**, 4448 (1996).

30. T. Fang, "Near-Surface Mechanical Properties of Optical Materials in Deterministic Microgrinding," Ph.D. thesis, University of Rochester, 1997, Chap. 3.

31. K. Sangwal *et al.*, J. Mater. Res. **14**, 3973 (1999).

32. F. Dahmani, J. C. Lambropoulos, A. W. Schmid, S. J. Burns, and C. Pratt, J. Mater. Sci. **33**, 4677 (1998).

33. J. H. Westbrook, Phys. Chem. Glasses **1**, 32 (1960).

34. D. Tabor, Proc. Phys. Soc., Sec. B **67**, 249 (1954).

35. W. D. Callister, *Materials Science and Engineering*, 2nd ed. (Wiley, New York, 1991), pp. 131-141.

36. S. Ramarajan *et al.*, Surf. Eng. **15**, 324 (1999).

37. L. B. Pfeil, *Symposium on Powder Metallurgy*, 47, The Iron and Steel Institute, Grosvenor Gardens, London, Special Report No. 38 (1947).

38. F. L. Ebenhoech, Prog. Powder Metall. **42**, 133 (1986).

39. J. E. Japka, J. Met. **40**, 18 (1988).

40. G. Boehm, Fachber. Huettenprax. Metallweiterverarb. **20**, 146 (1982).

41. K. Okuyama and Y. Kousaka, in *Powder Technology Handbook*, edited by K. Iinoya, K. Gotoh, and K. Higashitani (Marcel Dekker, New York, 1991), pp. 57–61.

42. G. K. Nathan and W. J. D. Jones, Proc. Instn. Mech. Engrs. **181**, 215 (1966–67).

43. J. N. Brecker, R. Komanduri, and M. C. Shaw, Ann. CIRP **22**, 219 (1973).

44. K. Nassau, Lapidary J. **35**, 1194 (1981).

45. C. A. West, Can. Chem. Process Inds. **28**, 3 (1944).

46. Corning 7940, Corning, Inc., Corning, NY 14831-0002.

47. LHG8, Hoya Corporation USA, San Jose, CA 95131.

48. KDP provided by Cleveland Crystals, Inc. (CCI), Cleveland, OH 44110. Indents were done on a fractured surface (Type-II cut).

49. BASF Corporation, Mt. Olive, NJ 07828-1234.

50. ISP International, Wayne, NJ 07470.

51. Novamet, Wyckoff, NJ 07481.

52. Personal communication with Dr. Al Friederang, BASF Corporation, 28 July 1998.

53. Exolon-Esk Company, Tonawanda, NY 14151-0590.

54. Microabrasives Corporation, Westfield, MA 01085.

55. Zirconia I, batch #1502792, courtesy of Saint Gobain/Norton Industrial Ceramics Corporation, Worcester, MA 15136.

56. 1.0-μm C, alumina polishing compound, Praxair Surface Technologies, Indianapolis, IN 46222-3274.

57. Transelco Division of Ferro Corporation, Penn Yan, NY 14527.

58. C. R. Brooks, *Heat Treatment of Ferrous Alloys* (Hemisphere, Washington, 1979).

59. T. Fujihana *et al.*, Surf. Coat. Technol. **51**, 19 (1992).

60. J. D. Verhoeven, *Fundamentals of Physical Metallurgy* (Wiley, New York, 1975), Chaps. 11 and 14.

61. Personal communication with Prof. James C. Li, Materials Science Program, University of Rochester, 1998.

62. Personal communication with Dr. James Knapp, Praxair Surface Technologies, 1999.

63. Personal communication with Ms. Dana Zagari, Transelco Division of Ferro Corporation, 1999.

Imaging of Laser–Plasma X-Ray Emission with Charge-Injection Devices (CID's)

Introduction

X-ray imaging and x-ray spectroscopy are used in laser–plasma-generated physics research to diagnose conditions in the laser targets. Examples of techniques used to image x-ray emission are pinhole cameras, Kirkpatrick–Baez (KB) microscopes, curved crystal optics, and Wölter microscopes.[1–3] All spectroscopic diagnostics rely also on spatial resolution to record an x-ray spectrum. Examples of spectroscopic techniques are Bragg crystal diffraction and grating diffraction. The simplest method of recording images is time-integrated exposure of film, a common example being the calibrated Kodak direct exposure film (DEF).[4] Alternatively, images can be recorded by a solid-state device that is either directly sensitive to x rays (photons absorbed in the device) or indirectly sensitive (photons absorbed in a phosphor coating, generating visible range photons that are then absorbed in the device).

This work details the method of obtaining time-integrated images of laser–plasma x-ray emission using charge-injection devices (CID's), as has been demonstrated on the University of Rochester's 60-beam UV OMEGA laser facility.[5] The CID has an architecture similar to a charge-coupled device (CCD). The differences make them more resistant to radiation damage and, therefore, more appropriate for some applications in laser–plasma x-ray imaging. Images were obtained with pinhole cameras, KB microscopes,[2] and a tunable monochromatic x-ray microscope.[6] Simultaneous images obtained on these systems with calibrated x-ray film have enabled determination of the absolute detection efficiency of the CID's in the energy range from 2 to 8 keV.

Charge-Injection Devices (CID's)

The CID cameras used in this work are manufactured by CID Technologies, Inc. of Liverpool, NY.[7] The model CID4150 is an 812 × 604 array having square pixels with 38.5-μm center-to-center spacing and overall array dimensions of 31.3 × 23.2 mm. Details of the pixel architecture found in the literature[8–11] are summarized as follows: Each pixel contains two storage areas (pads). At the start of integration, voltage applied to both pads injects any stored charge into the substrate layer. Next, charge is accumulated under a negatively biased column storage pad until the bias is changed to transfer the stored charge to a row pad. The row pad is attached to a row preamplifier from which the signal is output and digitized. The CID's used in this work were operated at room temperature and with no conversion phosphor coating on the detector surface (direct x-ray detection). A PC-based analog-to-digital converter with 16-bit resolution, operating at 500 kHz, accomplished the camera readout. The relatively high-speed readout was employed to minimize dark current in the uncooled detectors.

Figure 83.1 shows a CID camera in its housing and an epoxy-encased dental imaging version,[11] for comparison, alongside a film pack and film pack positioner, illustrating the relative compactness of the CID camera. All signal amplification and switching electronics are contained in the CID camera. An overview of the installation on the OMEGA target chamber and surrounding structure is shown in Fig. 83.2. The

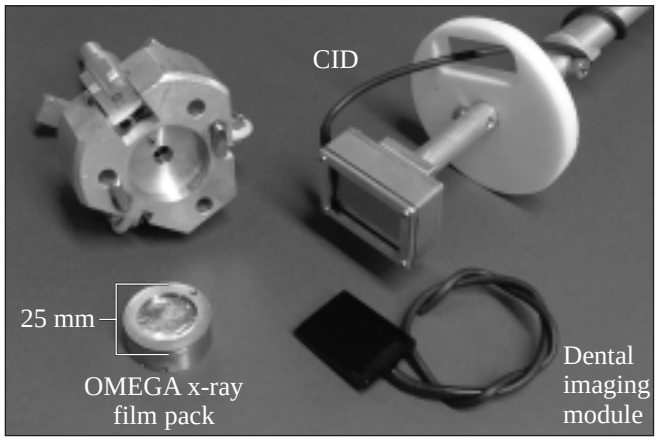

E10257

Figure 83.1
Picture of CID camera mounted on the end of a pinhole camera positioner. The CID camera replaces the film pack holder (upper left) and film pack (lower left). The CID camera was designed to be compact, as evidenced by the dental imaging version (lower right).

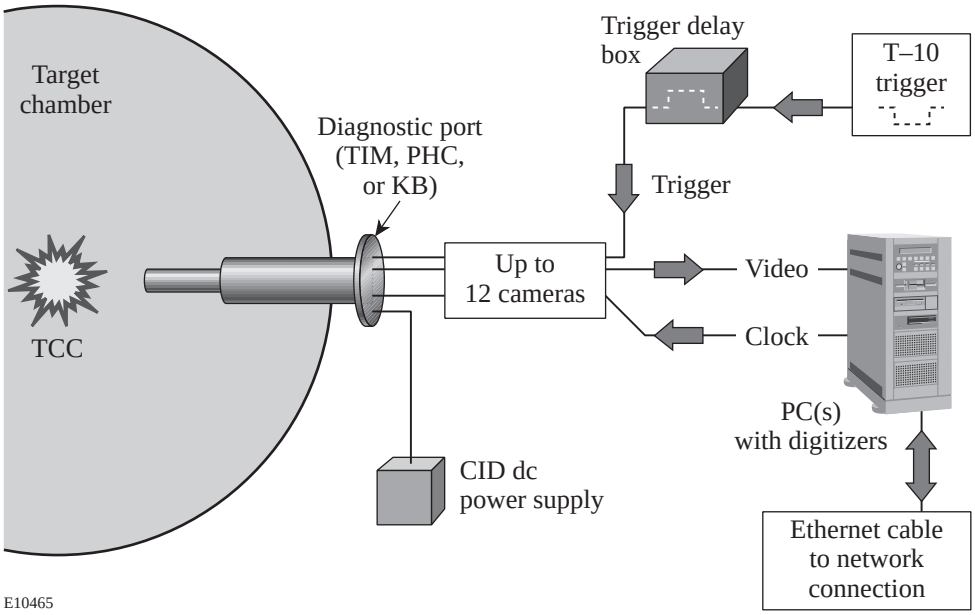

Figure 83.2
Schematic of the CID camera interface to an OMEGA x-ray diagnostic.

dc power is supplied along with a clocking line and an integration trigger line. The common integration trigger supplies each camera in use with a pre-shot pulse to acquire a background image and an on-shot pulse to acquire an image on the laser target shot. The two images are subtracted to provide the final image. The single output line contains the unformatted video signal, which is sent to a PC-based analog-to-digital converter card (ADC). Up to two PC's are used to acquire six CID camera outputs per PC, on as many as 12 CID cameras for the currently planned system.

Experiments

The CID cameras were used to obtain images of laser–plasma x-ray emission on OMEGA. Three different diagnostics were used as platforms for these tests: x-ray pinhole cameras and two different KB microscopes. One microscope was outfitted with a grating and used to obtain grating-dispersed images of target implosion cores.[12] The other microscope was outfitted with metal multilayer monochromators and used to obtain narrow-energy-band (monochromatic) x-ray images of target implosion cores.[6]

Figure 83.3 shows two images obtained with pinhole cameras located on opposite sides of the target chamber. The pinhole cameras have 11-μm pinholes and were located 170 mm from the target. The CID's were located to provide images with a magnification of 4.0 (~10 μm/pixel at the target plane). The images are of x-ray emission from a 4-mm-diam, Au-coated plastic sphere. The OMEGA beams were surface focused onto the target using the standard OMEGA optics and distributed phase plates designed to produce Gaussian-like focal spots with a diameter of ~900 μm (containing 95% of the energy). These produce x-ray spots with diameters of ~600-μm full width at half-maximum (FWHM). The images are analyzed to determine the relative pointing of each beam compared to the desired pointing (all beams pointed so as to converge at the target center, in the spherical-implosion-pointing mode). Typically six or more film-based cameras are used to obtain like images, necessitating film loading, unloading, developing, drying, and finally digitizing. Although these processes are streamlined by using auto film developers, quick drying, and video camera digitizing, the typical minimum processing time of ~40 min cannot compete with the several-minute time scale required to store and redisplay multiple digital image files.

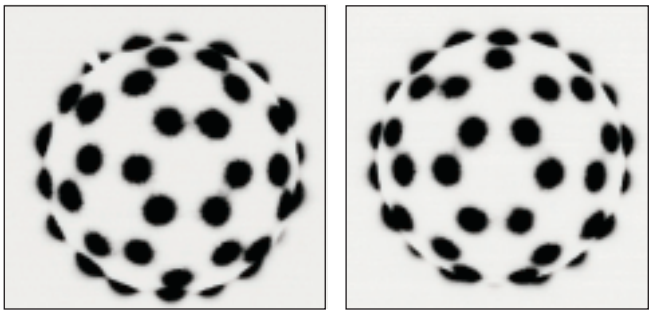

Figure 83.3
CID images taken from two opposing pinhole cameras on an OMEGA pointing shot.

Another example of CID-camera-obtained x-ray images is shown in Fig. 83.4. The CID's were located behind the same pinhole cameras described above, but farther away at a magnification of 8.0. The images are of the time-integrated x-ray emission from an imploded laser fusion target (in this case, a 3-atm-D_2-filled, 20-μm-thick CH shell). Figure 83.4(a) was taken with minimum filtration in front of the CID sensor (150 μm of Be, mostly in the pinhole camera itself), while Fig. 83.4(b) was taken with a CID on a pinhole camera on the opposite side of the target chamber and additional filtration of 50 μm of Al was used to limit the soft x-ray component of the image. Figure 83.4(a) clearly shows the target's outer-shell emission plus stalk emission (all of which occurs during target acceleration). Figure 83.4(b) shows only the harder x-ray emission that is confined to the high-density, high-temperature implosion core region.

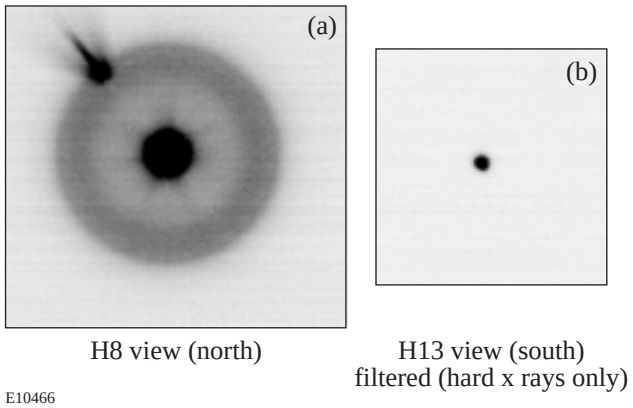

Figure 83.4
CID images of a directly driven imploding OMEGA laser target (from opposing pinhole cameras): (a) soft x-ray image containing emission from the outer shell region, the stalk, and a saturated core region; (b) hard x-ray image containing only emission from the core.

Pairs of images, one on film and one with a CID on the same x-ray microscope, have been obtained on a series of OMEGA target shots. The KB microscope was outfitted with a diffraction grating that yielded dispersed spectra of the implosion cores.[12] The magnification of the images is 20.3. Since the KB microscope is a four-mirror, four-image version with image views separated by 1.4° on the target chamber sphere, the images are nearly identical except for differences in the recording media. Figure 83.5 shows a pair of such images: (a) a film-recorded image (Kodak DEF) and (b) a CID-camera-recorded image. Both images are produced by the KB microscope, which has Ir-coated mirrors operating at grazing angles of 0.70°. Attenuation by 140 μm of Be is common to both, as is diffraction by the 0.2-μm-period transmission grating. The CID camera had an additional 25 μm of Be acting as a light shield and housing cover. Both images show nearly identical features. The main features captured by the grating-dispersed microscope (zeroth-order image of implosion and first-order diffracted image of the core) are seen in both images. Since the film and microscope have been absolutely calibrated, comparison of the film- and CID-recorded core spectra can be used to infer the absolute sensitivity of the CID pixels. Figure 83.6(a) shows such a comparison taken along the core spectrum and plotted as a function of photon energy. The CID pixel's inferred quantum efficiency dependence on energy is shown in Fig. 83.6(b). Although a precise model for the CID pixels has not been developed, the results of Janesick *et al.*[13] for the case of a front-side-illuminated, thin-depletion-region CCD are shown for comparison in Fig. 83.6(b). This model should be representative of the CID sensitivity.

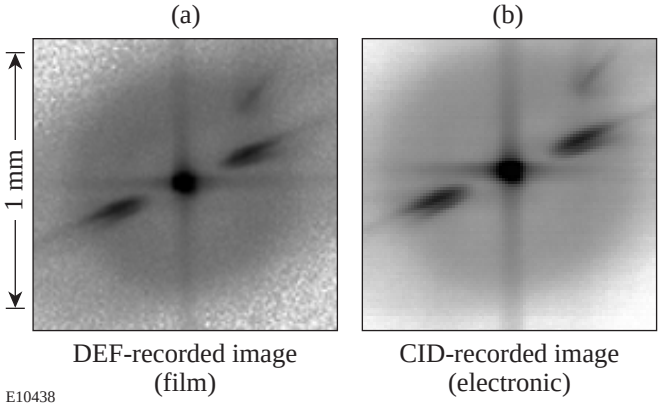

Figure 83.5
A pair of simultaneously recorded x-ray microscope images taken with (a) Kodak DEF film and (b) a CID camera. The image is an imploding OMEGA target with dispersion of the core emission by an x-ray transmission grating (evidenced by the features ~30° from the horizontal to the upper right and lower left). The horizontal and vertical streaks are due to small-angle specular scattering from the microscope mirrors.

Lastly, a pair of images taken with the KB microscope outfitted with metal multilayer monochromators is shown in Fig. 83.7. The imaging system has been previously described.[4] WB_4C multilayers with a 2d spacing of 26.5 Å were used, and the magnification of the images is 13.6. The monochromators were tuned so as to produce images of target emission centered on the Ar He-like β-line (3.683±0.011 keV) and the Ar H-like

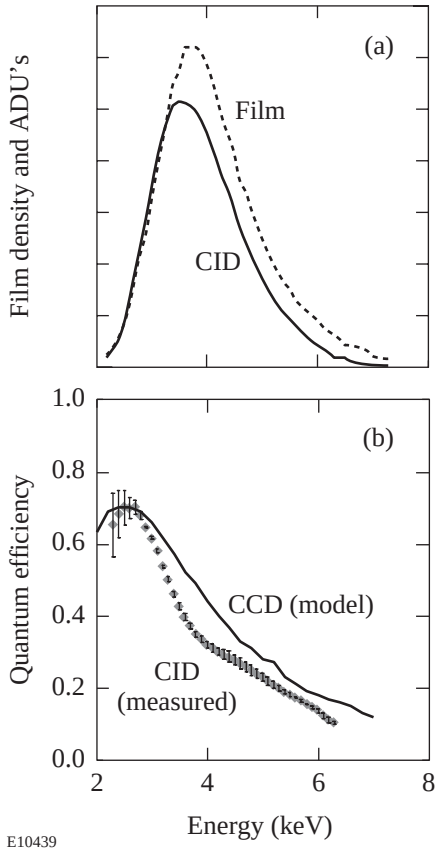

Figure 83.6
Comparison of CID- and film-recorded spectra. (a) Lineouts through the two spectral features; (b) inferred CID quantum efficiency, derived from the calibrated constants of the microscope/grating/film system.

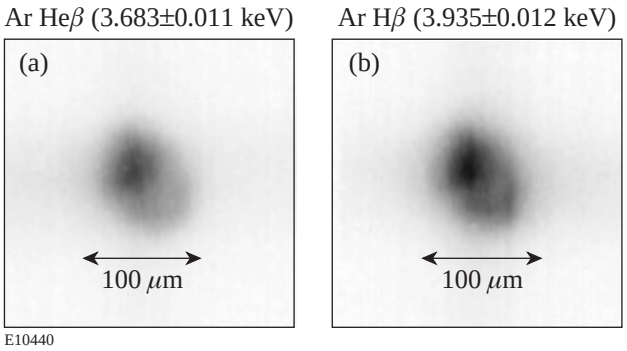

Figure 83.7
Monochromatic images of an imploding OMEGA laser target taken with two CID cameras. (a) Image of emission at 3.683±0.011 keV, centered on the Ar He-like β-line; (b) image of emission at 3.935±0.012 keV, centered on the Ar H-like β-line.

β-line (3.935±0.012 keV), where the indicated energy range is determined by the FWHM's of the monochromator diffraction peaks. The target was a 15-atm, D_2-filled, 20-μm-thick, 1-mm-diam CH shell containing 0.35% by atomic number of Ar gas as a dopant. The images show the enhanced line-plus-continuum emission from the implosion core region. The asymmetry of the core is ascribed to the lack of perfect direct-drive beam balance on this shot, aggravated by several lower-intensity beams being near each other on the target chamber sphere. The images show a clear core region whose size and morphology can be easily measured.

Conclusion

CID cameras have been used to obtain time-integrated x-ray images on a variety of imaging and spectroscopic diagnostics on the OMEGA laser facility's target chamber. Cross calibration of the CID camera with film shows that the CID pixels, when used in direct-detection mode (i.e., without a phosphor), have a useful energy range of better than 2 to 8 keV, with additional sensitivity to be expected, especially at higher energies. Currently, all existing OMEGA time-integrated x-ray diagnostics are being outfitted with CID cameras as an optional recording medium.

ACKNOWLEDGMENT

The authors acknowledge the support of the OMEGA laser operations group and the staff at the University of Rochester's Laboratory for Laser Energetics. This work was supported by the U. S. Department of Energy Office of Inertial Confinement Fusion under Cooperative Agreement No. DE-FC03-92SF19460, the University of Rochester, and the New York State Energy Research and Development Authority. The support of DOE does not constitute an endorsement by DOE of the views expressed in this article.

REFERENCES

1. J. A. Koch *et al.*, Appl. Opt. **37**, 1784 (1998).
2. F. J. Marshall and Q. Su, Rev. Sci. Instrum. **66**, 725 (1995).
3. N. M. Ceglio, A. M. Hawryluk, and R. H. Price, Appl. Opt. **21**, 3953 (1982).
4. B. L. Henke *et al.*, J. Opt. Soc. Am. B **3**, 1540 (1986).
5. T. R. Boehly, D. L. Brown, R. S. Craxton, R. L. Keck, J. P. Knauer, J. H. Kelly, T. J. Kessler, S. A. Kumpan, S. J. Loucks, S. A. Letzring, F. J. Marshall, R. L. McCrory, S. F. B. Morse, W. Seka, J. M. Soures, and C. P. Verdon, Opt. Commun. **133**, 495 (1997).
6. F. J. Marshall and J. A. Oertel, Rev. Sci. Instrum. **68**, 735 (1997).
7. CID Technologies, Inc., Liverpool, NY 13088.

8. Z. Ninkov, C. Tang, and R. L. Easton, in *Charge-Coupled Devices and Solid State Optical Sensors IV*, edited by M. M. Blouke (SPIE, Bellingham, WA, 1994), Vol. 2172, pp. 180–186.

9. J. J. Zarnowski *et al.*, in *Charge-Coupled Devices and Solid State Optical Sensors IV*, edited by M. M. Blouke (SPIE, Bellingham, WA, 1994), Vol. 2172, pp. 187–198.

10. J. Carbone *et al.*, in *Solid State Arrays and CCD Cameras*, edited by C. N. Anagnostoupoulos, M. M. Blouke, and M. P. Lesser (SPIE, Bellingham, WA, 1996), Vol. 2654, pp. 131–138.

11. J. Carbone *et al.*, in *Solid State Sensor Arrays: Development and Applications II*, edited by M. M. Blouke (SPIE, Bellingham, WA, 1998), Vol. 3301, pp. 90–99.

12. F. J. Marshall, J. A. Delettrez, R. Epstein, and B. Yaakobi, Phys. Rev. E **49**, 4381 (1994).

13. J. R. Janesick *et al.*, Opt. Eng. **26**, 156 (1987).

X-Ray Spectroscopic Measurements of Areal Density and Modulations of Compressed Shells in Implosion Experiments on OMEGA

Introduction

In inertial confinement fusion (ICF), spherical targets are driven either directly with laser beams[1] or indirectly with x-ray drive.[2] Initial target nonuniformities, either existing or created by the drive, can grow because of hydrodynamic instabilities disrupting the implosion and reducing its thermonuclear yield.[3] Therefore, it is important to measure the effects of these instabilities on the target performance and particularly on the shell integrity. Fusion reactions occur during the stagnation phase, at peak compression, when the maximum density and temperature are achieved. Simultaneously, the hot core and the inner surface of the shell emit most of their radiation in x rays.[3] This emission not only contains information about important parameters such as areal density, temperature, and their uniformity in the region from where the emission originates (hot core and inner shell), but can also be used to probe the rest of the cold shell.[4] While the shell's final areal density, neutron yield, and core temperature are important parameters of the target performance, the shell's integrity provides a more direct signature of instability.

Cold-shell integrity has been measured for shells with Ti-doped layers.[5] Monochromatic core images were obtained at energies below and above the *K*-edge energy of Ti with a pinhole-array x-ray spectrometer.[6] The ratio between such images reflects the nonuniformity of the cold shell; however, these measurements were limited to implosions with 20-μm-thick shells and 1-ns square pulse shape, which had the highest-intensity x-ray emission from the core. Slowly rising pulse shapes and thicker shells produce implosions with lower core intensity. When measured with a pinhole-array spectrometer, this intensity was insufficient to perform meaningful analysis.

In the present experiments the sensitivity of the measurements is increased by replacing the diffracting crystal in the pinhole-array spectrometer with filters for sampling the spectrum below and above the Ti *K* edge. This allows for measurements of shell integrity for 20- and 24-μm-thick shells with both the 1-ns square pulse shape and a slower-rising, 2.3-ns pulse that has a 1:6 foot-to-main-pulse intensity ratio (PS26). Pure CH targets were used to measure nouniformities in radiation temperature and uniformity of the emitting (hot) part of the target, which consists of the core and inner part of the shell.

In this article three measurement methods are described: (1) Imaging of the cold-shell modulations is based on the imaging of core radiation in two x-ray energies, absorbed and nonabsorbed by the shell. The ratio of intensities in the two narrow-energy-band x-ray images is used to infer modulation in the areal density of the absorbing shell. (2) Measurements of temperature nonuniformities in the core radiation use core images from two energy bands, both unattenuated by the shell. (3) Imaging of the hot-shell modulations measures emission nonuniformities at x-ray energies unattenuated by the shell. Since most of this emission comes from the inner, hot shell, the modulations in the images are related to the hot shell's areal-density nonuniformities.

Experiments

The targets used in these experiments were CH shells of ~450-μm inner radius and 20- and 24-μm shell thickness. Targets with Ti had 2-μm, Ti-doped CH (6.2% by atom) layers at the inner part of the shell. Targets were filled with 3 or 15 atm of D_2. Targets were irradiated with 351-nm laser light using the 60-beam OMEGA laser system.[7] Two pulse shapes were used in these experiments: a 1-ns square pulse shape with total on-target energy of about 25 kJ and PS26 with a duration of ~2.5 ns and total on-target energy of about 20 kJ. Beam-smoothing techniques used during these experiments included distributed phase plates[8] (DPP's) and smoothing by spectral dispersion[9] (SSD). The 2-D SSD had an IR bandwidth of 1.25 Å × 1.75 Å, producing a 0.2-THz bandwidth at 351 nm. The estimated illumination uniformity for 60 overlapping OMEGA beams with DPP's and SSD was $\sigma_{rms} \sim 2.5\%$, which was calculated from the on-target single-beam distribution and averaged over the length of the pulse.[10] Beam-to-beam energy variations were typically ~7%, which produces an additional on-target illumination nonuniformity of $\sigma_{rms} \sim 2.5\%$, with most of that contribution in modes 1 through 5.[10]

The thin solid line in Fig. 83.8 shows the measured spectrum of the core emission integrated over the time of a stagnation phase at peak compression (~300 ps) and integrated over the area of the core (~80 μm). The spectrum is from the implosion of a 24-μm-thick shell, with a 2-μm inner Ti-doped layer and an initial D_2 fill pressure of 3 atm by 1-ns-square-pulse illumination. The spectrum was measured with a spectrometer fitted with an ammonium dihydrogen phosphate (ADP) crystal and a 15-μm-wide slit. The spectrum contains absorption lines due to 1*s*–2*p* transitions in Ti ions near the 4.6-keV energy.[11] These lines are absorbed within the warm Ti-doped region (T ~ 300 to 600 eV), whereas radiation above the Ti *K* edge at 4.96 keV is absorbed by much colder Ti. The intensity above the *K* edge falls down gradually rather than abruptly, indicating a temperature gradient in the absorbing region and an associated gradual *K*-edge shift to higher energies due to ionization.[11] The electron temperature of the emission region ($T_e = 0.86 \pm 0.04$ keV) and the areal density of cold Ti in the shell ($\rho R_{\mathrm{Ti}} = 2.1 \pm 0.1$ mg/cm^2) have been derived from the fit to the measured spectrum, shown by the thick solid line outside absorption areas of warm Ti (at ~4.6 keV) and shifted *K* edge.

This spectrum was used not only to identify the spectral regions of x rays appropriate for imaging but also to calculate imaging sensitivity in order to convert intensity modulations in the image to modulations of the shell's areal density.

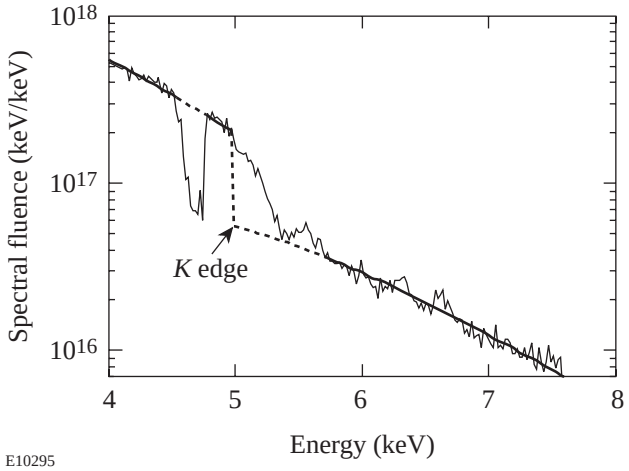

Figure 83.8
Measured time-integrated spectrum of the core emission taken with a 24-μm-thick shell with a 2-μm inner Ti-doped layer, at an initial fill pressure of 3 atm D_2, and 1-ns-square-pulse illumination.

Imaging of Cold-Shell Modulations

To measure the shell's integrity, the target is imaged at energies weakly absorbed by the shell, below the Ti *K* edge, and at energies strongly absorbed by the shell (above the Ti *K* edge at about 6.5 keV). The compressed core radiation serves as a backlighter for the shell.[5] Any modulations in this emission are measured from the core image below the *K* edge. The image above the *K* edge has approximately the same modulations in the backlighter and additional modulations in the absorbing shell.

Time-integrated images of core emission were taken with a 6-μm pinhole array, at 4× magnification, and recorded on DEF film. Two images were taken with a Ti filter at energies below the Ti *K* edge (~4.9 keV); the other two images were taken with an iron filter at energies above the Ti *K* edge (~6.5 keV). A schematic of the instrument is shown in Fig. 83.9. Instead of one image per energy channel, a pair of images were taken not only to reduce noise by averaging images but also to estimate the noise itself by subtracting one image from another. The calculated resolution for the imaging system was ~6 μm, with modulation transfer functions (MTF's) very similar for both 4.9- and 6.5-keV energy channels. The noise spectrum has been used in the Wiener filter applied to reduce noise during image processing. The thicknesses of both the Ti and the Fe filters were varied for different shots in order to achieve an optimum intensity on the film since intensity levels were different for different shot conditions.

The energy spectrum was measured for each target experiment using the crystal spectrometer. The approximate x-ray energy spectra of the images for each energy channel were calculated by multiplying this spectrum by the filter response. Figure 83.10(a) shows the spectra calculated for the lower-energy filter (solid line) and the higher-energy filter (dotted line). The conditions of the target experiment were a 20-μm-thick CH shell with a 2-μm inner Ti-doped layer, filled with 3 atm of D_2, irradiated by a 1-ns square pulse. Lineouts of two lower-energy-band images (solid lines) and two higher-energy-band images (dotted lines) are shown in Fig. 83.10(b). Note that the lineouts from the same energy band have similar features that are different from the features in the other energy band. This indicates that the features seen in the images are not noise, and that the differences between the images at different energies are likely due to modulations in the absorbing shell. (It is assumed that the core-emission image does not change appreciably over an ~1.6-keV interval in photon energy between the two energy bands, i.e., the features of the core

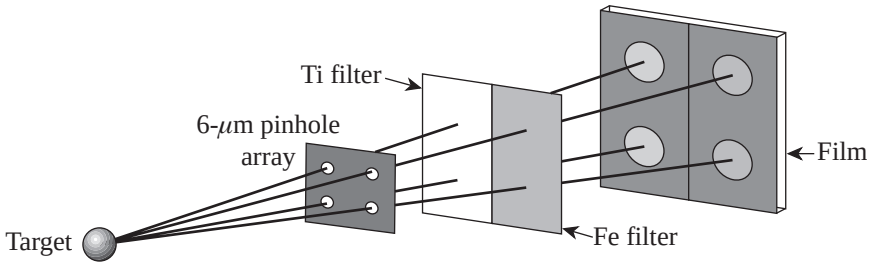

Figure 83.9
Schematic of the 6-μm filtered pinhole array. Two time-integrated images are obtained with a Ti filter at energies below the Ti *K* edge (~4.9 keV); the other two images are obtained with an Fe filter at energies above the Ti *K* edge (~6.5 keV). The magnification of the images is 4× and the images are recorded with DEF film.

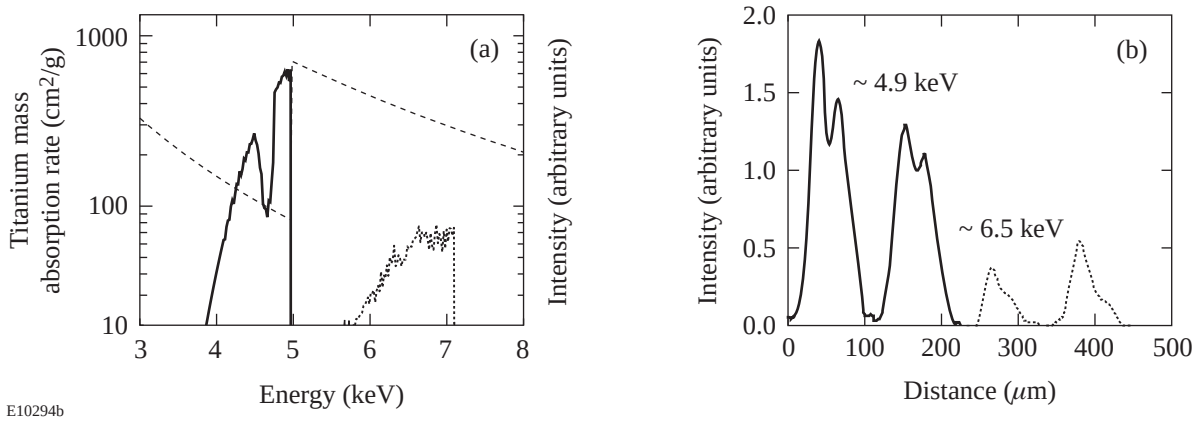

Figure 83.10
(a) The calculated spectra of the images below the Ti *K* edge (solid line) and above the Ti *K* edge (dotted line). The Ti mass absorption rate is shown by the dashed line. (b) The lineouts of two images taken below the Ti *K* edge (solid line) and above the Ti *K* edge (dotted line).

emission are the same at ~4.9 and ~6.5 keV. (This assumption is confirmed in the next section.)

The images were processed with the Wiener-filtering technique.[12] If $C(\mathbf{f})$ is the signal plus noise of the image (obtained by averaging two images for a particular x-ray energy channel) in Fourier space with coordinates $\mathbf{f}$, and $\langle N(\mathbf{f})\rangle$ is the average spectrum of the noise (calculated from the difference of two images for a particular energy band), then the restored signal spectrum $R(\mathbf{f})$ is given by the Wiener-filter formula[12]

$$R(\mathbf{f}) = \frac{C(\mathbf{f})}{\mathrm{MTF}(\mathbf{f})} \bullet \frac{|C(\mathbf{f})|^2 - |\langle N(\mathbf{f})\rangle|^2}{|C(\mathbf{f})|^2}, \qquad (1)$$

where MTF($\mathbf{f}$) is the modulation transfer function of the pinhole camera calculated for a particular x-ray energy channel. The filtered images are obtained by transforming the restored spectrum $R(\mathbf{f})$ back to real space.

The modulations of the ratio of intensities for filtered images below the *K* edge [$I_{<K}(\mathbf{x})$] and above the *K* edge [$I_{>K}(\mathbf{x})$] are related to the shell-areal-density modulations $\delta[rR(\mathbf{x})]$ by

$$\delta\left[\rho R(\mathbf{x})\right] = \delta \frac{\left\{\ln\left[\frac{I_{<K}(\mathbf{x})}{I_{>K}(\mathbf{x})}\right]\right\}}{\mu_{>K} - \mu_{<K}}, \qquad (2)$$

where $\mu_{>K}$ and $\mu_{<K}$ are the spectrally weighed mass absorption coefficients of cold Ti at energies above and below *K* edge, respectively, which were calculated for each shot using the measured x-ray spectra [Fig. 83.10(a)].

Figure 83.11 shows the power per mode of the measured modulation as a function of spatial frequency of the cold, Ti-doped shell areal density at peak compression. The data are from three target experiments, measured using core images taken at x-ray energies above and below the Ti *K* edge. For each

target experiment, the areal-density modulations were normalized to the measured cold-shell areal densities, which were deduced from the crystal spectrometer data, similar to that shown in Fig. 83.8, yielding relative modulations in the cold-shell areal density $\delta[\rho R(\mathbf{x})]/\rho R(\mathbf{x})$. To minimize errors due to spherical effects in the analysis of the outer section of the core images, only the 60-μm-diam central portion of each 100-μm-diam image was analyzed. The spectra in Figs. 83.11(a) and 83.11(b) correspond to 20- and 24-μm-thick-shell targets driven with a 1-ns square pulse shape. The spectrum in Fig. 83.11(c) corresponds to a 24-μm-thick-shell target driven with pulse shape PS26. All three targets were filled with 3 atm of D_2. To obtain the power per mode, shown in Fig. 83.11, absolute values of the Fourier amplitudes squared were summed at each spatial frequency. The σ_{rms} of the total nonuniformity is the square root of the sum of the power per mode over the spatial frequency. The spectra shown in Fig. 83.11 are very similar. They are peaked at a spatial frequency of 20 mm^{-1} (corresponding to a wavelength of 50 μm or mode number $\ell \sim 5$) with spatial features extending down to a wavelength of about 15 μm. The total σ_{rms} of the nonuniformities is similar for all three shots and is ~50%±20%. Adding previous data[5] to these measurements, we conclude that the nonuniformity σ_{rms} ranges from the noise level of ~20% up to ~50% and is similar for target experiments with a 20- or 24-μm-thick shell and with 1-ns square or PS26 pulse shapes.

Measurements of Temperature Nonuniformities

Measurements of the cold-shell integrity are based on the assumption that the distribution of core emission does not change appreciably over an ~1.6-keV interval in photon energy between the two energy bands at ~4.9 and ~6.5 keV. This assumption is valid if the effective emission temperature is constant over the whole area of the image. We use the term "effective" with respect to temperature in order to emphasize that the measured images of the cores are two dimensional, and

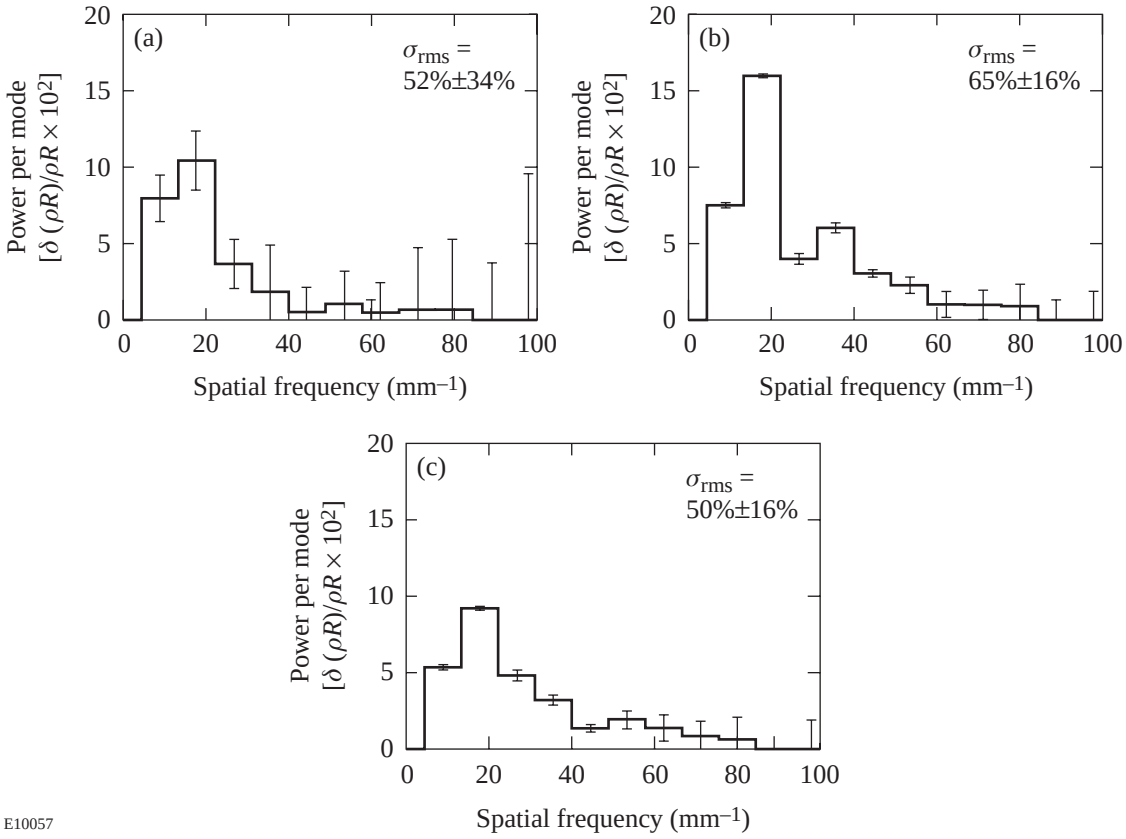

Figure 83.11
Power per mode of the measured modulation as a function of spatial frequency for target experiments with (a) 20-μm-thick shells and 1-ns square pulse shape, σ_{rms} = 52%±34%, (b) 24-μm-thick shells and 1-ns square pulse shape, σ_{rms} = 65%±16%, and (c) 24-μm-thick shells and PS26 pulse shape, σ_{rms} = 50%±16%. All experiments were taken with 3-atm-D_2-filled shells with a 2-μm-thick, inner-Ti-doped (6.2% by atom) layer.

not three dimensional as the cores are themselves. The intensity at each point is an integral over the core in the direction of the imaging system. Regions with different temperatures may exist inside the core; however, when integrated along the path toward the imaging system, only an integrated or effective temperature is observable.

Figure 83.12 represents the lineouts of the core images measured with Sn filters at an x-ray energy of about 3.5 keV (solid lines) and with Fe filters at an x-ray energy of about 6.5 keV (dashed lines). These data are from a target experiment with a 24-μm-thick CH shell (no Ti doping), filled with 15 atm of D_2 and driven by a 1-ns square pulse shape. At x-ray energies of $\gtrsim$3 keV, the core emission is not significantly absorbed by the outer shell. Differences in the shapes of the images as a function of energy band would indicate the presence of nonuniformities in the effective temperature. Lineouts of the captured images shown in Fig. 83.12 are, in fact, very similar. The image features are similar for the two images taken from the same energy band, indicating that these features are not noise. The fact that these features have the same shape for both energy bands indicates that the effective temperature is nearly constant over the entire area of the images. The measured effective temperature $T_{\text{eff}} = 0.86 \pm 0.04$ keV was found from the ratio of two different energy-band images shown in Fig. 83.12.

A similar analysis was performed on results from experiments with other conditions, including different CH-shell thicknesses and different pulse shapes. For all of these shots effective temperatures were constant over the whole area of the images within the experimental error determined by the noise in the images.

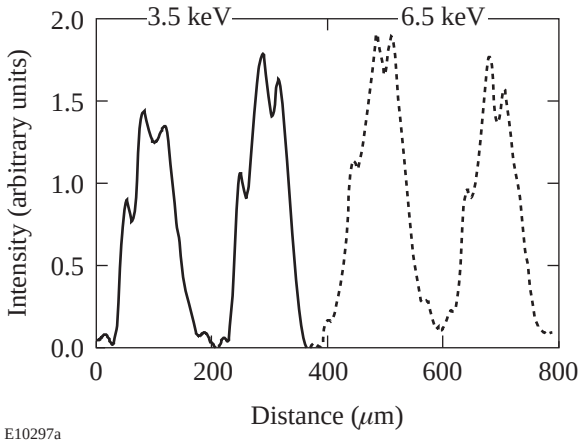

Figure 83.12
The lineouts of two images taken at ~3.5 keV (solid line) with a Sn filter, and at ~6.5 keV (dashed line) with an Fe filter for a target experiment on a 24-μm-thick shell, filled with 15 atm of D_2, driven by a 1-ns square pulse shape.

Imaging the Hot-Shell Modulations

As shown above, the core images have no temperature nonuniformities within the experimental resolution and sensitivity; the modulations seen in the high-energy, unattenuated images are due to areal-density modulations in the emission region. The core images are produced by the emission from the hot core and dominated by the emission from the inner hot shell; therefore, modulations in the image lineouts shown in Fig. 83.12 are mostly due to hot-shell areal-density modulations. Assuming that the absorption of x rays in the core and the shell is negligible, the intensity at the detector is proportional to the areal density of the emission region in the direction of x-ray propagation.

To analyze the areal-density nonuniformity of the hot inner shell, the smooth envelope of the core image $I_{\text{env}}(\mathbf{x})$ (obtained by filtering the image in Fourier space) was subtracted from the core image $I(\mathbf{x})$. The relative areal-density nonuniformity of the hot shell is given by the relation

$$\frac{\delta[\rho R(\mathbf{x})]}{\rho R(\mathbf{x})} = \sqrt{2}\left(\frac{I(\mathbf{x}) - I_{\text{env}}(\mathbf{x})}{I_{\text{env}}(\mathbf{x})}\right). \tag{3}$$

Since the signals from both "walls" of the hot shell are added to give $I(\mathbf{x})$, the relative nonuniformities in the captured image $\left[I(\mathbf{x}) - I_{\text{env}}(x)\right]/I_{\text{env}}(\mathbf{x})$ are multiplied by the factor of $\sqrt{2}$ in order to analyze modulations corresponding to only one wall of the shell (the assumption made here was that areal-density perturbations in the shell region are uncorrelated).

Figure 83.13 shows the measured power per mode of the areal-density nonuniformities as a function of spatial frequency for the hot inner shell. The spectrum is peaked at spatial scale lengths of 40 to 50 μm with a total σ_{rms} of 30%±15%. It is similar to the measured cold-shell spectra in both magnitude and shape.

Conclusions

Time-integrated measurements of the shell integrity are presented at peak compression, the final stage of a spherical implosion. Perturbations in the cold, or absorbing, part of the shell were studied using shells with and without inner Ti-doped layers. The hot, or emitting, part of the shell was studied using pure plastic shells. It is found that modulations in both

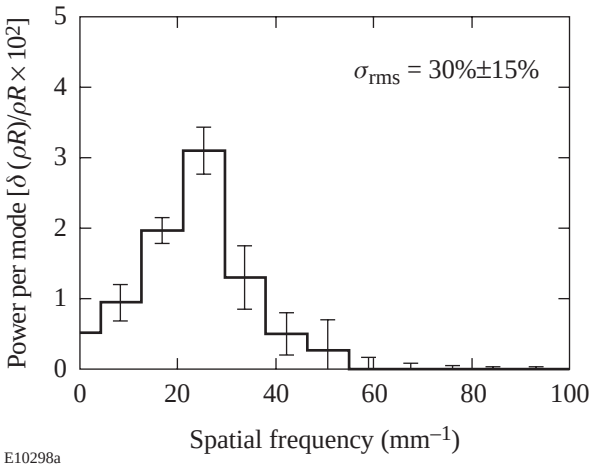

Figure 83.13
Power per mode of hot CH plasma emission as a function of spatial frequency for a target experiment on a 24-μm-thick shell, filled with 15 atm of D_2, driven by a 1-ns square pulse shape, σ_{rms} = 30%±15%.

the cold and hot parts of the shell are peaked at spatial scale sizes of 40 to 50 μm, with nonuniformities extending to ~15 μm. The magnitude of relative areal-density perturbations is in the range from the noise level of ~15% to 20% up to ~50% for both 1-ns square and PS26 pulse shapes. Time-resolved measurements at peak compression and earlier, in the deceleration phase, will aid in understanding the present findings.

ACKNOWLEDGMENT

This work was supported by the U.S. Department of Energy Office of Inertial Confinement Fusion under Cooperative Agreement No. DE-FC03-92SF19460, the University of Rochester, and the New York State Energy Research and Development Authority. The support of DOE does not constitute an endorsement by DOE of the views expressed in this article.

REFERENCES

1. S. E. Bodner, D. G. Colombant, J. H. Gardner, R. H. Lehmberg, S. P. Obenschain, L. Phillips, A. J. Schmitt, J. D. Sethian, R. L. McCrory, W. Seka, C. P. Verdon, J. P. Knauer, B. B. Afeyan, and H. T. Powell, Phys. Plasmas **5**, 1901 (1998).
2. J. D. Lindl, Phys. Plasmas **2**, 3933 (1995).
3. D. K. Bradley, J. A. Delettrez, R. Epstein, R. P. J. Town, C. P. Verdon, B. Yaakobi, S. Regan, F. J. Marshall, T. R. Boehly, J. P. Knauer, D. D. Meyerhofer, V. A. Smalyuk, W. Seka, D. A. Haynes, Jr., M. Gunderson, G. Junkel, C. F. Hooper, Jr., P. M. Bell, T. J. Ognibene, and R. A. Lerche, Phys. Plasmas **5**, 1870 (1998).
4. B. Yaakobi, F. J. Marshall, D. K. Bradley, J. A. Delettrez, R. S. Craxton, and R. Epstein, Phys. Plasmas **4**, 3021 (1997).
5. B. Yaakobi, V. A. Smalyuk, J. A. Delettrez, R. P. J. Town, F. J. Marshall, V. Yu. Glebov, R. D. Petrasso, J. M. Soures, D. D. Meyerhofer, and W. Seka, in *Inertial Fusion Sciences and Applications '99*, edited by W. J. Hogan C. Labaune, and K. A. Tanaka (Elsevier, Paris, 2000), pp. 115–121.
6. B. Yaakobi, F. J. Marshall, and D. K. Bradley, Appl. Opt. **37**, 8074 (1998).
7. T. R. Boehly, D. L. Brown, R. S. Craxton, R. L. Keck, J. P. Knauer, J. H. Kelly, T. J. Kessler, S. A. Kumpan, S. J. Loucks, S. A. Letzring, F. J. Marshall, R. L. McCrory, S. F. B. Morse, W. Seka, J. M. Soures, and C. P. Verdon, Opt. Commun. **133**, 495 (1997).
8. Y. Lin, T. J. Kessler, and G. N. Lawrence, Opt. Lett. **20**, 764 (1995).
9. S. Skupsky, R. W. Short, T. Kessler, R. S. Craxton, S. Letzring, and J. M. Soures, J. Appl. Phys. **66**, 3456 (1989).
10. F. J. Marshall, J. A. Delettrez, V. Yu. Glebov, R. P. J. Town, B. Yaakobi, R. L. Kremens, and M. Cable, Phys. Plasmas **7**, 1006 (2000).
11. B. Yaakobi, R. S. Craxton, R. Epstein, and Q. Su, J. Quant. Spectrosc. Radiat. Transfer **58**, 75 (1997).
12. V. A. Smalyuk, T. R. Boehly, D. K. Bradley, J. P. Knauer, and D. D. Meyerhofer, Rev. Sci. Instrum. **70**, 647 (1999); W. H. Press *et al.*, *Numerical Recipes in FORTRAN: The Art of Scientific Computing*, 2nd ed. (Cambridge University Press, Cambridge, England, 1992), pp. 701–715.

Secondary D-^{3}He Proton Spectra from D_2-Filled OMEGA Targets

Introduction

Two new diagnostic techniques now provide the first high-quality spectra of secondary fusion protons from imploded D_2-filled capsules in inertial confinement fusion (ICF) experiments. The potential utility of secondary neutrons and protons for diagnosing such capsules has been recognized for more than two decades,[1–8] but practical use of protons has previously been limited by the lack of accurate spectroscopic measurements. The first new technique utilizes a magnet-based charged-particle spectrometer; the second involves "wedge-range-filter"–based spectrometers utilizing special filters and CR39 nuclear track detectors. These spectrometers were recently used to acquire data from target capsules with about 14 atm of D_2 fuel in 19-μm-CH shells, imploded at the 60-beam OMEGA laser facility by irradiation with 22 kJ of laser energy. Results of that work, presented in this article, are important for the information they give about current experiments and for the potential they show for characterization of the cryogenic D_2-filled capsules to be used in the near future.

The general value of charged-particle spectrometry for capsule diagnostics has recently been demonstrated with magnet-based charged-particle spectrometers (CPS's), which are now used on a regular basis to measure spectra of primary fusion products (p, D, T, α) and "knock-on" particles (p, D, T, and ^{3}He elastically scattered by 14.1-MeV neutrons[3])[9,10] for a wide range of capsule types and implosion conditions on OMEGA.[11] Measured spectra provide a number of important implosion parameters such as primary yields, fuel ion temperature, and areal density (ρR) of fuel, shell(s), or fuel plus shell. Areal densities are determined by measuring the energy loss of charged fusion products as they pass out through the fuel and shell[9] or by measuring the yields of knock-on particles.[10]

In the most important future ICF experiments utilizing cryogenic capsules with DT or D_2 fuel, large areal densities will limit the number of diagnostic measurements that can be made of charged particles. On the National Ignition Facility (NIF), ρR_{total} of imploded DT capsules is eventually expected to exceed 1 g/cm^2. In this case, the only charged particles that could escape and be detected for studying ρR are tertiary protons,[12] which have energies as high as 30.8 MeV. DT capsules planned for OMEGA may (based on 1-D simulations) reach ρR_{total} of 0.2 to 0.3 g/cm^2. In this case, knock-on deuterons and tritons, resulting from elastic collisions with primary 14.1-MeV neutrons, could be detected and used to study ρR with CPS's.[10]

In the shorter term, cryogenic experiments will be carried out with pure-D_2 fuel. No charged primary fusion products will be energetic enough to escape and be detected, and there will be no high-energy primary neutrons to generate energetic knock-on particles. In addition, the method of determining ρR_{fuel} by measuring secondary-neutron yields[6] will fail for $\rho R_{\text{fuel}} \gtrsim 0.1$ g/cm^2. Fortunately, secondary D-^{3}He protons (12.6 to 17.5 MeV) *will* escape from D_2-filled capsules with relatively high ρR. These protons are created in the two steps indicated in reactions (1) and (2):

$$\mathrm{D} + \mathrm{D} \rightarrow n\,(2.45\ \mathrm{MeV}) + {}^3\mathrm{He}\,(0.82\ \mathrm{MeV}); \tag{1}$$

$${}^3\mathrm{He}\,(0.82\ \mathrm{MeV}) + \mathrm{D} \rightarrow \alpha\,(6.6\ \text{to}\ 1.7\ \mathrm{MeV}) + p\,(12.6\ \text{to}\ 17.5\ \mathrm{MeV}). \tag{2}$$

In one of the primary branches of the D-D reaction, ^{3}He is created with 0.82 MeV of kinetic energy. Some of the ^{3}He ions then react in-flight with thermal D ions, creating protons that, because of the kinetic energy of the ^{3}He, have a range of energies. Measured spectra of these protons can be used to measure ρR_{fuel} and ρR_{total}.

The remainder of this article will discuss the use of spectral measurements. Although the emphasis throughout is on secondary protons, there is also discussion of how they relate to the secondary neutrons created through reactions (3) and (4):

$$\mathrm{D} + \mathrm{D} \rightarrow p\,(3.02\ \mathrm{MeV}) + \mathrm{T}\,(1.01\ \mathrm{MeV}); \tag{3}$$

$$\mathrm{T}(1.01\ \mathrm{MeV}) + \mathrm{D} \rightarrow \alpha(6.7\ \text{to}\ 1.4\ \mathrm{MeV}) + n(11.9\ \text{to}\ 17.2\ \mathrm{MeV}). \quad (4)$$

The following sections discuss (1) how the characteristics of secondaries are related to the physical parameters of capsules; (2) how accurately measured spectra of secondary protons are made with the magnet-based CPS's and with "wedge-range-filter"–based spectrometers; (3) measurements during OMEGA shots; (4) physical interpretation of data; and (5) future application to cryogenic-target experiments.

Secondary Spectra and Capsule Characteristics

Two simple models of plasma structure are used here to illustrate how measurements of secondary yields and spectra are related to properties of compressed capsules. In the "hot-spot" model, all primary fusion reactions take place in a small region at the center of the spherical fuel, and the fuel outside the hot spot, where the primary fusion products react with cooler fuel to create secondaries, has uniform density and temperature. In the "uniform" model, the fuel is uniform over its entire spherical volume so that primary and secondary reactions take place everywhere. In both cases, there can be a spherical shell or pusher of a different material outside the fuel (generally CH, in most current OMEGA experiments). It is assumed in these simple models that the capsule is spherically symmetric, with no mixing of fuel and shell material, although numerical work currently underway indicates that fuel/shell mixing could be important. In future work, more-sophisticated models will be used.

The slowing down of primary ^{3}He and T in D fuel is modeled with the formalism described in Ref. 13, with results shown in Fig. 83.14. The production rates for secondaries are then determined by the cross sections shown in Fig. 83.15 (calculated from Ref. 14). The resultant yields, and the shapes of spectra as they are created in the fuel, are discussed below. Modifications to the spectrum of protons as they slow down on their way out of the fuel and shell are then determined by the stopping power illustrated in Fig. 83.16 (calculated according to Ref. 13).

1. Yields

By integrating over the appropriate paths of primary fusion products ^{3}He and T and using the foregoing assumptions to calculate their energies as a function of position, and then utilizing the secondary production rates, we can calculate yields Y_{2p} and Y_{2n} of secondary protons and neutrons as fractions of the primary-neutron yield Y_{1n} and obtain the results shown in Fig. 83.17. Related calculations were carried out previously[1–8] for some of these cases, utilizing older models for the slowing down of ^{3}He and T. The authors pointed out that a nearly linear relationship exists between ρR_{fuel} and the secondary-to-primary-yield ratios as long as ρR_{fuel} is low enough that the primary particles (^{3}He or T) escape the fuel. Each yield ratio reaches a saturation level (as shown in Fig. 83.17) when the appropriate primary particle is completely slowed down in the fuel, but measurements of yield can be used to infer ρR_{fuel} as long as saturation has not been reached. The results are weakly dependent on plasma density, but the plasma temperature has a strong impact on the value of ρR_{fuel} at which the linear relationship fails because of com-

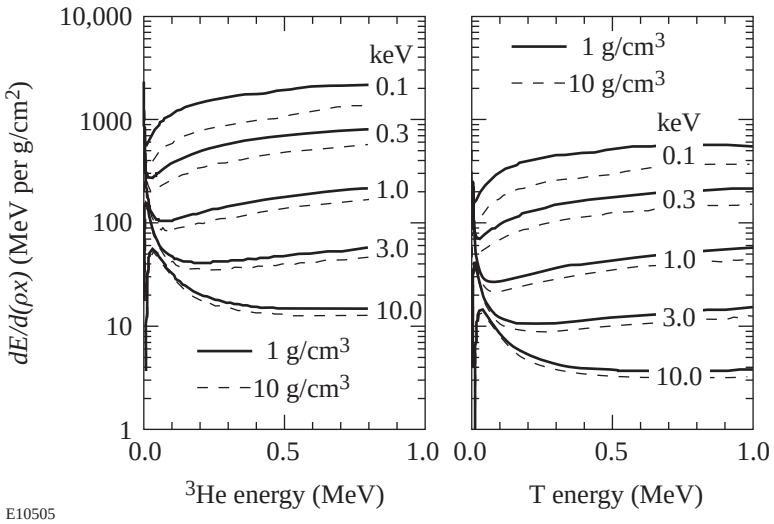

Figure 83.14
Stopping powers for ^{3}He (left) and T (right) in D plasmas of various temperatures (calculated according to Ref. 13). Note that at higher temperatures there is an important peak in the stopping power at low energies, due to ion-induced slowing.

plete slowing down of the primary particles in the fuel. This is a consequence of the temperature dependence of the total particle ranges, as illustrated in Fig. 83.18. Because of the magnitude of the cross sections (Fig. 83.14), secondary protons are preferentially produced close to the birth position of primary ^{3}He, while secondary neutrons are preferentially created near the end of the range of the primary T (see Fig. 83.19).

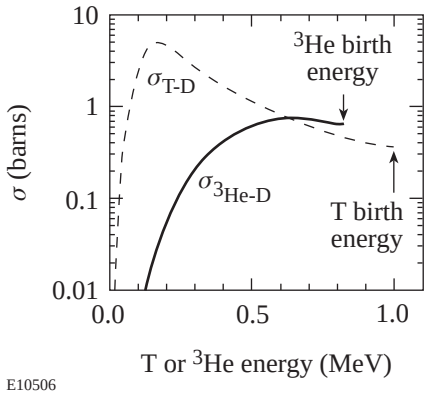

Figure 83.15
Fusion cross sections (σ) for energetic ^{3}He or T with cold D plasma (calculated according to information in Ref. 14).

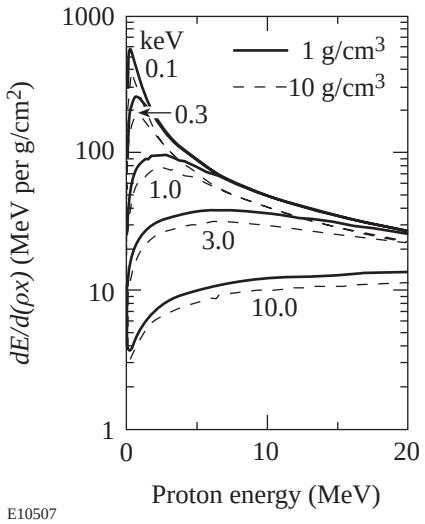

Figure 83.16
Stopping power for protons in D plasmas of various temperatures (calculated according to Ref. 13). The values for CH plasmas are almost identical except for being higher by a factor of about 14/13 (the ratio of the numbers of electrons per unit mass).

Two differences between the hot-spot and uniform models are apparent in Fig. 83.17: (1) The value of ρR_{fuel} for a given yield is slightly higher in the uniform model, reflecting the fact that the mean distance traveled by primary particles before they encounter the fuel–pusher interface is smaller by a factor of 0.75. (2) Complete saturation of yield at high values of ρR_{fuel} in the uniform model is approached asymptotically, but never reached, because some primaries are always created close enough to the surface to escape the fuel.

Although a measured secondary-proton yield can be used in the context of our models to infer ρR_{fuel} only in regimes where the primary ^{3}He escapes the fuel before stopping, another kind of information can be inferred when complete stopping occurs in the fuel. As seen in Fig. 83.17, the electron temperature T_e determines the maximum possible secondary-to-primary ratio Y_{2p}/Y_{1n}. If it is known that yield saturation has been reached, it is possible to estimate the effective electron temperature as illustrated in Fig. 83.20. A similar relationship between electron temperature and yield saturation holds for secondary neutrons.

2. Birth Spectra

Going beyond the calculation of yields, we can investigate the shapes of secondary-particle spectra at their birth. Consider first the protons. If ρR_{fuel} is small, so that primary ^{3}He particles escape the fuel before losing much of their 0.82-MeV birth energy, then the protons they produce by fusing with fuel deuterons are equally distributed between limiting energies of about 12.6 and 17.5 MeV. The energy limits are defined by kinematics and are determined by ^{3}He energy at the time of interaction with D. The flat distribution as a function of energy between the limits can be demonstrated by assuming that fusion products are distributed isotropically in the D–^{3}He center-of-mass frame, transforming to the lab frame, and calculating the number of particles per unit energy. The number of protons produced during the slowing down of ^{3}He from energy $E_{^3\text{He}}$ to $E_{^3\text{He}} - \Delta E_{^3\text{He}}$ is proportional to

$$\Delta E_{^3\text{He}} \sigma_{^3\text{He–D}}\left(E_{^3\text{He}}\right) \Big/ \left[dE_{^3\text{He}} / d(\rho x)\right],$$

where $\sigma_{^3\text{He–D}}\left(E_{^3\text{He}}\right)$ is as shown in Fig. 83.15, X is the distance along the trajectory of ^{3}He in the plasma, and $dE_{^3\text{He}} / d(\rho x)$ is as shown in Fig. 83.14.

For larger values of ρR_{fuel}, some of the ^{3}He will slow down before leaving the fuel; when they interact with the fuel, the kinematically defined width of the resultant proton spectrum

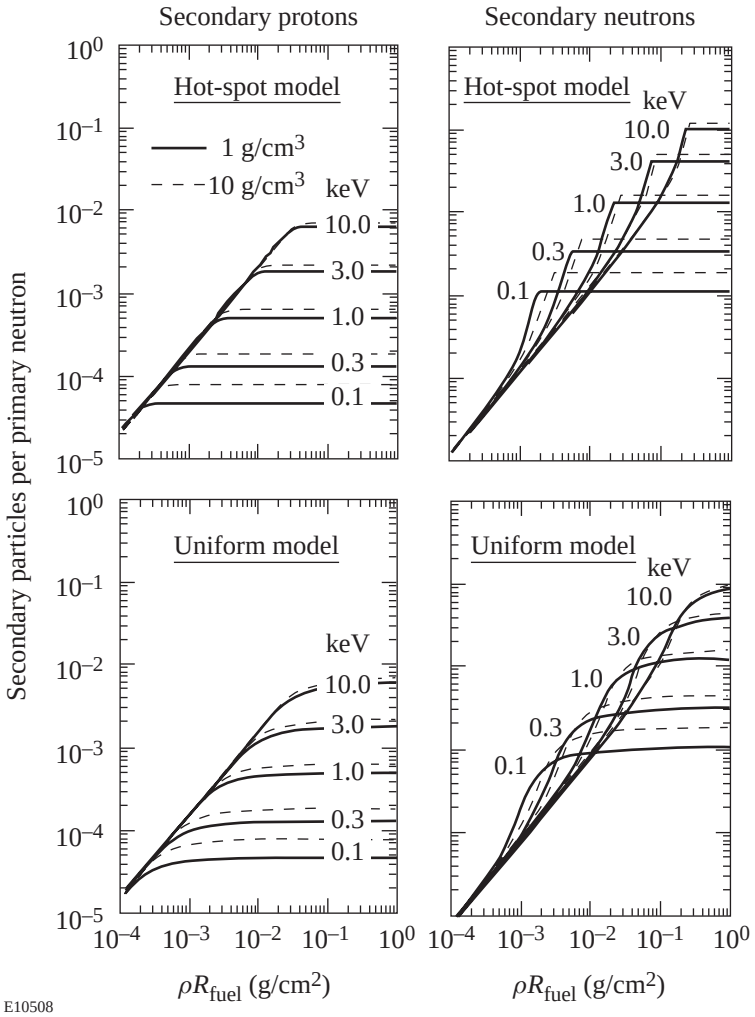

Figure 83.17
Yields of secondary protons (left) and neutrons (right), calculated using Li and Petrasso's ion-slowing formalism[13] to model the slowing down of primary fusion products in a D plasma. The two top plots assume the "hot-spot" model, in which all primary reactions take place in a small region at the center and secondary reactions take place outside the hot spot in a cooler region that is uniform in density and temperature. The two bottom plots assume the "uniform" model in which primary and secondary reactions take place throughout the uniform plasma. Plasma densities and electron temperatures T_e are as indicated.

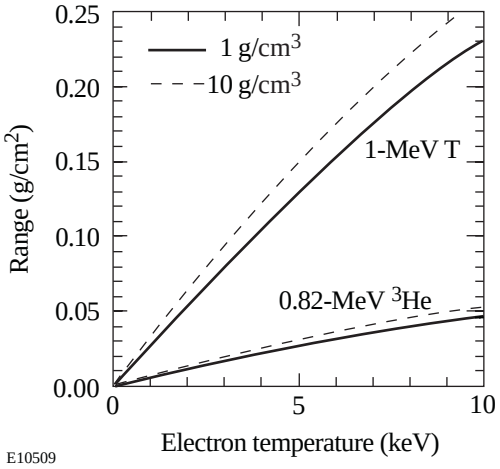

Figure 83.18
Ranges of primary D-D fusion products in a D plasma for different plasma densities and temperatures (from the stopping-power curves in Fig. 83.14).

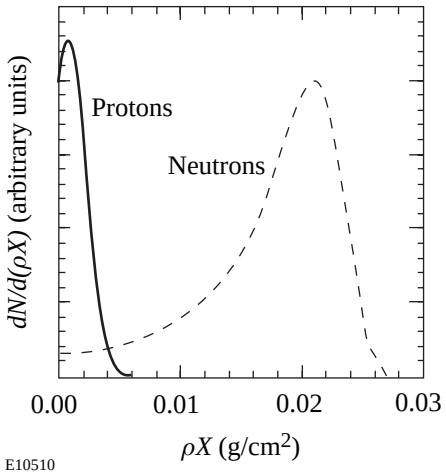

Figure 83.19
Illustration of how secondary protons are created mostly near the birth position of the primary ^{3}He, while secondary neutrons are created mostly toward the end of the range of primary T. The vertical axis is in arbitrary units that are different for the two curves; the horizontal axis unit ρX is the distance from primary birth position in g/cm^2 for a 1-keV, 3-g/cm^3 D plasma.

will be smaller. But since $\sigma_{^3\mathrm{He-D}}\left(E_{^3\mathrm{He}}\right)$ decreases rapidly as $E_{^3\mathrm{He}}$ goes below about 0.5 MeV, the contributions to the final proton spectrum become very small for lower-energy ^{3}He and the shape of the total proton spectrum remains relatively insensitive to the amount of slowing down, or equivalently the value of ρR_{fuel}. This is demonstrated in Fig. 83.21, which shows how, in the case of a hot-spot model, the shape of the spectrum gets built up as a contribution of parts due to ^{3}He slowed down by different amounts. Figure 83.21 also illustrates that the shape of the birth spectrum is relatively insensitive to the plasma temperature. The mean energy of the spectrum varies slightly with the amount of slowing down of ^{3}He, as shown in Fig. 83.22.

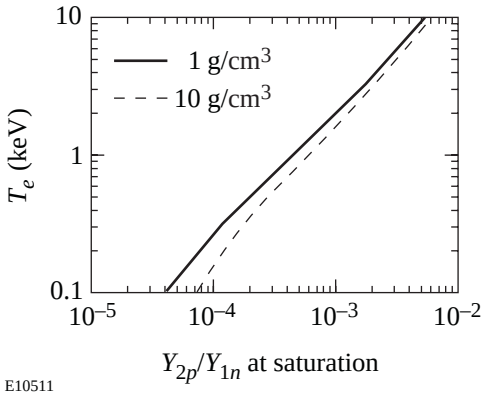

Figure 83.20
Electron temperature for which Y_{2p}/Y_{1n} cannot exceed a given saturation value (see Fig. 83.17). Under some circumstances, this relationship can be used to estimate T_e.

The secondary-neutron birth-spectrum shape is significantly more sensitive to ρR_{fuel} because the reaction cross section of primary T with fuel D increases rapidly as T energy decreases (down to about E_T = 0.2 MeV, as shown in Fig. 83.15). As discussed in Refs. 6–8, this means that the neutron spectrum gets narrower as ρR_{fuel} increases (and the exiting T energy decreases). Figure 83.21 illustrates this for the case of the hot-spot model.

3. Measured Spectra

A proton birth spectrum is never measured directly because it is modified by passage through the fuel and shell before being measured in a real experiment. Since the birth spectrum is relatively insensitive to fuel conditions, a measured spectrum contains diagnostic information about fuel and shell by virtue of the changes in the spectrum that can be inferred.

The mean energy of the secondary protons decreases according to the amount of material they traverse (Fig. 83.16

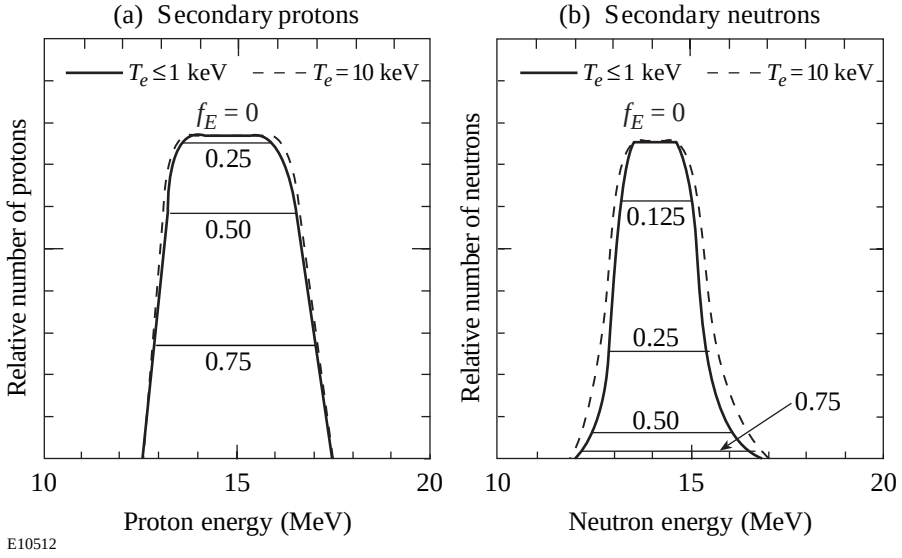

Figure 83.21
Calculated shapes of secondary-proton and -neutron spectra. These curves were generated by assuming that (a) the slowing of T or ^{3}He in a D plasma varies with energy as shown in Fig. 83.14, and (b) the primary particles are created near the center and pass through a uniform fuel that ranges their energies down to some fraction f_E of their birth energy (hot-spot model). The plasma density was assumed to be 3 g/cm^3. On each plot, the different curves show how the spectrum shape is built up as the primary particle gets ranged down; the curves *do not* show how the *number* of secondary particles varies with ρR. Each plot has one curve for plasma temperature 10 keV, corresponding to $f_E = 0$. This curve is arbitrarily normalized so its amplitude is the same as the corresponding curve for lower temperature to demonstrate that the shape is not strongly dependent on temperature.

showed how the stopping power of fuel or shell plasma for protons varies with proton energy and plasma temperature). For the case of a D plasma with ρ = 3 g/cm^3, Fig. 83.23 illustrates the slowing down of secondary protons as a function of T_e and ρX, where X is distance traveled through the plasma. The dependence on ρ is weak; the ratio of ρX to the mean energy loss $<\Delta E_{2p}>$ varies approximately as $\rho^{0.07}$ for $\rho X \leq 0.1$ g/cm^2. The dependence on temperature is weak for $T_e \leq 1$ keV and becomes progressively stronger for increasing T_e. For a CH plasma, the ratio of ρX to $<\Delta E_{2p}>$ is lower by about 13/14. If we assume that most of the protons are generated near the center of the fuel, then we can relate $<\Delta E_{2p}>$ to a sum of contributions from ρR_{fuel} and ρR_{shell}.

The protons are not all generated precisely at the center of the fuel, so they pass through slightly different amounts of material while leaving the capsule. This affects the mean energy, but that effect is fairly small for the OMEGA data discussed here. It also causes a broadening of the spectrum, and in future work that broadening will be used as another constraint on capsule structure.

A secondary-neutron birth spectrum can be measured directly.[15] The shape of this spectrum is sensitive to fuel conditions, so it has potential diagnostic value.[8] Figure 83.24 summarizes the plasma parameter regimes in which the measurement methods described above are applicable.

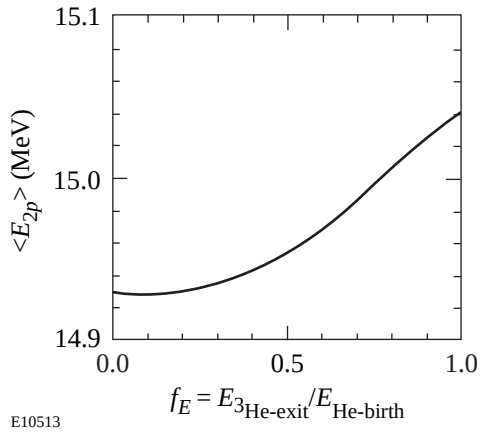

Figure 83.22
Dependence of the mean energies of the proton birth spectra (shown in Fig. 83.21) on the fraction of ^{3}He energy remaining when the ^{3}He reaches the fuel–pusher interface. Plasma temperature was assumed to be 3 keV, and the density was 3 g/cm^3. If the appropriate value of f_E (defined in the previous figure caption) is unknown, the effective mean energy will be uncertain. In such a case, we could use the value 14.97±0.04 MeV, which corresponds to the assumption of equal probability for all values of f_E.

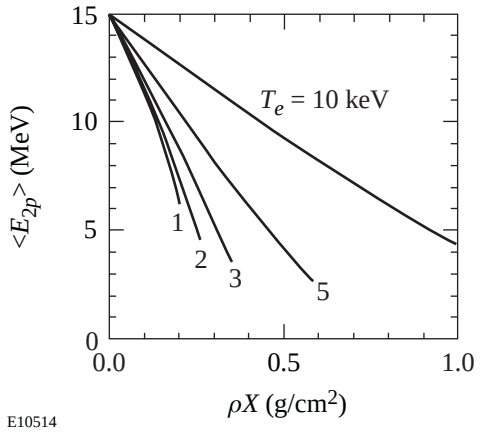

Figure 83.23
The mean energy of a secondary-proton spectrum after slowing down in a D plasma with ρ = 3 g/cm^3. The horizontal axis unit ρX is distance from birth position in g/cm^2. For a CH plasma, the value of ρX corresponding to a given energy should be reduced by the factor 13/14 (the ratio of electrons per unit mass for D to the value for CH). The dependence on ρ is weak; for $\rho X \leq 0.1$, the value of ρX corresponding to a given energy varies approximately as $\rho^{0.07}$.

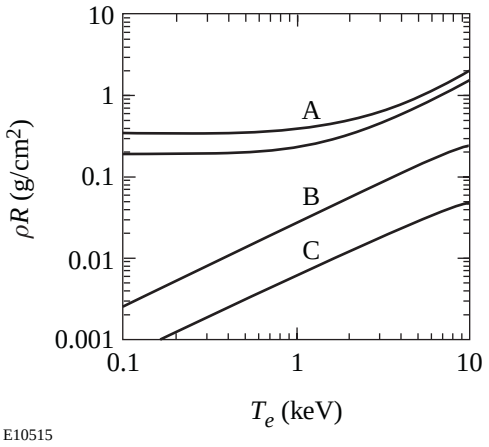

Figure 83.24
Boundaries of regimes in which various measurements can give diagnostic information about a 3-g/cm^3, pure-D plasma (assuming the hot-spot model). Note that ρR refers to ρR_{total} for curve A, but ρR_{fuel} for curves B and C. (A) Measurements of Y_{2p}/Y_{1n} and secondary-proton energy shift can be made only in the region *below* these curves, which show the ρR_{total} at which secondary protons fail to escape from the plasma (one curve each for the upper and lower limits of the birth spectrum). (B) Measurements of Y_{2n}/Y_{1n} give information about ρR_{fuel} only in the region *below* this curve, which shows where primary T is ranged out completely by the fuel and where the "saturated" regions of Fig. 83.17 are reached. *Above* this curve, measurement of Y_{2n} could give information about the fuel electron temperature. (C) Measurements of Y_{2p}/Y_{1n} give information about ρR_{fuel} only in the region *below* this curve, which shows where primary ^{3}He is ranged out completely by the fuel and where the saturated regions of Fig. 83.17 are reached. *Above* this curve, measurement of Y_{2p} can give information about the fuel electron temperature (see Fig. 83.20).

Instruments for Measuring Secondary-Proton Spectra

1. A Magnet-Based Charged-Particle Spectrometer

Two magnet-based spectrometers (CPS1 and CPS2) are installed on OMEGA. More information about CPS1 and CPS2 is available elsewhere,[16,17] but the principle of operation is illustrated in Fig. 83.25, which shows how a magnet is used to separate protons (or other charged particles) of different energies into different trajectories. The particles are stopped in CR39 nuclear track detectors, which are subsequently etched in a solution of NaOH and water, and then scanned with a microscope. A small hole appears at the location of the track of each individual proton. The position of a particle track gives the particle energy directly by virtue of the trajectory followed through the magnet. Final determination of an energy spectrum involves subtracting a background noise level, which includes neutron-induced noise and "intrinsic track noise." The neutron noise consists of tracks caused by protons elastically scattered by primary fusion neutrons, either in the CR39 itself or in surrounding materials; it scales with primary-neutron yield. The intrinsic track noise is caused by structural defects in the CR39, which look like particle tracks after etching; it is independent of implosion yields. Both types of noise are uniformly distributed on the CR39, subject to statistics.

Measuring secondary-proton spectra with CPS2 is more difficult than measuring other spectra, such as those of primary D-^{3}He protons,[9] for two reasons: (1) CR39 is not very sensitive to protons with energies higher than about 7 MeV, so when detecting protons with higher energies it is necessary to use a filter to range the protons down in energy just before they impact the detector. This is not difficult for primary D-^{3}He protons, which are nearly monoenergetic. But for the wide interval of incident energies associated with secondary protons, no single-filter thickness will range all protons down to the 0.5- to 7-MeV interval for which the detector is efficient. For this reason, a new filter whose thickness varies with position (or, equivalently, energy) was fabricated of aluminum. (2) Statistical noise is a significant problem. Typical primary D-D neutron yields in the OMEGA experiments have been of the order of 10^{11}, and the secondary-proton yield is usually in the vicinity of 10^8. With a spectrometer slit width of 3 mm, a slit length of 15 mm (perpendicular to the magnet dispersion direction), and a target-to-slit distance of 100 cm, the maximum total number of detected protons per shot is about 360—enough to give reasonable statistical errors for the total yield and the mean energy, but the error bars on individual energy bins in a spectrum will be large. In addition, the number of background noise events that must be subtracted is comparable to the number of true proton events, making the statistical noise even worse. After dispersion by the magnet, the 360 protons are spread out over an area of about 3 cm^2 on the CR39, giving 120 protons/cm^2. This has to be compared with noise that comes from intrinsic defects and from neutrons. Intrinsic noise events generally appear at a density of the order of 50 per cm^2. Neutron-induced events occur at about one per 10^4 neutrons, or about 45 per cm^2 on the CR39 (which is about 135 cm from the target); thus, for a single shot, the ratio of noise events to secondary-proton events is of the order of 1.

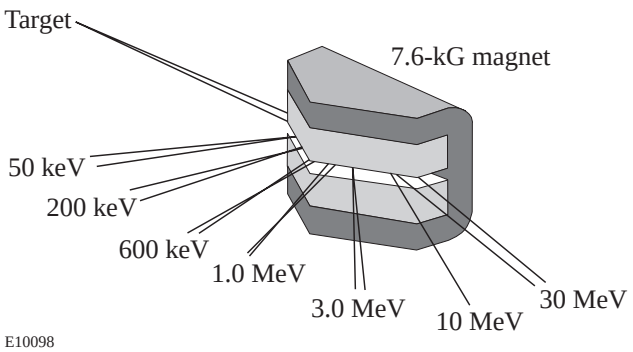

Figure 83.25
Concept of the magnet-based charged-particle spectrometers, showing how the magnetic field separates protons of different energies. Particles from the target capsule pass through a collimating aperture (not shown) before entering the magnet. After leaving the magnet, they are stopped in pieces of CR39 nuclear track detectors (not shown). The positions of the detected particles then indicate their energies by virtue of the trajectories followed.

2. Wedge-Range-Filter Spectrometers

Another new type of spectrometer, a wedge-range-filter spectrometer (WFS), has recently been tried for the first time. In a WFS (which will be described in detail elsewhere[18]), CR39 is again used as the particle detector, and special filters are used to range down the proton energies so they fall within the interval of sensitivity of the detector. The advantages of using range-filter measurements are simplicity and the ability to operate at lower yields by getting closer to the target. The disadvantages are (1) the interval of incident energies that can be detected with a single-filter thickness is not wide enough to cover the entire secondary-proton spectrum, and (2) it is difficult to get accurate spectral information. Secondary-proton yields have previously been estimated in this way by counting proton tracks behind a constant-thickness filter,[3–6] and Azechi *et al.*[6] used such data to make broadband estimates of different parts of the proton spectrum.

To find an improved approach, we have recently performed highly detailed calibrations of the response of CR39 to protons of different energies (different energies result in different track sizes)[19] and calibrations of the transmission characteristics of various filters. This information allows us to define a direct mapping between track diameter and incident proton energy for a given filter thickness. That mapping can be used to reconstruct part of the incident spectrum from a histogram of track diameters, but for each filter thickness the incident energy interval that is most accurately reconstructed is less than 1 MeV wide. To accurately reconstruct the entire secondary-proton spectrum, which is more than 5 MeV wide, it is necessary to have data from many different filter thicknesses. For this reason we use a special ranging filter with continuously varying thickness, making it possible to reconstruct a continuous spectrum over a wide energy interval. The filters used here were machined from aluminum, with thicknesses varying from 400 μm to 1800 μm. The fabrication tolerances turned out to be worse than desired, and the filters were slightly too thin. For the purposes of this first study, it was therefore necessary to estimate the thickness error by cross-calibrating the measured spectra with spectra acquired with the magnet-based CPS2. This single correction parameter was then applied to all data from WFS's. More-accurate fabrication and calibration techniques will make this unnecessary in the future.

A simple estimate of statistical errors can be made, assuming that a WFS is 15 cm from a capsule producing $Y_{1n} \simeq 10^{11}$ and $Y_{2p} \simeq 10^8$. With an effective area of about 3 cm^2 for the bulk of our spectrum, the number of incident protons will be about 10^5. These are spread out over at least 5 MeV, and at each filter thickness only about 1/3 of the spectrum is detected, so the number of protons actually counted is $\sim 3 \times 10^4$. This makes intrinsic noise totally irrelevant, but the number of neutron-induced events is $\sim 1 \times 10^4$. By restricting ourselves to an appropriate subset of track diameters, the number of proton events can be reduced by a factor of 2 and the number of neutron events by a factor of 4. The ratio of noise events to secondary-proton events is thus only ~0.15, and the large number of events guarantees very small statistical errors even after background subtraction.

Spectrum Measurements

1. Experiments

To illustrate the measurement and interpretation of secondary-proton spectra with our two new types of spectrometers, we present data from a recent series of four similar OMEGA shots. Table 83.I lists some basic shot parameters. The target capsules had ~14 atm of D_2 fuel in 19-μm-thick CH shells with outer diameters of ~910 μm. Each capsule was imploded by irradiation with ~22 kJ of 0.35-μm UV light applied in 60 beams for 1 ns (in a square-top pulse). The light was smoothed by spectral dispersion (2-D SSD with 0.3-THz bandwidth[20]). Primary-neutron yields Y_{1n} (measured via indium activation) varied from 8.1 to 9.8×10^{10}, while secondary-neutron yields Y_{2n} (measured with a time-of-flight diagnostic or Cu activation) were in the range of 1.1 to 1.8×10^8. Yield-weighted ion temperatures were 3.2 to 3.5 keV (measured with a neutron time-of-flight diagnostic).

CPS2 proton data were acquired by exposing one piece of CR39 to the protons from all four shots in order to sum the yields and minimize errors due to counting statistics. The background noise level was determined by measuring the number of apparent events at energies higher than the upper energy of the secondary-proton spectrum, and this mean noise level was subtracted from the total spectrum to give the results shown in Fig. 83.26. Table 83.I lists the mean energy and the yield of this proton spectrum.

WFS data for each of the four shots were taken at a distance of 15 cm from the target. Resultant spectra are shown in Fig. 83.27, and measured parameters are listed in Table 83.I. Figure 83.28 shows how the average of these spectra compares to the spectrum from the magnet-based CPS2.

2. Measurement Uncertainties

The proton yields obtained with CPS2 or with one of the WFS's have measurement uncertainties due to counting statistics. In addition, each measurement represents an average over a small solid angle, and measurements made at multiple positions during the same shot have shown that there are angular variations in particle fluxes that substantially exceed uncertainties due to counting statistics. This spatial variation

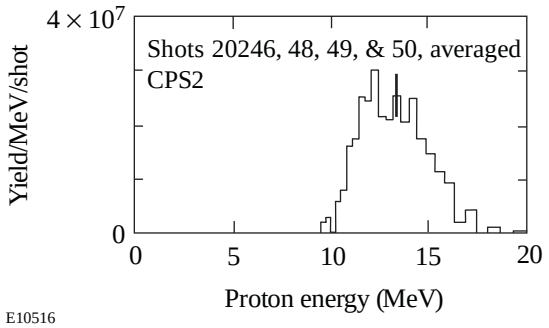

Figure 83.26
Spectrum of secondary protons for four shots, measured with the magnet-based spectrometer CPS2. One typical statistical error bar is shown.

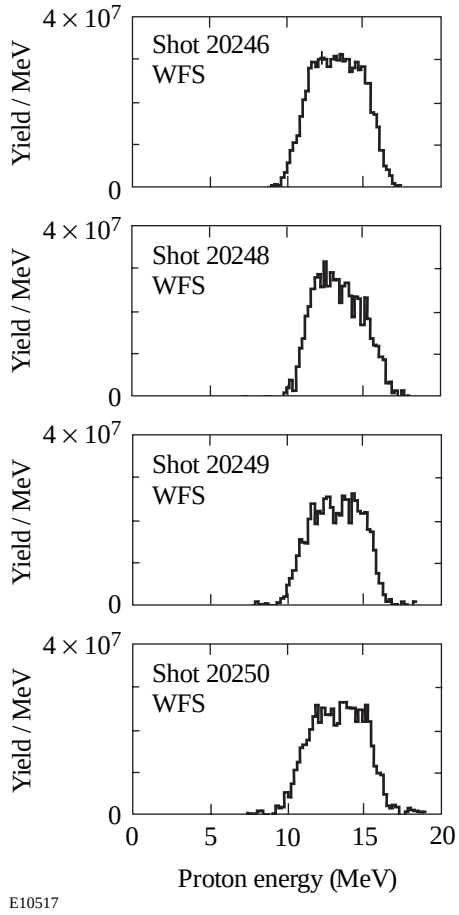

Figure 83.27
Spectra of secondary protons for the four individual OMEGA shots, as measured with the wedge-range-filter spectrometers (WFS's). One typical statistical error bar is shown in the top plot. The statistical errors in the lower three plots are slightly higher because only 1/3 of the available data were used.

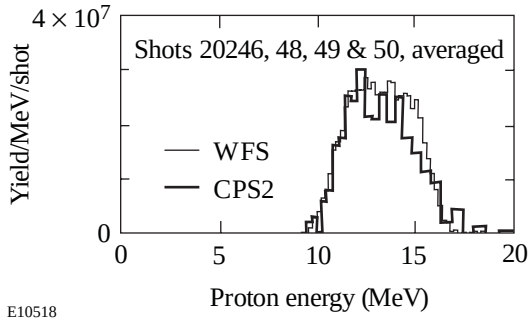

Figure 83.28
Comparison of the average spectrum measured with CPS2 (from Fig. 83.26) and the average of the individual WFS-measured spectra of Fig. 83.27.

of proton flux has been noted for a wide variety of shots and will be described in detail elsewhere. The standard deviation within measured spatial distributions of secondary-proton yield during individual shots tends to be in the vicinity of 20%. This puts a fundamental limit on the accuracy of any single yield measurement (as an indicator of total yield) and provides motivation for using multiple detectors.

The CPS2 yield measurements are affected by counting statistics in the measured spectra, including the subtracted background levels. The CPS2-measured proton-yield uncertainties quoted in Table 83.I were determined by adding, in quadrature, the statistical uncertainty (about 5%) and the expected standard deviation due to spatial variations (20% for a single shot, but 10% here for an average over four statistically independent shots). CPS2 measurements of mean energies have an uncertainty due to counting statistics (about 0.1 MeV here) and also due to any systematic energy calibration errors. Absolute calibration is accurate to about 0.1 MeV at 15 MeV.[21] The spatial variations in particle flux mentioned above do not seem to be accompanied by energy variations, so the energy measurement uncertainties quoted in Table 83.I are obtained by adding the statistical error to the calibration uncertainty in quadrature.

The WFS yield measurements are subject to the same 20% uncertainty due to spatial variations. Statistical errors for these measurements tend to be much smaller (near 1% for each shot), so in Table 83.I a 20% uncertainty is assigned to each individual measurement. Since there are four individual and statistically independent measurements (for the four shots), the error assigned to the shot-averaged yield is 10%. Errors in the measurement of mean energy are caused by counting statistics, but these statistical errors are quite small (about 0.02 MeV for shot 20246). The calibration error is larger, and since the energy calibration for these preliminary measurements was artificially tied to the calibration of the magnet-based CPS2, we do not list errors here (this will be remedied in the future).

3. Performance of the Spectrometer Types

Overall, the secondary-proton spectra obtained with the WFS's have less noise than those from CPS2. Statistical errors per shot are a factor of 10 smaller because the detector can be closer to the target, can use a larger active area, and has a higher ratio of true signal events to noise events. This advantage will diminish when secondary yields increase, as they are expected to for cryogenic targets. For current yields, the performance benefits combine with simplicity to make this approach very useful as a complement to the CPS's and particularly attractive

for studying the spectrum from many directions simultaneously for symmetry characteristics.[22] Theoretically, the WFS's should work at yields of ~10^6 and up to ~10^{10} (by moving farther from the target). They will not work for yields of 10^{11} or more, unless they can be moved well outside the target chamber, because of track overlap problems in the CR39. This probably limits their use to secondary (and tertiary) protons and, occasionally, primary protons from low-yield D-^{3}He shots. The primary charged products of many other targets will have yields that are too high, and the measurement of knock-on particles from DT targets,[10] which is of great interest to the ICF program, requires a separation of different particle types (D, T, and *p*), which cannot be performed with this approach.[19] These are appropriate applications for the magnet-based CPS's.

Interpretation of Measured Proton Spectra

1. Yield and Fuel Parameters

The measurements described above reflect properties of compressed targets, and in this section we look at implications

Table 83.I: OMEGA shot parameters, measurements, and inferred properties.

Parameter	Shot 20246	Shot 20248	Shot 20249	Shot 20250	<20246,48,49,50>
Fuel	14.2 atm D_2	14.3 atm D_2	14.3 atm D_2	14.3 atm D_2	14.3 atm D_2
Shell	19 μm CH	19 μm CH	19 μm CH	19 μm CH	19 μm CH
Outer Diameter	911 μm	909 μm	913 μm	905 μm	909.5 μm
Laser Energy	21.9 kJ	21.0 kJ	22.1 kJ	21.9 kJ	21.7 kJ
Laser Pulse	1 ns, square	1 ns, square	1 ns, square	1 ns, square	1 ns, square
T_i (keV)	3.2±0.5	3.5±0.5	3.5±0.5	3.2±0.5	3.3±0.5
Y_{1n} ($\times 10^{10}$)	9.76±0.07	8.06±0.06	8.28±0.06	9.17±0.07	8.82±0.03
Y_{2n} ($\times 10^{7}$)	17.7±1.2	11.6±0.9	11.1±0.9	12.4±1.0	13.1±0.5
Y_{2p} ($\times 10^{7}$)	15.8±3.1^{A,WFS}	11.8±2.4^{A,WFS}	12.1±2.4^{A,WFS}	12.1±2.4^{A,WFS}	11.4±1.3^{A,CPS2} 12.9±1.3^{A,WFS}
$\langle E_{2p}\rangle$ (MeV)	13.24^{B,WFS}	13.36^{B,WFS}	13.23^{B,WFS}	13.24^{B,WFS}	13.32±0.15^{CPS2} 13.27^{B,WFS}
ρR_{fuel} (mg/cm^2) from Y_{2n}/Y_{1n}	≤ (18±2)	≤ (15±2)	≤ (15±2)	≤ (14±2)	≤ (16±1)
ρR_{fuel} (mg/cm^2) from Y_{2p}/Y_{1n})	≥ (8±2)^{WFS}	≥ (7±2)^{WFS}	≥ (7±2)^{WFS}	≥ (6±2)^{WFS}	≥ (6±1)^{CPS2} ≥ (7±1)^{WPS}
ρR_{total} (mg/cm^2) from $\langle E_{2p}\rangle$	55$^{B,\ WFS}$	52$^{B,\ WFS}$	56$^{B,\ WFS}$	55$^{B,\ WFS}$	53±6^{CPS2} 54$^{B,\ WFS}$

^{CPS2}Measured with the magnet-based spectrometer CPS2.

^{WFS}Measured with a "wedge-range-filter" spectrometer.

^{A}Statistical errors are much smaller, but a 20% uncertainty is assumed because of known spatial nonuniformities (see pg. 138).

^{B}Statistical errors are very small, but systematic calibration errors have not been quantified (see pg. 138).

for physical parameters. The measured ratios Y_{2n}/Y_{1n} can be used to estimate ρR_{fuel}, with the information in Fig. 83.17, subject to two caveats. First, preliminary numerical simulations have suggested that any mixing at the shell–fuel boundary may result in an increase in secondary-neutron yield for a given ρR_{fuel}, meaning that the values in Fig. 83.17 could give us a value of ρR_{fuel} that is too high. For this reason, we will interpret our secondary-neutron-derived values of ρR_{fuel} as upper limits. Second, the results are slightly dependent on assumptions we make about temperature and density in the fuel. We know from neutron measurements that the ion temperatures are slightly higher than 3 keV; we assume the electron temperatures are the same. The mass density can't be determined directly, but we will find that the maximum possible value of ρR_{fuel} for these shots is about 18 mg/cm^2. This information can be used with the capsule dimensions and fill pressure to estimate that ρ is unlikely to exceed 10 g/cm^3. Inferred ρR_{fuel} increases slowly with increasing assumed ρ here, so using this upper limit on density will once again give us an upper limit on ρR_{fuel}. Since we don't know whether the radial profiles correspond more nearly to a uniform or hot-spot model, we can choose the larger results of the uniform model as an upper limit. Under these assumptions, we calculate upper limits on ρR_{fuel} in our four individual shots of 14 to 18 mg/cm^2, as listed in Table 83.I.

The measurements of Y_{2p}/Y_{1n} can also be used in conjunction with Fig. 83.17 to study ρR_{fuel}. In this case, there are reasons to interpret our results as lower limits. First, the values of Y_{2p}/Y_{1n} are very close to saturation. Second, preliminary work indicates that mixing at the shell–fuel boundary may sometimes result in a small decrease in secondary-proton yield for a given ρR_{fuel}, meaning that Fig. 83.17 could give us an inferred value of ρR_{fuel} that is too low. We therefore quote values from the hot-spot model (which gives lower numbers than the uniform model), using again the upper limit on ρ of 10 g/cm^3 (inferred ρR_{fuel} decreases slowly with increased assumed ρ here). The resulting lower limits for our shots fall in the interval from 6.3 to 8 mg/cm^2, as indicated in Table 83.I. These values are very similar to values for DT-filled capsules with similar shells and fill pressures, using CPS-measured spectra of knock-on particles.[10]

2. Energy Shift and ρR_{total}

The energy shift of a measured spectrum, relative to the birth spectrum, is due to proton slowing in both D fuel and CH shell. Figure 83.16 shows that the proton stopping powers normalized to ρ are almost the same for both D and CH, and in the vicinity of the birth energies of the protons there is little variation with plasma temperature for $T_e < 3$ keV. In addition, it will turn out that the shell ρR dominates the total ρR and that the amount of slowing down in the fuel is small. We therefore estimate ρR_{total} from the shift in mean energy by using the relationship for CH described in Fig. 83.23 and its caption, together with parameters appropriate for the shell. The result is weakly dependent on electron temperature and density in the shell, and we assume that $T_e = (1\pm0.5)$ keV and $\rho = (20\pm10)$ g/cm^3. These assumptions, together with the assumptions behind Fig. 83.23, lead to the inferred values of ρR_{total} shown in Table 83.I, which are all in the vicinity of 55 mg/cm^2. We note that this is similar to values measured for D-^{3}He–filled capsules and DT-filled capsules with similar shells and fill pressures.[9,10]

3. Future Improvements

Future data-interpretation work will involve more-detailed analytical and numerical modeling and the utilization of more information from proton spectra. The WFS-measured spectra for single shots are clean enough to allow detailed comparisons of spectrum shapes with model predictions. The important fact is that the combination of neutron and proton measurements provides a strong set of constraints that must be addressed in any complete model of the physics of capsule behavior.

Conclusions

We have shown the first detailed measurements of secondary-proton spectra from D_2-filled capsules in ICF experiments and demonstrated that charged-particle spectrometry can be used to provide useful diagnostic information about D_2-filled capsules in OMEGA. The energy downshift of a spectrum is directly related to the total areal density of the capsule, and the secondary-proton yield gives diagnostic information about fuel parameters such as the fuel areal density (especially in conjunction with primary- and secondary-neutron yields).

This first feasibility demonstration is particularly important because measurement of secondary-proton spectra may be the only diagnostic method for studying the areal densities of imploded, cryogenic D_2 capsules if ρR_{fuel} exceeds the limit for usefulness of secondary-neutron measurements (of the order of 0.1 g/cm^2, as shown in Figs. 83.17 and 83.24). It is expected that cryogenic, D_2-filled capsules will be imploded on OMEGA in the near future. Estimates of total areal densities, made from 1-D simulations, are as high as 0.2 to 0.3 g/cm^2. Under such circumstances, the measurement of secondary-proton spectra will still be possible with the techniques described here (and the increased yields will substantially decrease the statistical errors). This can be seen in Fig. 83.24, which

indicates the range of conditions under which the protons will escape the capsule and be measurable.

ACKNOWLEDGMENT

We thank Brock Bose for assistance in scanning CPS2 data. The work described in this article was performed in part at the LLE National Laser Users' Facility (NLUF) and was supported in part by U.S. Department of Energy Contract Number DE-FG03-99SF21782, LLE subcontract number PO410025G, LLNL subcontract number B313975, and the U.S. Department of Energy Office of Inertial Confinement Fusion under Cooperative Agreement No. DE-FC03-92SF19460. Part of this work was also performed under the auspices of the U.S. Department of Energy by University of California Lawrence Livermore National Laboratory under contract No. W-7405-Eng-48.

REFERENCES

1. H. D. Campbell and F. H. Southworth, in *1st Topical Meeting on the Technology of Controlled Nuclear Fusion* (American Nuclear Society, Hinsdale, IL, 1974), pp. 75–76.
2. E. G. Gamalii *et al.*, JETP Lett. **21**, 70 (1975).
3. S. Skupsky and S. Kacenjar, J. Appl. Phys. **52**, 2608 (1981).
4. T. E. Blue and D. B. Harris, Nucl. Sci. Eng. **77**, 463 (1981).
5. T. E. Blue *et al.*, J. Appl. Phys. **54**, 615 (1983).
6. H. Azechi *et al.*, Appl. Phys. Lett. **49**, 555 (1986).
7. H. Azechi, M. D. Cable, and R. O. Stapf, Laser Part. Beams **9**, 119 (1991).
8. M. D. Cable and S. P. Hatchett, J. Appl. Phys. **62**, 2233 (1987).
9. C. K. Li, D. G. Hicks, F. H. Séguin, J. A. Frenje, R. D. Petrasso, J. M. Soures, P. B. Radha, V. Yu. Glebov, C. Stoeckl, D. R. Harding, J. P. Knauer, R. L. Kremens, F. J. Marshall, D. D. Meyerhofer, S. Skupsky, S. Roberts, C. Sorce, T. C. Sangster, T. W. Philips, M. D. Cable, and R. J. Leeper, Phys. Plasmas **7**, 2578 (2000).
10. C. K. Li *et al.*, "Study of Direct-Drive, DT-Gas-Filled-Plastic-Capsule Implosions Using Nuclear Diagnostics on OMEGA," to be submitted to Physics of Plasmas.
11. T. R. Boehly, D. L. Brown, R. S. Craxton, R. L. Keck, J. P. Knauer, J. H. Kelly, T. J. Kessler, S. A. Kumpan, S. J. Loucks, S. A. Letzring, F. J. Marshall, R. L. McCrory, S. F. B. Morse, W. Seka, J. M. Soures, and C. P. Verdon, Opt. Commun. **133**, 495 (1997).
12. R. D. Petrasso, C. K. Li, M. D. Cable, S. M. Pollaine, S. W. Haan, T. P. Bernat, J. D. Kilkenny, S. Cremer, J. P. Knauer, C. P. Verdon, and R. L. Kremens, Phys. Rev. Lett. **77**, 2718 (1996).
13. C. K. Li and R. D. Petrasso, Phys. Rev. Lett. **70**, 3059 (1993).
14. S. Glasstone and R. H. Lovberg, *Controlled Thermonuclear Reactions: An Introduction to Theory and Experiment* (Van Nostrand, Princeton, NJ, 1960), Chap. 2.
15. F. J. Marshall, J. A. Delettrez, R. Epstein, V. Yu. Glebov, D. R. Harding, P. W. McKenty, D. D. Meyerhofer, P. B. Radha, W. Seka, S. Skupsky, V. A. Smalyuk, J. M. Soures, C. Stoeckl, R. P. Town, B. Yaakobi, C. K. Li, F. H. Séguin, D. G. Hicks, and R. D. Petrasso, Phys. Plasmas **7**, 2108 (2000).
16. D. G. Hicks, "Charged Particle Spectroscopy: A New Window on Inertial Confinement Fusion," Ph.D. thesis, Massachusetts Institute of Technology, 1999.
17. D. G. Hicks, C. K. Li, R. D. Petrasso, F. H. Séguin, B. E. Burke, J. P. Knauer, S. Cremer, R. L. Kremens, M. D. Cable, and T. W. Phillips, Rev. Sci. Instrum. **68**, 589 (1997).
18. F. H. Séguin *et al.*, "A Proton Spectrometer Based on a Wedge-Shaped Range Filter and CR-39 Nuclear Track Detectors," to be submitted to Review of Scientific Instruments.
19. J. A. Frenje *et al.*, "Charged Particle Measurements in DD, D^{3}He, and DT Implosions at the OMEGA Laser Facility Using Diagnostic Techniques Based on CR-39 Track Detection," to be submitted to Review of Scientific Instruments.
20. S. Skupsky and R. S. Craxton, Phys. Plasmas **6**, 2157 (1999).
21. D. G. Hicks *et al.*, "Charged-Particle Acceleration and Energy Loss in Laser-Produced Plasmas," to be published in Physics of Plasmas.
22. P. B. Radha, J. A. Delettrez, R. Epstein, S. Skupsky, J. M. Soures, S. Cremer, and R. D. Petrasso, Bull. Am. Phys. Soc. **44**, 194 (1999).

Comparison of a Liquid Crystal Point-Diffraction Interferometer and a Commercial Phase-Shifting Interferometer

Introduction

Fusion-class lasers, such as OMEGA, typically require hundreds, or even thousands, of high-performance optical elements ranging in diameter from several millimeters to tens of centimeters. To obtain high irradiation uniformity required for direct-drive ICF, it is critical that (1) the optical performance of these elements and associated optical subsystems be well characterized before being installed in the laser, and (2) their high performance be maintained throughout their lifetime in the laser system. Commercially available Fizeau phase-shifting interferometers[1] with aperture sizes of between 4 and 18 in. have been used to characterize the laser beam wavefront before optical elements are installed on OMEGA. Although these interferometers have high sensitivity, their expense and susceptibility of the measurement to environmental disturbance scale significantly with aperture size. Once optical elements are installed into OMEGA, wavefront characterization of OMEGA beamlines is performed at $\lambda = 1054$ nm with a shearing interferometer,[2] but the method suffers from (1) an inability to perform gradient measurements in more than two directions, (2) a sensitivity to only low-order phase errors, and (3) low spatial resolution. We have investigated the use of a phase-shifting, point-diffraction interferometer (PDI) both as a replacement to the shearing interferometer and as a low-cost alternative to commercially available phase-shifting interferometers.

The PDI[3,4] is an elegantly simple device that consists of a pinhole, upon which a laser beam under test is focused, and a region of high optical density surrounding the pinhole, which is used to attenuate a portion of the incident beam. Light diffracted from the pinhole generates a reference wavefront, while light that propagates around the pinhole is the object beam under test. Interference fringes of high contrast are obtained by attenuating the object beam such that object and reference beam intensities are nearly equal. A distinct advantage of the PDI design is its truly common-path nature, i.e., both object and reference beams follow the same path as opposed to two different paths, such as in the Mach–Zehnder, Michelson, or Fizeau interferometers.[5] This attribute makes the PDI an attractive alternative to other interferometers for several reasons: (1) sensitivity to environmental disturbances such as mechanical vibration, temperature fluctuations, and air turbulence is reduced; (2) very short coherence length lasers can be used, without the need for path-length-adjusting optics to maintain high fringe visibility; and (3) fewer optical elements are required, reducing the size and cost of the instrument. Several modifications of the PDI to incorporate the phase-shifting technique are described in the literature;[6] however, the liquid crystal point-diffraction interferometer (LCPDI), introduced by Mercer and Creath,[7,8] is particularly attractive because of its simplicity, ease of use, and low manufacturing cost. The LCPDI maintains the advantages of the standard PDI, while providing an ability to phase-shift the object beam wavefront relative to the reference wavefront. It is a modification of the PDI, where the pinhole that generates the reference wavefront is replaced by a glass or plastic microsphere that is embedded within a nematic liquid crystalline "host" (see Fig. 83.29). A voltage applied to the liquid crystal (LC) cell

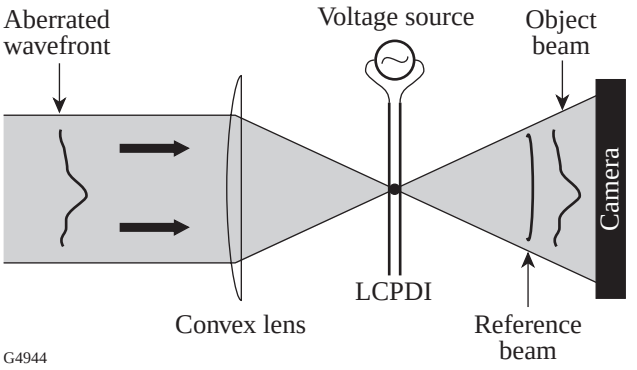

Figure 83.29
Schematic diagram of the liquid crystal point-diffraction interferometer (LCPDI). The laser beam is focused onto an area of the device containing a glass or plastic microsphere in the LC fluid gap that takes the place of the pinhole in the standard point-diffraction interferometer (PDI). The portion of the beam passing through the microsphere forms the reference wavefront of the interferometer, and light passing around the microsphere forms the object beam under test. Phase-shifting is accomplished through the application of an electric field to the LCPDI, as described in Fig. 83.30.

causes a phase shift of the object beam relative to the diffracted reference beam by an effective refractive index change of the LC. A "guest" dye that is added to the liquid crystalline host improves fringe contrast by attenuating the object beam intensity. Notably, the phase-shifting LCPDI was shown by Mercer and Rashidnia to be significantly more robust when compared with a phase-shifting Mach–Zehnder interferometer.[9]

We compared a visible-wavelength LCPDI to a commercially available, Mark IV XP Fizeau phase-shifting interferometer[10] and found that LCPDI measurements of a witness sample were in close agreement with measurements of the same sample made using the commercially available interferometer. Two systematic, phase-shift error sources in the LCPDI that contributed to measurement discrepancies were (1) an intensity modulation from frame to frame caused by the dichroism of the dye[8] and, to a lesser extent, (2) molecular alignment distortions of the host liquid crystal around the microsphere.[11] These phase-shift errors currently produce a spatially dependent accuracy in the LCPDI that, in some regions, closely compares with the Mark IV, but departs from the Mark IV measurements by approximately 50 nm in regions of highest systematic error. A smaller departure of the measurement from that of the Mark IV at higher spatial frequencies was due to interference effects caused by residual reflections between the CCD array and the final imaging lens. By modifying LCPDI fabrication parameters and through judicious choice of phase acquisition and analysis methods, these systematic errors can be significantly reduced.

LCPDI Construction

LCPDI cells were fabricated with liquid crystal Merck E7, a eutectic composition of rodlike molecules that has a nematic phase at room temperature. The long axes of the molecules in the nematic phase have a preferred orientation characterized by a unit vector called the *director*. A thin film of nylon or polyimide was applied to the inner surfaces of indium-tin oxide (ITO)–coated glass substrates and subsequently buffed unidirectionally, causing the director to preferentially lie in the plane of the substrates. Long-range orientational order, which is homogeneous and coincides with the direction of the crystal optic axis, is thereby imparted to the molecules. The means by which the LCPDI phase shifts is shown conceptually in Fig. 83.30. For a homogeneously aligned nematic LC with molecular axis parallel to the cell walls, linearly polarized light along the long axis of the molecule in Fig. 83.30 will see extraordinary refractive index n_e. As voltage is applied to the cell, the LC molecules will reorient, as shown. The effective refractive index approaches the value of the ordinary refractive index n_o when the molecules in the bulk of the fluid are nearly perpendicular to the cell walls. Cell parameters that determine the maximum phase shift are primarily the LC birefringence and fluid path length, assuming that the microsphere diameter and fluid path length are equal. If the microsphere diameter is less than the path length of the cell, phase modulation will be less. In addition, strong anchoring of interfacial LC molecules to the cell walls prevents complete reorientation of the director throughout the fluid path length, resulting in an effective refractive index that is somewhat less than n_o.

Fluid path lengths and microsphere diameters of either 10 or 20 μm were used, and cell gap was maintained by placement of fiber spacers or glass microspheres at the outer edges of the cell. The use of fiber spacers instead of glass microspheres at the corners of the device improved cell gap uniformity and reduced wedge across the clear aperture of the LCPDI device. Glass substrates, 2.4 cm × 2.8 cm × 1 mm thick, had inner walls that were coated with electrically conductive ITO prior to application of the alignment layer. We determined that in this application polyimide alignment layers offer an advantage over nylon layers because (1) they are more resistant to scratches that can be produced while manipulating the microspheres during assembly, and (2) they are easier to spin-deposit and buff, yielding devices with higher alignment

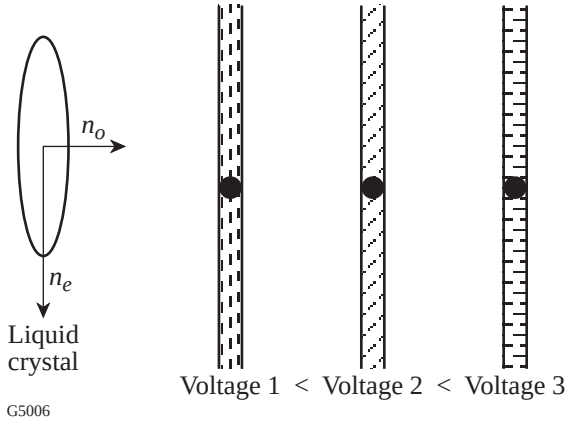

Figure 83.30
An electric field applied to the LCPDI produces a controlled reorientation of the birefringent LC molecules, thereby shifting the phase of the object wavefront relative to the reference wavefront. Light that is polarized along the buff direction of the cell will first see extraordinary refractive index n_e, followed by refractive index values approaching the ordinary refractive index n_o as voltage is applied. Attenuation of the object beam intensity by adding a "guest" dye to the LC fluid "host" allows high-contrast fringes to be obtained.

quality and contrast. Antiparallel buffing on opposing substrate surfaces generally provided better alignment quality than parallel-buffed surfaces. Bonding the wire leads to the devices with conductive epoxy *before* rather than after filling with LC eliminated the infiltration of air into the devices caused by the expansion and contraction of the fluid-filled cell during the epoxy thermal cure process. Visible-wavelength absorbing dye, Oil Red O, at 1% wt/wt concentration, was used for the device designed to operate at $\lambda = 543$ nm and produced an optical density of 2.1 in a 10-μm-path-length cell with no voltage applied. The blocking extinction, or optical density (OD), of this cell at $\lambda = 543$ nm with light polarized along the buffing direction as a function of applied voltage is shown in Fig. 83.31. Because of the absorption dichroism of the dye, the OD of the cell varied between 2.1 and 0.8 as voltage was raised from 0 to 6 V (rms) using a 2-kHz sine wave.

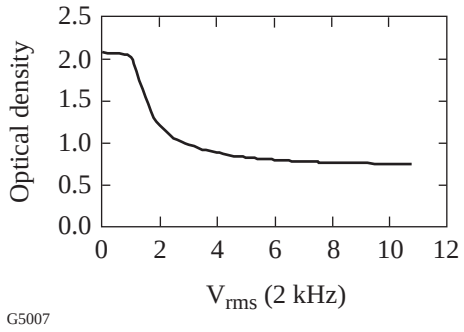

Figure 83.31
Absorbance at $\lambda = 543$ nm of the LCPDI with 1% wt/wt concentration of Oil Red O dye in the nematic E7 host LC as a funtion of voltage applied to the device. The dichroism of the dye produces voltage-dependent changes in fringe intensity and contrast.

Microspheres were placed in the cell using one of two different techniques: In the first method, a large quantity of microspheres were spin deposited onto one of the substrate surfaces before the cell was assembled. This ensured that a microsphere could later be found that would phase modulate satisfactorily upon optical testing and was quite easy to do compared with the manual deposition technique described below. A disadvantage of this approach is the possibility of microsphere agglomeration resulting in optical interference from adjacent microspheres during device testing. The current device assembly protocol calls for a single microsphere to be placed manually in the center of the substrate using a high-power microscope. In this method, the sphere is positioned using a single fiber from a camel's-hair brush. Custom assembly tooling helps to keep the two substrates in registration with each other as they are lowered to help eliminate the scratching of the alignment coating caused by microsphere displacement when the substrates are inadvertently sheared. We have found that the use of glass microspheres rather than plastic ones as the central element reduces the number of scratches in the alignment coating caused by movement of the central sphere during device assembly operations. Plastic spheres also had a slightly elliptical appearance in some cells and showed a uniaxial conoscopic figure, likely due to stress-induced birefringence imparted by the substrates during cell fabrication and epoxy cure. The custom tooling used to maintain substrate registration remedied this by preventing excessive force from being applied during the assembly operation.

Test Sample Measurements

The LCPDI cell used for these measurements had a glass microsphere diameter and fluid gap of 10 μm and was placed in the experimental setup shown in Fig. 83.32. The $\lambda = 543$-nm HeNe laser beam was spatially filtered and up-collimated to slightly overfill a 1-in.-diam *f*/16 doublet lens used to focus the beam into the LCPDI. A Tamron SP60 300-mm telephoto zoom lens was used to image the cavity region to the CCD camera. The beam diameter at the focus of the doublet was 41 μm at $1/e^2$ of peak intensity, as measured with a scanning slit. The intensity onto the LCPDI was adjusted, and linear polarization was maintained along the extraordinary axis of the LC by using two polarizers placed before the spatial filter. Fringe data were acquired through a sequence of five images, each shifted incrementally in phase by a relative amount $\pi/2$, and resultant phase ϕ computed using the five-frame algorithm[8,12,13]

$$\tan(\phi) = \left(\frac{\Delta I_3 - \Delta I_1}{\Delta I_0 + \Delta I_4 - 2\Delta I_2} \right) \times \left(\frac{\sqrt{I_0^{\text{obj}}} + \sqrt{I_4^{\text{obj}}} + 2\sqrt{I_2^{\text{obj}}}}{\sqrt{I_3^{\text{obj}}} + \sqrt{I_1^{\text{obj}}}} \right), \quad (1)$$

where I_k^{obj} is the kth object beam intensity distribution and $\Delta I_k = I_k - I_k^{\text{obj}}$ is the kth interferogram in the five-frame sequence. Equation (1) is normalized to the intensity distribution of the object beam in order to reduce the effect of intensity and contrast changes caused by the dichroism of the dye, as described by Mercer.[8] The object beam intensity was obtained by moving the LCPDI a short distance laterally so that the incident beam did not intersect the microsphere and by acquiring five frames of data at the same voltages used for acquiring interferometric phase data. Table 83.II gives a relative com-

parison of several different phase unwrapping algorithms that were tested with intentionally noisy data (i.e., low-contrast fringes with focus at the microsphere) in order to compare the robustness of the various unwrapping algorithms. In Table 83.II, the relative processing speed of these algorithms is compared to a simple path-dependent, linear algorithm that began at the edge of the CCD array and propagated unacceptably large unwrapping errors throughout the array. The large residual errors for the algorithms listed in the table are primarily from unwrapping errors at the edge of the CCD array. Although a tiled, path-dependent unwrapping algorithm that began in the center of the array, combined with a masking technique, produced the least phase error, the tiled algorithm was chosen without masking because it required significantly less processing time and had only marginally greater residual error. Data acquisition was automated using a personal computer, in-house data acquisition and analysis software, and graphical user interface. With no test sample in the cavity region between the collimating lens and the focusing doublet, several focus and voltage conditions were investigated, as described in Table 83.III. The least amount of residual phase error in empty cavity measurements was found in the low-voltage regime (<1.2-V rms at 2 kHz) with 3 to 4 fringes on the camera. Greater phase error was observed in the high-voltage regime (3.8 to 7 V) because of the loss of fringe contrast caused by the absorption dichroism of the dye.

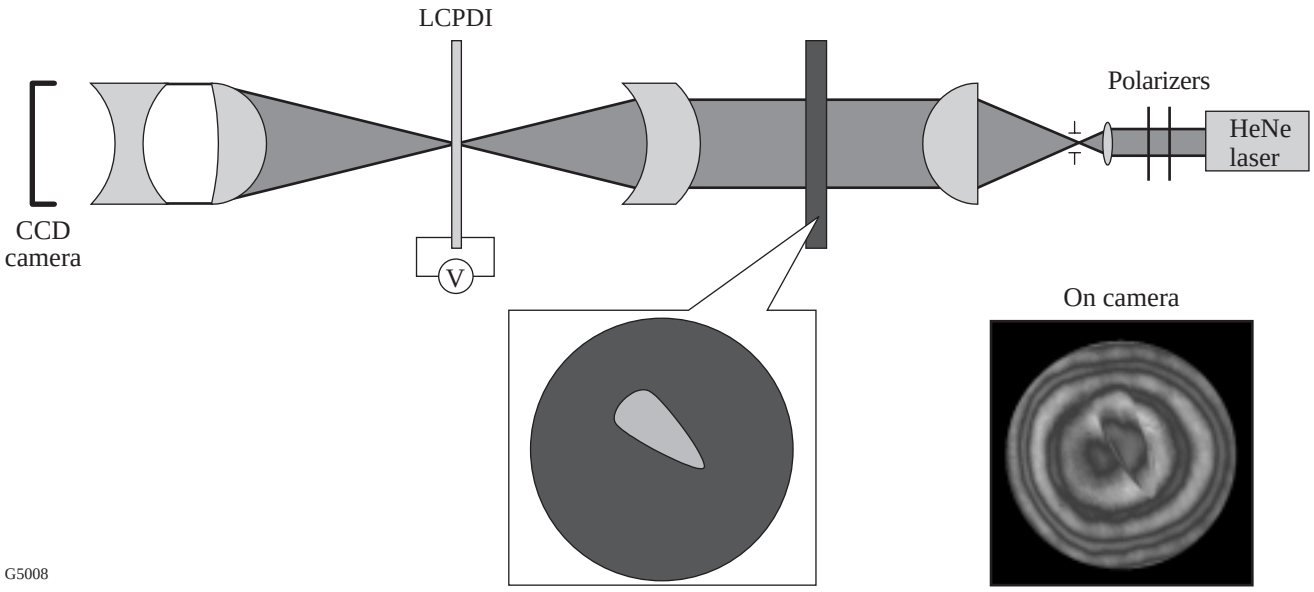

Figure 83.32
Experimental setup used for LCPDI measurements. The inset shows interference fringes from the test sample with an MRF-polished spot.

Table 83.II: Relative comparison of different unwrapping algorithms with intentionally noisy data (low-contrast fringes). Among the algorithms tested, the tile unwrapping algorithms showed the least number of unwrapping errors. The tile unwrapping algorithm with a tile size of 10×10 pixels was used for the experimental results reported.

	Centered Linear, Path Dependent	Box Mask and Linear, Path Independent	Tile Unwrap	Tile Unwrap and Box Mask
p–v (2π rad)	9.07	3.23	2.77	2.670
rms (2π rad)	0.45	0.13	0.10	0.094
Computation time (compared to standard unwrap starting at edge of array)	1:1	3:1	5:2	4:1

To characterize the empty cavity, two sets of ten phase measurements were taken approximately 5 min apart, the ten measurements averaged, and the two sets of phase averages subtracted to give residual peak-to-valley (p–v) and rms phase errors of 22 nm and 1.7 nm, respectively, as shown in Fig. 83.33. The quality of the interference fringes used for the five-frame sequence is shown in Fig. 83.33(a). As evident from the horizontal lineout in Fig. 83.33(b), a residual amount of tilt is present in the phase difference. With tilt removed, p–v and rms phase errors drop to 19 nm and 1.1 nm, respectively. The dominant phase error in Fig. 83.33(b) has a spatial period equal to that of the interference fringes, suggesting that the effect of the dye has not been entirely eliminated through the use of Eq. (1). Also apparent in the phase image is an error term equal to twice the frequency of the fringes, indicating that there is some amount of phase-shift error related to the host LC in addition to the dye-induced error. Because these systematic error sources are present, their removal through subtraction of a reference phase requires stringent control of environmental parameters. Although air turbulence was reduced by placing a plastic enclosure around the setup in Fig. 83.32, the setup was not supported by an air-isolation table and was located in a

Table 83.III: Several focus and voltage conditions were investigated for the LCPDI in empty-cavity measurements.

Focus	– Close to best focus (1 to 2 fringes) – Intermediate focus position (3 to 4 fringes) – Far from best focus (8 to 9 fringes) - Off center (lateral movement of the LCPDI) - On center (no lateral movement)
Voltage (rms at 2 kHz)	– Low-voltage regime (0–1.21 V) – High-voltage regime (3.8–7 V)

Conditions giving least residual phase error: intermediate focus with low-voltage regime.

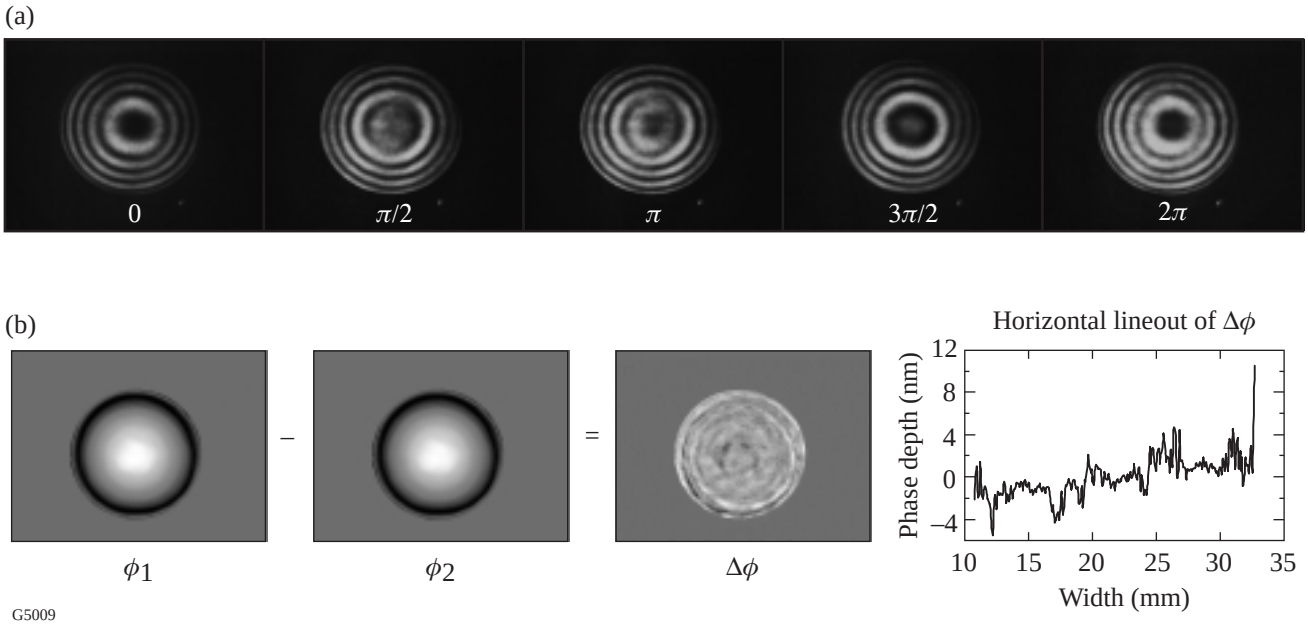

Figure 83.33
(a) LCPDI interference fringes obtained by phase-shifting through 2π rad, from 0.98 V (0) to 1.21 V (2π). (b) Two empty-cavity phase images ϕ_1 and ϕ_2 were subtracted to obtain the residual phase error $\Delta\phi$ in the LCPDI. The phase-difference image reveals phase-error contribution from both dye- and host-induced phase-shift error.

room without strict air-handling requirements. It is expected that more rigorous environmental standards and improvements to LCPDI packaging and mounting will significantly improve its precision. Further improvements to both accuracy and precision of the LCPDI can be achieved through removal or mitigation of systematic error sources, as discussed below.

A test object was next inserted into the cavity that consisted of a 2-in.-diam × 0.25-in.-thick fused-silica wedged window with a central "spot" polished into the window using the magnetorheological finishing method (MRF).[14] The geometry of the polished spot is characteristic of this technique and was well suited for this test because of the co-existence of steep and gradual gradient features (see Fig. 83.32). An empty-cavity phase measurement was subtracted from the phase measurement of the test object for all measurements reported here. In contrast to the empty-cavity measurements described previously, however, acquisition of both the test object phase and associated reference phase incorporated a $\pi/2$ phase-offset technique[12] that reduced residual phase-shift errors at twice the fringe frequency that were apparent in initial measurements of the test piece. In this method, ten phase measurements were acquired per Eq. (1) and averaged, followed by an additional set of ten phase measurements acquired with the first frame of the five-frame sequence offset in phase by $\pi/2$. Averaging the first set of ten measurements with the set of measurements acquired with $\pi/2$ offset produced the phase plot shown in Fig. 83.34. This figure shows that the LCPDI results are in close agreement with those from a 4-in.-aperture Zygo Mark IV XP operating at $\lambda = 633$ nm and located on an air-supported table in the Center for Optics Manufacturing (COM). The close comparison of the high gradient features on the left of the lineout is especially notable. The large peak on the right of the LCPDI lineout appears to approach a discrepancy of 100 nm, but it is near the edge of the aperture, where a valid comparison cannot be made because of the absence of Mark IV XP data. The remaining discrepancies on the right of the lineout are attributed to the following sources: (1) Phase-shift errors likely related to the dichroism of the dye produced an approximately 50-nm residual phase error at the same spatial frequency as the fringe pattern, which can be seen in the LCPDI phase image in Fig. 83.34. (2) The high-spatial-frequency ripple in the LCPDI lineout of Fig. 83.34 was caused by an interference pattern observed during data acquisition whose origin appeared to be multiple reflections between the zoom lens and the CCD array. (3) To a lesser extent, alignment distortions of the host LC molecules may also contribute residual phase-shift error, as discussed below. As noted previously, accounting for object beam intensity changes through the use of Eq. (1) has not completely removed the phase error related to the absorption dichroism of the dye. The phase-offset method, however, reduced the appearance of LC host-induced phase-shift errors at twice the fringe frequency, although higher-order phase-shift error not compensated using this technique may still be present.[15] Because the dominant error has periodicity equal to the interference fringes, the current LCPDI device incorporating the highly dichroic Oil Red O dye would be most useful for characterizing aberrations whose Zernike fit is not significantly affected by the presence of this error.

Discussion

1. Dye-Induced Measurement Error

The predominant phase error in Fig. 83.34 has a periodicity equal to that of the interference fringes, indicating that its most likely origin is an intensity change between phase shifts caused by absorption dichroism of the Oil Red O dye.[8] The use of Eq. (1) significantly reduces the contribution of this effect to the phase error but does not eliminate it entirely. Equation (1) is exact provided that (1) the reference beam

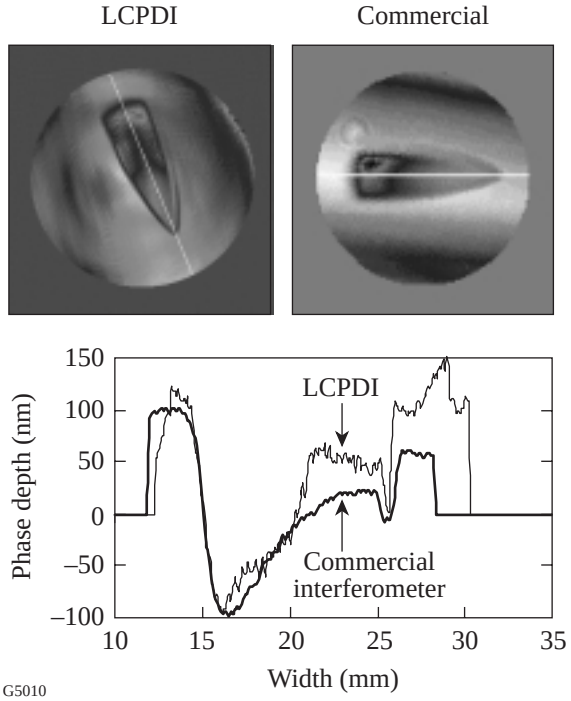

Figure 83.34
Phase measurements of a wedged window containing an MRF polishing spot comparing the LCPDI to a commercial interferometer (Zygo Mark IV XP). The LCPDI lineout matches that of the Zygo Mark IV in some areas and is ≤50 nm discrepant in other areas primarily due to the absorption dichroism of the dye used.

intensity remains constant with applied voltage and (2) the object beam intensity can be accurately measured. Although the object beam intensity is fairly well approximated using the procedure described above, a ray-trace model has shown that the intensity of the reference beam changes with voltage applied to the cell.[16,17] This model has also indicated that refraction through the microsphere cannot produce sufficient intensity in the reference beam to obtain the experimentally observed high fringe contrast, and diffraction must also be considered.[17] This suggests that by measuring fringe contrast and object-beam-intensity changes with voltage, it may be possible to accurately account for changes in reference beam intensity and thereby further reduce the phase error contributed by the absorption dichroism of the dye. Nonetheless, frame-to-frame absorbance changes in the LCPDI can be substantially reduced through the use of either a non-dichroic dye or a mixture of both positive and negative dichroic dyes. In Fig. 83.35, the absorbance as a function of wavelength for two such positive and negative dichroic dye combinations in E7 is shown for different voltages applied to the cell.[18] Figure 83.35(a) shows that when the Oil Red O dye, having positive dichroism, was combined with a negative dichroic Orasol dye mixture, the OD at 543 nm in a 22-μm-path cell changed by only 0.03 as the voltage was increased from 0 to 5-V rms. This result represents a factor-of-40 improvement compared with absorbance changes observed in the cell with the single dye component Oil Red O (compare with Fig. 83.31). An Orasol/Sudan dye mixture in Fig. 83.35(b) showed a change in OD of only 0.08 as voltage changed by 9-V rms. These results are summarized in Table 83.IV. We are currently in the process of purifying the Orasol dyes in order to reduce ionic conduction in the LC that has contributed to hydrodynamic-induced scattering observed in devices made with the new dye mixtures. Because the molecular structure of the Orasol dyes is not well known, the effect of these dyes on the long-range orientational order of the LC is currently unknown. Other visible-wavelength dye candidates with negative absorption dichroism that are expected to minimally perturb the liquid crystalline order parameter have also recently been identified.[19] For applications at λ = 1054 nm, LCPDI's fabricated using recently synthesized nickel dithiolene dyes with various terminal functional groups[20] also show significantly less intensity change as a function of voltage applied to the cell. It is anticipated that appropriate combinations of purified positive and negative dichroic dyes will substantially reduce, or even eliminate, the primary source of systematic error in the LCPDI.

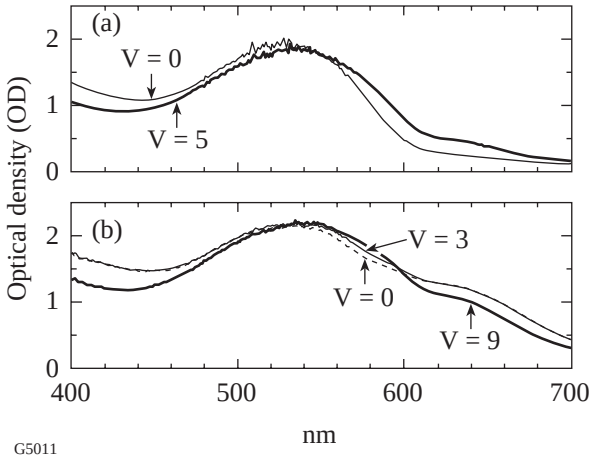

Figure 83.35
Absorbance (OD) of two different dye mixtures containing both positive and negative dichroic dye components in E7 shows very little change with applied voltage. Such mixtures can be used to significantly reduce phase-shift error in the LCPDI caused by the absorption dichroism of a single dye. (a) 1.3% Orasol Red BL, 0.55% Orasol Black RLI, + Oil Red O; (b) 1.3% Orasol Red BL, 0.55% Orasol Black RLI + 0.2% Sudan III, 0.38% Sudan Black B. In each case fluid path length was 22 μm.

2. LC Host-Induced Measurement Error

Although the long-range orientational order of the LC is homogeneous and planar, we have observed a distortion in the molecular alignment locally around the microsphere that is voltage dependent and can lead to phase-shift errors.[11] This alignment distortion is caused by a competition between anchoring forces on the surface of the sphere, the cell walls, and elastic forces of the LC.[21] Viewed through a polarizing microscope with 100× magnification, the liquid crystal alignment around the microsphere has the appearance shown in Fig. 83.36. These images are of a 10-μm-diam silica micro-

Table 83.IV: Absorbance (OD) at 543 nm.

V (rms at 2 kHz)	Mixture A	Mixture B
0	1.854	2.13
1	–	–
3	–	2.2
5	1.823	–
9	–	2.21
A = 1.3% Orasol Red BL, 0.55% Orasol Black RLI, + ORO		
B = 1.3% Orasol Red BL, 0.55% Orasol Black RLI + 0.2% Sudan III, 0.38% Sudan Black B		

sphere within the 10-μm path cell of E7 with 1% wt/wt Oil Red O dye used for the comparison tests described in the previous section. The alignment perturbation has quadrupolar symmetry, most apparent at intermediate rms voltages (2.38 V and 3.9 V in Fig. 83.36). The buff direction of the cell can be seen as oriented diagonally from the lower left to the upper right of these images. Regions of director distortion that have the appearance of large "ears" and extend outward from the sphere in the buff direction can also be seen in these images. This alignment distortion is enhanced in a thicker, 20-μm path cell with 20-μm-diam glass microspheres, shown in Fig. 83.37. In the thicker cell, the planar anchoring force of the substrate walls has less effect in the bulk of the fluid, and the alignment perturbation at intermediate voltages is more pronounced than in the 10-μm path cell. The director distortion appearing as large ears in these images again extends parallel to the buff direction. In Figs. 83.36 and 83.37, the increased electric-field strength encountered at higher voltages imparts sufficient torque to the molecules to overcome the competing surface-anchoring forces and elastic distortions of the liquid crystal, and the perturbation becomes less severe.

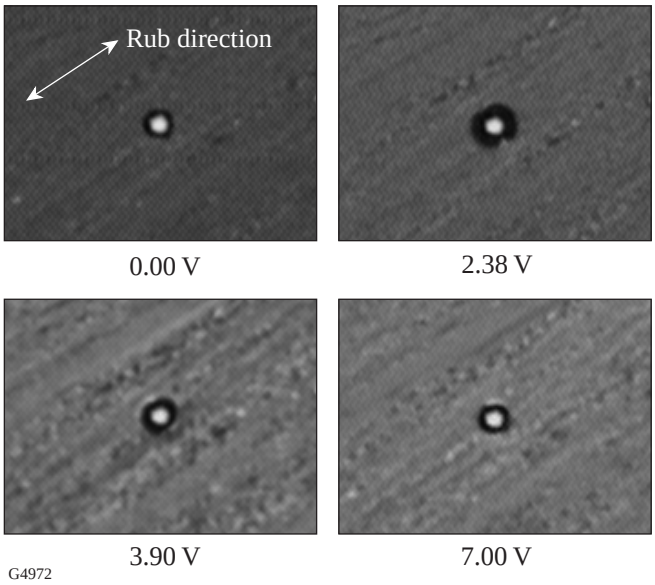

Figure 83.36
Polarizing microscope images of a 10-μm silica microsphere in 10-μm-path E7 host showing the quadrupolar alignment perturbation of the nematic director around the microsphere. This alignment perturbation produces a phase-shift error in the LCPDI that is dependent upon focusing conditions and the voltage applied to the cell. The quadrupolar symmetry is greatest at intermediate voltages, gradually becoming more circular with increasing electric-field strength. Voltage waveform was a 2-kHz sine wave.

The structures observed in Figs. 83.36 and 83.37 are similar to those described by other authors in the context of colloidal suspensions in nematic solvents[22,23] and inverted nematic emulsions.[21,24] The existence of planar or normal anchoring of the director to the sphere's surface plays a critical role in determining the director field configuration around the sphere[21] as does the anchoring strength.[25] For strong anchoring conditions, topological defects are known to form at the sphere's surface in addition to director distortions in the region surrounding the sphere.[21] With no voltage applied to the cell in Fig. 83.37, two such surface defects can be seen at the poles of the spheres that are diametrically opposed in a direction orthogonal to the long-range orientational order imposed by the substrates. We observed that altering the procedure by which the microspheres were applied to the surface of the substrates changed the topological orientation of the defects. In the images of Figs. 83.36 and 83.37, spheres were spin-deposited in a high-performance liquid chromatography-grade hexane solution onto one of the substrates, and the hexane was allowed to evaporate before the cells were filled with liquid crystal *via* capillary action. The alignment of the defects orthogonal to the rub direction of the substrates and the concomitant quadrupolar symmetry around the microsphere resemble structures characteristic of weak normal anchoring.[25] When a manual deposition method was used without hexane, however, the two surface defects appeared *along* the rub direction, providing evidence of planar anchoring at the surface of the sphere.[21] The change in anchoring conditions is

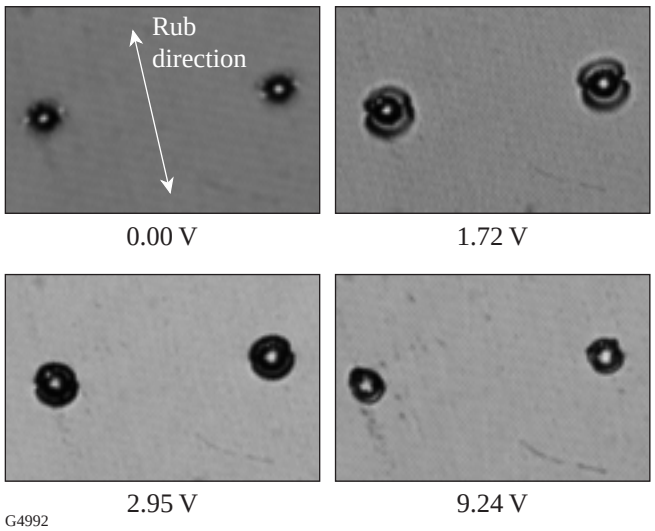

Figure 83.37
Polarizing microscope images of a 20-μm silica microsphere in 20-μm-path E7 host. The alignment distortion is enhanced, compared with the thinner LC cell of Fig. 83.36. Voltage waveform was the same as in Fig. 83.36

likely related to trace impurities that remained on the surface of the sphere after solvent evaporation since no attempt was made to further purify the hexane prior to use.

The effect of the quadrupolar alignment around the microsphere on a laser beam, when focussed close to the sphere, is clearly seen in Fig. 83.38. These interference fringes were obtained by using the setup shown in Fig. 83.32, and the small diffraction rings in Fig. 83.38 are from the final telephoto imaging lens. No measurable amount of light was observed to couple into the orthogonal polarization due to localized director distortions. Because the dye molecules rotate with the liquid crystal molecules, the dichroism of the Oil Red O dye in this cell may also have a contributing effect on the intensity and contrast changes observed. Focusing at a greater distance from the sphere produced fringes where the quadrupolar symmetry was less evident, as shown in Fig. 83.39. The loss of contrast caused by lower dye absorption of the object beam intensity can be clearly seen at 7.17 V in Fig. 83.39. As in Figs. 83.36 and 83.37, the effect of director distortions on the fringes in Figs. 83.38 and 83.39 is greatest at intermediate voltages. As the size of the Airy disk becomes increasingly larger compared with the size of the diffracting region, the reference wavefront becomes increasingly spherical,[8] with the optimum focusing condition for this device shown in Fig. 83.33(a).

These director distortions produce a phase-shift error that is both spatially nonuniform and nonlinear and can contribute significant residual phase error when the focus is placed very close to the microsphere. We have investigated the use of phase-shift algorithms designed for nonlinear and spatially nonuniform phase shifts, such as described by Hibino *et al.*,[26] to reduce these errors in the LCPDI. As described below, a six-frame algorithm designed to reduce the contribution of higher-order nonlinearity in the phase shift generally did not experimentally produce lower residual phase error than the five-frame algorithm produced. To explore the cause of this result, we have empirically derived a general form of the LCPDI phase-shift error with which we have compared the ability of each algorithm to reduce the contribution of director distortions to the phase measurement. A comparison of the residual phase error produced using these two algorithms in the absence of absorption dichroism was performed by subtracting a reference phase image created using error-free simulated fringes from the simulated phase image generated using the empirically derived phase-shift error.

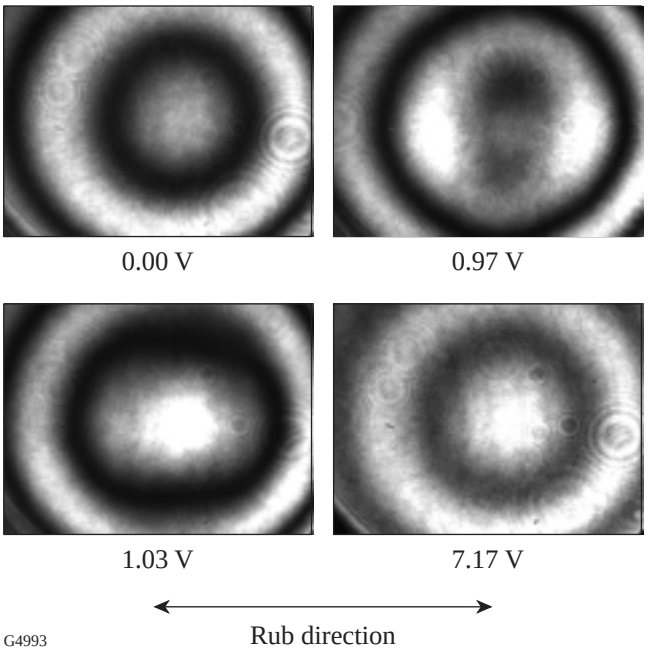

Figure 83.38
Interference fringes obtained by focusing a 543-nm laser beam at *f*/16 into the LCPDI of Fig. 83.36, revealing the effect of director distortions having quadrupolar symmetry.

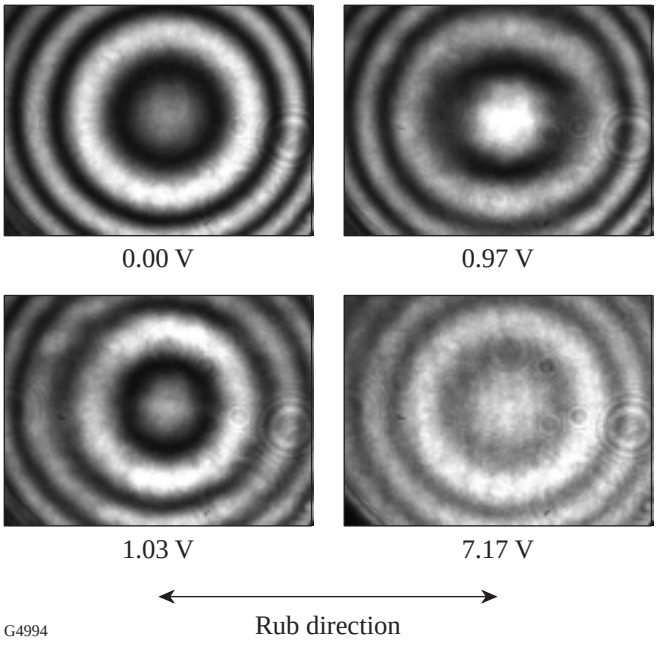

Figure 83.39
Interference fringes as in Fig. 83.38, but with displaced focal position. Quadrupolar symmetry is less evident at intermediate voltages than in Fig. 83.38. Loss of contrast due to dichroism of the Oil Red O dye molecules is observed at high voltage.

Neglecting frame-to-frame intensity and contrast changes, the intensity $I(x,y,\alpha_r)$ of each frame of data can be written as

$$I(x,y,\alpha_r) = I_0(x,y)\{1+\gamma(x,y)\cos[\alpha_r - \phi(x,y)]\}$$

$$\text{for } r = 1, 2, \ldots, m, \tag{2}$$

where $I_0(x,y)$ is the mean intensity, γ is the interference fringe visibility, α_r is the phase shift at each discrete frame r, ϕ is the phase of the wavefront being measured, and m is the total number of frames. Here the phase-shift parameter α_r is spatially nonuniform and changes nonlinearly from frame to frame. Following Ref. 26, α_r can be given by a polynomial expansion of the unperturbed phase-shift value α_{0r} as

$$\alpha_r = \alpha_{0r}[1+\varepsilon(\alpha_{0r})]$$

$$= \alpha_{0r}\left[1+\varepsilon_1(x,y)+\varepsilon_2(x,y)\frac{\alpha_{0r}}{\pi}+\varepsilon_3(x,y)\left(\frac{\alpha_{0r}}{\pi}\right)^2\right.$$

$$\left.+\ldots+\varepsilon_p(x,y)\left(\frac{\alpha_{0r}}{\pi}\right)^{p-1}\right]$$

$$\text{for } r = 1, 2, \ldots m, \tag{3}$$

where p ($p \le m-1$) is the maximum order of the nonlinearity, ε_q ($1 \le q \le p$) are the error coefficients, which can be spatially nonuniform, and $\alpha_{0r} = 2\pi[r-(m+1)/2]/n$ is the unperturbed phase shift with n equal to an integer. For the five-frame algorithm in Eq. (1), for example, $m = 5$, $n = 4$, and the unperturbed phase shifts are therefore

$$\begin{aligned}
\alpha_{01} &= -\pi, \\
\alpha_{02} &= -\pi/2, \\
\alpha_{03} &= 0, \\
\alpha_{04} &= \pi/2, \\
\alpha_{05} &= \pi.
\end{aligned} \tag{4}$$

The offset value $(m + 1)/2$ was introduced in Ref. 26 for convenience of notation and adds only a spatially uniform piston term to the calculated phase when no phase-shift error is introduced. In the simulation that follows, the functional form of the phase-shift error and the starting phase value were chosen to closely represent the experimentally observed phase-shift error. Equation (1) can correct for linear phase-shifter miscalibration (i.e., $p = 1$) that is spatially nonuniform but is sensitive to the effect of spatial nonuniformity for higher orders of phase-shift error.[26] The six-frame algorithm [Eq. (39)][26] given by

$$\tan\phi = \frac{\sqrt{3}(5I_1 - 6I_2 - 17I_3 + 17I_4 + 6I_5 - 5I_6)}{I_1 - 26I_2 + 25I_3 + 25I_4 - 26I_5 + I_6} \tag{5}$$

has greater immunity to both linear and quadratic nonlinearity ($p = 2$) of the phase shift that is spatially nonuniform. For this algorithm, the phase-shift interval is $\pi/3$, and $m = n = 6$. For both the five- and six-frame algorithms given by Eqs. (1) and (5), respectively, the phase ϕ was calculated using fringes simulated with Eq. (2), where the object beam intensity in Eq. (1) was taken as constant from frame to frame. As noted previously, a comparison of the residual phase error from these two algorithms was performed by subtracting a reference phase image ϕ_{ideal}, created by using error-free simulated fringes, from the phase image $\phi_{\text{perturbed}}$, generated using the empirically derived phase-shift-error coefficient

$$\varepsilon(\alpha_{0r}) = H\exp[-A\alpha_{0r}] \times f(x,y), \tag{6a}$$

where α_{0r} is the unperturbed phase shift and the spatial nonuniformity is given as

$$f(x,y) = \left[1-\exp\left(-\left|Bx^2+Cy^2\right|\right)\right]$$

$$\left\{\exp\left[-\left|\left(Dx^2+Ey^2\right)^{1/2}/F\right|^G\right]\right\}$$

$$\times\left|\sin\left[\tan^{-1}(Kx/My)\right]\right|, \tag{6b}$$

where A–M are constants. The phase shift used in generating $\phi_{\text{perturbed}}$ was calculated by combining Eqs. (6) and (3):

$$\alpha_r = \alpha_{0r}[1+H\exp(-A\alpha_{0r})\times f(x,y)]. \tag{7}$$

Figure 83.40 shows the general form of $f(x,y)$ and the peak value of the phase error in Eq. (7) as a function of α_{0r} for one set of constants A–M with $A > 0$. The functional form of this phase error is qualitatively similar to the director distortion observed in Figs. 83.36 and 83.37; the interference fringes in

Fig. 83.41, simulated using Eqs. (2) and (7) and used to obtain $\phi_{\text{perturbed}}$, are similar in appearance to those in Figs. 83.38 and 83.39. It is likely that some of the experimentally observed spatial variations in fringe intensity and contrast when focused close to the microsphere can be attributed to spatially nonuniform absorbance caused by orientational coupling between the dye molecules and liquid crystal molecules. We have not attempted here to model dye-induced absorbance changes that may affect fringe intensity and contrast. The image containing the residual phase error is thus given as

$$\Delta\phi = \phi_{\text{perturbed}} - \phi_{\text{ideal}}. \tag{8}$$

By expanding the exponential term in Eq. (7) and comparing with Eq. (3), it can be shown that the linear and quadratic error terms are, respectively,

$$\varepsilon_1 = H f(x,y), \qquad \varepsilon_2 = -AH\pi f(x,y), \tag{9}$$

and Eq. (7) can be approximated by

$$\alpha_r = \alpha_{0r}\left[1+\varepsilon(\alpha_{0r})\right] \approx \alpha_{0r}\left[1+\varepsilon_1(x,y)+\varepsilon_2(x,y)\frac{\alpha_{0r}}{\pi}\right] \quad \text{for } r = 1,\ 2,\ \ldots, m, \tag{10}$$

where $\varepsilon_1(x,y)$ and $\varepsilon_2(x,y)$ are given by Eq. (9). The ability of this approach to determine which algorithm would experimentally show better immunity to LCPDI phase-shift errors in the absence of absorption dichroism was first tested theoretically using Eq. (10) with spatially uniform error coefficients ε_1 and ε_2 [i.e., $f(x,y) = 1$]. Table 83.V compares these results with the results of Hibino *et al.*[26] The residual errors shown in this table for the six-frame algorithm matched those of Ref. 26, and this algorithm performed significantly better than the five-frame algorithm when the quadratic phase-shift error shown in the table was introduced. The six-frame algorithm also produced less residual phase error when the spatially nonuniform error term given by Eq. (6b) was included in the simulated phase plots. When the phase error was exponentially increasing (i.e., ε_1, $\varepsilon_2 > 0$), the six-frame algorithm consistently yielded less residual error than the five-frame algorithm. When $\varepsilon_2 < 0$, however, the five-frame algorithm generally yielded less residual error. Table 83.VI gives a relative comparison of the algorithms using spatially nonuniform ε_1 and ε_2 given by Eq. (9) for both positive and negative values of ε_2. For the cases when $\varepsilon_2 < 0$, the sum of the phase-shift error terms in Eq. (10) yields an approximation to the shape of the curve shown in Fig. 83.40; the descriptive terms in Table 83.VI when $\varepsilon_2 < 0$ correspond to the different regions of this curve. Among the curve shapes listed in Table 83.VI, the "parabola" most closely approximates the observed LCPDI phase-shift error, and the five-frame algorithm gave less residual phase error in this case.

Residual phase errors from both algorithms using experimental fringes are compared in Table 83.VII with residual phase errors obtained using fringes simulated with the phase perturbation given by Eq. (7) and shown in Fig. 83.40. To avoid unwrapping errors observed when excessive phase error is introduced, an intermediate focusing regime that showed sufficient host-induced phase error was chosen for this test. Figure 83.42(a) compares two experimental interferograms from this series with their corresponding simulated interferograms. As shown in Table 83.VII, the five-frame algorithm produced lower residual rms phase error in both the experiment and the simulation by nearly the same factor. The larger p–v errors in

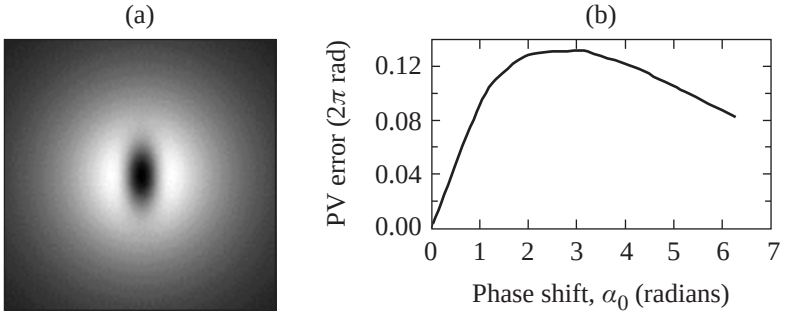

Figure 83.40
(a) Gray-scale image showing the spatial form of $f(x,y)$ defined in the text and used in Fig. 83.42. Black corresponds to $f(x,y) = 0$ with a maximum value of $f(x,y) = 1$. (b) Peak value of the phase-error function $\alpha_{0r}[\exp(-A\alpha_{0r})\ f(x,y)]$ versus α_{0r} for the set of constants A–M given in Table 83.VII.

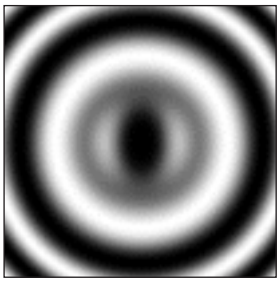

G5013

Figure 83.41
Simulated interference fringes computed using the empirically derived form of the LC alignment perturbation given by Eq. (7) and the two-beam interference expression given by Eq. (2). The simulated fringes are similar in appearance to the experimental fringes in Figs. 83.38 and 83.39.

the experimental results are attributed to spurious phase spikes. The ideal phase image ϕ_{ideal} in the experimental data set was determined from a five-term Zernike fit to the final phase image $\phi_{perturbed}$; the phase difference $\Delta\phi = \phi_{perturbed} - \phi_{ideal}$ is shown in Fig. 83.42(b). To reduce the contribution of dye-induced absorbance changes, each intensity interferogram in the experimental data set was normalized by a reference intensity image obtained adjacent to the microsphere at the same voltage. In both the experimental and simulated fringes, the phase perturbation was observed to first increase, then decrease in amplitude as the phase was shifted through the requisite number of frames, corresponding to $A = 0.37$ and $H = 1.21$ in Eq. (7). For the experiment, the starting phase corresponded to a voltage close to the Frederiks transition threshold where very little perturbation in the fringes was

Table 83.V: Peak-to-valley residual phase errors (2π rad) that are due to linear and quadratic spatially uniform phase-shift errors for the five- and six-frame algorithms.

ε_1	ε_2	Five-Frame	Six-Frame	Six-Frame*
0.1	0.0	0.0020	0.00005	0.00005
0.0	0.2	0.0265	0.0015	0.0015
0.1	0.2	0.0260	0.0025	0.0025
0.0	0.4	0.0610	0.0060	0.0060
0.1	0.4	0.0595	0.0050	0.0050

*From Table 3 of Ref. 26.

Table 83.VI: Residual phase error (2π rad) produced by the five- and six-frame algorithms for different values of the quadratic error coefficient ε_2. The error coefficients were multiplied by the spatial nonuniformity $f(x,y)$ in each case before computing residual error using the values of constants B–M indicated. The descriptive terms refer to the shape of the curve produced by plotting the induced phase error given in Eq. (10) versus the phase shift α_{0r}.

ε_1	ε_2	Type		Five-Frame	Six-Frame
0.0833	–0.0139	Decreasing positive slope	rms	0.00490	0.00464
			p–v	0.03250	0.03010
0.0833	–0.0417	Parabola	rms	0.00236	0.00313
			p–v	0.01510	0.02030
0.0833	0.4629	Increasing exponential	rms	0.0601	0.0280
			p–v	0.2390	0.1780
0.0833	0	Linear	rms	0.00642	0.00533
			p–v	0.04100	0.03470
$B = 0.03$; $C = 0.008$; $D = E = 0.002$; $F = 2$; $G = 3$; $M = 0$.					

observed. Thus, in the simulation, a starting phase of $\alpha_{0r} = 0$ was used. The superior performance of the five-frame algorithm by nearly the same factor in both the simulation and the experiment suggests that the form of the LCPDI phase-shift error represented empirically by Eq. (7) may be the underlying cause of the experimentally observed discrepancy.

Generally, an algorithm with more sample frames will be more effective in reducing measurement errors, depending upon the type of phase-shift error addressed by the algorithm and the type of error introduced during the measurement. Currently a period of 2 to 3 s is required between frames to ensure that the liquid crystal molecules have reached an equilibrated state, thus choosing a phase-shifting algorithm that addresses LCPDI device-specific phase-shift errors and minimizes the number of frames required is critical. Multiple applications of the phase-offset method can also reduce higher-order phase-shift errors;[15] however, this method is limited by the maximum retardance that can be obtained in an LCPDI device. This simulation and the experimental results (1) confirm the superior performance of the five-frame algorithm over the six-frame algorithm for this LCPDI, even though the six-frame algorithm was designed to address higher-order phase-shift error, and (2) emphasize the importance of understanding the underlying behavior of the phase-shift error in the LCPDI in order to choose effective phase-reduction algorithms and to optimize experimental conditions. For example, further reduction of phase errors related to the liquid crystalline host

Table 83.VII: Comparison of residual errors (2π rad) obtained using the five- and six-frame algorithms with both experimental and simulated interference images. Simulated images were obtained using the indicated values of constants *A*–*M*, corresponding to the phase perturbation shown in Fig. 83.40.

	Experiment			Simulation	
	Five-Frame	Six-Frame		Five-Frame	Six-Frame
p–v	0.1450	0.278		0.1001	0.1314
rms	0.0167	0.022		0.0164	0.0223
$H = 1.21498$; $A = 0.37$; $B = 0.06$; $C = 0.016$; $D = E = 0.002$; $F = G = 1$; $M = 0$.					

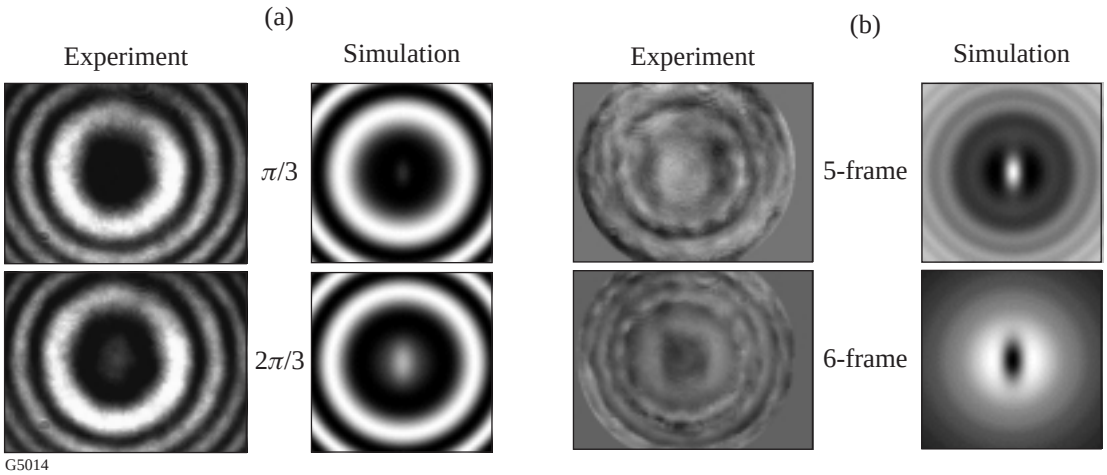

Figure 83.42
(a) Two interferograms from the six-frame series used in comparing five- and six-frame algorithms. For the images shown, the phase shift $\alpha_{0r} = \pi/3$ and $2\pi/3$, corresponding respectively to $r = 2, 3$ for the six-frame algorithm. Focusing conditions were chosen so as to introduce only a moderate amount of LC host-induced phase-shift error to avoid possible phase unwrapping errors. (b) Gray-scale images of the residual phase error $\Delta\phi = \phi_{\text{perturbed}} - \phi_{\text{ideal}}$ for the five- and six-frame algorithms. For the experimental results shown, ϕ_{ideal} was determined by a five-term Zernike fit to the phase data. Table 83.VII gives p–v and rms errors.

alignment distortions may be possible by tailoring an algorithm for the observed phase-shift error. In addition, operating the device well above the Frederiks transition threshold will reduce the alignment perturbation and thus also reduce the measurement error, once high-contrast fringes can be maintained in the higher-voltage regime through the use of a dye system without absorption dichroism. We have also begun to investigate the use of chiral-smectic-A LC's in place of nematic-phase LC's because of their faster response time, high birefringence, and gray-scale capability.[27,28] Liquid crystal systems with a faster response time would make algorithms with a greater number of sample frames more practical.

Summary

The liquid crystal point-diffraction interferometer is attractive in that it combines the common-path design of the PDI with the high resolution that can be achieved through modern phase-shifting techniques; it is also a low-cost alternative to commercially available phase-shifting interferometers. Empty-cavity measurements using the LCPDI designed for 543 nm with a dye having large absorption dichroism produced residual p–v and rms phase errors of 19 nm (0.035 λ) and 1.1 nm (0.002 λ), respectively, without using a phase-offset averaging technique and with nonideal environmental conditions. This suggests that LCPDI devices to be fabricated using newly available near-IR dyes[20] will satisfy the desired accuracy of 105 nm at λ = 1054 nm for *in-situ* analysis of OMEGA beamlines. Using the visible-wavelength LCPDI for phase measurement of a wedged window with a polished spot yielded results that were comparable to those of the Zygo Mark IV XP, showing the current LCPDI to be a useful optical metrology tool. The LCPDI measurement matched the Mark IV measurement nearly exactly in some regions but was ≤50 nm discrepant in other regions. This spatially dependent error had periodicity equal to that of the interference fringes, suggesting an intensity change from frame to frame caused by the absorption dichroism of the dye as the primary cause of the discrepancy. Additional error contributors in these measurements were interference effects of multiple beams and LC molecular alignment distortions around the mircrosphere.

The use of a non-dichroic dye or a combination of positive and negative dichroic dyes will significantly reduce errors related to intensity changes from frame to frame. For visible-wavelength applications, the high absorbance necessary to achieve high-contrast fringes has been available from commercially available dyes, whereas for applications in the near-IR, we have synthesized several dyes showing significantly greater absorbance than can be obtained from commercial dyes.[20] Two visible-wavelength dye mixtures that combine commercially available dyes having positive dichroism with Orasol dyes exhibiting negative dichroism were shown to have negligible change in absorbance over the voltage range of interest. Synthesis by-products not removed from the Orasol dyes may be the cause of the high ionic conduction measured in LCPDI cells made with these components, giving rise to a scattering texture that appeared when voltage was applied to the device. Purification of these dye components is in process, and it is expected that future LCPDI devices incorporating these purified dyes or other dye candidates will produce significantly less scatter. For wavefront analysis of OMEGA beamlines, initial tests of LCPDI devices fabricated using the newly synthesized near-IR dye mixtures show much less intensity change with voltage applied to the cell than that seen in the visible-wavelength devices, suggesting that some of these dye components may have negative dichroism.[20]

Our investigation has also shown that director distortions in the vicinity of the microsphere can affect phase-measurement accuracy of the LCPDI and suggests that it is possible to tailor device fabrication and experimental testing parameters to reduce the effect of nematic director distortions on phase measurements. Stronger anchoring in the bulk of the fluid, achieved by using a thinner path cell, was shown to reduce the spatial extent of the alignment distortion. Obtaining weaker anchoring at the sphere surface will likely reduce phase-measurement errors by eliminating topological defects and minimizing director distortions as voltage is applied to the cell.[25] These director distortions were observed to perturb the interference fringes when the focus was placed very close to the microsphere, although by judicious choice of focusing regime, the contribution of alignment distortions to the phase error was significantly reduced. Our simulation using the empirically derived phase-shift error suggests that phase-measurement error due to host alignment distortions can be further reduced through the use of device-specific phase-shifting algorithms, once these distortions become the dominant contribution to the measurement error.

It is expected that (1) the use of dyes that eliminate absorbance changes during data acquisition and (2) the reduction of acoustic vibration through the use of an air-supported table and more rigid mounting of the device will greatly improve LCPDI accuracy and precision, making the LCPDI a low-cost alternative for evaluation of high-performance optical elements, such as required for OMEGA. The use of phase-shifting algorithms and averaging methods tailored for device-specific phase-shift errors can further improve LCPDI performance.

ACKNOWLEDGMENT

This work was supported by the U.S. Department of Energy Office of Inertial Confinement Fusion under Cooperative Agreement No. DE-FC03-92SF19460, the University of Rochester, and the New York State Energy Research and Development Authority. The support of DOE does not constitute an endorsement by DOE of the views expressed in this article.

REFERENCES

1. K. Creath, in *Progress in Optics XXVI*, edited by E. Wolf (North-Holland, Amsterdam, 1988), Chap. V.
2. M. V. R. K. Murty, in *Optical Shop Testing*, edited by D. Malacara, Wiley Series in Pure and Applied Optics (Wiley, New York, 1978), Chap. 4, pp. 105–148.
3. V. P. Linnik, C.R. Acad. Sci. (USSR) **1**, 208 (1933).
4. R. N. Smartt and W. H. Steel, Jpn. J. Appl. Phys. **14**, 351 (1975).
5. D. Malacara, ed. *Optical Shop Testing*, Wiley Series in Pure and Applied Optics (Wiley, New York, 1978).
6. See, for example, several references in Ref. 8.
7. C. R. Mercer and K. Creath, Opt. Lett. **19**, 916 (1994).
8. C. R. Mercer and K. Creath, Appl. Opt. **35**, 1633 (1996).
9. C. R. Mercer and N. Rashidnia, in *8th International Symposium on Flow Visualization 1998*, edited by G. M. Carlomagno and I. Grant (Edinburgh, Scotland, 1998), CD-ROM, pp. 256.1–256.9.
10. Zygo Mark IVxp™, Zygo Corporation, Middlefield, CT 06455.
11. M. J. Guardalben and N. Jain, Opt. Lett. **25**, 1171 (2000).
12. J. Schwider *et al.*, Appl. Opt. **22**, 3421 (1983).
13. P. Hariharan, B. F. Oreb, and T. Eiju, Appl. Opt. **26**, 2504 (1987).
14. S. D. Jacobs, S. R. Arrasmith, I. A. Kozhinova, L. L. Gregg, A. B. Shorey, H. J. Romanofsky, D. Golini, W. I. Kordonski, P. Dumas, and S. Hogan, Am. Ceram. Soc. Bull. **78**, 42 (1999).
15. J. Schwider, T. Dresel, and B. Manzke, Appl. Opt. **38**, 655 (1999).
16. A. C. Turner, 1998 Summer Research Program for High School Juniors at the University of Rochester's Laboratory for Laser Energetics, Laboratory for Laser Energetics Report No. 300, NTIS document No. DOE/SF/19460-299 (1998). Copies may be obtained from the National Technical Information Service, Springfield, VA 22161.
17. R. Rao, 1999 Summer Research Program for High School Juniors at the University of Rochester's Laboratory for Laser Energetics, Laboratory for Laser Energetics Report No. 311, NTIS document No. DOE/SF/19460-338 (1999). Copies may be obtained from the National Technical Information Service, Springfield, VA 22161.
18. The Orasol dyes were recommended by C. Mercer, private communication.
19. E. Prudnikova, B. Umanskii, and T. Plyusnina, Mol. Cryst. Liq. Cryst. **332**, 37 (1999).
20. Laboratory for Laser Energetics LLE Review **81**, 37, NTIS document No. DOE/SF/19460-335 (1999). Copies may be obtained from the National Technical Information Service, Springfield, VA 22161.
21. P. Poulin and D. A. Weitz, Phys. Rev. E **57**, 626 (1998).
22. P. Poulin, N. Frances, and O. Mondain-Monval, Phys. Rev. E **59**, 4384 (1999).
23. A. Glushchenko *et al.*, Liq. Cryst. **23**, 241 (1997).
24. H. Stark, J. Stelzer, and R. Bernhard, Eur. Phys. J. B **10**, 515 (1999).
25. O. Mondain-Monval *et al.*, Eur. Phys. J. B **12**, 167 (1999).
26. K. Hibino *et al.*, J. Opt. Soc. Am. A **14**, 918 (1997).
27. S. Garoff and R. B. Meyer, Phys. Rev. A **19**, 338 (1979).
28. A. Sneh, J. Y. Liu, and K. M. Johnson, Opt. Lett. **19**, 305 (1994).

Understanding the Mechanism of Glass Removal in Magnetorheological Finishing (MRF)

Introduction

Two magnetorheological (MR) fluids are currently in widespread industrial use for the commercial manufacture of high-precision optics using magnetorheological finishing (MRF). One composition, which consists of cerium oxide in an aqueous suspension of magnetic carbonyl iron (CI) powder, has been found appropriate for almost all soft and hard optical glasses and low-expansion glass-ceramics. The second composition, which uses nanodiamond powder as the polishing abrasive, is better suited to calcium fluoride, IR glasses, hard single crystals (i.e., silicon and sapphire), and very hard polycrystalline ceramics (i.e., silicon carbide).

The extension of MRF to a vast array of materials is possible because of the unique nature of this finishing process. The magnetic carbonyl iron particles may be thought of as a form of variable compliance lap that supports the nonmagnetic polishing abrasives. Lap stiffness may be increased or decreased by adjusting the CI concentration and/or the magnetic field strength.

Considerations leading to a choice of nonmagnetic polishing abrasive are more complex than those encountered in conventional pitch or pad polishing. Not only do the hardness and chemistry of the abrasive grains need to be appropriate to the workpiece, but the type of abrasive (median size, surface chemistry) can have a large or small effect on the out-of-field MR fluid rheology. Fluid properties in an MRF machine circulation system must be held constant to realize constant rates of material removal during polishing.

Advances have been made in understanding the mechanism of removal with MRF, based in part on the hardness of the CI powder, the magnetorheological properties of the MR fluid, and the interaction of cerium oxide or other abrasives with the workpiece surface. This article presents the results of recent studies, within the context of classical optical polishing operations.

The mechanisms of material removal important to glass polishing have been an area of study for years. Cumbo[1] describes the goals of precision polishing to be to shape the glass to within 0.1 μm of the desired form, to remove subsurface damage created by grinding operations, and to reduce the peak-to-valley (p–v) roughness to less than 5 nm. While there are several proposed mechanisms of material removal in polishing, none are widely accepted. Some authors describe polishing in terms of small-scale fracture,[2,3] while others describe it as "plastic scratching" of a hydrated layer[4] or a tribo-chemical wear process.[5] The goal of this work is to try to use some of these existing theories to understand the mechanisms of material removal in the MRF of glass.

Preston[6] gave a classic theory of removal in glass polishing that is still being studied today. He states, "(…the rate at which material is removed) is proportional to the rate at which work is done on each unit area of the glass." Furthermore, he defines the work done in time t as

$$w = \mu A p v t, \tag{1}$$

where w = work (N • m), μ = coefficient of friction, A = area of contact between the glass and polishing lap (m^2), p = pressure applied to the glass part (N/m^2), v = relative velocity between the lap and the part (m/s), and t = time in which work is done (s).

The term μp is the specific traction, or drag divided by the contact area, of the polishing lap (felt in this case) on the glass. The expression in Eq. (1) states that the work done on the material is proportional to the specific drag force multiplied by the area of contact and the velocity. He continues to say that if the specific drag force remains constant, then the removal rate is proportional to "…the amount of felt that passes over it…this is independent of velocity, except in so far as velocity may affect the amount of felt passing over."[6] In general, these statements are true in MRF as well: namely, that the

material removal scales with the drag force and is primarily controlled by the time of contact between the abrasive and the glass surface.

Preston's equation is commonly written in a slightly different form,

$$\frac{dz}{dt} = C_P \frac{L}{A}\frac{ds}{dt}, \tag{2}$$

where dz/dt = the change in height in time, or removal rate (m/s), C_P = Preston's coefficient (m^2/N), L = total normal load applied (N), A = area over which wear occurs (m^2), and ds/dt = velocity of the work piece relative to the tool (m/s).

The difficulty comes in defining Preston's coefficient in Eq. (2). The discussion above shows that a friction coefficient makes up part of it, but several other things are accounted for in this coefficient. The importance of various effects that make up Preston's coefficient in MRF will be demonstrated here. One of these is the chemical effects associated with the presence of water in the MR fluid. The mechanics associated with how different abrasive types affect the removal of material in MRF are also given. Before describing the mechanisms of material removal in MRF, it is instructive to discuss proposed mechanisms in other polishing processes.

Review of Mechanisms of Material Removal

Silvernail and Goetzinger[7,8] summarize various factors that are important to glass polishing. Aside from pressure and velocity, they note that the polishing agent, liquid carrier fluid, and polishing lap are all important. Their results show that adding water to the slurry dramatically increases the removal rate of a crown glass. They conclude that the improved removal rate due to the addition of water is independent of the other parameters in the system (e.g., abrasive concentration, pressure, etc.) and that the interaction is primarily with the glass. The results that show changes in the polishing due to lap type are inconclusive. An increase in removal rate is seen with an increase in cerium oxide content, showing that the concentration of the slurry is important to material removal. This effect generally levels off at a concentration between 10 wt% and 20 wt% (approximately 1 vol% to 3 vol%). Furthermore, they discuss how cerium oxide behaves as an excellent abrasive while other rare earth oxides that are similar in structure are not good abrasives. They cannot explain the increased polishing effect of cerium oxide.

Other authors describe glass material removal in terms of small fracture events caused by the abrasive interacting with the glass surface. Buijs and Korpel-Van Houten[2] describe material removal of glass surfaces by abrasive particles through an indentation fracture theory. This process is intended to explain lapping, but a polishing process based on a similar theory could be envisioned. Essentially they describe how the abrasive particle acts like a Vickers indenter under a normal load. Material removal occurs through lateral cracking of the glass under the indenter-like abrasive. Removal rates in this model depend on the shape of the particle and material properties of the glass (namely, elastic modulus, hardness, and fracture toughness). While this explanation is typically used to explain grinding and microgrinding, Lambropoulos *et al.*[3] show that removal rates obtained with MRF correlate with the same material properties described by Buijs and Korpel-Van Houten. They explain the fracture occurring through mechanisms other than indentation, however. Asperities on the surface can be modeled as nanometer-sized cracks. The abrasive contacts the asperity through shear and normal loads. In this geometry, the shear load works to drive the crack, while the normal load tends to close the crack. If the shear force is large enough relative to the normal load, fracture of the asperity will occur. This is different from Buijs *et al.* in that this mechanism is shear driven, while their work is controlled by lateral cracking from normal loads indenting the particle. The work of Lambropoulos *et al.* is in its early stages, but it gives a plausible explanation of how removal rates in polishing correlate with parameters used to describe fracture.

Water's positive impact on polishing is discussed in several other references. If polishing is thought to consist of small fracture events, then the effect of water can be explained by Michalske and Bunker.[9] The authors (and references) describe how water can attack the Si-O-Si bonds at the crack tip, which results in a reduced fracture toughness of the glass. Furthermore, the hydrolysis rate increases as the stress of the bond increases. Consider the model proposed by Lambropoulos *et al.*[3] and/or Buijs *et al.*[2] According to Michalske and Bunker's theory, the presence of the water as well as the stresses applied by the abrasive to the glass surface would dramatically reduce the fracture toughness of the material as well as speed up the kinetics of the process.[9] This possibly explains why water enhances the removal of glass in polishing.

A second, possibly related, mechanism of material removal also involves hydration of the glass surface due to chemical interaction between the carrier fluid (water) and the glass surface. Cook[10] describes how the water molecule breaks Si-

O-Si bonds and how this helps to create a hydrated layer in the glass surface. Cumbo[1,11] gives a summary of Cook's work and extends it with a study of the chemical effects in polishing experiments. Cook's[10] process basically describes how the loads applied to the surface by the abrasive promote diffusion of water into the silica network. As the water dissociates, it attacks the bonds within the network, weakening the structure. This promotes bond breakage and material removal. Cerium oxide and zirconia particles are described as having "chemical tooth," which promotes bonding of the abrasive to the silica. This promotes material removal from the silica network as well as inhibits redeposition of material back onto the surface. For chemically inactive materials, such as diamond, removal is said to depend on the carrier fluid's ability to carry the removed material away since the silica does not bond with the abrasive.

Izumitani's theory of the mechanism of material removal is also based on the idea of the hydrated layer.[4] This hydrated layer is caused by a chemical reaction between modifier ions in the glass and the hydrogen ions in the water. Material removal occurs by abrasive particles scratching away this layer. The speed at which material is removed depends on how quickly the hydrated layer is formed (chemical durability of the glass) and the hardness of the hydrated layer as well as the hardness and/or friability of the abrasive. He showed that a softer abrasive that is more easily crushed but still harder than the hydrated layer is most effective. His explanation is that the crushing provides more particles and therefore a higher frequency of scratching events. He also describes the necessary properties of the lap used in polishing. The lap must be hard enough to support the abrasive and transmit pressure, but soft enough to allow the particle to embed into the polishing lap.

Evidence in the literature supports the existence of a surface layer that is created by hydration of the surface during polishing. Izumitani[4] creates a hydrated layer by immersing the glass surfaces in 0.1 N solution of HCl. Subsequent Vickers microhardness tests show a reduction in microhardness of this layer with increased immersion time. Furthermore, he shows that the polishing rate increases as the microhardness of the hydrated layer decreases. Yokota *et al.*[12] use ellipsometry to show the existence of the hydrated layer after polishing. They demonstrate a reduction in refractive index in a small surface layer in glasses that are susceptible to chemical attack. The size of these layers is of the order of tens of nanometers deep. Glasses of interest to this work, borosilicate crown and silica, each reportedly have hydrated layers of approximately 40 nm with the polishing conditions studied. Maaza *et al.*[13] use grazing-angle neutron reflectometry (GANR) to study the hydrated layer. They also show evidence of a hydrated layer from the polishing process. The hydrated layer of their Borkron surfaces was approximately 5 nm (Borkron is a special borosilicate glass used for neutron optics applications[13]). It is 15 nm for the floated face of float glass and 40 nm for the nonfloated face. They also report on the existence of 2-nm cracks in the float glass from the polishing process. Yokota *et al.*[12] describe how some chemically resistant glasses like fused silica (FS), Vycor, and Pyrex actually show densification of the material in these layers. They explain this densification to be caused by high local pressures on the glass surface due to polishing. Shorey *et al.*[14] provide more evidence of densification in fused silica by comparing numerical simulations with nanoindentation experiments. Densification apparently depends on the state of stress from both normal and shear loading.

Kaller[5,15] describes a process he refers to as a tribo-chemical friction wear process. According to Kaller, the abrasive should be softer than the surface being polished, and the most important property of a polishing agent is its ability to "grip" the surface. He states that the most effective polishing abrasives (mostly cerium oxide and iron oxide) have a large number of lattice defects produced during manufacture, and it is the presence of these defects that promotes the gripping of the abrasive to the surface. He describes three steps: The first is intimate contact between polishing grains and the glass surface. This coupled with friction or shear forces promotes lattice deformation and partial removal of surface layers of the abrasive grain. Second, removal of these surface layers exposes ionic vacancies in the lattice, which bond with the glass. Finally, the continued motion of the polishing wheel produces continuous removal of glass. He continues his discussion to address how manufacturing methods can produce more, or fewer, lattice defects, as well as determine the primary crystallite size. Important additional lattice defects are created through (1) valance change of the oxide, (2) incorporation of metal ions or molecules into the lattice, and (3) quenching. Finally, he discusses how careful control of processing allows control of crystallite size, number of defects, and rubbing resistance. For a given process a particle could be manufactured with the appropriate number of lattice defects so that the abrasion resistance matches the process for which it is intended. In other words, a cerium oxide particle can be produced that will provide a low rubbing resistance (soft particle), which means low removal, but a high precision surface. A (hard) cerium oxide particle could also be produced to provide a high rubbing stress, which would give higher removal, but less precise (rougher) surfaces. He states that the first abrasive would be used in low shear to be most effective, but that the second one

would increase its effectiveness at very high shear, presumably due to the exposure of new lattice defects. His only discussion of a hydrated layer is to say that experiments that were supposed to prove the existence of the hydrated layer did not. To explain other observations of a densified surface layer resulting from the pressure of polishing, Kaller claims evidence for nanometer-scale abrasive particles left on or in the surface after polishing. He refutes the idea of a smallest-size limit in milling of abrasives.

Kaller's ideas are at least partially supported by Kirk and Wood.[16] In their paper, they describe the calcination of cerium oxide sol-gels and show evidence of significant changes in the crystallography due to calcination temperature. Before calcination, the particles are loosely bonded and of the order of 5 to 10 nm in size. After calcination at 850°C for 1800 s, the crystallite size increases to about 60 to 80 nm, and they become strongly bonded together. Furthermore, they show that the {111}-type planes grow faster than {200} planes at elevated temperatures. The {111} planes have a higher atom density than the {200} planes, which means that more cerium atoms are exposed. The hypothesis is that this explains the increased polishing efficiency of properly calcined cerium oxide.

Several views on the roles of the various constituents in the polishing process clearly exist. Water plays a major role in glass polishing. It is not clear whether this is due to the reduced fracture toughness at the glass surface or a softening due to chemical attack of the silica network. Actually, each process description is similar, and there may be two ways of saying the same thing. The type of abrasive is also important. The wide acceptance of cerium oxide in glass polishing is explained to be due to its chemical tooth, which could be explained by Kaller's lattice defect theory. Also, both Izumitani[4] and Kaller[5] show that it is possible to polish hard materials with relatively soft abrasives; however, hard materials such as diamond can also be used. The relative effectiveness of an abrasive is not solely due to its hardness.

Much of this discussion is as appropriate for MRF as it is for the more common pitch or pad polishing. The ability of abrasives softer than the glass to polish, even in the absence of water, will be shown. Furthermore, without water, abrasives harder than the glass surface have difficulty maintaining contact with the surface and actually have a lower material removal rate than the softer abrasive. This will be explained the same way Preston did for Eq. (1); namely, removal rate is proportional to how long the abrasive is in contact with the glass surface. The importance of water in MRF and how it allows abrasives to more easily abrade material away from the surface will be shown. Finally, the interactions of different abrasives with the glass surface are demonstrated. An increase in abrasive concentration increases the time the abrasives are in contact with the glass surface. This results in increased removal. The hypothesis that cerium oxide grips the glass better and that this leads to an increase in measured drag force under identical experimental conditions as aluminum oxide and diamond is experimentally substantiated. Diamond drastically reduces drag but gives an increased removal rate.

Overview of MRF

Several references describe the evolution of MRF in recent years.[17–19] This process utilizes magnetic particles, nonmagnetic polishing abrasives in either an aqueous or nonaqueous carrier fluid, and a magnetic field to polish materials. The "standard" MR fluid consists of 36 vol% of carbonyl iron (CI) as the magnetic component and 6 vol% of cerium oxide as the abrasive with the balance made up of de-ionized (DI) water and fluid stabilizers.[19,20] Figure 83.43 shows an SEM and size distributions of particles after being used in MRF for one week. The dark spherical particles are the magnetic CI and have a median particle size of 4.5 μm. The lighter, small particles are the nonmagnetic abrasive, which in this case is cerium oxide. The cerium oxide starts with a median size of 3.5 μm with a fairly broad distribution. The SEM shows several significantly smaller particles that are likely due to milling of the abrasives during use. Proper manipulation and control of the MR fluid allows MRF to successfully polish a wide variety of materials with commercially viable removal rates.[18,19] Removal rates obtained with the standard MR fluid vary from about 2 μm/min for a hard silica glass like fused silica to more than 9 μm/min for a soft laser glass like LHG8.[17]

The primary concern of this work is to study how MRF polishes glass. Figure 83.44(a) shows a photo of an MRF machine with a vertical wheel [schematic of this machine shown in Fig. 83.44(b)]. MR fluid is pumped from the fluid conditioner (1) up to the nozzle (2), where it is ejected onto the rotating vertical wheel as a ribbon. The wheel shape is that of a portion of a 150-mm-diam sphere. At the initial point of contact, the MR fluid is a viscous fluid with the approximate consistency of honey (viscosity ≈ 0.5 Pa•s, yield stress ≈ 0 kPa). The rotation of the wheel drags the fluid under the part in region (3), where it is acted upon by the magnetic field. The MR fluid ribbon flows through the converging gap between the lens and the wheel. The magnetic field stiffens the ribbon in this region, giving it the approximate consistency of clay (yield stress ≈ 10 kPa). Significant forces are created by the interac-

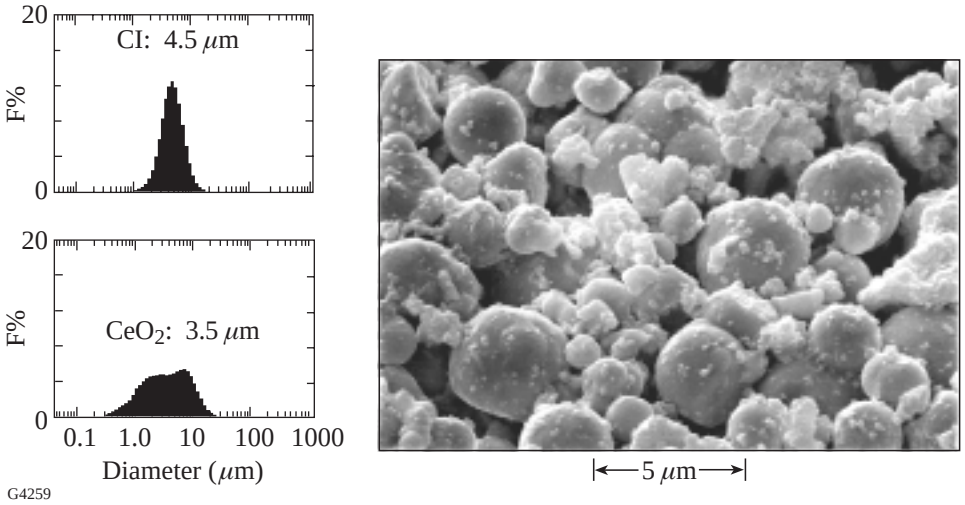

Figure 83.43
SEM of particles and their initial size distributions after one week of use in MRF. The dark spherical particles are the hard magnetic carbonyl iron particles. They have a median size of 4.5 μm. The smaller, light particles are the cerium oxide abrasives. They initially have a broad size distribution with a median particle size of 3.5 μm. The large amount of small particles in the SEM suggests that milling of the cerium oxide occurs during use.

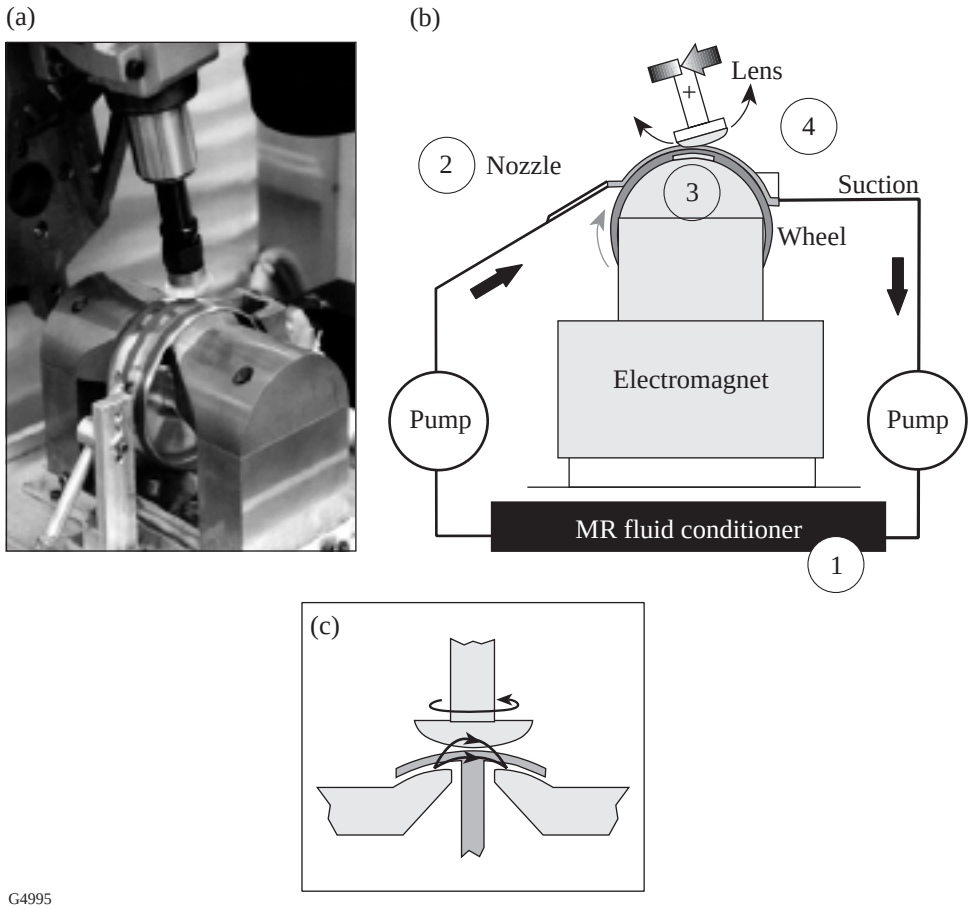

Figure 83.44
The setup used in MRF with a vertical wheel. (a) A photo of an actual MRF machine. (b) A schematic of the MRF machine. Fluid is pumped from the conditioner at (1) to the nozzle at (2) onto the rotating wheel. The wheel carries the fluid between the part and wheel into the magnetic field at (3), where the field causes it to stiffen. Hydrodynamic flow in this region causes stresses sufficient to cause removal to occur. The wheel continues to carry the fluid outside of the field region, where it is removed from the wheel at (4). This fluid is again pumped to the conditioner to complete the circuit. (c) Cross-sectional view showing the relative orientation of the 150-mm-diam spherical MRF wheel, pole pieces, and part. Field lines in the polishing zone are schematically shown.

tion between the wheel, MR fluid, and glass surface since the MR fluid ribbon flows through a converging gap, deforming from a thickness of 2 mm to one of 1.5 mm. Rotation of the wheel continues to drag the MR fluid from region (3) over to region (4), where it is removed from the wheel through suction. Here, the magnetic field does not act on the MR fluid, so it again has the consistency of honey. The MR fluid is pumped back to the fluid conditioner, where it is cooled to a setpoint temperature and any evaporative losses are replaced. Our primary area of concern is region (3) inside the magnetic field where polishing occurs. Figure 83.44(c) shows a cross-sectional view of this region. The pole pieces provide the magnetic field to stiffen the MR fluid. This fringing field between the gap of the pole pieces has a strong vertical gradient. The field is higher at the wheel surface than it is at the part surface, which causes the CI to be pressed against the wheel surface and the nonmagnetic abrasive to move to the glass surface.

Figure 83.45(a) shows a photo of the MR fluid contacting a meniscus lens surface (flow direction is left to right for all of Fig. 83.45). The fluid contacts the surface in the shape of a backward D. This is the shape of the removal under the action of the rotating wheel if the part is held stationary in the fluid. This D-shaped region is referred to as the "spot" from this point on. The white regions surrounding the spot and extending downstream (to the right) from the spot are abrasive particles. This is evidence of the fact that abrasives move to the part surface under the action of the magnetic field. Figure 83.45(b) shows an interferogram of a removal spot; its oblique view is shown in Fig. 83.45(c) (adapted from Ref. 18). The surface before and after a removal experiment is evaluated using a phase-shifting interferometer.[21] The instrument software is used to subtract the initial surface from the final surface containing the spot. Height variations on the resulting image are due to material removed from the initial surface. The peak removal rate is found by dividing the depth of deepest penetration by the contact time between the part and MR fluid ribbon.

The proximity of the part and wheel surface changes due to the curvature of the wheel (and part, if polishing a lens). The location of the deepest and widest part of the spot shown in this figure is approximately the position of closest approach between the part and the wheel surface. During polishing, the part is rotated and swept through the polishing zone, allowing material to be removed in annular regions over the entire part surface. Computer-controlled dwell times allow control of the surface figure of the polished surface to a precision of $\lambda/20$.[18]

Removal mechanisms on a macroscopic scale have been previously considered.[22,23] Since the normal force on an abrasive particle is low compared with conventional polishing,[24] a shear-controlled mechanism has been described.[22,23] MR fluids are modeled as Bingham fluids with a yield stress (~10 kPa) and small plastic viscosity (~0.5 Pa•s).[17,22,23,25] The flow of a fluid with a yield stress through a converging gap, like the one between the rotating wheel and part surface in MRF, allows the possible formation of unsheared regions called "cores" (see Fig. 83.46). These cores effectively reduce the gap between the wheel and part surface and cause increased shear stresses on the downstream end of flow. While the opacity of the MR fluid prevents visual confirmation of the presence of these cores, material removal has been shown to increase in the region where these cores are expected to be located.[23] In general, the low normal loading in MRF keeps an abrasive particle in contact with the glass surface, but material removal is primarily controlled by the shear stresses applied to the abrasive through the bulk flow of the MR fluid.

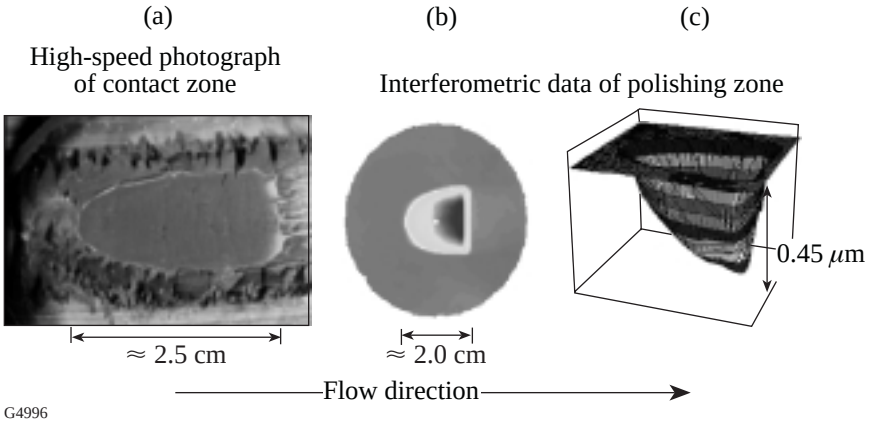

Figure 83.45
The spot in MRF. Flow is from left to right in all parts of this figure. (a) An actual photo of the contact region, or "spot," on a stationary meniscus lens. (b) Interferogram of the material removed from the spot. Interferometric characterization of the spot gives a removal function that a computer program can use to vary dwell time of this spot over the surface. This allows precise control of the figure during polishing. (c) An oblique view of the spot. The deepest region is at the trailing edge of the flow and is approximately the position of closest approach between the part and wheel.

Experimental Considerations and Earlier Screening Studies

The spot-taking machine (STM)—a machine similar to the commercial MRF polishing machine[26]—is used to perform these material removal experiments [see Fig. 83.44(a)].[19] The only automated degree of freedom in the part motion on the STM is the height of the part above the rotating wheel. There is no rotation or swing of the part, so a removal experiment consists simply of making a spot on a flat part. Important machine parameters are held constant for all removal experiments. The vertical wheel rotates at 150 rpm, the MR fluid ribbon height is 2.0 mm, and the part surface is placed 0.5 mm into the MR fluid. The current to the electromagnet is kept at 15 A. This results in the magnetic flux density having a horizontal component of about 260 kA/m, 1 mm above the wheel surface.[27]

Water loss due to evaporation from aqueous MR fluids is a concern during removal experiments. If this evaporation is left unchecked, the actual CI concentration of the MR fluids, and therefore the viscosity and yield stress, will increase. The STM monitors the viscosity in real time and maintains the appropriate CI concentration. An off-line moisture analyzer is used at the beginning of each experiment to measure moisture content in the MR fluid.[28] It is therefore possible to calculate the actual CI concentration for data analysis.

The viscosity outside of the magnetic field is measured off-line before each set of experiments using a cone and plate viscometer[29] whose shear rate may be varied from 0 to 960 1/s. These MR fluids are shear thinning, which means that the apparent viscosity decreases as the shear rate increases. Because of this, the viscosity is monitored at only the maximum shear rate since this is the approximate shear rate both in the fluid delivery system and underneath the part during polishing. For all the experiments performed, the viscosity at 960 1/s is 60±20 cps. As expected, the viscosity tends to increase with the amount of solids in an MR fluid. This viscosity is kept low so that it is easily pumped by the fluid delivery system.

Roughness measurements are made with two instruments. One is a white-light interferometer, which measures the roughness over a 0.25-mm × 0.35-mm area and has a lateral resolution of 1.1 μm.[30] This interferometer is a valuable tool in measuring the microroughness of a part. The second instrument is an atomic force microscope (AFM), which measures the roughness over a smaller region.[31] Scans are performed in contact mode over a 5-μm × 5-μm-square region using 256 samples, at a rate of 1 Hz. This allows us to investigate submicron features from polishing with a lateral resolution approaching 20 nm. The vertical scale is 15 nm for all AFM scans presented here.

Each fluid is characterized on the magnetorheometer described in previous work[23,25] to determine the dynamic yield stress of the fluid. The MR fluids are tested at magnetic fields with flux densities of 200 kA/m and 250 kA/m only, since this is the nominal flux density at 15 A on the STM in the region of fluid/part interaction. Fixed conditions for other experimental parameters on the magnetorheometer are polishing configuration, 0.5-mm gap, and 3.33-rpm cup speed. The results of our work on the magnetorheometer are shown in Fig. 83.47. The data from this experiment were taken in the range of 40 vol% to 45 vol% CI. The dynamic yield stress does not change for CI compositions greater than about 35 vol% CI but asymptotically approach values of about 15 kPa at 200 kA/m and 20 kPa at 250 kA/m for a variety of commercial CI powders. The yield stress of the MR fluid is also unaffected by the incorporation of nonmagnetic abrasives at the low loading used for these experiments.

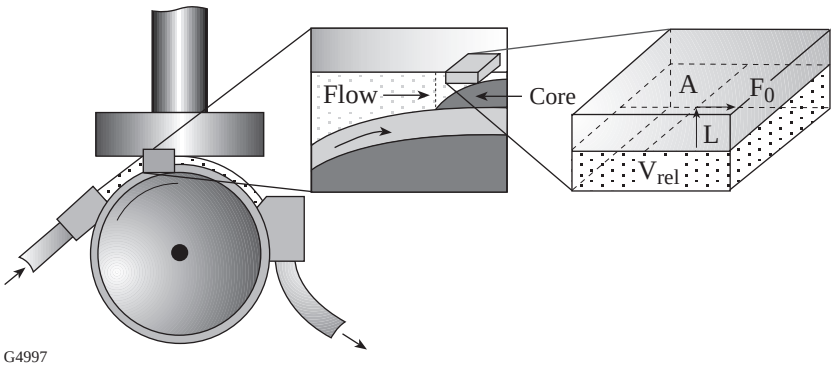

Figure 83.46
Schematic showing the contact between the MR fluid and the glass. The first callout shows the internal structure of the flow. The removal rate increases in the region of the core due to the increased shear stresses that result from the throttling action of the core. If material removal is considered over a small material volume, a Preston-type equation based on the shear stress at the part surface can be used to describe the removal process.

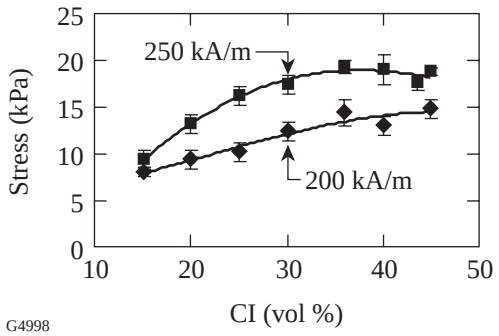

Figure 83.47
Dynamic yield stress measured on the magnetorheometer for the MR fluids used in removal experiments. Measurements were taken in the polishing configuration, 0.5-mm gap and 3.33-rpm cup speed at fields with a flux density of 200 kA/m and 250 kA/m. The yield stress is approximately 15 kPa at 200 kA/m and 20 kPa at 250 kA/m for the fluids between 40% and 45% CI concentration—the region of interest for these experiments. This data is for a variety of CI types, both with and without abrasives. The type of CI and presence of abrasives in this low loading have no effect on the dynamic yield stress of the MR fluid. Solid lines have been added only to aid the eye.

The flow of an MR fluid between the part surface and wheel is complicated. The yield stress does not give a full representation of the forces applied to the part by the fluid during removal.[22,23] Because of this, the pressure and the total drag force applied to the part by the fluid are measured as well. A pressure-sensing pad[32] is used to measure the pressure distribution applied to the part by the MR fluid. Measurements are taken by adhering the sensor to the part surface and lowering it into the MR fluid ribbon.

The drag force is measured using a linear translation stage,[33] a sapphire flat, and a 5-lb (≈ 22.2 N) load cell.[34] The interaction between the sapphire flat and the MR fluid forces the linear stage in the direction of flow. The linear stage, free to move horizontally, is driven into the load cell with a force equal to the drag force applied by the MR fluid. Drag force measurements are taken with the part at a depth of 0.5 mm into the MR fluid for experiments with nonaqueous MR fluids and a 1.0-mm depth with aqueous MR fluids (drag force measurements reported later for aqueous MR fluids without abrasives were done at both 0.5-mm and 1.0-mm depths). While this does not allow a direct comparison between pressure and drag measurements, it is sufficient for an evaluation of the relative performance of each fluid where the pressure and drag force are considered separately.

To fully understand mechanisms of material removal in MRF, the roles of the various constituents of the MR fluid need to be separated and evaluated. In previous work, we described how the nanohardness (H_{nano}) of the magnetic carbonyl iron (CI) and nonmagnetic polishing abrasives could be determined through novel nanoindentation techniques.[35,36] These results were used to conduct initial screening experiments on the importance of (1) the nanohardness of the CI in nonaqueous MR fluids without abrasives and (2) the effect of gradually adding DI water to the MR fluid and how the DI water changed abrasive interactions with the glass surface.[36] It was found that in nonaqueous MR fluids, CI that was softer than the glass surface slowly abraded material but did not penetrate the glass surface. Harder CI penetrated the glass surface. Adding DI water turned on chemistry and changed the way hard particles were seen to interact with the glass surface, due to the evolution of a hydrated or underdense (corroded) layer that enhanced rates of material removal. Removal rates were related to the mechanical properties of the CI and the glass. Surface morphologies resulting from abrasive/part interaction were consistent for three different glass types: BK7, LHG8, and FS.

Mechanisms of Removal in MRF

The work described in this section is based upon our previous screening studies. Aqueous MR fluids are used to remove material from a fused-silica (FS)[37] surface. These MR fluids are made up separately of hard CI (H_{nano} = 11.7±0.8 GPa), soft CI (H_{nano} = 2.2±1.0 GPa), and varying amounts of nonmagnetic polishing nano-abrasives (cerium oxide, aluminum oxide, and diamond). Variations in the material removal of FS (H_{nano} = 9.9±0.1 GPa) are monitored as a function of abrasive type and amount.

To study the effects of DI water in polishing requires a carrier fluid that suppresses the chemical effects. A dicarboxylic acid ester (DAE) has a density of 1.189 g/ml at 20°C[38] and a viscosity of 2.85 cps at 23°C,[39] which is similar to the density and viscosity of water, 0.982 g/ml and 1.0 cps, respectively.[38] This allows the nonaqueous DAE-based MR fluid to have a solids loading and rheology similar to the aqueous MR fluid. Another advantage of the DAE is that water is soluble up to 8.3 wt% (≈ 7 vol%), which makes it possible to study the chemical effects of water incrementally. Removal rates of BK7 glass were shown to increase exponentially with water concentration in this range (see Ref. 40).

The nine MR fluids studied here are summarized in Table 83.VIII. MR fluids 1 through 5 are made up with a carrier fluid and CI only. MR fluid 1 has 40 vol% soft CI and 60 vol% DAE; MR fluid 2 contains 40 vol% of the hard CI and 60 vol% DAE. MR fluid 3 is the same as MR fluid2, except

that 1 vol% DI water is added to the composition. MR fluids 4 and 5 are the same as MR fluids 1 and 2 except that MR fluids 4 (soft CI) and 5 (hard CI) utilize an aqueous carrier fluid (made up of DI water and <1 vol% of stabilizing agents).

1. Removal Experiments Without Polishing Abrasives

Each MR fluid was used on the STM to put a removal spot on a 50-mm-diam FS surface initially polished flat to within $\lambda/4$[21] and 0.9±0.1-nm rms roughness.[30] Normal stresses were measured as previously described. The peak pressure was found to be 129±4 kPa for all tests. The drag force was measured at a 0.5-mm gap and found to be 0.6±0.2 N. This 0.2-N variation is measured within three repetitions of a single experiment and is due to the resolution of the cell. Removal rates were determined interferometrically as described on p. 162. Stated removal rates are the peak removal rate for a single spot. Removal rates under identical conditions in MRF have been found to be repeatable to within 2.5% error.[23]

The results of this study are shown in Fig. 83.48. The areal rms roughness is plotted against the peak removal rate with the profilometer maps[30] given. The number on each profilometer map corresponds with the MR fluid number of the experiment, and the arrow gives the flow direction of the MR fluid. MR fluid 1, with soft CI, gives a low removal rate of 0.003 μm/min and a relatively low roughness (2.3±0.1 nm) and leaves faint grooves in the direction of flow. No sleeks are apparent (sleeks are defined as the pit-like features with comet tails). The removal rate is still low for MR fluid 2 (0.004 μm/min) but the areal rms roughness increases to 22.6±1.7 nm. Large numbers of pits and sleeks are seen as a result of the hard CI. The effect of adding a small amount of water to MR fluid 2 is shown with the result for MR fluid 3. The removal rate increases 2.5× to 0.010 μm/min, and the areal roughness drops to 7.0±1.0 nm rms. Also, the numbers of sleeks is reduced, and they tend to become longer scratches. Using MR fluids 4 and 5 for removal experiments further emphasizes the effect of the DI water. The removal rate increases from 0.01 μm/min (MR fluid 3) to 0.23 μm/min for MR fluid 4 and 0.14 μm/min for MR fluid 5. The 0.25-mm × 0.35-mm areal rms roughness values for these two aqueous MR fluids are greatly reduced (0.8±0.2 nm for MR fluid 4, and 1.3±0.3 for MR fluid 5). Also, the profilometer scans clearly indicate many fewer sleeks than for the nonaqueous MR fluids. It is interesting to note that the soft CI-based MR fluid 4 actually has a higher removal rate than the hard CI-based MR fluid 5. Otherwise, the presence of the DI water significantly diminishes the effect of the CI particle hardness in these experiments. Atomic force microscope images over 5-μm × 5-μm areas show no significant differences in the FS surface for removal experiments with MR fluids 4 or 5.

Table 83.VIII: Summary of the MR fluids used for material removal experiments.

MR Fluid Number	Vol% CI	†CI Nanohardness (Gpa)	DAE (Vol%)	*Water (Vol%)	Abrasive Type (Amount, Vol%)
1	40	2.2±1.0	60	0	None
2	40	11.7±0.8	60	0	None
3	40	11.7±0.8	59	1	None
4	40	2.2±1.0	0	60	None
5	40	11.7±0.8	0	60	None
6	40–45	11.7±0.8	0	Balance	Cerium oxide (0–1.0)
7	40–45	11.7±0.8	0	Balance	Aluminum oxide (0–1.0)
8	40–45	11.7±0.8	0	Balance	Diamond (0–0.1)
9	40–45	2.2±1.0	0	Balance	Cerium oxide (0–1.0)

*Aqueous MR fluids contain DI water and <1 vol% fluid stabilizers.

†Hardness measured with nanoindentation at 1 and 5 mN; FS nanohardness is 9.9±0.1 Gpa at these loads.[35,36]

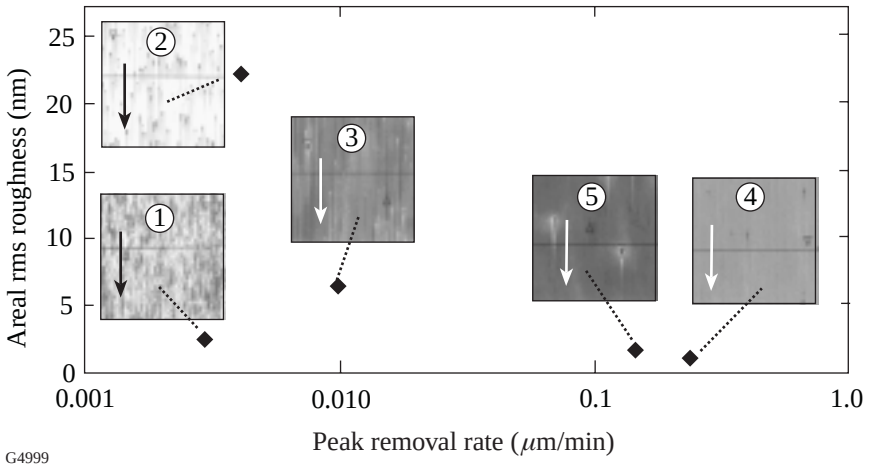

Figure 83.48
Areal (0.25-mm × 0.35-mm) rms roughness versus peak removal rate on FS for MR fluids 1 through 5. The soft CI (MR fluid 1) is able to remove material at a very low rate in the absence of the chemical effects of water, but does not pit the surface. The hard CI without water (MR fluid 2) gives low removal and high roughness as the hard CI leaves pits and sleeks in the softer FS surface. The addition of 1 vol% DI water to MR fluid 3 decreases the number of sleeks, which results in a decrease in roughness, and increases removal rate. Fully aqueous MR fluids 4 and 5 show a decrease in pits and sleeks, decrease in roughness, and dramatic increase in removal rate.

2. Removal Experiments with 40 vol% to 45 vol% CI and Nonmagnetic Nano-Abrasives

Table 83.VIII also lists the composition information for MR fluids 6 through 9. The same hard and soft CI powders that were used in the previous experiments are used here. Table 83.IX summarizes the properties of three different types of nonmagnetic abrasives used in combination with the CI's. These abrasives are nano-cerium oxide,[41] nano-aluminum oxide,[42] and nano-polycrystalline diamonds.[43] The cerium oxide and aluminum oxide abrasives are described in the product literature[44] as loosely bound agglomerates approximately 10 μm in size. It should be possible to disperse them down to agglomerates of a few hundred nanometers with moderate milling. Cerium oxide from an MR fluid was recently sized after being used in the STM. The mean diameter of the cerium oxide used for 10 days was found to be 0.125 μm and that used for only 2 h was >0.3 μm.[45] The milling that occurs in the STM among these particles and the CI breaks up any loose agglomerates. The stated primary particle sizes are 37 nm for the alumina and 11 nm for the cerium oxide.[44,46] The polycrystalline diamonds have a particle size of about 0.125 μm and are made up of crystals approximately 10 nm in size.[47] The advantage of using these nanoabrasives is that their particle sizes are similar, and they can be introduced in small quantities to the aqueous MR fluid without causing large changes in MR fluid rheology.

Notice from Table 83.VIII that the cerium oxide and aluminum oxide are added in concentrations ranging from 0 vol% to 1.0 vol%, while the diamonds are added in a volume loading up to only 0.1 vol%. This is due to the fact that the diamonds have an immediate and dramatic effect, whereas the other, softer abrasives have a more gradual effect. Also, due to the high cost of diamonds (≈ \$10/gram versus ≈ \$0.10/gram for cerium oxide), their addition into the MR fluid was halted as soon as the removal rate appeared to be unaffected by the addition of more diamonds. The difference in the performance of these abrasives is found to be significant even in the small volume loadings given here.

The next step in these experiments is to gradually add the nonmagnetic abrasives into the MR fluid. Figure 83.49 shows the removal rate for FS as a function of cerium oxide concentration for experiments done with MR fluid 6 at a 45 vol% hard CI concentration. The 5-μm × 5-μm AFM scans representative of the FS surface at a given concentration of cerium oxide and their cross-sectional profiles are also given in this figure. The 15-nm scale length given in Fig. 83.49 (and Fig. 83.50) is appropriate for each profile in the figure. The AFM scans are shown because their lateral resolution (approximately 20 nm) allows for better characterization of an abrasive's performance than the 0.25-mm × 0.35-mm profilometer maps do (lateral resolution = 1.1 μm). The white arrows in these AFM scans indicate the direction of flow. The removal rate increases from 0.62 μm/min with no cerium oxide to 0.94 μm/min with only 0.05 vol% cerium oxide. Distinct scratches caused by the small amount of cerium oxide in the MR fluid become apparent. The removal rate climbs to 3.01 μm/min when the cerium oxide concentration is increased 10× to 0.5 vol% cerium oxide. The removal rate increases further, to 3.51 μm/min, as the cerium oxide concentration is increased to 1.0 vol%. The areal rms is 0.9±0.1 nm for the scans in this figure. It is clear that not only does the cerium oxide become responsible for material removal but also a change in the surface morphology becomes apparent. These scans give more evidence that cerium oxide moves into the layer between the CI and the glass surface and becomes the primary agent for material removal. When cerium oxide is added to the MR fluid, the CI particle is no longer a primary abrasive. The increase in the number of polishing

grooves or scratches caused by the increase in nonmagnetic abrasive concentration is seen for all three types of nonmagnetic abrasives.

Additional information can be gained by considering the differences in morphology of the FS surfaces for the different abrasives used in polishing. Figure 83.50 shows the removal rates from experiments using the MR fluids with 45 vol% hard CI and the maximum loading of the three nano-abrasives used for these experiments. The lowest removal rate here (0.62 μm/min) is for the MR fluid without nonmagnetic abrasives. When 1.0 vol% aluminum oxide is added, the removal rate increases to 1.0 μm/min. Removal rates are even higher for the other nonmagnetic abrasives: 3.51 μm/min for 1.0 vol% cerium oxide, and 4.66 μm/min for 0.1 vol% diamond. An examination of the 5-μm × 5-μm AFM maps in Fig. 83.50 shows differences in how these three nonmagnetic abrasives interact with the glass surface. The scan for the MR fluid with 45 vol%

Table 83.IX: Summary of particle size information for the nano-abrasives used.

	Primary Particle Size (nm)	Aggregate Size (μm)	Agglomerate Size (μm)
Cerium Oxide	11	1.5	3.0
Alumina	37	0.3	N/A
Diamond	10	0.125	N/A

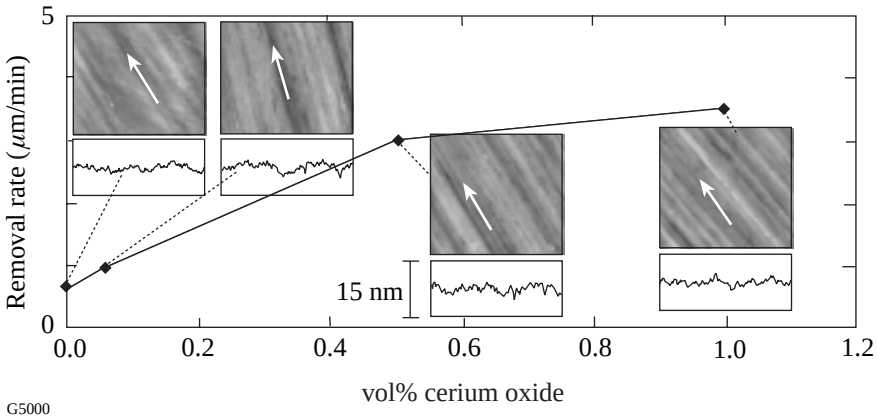

Figure 83.49
Removal rate versus concentration of cerium oxide for experiments using MR fluid 6 (each MR fluid contained 45 vol% hard CI and the aqueous carrier fluid). The removal rate increases with cerium oxide concentration, leveling off at about 3 μm/min. The inset AFM scans and accompanying profiles show evolution of the morphology of the FS surface as the abrasive is added. The cerium oxide moves to the interface between the CI and the glass to control removal. The 15-nm scale applies to all profile plots.

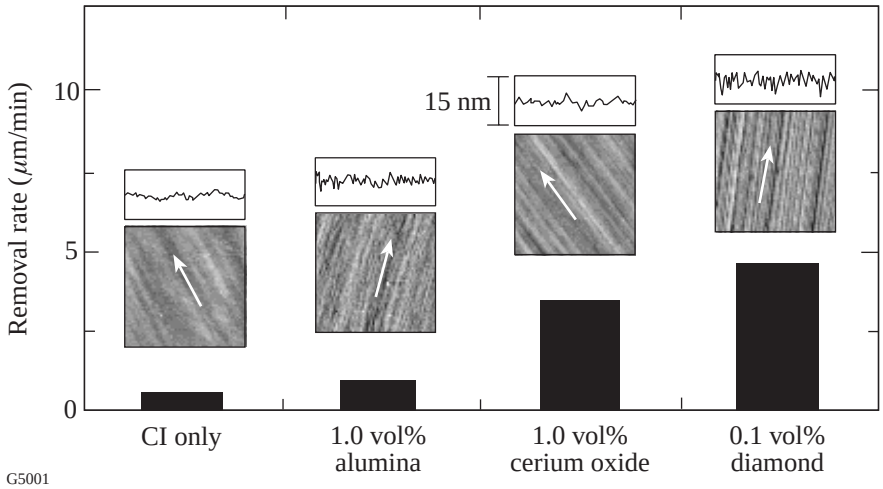

Figure 83.50
Removal rate as a function of abrasive type for MR fluids with 45 vol% hard CI and the maximum amount of abrasive used during these experiments (only up to 0.1 vol% diamond was used due to its high cost and high removal rates). The three abrasive types affect removal rates to varying degrees due to differences in how each interacts with the FS surface. Aluminum oxide gives deep (≈ 4 nm) discontinuous grooves; cerium oxide gives shallower (≈1 to 2 nm), continuous grooves; and diamond gives deep (≈4 nm) continuous grooves in the direction of flow. Characteristics of the polishing grooves help explain differences in removal rates for the three types of nano-abrasives.

hard CI without nonmagnetic abrasives is the same scan shown in Fig. 83.49. It has an areal rms of 0.8 nm. The aluminum oxide does not appear to continuously scratch the surface; instead, there appear to be several small discontinuous scratches at the FS surface. This leads to the lowest removal rates for the MR fluids containing nonmagnetic abrasives and an areal rms roughness of 1.2 nm. The cerium oxide gives wide, continuous scratches over the scanned region and an rms roughness of 0.9 nm. Finally, the diamond gives distinct narrow, continuous scratches along the direction of flow. The areal rms roughness for this scan is 1.4 nm. More differences in the behaviors of the abrasives are observed and are discussed below.

Differences in the Mechanics of Removal for Aqueous MR Fluids

Figure 83.51 shows the removal rate for MR fluids made up of 45 vol% hard CI and increasing amounts of nonmagnetic abrasives. Small amounts of diamond cause dramatic increases in removal rates. Cerium oxide increases removal to a lesser degree, and the aluminum oxide increases removal to an even lesser degree. These removal rates tend to level off at higher nonmagnetic abrasive concentrations. A certain minimum amount of nonmagnetic abrasive is needed to maximize the effectiveness, but there is a point where the addition of more abrasive has little or no effect on the removal rate. This has been shown to be true in more conventional polishing methods as well. Izumitani[4] showed a maximum in polishing efficiency of BK7 glass at about 1.5 vol% (10 wt%) cerium oxide. It is not clear whether this polishing was done on pitch or on a polyurethane lap. Silvernail and Goetzinger[8] show similar behavior on felt and Pellon laps. Their result depends on the applied pressure, but most of their removal rates level off above 1.5 vol% cerium oxide. Presumably this means that once the contact zone between the CI and the glass surface is saturated with nonmagnetic abrasive, further addition of abrasives is unnecessary.

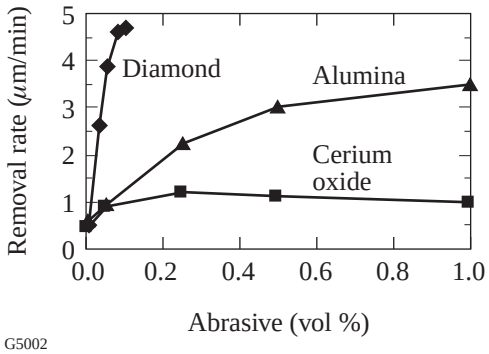

Figure 83.51
Removal rate versus vol% abrasive for 45 vol% hard CI and the aqueous carrier fluid. The diamonds are shown to have an immediate impact, dramatically increasing removal with less than 0.1 vol% concentration. The cerium oxide gradually increases removal. The aluminum oxide proves ineffective at increasing removal rates.

The reason for the relative effectiveness of each particle type is not clear, but these results do agree with AFM measurements as well as with the experiments with nonaqueous MR fluids. The cerium oxide grooves are approximately 1 nm to 2 nm deep, whereas the aluminum oxide and diamond grooves are approximately 4 nm deep.[40] The diamonds, the hardest particles, exhibit distinct continuous scratches, which leads to high removal rates. The cerium oxide also scratches the material in a continuous manner, but the scratches are less severe, which leads to an intermediate removal rate. The lowest removal rate is for the aluminum oxide particles, even though they give features deeper than those from cerium oxide and as deep as those from diamond. The scratches associated with these aluminum oxide particles are discontinuous. The relative hardness values of the aluminum oxide and cerium oxide particles are not known because these particles are too small for nanoindentation experiments. Nanohardness tests done in a previous work[35] showed that it is possible for an aluminum oxide particle to be either very much harder than a cerium oxide particle or of comparable hardness. Even if the relative hardness values are not known, however, differences in removal rates should not be surprising after viewing the AFM scans. The continuity of contact between the abrasives and glass surface is important for high removal rates.[6] The diamond and cerium oxide have this continuous contact while the aluminum oxide does not. The previous study[36] with the nonaqueous MR fluids without nonmagnetic abrasives (MR fluids 1 and 2) gave a similar result. The soft CI removed material from BK7 and LHG8 more efficiently than the hard CI. This trend changed somewhat when FS was used, probably because removal rates were so low and the hardness of FS is nearly the same as the hard CI. The proposed phenomenological explanation was that the soft CI could not penetrate the surface and was able to maintain contact with a shallow surface layer. The hard CI gave sleeks and pits and seemed to "skip" along the surface, causing discontinuity of contact between the abrasive and the glass surface. The reduced removal rate for aluminum oxide caused by discontinuity of abrasive/glass contact is consistent with these results. This may also be a partial explanation as to why Kaller[15] recommends abrasives that are softer than the bulk material and Izumitani[4] recommends abrasives with the same hardness of the hydrated layer.

Several references support these relative removal rates. The aqueous MR fluids have an approximate pH of 9. In Ref. 10 Cook analyzes work from others that shows cerium oxide is a much more efficient polisher than aluminum oxide in the pH range of 7 to 9. Cumbo[11] shows that cerium oxide has a higher removal rate on FS than aluminum oxide on FS at pH 10. Kaller and Cook give possible explanations for the effectiveness of cerium oxide. Kaller[15] explains that lattice defects in cerium oxide crystals allow cerium oxide to grip the material better and therefore enhance removal rates. Cook's[10] explanation is that the near neutral charge on the cerium oxide surface at this pH improves its ion exchange ability. The increased removal rate for diamond could be due to similar reasons. Its high hardness gives an explanation for the deep, distinct polishing grooves. The continuous contact maintained by the diamond could be explained by the fact that these diamonds are created by an explosion process,[47] which would likely result in many lattice defects. Kaller's explanation for cerium oxide provides support for the efficient removal seen with the MR fluids with diamond abrasives.

Figure 83.52 shows the removal rate as a function of CI concentration at the maximum nonmagnetic abrasive concentrations for the three abrasives used during these experiments. Notice that the data for MR fluids 6 (hard CI and cerium oxide) and 9 (soft CI and cerium oxide) coincide. This is more evidence that the type of CI is unimportant in aqueous environments with nonmagnetic abrasives, when the CI acts only as a lap. This plot shows the general trend that an increase in CI concentration leads to higher removal rates and that the relative increase in removal rate is largely related to the abrasive type. The nonmagnetic abrasives efficiently increase removal rate and decrease roughness. The diamonds are 10× more efficient than cerium oxide and aluminum oxide.

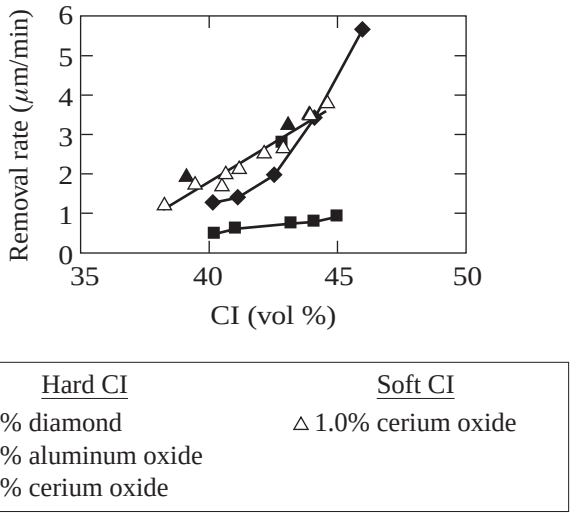

Figure 83.52
Effect of the CI concentration on removal with maximum amount of abrasive present. Once again the diamonds prove to be the most efficient, reacting strongest to the increase in CI concentration. The cerium oxide data consist of both hard and soft CI. This shows that the hardness of CI is unimportant in the presence of the abrasive.

Figure 83.53 shows how the removal rate changes with pressure and drag force (pressure and drag force changed as a result of varying CI concentration but keeping the nonmagnetic abrasive concentration and wheel velocity constant). Figure 83.53(a) shows the removal rate as a function of drag force at the maximum nonmagnetic abrasive concentration used for these experiments. Figure 83.53(b) shows the removal rate as a function of the peak pressure. Both drag force and pressure scale with removal rate in a linear way, which is consistent with considerations such as Preston's equation[6] discussed at the beginning of this article. The slopes of these lines (related to a Preston-type coefficient) depend on the type of abrasive used. The linear fits for the drag force tend to go through the origin, whereas they do not for the pressure. This supports the theory that in MRF the shear stress controls removal of material.

The drag force as a function of nonmagnetic abrasive content at a constant CI concentration is plotted in Fig. 83.54 for MR fluids 6, 7, and 8. As nonmagnetic abrasives are added, the drag force is reduced. This is once again consistent with the idea that nonmagnetic abrasives move to the region between the CI and the glass surface. All of the curves start at approximately the same initial drag force of about 5.5 N without nonmagnetic abrasive. While the MR fluid lap yields and conforms to the part surface, the magnetic field gives it a certain rigidity that makes it relatively difficult to shear. It is almost a two-body abrasion problem. This changes when nonmagnetic abrasives are added. They are forced to the glass surface because of the gradient in the magnetic field. At this point, the process becomes a three-body abrasion system. The magnetically stiffened CI forms the polishing lap that supports the free abrasives against the glass surface. This is similar to loose abrasive polishing on a conformal lap.

Consider the relative reductions in the drag force. The diamonds are seen to reduce the drag force dramatically, while increasing the removal rate just as dramatically. Adding aluminum oxide to the MR fluid also significantly reduces the drag

force, but adding cerium oxide has very little effect. This does not correlate with removal but may be interesting for a different reason. Several authors (see, for example, Refs. 10 and 15) hypothesize that one of the reasons cerium oxide is a successful polishing agent is because of its ability to chemically bond with the glass surface. This plot may begin to give physical evidence of this phenomenon.

All of these results suggest the use of a modified Preston equation to describe material removal in MRF. Consider Eq. (2). If a coefficient of friction is pulled out of C_P, it can be written as

$$\frac{dz}{dt} = C'_P \frac{\mu L}{A} \frac{ds}{dt}. \tag{3}$$

The term C'_P is a new Preston coefficient and μ is a coefficient of friction. The friction coefficient multiplied by a normal load gives a drag force (F_D) and Eq. (3) becomes

$$\frac{dz}{dt} = C'_P \frac{F_D}{A} \frac{ds}{dt}. \tag{4}$$

Finally, if this is considered over a very small volume of material (see callout on right in Fig. 83.46), the term F_D/A is simply the local shear stress at the part surface. This would give a removal rate description similar to Preston's equation based on the local shear stress (τ) at the part surface

$$\frac{dz}{dt} = C'_P \tau \frac{ds}{dt}. \tag{5}$$

Previous work[22,23] has shown that spot profiles are consistent with the shear stress distribution at the part surface. The remaining two terms in Eq. (5) are not yet fully understood. The relative velocity (ds/dt) is difficult to define in MRF. This velocity could be the relative velocity between the wheel and the part surface, but since the CI in the MR fluid actually supplies the lap, it is more correct that ds/dt is the relative velocity between the CI and the glass surface. This is not easily determined at this time. In fact, the behavior of the different abrasives in different MR fluids may indicate that this relative velocity depends on the abrasive type used. The wheel velocity was the same for all of the experiments described here, so this term was held as constant as possible in terms of controllable experimental parameters.

This work has also shown that, as for other polishing processes, it is difficult to define the Preston coefficient $\left(C'_P\right)$ in MRF. This term contains information on the chemistry of the carrier fluid, abrasive type, and glass type. Lambropoulos *et al.*[3] showed that the removal rate in MRF is proportional to the term $E/K_c H_K^2$ of the glass (E = elastic modulus, K_c = fracture toughness, and H_K = Knoop hardness of the glass). The experiments described here show that the removal rate depends on the abrasive type as well as the concentration. As a result, this coefficient would also have to contain information about the abrasive type used for a given MR fluid (probably size, shape, and hardness as well as the tribochemical "gripping"[15] power). Finally, it was shown that the presence of DI water dramatically changes how the abrasive interacts with the glass surface. Therefore, information on the chemical make-up of the carrier fluid must also be contained in this coefficient.

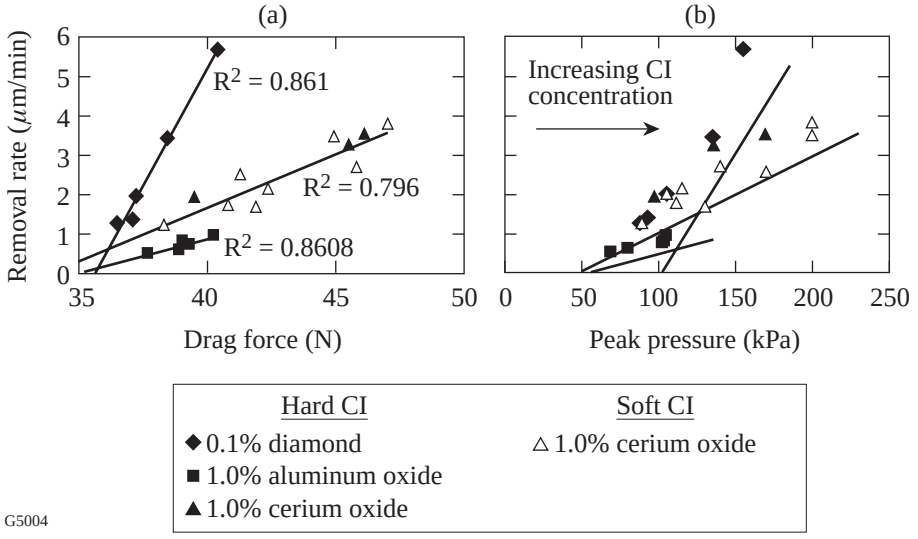

Figure 83.53
Removal rate versus drag force (a), and removal rate versus peak pressure (b). Removal rate increases linearly with pressure and drag force. The linear fits for the drag force go through the origin with high correlation coefficients, but do not for the pressure. This means that there can be removal with a nonzero pressure, but with no drag force (therefore no shear stress) there will be no removal. This supports the idea that shear stress controls removal rate in MRF.

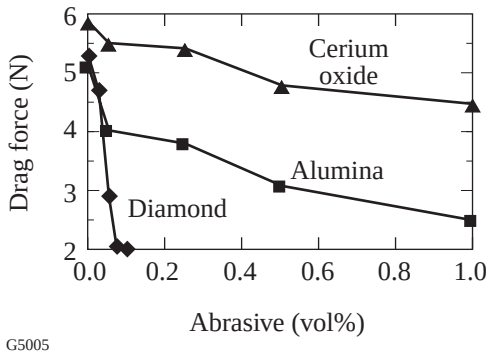

Figure 83.54
Effect of adding abrasive to MR fluids 4, 5, and 6 containing 45 vol% CI. In each case the addition of abrasive reduces the drag force, supporting the idea that MRF becomes a three-body abrasion problem. The cerium oxide maintains a high drag force, which supports the theories that cerium oxide has "chemical tooth."

Summary

The mechanisms of material removal in MRF have been presented. Previous work describes how the shear stress due to the hydrodynamic flow of the MR fluid between the rotating wheel and the part surface controls the removal rate. The idea that material removal depends on the shear stress at the part surface is supported by the linear relation between removal rate and the total drag force shown here. It has also been shown previously that the nanohardness of the CI is important in material removal with nonaqueous MR fluids. We show here that as DI water is added to the MR fluid, the differences in the behavior of the hard and soft CI become less significant as the removal rate dramatically increases for both. This is due to either the presence of a hydrated layer or reduced fracture toughness of the glass in aqueous MR fluids. The addition of nonmagnetic nano-abrasives increases removal rates further since they move to the interface between the CI and the glass surface to control material removal. A transition from two-body to three-body removal is hypothesized. The relative increase in removal depends on the amount and type of the abrasive since different abrasives interact with the glass surface in different ways. This behavior of the abrasive is evident from both AFM scans as well as drag force measurements. More work should allow these results to be summarized in a modified Preston equation based on the local shear stress at the part surface.

ACKNOWLEDGMENT

The authors would like to thank Rebecca Coppens, Henry Romanofsky, Leslie Gregg, Irina Kozhinova, Steven Arrasmith, Caleb Farny, and Susan Brandt of the Center for Optics Manufacturing for their help in this work. We would also like to thank Alexander Maltsev of LLE for his assistance in sample preparation. Support for this work was provided in part by the Center for Optics Manufacturing (COM), QED Technologies, U.S. Army Materiel Command, and DARPA (Defense Advanced Research Project Agency).

REFERENCES

1. M. J. Cumbo, "Chemo-Mechanical Interactions in Optical Polishing (Glass Finishing)," Ph.D. thesis, University of Rochester, 1993, Chap. 1.
2. M. Buijs and K. Korpel-van Houten, J. Mater. Sci. **28**, 3014 (1993).
3. J. C. Lambropoulos, S. D. Jacobs, and J. Ruckman, in *Finishing of Advanced Ceramics and Glasses*, edited by R. Sabia, V. A. Greenhut, and C. G. Pantano, Ceramic Transactions, Vol. 102 (The American Ceramic Society, Westerville, OH, 1999), pp. 113–128.
4. T. S. Izumitani, *Optical Glass*, American Institute of Physics Translation Series (American Institute of Physics, New York, 1986), Chap. 4, pp. 92–98.
5. A. Kaller, Glastech. Ber. **64**, 241 (1991).
6. F. W. Preston, J. Soc. Glass Technol. **XI**, 214 (1927).
7. W. L. Silvernail and N. J. Goetzinger, The Glass Industry **52**, 130 (1971).
8. *ibid.*, 172.
9. T. A. Michalske and B. C. Bunker, J. Am. Ceram. Soc. **76**, 2613 (1993).
10. L. M. Cook, J. Non-Cryst. Solids **120**, 152 (1990).
11. M. J. Cumbo, D. Fairhurst, S. D. Jacobs, and B. E. Puchebner, Appl. Opt. **34**, 3743 (1995).
12. H. Yokota *et al.*, Surf. Sci. **16**, 265 (1969).
13. M. Maaza *et al.*, Opt. Commun. **100**, 220 (1993).
14. A. B. Shorey, K. Xin, K.-H. Chen, and J. C. Lambropoulos, in *Inorganic Optical Materials*, edited by A. J. Marker III (SPIE, Bellingham, WA, 1998), Vol. 3424, pp. 72–81.
15. A. Kaller, Glass Sci. Technol. **71**, 174 (1998).
16. N. B. Kirk and J. V. Wood, J. Mater. Sci. **30**, 2171 (1995).
17. D. Golini, S. Jacobs, W. Kordonski, and P. Dumas, in *Advanced Materials for Optics and Precision Structures*, edited by M. A. Ealey, R. A. Paquin, and T. B. Parsonage, Critical Reviews of Optical Science and Technology (SPIE, Bellingham, WA, 1997), Vol. CR67, pp. 251–274.
18. S. D. Jacobs, S. R. Arrasmith, I. A. Kozhinova, L. L. Gregg, A. B. Shorey, H. J. Romanofsky, D. Golini, W. I. Kordonski, P. Dumas, and S. Hogan, in *Finishing of Advanced Ceramics and Glasses*, edited by R. Sabia, V. A. Greenhut, and C. G. Pantano, Ceramic Transactions, Vol. 102 (The American Ceramic Society, Westerville, OH, 1999), pp. 185–199.

19. S. R. Arrasmith, I. A. Kozhinova, L. L. Gregg, A. B. Shorey, H. J. Romanofsky, S. D. Jacobs, D. Golini, W. I. Kordonski, S. J. Hogan, and P. Dumas, in *Optical Manufacturing and Testing III*, edited by H. P. Stahl (SPIE, Bellingham, WA, 1999), Vol. 3782, pp. 92–100.

20. S. D. Jacobs, W. Kordonski, I. V. Prokhorov, D. Golini, G. R. Gorodkin, and T. D. Strafford, "Magnetorheological Fluid Composition," U.S. Patent No. 5,804,095 (8 September 1998).

21. Zygo Mark IVxp™ or Zygo GPI xpHR™ phase-shifting interferometer system was used for all data acquisition and analysis related to polishing spots, HeNe laser source with $\lambda = 632.8$ nm, Zygo Corporation, Middlefield, CT 06455.

22. V. W. Kordonski, D. Golini, P. Dumas, S. J. Hogan, and S. D. Jacobs, in *Smart Structures and Materials 1998: Industrial and Commercial Applications of Smart Structures Technologies*, edited by J. M. Sater (SPIE, Bellingham, WA, 1998), Vol. 3326, pp. 527–535.

23. A. B. Shorey, "Mechanisms of Material Removal in Magnetorheological Finishing (MRF) of Glass," Ph.D. thesis, University of Rochester, 2000, Chap. 3.

24. *ibid.*, Chap. 2.

25. A. B. Shorey, W. I. Kordonski, S. R. Gorodkin, S. D. Jacobs, R. F. Gans, K. M. Kwong, and C. H. Farney, Rev. Sci. Instrum. **70**, 4200 (1999).

26. Q22, QED Technologies, LLC, Rochester, NY 14607.

27. Field measurements were taken with the F. W. Bell Model 9500 Gaussmeter, Bell Technologies Inc., Ontario, FL 32807.

28. Computrac Max-1000 moisture analyzer, Arizona Instruments, Phoenix, AZ 85040-1941.

29. Brookfield DV-III cone and plate viscometer, Brookfield Engineering Laboratories, Inc., Stoughton, MA 02072.

30. Zygo NewView™ White Light Optical Profiler, areal over 0.25 mm × 0.35 mm with a 20× Mirau objective, 1.1-μm lateral resolution, Zygo Corporation, Middlefield CT 06455.

31. Nanoprobe III atomic force microscope (AFM), Digital Instruments, Santa Barbara, CA 93117.

32. Measured with the I-scan pressure measurement system, Tekscan, Inc., Boston, MA 02127. We used a 0.1-mm-thick 5051 pressure film with a maximum allowable load of 345 kPa (50 psi) and a lateral resolution of 1.27 mm.

33. Linear ball slide, Parker Hannafin Corporation, Cleveland, OH 44124-4141.

34. LKCP 475 5-lb load cell, Cooper Instruments, Warrenton, VA 20188.

35. A. B. Shorey, K. M. Kwong, K. M. Johnson, and S. D. Jacobs, Appl. Opt. **39**, 5194 (2000).

36. A. B. Shorey, L. L. Gregg, H. J. Romanofsky, S. R. Arrasmith, I. Kozhinova, J. Hubregsen, and S. D. Jacobs, in *Optical Manufacturing and Testing III*, edited by H. Stahl (SPIE, Bellingham, WA, 1999), Vol. 3782, pp. 101–111.

37. Corning 7940, Corning, Inc., Corning, NY 14831-0002.

38. R. S. Higgins and S. A. Kilinger, *High Purity Solvent Guide*, 3rd ed. (Baxter Diagnostics, Muskegon, MI, 1990).

39. Brookfield DV-II Digital Viscometer, Brookfield Engineering Laboratories, Inc., Stoughton, MA 02072.

40. A. B. Shorey, "Mechanisms of Material Removal in Magnetorheological Finishing (MRF) of Glass," Ph.D. thesis, University of Rochester, 2000, Chap. 5.

41. NanoTek Cerium Oxide, Nanophase Technologies Corporation, Burr Ridge, IL 60521.

42. NanoTek Aluminum Oxide, Nanophase Technologies Corporation, Burr Ridge, IL 60521.

43. 0.125-μm Hyprez-type PC diamonds, Engis Corporation, Wheeling, IL 60090.

44. NanoTek Cerium Oxide and Aluminum Oxide product literature of Nanophase Technologies Corporation, Burr Ridge, IL 60521, http://www.nanophase.com/products.shtml.

45. I. Kozhinova, L. Gregg, and J. Hesterman, "CPD-012 Cerium Oxide Powder Particle Size Measurements Using the Variety of Relative Refractive Indexes," Magnetorheological Finishing Laboratory internal report, Center for Optics Manufacturing, Rochester, NY, 25 February 2000.

46. "Fundamentals of Particle Sizing," product literature of Nanophase Technologies Corporation, Burr Ridge, IL 60521.

47. Engis diamond product literature, Engis Corporation, Wheeling, IL 60090, http://www.engis.com/hyprez/powders.html.

Optical and Plasma Smoothing of Laser Imprinting in Targets Driven by Lasers with SSD Bandwidths up to 1 THz

Introduction

A key issue for inertial confinement fusion (ICF)[1–3] is the Rayleigh–Taylor (RT) hydrodynamic instability.[4,5] In direct-drive ICF, nonuniformities in the drive laser produce pressure variations that "imprint" perturbations into the target. Unstable RT growth can amplify these perturbations, resulting in sufficient distortion of the target shell to degrade implosion performance. As coronal plasma is formed around the target, a region of thermal conduction is produced where nonuniform energy deposition can be thermally smoothed[6–8] before perturbations reach the ablation surface. A mode of laser nonuniformity couples to (or seeds) a mode of hydrodynamic instability up to the time that sufficient plasma smoothing occurs, and then imprinting ceases.[8] The time to produce this plasma and decouple the laser nonuniformities from the unstable ablation region depends on the perturbation wavelength and the energy deposition rate, i.e., the laser pulse shape. Fast-rising pulses produce plasma more rapidly than slow-rising pulses and therefore cause imprinting over shorter times.[9] During the time that this plasma evolves, nonuniformities in the drive must be minimized. To do so, many ICF target designs employ laser-beam-smoothing techniques,[10] most of which are time dependent. These techniques are quite effective and have produced marked improvements in the performance of direct-drive targets.[11]

As a result of these smoothing effects, the amount of imprint experienced by a target depends on the temporal behavior of both the laser uniformity and the plasma evolution. This article describes measurements of the effect of beam smoothing and pulse shape on imprinting, and the results are used to demonstrate the dependence of imprinting on the plasma formation rate. It extends the measurements described in Ref. 9 to the higher smoothing rates of 1-THz smoothing by spectral dispersion (SSD).[10]

Laser imprinting begins when nonuniformities in the laser produce variations in the initial pressure, launching nonuniform shocks into the target. These shocks produce velocity perturbations in the target that distort the shock and ablation fronts. (Regions of higher intensity produce stronger shocks that propagate faster than those driven at lower intensities.) These distortions create lateral mass flow in the shock-compressed material that in turn creates differential pressures that perturb the acceleration profile at the ablation surface. The RT instability exponentially amplifies these acceleration and velocity perturbations, producing additional mass perturbations in the target. (This redistribution of mass can be responsible for degrading the target performance and is observable in many experiments.) In addition to the above, effects such as dielectric breakdown in the target and laser filamentation[12] may create target perturbations that can seed the RT instability.

As the interaction proceeds, more plasma is formed and the laser light is absorbed at increasing distances from the ablation surface. The nonuniformities in intensity continue to drive acceleration perturbations at the ablation front, but thermal smoothing in the intervening plasma (between the absorption and ablation regions) reduces the magnitude of the pressure variations that reach the ablation surface. Eventually, the size of this conduction zone is sufficient to completely smooth the pressure perturbations, and imprinting stops. The calculated condition for the cessation of imprinting is[8]

$$kd_c \sim 2, \tag{1}$$

where k is the wave number of the imprinted perturbation and d_c is the average distance between the absorption region and the ablation surface.[13] In this article, the effect of the plasma formation rate and beam smoothing on imprinting is experimentally studied and found to be in good agreement with the condition of Eq. (1).

Experiments on the OMEGA laser system[14] measured an equivalent surface roughness of imprinting in planar targets using the growth of preimposed modulations for calibration.[9] This surface roughness is defined as the mass perturbation that produces similar resultant amplitudes after the linear RT growth phase.[15] Using this measure, the imprinting produced by different temporal pulse shapes and beam-smoothing tech-

niques is compared. Rapidly rising (~100 ps/decade) pulses produce less imprint than slowly rising pulses (~2.5-ns rise time) when no temporal beam smoothing is employed. Furthermore, the effect of SSD is less pronounced for these rapid-rise pulses. These are consistent with plasma smoothing[6–8] by thermal conduction and the intensity-dependent rate of plasma production.[9]

Simulations[15,16] that investigated imprinting have indicated that, for a given laser wavelength, the imprint efficiency (equivalent imprint level per fractional laser nonuniformity) depends linearly on the drive nonuniformity (i.e., $\delta m \propto \delta I/I$) for the intensities relevant to direct-drive ICF. The duration of imprinting, however, depends on the time required to produce a sufficiently sized plasma [Eq. (1)] to completely smooth pressure variations created by laser nonuniformities. As the thermal conduction region grows, longer wavelengths can be smoothed; thus, for each wavelength the duration of laser imprinting (and therefore its total magnitude) depends on the time required to develop a sufficiently large conduction zone. The plasma formation rate therefore affects the wavelength dispersion of imprinting. For a given wavelength of interest, imprinting ultimately ceases when the conduction region grows to a sizable fraction of the wavelength, satisfying Eq. (1). Thus, in order to reduce imprinting, it is also important that significant optical beam smoothing occurs while this plasma is forming. The experiments described below demonstrate the interplay between these two effects.

Experiments

In these experiments, six overlapping UV OMEGA beams irradiated 20-μm-thick CH (ρ = 1.05 g/cm^3) targets with preimposed modulations at 30- and 60-μm wavelengths. These wavelengths correspond to ℓ modes of 50 and 100 on millimeter-sized targets, which are important for direct-drive ICF on OMEGA. Experiments were performed with two laser temporal pulse shapes: a 3-ns square pulse and a 2.5-ns ramp pulse. The square pulse had a rise time of 100 ps per decade of intensity and an intensity of 2×10^{14} W/cm^2. The ramp pulse rose linearly from ~10^{13} to 2.5×10^{14} W/cm^2 in 2.5 ns after a 100-ps rise to ~10^{13} W/cm^2. For each pulse shape, experiments were performed with and without single-cycle, 2-D SSD beam smoothing at 0.2- and 1.0-THz bandwidths with modulation frequencies of 3×3 GHz and 1.6×11 GHz, respectively. In some cases, polarization smoothing (PS)[17] was added by using wedged birefringent plates.[18]

The driven targets were radiographed with x rays produced by a uranium backlighter irradiated at 2×10^{14} W/cm^2. X rays transmitted through the target and a 3-μm-thick Al blast shield were imaged by a framing camera with 8-μm pinholes filtered with 20 μm of Be and 6 μm of Al.[19] This filtration provided highest sensitivity at 1.3 keV and a resolution of at least 12 μm.

Since the initial perturbations produced by the laser are quite small, it is difficult to directly measure laser imprint. Measurements often rely on RT growth to produce detectable modulations in the target areal density. Relying on this nonlinear process as an "amplifier" makes it difficult to determine the initial amplitude of the seed, i.e., the amplitude of imprinting. The spectrum of laser nonuniformities is determined by the interference produced by the distributed phase plates (DPP's)[20] and the smoothing produced by SSD. These spectra were measured for a variety of conditions.[18,21] For the DPP-only case, the power spectrum of nonuniformities peaks at about 6 μm. SSD begins smoothing the shortest wavelengths, almost immediately (~25 ps) producing a spectrum that first flattens, then monotonically falls with frequency. These nonuniformities produce target perturbations that evolve due to dispersion in the RT growth and saturation mechanisms. As a result, the perturbation spectra for the various uniformity conditions are similar because the competing effects preferentially amplify the mid-frequencies (i.e., wavelengths from ~20 to 100 μm). The primary difference is the amplitude at a given time. Smoother irradiation profiles eventually produce features similar (albeit at later times) to those with higher irradiation nonuniformities. This evolution was shown for various uniformities in Refs. 18 and 22 and discussed at length in Ref. 23. As the spectra evolve, their peak moves to longer wavelengths. For these measurement times the spectral peak typically reaches 30 μm but seldom reaches 60 μm. These wavelengths are therefore of great interest because they can be most damaging to the target.

Low-amplitude, single-mode, preimposed target perturbations (at 30 and 60 μm) were used as a "control" for calibration, from which the initial amplitude of laser imprinting was determined. The basis of this calibration is that, in the linear regime of RT instability, imprinted perturbations grow at the same rate as preimposed modulations.[9,15,24] Although imprinting also produces velocity and acceleration perturbations, it is useful to assign it an equivalent surface roughness (mass modulation) to imprinting.[15]

Imprint was measured in this work by the method illustrated in Fig. 84.1(a), which shows a plot of the amplitude of single-mode target perturbations predicted by the 2-D code *ORCHID*.[25] The green curve shows the amplitude evolution

in a target having a 60-μm, single-mode mass perturbation and driven with a spatially perfect laser. The blue curve shows a similar evolution in an initially perfect target (no perturbations) driven by a laser having a single-mode intensity modulation (again with 60-μm wavelength). The blue curve starts at zero amplitude and rises as imprinting begins. At ~400 ps, RT growth begins and the evolution of imprint amplitude is parallel to the green curve. The RT instability amplifies both perturbations, imposed or imprinted, in the same manner. The equivalent surface roughness of imprinting can be deduced by extrapolating (dashed curve) the temporal evolution of the imprinted amplitudes (blue curve) back to t = 0 using the behavior of the preimposed mode (green curve). In the linear regime, modes of the same wavelength grow at the same rate, and the ratio of amplitudes for these two modes remains constant. Thus, an equivalent initial amplitude for imprinting can be deduced by comparing (after some RT growth) the amplitude of the imprinted mode to a preimposed mode of known initial value. Figure 84.1(b) shows the result of an experiment[23] where a target with a preimposed 60-μm perturbation was driven by a laser with 0.2-THz SSD without polarization smoothing. The upper two curves show the amplitude of the imposed modulations in two different experiments: one with an initial amplitude of 1250 Å and the other with 500 Å. The lower curve is the amplitude of the imprinted modes (at the same wavelength) for six different experiments. All experiments were performed under similar laser and target conditions.[23,26] The points at the lower left have large error bars because the signal is very near the noise level.

Since the imposed and imprinted perturbations grow at the same rate, the upper two curves in Fig. 84.1(b) are parallel to the lower curve. The ratio of the amplitudes for the two preimposed modes (initial amplitudes of 1250 Å and 500 Å) is constant and equal to their ratio at $t = 0$, showing that the RT growth is in the linear regime. This method requires that, for the modes of interest, the RT instability remain in the linear regime and that they experience no saturation or nonlinear effects.[27] Saturation of RT growth is discussed at length in Refs. 23 and 26, where it was shown that at $\lambda = 60$ μm, both the single-mode and the imprinted perturbations behaved linearly for the experimental conditions and observation times described in this article. For this experiment the 30-μm-wavelength imprinting data was measured before the onset of its saturation as observed in Refs. 23 and 26.

The amplitude of the equivalent surface roughness for a specific wave number is defined as[15]

$$A_{\mathrm{eq}}(k,0) = \left[A_{\mathrm{imprint}}(k,t)/A_{\mathrm{pre}}(k,t)\right]A_{\mathrm{pre}}(k,0), \qquad (2)$$

where $A_{\mathrm{imprint}}(k,t)$ is the measured amplitude of the imprinted features, $A_{\mathrm{pre}}(k,t)$ is the measured amplitude of the preimposed modulation, and $A_{\mathrm{pre}}(0)$ is the known initial amplitude of the preimposed modulation. A measure of imprint efficiency,[15] which can be readily compared to simulations, is $\eta_i(k) = A_{\mathrm{eq}}(k,0)/(\delta I/I)$, where $\delta I/I$ is the measured fractional irradiation nonuniformity at the same wavelength.

The amplitudes of the perturbations are obtained by Fourier analysis of the x-ray radiographed images.[19] The Fourier amplitude of the imprinted features at a given wavelength is the rms of all mode amplitudes at that wavelength, i.e., those modes at a given radius (centered at zero spatial frequency) in spatial-frequency space (the contribution of the preimposed

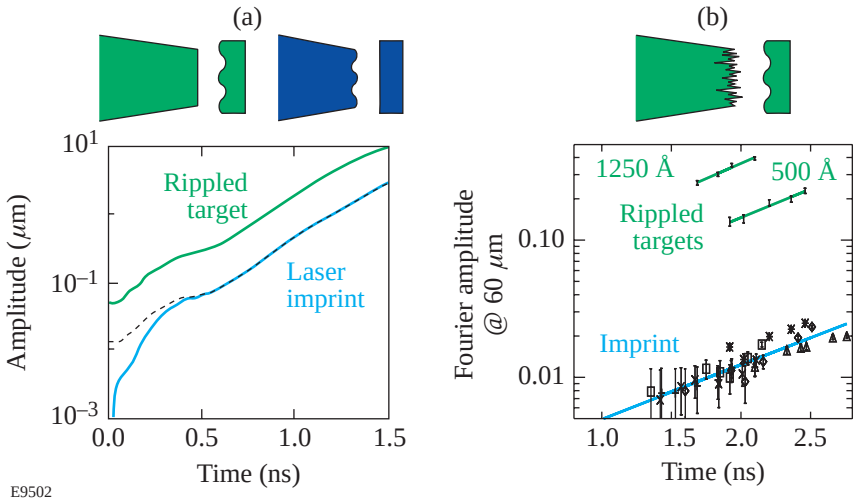

Figure 84.1
Derivation of equivalent surface finish. (a) Simulations of the perturbation amplitude evolution: T'm green curve is a 60-μm, single-mode mass perturbation driven with a spatially perfect laser. The blue curve shows the similar evolution in an initially perfect target (no perturbations) driven by a laser having a 60-μm, single-mode intensity modulation. The equivalent surface finish is defined as the point where the dashed curve intercepts t = 0. (b) Experimental results showing the measured amplitudes (optical depth) for imprinted (lower set) and imposed modulations (upper two sets). All are at 60-μm wavelength.

modulation is not included). The features of interest at 30 μm and 60 μm are easily observed by the camera, which has ~15-μm resolution.

The preimposed single-mode modulations appear as localized features along a single axis in the Fourier plane and at the spatial frequency of their modulation. The time-dependent amplitude of the preimposed mode is obtained by subtracting (in quadrature) the rms amplitude of the imprinted modes at the same time. The analysis box is ~300 μm in the target plane; thus, in Fourier space, the pixel size is ~3.3 mm^{-1}. (The box size is optimized to ensure that all the power in the preimposed mode is contained in a single pixel in each Fourier half-plane.)

For these experiments a variety of beam-smoothing techniques were used. A single-beam laser with a DPP and no SSD provides a static speckle pattern with ~80% to 100% nonuniformity in wavelengths from 2 μm to 250 μm.[21] The speckle results from the interference of many beamlets produced by diffraction in the DPP optic. The speckle pattern is statistical in nature with a sufficiently short correlation length that multiple overlapped beams can be treated as statistically independent patterns. Thus six-beam irradiation reduces this nonuniformity to $\sqrt{6}$ times lower than the single-beam value. Additional beam smoothing is provided by SSD, which, by introducing bandwidth onto the laser, produces a statistically independent speckle pattern every $\Delta t = t_c$, where $t_c \sim 1/\Delta\nu$ is the correlation time and $\Delta\nu$ is the UV laser bandwidth.[10] SSD does not reduce nonuniformities instantaneously, rather the time-averaged rms uniformity is reduced by $\sqrt{t_c/\langle t\rangle}$, where $\langle t\rangle$ is the averaging time. Thus, the drive uniformity is time dependent and varies with the amount of bandwidth applied to the laser. These experiments were performed with one of two laser bandwidths, either $\Delta\nu = 0.2$ THz$_{UV}$ or 1.0 THz$_{UV}$. (All experiments with SSD used two-dimensional SSD.) In the former case the IR bandwidths were 1.25 Å × 1.75 Å and in the latter case 1.6 Å × 11 Å. In some cases, polarization smoothing (PS) using birefringent wedges[18] was added to the drive beams. Polarization smoothing provides an instantaneous $\sqrt{2}$ reduction in nonuniformity by dividing each beam into two orthogonal polarizations that are separated by 80 μm in the target plane.[18]

Figure 84.2 shows the equivalent surface roughness (in μm) of imprinting measured at 60-μm wavelength for a series of shots that used a 3-ns square pulse with four different smoothing conditions (all with similar drive intensities). The temporal axis is the time at which each measurement was taken. These data separate into distinct sets associated with each uniformity condition and are constant in time. Both these observations are expected and confirm the utility of this technique. When the growth of the imprinted features is in the linear regime, their amplitude should remain a constant fraction of that of the preimposed mode, leading to a constant inferred surface roughness. This quantity's dependence on the initial uniformity produced by the various beam-smoothing techniques indicates the sensitivity of the method. For example, the addition of polarization smoothing (diamonds) to the 0.2-THz SSD experiments (blue squares) reduced the equivalent surface roughness by the expected factor of $\sqrt{2}$. Similarly, the increase in the SSD bandwidth from 0.2 (blue squares) to 1.0 (**x**'s) THz without polarization smoothing reduced the equivalent surface roughness by ~0.60. This is the reduction expected from models of the optical smoothing by SSD (see below). The results for all conditions are listed in Table 84.I.

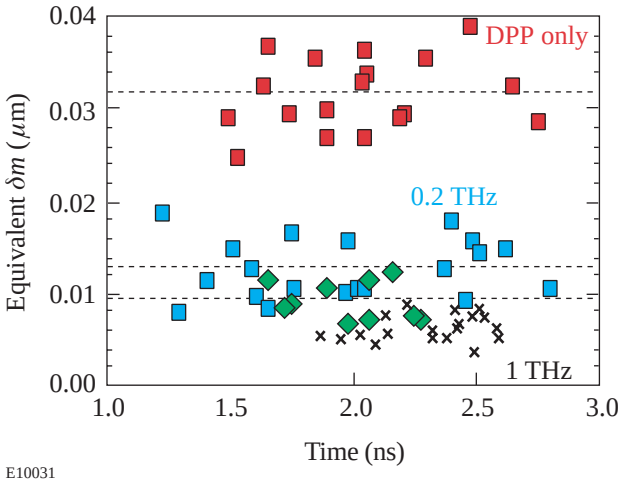

Figure 84.2
The equivalent surface roughness (in μm) at 60-μm wavelength derived from planar targets driven by laser beams having a 3-ns square pulse and four types of beam smoothing applied: DPP only (red squares), DPP + 0.2-THz SSD (blue squares), DPP + 0.2-THz SSD + PS (diamonds), and DPP + 1-THz SSD (**x**'s). The data segregate according to the laser nonuniformity with the total amount of imprinting decreasing with increased beam smoothing.[9]

The effect of pulse shape on imprinting was studied by repeating these measurements with a slowly rising pulse, i.e., with a ~2.5-ns rise to the maximum intensity. Figure 84.3 shows the equivalent surface roughness as a function of time for the two pulse shapes, each with and without 0.2-THz SSD. Again the data group according to laser conditions (pulse shape or SSD) and exhibit an approximately constant value over a considerable time.

These data show that without SSD the ramp pulse (red triangles) produces about 50% more imprinting (rougher equivalent surface) than the square pulse (red squares). They also indicate that 0.2-THz SSD produces a greater reduction of imprinting (~2.5×) on the ramp pulse (blue triangles) than for the factor of 2.2 observed for the square pulse (blue squares). Similar experiments were performed using preimposed modulations with $\lambda = 30$ μm.

The imprint efficiency was calculated for the experiments without SSD using the single-beam irradiation nonuniformities reported in Ref. 21. The uniformity results were scaled by the differences in analysis boxes between the x-ray radiography ($L = 300$ μm; $\Delta k = 0.021$ μm^{-1}) and the optical experiments ($L = 440$ μm; $\Delta k = 0.0143$ μm^{-1}). In addition, the values obtained in Ref. 21 were reduced by $\sqrt{6}$ since these experiments utilized six overlapped beams. Thus, $\delta I/I$ was 0.0068 for 30 μm and 0.0049 for 60 μm. Lastly, a factor of 2 was included to relate the complex amplitude for $\delta I/I$ to the equivalent surface roughness, which was normalized using a real (cosine) function. The measured imprint efficiencies are shown in Table 84.I. Since the SSD produces time-varying uniformity, it is difficult to assign a single number to the uniformity; therefore, the imprint efficiency is not quoted for those cases. The effect of SSD will be discussed below.

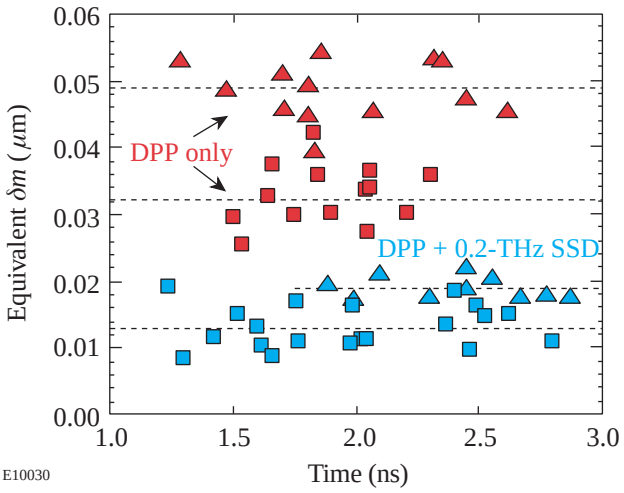

Figure 84.3
The deduced equivalent surface roughness of the imprinted features (at 60 μm) for two pulse shapes: 3-ns square (squares) and ramp (triangles). These data show that for the same laser nonuniformity, a ramp pulse produces more imprinting. The blue and red symbols correspond, respectively, to each of the pulses with and without 2-D SSD. They indicate that the effect of SSD is greater for the ramp pulse.[9]

As discussed above, the duration of imprinting depends on the time required to produce sufficient plasma atmosphere to enable smoothing. As a result, the ramp pulse imprints for a longer duration than the square pulse because it delivers energy at a slower rate and therefore generates the smoothing plasma more slowly. Thus the ramp pulse will imprint for a longer duration, leading to a higher equivalent roughness. The imprint efficiencies measured here are lower, as expected, than those observed by Glendinning *et al.*[24,28] using an even slower rise and lower-intensity ramp pulse.

Simulations of Imprint and Plasma Smoothing

The experiments were simulated with the 2-D hydrodynamics code *ORCHID* to determine the predicted imprint efficiency and the effects of plasma smoothing. The imprint efficiencies were calculated by imposing a single-mode nonuniformity in the laser irradiation. The evolution of the resulting perturbations was compared to that of preimposed mass perturbations at the same wavelength. The experimental temporal pulse shapes were used in the simulations. The simulation results shown in Table 84.I are in reasonable

Table 84.I: Equivalent surface roughness and imprint efficiency for various conditions.

Pulse-Shape Uniformity	Equivalent Surface Roughness (μm)		Imprint Efficiency: $(\delta m/\rho)/(\delta I/I)$ (μm)			
			Experiment		Simulation	
	60 μm	30 μm	60 μm	30 μm	60 μm	30 μm
Square (no SSD)	0.032±005	0.022±004	3.3±0.4	1.6±0.3	1.7	1.1
Ramp (no SSD)	0.049±008	0.023±005	5.0±0.6	1.7±0.4	3.1	2.3
Square (0.2-THz SSD)	0.013±003	0.010±003				
Ramp (0.2-THz SSD)	0.017±005	0.011±004				
Square (1-THz SSD)	0.009±0.0018	0.0044±0.0015				
Ramp (1-THz SSD)	0.0105±0.0022	0.0054±0.0019				

agreement with the measured values. Similar imprint efficiencies were calculated with the 2-D hydrodynamics code *LEEOR*.[29] The 2-D simulations underestimate the imprint efficiency at 60 μm, similar to the observations of Glendinning *et al.*[24,28] For the 30-μm perturbations, the simulations also underestimate the square-pulse data but overestimate the ramp-pulse data.

The inherent real surface roughness of these foils (transverse to the imposed modulations) was measured to be less than 1% of the imposed mode and, therefore, did not contribute significantly to the error in the measurements of either the imprinted or the imposed modes. The measured signal for the preimposed mode also has a contribution from the imprinted signal at that distinct mode. Since the relative phase of these two signals is arbitrary, the resultant signal can vary significantly when the imprint is a sizable fraction of the preimposed mode.To minimize this effect, the imprinted modes were kept below 30% of the imposed mode by increasing the amplitude of the imposed modes on shots without SSD. Most experiments were performed with the imprint between 0.1 and 0.25 of the imposed mode. This represented a trade-off between the noises from either too low a signal in the imprinted modes or that affecting determination of the imposed mode, while keeping both signals below the saturation limits.

The effect of plasma formation rate on thermal smoothing of nonuniform energy deposition was investigated using *ORCHID*. Figure 84.4 shows the calculated amplitude of pressure perturbations (solid curves) at the ablation surface as a function of time for two cases: a ramp pulse and a square pulse, both without SSD. In these simulations a static 60-μm-wavelength, 5% spatial-intensity modulation was imposed on the irradiation profile. The pressure perturbations that reach the ablation surface diminish as the plasma expands. Note that for the ramp pulse, the smoothing rate is slower and the perturbations persist for a longer period. The temporal evolution (dashed curves) of the normalized conduction zone (kd_c) for the two pulse shapes is also shown. This is defined as the distance between the ablation surface and the mean of the energy deposition profile as weighted by a diffusion length e^{-kz} and is normalized to the wave number.[13] (The energy deposition profile must also be accounted for since considerable smoothing can take place in the plasma region outside the critical surface.) Imprinting ceases when pressure perturbations at the ablation surface are reduced to negligible levels. Figure 84.4 shows that for both pulse shapes this occurs when $kd_c \sim 2$, providing a measure of the decoupling time for the case of constant uniformity (no SSD). This analysis has also been applied to other wavelengths and both pulse shapes, and found to confirm that $kd_c \sim 2$ is the applicable condition. Figure 84.5 shows the simulations of the normalized smoothing length (kd_c) as a function of time for the square (dashed) and ramp (solid) pulses for three wavelengths: 30, 60, and 120 μm. The solid points indicated the time at which the modulations in ablation pressure diminish to zero for each case. This occurs for $kd_c \sim 2$ for all six cases. As the plasma evolves, shorter wavelengths are smoothed sooner than longer wavelengths; this in part determines the dispersion in wavelength of the imprint efficiency. Thus, for the broad spectrum of laser

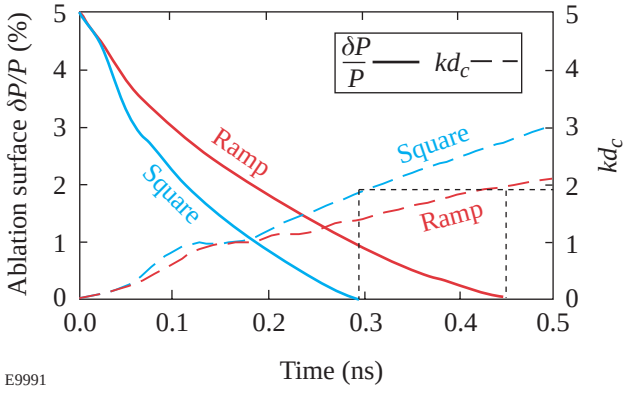

Figure 84.4
The calculated amplitude of 60-μm perturbations (solid curves) in the pressure at the ablation surface as a function of time. The size of the conduction zone (dashed curves) as a function of time in CH targets driven by the square and ramp pulses. These graphs show that, for 60-μm perturbations, decoupling occurs at 290 ps for the square pulse and 450 ps for the ramp pulse.[9]

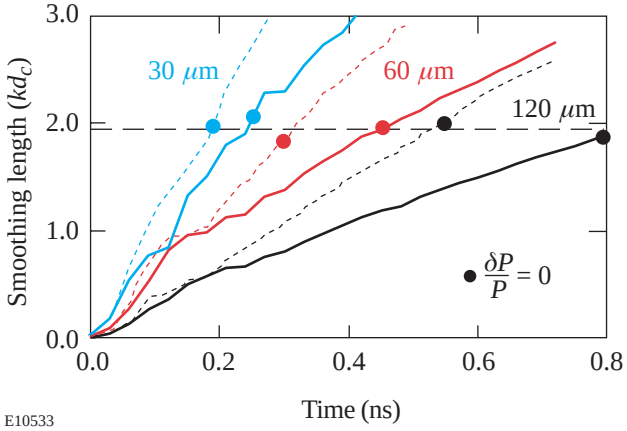

Figure 84.5
Simulations of the normalized smoothing length (kd_c) versus time for square (dashed) and ramp (solid) pulses. The points indicate the time at which the modulations in ablation pressure diminish to zero. Perturbations with wavelengths of 30, 60, and 120 μm are all smoothed when $kd_c \sim 2$.

nonuniformities present in laser speckle, the short-wavelength modes are smoothed first. These modes also have faster growth rates and experience saturation sooner than longer-wavelength modes. In contrast, the longer-wavelength modes are smoothed less, but also grow at slower rates. As a result, intermediate wavelengths (ℓ modes of 50 to 100 on millimeter-sized targets) become dominant and, therefore, are of most concern for target stability. The calculated decoupling times for 60-μm wavelengths were found to be 290 and 450 ps for the square and ramp pulses, respectively. For 30-μm wavelengths, the respective times were 190 and 270 ps.

Decoupling and the Dynamics of Smoothing

Plasma smoothing and decoupling of imprinted perturbations are confirmed experimentally by analyzing experiments with time-dependent beam smoothing. By matching the observed reduction of imprinting to the smoothing rate of SSD, the effect of thermal smoothing by the plasma atmosphere is observed. Figure 84.6 shows the imprint reduction [at (a) 60-μm and (b) 30-μm wavelengths] as a function of time for SSD bandwidths of 0.2 (red solid points) and 1.0 (blue solid points) $\mathrm{THz}_{\mathrm{UV}}$. In each, the curves are the irradiation nonuniformity (normalized to that at $t = 0$) predicted by an optical model[21] (basically a $1/\sqrt{t\Delta\nu}$ dependence). The points are the measurements of the reduction in imprinting due to SSD. This reduction is calculated by normalizing the SSD data to measurements without SSD. Reference 21 demonstrated that the optical model accurately predicts the smoothing rate and the ultimate uniformity achieved with 0.2-THz SSD (red curve). It is expected that it represents the performance of 1.0 THz (blue curve) as well. The imprint data are plotted at the calculated decoupling times described above. The square-pulse data (squares) are shown for 0.2 THz (red points) and 1.0 THz (blue points). The ramp-pulse data (triangles) are similarly coded for SSD. The predictions (open symbols) are shown slightly displaced in time for clarity. Figure 84.6 shows that (1) for 60 μm the calculated decoupling times are consistent with the optical data and (2) the hydrocode models the effect of SSD and the plasma production rate (pulse shape) quite well. The 30-μm data for the ramp pulse are above both the optical smoothing rate and the hydrocode results, i.e., the reductions are less than expected. This may be caused by the imprinting measurement for the no-SSD, 30-μm case (denominator for reduction calculation) being too low. A possible mechanism for error in the measured imprint is the onset of saturation in the imprinted (3-D) modes that has not yet affected the preimposed (2-D) modes. Reference 23 showed that for these conditions the 30-μm perturbations can experience saturation if the amplitudes are high enough. Furthermore, the ramp pulse, because of its late decoupling time, imprints more readily and therefore would be most susceptible to saturation. Unfortunately, the spread in data does not allow its temporal trend to be discerned with precision and saturation cannot be easily detected.

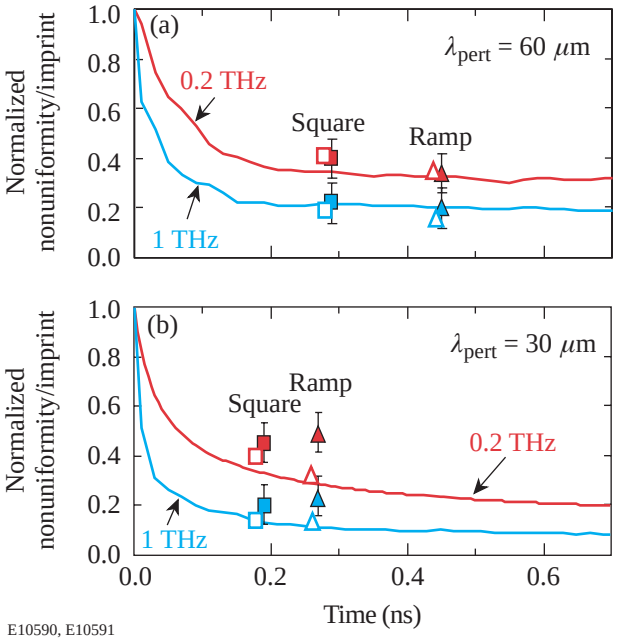

Figure 84.6
The normalized nonuniformity [(a) for 60 μm and (b) for 30 μm] as predicted by the optical model (curves) with the measured reductions in imprint for 0.2 THz (solid points) and 1 THz (shaded points) for square (squares) and ramp (triangles) pulse shapes. The predictions by *ORCHID* are shown as open points (similarly identified).

Conclusion

Using preimposed modulations on planar targets to calibrate imprinting amplitudes, this work has confirmed imprinting's expected dependence on drive-laser nonuniformity, showing the utility of the equivalent-surface technique. It has demonstrated that imprinting depends on the temporal shape of the drive laser. This occurs because thermal smoothing in the coronal plasma ultimately limits the duration of imprinting and therefore its total amplitude. Once there is sufficient plasma, the pressure perturbations no longer reach the unstable ablation surface and imprinting stops. Steeply rising pulses produce plasma more rapidly than slowly rising pulses and therefore produce less imprinting. The simulations of the static cases (DPP's only) show behavior that is consistent with the decoupling times predicted for these conditions. Moreover, using the dynamic case of 2-D SSD, the improvements in uniformity inferred by measuring imprint are consis-

tent with both the measured rate of smoothing by SSD and the decoupling times predicted by the hydrocodes; they also verify the predictions of Eq. (1). The increase in laser bandwidth to 1 THz has produced reductions in the imprint level that agree with expected performance. These results provide confidence in our ability to model and control imprinting in direct-drive ICF targets.

ACKNOWLEDGMENT

This work was supported by the U.S. Department of Energy Office of Inertial Confinement Fusion under Cooperative Agreement No. DE-FC03-92SF19460, the University of Rochester, and the New York State Energy Research and Development Authority. The support of DOE does not constitute an endorsement by DOE of the views expressed in this article.

REFERENCES

1. J. Nuckolls *et al.*, Nature **239**, 139 (1972).
2. J. D. Lindl, Phys. Plasmas **2**, 3933 (1995).
3. S. E. Bodner, D. G. Colombant, J. H. Gardner, R. H. Lehmberg, S. P. Obenschain, L. Phillips, A. J. Schmitt, J. D. Sethian, R. L. McCrory, W. Seka, C. P. Verdon, J. P. Knauer, B. B. Afeyan, and H. T. Powell, Phys. Plasmas **5**, 1901 (1998).
4. Lord Rayleigh, Proc. London Math Soc. **XIV**, 170 (1883).
5. G. Taylor, Proc. R. Soc. London Ser. A **201**, 192 (1950).
6. K. A. Brueckner and S. Jorna, Rev. Mod. Phys. **46**, 325 (1974).
7. S. E. Bodner, Phys. Rev. Lett. **33**, 761 (1974).
8. V. N. Goncharov, S. Skupsky, T. R. Boehly, J. P. Knauer, P. McKenty, V. A. Smalyuk, R. P. J. Town, O. V. Gotchev, R. Betti, and D. D. Meyerhofer, Phys. Plasmas **7**, 2062 (2000).
9. T. R. Boehly, V. N. Goncharov, O. Gotchev, J. P. Knauer, D. D. Meyerhofer, D. Oron, S. P. Regan, Y. Srebro, W. Seka, D. Shvarts, S. Skupsky, and V. A. Smalyuk, "The Effect of Plasma Formation Rate and Beam Smoothing on Laser Imprinting," submitted to Physical Review Letters.
10. S. Skupsky and R. S. Craxton, Phys. Plasmas **6**, 2157 (1999).
11. D. D. Meyerhofer, J. A. Delettrez, R. Epstein, V. Yu. Glebov, R. L. Keck, R. L. McCrory, P. W. McKenty, F. J. Marshall, P. B. Radha, S. P. Regan, W. Seka, S. Skupsky, V. A. Smalyuk, J. M. Soures, C. Stoeckl, R. P. J. Town, B. Yaakobi, R. D. Petrasso, J. A. Frenje, D. G. Hicks, F. H. Séguin, C. K. Li, S. Haan, S. P. Hatchett, N. Izumi, R. Lerche, T. C. Sangster, and T. W. Phillips, "Core Density and Temperature Conditions and Fuel–Pusher Mix in Direct-Drive ICF Implosions," to be published in Physics of Plasmas.
12. H. A. Rose and D. F. DuBois, Phys. Fluids B **5**, 3337 (1993).
13. H. Azechi *et al.*, Phys. Plasmas **4**, 4079 (1997).
14. T. R. Boehly, D. L. Brown, R. S. Craxton, R. L. Keck, J. P. Knauer, J. H. Kelly, T. J. Kessler, S. A. Kumpan, S. J. Loucks, S. A. Letzring, F. J. Marshall, R. L. McCrory, S. F. B. Morse, W. Seka, J. M. Soures, and C. P. Verdon, Opt. Commun. **133**, 495 (1997).
15. S. V. Weber, S. G. Glendinning, D. H. Kalantar, M. H. Key, B. A. Remington, J. E. Rothenberg, E. Wolfrum, C. P. Verdon, and J. P. Knauer, Phys. Plasmas **4**, 1978 (1997).
16. R. J. Taylor *et al.*, Phys. Rev. Lett. **79**, 1861 (1997).
17. Y. Kato, unpublished notes from work at LLE, 1984.
18. T. R. Boehly, V. A. Smalyuk, D. D. Meyerhofer, J. P. Knauer, D. K. Bradley, R. S. Craxton, M. J. Guardalben, S. Skupsky, and T. J. Kessler, J. Appl. Phys. **85**, 3444 (1999).
19. V. A. Smalyuk, T. R. Boehly, D. K. Bradley, J. P. Knauer, and D. D. Meyerhofer, Rev. Sci. Instrum. **70**, 647 (1999).
20. Y. Lin, T. J. Kessler, and G. N. Lawrence, Opt. Lett. **20**, 764 (1995).
21. S. P. Regan, J. A. Marozas, J. H. Kelly, T. R. Boehly, W. R. Donaldson, P. A. Jaanimagi, R. L. Keck, T. J. Kessler, D. D. Meyerhofer, W. Seka, S. Skupsky, and V. A. Smalyuk, J. Opt. Soc. Am. B **17**, 1483 (2000).
22. T. R. Boehly, R. L. McCrory, C. P. Verdon, W. Seka, S. J. Loucks, A. Babushkin, R. E. Bahr, R. Boni, D. K. Bradley, R. S. Craxton, J. A. Delettrez, W. R. Donaldson, R. Epstein, D. Harding, P. A. Jaanimagi, S. D. Jacobs, K. Kearney, R. L. Keck, J. H. Kelly, T. J. Kessler, R. L. Kremens, J. P. Knauer, D. J. Lonobile, L. D. Lund, F. J. Marshall, P. W. McKenty, D. D. Meyerhofer, S. F. B. Morse, A. Okishev, S. Papernov, G. Pien, T. Safford, J. D. Schnittman, R. Short, M. J. Shoup III, M. Skeldon, S. Skupsky, A. W. Schmid, V. A. Smalyuk, D. J. Smith, J. M. Soures, M. Wittman, and B. Yaakobi, Fusion Eng. Des. **44**, 35 (1999).
23. V. A. Smalyuk, T. R. Boehly, D. K. Bradley, V. N. Goncharov, J. A. Delettrez, J. P. Knauer, D. D. Meyerhofer, D. Oron, D. Shvarts, Y. Srebro, and R. P. J. Town, Phys. Plasmas **6**, 4022 (1999).
24. S. G. Glendinning, S. N. Dixit, B. A. Hammel, D. H. Kalantar, M. H. Key, J. D. Kilkenny, J. P. Knauer, D. M. Pennington, B. A. Remington, R. J. Wallace, and S. V. Weber, Phys. Rev. E **54**, 4473 (1996).
25. R. L. McCrory and C. P. Verdon, in *Inertial Confinement Fusion*, edited by A. Caruso and E. Sindoni (Editrice Compositori, Bologna, Italy, 1989), pp. 83–124.
26. V. A. Smalyuk, T. R. Boehly, D. K. Bradley, V. N. Goncharov, J. A. Delettrez, J. P. Knauer, D. D. Meyerhofer, D. Oron, and D. Shvarts, Phys. Rev. Lett. **81**, 5342 (1998).
27. S. W. Haan, Phys. Rev. A **39**, 5812 (1989).
28. S. G. Glendinning, S. N. Dixit, B. A. Hammel, D. H. Kalantar, M. H. Key, J. D. Kilkenny, J. P. Knauer, D. M. Pennington, B. A. Remington, J. Rothenberg, R. J. Wallace, and S. V. Weber, Phys. Rev. Lett. **80**, 1904 (1998).
29. D. Shvarts, U. Alon, D. Ofer, R. L. McCrory, and C. P. Verdon, Phys. Plasmas **2**, 2465 (1995).

Analysis of a Direct-Drive Ignition Capsule Designed for the National Ignition Facility

Introduction

One of the primary missions of the National Ignition Facility[1] (NIF) is to achieve fusion ignition and moderate gain by means of inertial confinement fusion (ICF). A typical ICF experiment involves the implosion of a small spherical capsule containing deuterium–tritium (DT) fuel using high-power laser light. The energy is absorbed in a thin, outer region of the capsule, which quickly heats and ablates, expanding outward and accelerating the remainder of the capsule inward, compressing the contained DT fuel to ignition conditions. The implosion can be tailored to give a number of assembled fuel configurations of which the most energy efficient[2] is isobaric with a central high-temperature hot spot surrounding a low-temperature main fuel layer. The central hot spot initiates the fusion reaction, which leads to a burn wave propagating into the main fuel layer. For direct-drive target designs two main effects can prevent the correct assembly of the fuel: (1) preheat of the fuel[3] and (2) hydrodynamic instabilities of the imploding shell.[2,4–6]

Hydrodynamic instabilities, and their effects on imploding ICF capsules, have been the subject of extensive studies in the past.[2,6–11] Nonuniformities in the applied drive, coupled with imperfections at the target surface, seed Rayleigh–Taylor (RT) unstable growth at the ablation front. In addition, rarefaction waves generated at the perturbed inner ice surface, due to the breakout of the first shock, return to the ablation region and contribute to the instability there.[12–14] These perturbations feed through the shell and couple with the existing perturbations on the inner ice surface. This combination serves as the seed for RT growth at the ice/vapor interface when the ice layer begins to decelerate around the hot spot.

A good understanding of how the unstable growth of perturbations affects target performance (ignition and gain) is required to guide the development of the laser and target systems' specifications. Of specific importance is the designation of parameters dealing with the allowable levels of roughness at both the outer and inner surfaces of the capsule, the allowable limit on laser power imbalance and beam mistiming, and the amount of bandwidth requirements for single-beam uniformity. A consistent scaling that includes the net effect of all of these mechanisms acting together is developed. Such a "nonuniformity budget" adds flexibility in the design of the laser and target systems, allowing trade-offs to be made among the four sources of nonuniformity.

This article will first examine briefly the current direct-drive point design[3,6,15] for the NIF. Using one-dimensional 1-D *LILAC*[16] results, we show that the capsule design is robust. Next we examine the scaling of target gain in terms of a spectral ensemble of the rms surface roughness of the inner ice surface ($\bar{\sigma}$) at the end of the acceleration phase of the implosion. The scaling of gain with $\bar{\sigma}$, developed using the results of many two-dimensional (2-D) *ORCHID*[17] simulations, allows for the definition of a global nonuniformity budget that can ascertain the relative significance of the different nonuniformity sources in reducing capsule performance. In addition, the modeling of each of the four perturbation mechanisms is discussed. Overall target gain results are evaluated, and the scaling of the physical specification being modeled (e.g., outer-surface roughness) with $\bar{\sigma}$ is established. We also discuss the physical mechanisms that determine why target gain scales with $\bar{\sigma}$. Finally, we construct an overall nonuniformity budget for NIF systems, using the combined effects of each of the four perturbation mechanisms.

Point Direct-Drive Target Design for NIF

The base-line direct-drive designs for NIF employ a solid (cryogenic) DT-shell target with a thin polymer ablator (required to fabricate the cryogenic shell) surrounding the DT-ice shell.[3,15] The designs use shock preheat to control the isentrope of the ablation surface and the fuel. Variation in the isentrope ($\alpha = 1$ to 4, where α is the ratio of the fuel pressure to the Fermi-degenerate pressure) is achieved by varying the incident laser pulse shape. Based on the results of current OMEGA experiments and theoretical calculations of these NIF designs, we have selected the 1.5-MJ, $\alpha = 3$ design to be the point design for further study.

The point design has been shown[3] to be robust to several design uncertainties including control of laser pulse shape, material equation-of-state modeling, operating temperature, and the effects of hot electrons produced by laser–plasma instabilities (LPI). Figure 84.7(a) shows the target specification; Fig. 84.7(b) shows the pulse shape for this design. The DT-ice thickness and adiabat of the implosion determine the intensity and duration of the foot. In this design, the foot is 4.25 ns long at a power of 10 TW. This region launches a 10-Mbar shock through the DT ice. At the time of shock breakout at the rear surface of the DT ice, the pulse ramps up to the drive region, which lasts for 2.5 ns at a power of 450 TW. This rapid rise in intensity generates pressures of approximately 80 Mbar and thus accelerates the DT ice inward. The $\alpha = 3$ design is predicted, by 1-D calculations, to have a gain of 45, a neutron-averaged ion temperature of 30 keV, and a peak fuel ρR = 1.3 g/cm^2. The peak in-flight aspect ratio (IFAR) of this design is 60, and the hot-spot convergence ratio is 29.

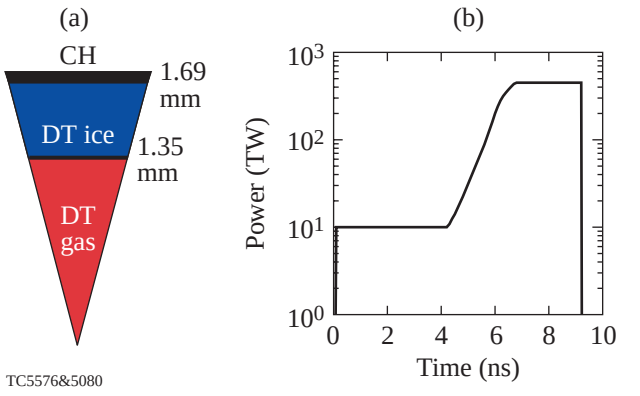

Figure 84.7
The base-line, $\alpha = 3$, "all-DT," 1.5-MJ target design. (a) The target specification and (b) the pulse shape.

Modeling Sources of Nonuniformities

During the foot pulse, the laser intensity is constant and the ablation front travels at constant velocity. While no RT unstable growth is present during this time, perturbations could still grow due to the presence of power imbalance, outer-surface roughness [Ritchmyer–Meshkov (RM)-like instability][18] and laser nonuniformity (laser imprint).[18–20] Later, when the laser intensity ramps up to drive conditions, the ablation front starts to accelerate, producing conditions for RT growth that amplify the target nonuniformities seeded during the foot pulse. Establishing the relative importance of each source of nonuniformity requires that a time in the implosion at which all sources complete their contribution to the total nonuniformity be identified. Since perturbations due to power imbalance grow through the whole laser pulse, laser imprint and RM growth occur only during the foot pulse, and the feedout brings perturbation to the unstable ablation front during the main pulse, the best choice is at the end of the acceleration phase. At this time the ice/vapor surface perturbations decouple from the now-stable ablation surface. To construct a scaling of gain versus mode spectrum at the ice/vapor surface ($\bar{\sigma}$), 2-D *ORCHID* burn calculations were compiled to examine the effects of various, initially applied, ice/vapor-interface perturbation spectra ($\ell = 2$–50) on target gain. It was found that the target gain can be well represented in terms of an effective nonuniformity ($\bar{\sigma}$) that gives a reduced weight to the low-order modes ($\ell < 10$):

$$\bar{\sigma} = \sqrt{0.06\,\sigma^2_{\ell<10} + \sigma^2_{\ell>9}}\,, \qquad (1)$$

where $\sigma^2_{\ell<10}$ is the sum-in-quadrature of all modes of nonuniformity with $\ell < 10$ and $\sigma^2_{\ell>9}$ is the corresponding sum for $\ell > 9$. Results of this scaling, shown in Fig. 84.8, indicate that the gain threshold for point design occurs at a value of $\bar{\sigma} = 2.5$.

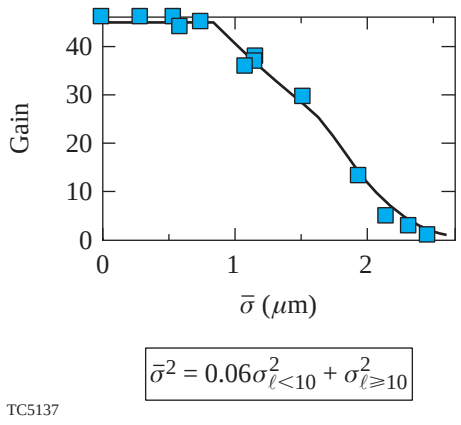

Figure 84.8
The reduction in target gain is drawn as a function of an ensemble of modal amplitudes taken at the ice/vapor interface at the end of the acceleration phase of the implosion.

From Eq. (1), it can be seen that the high-order modes can be significantly more damaging to capsule gain than that due to the low-order modes. The small $\bar{\sigma}$ weighting of the low-order modes is just a reflection of two effects. First, as has been shown in several single-mode studies,[21,22] capsule gain is far more tolerant of levels of low-order modes than the high-order modes. Secondly, during the deceleration phase of the implosion, low-order modes experience less growth than the high

ℓ modes.[23,24] During the acceleration phase at the ablation front, the development of the high-order modes, seeded from the laser imprint, feedout from the inner ice surface, and the outer-surface roughness, is critical in determining the integrity and survivability of the shell. Due to lateral smoothing, however, the high-order modes do not feed through efficiently to the inner ice surface. The result is that the low-order modes tend to dominate the inner ice roughness at the end of the acceleration phase.[8]

These results help construct 2-D simulations of the four main perturbation mechanisms: laser imprint, power imbalance, and inner- and outer-target-surface roughness. Each of the four mechanisms was studied independently to evaluate the sensitivity of gain to variations in the laser and target system specifications. Applying the $\bar{\sigma}$ scaling to the results allows a nonuniformity budget for NIF to be determined. By establishing a global budget in terms of $\bar{\sigma}$, it is possible to evaluate the contribution of each source to the problem as a whole, providing insight into the mission-critical nonuniformities, and giving direction for trade-offs between the various sources of nonuniformity. A discussion of the modeling, sample numerical results, and how gain scales with $\bar{\sigma}$ for each perturbation mechanism follows.

1. Power Balance

The term "power balance" can be applied to a wide range of temporal, beam-to-beam intensity differences, arising from laser amplifier saturation, beam mistiming, variations in frequency conversion (angular or polarization tuning), and/or the transport of the UV energy to the target. The effects of power imbalance on the applied irradiation are modeled by determining the on-target power variations between the beams due to their propagation through the laser system. Each beam develops a unique temporal power history, which is used to calculate the irradiation nonuniformity on-target over the entire implosion. Many NIF laser power histories were calculated by Jones[25] and supplied to the authors.

Further modeling uses 1-D *LILAC* density and temperature profiles and a 2-D laser absorption routine from *ORCHID* to determine the absorbed energy at the critical surface for a single beam. This absorption profile is scaled for each beam and, using the orientation of the beam, mapped onto a sphere representing the critical surface of the target. All 192 beamlets of the NIF system are mapped to 48 unique positions on the sphere. The resulting spherical intensity distributions are then decomposed for each time and used as input to 2-D *ORCHID* simulations.

Two series of 2-D *ORCHID* runs were completed using each of the NIF power histories. The first series used the calculated power imbalance as supplied by Jones,[25] while the second series artificially doubled the power imbalance to determine ignition thresholds. In addition, further runs were compiled to assess the effects of beam mistiming for each series. A contour plot of mass density at stagnation from a typical power imbalance *ORCHID* simulation, illustrated in Fig. 84.9, clearly shows the presence of low-order modes distorting the core region. Compiling the results of these simulations, shown in Fig. 84.10, illustrates the degradation of yield with increasing on-target nonuniformities and beam-to-beam mistiming. The target gain is shown plotted against the on-target rms perturbation. The base-line NIF requirements for power balance and beam mistiming have been given as 8% rms beam-to-beam and 30-ps rms beam-to-beam, respectively.[26] The reduction in gain for these requirements is low (~10%). The results are also plotted against their calculated values of $\bar{\sigma}$ in Fig. 84.10(b). A $\bar{\sigma}$ value of ~0.85 corresponds to the NIF requirements for power imbalance.

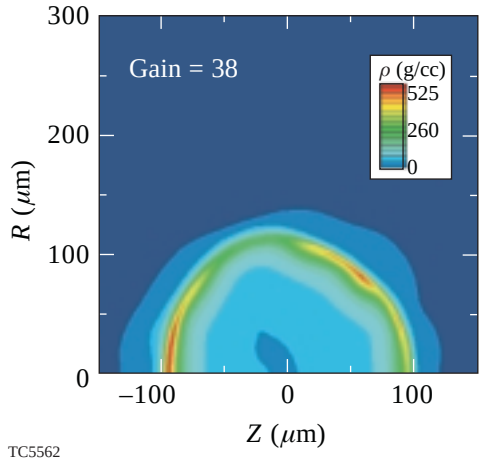

Figure 84.9
Core disruption due to NIF specifications of power imbalance and beam mistiming is dominated by low-order modes but has little effect on target gain.

2. Ice/Vapor Surface Roughness

Since there is uncertainty in the initial ice spectrum, 2-D *ORCHID* simulations were completed assuming an initial prescription for the spectral behavior and amplitude of the roughness of the form $a = a_0/\ell^{\beta}$. Variations in β and total σ_{rms} were examined from 0 to 1.5 and 0.5 to 12 μm, respectively. These simulations assumed smooth outer surfaces and perfect laser illumination. Figure 84.11 shows an example where the initial surface roughness of the ice/vapor interface was 3.8-μm rms (2.0-μm rms summed over modes 10 to 50) with $\beta = 0.75$.

Figure 84.11(a) illustrates the density contours of the imploding shell at stagnation. Perturbations at the ablation front are clearly visible. Comparing the roughness spectrum ice/vapor interface at the end of the acceleration phase with that of the initial spectrum, illustrated in Fig. 84.11(b), it can be seen to have increased in magnitude and steepened to a higher order of β. These results are typical of the behavior of the inner ice perturbations. They can be attributed to the unique process of feeding out to the ablation surface, undergoing RT growth, and then feeding back into the original surface. The low modes dominate with the high modes being filtered by lateral smoothing while traversing the ice layer.

The results from this series of 2-D *ORCHID* runs are compiled in Fig. 84.12. In Fig. 84.12(a), the behavior of target gain is drawn as a function of the rms of just the low-order modes (ℓ = 2–10). These curves indicate that while the low-order modes are dominant, the high-order modes, as the applied spectra flatten, cannot be ignored. However, Fig. 84.12(b) shows the gain can be well represented by the behavior of $\bar{\sigma}$, regardless of the applied spectrum.

3. Outer-Surface Roughness

The direct-drive point design has traditionally been called the "all-DT" design, which is a misnomer. The DT-ice capsule

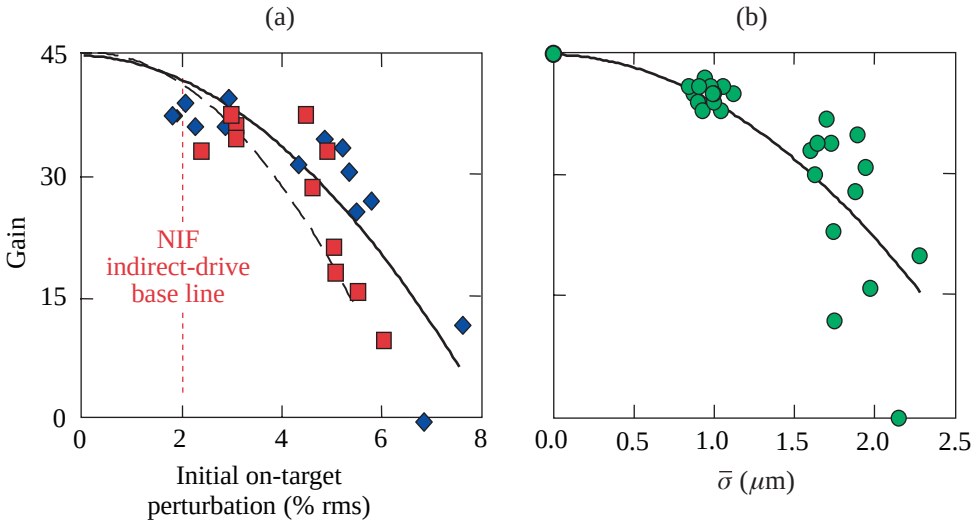

Figure 84.10
NIF laser power histories have been used to validate the NIF base-line power imbalance specifications. (a) Calculated target gain is drawn as a function of the on-target rms perturbation for beams with perfect timing (◆) and beams with a 30-ps rms (beam-to-beam) mistiming (■). (b) Calculated target gain is shown to scale well with $\bar{\sigma}$.

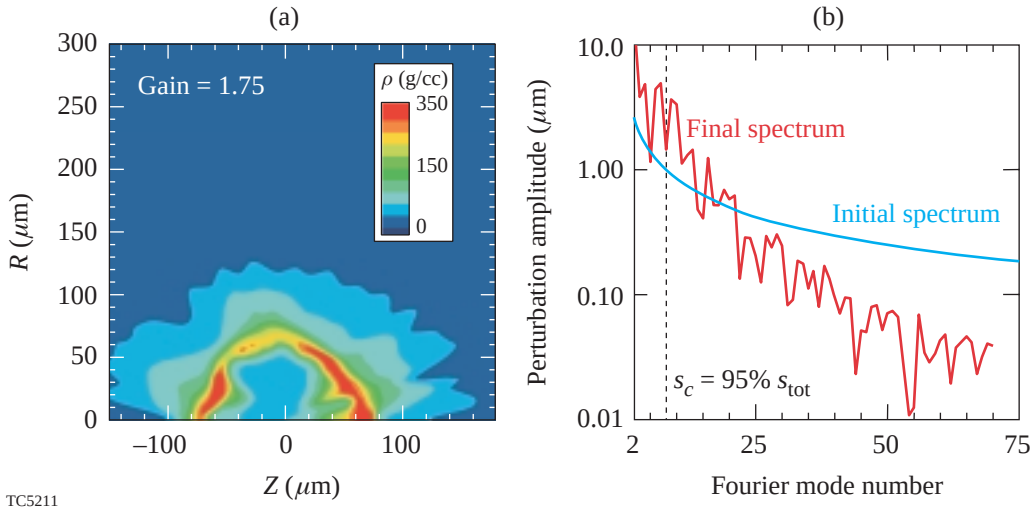

Figure 84.11
Results from *ORCHID* simulation indicate target gain depends strongly on the development of the low-order modes. (a) Density contours drawn at the time of stagnation. Note that the gain for this target was reduced from 45 to ~2. (b) Spectra of ice/vapor interface at the beginning and end of the implosion. Note the concentration of power in the low-order modes at stagnation.

is actually fabricated within a thin (1- to 2-μm) plastic microballoon, which serves, albeit for a short time, as an ablator. The density mismatch at the CH/DT interface can lead to additional perturbation growth at the ablation front. Indeed, when the shock reaches the interface, it produces a transmitted shock into the DT and a reflected rarefaction wave that moves back out toward the ablation surface. After the rarefaction wave breaks out at the ablation front, the latter starts to accelerate at $a \sim \left(p^{\mathrm{CH}} - p^{\mathrm{DT}}\right)/(\rho d)$, where ρ and d are initial density and thickness of CH layer, and p^{CH} and p^{DT} are the post-shock pressures in CH and DT, respectively. The acceleration occurs for a time interval $\Delta t_{\mathrm{acc}} \sim d/c_s$ (until the compression wave is generated at the ablation front), where c_s is the sound speed of the compressed ablator material. During the acceleration, the ablation surface is RT unstable, and perturbations in the front grow by a factor $\exp\left(\sqrt{ka\Delta t_{\mathrm{acc}}^2}\right) \sim \exp\left(\varepsilon\sqrt{kd}\right)$, where the coefficient ε depends on the shock strength. Furthermore, since the ablation front is rippled, the rarefaction wave breaks out first at the front's valleys and then at the peaks. Thus, there is a delay Δt_{rw} between accelerating the peaks and valleys of the ablation front. This delay creates an additional velocity perturbation $\delta v = a\Delta t_{\mathrm{rw}}$. The RT growth and δv increase the kinetic energy of the front ripple, leading to a higher perturbation amplitude. Since the RT growth factor increases with the ablator thickness d, minimizing the perturbation growth during the foot pulse requires the minimum thickness of the ablator layer.

Modeling the effects of these perturbations on indirect-drive target performance[7–10] has led to an outer-surface spectrum that is considered by target fabrication groups to be the "NIF standard." A series of 2-D *ORCHID* simulations were compiled using the NIF standard as a base-line level of surface roughness (σ = ~115 nm). The power spectrum of the nonuniformity was then doubled and quadrupled to determine the resultant ice/vapor surface distortion at the end of the acceleration phase. As can be seen in Fig. 84.13, the effect of these

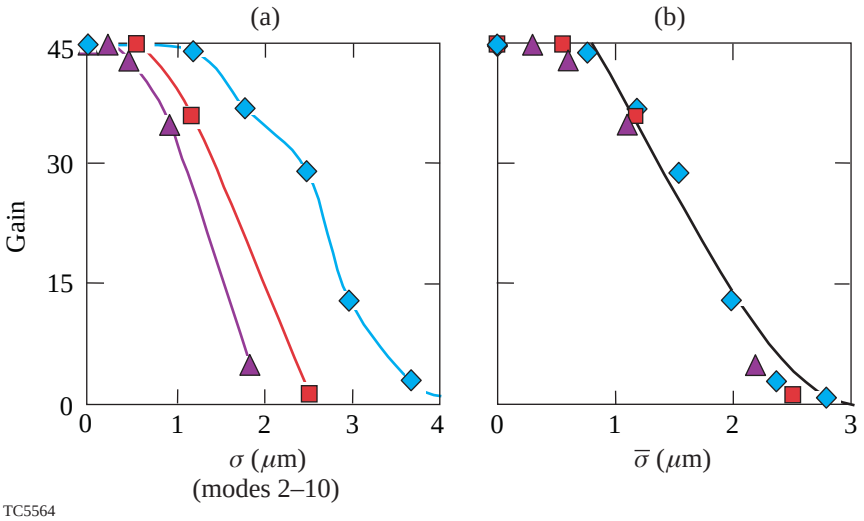

Figure 84.12
Results from *ORCHID* simulation of inner-ice-surface roughness indicate that high-order modes contribute to the reduction of capsule gain. Mode amplitudes obey $a = a_0/\ell^{\beta}$, $\beta = 0.00$ (▲), 0.75 (■), and 1.50 (◆). (a) Calculated target gain is drawn as a function of the initial rms finish of the ice layer in modes 2–10. (b) Calculated target gain is now drawn as a function of the calculated values of $\bar{\sigma}$.

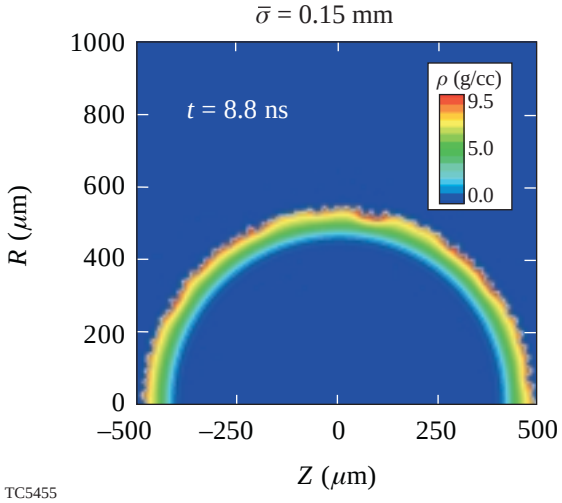

Figure 84.13
ORCHID simulations, using twice the NIF standard surface roughness (230 nm), reveal no significant disruption of the ice/vapor interface at the end of the acceleration phase of the implosion.

levels of surface roughness on the ice/vapor interface has been minimal. While the density contours show a ~4-μm perturbation at the ablation surface, the inner-ice-surface layer shows no appreciable disruption. After analysis, the rms value of the resultant spectrum results in a value of $\bar{\sigma} \sim 0.15$. These results are consistent with Goncharov's analytic model[18,27] and indicate that the gain of the direct-drive point design is insensitive to outer-surface roughness below our calculations of ~250 nm. These results indicate that, if given the NIF standard roughness, the outer surface of the direct-drive point design will not contribute significantly to the global nonuniformity budget.

4. Laser Imprint

The last, and possibly most important, source of nonuniformity for the direct-drive point design is the imprinting of variations in the laser-beam profile onto the surface of the capsule. Our understanding of imprint is based on both theory[18,20] and experiment.[19,28] These studies have shown that, without any temporal smoothing of laser profiles, imprinted perturbations will lead to shell failure during the implosion. Smoothing of individual laser profiles is a major issue for direct drive. The direct-drive design for NIF includes the combined application of a distributed phase plate (DPP),[29,30] polarization smoothing,[31] and smoothing by spectral dispersion (SSD)[32] within each of its 192 beams.

In modeling the irradiation nonuniformity, the single-beam DPP spectrum[33] (modes 2 to 200) is modified for the 40-beam overlap and the use of polarization smoothing. The application of SSD produces statistically independent speckle patterns every $\Delta t = t_c$, where $t_c = 1/\left[\Delta\nu \sin\left(kn\delta/2\right)\right]$ is the correlation time ($\Delta\nu$ is the laser bandwidth, n is the number of color cycles, and δ is the speckle size, which is 7 μm for NIF). The NIF specification for smoothing has been given as 1-THz bandwidth and two color cycles. In the case of the constant-intensity foot pulse, this reduces the time-averaged laser nonuniformity by a factor $\sqrt{\left(t_c/\langle t\rangle\right)}$, where $\langle t\rangle$ is the averaging time. The longest wavelength that can be smoothed by SSD is determined by the maximum angular spread $\Delta\theta$ of the light propagating through the laser.[34] Using $\Delta\theta = 100$ μrad and a laser focal length $F = 700$ cm, SSD can smooth spherical-harmonic modes down to $\ell_{\text{cut}} = 15$. To model these intensity variations, a series of *ORCHID* simulations were compiled, randomly changing the sign of the individual laser mode amplitudes every $\Delta t = t_c$. The laser power histories for these runs were then averaged giving a smoothing rate similar to that of SSD, which was then applied to a single simulation.

Calculations for the effect of laser imprint have been performed to determine the ice/vapor distortion at the end of the acceleration phase of the implosion. Comparing the density contours of two separate implosions of the same shell, driven under different imprint scenarios, illustrates the need for this level of smoothing. The majority of *ORCHID* simulations below were performed with one color cycle to determine the minimal level of smoothing. Figure 84.14 shows the density contours for two implosions of the same shell using (a) no bandwidth and (b) 1-THz bandwidth (one color cycle). The calculated values of $\bar{\sigma}$, compiled from a series of *ORCHID* simulations, can be used to project the target gain as a function of applied bandwidth as shown in Fig. 84.15. From this graph it can be seen that deploying 1-THz bandwidth at one color cycle results in a 30% reduction in gain. For the same bandwidth higher uniformity can be achieved in the spectral range of interest by increasing the number of color cycles[31,35] (usually achieved by increasing the SSD modulator frequency). An additional *ORCHID* simulation, employing 1 THz and two

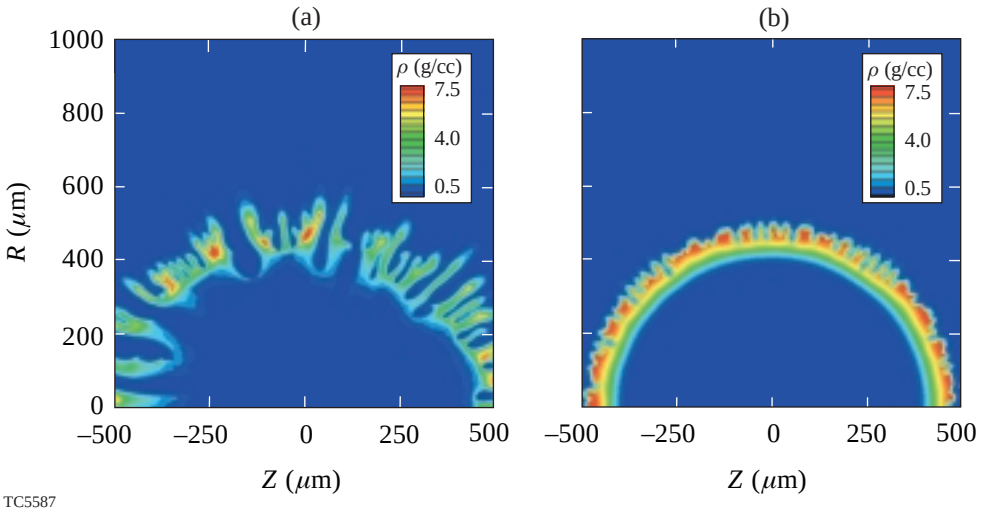

Figure 84.14
The need for high levels of bandwidth and multiple color cycles is evident when comparing density contours for two implosions of the same shell, applying (a) no bandwidth or (b) 1-THz bandwidth (one color cycle).

color cycles, was analyzed, and the result is plotted as the single annotated point in Fig. 84.15. It can be seen that either doubling the bandwidth or deploying two color cycles would recover almost the full design gain for the capsule. The NIF specifications, 1-THz bandwidth with two color cycles, correspond to a $\bar{\sigma}$ value of 1.0.

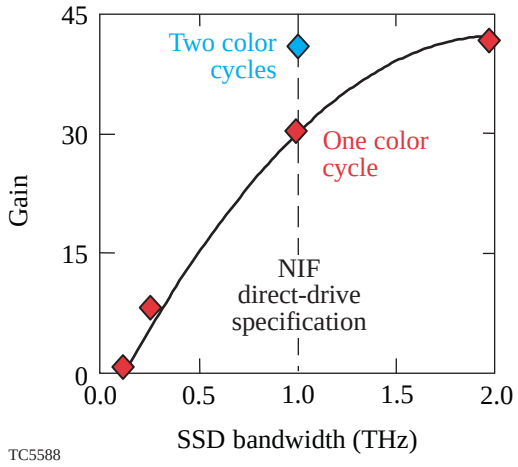

Figure 84.15
Projected target gain, using $\bar{\sigma}$ scaling, drawn as a function of the applied laser bandwidth for the direct-drive NIF point design capsule

Gain Reduction

There are three distinct regions in the behavior of the gain as a function of $\bar{\sigma}$. The first extends from $\bar{\sigma}$ equal to zero out to about to 1, the second from 1 out to about 2.5, and the third for $\bar{\sigma}$ above 2.5. While the first and third regions are easily explained by minimal effect of small perturbations on gain in the first region and total ignition failure in the third, a consistent argument to connect the two regions while explaining the middle ground can be found by examining the sequence of events leading to high gain in an unperturbed implosion.

It is well known that the main precursor to ignition is the incoming shell motion providing PdV work to the hot spot. As the shell moves in and heats the hot spot, it also provides the necessary ρR, enabling efficient absorption of α-particle energy.[2] The combination of these two must exceed any losses due to thermal conduction and radiation transport out of the hot spot. If done correctly, ignition occurs and a burn wave begins to move out into the cold fuel shell. It is at this point, however, that the disposition of the shell re-enters the problem. As the burn wave moves out into the ice layer, it exerts a tremendous pressure on the shell. In ICF targets it is typically the hydrodynamic expansion of the ignited fuel that quenches the burn.[23] If, however, the shell still retains some of its original radial kinetic energy, the inward momentum of the shell acts as a tamper to increase the ρR of the fuel while preventing the burn wave from decompressing the shell prematurely.

Levedahl and Lindl[36] have shown how excess kinetic energy in the shell, above that required for ignition, leads to a higher burn-up fraction. Their results show that the burn-up fraction can be drawn as a function of a dimensionless parameter that equals 1 for NIF capsules that marginally achieve ignition. As the retained kinetic energy in the shell is increased, the burn-up fraction climbs sharply until leveling off for kinetic energies in excess of 2 to 4 times the ignition energy. The sharp increase in burn-up fraction is referred to as the "ignition cliff" and indicates that NIF capsules need 1 to 2 times the kinetic energy above that which is required for ignition to achieve high gain. The ratio of excess radial kinetic energy to the maximum in-flight radial kinetic energy of the shell is referred to as "implosion margin" or simply "margin." To achieve burn-up fractions above 10% requires margins above 30%. The margin for the direct-drive point design is 40%, which results in a burn-up fraction of ~15%. The point design delivers a gain of 45, which is directly related to the burn-up fraction. The gain threshold ($G = 1$) for this target is roughly 1.1 times the ignition energy or a margin of roughly 10%.

Margin is directly related to the hydrodynamic stagnation of the incoming shell, and typically only the pressure associated with an ignited burn wave can force the shell off its normal trajectory. If, for a moment, we examine the point design with thermonuclear burn turned off, we can see, as shown in Fig. 84.16, that the stagnating shell can lose almost half of its radial kinetic energy or margin for every 100 ps traveled. As a result, there exists a critical timing involving the onset of ignition and the decreasing margin in the shell. If ignition is delayed beyond the time at which the point design would normally ignite ($t = 0$ in Fig. 84.16), the shell's margin drops and the final gain is diminished. If ignition is delayed too long, the shell will stagnate, the PdV work will cease, and the implosion will fail. Recalling that the margin for the gain threshold is roughly 10%, the high-gain window for this target, as shown in Fig. 84.16, is ~120 ps.

One of the roles of increasing perturbations at the ice/vapor interface is to delay the onset of ignition. As was pointed out by Levedahl and Lindl[37] and Kishony,[22] one can view increasing perturbation amplitudes as being an equivalent reduction in implosion velocity. The increased surface area and perturbed volume of the hot spot allow for an increase in the thermal

conduction losses and a decrease in the absorbed energy density of α particles within the hot spot. To reach ignition requires that the hot spot be driven to a higher ρR to recoup these losses. A high-gain shell, by our definition, still has excess kinetic energy to complete the task; however, this delays ignition and depletes the shell of valuable margin. The results of *ORCHID* simulations clearly show, as displayed in Fig. 84.17(a), how increasing $\bar{\sigma}$ affects ignition timing and the margin of the implosion. The point design resides in a linear, albeit steep, region of the ignition cliff. One should then expect a linear response of the burn-up fraction (i.e., gain) to changes in implosion margin. Such a linear behavior is clearly indicated in Fig. 84.17(b), where the calculated gains from the *ORCHID* simulations are drawn as a function of their calculated margin. The argument of increasing shell nonuniformities effectively depleting the shell margin explains the performance of targets giving intermediate gains for intermediate values of $\bar{\sigma}$.

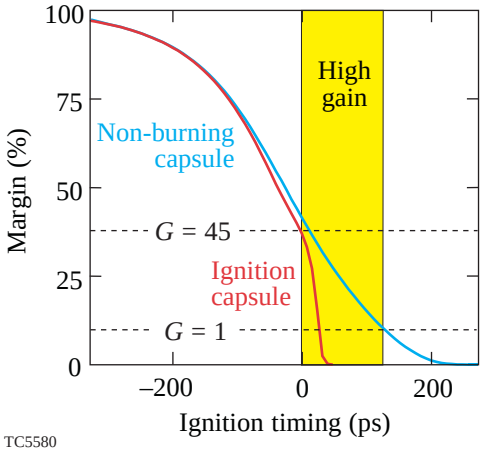

Figure 84.16
Shell stagnation determines the margin trajectory, which, in turn, defines the window for high gain.

Uniformity Budget for NIF

A global nonuniformity budget for the direct-drive point design on NIF can now be constructed in terms of $\bar{\sigma}$. If each of the four sources of nonuniformity acts independently, then the total effect can be measured by adding the individual $\bar{\sigma}$'s in quadrature $\bar{\sigma}_t$. Figure 84.18 displays the dependence of $\bar{\sigma}$ for each of the four main sources as a function of their individual laser and target specifications. Specification values have been scaled to reflect a universal multiplier that serves as the y axis. The sum-in-quadrature value $\bar{\sigma}_t = 1.4$ for this system (using current NIF specifications with two color cycles) is plotted as the solid dot on the inset graph of gain versus $\bar{\sigma}_t$ and represents a capsule gain of slightly greater than 30. The largest contributor can be seen to be the effects of laser nonuniformity. While the on-target power imbalance also makes a strong contribution, the effects due to the roughness of the ice/vapor interface are manageable and those due to outer-surface roughness are of no real consequence. If the NIF specifications of two color cycles are not achieved and only one color cycle is used, then the combined $\bar{\sigma}_t$ increases from 1.4 to 1.75, as seen in Fig. 84.10. The resultant target gain drops from 30 to 20. At one color cycle, the gain could be brought back to 30 by

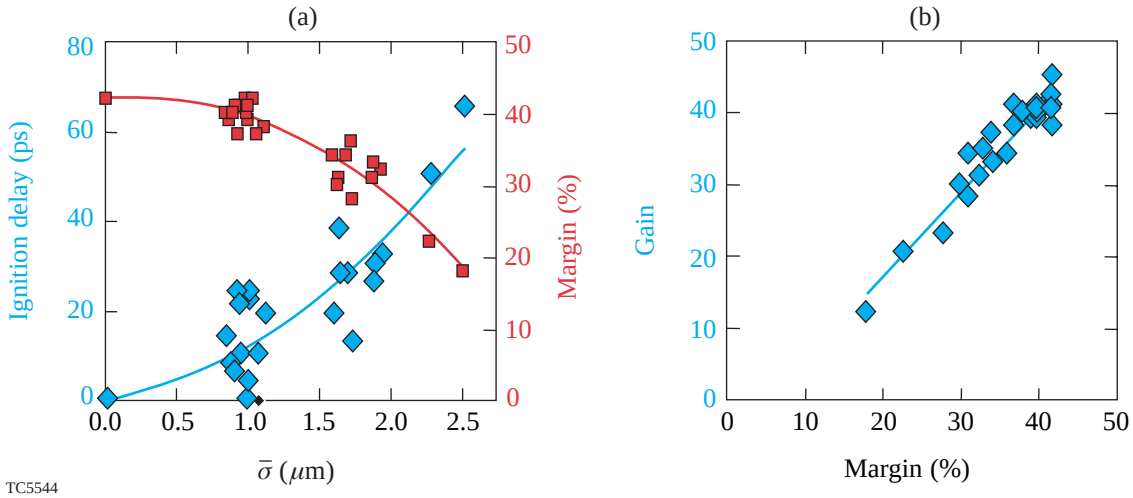

Figure 84.17
ORCHID simulations indicate that hot-spot ignition is delayed as ice/vapor interface perturbations increase. (a) Increasing shell perturbations ($\bar{\sigma}$) act to increase ignition delay (◆). This delay causes the burn wave to sample a shell with decreased margin (■). (b) Capsule gain depends strongly on the shell margin at ignition.

doubling the bandwidth, but this has been precluded by the efficiency of the frequency-tripling crystals. The achievement of two color cycles is consistent with current-day technology, but propagation issues through the laser chain must still be examined. At the two-color-cycle level, even higher gains can be achieved with improvements in power-balance technology.

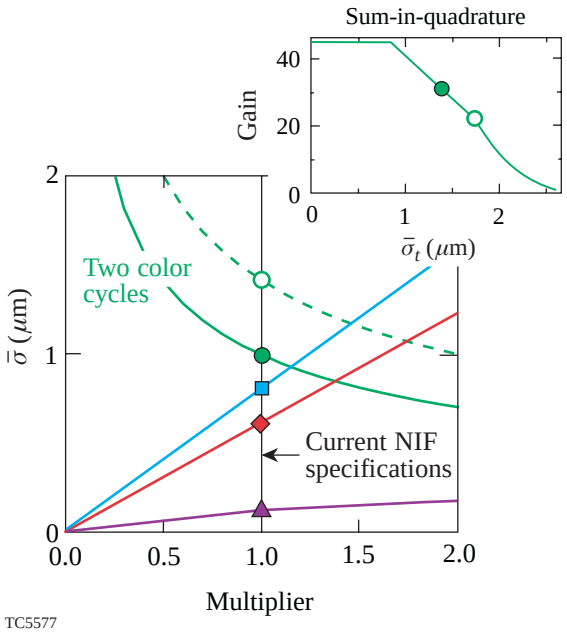

Figure 84.18
ORCHID results can be used to scale the target gain with $\bar{\sigma}$ to form a global nonuniformity budget for the direct-design point design. The *y* axis scales to the parameters: SSD bandwidth, one color cycle (○, × 1 THz); SSD bandwidth, two color cycles (●, × 1 THz); on-target power imbalance (■, × 2% rms); inner ice roughness (◆, × 1 μm rms); and outer-surface roughness (▲, × 80 nm).

Conclusions

Capsule gain can be directly related to the kinetic energy of the incoming shell that is in excess of the energy required to achieve ignition. When related to the peak kinetic energy of the implosion, this excess kinetic energy can be cast in terms of an implosion margin. Shell margin, prior to ignition, depends only on the temporal stagnation of the shell. As such, high gain requires the onset of ignition to coincide with significant (~40%) retained shell margin. Our analysis indicates that increasing perturbations in the incoming shell delay the onset of ignition within the hot spot. During this delay, the shell continues to stagnate and lose valuable margin. When ignition does occur, the burn wave samples the depleted shell margin allowing the high ignition pressure to decompress the main fuel layer prematurely, which leads to reduced gain. If the perturbations of the incoming shell delay ignition too long, the shell will stagnate, the PdV work will cease, and the implosion will fail.

The two-dimensional hydrodynamics code *ORCHID* has been used to examine the target performance of the NIF direct-drive point design driven under the influence of the four main sources of nonuniformity: laser imprint, power imbalance, and inner- and outer-target-surface roughness. Results from these studies indicate that capsule gain can be scaled to the rms spectrum of the ice/vapor surface deformation at the end of the acceleration stage of the implosion. Applying this scaling shows that NIF direct-drive point design performance is most sensitive to the effects of SSD smoothing, followed by power imbalance, inner-ice-surface roughness, and outer-surface roughness. A global nonuniformity budget was constructed using the scaling of a varied set of *ORCHID* simulations to evaluate the net effect of all nonuniformities acting together. This budget indicates that, if laser smoothing, power imbalance, and both inner- and outer-surface roughness stay within the limits specified by NIF direct-drive requirements, the capsule shell remains intact during the implosion and the implosion results in $G \sim 30$.

REFERENCES

1. M. D. Campbell and W. J. Hogan, Plasma Phys. Control. Fusion **41**, B39 (1999).
2. J. D. Lindl, Phys. Plasmas **2**, 3933 (1995).
3. Laboratory for Laser Energetics LLE Review **79**, 121, NTIS document No. DOE/SF/19460-317 (1999). Copies may be obtained from the National Technical Information Service, Springfield, VA 22161.
4. Lord Rayleigh, in *Scientific Papers* (Cambridge University Press, Cambridge, England, 1900), Vol. II, pp. 200–207.
5. M. S. Plesset, J. Appl. Phys. **25**, 96 (1954); G. I. Bell, Los Alamos National Laboratory, Report No. LA-1321 (1951).
6. S. E. Bodner, D. G. Colombant, J. H. Gardner, R. H. Lehmberg, S. P. Obenschain, L. Phillips, A. J. Schmitt, J. D. Sethian, R. L. McCrory, W. Seka, C. P. Verdon, J. P. Knauer, B. B. Afeyan, and H. T. Powell, Phys. Plasmas **5**, 1901 (1998).
7. S. W. Haan *et al.*, Phys. Plasmas **2**, 2480 (1995).
8. M. M. Marinak *et al.*, Phys. Plasmas **5**, 1125 (1998).
9. T. R. Dittrich *et al.*, Phys. Plasmas **5**, 3708 (1998).
10. S. V. Weber, S. G. Glendinning, D. H. Kalantar, M. H. Key, B. A. Remington, J. E. Rothenberg, E. Wolfrum, C. P. Verdon, and J. P. Knauer, Phys. Plasmas **4**, 1978 (1997).

11. V. N. Goncharov, S. Skupsky, P. W. McKenty, J. A. Delettrez, R. P. J. Town, and C. Cherfils-Clérouin, in *Inertial Fusion Sciences and Applications 99*, edited by C. Labaune, W. J. Hogan, and K. A. Tanaka (Elsevier, Paris, 2000), pp. 214–219.

12. R. Betti, V. Lobatchev, and R. L. McCrory, Phys. Rev. Lett. **81**, 5560 (1998).

13. D. P. Smitherman *et al.*, Phys. Plasmas **6**, 932 (1999).

14. K. Shigemori *et al.*, Phys. Rev. Lett. **84**, 5331 (2000).

15. C. P. Verdon, Bull. Am. Phys. Soc. **38**, 2010 (1993).

16. M. C. Richardson, P. W. McKenty, F. J. Marshall, C. P. Verdon, J. M. Soures, R. L. McCrory, O. Barnouin, R. S. Craxton, J. Delettrez, R. L. Hutchison, P. A. Jaanimagi, R. Keck, T. Kessler, H. Kim, S. A. Letzring, D. M. Roback, W. Seka, S. Skupsky, B. Yaakobi, S. M. Lane, and S. Prussin, in *Laser Interaction and Related Plasma Phenomena*, edited by H. Hora and G. H. Miley (Plenum Publishing, New York, 1986), Vol. 7, pp. 421–448.

17. R. L. McCrory and C. P. Verdon, in *Inertial Confinement Fusion*, edited by A. Caruso and E. Sindoni (Editrice Compositori, Bologna, Italy, 1989), pp. 83–124.

18. V. N. Goncharov, Phys. Rev. Lett. **82**, 2091 (1999); R. Ishizaki and K. Nishihara, Phys. Rev. Lett. **78**, 1920 (1997); R. J. Taylor *et al.*, Phys. Rev. Lett. **79**, 1861 (1997); A. L. Velikovich *et al.*, Phys. Plasmas **5**, 1491 (1998).

19. S. P. Obenschain *et al.*, Phys. Rev. Lett. **46**, 1402 (1981); S. G. Glendinning, S. N. Dixit, B. A. Hammel, D. H. Kalantar, M. H. Key, J. D. Kilkenny, J. P. Knauer, D. M. Pennington, B. A. Remington, R. J. Wallace, and S. V. Weber, Phys. Rev. E **54**, 4473 (1996); R. J. Taylor *et al.*, Phys. Rev. Lett. **76**, 1643 (1996); C. J. Pawley *et al.*, Phys. Plasmas **4**, 1969 (1997); V. A. Smalyuk, T. R. Boehly, D. K. Bradley, V. N. Goncharov, J. A. Delettrez, J. P. Knauer, D. D. Meyerhofer, D. Oron, D. Shvarts, Y. Srebro, and R. P. J. Town, Phys. Plasmas **6**, 4022 (1999).

20. V. N. Goncharov, S. Skupsky, T. R. Boehly, J. P. Knauer, P. McKenty, V. A. Smalyuk, R. P. J. Town, O. V. Gotchev, R. Betti, and D. D. Meyerhofer, Phys. Plasmas **7**, 2062 (2000).

21. Laboratory for Laser Energetics LLE Review **23**, 125, NTIS document No. DOE/SP40200-03 (1985). Copies may be obtained from the National Technical Information Service, Springfield, VA 22161.

22. R. Kishony, "Ignition Criterion in Inertial Confinement Fusion Using Self-Similar Solutions, and the Effect of Perturbations on Ignition," Ph.D. thesis, Tel Aviv University, 1999.

23. J. D. Lindl, *Inertial Confinement Fusion: The Quest for Ignition and Energy Gain Using Indirect Drive* (Springer-Verlag, New York, 1998), p. 3.

24. V. Lobatchev and R. Betti, "Ablative Stabilization of the Deceleration-Phase Rayleigh-Taylor Instability," to be published in Physical Review Letters.

25. O. S. Jones, Lawrence Livermore National Laboratory, private communication (2000).

26. O. S. Jones *et al.*, in *NIF Laser System Performance Ratings*, Supplement to Third Annual International Conference on Solid State Lasers for Application to Inertial Confinement Fusion (SPIE, Bellingham, WA, 1998), Vol. 3492, pp. 49–54.

27. V. N. Goncharov, P. McKenty, S. Skupsky, R. Betti, R. L. McCrory, and C. Cherfils-Clérouin, "Modeling Hydrodynamic Instabilities in Inertial Confinement Fusion Targets," to be published in Physics of Plasmas.

28. T. R. Boehly, V. N. Goncharov, O. Gotchev, J. P. Knauer, D. D. Meyerhofer, D. Oron, S. P. Regan, Y. Srebro, W. Seka, D. Shvarts, S. Skupsky, and V. A. Smalyuk, "Optical and Plasma Smoothing of Laser Imprinting in Targets Driven by Lasers with SSD Bandwidths Up to 1 THz," to be published in Physics of Plasmas.

29. Y. Kato *et al.*, Phys. Rev. Lett. **53**, 1057 (1984).

30. Laboratory for Laser Energetics LLE Review **33**, 1, NTIS document No. DOE/DP/40200-65 (1987). Copies may be obtained from the National Technical Information Service, Springfield, VA 22161.

31. T. R. Boehly, V. A. Smalyuk, D. D. Meyerhofer, J. P. Knauer, D. K. Bradley, R. S. Craxton, M. J. Guardalben, S. Skupsky, and T. J. Kessler, J. Appl. Phys. **85**, 3444 (1999).

32. Laboratory for Laser Energetics LLE Review **36**, 158, NTIS document No. DOE/DP/40200-79 (1988). Copies may be obtained from the National Technical Information Service, Springfield, VA 22161.

33. R. Epstein, J. Appl. Phys. **82**, 2123 (1997).

34. S. Skupsky and R. S. Craxton, Phys. Plasmas **6**, 2157 (1999).

35. R. H. Lehmberg, A. J. Schmitt, and S. E. Bodner, J. Appl. Phys. **62**, 2680 (1987).

36. W. K. Levedahl and J. D. Lindl, Nucl. Fusion **37**, 165 (1997).

37. *ibid.*, p. 171.

Core Performance and Mix in Direct-Drive Spherical Implosions with High Uniformity

Introduction

In the direct-drive approach to laser-driven inertial confinement fusion (ICF)[1] a spherical target is symmetrically illuminated by a number of individual laser beams. One of the primary determinants of target performance is illumination uniformity, both individual-beam uniformity and on-target beam-to-beam power history differences (power balance). Illumination nonuniformities lead to distortions in the compressed core due to secular growth of low-order ($\ell \lesssim 10$) modes and shell breakup and mix due to the Rayleigh–Taylor (RT)[2,3] growth of perturbations imprinted by high-order ($\ell > 10$) nonuniformities. To reduce the effect of imprinting, a number of beam-smoothing techniques have been employed, including distributed phase plates (DPP's),[4] polarization smoothing (PS) with birefringent wedges,[5,6] smoothing by spectral dispersion (SSD),[7] and induced spatial incoherence (ISI).[8] Ultimately to ignite a direct-drive cryogenic pellet, the on-target beam nonuniformity must be less than 1%.[3,9,10]

An ICF target is RT unstable during two phases of the implosion: During the acceleration phase, surface nonuniformities seeded by laser nonuniformities, outer-target-surface roughness, and feedout of inner-target-surface roughness grow at the ablation front. Under extreme conditions, the perturbations can grow to be comparable to the in-flight shell thickness disrupting the shell or by feeding perturbations through the remaining shell material, seeding the deceleration-phase RT instability. During the deceleration and core assembly phases the boundary between the high-temperature, low-density hot spot and the colder, high-density pusher (shell) is RT unstable.

Beam uniformity's effect on target performance is studied in direct-drive implosions of gas-filled plastic shells on the OMEGA laser system.[11] These targets are surrogates[12,13] for cryogenic implosions that have recently commenced on OMEGA. These cryogenic implosions are energy-scaled surrogates for direct-drive ignition targets on the National Ignition Facility.[3,9,10,14] Implosions of 20-μm-thick, gas-filled plastic shells driven with a 1-ns square laser pulse have ratios of the thickness of the ablation-surface mix region due to RT growth to the in-flight shell thickness that are similar to those predicted for OMEGA cryogenic implosions (see Fig. 84.19). The in-flight shell thickness was calculated using the 1-D hydrodynamic code *LILAC*,[15] and the mix width was calculated using a postprocessor that includes the effects of mass ablation, finite shell thickness, and spherical convergence.[16] Three different CH-shell-implosion conditions were calculated. Plastic shell implosions are useful because a wide variety

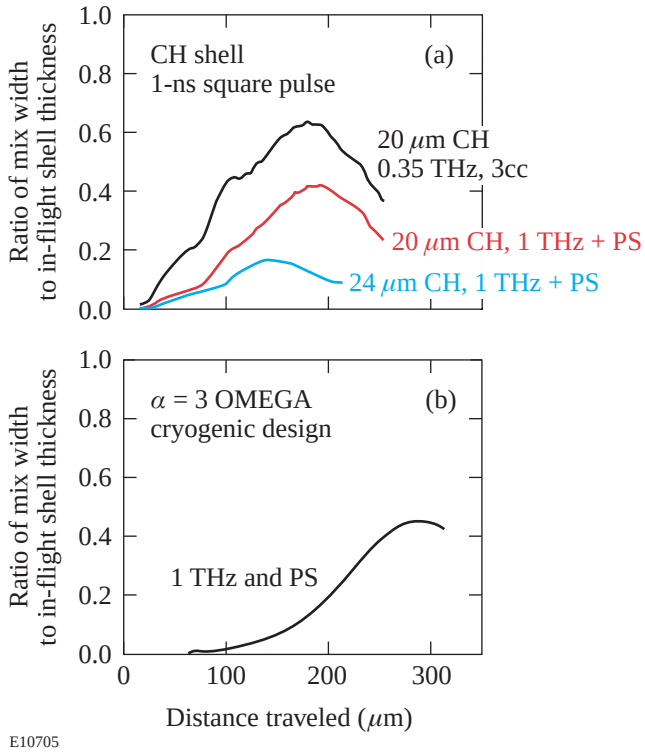

Figure 84.19
(a) Ratio of the calculated acceleration phase "mix" width to the in-flight shell thickness for 20-μm-thick CH shells illuminated by 1-ns square pulses with 1-THz SSD and PS (red line); 0.35-THz, three-color-cycle SSD without PS (black line); and for a 24-μm-thick CH shell illuminated with 1-THz SSD and PS (blue line). For full smoothing, the width of the mix region is significantly smaller than the in-flight shell thickness. (b) A similar comparison for NIF-scaled cryogenic targets planned for OMEGA is shown.

of shell/gas conditions and diagnostics can be applied to study the details of the implosion.[17–19]

This article describes a series of OMEGA direct-drive plastic shell implosions with high-quality beam smoothing and power balance. These experiments suggest that the shell remains reasonably integral during the acceleration phase and that single-beam nonuniformity is no longer the primary limitation on target performance. A wide variety of target types and fill gasses are used to build a model of core conditions and fuel–shell mixing.

The sections that follow describe the targets and diagnostics applied to the spherical implosions, the laser conditions for the implosions, the target performance, and a static mix model. This work is summarized in the last section.

Targets and Diagnostics

The philosophy of the experiments reported here is to first choose a laser pulse shape, smoothing conditions, target-shell thickness, and gas-fill pressure, and then vary the make-up of the fill gas or details of the shell layers so that many diagnostics can be applied to the nearly identical implosions. OMEGA produces very reproducible implosions suggesting that the implosion hydrodynamics is unchanged for different target types and fill-gas make-up.

1. Core Diagnostics

The primary (N_p) and secondary neutron (N_s) yields were measured using scintillator counters coupled to fast photomultipliers.[20] Indium and copper activation provided additional yield measurements.[21] For the range of yields recorded, the typical uncertainty in these measurements was 10%. The fast scintillator counters also measured the neutron-averaged ion temperature with an uncertainty ~0.5 keV.

The secondary proton and knock-on particle yields were measured with range filters[22] and charged-particle spectrometers (CPS's).[23] CR-39 nuclear emulsion was used in both detectors to determine the yield and the energy spectrum.

For DT-filled implosions, the fuel areal density is determined from the number of elastically scattered knock-on fuel particles:[24,25]

$$n + \mathrm{T}(\mathrm{D}) \rightarrow n' + \mathrm{T}'(\mathrm{D}'). \tag{1}$$

The yield of knock-on particles is insensitive to the electron temperature profile.[24,25]

Limits on fuel areal density (ρR_f) in D_2-filled implosions can be inferred from the secondary neutron (N_s) production[22,26]

$$\mathrm{D} + \mathrm{D} \rightarrow \mathrm{T} + p, \tag{2}$$

followed by

$$\mathrm{T} + \mathrm{D} \rightarrow n(12 \sim 17\ \mathrm{MeV}) + {}^4\mathrm{He}, \tag{3}$$

and secondary proton production (p_s)[22,26]

$$\mathrm{D} + \mathrm{D} \rightarrow {}^3\mathrm{He} + n, \tag{4}$$

followed by

$${}^3\mathrm{He} + \mathrm{D} \rightarrow p(12 \sim 17\ \mathrm{MeV}) + {}^4\mathrm{He}. \tag{5}$$

The secondary proton and neutron yields depend on the electron temperature profile in the core and typically provide limits on the ρR_f and the core electron temperature.[22,26]

The inferred value of ρR_f depends on whether a hot spot (point-like source surrounded by uniform fuel) or uniform (uniform fuel and source) "ice-block" model is used. The ρR_f inferred with the uniform model is ~34% larger than with the hot-spot model.[22,26] Simulations using *LILAC*[15] suggest that the uniform model is more appropriate for inferring ρR_f under the experimental conditions described in this work.

2. Shell Diagnostics

The areal density of the plastic shell, ρR_s, during stagnation was measured with charged-particle spectroscopy. Secondary protons from D_2 implosions (produced with 12- to 17-MeV energies) are slowed down predominantly in the shell by an amount proportional to ρR_s.[22] For CH shells with DT fill, the number of knock-on protons determines ρR_s.[25] In addition, knock-on deuterons and tritons are slowed in the shell, providing another measure of ρR_s and, coupled with the knock-on proton yield, provide an estimate of the shell electron temperature.[25]

3. Mix Diagnostics

The core–fuel mix characteristics are inferred in a number of ways. CD layers in D_2-filled CH targets are probed with tritons and ^{3}He particles produced in the D_2 reaction in the fuel region [Eqs. (2)–(5)].[27] The measured secondary yields from the shell regions are compared to 1-D simulations. When the yields are significantly different than those predicted, they

provide information about fuel–shell mix. The secondary DT neutrons and D-^{3}He protons produced directly in the shell can be subtracted using H_2-filled implosions with the same shell conditions. An implosion of a plastic shell with a CD layer and a pure-^{3}He fill provides a primary D-^{3}He proton signal only if the shell and fuel regions are microscopically mixed. This yield depends on the characteristics of the mix, either microscopic (diffusive) or macroscopic, where islands of shell material penetrate the core.

Laser Conditions

An ~23-kJ, 1-ns square pulse delivered by the 60-beam OMEGA laser system[11] was used to drive the implosions described in this work. Figure 84.20 shows the measured pulse shapes for 50 of the 60 beams. The beam-to-beam UV energy balance (thick line in Fig. 84.20) is typically ≤5% rms. When beam overlap on target is included, the on-target nonuniformity due to beam-to-beam power imbalance is <2% ($\ell \leq 12$). Individual-beam smoothing was accomplished by combining DPP's, SSD, and PS (in most cases). The DPP's produce a third-order supergaussian profile with 95% of the energy enclosed in an ~936-μm diameter. When 2-D SSD and PS are added, the spot diameter increases somewhat due to the angular divergence associated with these techniques. Two different, two-dimensional (2-D) SSD configurations were used: a single color cycle with 1-THz bandwidth at 3- and 10-GHz modulation frequencies or a three-color-cycle configuration with 0.35-THz bandwidth with 3- and 3.3-GHz modulation frequencies. Polarization smoothing with birefringent wedges was employed on the implosions with 1-THz SSD.

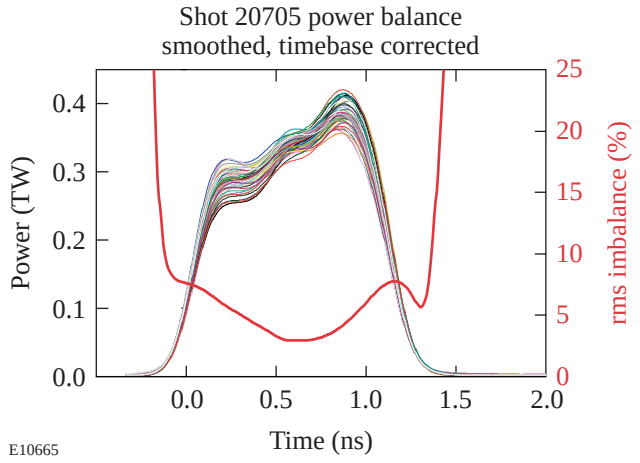

Figure 84.20
The measured 1-ns square pulse from 50 of the 60 OMEGA beams for shot 20705 (thin lines). The red line shows the rms beam-to-beam power imbalance inferred for the same shot. For most of the pulse, the power imbalance is ~5%.

The calculated time-dependent, on-target nonuniformity ($\ell = 1 \sim 500$) due to single-beam nonuniformity assuming perfect beam-to-beam power balance for 1-THz SSD with PS is less than 1% after 300ps.[28] Additional on-target nonuniformities are due to beam-to-beam power imbalance and differences in DPP spot sizes.

Implosion Results

This section describes a series of gas-filled plastic (CH) shell implosions driven with a ~23 kJ, 1-ns square pulse. Most of the implosions were driven with full beam uniformity (1-THz SSD and PS), while 0.35-THz SSD (three color cycles without PS) was used for the others. The ~940-μm-diam plastic targets had 18~24-μm wall thicknesses and were filled with fuel pressures of 3~15atm. The targets were predicted to have gas convergence ratios of ~35 and ~14, respectively, from 1-D hydrodynamic simulations.[15]

The ratio of the measured primary neutron yield to that predicted by 1-D simulations ["yield over clean" (YOC)] for CH shells with D_2 fills as a function of the calculated convergence ratio (initial to final radius of the fuel–shell boundary) for 1-THz SSD and PS is shown in Fig. 84.21. The 20- and 24-μm-thick shells were filled with either 3 or 15 atm of D_2. The OMEGA laser system provides highly reproducible implosions, as can be seen by the small spread in the YOC's for each condition. The implosions with 15-atm-filled, 20-μm-thick shells were taken over three experimental campaigns spanning two months and show an ~10% standard deviation of YOC's. The implosions with convergence ratio ~35 have YOC's of ~20%. The most-stable implosions (24-μm-thick shells with 15-atm fills) have YOC's $\gtrsim$ 40%.

The measured and calculated neutron-production rates for a 20-μm-thick CH shell filled with 15 atm of D_2 are compared in Fig. 84.22. The two temporal histories are in good agreement except that the measured neutron-production rate is ~35% of the calculated one. There is no evidence that the measured neutron burn rate decreases before the time predicted by 1-D simulations (i.e., no early burn termination). Over many target implosions, the measured time of peak neutron emission (bang time) is within 50 ps of that predicted.

For 20-μm-thick CH shells with 15-atm-D_2 or DT fill pressures, the predicted ρR_f is 16mg/cm^2 and ρR_s is 60mg/cm^2.

The measured charged-particle spectra used to determine the fuel, shell, and total areal densities of these implosions are shown in Figs. 84.23–84.25. Figures 84.23 and 84.24 show the measured knock-on D and *p* spectra for CH shells filled with DT. The ρR_f inferred from D knock-on yield is 16mg/cm ^{2}, while $\rho R_s \sim 61$mg/cm ^{2} from the knock-on protons. The total ρR can also be determined from the slowing down of D-^{3}He secondary protons from D_2-filled shells (Fig. 84.25), and it is found to be 76 mg/cm^2. These measurements show that the sum of fuel and shell areal densities for DT implosions is in good agreement with the total areal density independently inferred from D_2 implosions. The measured fuel and shell areal densities are close to those predicted from 1-D simulations.

These results were compared with target implosions driven with similar laser pulse shapes and with larger single-beam nonuniformities (0.35-THz, three-color-cycle SSD without PS). *LILAC* simulations predicted identical target performance. Table 84.II compares the measured implosion parameters for 20-μm-thick CH shells with 15-atm-gas fills of D_2 and DT driven under identical conditions, except for the single-beam nonuniformity. In all aspects, the implosions driven with more-uniform beams performed significantly better. In particular both the primary neutron yield and fuel areal density increased by ~70%.

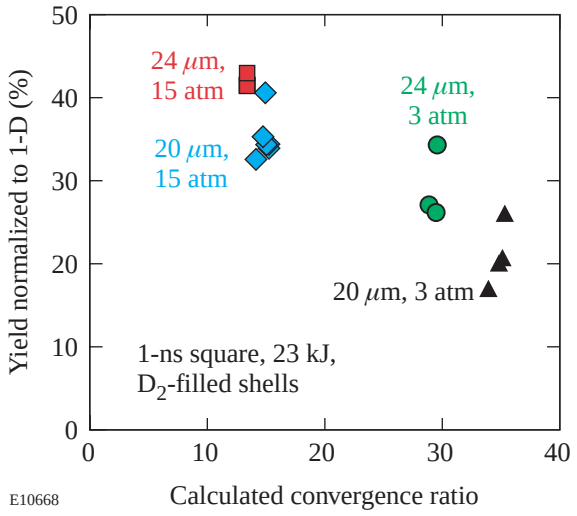

Figure 84.21
Ratio of the measured to calculated primary neutron yield (YOC) for D_2-filled CH capsule implosions as a function of calculated convergence ratio for 1-THz SSD and PS. This shows both the high reproducibility of the OMEGA laser system and good performance at convergence ratios of ~35.

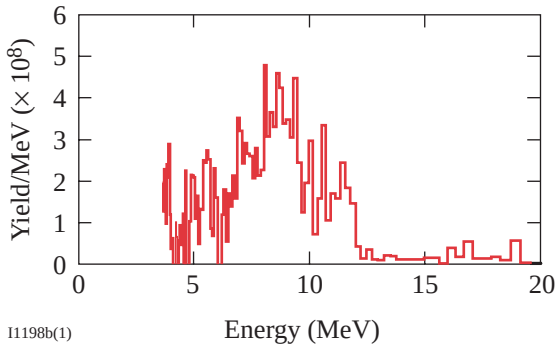

Figure 84.23
The measured "knock-on" deuteron spectrum for a 15-atm-DT fill in a 20-μm-thick CH shell. The estimated fuel areal density is 16mg/cm ^{2} (Ref. 25).

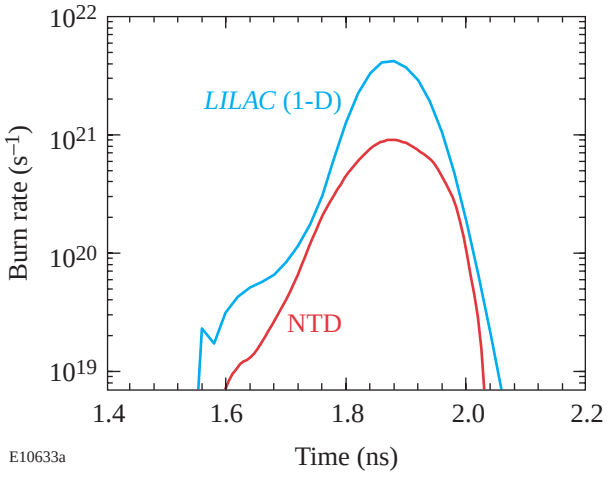

Figure 84.22
The time-dependent, measured (red) and predicted (blue) neutron-production rates for a 15-atm-DT fill in a 20-μm-thick CH shell are overlaid.

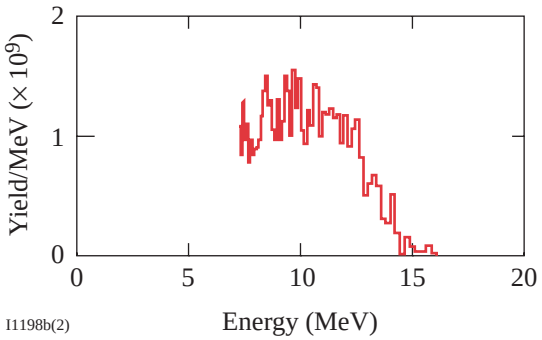

Figure 84.24
The measured knock-on proton spectrum for a 15-atm-DT fill in a 20-μm-thick CH shell. The estimated shell areal density is 61 mg/cm^2 (Ref. 25).

In summary, high-uniformity, moderate-convergence-ratio implosions with 15-atm-gas-fill pressure have YOC's of ~40% and compressed fuel and shell areal densities close to those predicted. Figure 84.19(a) shows the predicted ratio of the imprint-induced mix width to the shell thickness for three implosions. When full smoothing (1-THz SSD and PS) is applied to 20-μm-thick shells, the mix width is predicted to be ~42% of the in-flight shell thickness compared with 65% for 0.35-THz SSD without PS. The primary yields and fuel areal densities increased by ~70% for the 1-THz and PS implosion, indicating that the reduction of mix width and corresponding improvement in shell stability significantly affected the target performance. The 24-μm-thick CH shells with 15-atm fills show a further 25% improvement in YOC compared to 20-μm-thick shells using full beam smoothing. If the imprint-induced shell stability were still the dominant determinant of target performance, reducing the ratio of the mix width to in-flight shell thickness from 42% to 17% might have been expected to improve target performance significantly further. While shell stability still plays a role in target performance, it appears that other effects, such as power imbalance, play a comparable role.

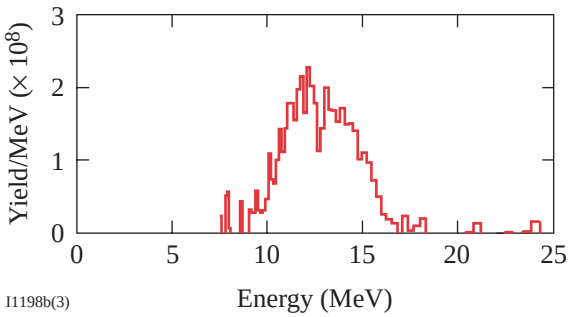

Figure 84.25
The measured secondary D-^{3}He proton spectrum for a 15-atm-D_2 fill in a 20-μm-thick CH shell. The estimated total areal density is 76 mg/cm^2 (Ref. 22).

Core Mix Model

In the preceding sections, the experimental results have been compared with the predictions of 1-D hydrodynamic simulations. While some observations are close to those predicted, others, such as the primary yield, are lower, while still others, such as the ratio of the secondary neutron yield to the primary neutron yield, are larger. The variation in observables provides constraints on the possible core conditions and fuel–pusher mix during stagnation. In this section, the experimental results are compared to a static model of the core to gain additional insight about target performance.[29]

The predictions of this static model are compared to neutron-burn-averaged observations. This model assumes that the compressed core can be divided into two regions: a "clean" region with only fuel material and a "mixed" region where some of the shell material is mixed with the fuel material. The clean region is characterized by a single temperature (electron and ion are assumed to be the same), fuel density, and radius. In the mix region, the fuel density decreases linearly from the edge of the clean region to the edge of the mix region, the shell material density decreases linearly from the edge of the mix region to the boundary of the clean region, and the temperature decreases linearly from the edge of the clean region to the edge of the mix region. Thus, the model has six parameters: the temperature, density, and radius of the clean region; the radius of the mix region; and the shell material density and temperature at the edge of the mix region. The total fuel mass is

Table 84.II: Comparison of implosion performance of ~19-μm-thick CH shells filled with 15 atm of D_2 or DT fill with 1-THz SSD and PS or 0.35-THz SSD (three color cycles) without PS.

Diagnostic	0.35-THz SSD	1-THz SSD and PS
D_2 primary yield (10^{10})	9±1	16±1
T_{ion} (D_2) (keV)	3.2±0.5	3.7±0.5
Secondary neutron ratio (Y_{2n}/Y_n 10^{-3})	1.5±0.4	2.5±0.2
Secondary proton ratio (Y_{2p}/Y_n 10^{-3})	1.4±0.2	1.9±0.2
DT primary yield (10^{12})	6±1	11±1
T_{ion} (DT) (keV)	3.7	4.4 keV
Knock-on fuel ρR (mg/cm^2)	9±2	15±2

assumed to be conserved. The nuclear and particle emission from the compressed core in the model must match the measured values of primary neutron burn rate, average neutron ion temperature, secondary neutron, proton, and knock-on yields (both for CH shells and CH shells with inner CD layers). CH shells with inner CD layers filled with ^{3}He fuel provide additional experimental observations. Approximately ten experimental observables are used to constrain the model's parameters. The core temperature and density profiles inferred from this model for 15-atm-filled, 20-μm-thick plastic shells are shown in Fig. 84.26. The range of allowable parameters is shown in the figure as the width of parameter estimates. The measured values of various parameters and their fraction (in percent) predicted by the model are shown in Table 84.III. The model predicts that the total compressed radius is 50 μm with approximately 1 μm (20% of the compressed shell areal density) of the original shell material mixed into the outer 50% of the fuel region. This model provides a picture of the stagnation conditions for the implosion. In the future it will be applied to other implosions to further understand the mix characteristics.

Conclusions

In summary, the implementation of full beam smoothing (1-THz SSD and PS) on OMEGA has produced moderate-convergence-ratio (CR~15) implosions that perform close to 1-D predictions. The primary neutron yield is ~35%–45% of that predicted, while the fuel and shell areal densities are close to their predicted values. When the shell is thickened to reduce the effect of the acceleration-phase RT instability, the perfor-

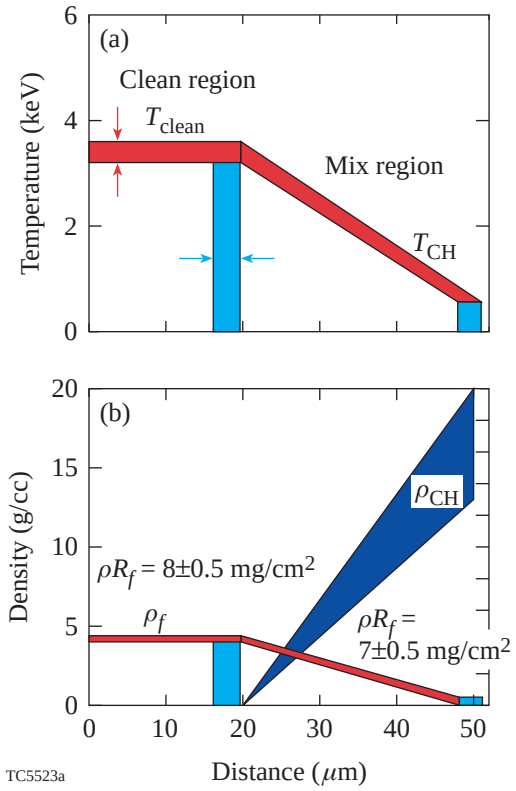

Figure 84.26
Inferred core and fuel–shell mix profiles from the mix model described in the text. The temperature profiles are shown in (a) and the density profiles in (b). The range of the parameters, which are consistent with the experimental observations, is shown by the width of the various parameter bands.

Table 84.III: Comparison of measured and mix-model–predicted implosion parameters for a ~19-μm-thick CH shell (with or without CD layers) filled with 15 atm of D_2 or DT, or ^{3}He for implosions with 1-THz SSD and PS.

Parameter	Measurement	Model (% of expt)
Fuel ρR (mg/cm^2)	15±2	100
T_{ion} (DT) (keV)	4.4±0.4±0.5 (sys)	86
Max. neutron burn rate (n/s)	$(9\pm1)\times10^{20}$	110
T_{ion} (D_2) (keV)	3.7±0.2±0.5 (sys)	89
Secondary neutron ratio	$(2.4\pm0.4)\times10^{-3}$	100
Secondary proton ratio	$(1.8\pm0.3)\times10^{-3}$	78
Secondary neutron ratio (D_2)	$(3.1\pm0.5)\times10^{-3}$	94
D-^{3}He proton yield (^{3}He fill)	$(1.3\pm0.2)\times10^{7}$	66
D_2 neutron yield (^{3}He fill)	$(8.5\pm0.4)\times10^{8}$	97

mance improves only slightly, suggesting that single-beam nonuniformities are no longer the dominant determinant of target performance. The stagnation conditions are reproduced by a tightly constrained static mix model.

Future research will address the effect of residual beam-to-beam power imbalances and target-manufacturing nonuniformities as limitations of target performance. Implosions that are less stable during the acceleration phase (e.g., more slowly rising pulses) will be used to further understand the fuel–shell mixing. In addition, x-ray diagnostics will be utilized and their results compared to the static mix model.

Cryogenic-target implosions have begun on the OMEGA laser system. An ignition target on a MJ-class laser system such as the National Ignition Facility will require a shell composed primarily of a frozen DT layer. The OMEGA experiments are energy-scaled versions of ignition implosions with ~100-μm-thick ice layers. The stability properties of these targets due to imprinting are similar to those described in this article. The results described here lead to confidence in the ability to obtain direct-drive ignition on the National Ignition Facility.[9]

ACKNOWLEDGMENT

The authors are extremely grateful to the staff of the Laboratory for Laser Energetics for their dedicated efforts in developing and providing the high-performance OMEGA laser system, including low-power imbalance and high single-beam uniformity, and high-quality diagnostics, operations, and target fabrication. This work was supported by the U.S. Department of Energy Office of Inertial Confinement Fusion under Cooperative Agreement No. DE-FC03-92SF19460, the University of Rochester, and the New York State Energy Research and Development Authority. The support of DOE does not constitute an endorsement by DOE of the views expressed in this article.

REFERENCES

1. J. Nuckolls *et al.*, Nature **239**, 139 (1972).
2. J. D. Kilkenny, S. G. Glendinning, S. W. Haan, B. A. Hammel, J. D. Lindl, D. Munro, B. A. Remington, S. V. Weber, J. P. Knauer, and C. P. Verdon, Phys. Plasmas **1**, 1379 (1994).
3. S. E. Bodner, D. G. Colombant, J. H. Gardner, R. H. Lehmberg, S. P. Obenschain, L. Phillips, A. J. Schmitt, J. D. Sethian, R. L. McCrory, W. Seka, C. P. Verdon, J. P. Knauer, B. B. Afeyan, and H. T. Powell, Phys. Plasmas **5**, 1901 (1998).
4. T. J. Kessler, Y. Lin, J. J. Armstrong, and B. Velazquez, in *Laser Coherence Control: Technology and Applications*, edited by H. T. Powell and T. J. Kessler (SPIE, Bellingham, WA, 1993), Vol. 1870, pp. 95–104.
5. Y. Kato, unpublished notes from work at LLE, 1984.
6. T. R. Boehly, V. A. Smalyuk, D. D. Meyerhofer, J. P. Knauer, D. K. Bradley, R. S. Craxton, M. J. Guardalben, S. Skupsky, and T. J. Kessler, J. Appl. Phys. **85**, 3444 (1999).
7. S. Skupsky, R. W. Short, T. Kessler, R. S. Craxton, S. Letzring, and J. M. Soures, J. Appl. Phys. **66**, 3456 (1989).
8. R. H. Lehmberg and S. P. Obenschain, Opt. Commun. **46**, 27 (1983).
9. P. W. McKenty, V. N. Goncharov, R. P. J. Town, S. Skupsky, R. Betti, and R. L. McCrory, "Analysis of a Direct-Drive Ignition Capsule Designed for the NIF," to be published in Physics of Plasmas.
10. S. V. Weber *et al.*, *ICF Quarterly Report*, **7**, 43, Lawrence Livermore National Laboratory, Livermore, CA, UCRL-LR-105821-97-2 (1997).
11. T. R. Boehly, D. L. Brown, R. S. Craxton, R. L. Keck, J. P. Knauer, J. H. Kelly, T. J. Kessler, S. A. Kumpan, S. J. Loucks, S. A. Letzring, F. J. Marshall, R. L. McCrory, S. F. B. Morse, W. Seka, J. M. Soures, and C. P. Verdon, Opt. Commun. **133**, 495 (1997).
12. F. J. Marshall, J. A. Delettrez, V. Yu. Glebov, R. P. J. Town, B. Yaakobi, R. L. Kremens, and M. Cable, Phys. Plasmas **7**, 1006 (2000).
13. J. A. Delettrez, V. Yu. Glebov, F. J. Marshall, C. Stoeckl, B. Yaakobi, and D. D. Meyerhofer, Bull. Am. Phys. Soc. **44**, 192 (1999).
14. C. P. Verdon, Bull. Am. Phys. Soc. **38**, 2010 (1993).
15. M. C. Richardson, P. W. McKenty, F. J. Marshall, C. P. Verdon, J. M. Soures, R. L. McCrory, O. Barnouin, R. S. Craxton, J. Delettrez, R. L. Hutchison, P. A. Jaanimagi, R. Keck, T. Kessler, H. Kim, S. A. Letzring, D. M. Roback, W. Seka, S. Skupsky, B. Yaakobi, S. M. Lane, and S. Prussin, in *Laser Interaction and Related Plasma Phenomena*, edited by H. Hora and G. H. Miley (Plenum Publishing, New York, 1986), Vol. 7, pp. 421–448.
16. V. N. Goncharov, P. McKenty, S. Skupsky, R. Betti, R. L. McCrory, and C. Cherfils-Clérouin, Phys. Plasmas **7**, 5118 (2000).
17. M. D. Cable *et al.*, Phys. Rev. Lett. **73**, 2316 (1994).
18. D. K. Bradley, J. A. Delettrez, R. Epstein, R. P. J. Town, C. P. Verdon, B. Yaakobi, S. Regan, F. J. Marshall, T. R. Boehly, J. P. Knauer, D. D. Meyerhofer, V. A. Smalyuk, W. Seka, D. A. Haynes, Jr., M. Gunderson, G. Junkel, C. F. Hooper, Jr., P. M. Bell, T. J. Ognibene, and R. A. Lerche, Phys. Plasmas **5**, 1870 (1998).
19. F. J. Marshall, J. A. Delettrez, R. Epstein, V. Yu. Glebov, D. R. Harding, P. W. McKenty, D. D. Meyerhofer, P. B. Radha, W. Seka, S. Skupsky, V. A. Smalyuk, J. M. Soures, C. Stoeckl, R. P. J. Town, B. Yaakobi, C. K. Li, F. H. Séguin, D. G. Hicks, and R. D. Petrasso, Phys. Plasmas **7**, 2108 (2000).
20. V. Yu. Glebov, D. D. Meyerhofer, C. Stoeckl, and J. D. Zuegel, "Secondary-Neutron-Yield Measurements by Current-Mode Detectors," to be published in the Review of Scientific Instruments.
21. S. M. Lane *et al.*, *Laser Program Annual Report 1986*, Lawrence Livermore National Laboratory, Livermore, CA, UCRL-50021-86, 3-100 (1987).

22. F. H. Séguin, C. K. Li, D. G. Hicks, J. A. Frenje, K. M. Green, R. D. Petrasso, J. M. Soures, D. D. Meyerhofer, V. Yu. Glebov, C. Stoeckl, P. B. Radha, S. Roberts, C. Sorce, T. C. Sangster, M. D. Cable, S. Padalino, and K. Fletcher, "Using Secondary Proton Spectra to Study Imploded D_2-Filled Capsules at the OMEGA Laser Facility," submitted to Physics of Plasmas.

23. D. G. Hicks, "Charged Particle Spectroscopy: A New Window on Inertial Confinement Fusion," Ph.D. thesis, Massachusetts Institute of Technology, 1999.

24. S. Skupsky and S. Kacenjar, J. Appl. Phys. **52**, 2608 (1981).

25. C. K. Li, D. G. Hicks, F. H. Séguin, J. A. Frenje, K. Green, R. D. Petrasso, D. D. Meyerhofer, J. M. Soures, V. Yu. Glebov, P. B. Radha, S. Skupsky, C. Stoeckl, S. Roberts, and T. C. Sangster, "Study of Direct-Drive, DT-Gas-Filled-Plastic-Capsule Implosions Using Nuclear Diagnostics on OMEGA," submitted to Physics of Plasmas.

26. H. Azechi, M. D. Cable, and R. O. Stapf, Laser Part. Beams **9**, 119 (1991).

27. V. Yu. Glebov, J. A. Delettrez, R. Epstein, P. W. McKenty, F. J. Marshall, D. D. Meyerhofer, P. B. Radha, V. A. Smalyuk, and C. Stoeckl, Bull. Am. Phys. Soc. **44**, 194 (1999).

28. S. Skupsky and R. S. Craxton, Phys. Plasmas **6**, 2157 (1999).

29. P. B. Radha, V. Yu. Glebov, F. J. Marshall, D. D. Meyerhofer, S. P. Regan, W. Seka, S. Skupsky, V. A. Smalyuk, J. M. Soures, C. Stoeckl, B. Yaakobi, and R. D. Petrasso, Bull. Am. Phys. Soc. **45**, 164 (2000).

Secondary-Neutron-Yield Measurements by Current-Mode Detectors

Introduction

The measurement of secondary deuterium–tritium (DT) neutrons from pure-deuterium targets in inertial confinement fusion (ICF) experiments was proposed more than two decades ago[1–3] as a method for determining fuel areal density and demonstrated experimentally more than a decade ago.[4,5]

The secondary neutron yield is typically several orders of magnitude less than the primary yield, necessitating the use of a very sensitive neutron detector. For this application several single-hit detectors consisting of an array of individual scintillator detectors and electronics for detecting the time of flight of the first neutron (single hit) were developed at major laser facilities: LaNSA[6] at Nova, MEDUSA[7] at OMEGA, and MANDALA[8] at GEKKO. MEDUSA saturates on high-yield, direct-drive implosion experiments currently carried out on the 30-kJ, 60-beam OMEGA laser system and is not suitable for future cryogenic capsules experiments on OMEGA. At LLE we have developed several current-mode detectors (e.g., a single scintillator and a photomultiplier tube) for secondary-neutron-yield measurements on current and future OMEGA experiments. This article describes the status of these detectors, including detector design and calibration.

Comparison of Two Mode Detectors

For ICF experiments, single-hit detectors have many advantages (i.e., they are very sensitive and they can measure secondary neutron spectra and ion temperature in addition to secondary yield) but they also have two major disadvantages: First, single-hit detectors are very expensive because of the large number of individual detectors (~1000) and associated electronics. Second, they have a very limited dynamic range, which stems from the principle that an individual detector registers only the first hit. At low yield the single-hit detector is limited by statistical error simply from the number of fired individual detectors. To obtain less than 20% statistical error, 30 or more hits are necessary. If the number of fired individual detectors exceeds 50% of the array elements (500 detectors) at high yield, the single-hit detector is limited by a high number of double hits on a single detector. This effect can be compensated for to a certain extent by statistical analysis, but this so-called "busy correction" can extend the dynamic range by only a factor of 2. Consequently the dynamic range of the single-hit detector is 15 to 30 (with busy correction).

Current-mode detectors, e.g., a single scintillator and a photomultiplier tube connected with a digital oscilloscope, are much cheaper than single-hit detectors. The dynamic range of the current-mode detector is restricted by the linear dynamic range of the photomultiplier and can exceed 1000 for many photomultipliers. The operational range of the current-mode detector can be adjusted by changing location, the high voltage on the photomultiplier, or the scintillator. Since current-mode detectors are relatively cheap, it is possible to create several such detectors—each designed for a different secondary-yield range—and, thus, cover a large range of secondary yields without any change in setup. A disadvantage of the current-mode detectors is the fact that a very high secondary yield is required to measure energy spectra of secondary neutrons.

The dynamic range limitations of the single-hit detectors can be compensated for by modifying the targets—for example, by diluting the D_2 with H_2 or ^3He in the gas mixture to suppress the primary yield. We use such modifications for direct-drive ICF experiments with MEDUSA; however, this reduces the yield of secondary protons, which provide additional ρR information. A proton yield of 5×10^7 or higher, which is well beyond the MEDUSA range, is required to measure secondary proton spectra with a charged-particle spectrometer (CPS).[9] Target modifications are not possible for the cryogenic-target experiments planned on OMEGA, necessitating the development of current-mode detectors for secondary-yield measurements at LLE.

Background for Secondary Neutrons

Several background processes complicate the measurement of secondary neutrons:

1. *Hard x rays*. The hard-x-ray signal from laser–plasma interaction and from the peak compression can be very large

on OMEGA: x-ray energies can reach 500 keV.[10] As a result, the secondary neutron signal appears on the tail of the hard-x-ray signal. This complicates background subtraction for the secondary neutron signal. The hard-x-ray signal can be suppressed by lead shielding the scintillator counter.

2. *Neutron-induced gamma rays from the target chamber wall*. The primary neutrons interact with the target chamber wall and produce gamma rays, which are detected in the scintillator. This gamma-ray signal is several order of magnitudes smaller than the primary neutron signal but larger than the secondary neutron signal. It is practically impossible to suppress this gamma-ray signal by shielding because of its high energy. The timing of the gamma-ray signal depends on the size of the target chamber and the location of the scintillator counter and can be chosen to be before or after the secondary neutron signal.

3. *Neutron-induced gamma rays from the target and other structures*. The interaction of the primary neutrons with the target and other structures (target positioner, other diagnostics, etc.) within the target chamber creates gamma rays. For the current-mode detectors within the target chamber or close to it, these gamma rays may create background for the secondary neutron signal. The amount of background and its arrival time can be measured in ICF experiments that produce high yields with very low areal densities. There is no shielding against these gamma rays, but the location of the detector can be adjusted to move the gamma-ray signal away from the secondary neutron peak. For the current-mode detectors located far from the target chamber these gamma rays are not an issue since they fall between the hard x rays and the gamma rays from the target chamber wall.

Current-Mode Detectors at LLE

At the present time LLE has five current-mode detectors plus MEDUSA to measure secondary neutron yield. Historically, LLE's neutron bang time (NBT) detector was the first current-mode detector used to measure secondary neutron yield. The NBT detector is located inside the OMEGA target chamber in a 1.5-in. reentrant tube. The first NBT channel has a BC-422Q scintillator with 4826-mm^3 volume located 55 cm from the target chamber center (TCC) and a Hamamatsu H5783 photomultiplier connected to a 1.5-GHz LeCroy 9362 scope. The NBT detector is shielded from hard x rays by 1.5 in. of lead in front and 0.5 in. of lead surrounding it. LLE's NBT detector was not originally designed for secondary-yield measurements but has been calibrated against MEDUSA on several low-yield DT shots. An example of a scope trace of the NBT detector for an indirect-drive DT shot with 3.4×10^7 yield is shown in Fig. 84.27. The DT peak on this scope trace was fit with a Gaussian function and is used for calibration. A scope trace of the NBT detector for a direct-drive DD shot with 8.0×10^{10} primary yield and 1.5×10^8 secondary yield is shown in Fig. 84.28. Figures 84.27 and 84.28 show that a lead thickness of 1.5 in. is not enough to shield from hard x rays on OMEGA. There are a few gamma-ray signals between the secondary-DT-neutron signal and the primary-DD-neutron signal. Because of the uncertainty in the gamma-ray background under the DT peak, the NBT error in the secondary neutron yield is estimated to be 20%. The NBT detector becomes nonlinear for secondary yields above 1.5×10^8, which was observed in comparison with other secondary-yield detectors described below. The NBT detector extends our measurable secondary yield beyond the MEDUSA range; it was used in comparison with the CPS diagnostic to measure secondary yield in direct-drive experiments. But recently another more

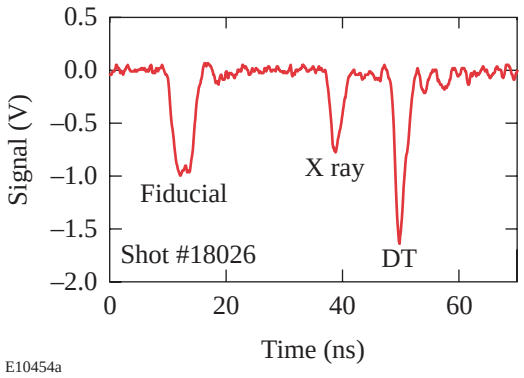

Figure 84.27
Scope trace of the NBT detector signal on a DT shot with a 3.4×10^7 yield.

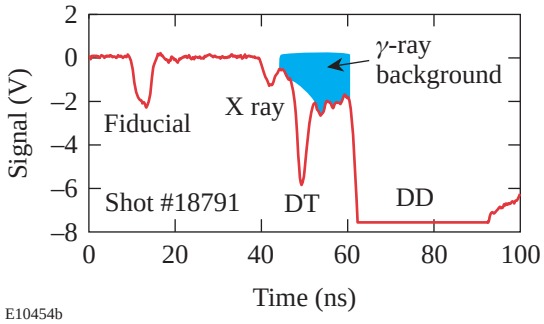

Figure 84.28
Scope trace of the NBT detector signal on a DD shot with a primary DD yield of 8.0×10^{10} and a secondary DT yield of 1.5×10^8.

precise and specially designed current-mode detector, 1.7MNTOF, replaced the NBT detector in secondary-neutron-yield measurements.

The other already existing scintillation counter that can be used as a current-mode detector to measure secondary neutron yield is the 3MLARD detector. It consists of a 17.78-cm-diam, 10-cm-thick scintillator coupled with an XP2020 photomultiplier connected to two channels of the Tektronix 684 scope. The 3MLARD detector is located 285 cm from the TCC and is shielded by a 0.75-in.-thick lead plate in front of the scintillator. An example of a scope trace for the direct-drive DD shot with 6.0×10^9 primary yield and 6.0×10^6 secondary yield is shown in Fig. 84.29. The signals from hard x rays, secondary DT neutrons, gamma rays from the target chamber wall, and primary DD neutrons (saturating the scope) are clearly seen. To measure secondary neutrons from the 3MLARD detector, the secondary neutron signal is integrated. We use in this detector a relatively low signal well below XP2020 saturation. The linearity of the 3MLARD was checked by comparison with other detectors. The 3MLARD detector was calibrated against MEDUSA for the secondary neutron yields; it does not extend MEDUSA's range but instead provides a second, independent measurement of the secondary neutron yield.

The 1.7MNTOF detector was designed specifically for measuring secondary neutron yield. It consists of a 40-mm-diam, 10-mm-thick fast BC 422Q scintillator coupled with a fast (250 ps) Photeck PMT240 microchannel-plate photomultiplier connected to two channels of a Tektronix 684 scope. This detector is heavily shielded from hard x rays by 2 in. of lead in front and 1 in. of lead surrounding it. The 1.7MNTOF detector is located on the target chamber wall, 170 cm from the TCC. Because of its location, the 1.7MNTOF has no background from neutron-induced gamma rays from the target chamber wall. A scope trace of the 1.7MNTOF detector for a direct-drive DD shot with 8.5×10^{10} primary yield and 1.5×10^8 secondary yield is shown in Fig. 84.30. The signals from secondary DT neutrons and primary DD neutrons (saturating the scope) can be seen in Fig. 84.30. The hard-x-ray signal is completely eliminated by the lead shielding. From Fig. 84.30 one can estimate a gamma-ray background of a few percent. To measure secondary neutrons from the 1.7MNTOF detector we integrated the signal in the appropriate time window. The 1.7MNTOF detector was calibrated using ride-along copper activation on pure-DD shots; the result of this calibration is shown in Fig. 84.31. The copper activation is a standard diagnostic[11] for 14.1-MeV neutrons in ICF experiments with DT-filled targets. The ^{63}Cu $(n,2n)$ ^{62}Cu reaction cross section has a threshold at 10.9 MeV, and, therefore, copper activation is insensitive to the primary DD neutrons and registers only secondary DT neutrons. The secondary DT neutrons have an energy spectrum from 11.8 MeV to 17.1 MeV. The ^{63}Cu $(n, 2n)$ ^{62}Cu reaction cross section increases as the neutron energy increases.[12] We estimate the error from the uncertainty in the energy spectrum of the secondary neutrons to be less than 10%. This 1.7MNTOF calibration error can be improved if necessary by special low-yield DT calibration shots. The PMT240 photomultiplier is linear up to 25 V into a 50 Ω load. This level of signal has not yet been reached, and one can see from Fig. 84.31 that the 1.7MNTOF detector is linear over the range of yields measured. The PMT240 gain is 6×10^5 and the sensitivity of the 1.7MNTOF detector is about 0.3 pC/neutron.

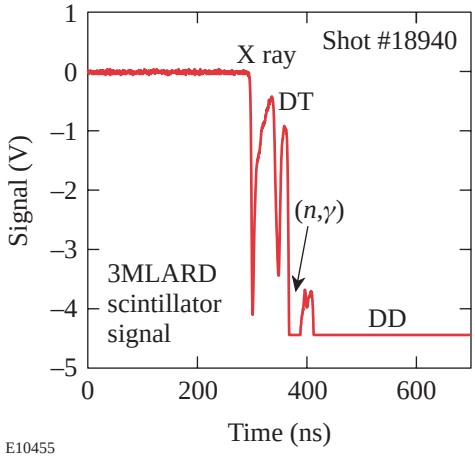

Figure 84.29
Scope trace of the 3MLARD detector signal on a DD shot with a primary DD yield of 6.0×10^9 and a secondary DT yield 6.0×10^6.

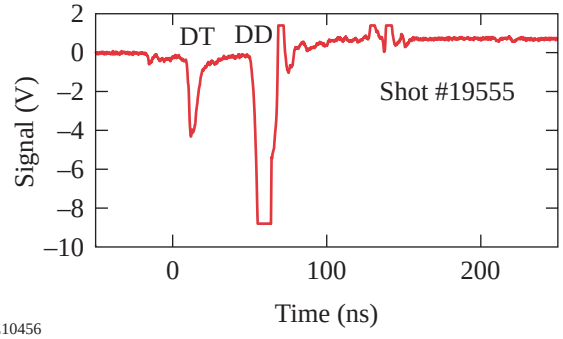

Figure 84.30
Scope trace of the 1.7MNTOF detector signal on a DD shot with a primary DD yield of 8.5×10^{10} and a secondary DT yield of 1.5×10^8.

The 20MLARD and 20M3×3 current-mode detectors are designed to extend the secondary-yield measurements to 5×10^{10}. The 20MLARD counter is identical to the 3MLARD counter. The 20M3×3 detector has a 3-in.-diam, 3-in.-thick scintillator and an XP2020 photomultiplier. Both detectors are located 20 m from the TCC behind the MEDUSA array and are shielded from hard x rays by 1.5-in. MEDUSA lead shielding and MEDUSA itself. Each of the detectors uses two channels of the Tektronix 2440 scope. A scope trace from the 20MLARD detector for the direct-drive DD shot with 1.0×10^{11} primary yield and 3.2×10^{8} secondary yield is shown in Fig. 84.32. The signals from hard x rays, gamma rays from the target chamber wall, secondary DT neutrons, and primary DD neutrons (saturating scope) along with small signals from the scattered neutrons can be seen in Fig. 84.32. A scope trace for the 20M3×3 detector looks very similar, but with lower signals. At this level of the secondary neutron yield there are just a few neutron hits in the 20MLARD and 20M3×3 current-mode detectors. We need higher yield for more precise calibration of these detectors. They can be calibrated with ride-along copper activation on moderate-yield DT shots. These two detectors will be used for the OMEGA cryogenic D_2 shots.[13]

The operating range of secondary yields of MEDUSA and all current-mode detectors at LLE together with the current status of the detectors is summarized in Table 84.IV. The lower limit of the yield range is determined by the neutron hit statistics, and the upper level is set by the measured or expected linearity threshold of the photomultiplier.

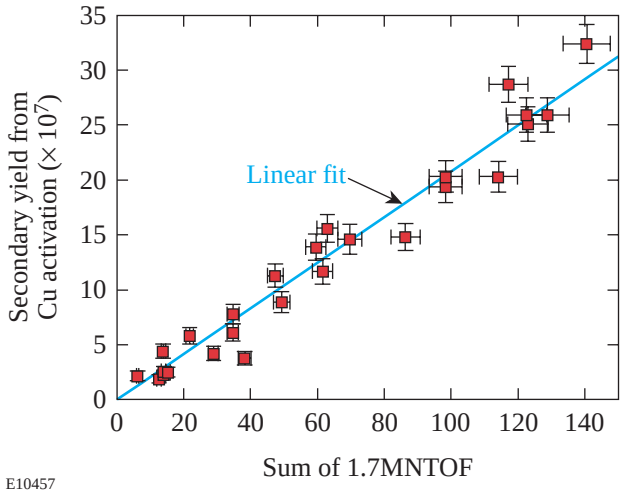

Figure 84.31
Calibration of the 1.7MNTOF detector against copper activation.

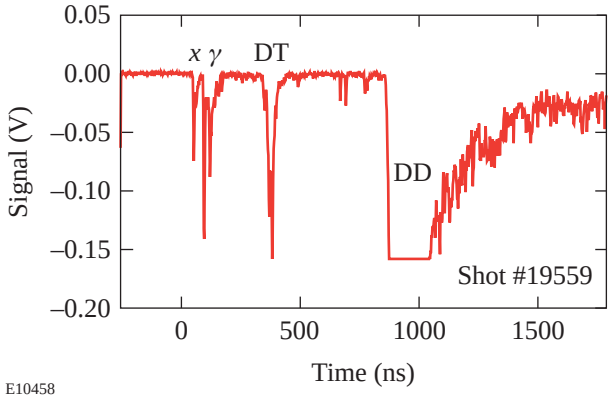

Figure 84.32
Scope trace of the 20MLARD detector signal on a DD shot with a primary DD yield of 1.0×10^{11} and a secondary DT yield of 3.2×10^{8}.

Table 84.IV: Detectors for secondary-yield measurements at LLE.

Detector	Yield Range	Current Status
MEDUSA	5.0×10^{5} to 1.5×10^{7}	Calibrated
3MLARD	5.0×10^{5} to 1.5×10^{7}	Calibrated
NBT	1.0×10^{7} to 1.5×10^{8}	Calibrated
1.7MNTOF	1.0×10^{7} to 1.0×10^{9}	Calibrated
20MLARD	2.0×10^{8} to 5.0×10^{9}	Future calibration
20M3×3	5.0×10^{8} to 5.0×10^{10}	Future calibration

Conclusions

Single-hit detectors like MEDUSA or LaNSA have a low dynamic range, which is inappropriate for the wide range of secondary yields obtained on OMEGA target shots. Current-mode detectors are an inexpensive alternative to single-hit detectors for measuring secondary neutrons over a wide range of yields. For the current direct-drive ICF experiments and future cryogenic experiments on OMEGA we have developed a set of current-mode detectors to measure secondary neutron yield from 5.0×10^5 to 5.0×10^{10} with an accuracy of 10%. The current-mode detectors have been used in several OMEGA direct-drive implosion experiments to measure secondary yield and will be used on future OMEGA cryogenic D_2 target shots.

ACKNOWLEDGMENT

This work was supported by the U.S. Department of Energy Office of Inertial Confinement Fusion under Cooperative Agreement No. DE-FC03-92SF19460, the University of Rochester, and the New York State Energy Research and Development Authority. The support of DOE does not constitute an endorsement by DOE of the views expressed in this article.

REFERENCES

1. E. G. Gamalii *et al.*, JETP Lett. **21**, 70 (1975).
2. T. E. Blue and D. B. Harris, Nucl. Sci. Eng. **77**, 463 (1981).
3. T. E. Blue *et al.*, J. Appl. Phys. **54**, 615 (1983).
4. H. Azechi *et al.*, Appl. Phys. Lett. **49**, 555 (1986).
5. M. D. Cable *et al.*, Bull. Am. Phys. Soc. **31**, 1461 (1986).
6. M. B. Nelson and M. D. Cable, Rev. Sci. Instrum. **63**, 4874 (1992).
7. J. P. Knauer, R. L. Kremens, M. A. Russotto, and S. Tudman, Rev. Sci. Instrum. **66**, 926 (1995).
8. N. Izumi *et al.*, Rev. Sci. Instrum. **70**, 1221 (1999).
9. Laboratory for Laser Energetics LLE Review **83**, 130, NTIS document No. DOE/SF/19460-357 (2000). Copies may be obtained from the National Technical Information Service, Springfield, VA 22161.
10. C. Stoeckl, V. Yu. Glebov, D. D. Meyerhofer, W. Seka, B. Yaakobi, R. P. J. Town, and J. D. Zuegel, "Hard X-Ray Detectors for OMEGA and NIF," to be published in the Review of Scientific Instruments.
11. R. A. Lerche, W. R. McLerran, and G. R. Tripp, *Laser Program Annual Report-1976*, Lawrence Livermore National Laboratory, Livermore, CA, UCRL 50021-76, 3-105 (1976).
12. H. Liskien and A. Paulsen, J. Nucl. Energy **19**, 73 (1965).
13. R. L. McCrory, R. E. Bahr, T. R. Boehly, T. J. B. Collins, R. S. Craxton, J. A. Delettrez, W. R. Donaldson, R. Epstein, V. N. Goncharov, R. Q. Gram, D. R. Harding, P. A. Jaanimagi, R. L. Keck, J. P. Knauer, S. J. Loucks, F. J. Marshall, P. W. McKenty, D. D. Meyerhofer, S. F. B. Morse, O. V. Gotchev, P. B. Radha, S. P. Regan, W. Seka, S. Skupsky, V. A. Smalyuk, J. M. Soures, C. Stoeckl, R. P. J. Town, M. D. Wittman, B. Yaakobi, J. D. Zuegel, R. D. Petrasso, D. G. Hicks, and C. K. Li, in *Inertial Fusion Sciences and Applications 99*, edited by C. Labaune, W. J. Hogan, and K. A. Tanaka (Elsevier, Paris, 2000), pp. 43–53.

Fourier-Space Image Processing for Spherical Experiments on OMEGA

Introduction

Measurements of shell integrity are very important for understanding and quantifying the performance degradation of spherical implosions in inertial confinement fusion (ICF).[1] Such measurements are performed at the peak of compression of the implosion, when maximum density and temperature are achieved. At this time, the hot core and the inner surface of the shell produce strong x-ray emission.[1] This radiation acts to backlight the rest of the shell. Imaging this emission at x-ray energies not absorbed by the shell provides measurements of the shape of this backlighter. Spatial modulations in the image taken at x-ray energies highly absorbed by the shell depend on modulations in both the backlighter emission and the shell's areal density.

The first measurements of shell-areal-density modulations were time integrated over the duration of the peak compression phase (~300 to 400 ps).[2–4] Core images were taken with either a monochromatic pinhole-array x-ray spectrometer[2,3] or a narrow-band filtered pinhole array[4] in targets with Ti-doped layers. The modulations in the cold, or absorbing, part of the shell's areal density $\delta[\rho R](\mathbf{r})$ are related to the modulation in the logarithm of the intensity ratio of two images taken at x-ray energies above (highly absorbing by the shell) and below (weakly absorbing by the shell) the Ti K edge:

$$\delta\left[\rho R\right](\mathbf{r}) = \delta\left\{\frac{\ln\left[I_{<K}(\mathbf{r})\right]/I_{>K}(\mathbf{r})}{\left(\mu_{>K}-\mu_{<K}\right)}\right\}, \qquad (1)$$

where $I(\mathbf{r})$ is the intensity in the image, μ is the mass absorption coefficient of Ti, and subscripts $<K$ and $>K$ designate energies just above and just below the Ti K edge, respectively.

The shell opacity and core size can vary significantly during the time of the stagnation phase, therefore time-resolved measurements of shell modulations are important. In this work, images above and below the Ti K edge are captured with a framing camera and recorded on film. The imaging system, composed of the pinhole array, the framing camera, the film, and the digitization process, is fully characterized. Image processing techniques are accomplished in spatial-frequency, or Fourier, space. In the sections that follow: (1) The image formation at all four stages of the imaging system is described along with approximations that enable the modulations in captured images to be related to shell-areal-density nonuniformities. (2) The pinhole camera and framing camera resolution are described. (3) The most important sources of experimental noise are investigated: the statistical x-ray photon noise from the core emission, the framing camera noise, the film noise, and the digitization noise. Methods of noise reduction are discussed. (4) A noise filtering and resolution deconvolution method based on Wiener filtering is formulated, and the experimental uncertainties along with the approximations are discussed. Conclusions are presented in the final section.

Experimental Configuration

The shell-areal-density modulation has been measured for shot 19669 in which a spherical target with an initial diameter of 921 μm, a 19.8-μm-thick shell, and 15-atm-D_2 fill was imploded by 351-nm laser light using the 60-beam OMEGA laser system.[5] A 1-ns square pulse shape with total on-target energy of about 23 kJ was used in this experiment. The target shell had a 2.4-μm-thick, Ti-doped (7.4% by atom) CH layer, which was separated from the inner surface by a 1.1-μm-thick pure-CH layer. The 15.3-μm outer layer was pure CH. Beam-smoothing techniques used during these experiments included distributed phase plates (DPP's)[6] and 0.2-THz smoothing by spectral dispersion (SSD).[7]

The target emission during the peak of compression was imaged by a 6-μm pinhole array (protected by a 203.2-μm Be filter) on a framing camera. The upper two strips of the framing camera were filtered by a 75-μm-thick Ti filter and the lower two strips by a 50-μm-thick Fe filter to image core radiation above (~6.5 keV) and below (~4.9 keV) the Ti K edge, simultaneously. The spectral bandwidth of these two x-ray energy channels was about $\Delta E/E \approx 0.2$ and similar to the time-

integrated measurements.[4] The distance between the target and the pinhole array was 3 cm, and the distance between the pinhole array and the framing camera was 36 cm, resulting in a magnification of 12 (Fig. 84.33). Each image taken with a framing camera had a temporal resolution of ~40 ps.[8] The use of optical fiducial pulses coupled with an electronic monitor of the framing camera produced a frame-timing precision of ~70 ps. The framing-camera output was captured on Kodak T-Max 3200 film, which was then digitized with a Perkin-Elmer microdensitometer (PDS) equipped with a 20-μm-square scanning aperture.

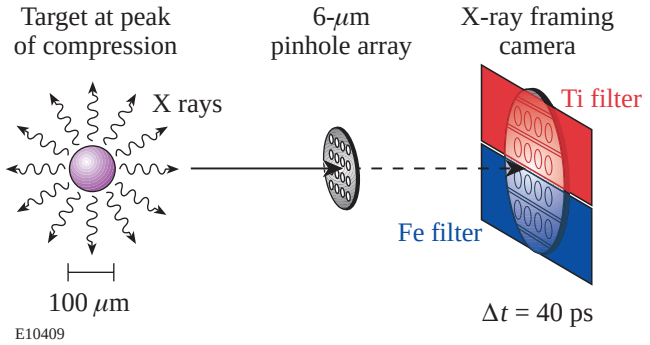

Figure 84.33
Schematic of the framing camera.

Figure 84.34 shows "raw" core images at the peak of compression below [(a), (b)] and above [(c), (d)] the Ti *K* edge, taken at 2.25 ns [(a), (c)] and at 2.30 ns [(b), (d)]. Notice that the two images within a particular energy channel have similar features that are different from the features in the other energy channel. This indicates that the features seen in the images are not noise and that the difference between the images at different energies is due to modulations in the absorbing shell. The main purpose of this article is to characterize the resolution and noise of all parts of the imaging system in order to distinguish signal from noise and relate detected modulations in the images to modulations in the shell. Figure 84.35 shows a block diagram of the entire detection system, which comprises four major parts: the 6-μm pinhole, the framing camera with a microchannel plate (MCP) and a phosphor plate, the film, and the digitization process. At each stage of the measurement, noise is added to the signal, and the signal with noise is convolved with the point-spread function (PSF) of each component of the system. In the spatial-frequency domain, the spectra of both the signal and the noise are multiplied by a modulation transfer function (MTF, defined here as the Fourier transform of the PSF) of that component of the imaging system.

The x-ray intensity leaving the target at time t and energy E is defined as

$$I_0(E,\mathbf{r},t) = I^{\text{core}}(E,\mathbf{r},t)\,\exp\left[-D_0(\mathbf{r},t)\right], \tag{2}$$

where $\mathbf{r}$ is the spatial coordinate, I_{core} $(E,\mathbf{r},t)$ is the core emission intensity integrated over the core size in the direction of light propagation from the target to the detector, and $D_0(E,\mathbf{r},t) = \mu(E)[\rho R](\mathbf{r},t)$ is the optical depth of the Ti in the shell. The absorption in CH is negligible compared to Ti in this experiment at an energy range from 5 to 7 keV.[4] The light intensity leaving the framing camera and incident on the film is

$$\begin{aligned} & I_{i2}(\mathbf{r},t) \\ & \sim \int dE \int d\mathbf{r}' R_{1,2}(E,\mathbf{r}-\mathbf{r}',t)\; f_1(E)\,\mu_{\text{Au}}(E)\,I_{i0}(E,\mathbf{r}',t) \\ & + I_{i\text{back}}(\mathbf{r},t), \end{aligned} \tag{3}$$

where the subscript i ($i = a$ or b) corresponds to images taken above and below the Ti *K* edge, respectively, $R_{1,2}(E,\mathbf{r},t)$ is the

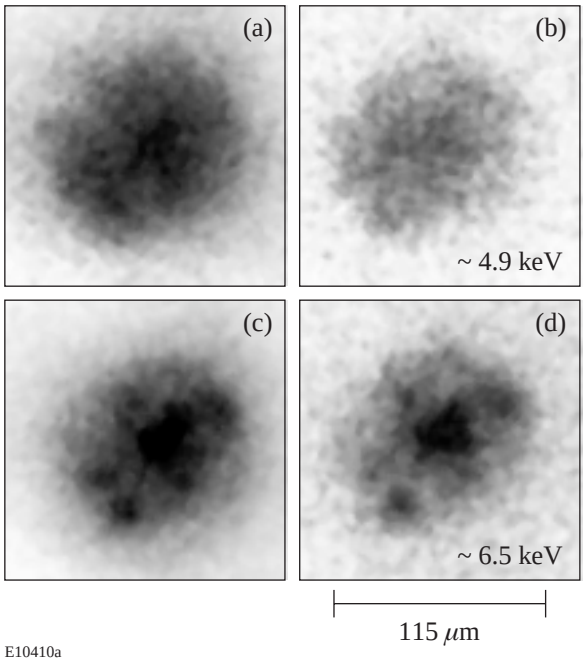

Figure 84.34
"Raw" core images at the peak of compression below [(a), (b)] and above [(c), (d)] the Ti *K* edge, taken at 2.25 ns [(a), (c)] and 2.30 ns [(b), (d)].

PSF of the pinhole and framing cameras that is in general a function of the x-ray energy E, $f_i(E)$ is the filter function of the ith energy channel, $\mu_{Au}(E)$ is the mass absorption rate of the gold photocathode (in the MCP), and $I_{i\text{back}}(E,\mathbf{r},t)$ is the background intensity for the ith channel. The background intensity is normally slowly varying and comes from hard x rays penetrating directly through the 25-μm-thick Ta substrate in which the pinholes are contained.

The film converts the incident light intensity $I_{i2}(\mathbf{r},t)$ into the film optical density O_{i3} $(\mathbf{r},t)$ according to its sensitivity [or D log(H)] curve W. Convolved with the PSF of the film $R_3(\mathbf{r},t)$, $O_{i3}(\mathbf{r},t)$ is given by

$$O_{i3}(\mathbf{r},t) = \int d\mathbf{r}' R_3(\mathbf{r}-\mathbf{r}')\, W\left\{\log_{10}\left[\int_{t-\tau/2}^{t+\tau/2} dt' I_{i2}(\mathbf{r}',t')\right]\right\}, \quad (4)$$

where τ = 40 ps is the temporal resolution of the framing camera. During film digitization, the optical density $O_{i3}(\mathbf{r},t)$ is convolved with the PSF $R_4(\mathbf{r})$ of the 20-μm-square aperture in the PDS to give the digitized or measured optical density

$$O_{i4}(\mathbf{r},t) = \int d\mathbf{r}' R_4(\mathbf{r}-\mathbf{r}') O_{i3}(\mathbf{r}',t). \quad (5)$$

The optical density of the film, $O_{i4}(\mathbf{r},t)$, is converted to intensity using the inverse film sensitivity W^{-1}; simultaneously the flat background intensity $I_{i\text{back}}(\mathbf{r},t)$ can be subtracted from the image because the constant $I_{i\text{back}}(\mathbf{r},t)$ is not affected by the convolutions in Eqs. (4) and (5). The measured optical depth $D_{i5}(\mathbf{r},t)$ of the target at a particular energy channel is obtained by taking the natural logarithm of that intensity-converted image,

$$D_{i5}(\mathbf{r},t) = \ln\left\{10^{W^{-1}[O_{i4}(\mathbf{r},t)]} - I_{i\,\text{back}}(\mathbf{r},t)\right\}. \quad (6)$$

Measured shell modulations $d_5(\mathbf{r},t)$ in optical depth are the differences in modulation optical depth of images above and below the Ti K edge,

$$d_5(\mathbf{r},t) = \delta\left[D_{a5}(\mathbf{r},t) - D_{b5}(\mathbf{r},t)\right]. \quad (7)$$

The blue line in Fig. 84.36 shows the measured shell modulation spectrum as a function of spatial frequency. This spectrum was obtained by azimuthally averaging the Fourier amplitude of the measured optical-depth-difference images above $[D_{a5}(\mathbf{r},t)]$ and below $[D_{b5}(\mathbf{r},t)]$ the Ti K edge. Each image was obtained by averaging two images below the K edge [shown in Figs. 84.34(a) and 84.34(b)] $D_{b5}(\mathbf{r},t) = [D_{b5}(\mathbf{r},t_1) + D_{b5}(\mathbf{r},t_2)]/2$, and two images above the K edge [shown in Figs. 84.34(c) and 84.34(d)] $D_{a5}(\mathbf{r},t) = [D_{a5}(\mathbf{r},t_1) + D_{a5}(\mathbf{r},t_2)]/2$. The noise level, shown by a red line in Fig. 84.36, was obtained by analyzing in Fourier space the differences in the two images above $[N_{a5}(\mathbf{r},t)]$ and below $[N_{b5}(\mathbf{r},t)]$ the K edge, respectively. It was assumed that there was little difference between images taken 50 ps apart. The black line represents the film noise, which was obtained by analyzing the same-size area as in the above images (1.4 mm × 1.4 mm) of uniformly exposed (optical density ~1) film.

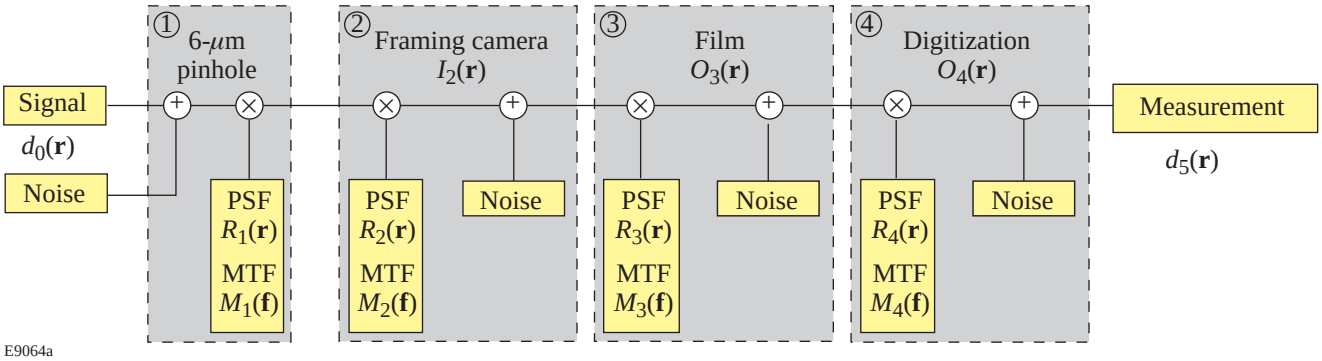

Figure 84.35
Block diagram of the experimental detection system, which comprises four major parts: a 6-μm pinhole, the framing camera, the film, and the digitization. At each stage of measurement, noise is added to the signal, and the signal with noise is convolved with the PSF. Variables $d_0^{sh}(\mathbf{r},t)$ and $d_5(\mathbf{r},t)$ are the optical-depth modulations in the shell and measured on a film, respectively. $I_2(\mathbf{r},t)$ is the light intensity in the framing camera's output. $O_3(\mathbf{r},t)$ and $O_4(\mathbf{r},t)$ are the optical density of the film, before and after digitization, respectively.

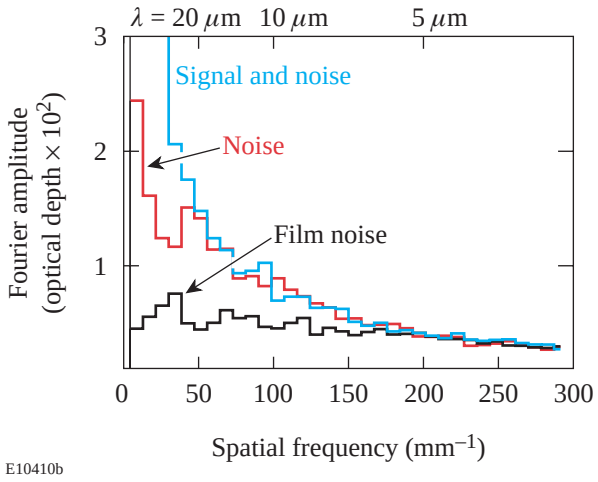

Figure 84.36
Azimuthally averaged Fourier amplitude as a function of spatial frequency for the signal with noise (blue line), the noise (red line) of the measured optical-depth modulations from the images in Fig. 84.34, and the film noise (black line).

One advantage of performing noise analysis in spatial-frequency space is the possibility of determining the origin of the noise from the shape of the noise spectrum. At each stage of the imaging system, the spectra of both the signal and the noise are multiplied by the MTF of that particular part of the system. Therefore, an initially flat noise spectrum—for example, the statistical x-ray photon noise from the core emission—will follow the shape of the pinhole camera's MTF after being imaged by the pinhole camera. Figure 84.36 shows that the film noise dominates at high spatial frequencies (>200 mm^{-1}), which slowly falls as a function of spatial frequency following the MTF of the 20-μm-square scanning aperture. At lower spatial frequencies (<200 mm^{-1}), the noise falls more steeply and, as will be shown later, is dominated by photon statistics from the core emission in this spectral region.

To recover the target optical depth $D_0(E,\mathbf{r},t)$ from the measured optical depth $d_5(\mathbf{r},t)$ it is, in general, necessary to work backward through all four stages of the imaging system, compensating for noise and system response (PSF). Additional complications arise during signal conversions from optical density to intensity and finally to the shell's optical depth. These conversions are nonlinear [see Eqs. (2), (4), and (6)]; therefore, additional noise is generated from the coupling of signal and noise during each conversion. However, if the modulations in the target's optical depth are small (which is the case in our experiment), the entire imaging system may be considered linear. This greatly simplifies the relation between the measured and target optical depths and enables a direct linear relationship between them. This method is justified when all of the nonlinear effects are small and may not be detected within system noise.

If the shell's optical-depth modulations are small for the energy channels above and below the Ti K edge, the core intensity consists of the smooth envelope and small modulations and has the same spatial and temporal structure for both the above- and below-K-edge energy channels, then can be summarized as

$$D_{i0}^{\mathrm{sh}}(\mathbf{r},t) = D_i^{\mathrm{sh}}(t) + d_{i0}^{\mathrm{sh}}(\mathbf{r},t), \tag{8}$$

$$I^{\mathrm{core}}(\mathbf{r},t) \sim I^{\mathrm{env}}(\mathbf{r},t)\,\exp\left[-d_0^{\mathrm{core}}(\mathbf{r},t)\right], \tag{9}$$

where $D_{i0}^{\mathrm{sh}}(\mathbf{r},t)$ is the total shell optical depth;

$$d_{i0}^{\mathrm{sh}}(\mathbf{r},t) = \mu_i \delta[\rho R](\mathbf{r},t) < 1$$

and $d_0^{\mathrm{core}}(\mathbf{r},t) < 1$ are the optical-depth modulations of the shell and the core, respectively; $I^{\mathrm{env}}(\mathbf{r},t)$ is the slowly varying envelope of the core emission; and μ_i is the spectrally weighed mass absorption rate of cold Ti at a particular energy channel [it is determined by the filter function $f_i(E)$ and core emission spectrum $I^{\mathrm{core}}(E,\mathbf{r},t)$]. The modulation in the shell's optical depth is simply the difference in optical-depth modulations above and below the K edge:

$$d_0^{\mathrm{sh}}(\mathbf{r},t) = d_{a0}^{\mathrm{sh}}(\mathbf{r},t) - d_{b0}^{\mathrm{sh}}(\mathbf{r},t). \tag{10}$$

Since the shell and core modulations are small, it is possible to expand the exponential functions in Eqs. (2) and (9) into Taylor series; retaining only zeroth and first orders in these expansions, we have the following expression for Eq. (3):

$$I_{i2}(\mathbf{r},t) \sim I^{\mathrm{env}}(\mathbf{r},t)\left\{2C - \left[\int d\mathbf{r}' R_{1,2}(\mathbf{r}-\mathbf{r}',t)\, d_{i0}^{\mathrm{sh}}(\mathbf{r}',t)\right.\right.$$

$$\left.\left. + \int d\mathbf{r}' R_{1,2}(\mathbf{r}-\mathbf{r}',t)\, d_0^{\mathrm{core}}(\mathbf{r}',t)\right]\right\}, \tag{11}$$

where $C = \int d\mathbf{r} R_{1,2}(\mathbf{r},t)$ is a normalization constant and the background intensity is assumed to be zero, $I_{i\mathrm{back}}(\mathbf{r},t) = 0$. T-MAX 3200 film has a constant MTF at least up to a spatial frequency of ~50 mm^{-1}, the highest spatial frequency considered in the experiment, so the PSF of the film is set to the delta function $\delta(\mathbf{r})$. Since only the "linear" part of the film sensitivity [D log(H)] curve is used, the modulations in measured optical

depth are linearly related to the optical-depth modulations in the target:

$$d_{i5}(\mathbf{r},t) = \int d\mathbf{r}' R_{\rm sys}(\mathbf{r}-\mathbf{r}',t)\, d_0^{\rm sh}(\mathbf{r}',t) + \int d\mathbf{r}' R_{\rm sys}(\mathbf{r}-\mathbf{r}',t)\, d_0^{\rm core}(\mathbf{r},t), \quad (12)$$

where $R_{\rm sys}(\mathbf{r},t)$ is the PSF of the entire system. It is normalized, $\int d\mathbf{r} R_{\rm sys}(\mathbf{r},t) = 1$, and proportional to the convolution of PSF's of the pinhole camera, the framing camera, and the digitizing aperture of the densitometer. In frequency space, the system MTF is the product of the MTF's of each of these components. Equation (12) was obtained by substituting Eq. (11) into Eqs. (4)–(6) and retaining only the zeroth-order and first-order terms of the Taylor series expansion of the logarithm function. Subtracting the optical-depth images above and below the *K* edge, the measured modulation in the cold-shell optical depth is given by

$$d_5(\mathbf{r},t) = d_{a5}(\mathbf{r},t) - d_{b5}(\mathbf{r},t) = \int d\mathbf{r}' R_{\rm sys}(\mathbf{r}-\mathbf{r}',t)\, d_0^{\rm sh}(\mathbf{r}',t). \quad (13)$$

The measured optical-depth modulations calculated from images above and below the Ti *K* edge are linearly related to the shell optical-depth modulations if these modulations are small. As mentioned earlier in this section, the core intensity $I^{\rm core}(\mathbf{r},t)$ has the same spatial and temporal structure for both the above- and below-*K*-edge energy channels. This assumption was experimentally confirmed in time-integrated experiments with pure-CH shells[4] and was used to derive Eq. (13) for time-resolved imaging.

In summary, approximations of the system performance have been used to find a straightforward relationship between the measured optical-depth modulations and the cold-shell areal-density modulations. Equation (13) has been derived by assuming that the shell's optical-depth modulations are small compared to unity. Since Eq. (13) is a linear approximation, it does not treat the generation of harmonics and coupling of modes produced by system nonlinearities. These nonlinearities have been simulated for amplitudes of modulations similar to that in data shown in Fig. 84.34, and the nonlinear effects were found to be negligible compared to the system noise.

System Resolution

The system resolution is determined from the point-spread function (PSF) in real space or the modulation transfer function (MTF) in spatial-frequency space, which is defined in this article as the Fourier transform of the PSF. The system MTF is the product of the MTF's of each of these components: the pinhole camera, the 20-μm-square scanning aperture, and the framing camera. The first two are determined from calculations based on geometry and spectral energy.

The digitizing PSF is proportional to Δx = 20-μm-square aperture; therefore, the MTF, which is the Fourier transform of the aperture, is given by[9]

$$M_{\rm dig}(f_x, f_y) = \left[\frac{\sin(\pi \Delta x\, f_x)}{\pi \Delta x\, f_x}\right]\left[\frac{\sin(\pi \Delta x\, f_y)}{\pi \Delta x\, f_y}\right], \quad (14)$$

where f_x, f_y are the spatial-frequency components of the vector **f**.

The MTF of the framing camera was determined by measuring the camera response to an edge placed ~1 mm in front of the camera and backlit by x rays. This output of the framing camera was measured with a charge-coupled-device (CCD) camera[10] with 9-μm-square pixel size. The edge was close enough to the framing camera so that diffraction effects can be neglected. The dashed line in Fig. 84.37(a) represents the light intensity incident on the edge. The blue line is the measured light intensity propagated through the system (and averaged in the direction parallel to the edge), and the red line is the fit to experimental data assuming the framing camera MTF as a two-Gaussian function,[11]

$$M_{\rm fc}(f) = \alpha_1 \exp\left[-(\sigma_1 f)^2\right] + \alpha_2 \exp\left[-(\sigma_2 f)^2\right], \quad (15)$$

where $\alpha_1 = 0.89 \pm 0.01$, $\alpha_2 = 0.22 \pm 0.01$, $\sigma_1 = 105.4 \pm 0.4\ \mu$m, and σ_2 = 2356.8±0.4 μm. The measured MTF of the framing camera is shown in Fig. 84.37(b). This MTF is similar to that measured in the earlier experiments.[12] The only difference is that CCD measurements are more sensitive than film measurements, and it was possible to detect the long-scale-length scattering of photons and electrons between the phosphor and microchannel plates.[13] This scatter is given by the second term in Eq. (15), and it reduces the MCP resolution by about 10% at low spatial frequencies <5 mm^{-1}.

The resolution of the pinhole camera was calculated using the Fresnel approximation (which should work well for the parameters of our imaging system) for the light propagation.[9] The pinhole PSF is given by the following equation:[9]

$$P_{\mathrm{ph}}(x,y,z_2) \sim \frac{1}{\left(\lambda^4 z_1^2 z_2^2\right)} \cdot \left| \iint dx'dy' \mathrm{circ}\left(\frac{x',y'}{d}\right) \exp\left[-\frac{i\pi}{\lambda}\left(x'^2+y'^2\right)\left(\frac{1}{z_1}+\frac{1}{z_2}\right)\right] \exp\left[\frac{2i\pi}{(\lambda z_2)}(xx'+yy')\right]\right|^2, \quad (16)$$

where circ($x,y/d$) is the circular aperture function with diameter d, λ is the x-ray wavelength, and z_1, z_2 are the distances from the object to the pinhole and the pinhole to the image, respectively. Because the pinhole size d in the pinhole array was varying typically within a specification of 0.5 μm, d = 6±0.5 μm, it was important that the pinhole-size variation not affect the pinhole resolution. Figure 84.38(a) shows the calculated pinhole MTF's of 5-, 6-, and 7-μm-diam pinholes at an x-ray energy of 5 keV. Even though the MTF's are different at high spatial frequencies, there is little difference (<5%) for all three MTF's at low spatial frequencies (<50 mm^{-1}), where all detected above the noise signal are located (see Fig. 84.36). Figure 84.38(b) shows that calculated MTF's of 6-μm pinholes at 5 and 7 keV are very close (with differences also <5%) at low spatial frequencies (<50 mm^{-1}). The pinhole depth's effect on the resolution was found to be negligible for the experimental conditions. This confirms the assumption made in the previous section that the system resolution is the same for images above and below the K edge.

System Noise

To determine the origin of noise shown by the black line in Fig. 84.36, the noise of the entire imaging system and in its individual parts was characterized by Fourier space analysis of uniformly exposed areas with the same box size (1.4 mm × 1.4 mm in image plane) as the data in Fig. 84.36. To measure noise in the entire system, images of a large area (~1 mm in diameter) of a uranium backlighter were used. The backlighter target was illuminated by 12 overlapping beams at an intensity of ~10^{14} W/cm^2, in a configuration similar to the noise measurements for planar-foil experiments.[12] Since the backlighter

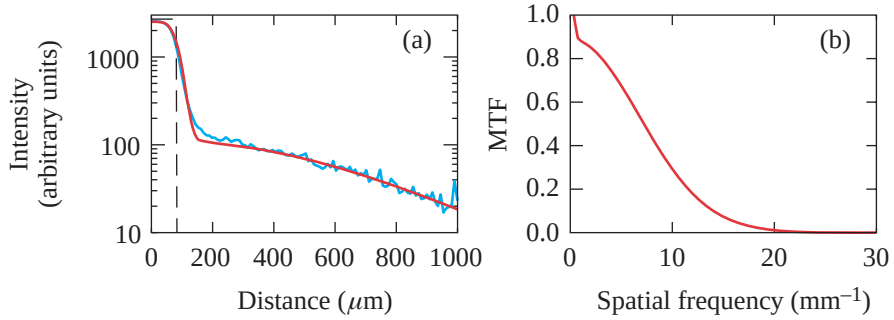

Figure 84.37
The framing camera resolution. The blue line in (a) represents the light intensity incident on the edge. The red line is the measured light intensity propagated through the system (and averaged in the direction parallel to the edge). The red line is the fit to experimental data assuming the framing camera MTF shown in (b).

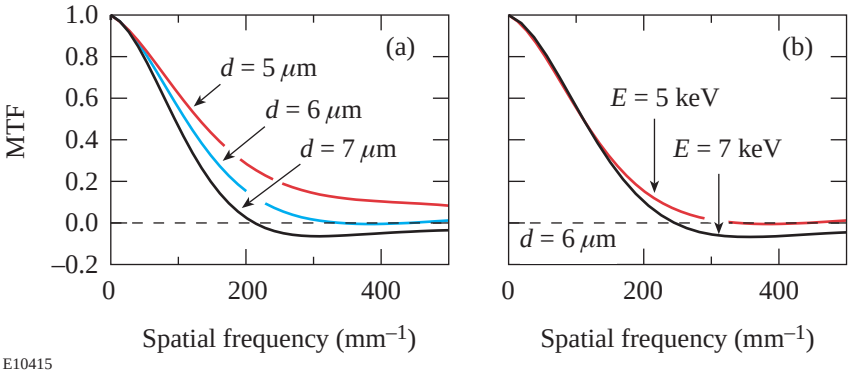

Figure 84.38
The resolution of the pinhole camera. (a) The calculated pinhole MTF's of 5-, 6-, and 7-μm-diam pinholes at an x-ray energy of 5 keV. (b) The calculated 6-μm pinhole MTF's at x-ray energies of 5 and 7 keV.

emission was smooth, the nonuniformities in the images were considered to be caused by noise. A 25-μm "strip" of CH_2 was placed between the backlighter and the pinhole to attenuate the backlighter emission by a factor of ~8 at 1.3 keV (see Fig. 84.39). The filters in front of the framing camera were also varied to change the exposure levels by a predetermined amount.

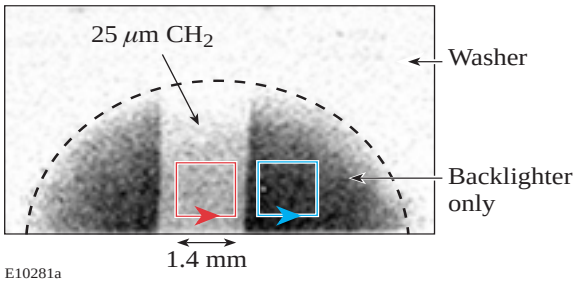

Figure 84.39
The image of the 25-μm CH_2 "strip" target taken with a U backlighter. Two boxes in the strip and backlighter-only regions represent image areas taken for analysis.

Figure 84.40 shows the azimuthally averaged Fourier amplitudes of the optical depth for two square regions with 1.4 mm in image plane, through (blue lines) and around (red lines) the strip. The total filtration in front of the framing camera included 20 μm of Be and 12 μm of Al for the data shown in Fig. 84.40(a) and 9 μm of Al for the data in Fig. 84.40(b). As a result of the filters, a relatively narrow band ($\Delta E/E \approx 0.2$) of x rays around 1.3 keV is used for radiography. At high spatial frequencies ($f > 200$ mm^{-1}), the noise spectrum is nearly constant, indicative of the noise from film and digitization. At lower spatial frequencies the noise amplitudes depend on the MTF's of pinhole and framing cameras and have contributions from both the photon statistical noise of the backlighter x rays and framing camera noise. It will be shown later in this section that the amplitude of framing camera noise is proportional to the output intensity. This means that in optical-depth space the framing camera noise is independent of the intensity (because the optical depth is the logarithm of the intensity), and it is expected to be the same in the areas through and around the strip. In optical-depth space, the photon noise of backlighter x rays is inversely proportional to the square root of the number of photons.[12] There is more photon noise in the region of the strip with fewer x-ray photons than in the region out of the strip [shown in Fig. 84.40(a)]. The noise falls even more with decreasing amount of filtration reaching the film noise level. This indicates that photon noise is dominant in the low-spatial-frequency region of the data shown in Figs. 84.36 and 84.40.

Figure 84.41 shows spectra of digitizing noise and the film noise in optical density versus spatial frequency. The digitizing noise [Fig. 84.41(a)] has been measured by digitizing uniform light exposures (with no film) using six different filters with transmissions of 0.5, 1.1, 1.5, 1.9, 2.4, and 2.9 optical density. To measure the film noise, the film was exposed to uniform irradiation at five different exposure levels of 0.5, 1.1, 1.7, 2.9, and 3.8 optical density [Fig. 84.41(b)]. A 5-μm-square digitizing aperture was used, and the analysis box size was the same as for all other images in this article: 1.4 mm square in image plane. The digitizing noise spectra are flat functions of spatial frequency, as expected, because the digitizing noise is added to the measurement after the effect of the system resolution. The noise amplitudes increase at higher optical-density levels when light transmission through the filter decreases. The film noise, which is about ten times higher than the digitizing noise (as evident from Fig. 84.41), also depends weakly on the exposure level. At high spatial frequencies its amplitude decreases gradually, as expected, since they are multiplied by the 5-μm-square digitizing aperture MTF given by Eq. (14).

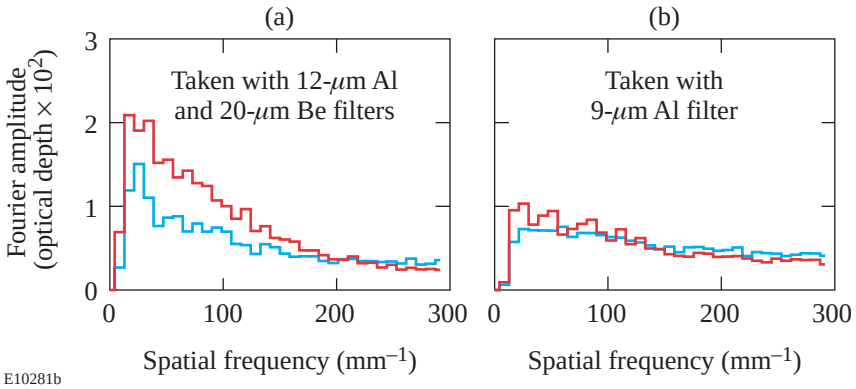

Figure 84.40
System noise. The measured noise spectra in areas through (blue lines) and around (red lines) the 25-μm-CH_2 strip target taken with (a) 20-μm-Be and 12-μm-Al filters, and (b) a 9-μm-Al filter.

Framing camera noise could be measured once the film was replaced by the CCD camera,[10] which allowed lower noise amplitudes to be detected. Figure 84.42(a) shows noise spectra of framing camera outputs taken with film and with the CCD. The framing camera was uniformly illuminated by x rays during two similar flat-field exposures (one exposure was taken with film, the other with a CCD). The incident x-ray flux was kept high to minimize the photon noise of incident x rays. The film exposure was converted to intensity in order to compare it with CCD data, which measures intensity, not optical density. Film data were digitized with a 10-μm-square digitizing aperture; the CCD's pixels were 9 μm. Film noise dominates framing camera noise at high spatial frequencies, and both noise levels are comparable at low spatial frequencies. The spectral shape of the framing camera noise follows the MTF (shown in Fig. 84.37).

Figure 84.42(b) shows the dependence of the framing camera noise on output intensity. By varying the gain of the framing camera, three different areas (with a typical square box of 1.4 mm) had average exposure levels of 200, 650, and 3600 counts measured with the CCD during one of the flat-field exposures. The noise spectra corresponding to these data are shown by three lines in Fig. 84.42(b). The noise levels scale as the average exposure levels on the CCD, indicating that the framing camera noise is proportional to the output intensity. This noise is dominated by the gain variations inside the MCP, which are reproducible from shot to shot. Figure 84.43 shows two images of the same area of the framing camera outputs taken during two different flat-field exposures. Images are virtually identical. Since this noise is reproducible, it can be removed from the images by subtracting two images. In Fig. 84.44 the noise spectra of these two images is shown by red and black lines. The blue line represents the noise from the difference of two images. The framing camera noise is reduced by a factor of 4 at low spatial frequencies. Such noise reduction can be useful in image processing when the framing camera noise is dominant (with the CCD).

In summary, the photon statistics of x rays are the dominant source of noise in our measurements. By increasing the inci-

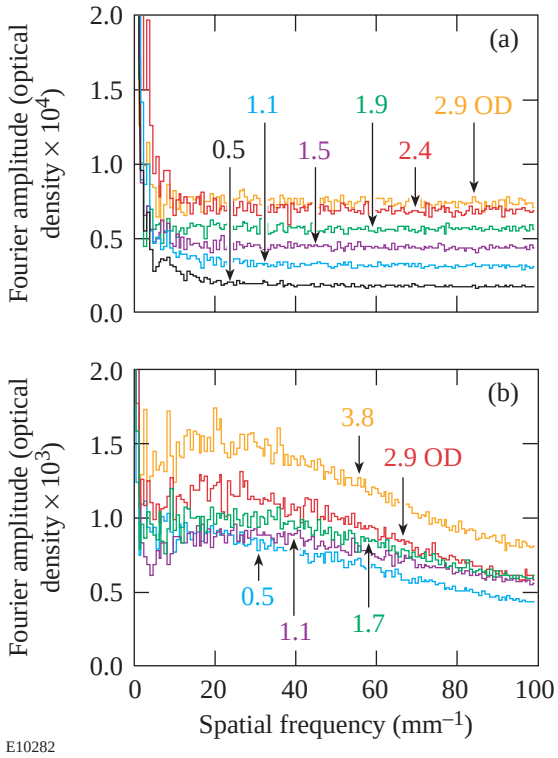

Figure 84.41
Fourier spectra of digitizing and film noise versus spatial frequency. (a) The digitizing noise measured by digitizing uniform light exposures (with no film) using six different filters with transmissions of 0.5, 1.1, 1.5, 1.9, 2.4, and 2.9 optical density. (b) The film noise measured by digitizing uniform film exposures at five different exposure levels of 0.5, 1.1, 1.7, 2.9, and 3.8 optical density.

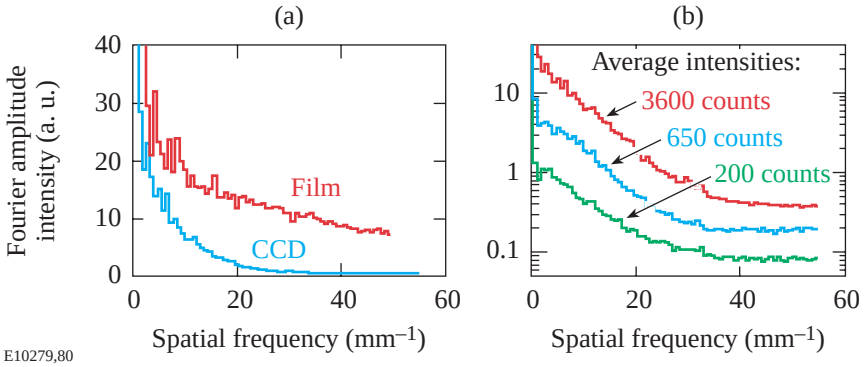

Figure 84.42
The framing camera noise. (a) The comparison of framing camera noise spectra taken with film and with a CCD. (b) The framing camera noise at different output intensities of 200, 650, and 3600 counts taken during a flat-field exposure with a CCD.

dent photon flux it was possible to reduce the noise to the levels where the framing camera and film noise became important. In this situation, an additional noise reduction was possible when the film was replaced by the CCD camera, and the framing camera noise was reduced by removing the shot-to-shot repeatable structure in the framing camera output.

Wiener Filtering

Using the measured system resolution and noise, it is possible not only to distinguish signal from noise in Fig. 84.36 but also to reduce it and deconvolve the resolution from the data detected above the noise. Such image processing is possible with Wiener filtering in spatial-frequency space. If $C(\mathbf{f})$ is the signal plus noise measured by the system (blue line in Fig. 84.36), $C(\mathbf{f}) = S(\mathbf{f}) + N(\mathbf{f})$, then the restored signal $R(\mathbf{f})$ is[14]

$$R(\mathbf{f}) = \frac{C(\mathbf{f})}{M_{\text{sys}}(\mathbf{f})} \bullet \frac{\left|S(\mathbf{f})\right|^2}{\left|S(\mathbf{f})\right|^2 + \left|N_{\text{avg}}(\mathbf{f})\right|^2}, \tag{17}$$

where $M_{\text{sys}}(\mathbf{f})$ is total system MTF, which is the product of the 6-μm pinhole camera MTF (Fig. 84.38), the framing camera MTF [Fig. 84.37(b) and Eq. (15)], and the 20-μm-square digitizing aperture MTF [Eq. (14)]. The last two MTF's are applied assuming a system magnification of 12. The term $\left|N_{\text{avg}}(\mathbf{f})\right|$ is the average noise spectrum (the black line in Fig. 84.36). During Wiener filtering the amplitudes that have $\left|C(\mathbf{f})\right| < 1.5\left|N_{\text{avg}}(\mathbf{f})\right|$ plus all amplitudes with spatial frequencies >50 mm^{-1} (this corresponds to wavelengths shorter than 20 μm) were filtered because the noise is dominant there. For the rest of the spectrum, it was assumed that the unknown variable $S(\mathbf{f})$ can be obtained by subtracting the noise in quadrature from the measured signal plus noise, $\left|S(\mathbf{f})\right|^2 = \left|C(\mathbf{f})\right|^2 - \left|N_{\text{avg}}(\mathbf{f})\right|^2$.

Figure 84.45 shows the result of such image processing, the image of the shell's optical-depth modulations. The level of shell modulations is similar to the time-integrated measurements,[4] which have detected ~20% perturbations in cold-shell areal density. The errors in determining these modulations, besides the system noise, include the uncertainty in the system

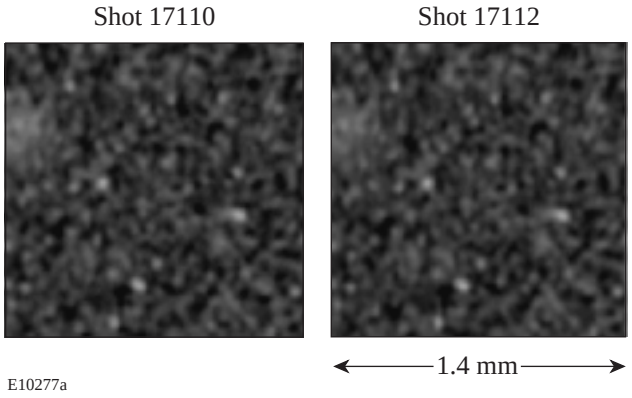

Figure 84.43
Two images of the same area of the framing camera outputs taken during two different flat-field exposures with a CCD. The images are nearly identical.

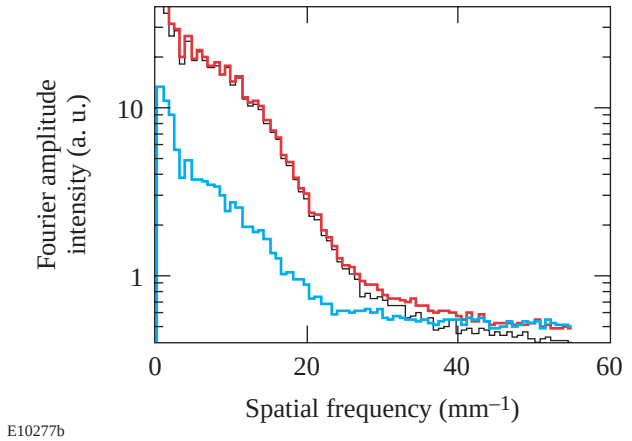

Figure 84.44
Reduction of the framing camera noise. The noise spectra of two images from Fig. 84.43 shown by red and black lines. The blue line represents noise from the difference of two images showing that framing camera noise can be reduced by a factor of 4 at low spatial frequencies.

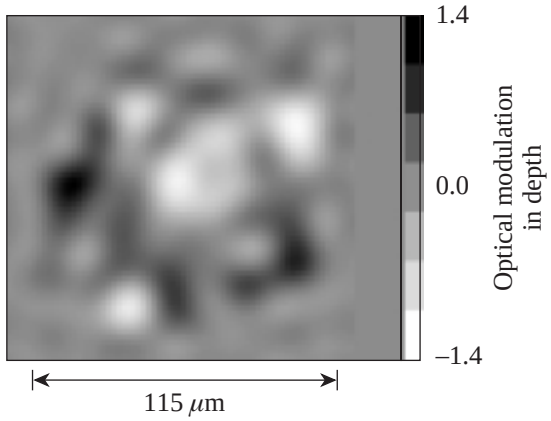

Figure 84.45
The Wiener-filtered image of the shell's optical-depth modulations.

MTF (which was about 5%) and the uncertainty in linearization of the nonlinear imaging system. This error was estimated by calculating the deviation of the sinusoidal shell modulation with an amplitude of 0.5 OD imaged by the system using Eqs. (2)–(7) without approximation and by using a linear approximation [Eq. (13)]. This calculated deviation is of the order of ~6%.

Conclusions

An imaging system based on the pinhole camera, framing camera, film, and digitization was characterized. This system has been used in spherical implosion experiments to measure shell integrity. Hot-core emission, which was used as a backlighter for the cold shell, was imaged at x-ray energies above and below the Ti *K* edge. The difference between the two images was related to perturbations in the cold, or absorbing, part of the shell. Based on the measured resolution and noise, a Wiener filter has been formulated that reduces noise, compensates for detector resolution, and facilitates measurement of shell nonuniformities.

ACKNOWLEDGMENT

This work was supported by the U.S. Department of Energy Office of Inertial Confinement Fusion under Cooperative Agreement No. DE-FC03-92SF19460, the University of Rochester, and the New York State Energy Research and Development Authority. The support of DOE does not constitute an endorsement by DOE of the views expressed in this article.

REFERENCES

1. D. K. Bradley, J. A. Delettrez, R. Epstein, R. P. J. Town, C. P. Verdon, B. Yaakobi, S. Regan, F. J. Marshall, T. R. Boehly, J. P. Knauer, D. D. Meyerhofer, V. A. Smalyuk, W. Seka, D. A. Haynes, Jr., M. Gunderson, G. Junkel, C. F. Hooper, Jr., P. M. Bell, T. J. Ognibene, and R. A. Lerche, Phys. Plasmas **5**, 1870 (1998).

2. B. Yaakobi, V. A. Smalyuk, J. A. Delettrez, R. P. J. Town, F. J. Marshall, V. Yu. Glebov, R. D. Petrasso, J. M. Soures, D. D. Meyerhofer, and W. Seka, in *Inertial Fusion Sciences and Applications 99*, edited by C. Labaune, W. J. Hogan, and K. A. Tanaka (Elsevier, Paris, 2000), pp. 115–121.

3. B. Yaakobi, V. A. Smalyuk, J. A. Delettrez, F. J. Marshall, D. D. Meyerhofer, and W. Seka, Phys. Plasmas **7**, 3727 (2000).

4. V. A. Smalyuk, B. Yaakobi, F. J. Marshall, and D. D. Meyerhofer, in *Atomic Processes in Plasmas: Twelfth Topical Conference*, edited by R. C. Mancini and R. A. Phaneuf (American Institute of Physics, New York, 2000), pp. 15–24.

5. T. R. Boehly, D. L. Brown, R. S. Craxton, R. L. Keck, J. P. Knauer, J. H. Kelly, T. J. Kessler, S. A. Kumpan, S. J. Loucks, S. A. Letzring, F. J. Marshall, R. L. McCrory, S. F. B. Morse, W. Seka, J. M. Soures, and C. P. Verdon, Opt. Commun. **133**, 495 (1997).

6. Y. Lin, T. J. Kessler, and G. N. Lawrence, Opt. Lett. **20**, 764 (1995).

7. S. Skupsky, R. W. Short, T. Kessler, R. S. Craxton, S. Letzring, and J. M. Soures, J. Appl. Phys. **66**, 3456 (1989).

8. D. K. Bradley, P. M. Bell, O. L. Landen, J. D. Kilkenny, and J. Oertel, Rev. Sci. Instrum. **66**, 716 (1995).

9. G. O. Reynolds *et al.*, *The New Physical Optics Notebook: Tutorials in Fourier Optics* (SPIE Optical Engineering Press, Bellingham, WA, 1989).

10. R. E. Turner *et al.*, "Comparison of CCD versus Film Readouts for Gated MCP Cameras," to be published in the Review of Scientific Instruments.

11. H. F. Robey, K. S. Budil, and B. A. Remington, Rev. Sci. Instrum. **68**, 792 (1997).

12. V. A. Smalyuk, T. R. Boehly, D. K. Bradley, J. P. Knauer, and D. D. Meyerhofer, Rev. Sci. Instrum. **70**, 647 (1999).

13. J. D. Wiedwald *et al.*, in *Ultrahigh- and High-Speed Photography, Videography, Photonics, and Velocimetry '90*, edited by L. L. Shaw, P. A. Jaanimagi, and B. T. Neyer (SPIE, Bellingham, WA, 1990), Vol. 1346, pp. 449–455.

14. W. H. Press *et al.*, *Numerical Recipes in FORTRAN: The Art of Scientific Computing*, 2nd ed. (Cambridge University Press, Cambridge, England, 1992), pp. 701–715.

LLE's Summer High School Research Program

During the summer of 2000, 14 students from Rochester-area high schools participated in the Laboratory for Laser Energetics' Summer High School Research Program. The goal of this program is to excite a group of high school students about careers in the areas of science and technology by exposing them to research in a state-of-the-art environment. Too often, students are exposed to "research" only through classroom laboratories, which have prescribed procedures and predictable results. In LLE's summer program, the students experience many of the trials, tribulations, and rewards of scientific research. By participating in research in a real environment, the students often become more excited about careers in science and technology. In addition, LLE gains from the contributions of the many highly talented students who are attracted to the program.

The students spent most of their time working on their individual research projects with members of LLE's technical staff. The projects were related to current research activities at LLE and covered a broad range of areas of interest including laser modeling and characterization, diagnostic development, hydrodynamics modeling, liquid crystal chemistry, superconductors, optical coatings, laser damage, and the development of a novel laser glass (see Table 84.V).

The students attended weekly seminars on technical topics associated with LLE's research. Topics this year included lasers, fusion, holography, optical materials, nonlinear optics, the OMEGA Cryogenic Target System, and scientific ethics. The students also received safety training, learned how to give scientific presentations, and were introduced to LLE's resources, especially the computational facilities.

The program culminated with the High School Student Summer Research Symposium on 23 August at which the students presented the results of their research to an audience including parents, teachers, and LLE staff. The students' written reports will be bound into a permanent record of their work that can be cited in scientific publications. These reports are available by contacting LLE.

One hundred and seventeen high school students have now participated in the program since it began in 1989. The students this year were selected from approximately 70 applicants.

In 1997, LLE added a new component to its high school outreach activities: an annual award to an Inspirational Science Teacher. This award honors teachers who have inspired High School Program participants in the areas of science, mathematics, and technology and includes a $1000 cash prize. Teachers are nominated by alumni of the High School Program. Mr. James Shannon of Pittsford Mendon High School was the recipient of LLE's 2000 William D. Ryan Inspirational Teacher Award. Mr. Shannon, a chemistry teacher, was nominated by three alumni of the Research Program—Mr. Chen-Lin Lee (participant 1994), Mr. Steven Corsello (participant 1998), and Ms. Leslie Lai (participant 1998). Mr. Lee writes, "One person (Mr. Shannon) stands out most in providing me encouragement and confidence to further my studies in engineering." He adds, "He loves interacting with students, he loves teaching, and he loves chemistry." Mr. Corsello writes, "Mr. Shannon's unique teaching style enables his students to better understand chemistry." Ms. Lai writes, "He devoted his time to each student and made it easier for everyone to learn the material," and "He is one of the most encouraging people I have ever met." Ms. Kathleen Walling, principal of Pittsford Mendon High School, adds, "Jim is one of the most talented and dedicated teachers at this high school and has long been a favorite of students and parents," and "Jim has gone far above and beyond the requirements of his job description time and time again."

Table 84.V: High School Students and Projects—Summer 2000.

Name	High School	Supervisor	Brief Project Title
Andrew Campanella	Webster	P. Jaanimagi	Large-Area, Low-Voltage X-Ray Source
Jill Daum	Rushville	D. Smith/J. Taniguchi	Experimental Simulation of Damage in Spatial-Filter Lenses
Abraham Fetterman	Pittsford Mendon	M. Skeldon	Modeling Pulse Shape Distortions in the OMEGA Laser
Ming-fai Fong	Pittsford Sutherland	S. Regan	Experimental Investigation of Smoothing by Spectral Dispersion (SSD) with Apertured Near Fields
Robert Forties	Irondequoit	F. Marshall	X-Ray Sensitivity Measurements of Charge Injection Devices
Binghai Ling	Brighton	R. Epstein	Simulation of Plasma Spectra and Images of Foil Targets Using the Prism SPECT3D Radiation-Transport Post-Processor
Anne Marino	Hilton	S. Jacobs	Developing a Durable Phosphate Glass with a Low Glass Transition Temperature
Elizabeth McDonald	Harley	J. Zuegel	Adapting ASBO/VISAR for Foam Targets
Ronen Mukamel	Brighton	S. Craxton	Modeling the Spectra of Frequency-Converted Broadband Laser Beams on OMEGA
Gloria Olivier	Honeoye Falls-Lima	K. Marshall	Improving the Visible Selective Reflection in Lyotropic Cellulose Urethane Liquid Crystals
Colin Parker	Brighton	J. Marozas	Dynamic Focal Spot Size Using a Static Phase Plate
Priya Rajasethupathy	Brockport	J. Delettrez	Improving Equation-of-State Tables
John Savidis	Gates-Chili	R. Sobolewski	Characterization of Ultrafast Superconducting Optoelectronic Devices
Stephanie Wolfe	Spencerport	D. Smith/J. Oliver	Coatings for Ultraviolet Lithography

FY00 Laser Facility Report

The three primary priorities on OMEGA in FY00 in addition to executing target shots (see Table 84.VI) were (1) activate and test the full suite of Cryogenic Target Handling System (CTHS) equipment, (2) improve single-beam uniformity by activating the first terahertz (THz)-bandwidth-capable SSD system, and (3) improve overall on-target uniformity by balancing the beam-to-beam power fluctuations.

The following system improvements and modifications were realized during FY00:

- Demonstration of all Cryogenic Target Handling System (CTHS) subsystems and integrated testing including shooting cryogenic DD test shots; demonstrated capability of up to three cryogenic target shots per week.
- Installation of 1-THz smoothing by spectral dispersion (SSD), characterization of improved beam smoothing, and utilization of THz SSD on many experimental campaigns.
- Installation of 60 modified frequency-conversion-crystal (FCC) assemblies for broad-bandwidth (THz) capability as well as refurbished and environmentally protected optical surfaces (three KDP crystals per beamline). This project virtually eliminated a scatter loss of up to 20% at the end of the beamlines.
- Installation of 60 distributed polarization rotators (DPR's) on the full-aperture UV system for time instantaneous beam smoothing on target.
- Consistent 3% rms energy balance achieved on-target by balancing gain stages to compensate for small-signal-gain variations.
- Installation of a P510 streak camera, which increased system coverage from 20 beams to 50 beams. In addition, the new cameras have higher dynamic range and better frequency response than the original two cameras.
- Improved beamline laser transport by fixing spatial-filter-lens coating degradation. Sequentially removed, repaired, and replaced 231 lenses in the laser chain. By replacing all sol-gel antireflective coatings with hard oxide coatings, the long-term transmission of the lenses will remain high.
- The OMEGA wavefront sensor was relocated to a new platform on top of the south-end mirror structure of the Target Bay and re-engineered for multiplexed diagnostic functions as well as the capability to capture any of five OMEGA beamlines.
- In March 2000 the pulse shaping system was replaced by integrated, electronically synchronized hardware. This |aperture-coupled-stripline (ACSL) system has improved performance and increased reliability over the previous pulse shaping system.

Table 84.VI: The OMEGA shot summary for FY00.

LLE-ISE	320
LLE-RTI	195
LLE-LPI	43
LLE-other	24
LLNL	284
LANL	131
NLUF	124
CEA	21
SNL	11
Total	1153

National Laser Users' Facility News

During FY00 external use of OMEGA increased by 12% and accounted for 50% of the total target shots carried out on the facility. The external users included six teams carrying out work under the National Laser Users' Facility (NLUF) program as well numerous other scientific teams from Lawrence Livermore National Laboratory (LLNL), Los Alamos National Laboratory (LANL), Sandia National Laboratory (SNL), the Nuclear Weapons Effects Testing (NWET) program, and Commissariat à l'Énergie Atomique (CEA) of France.

FY00 NLUF Experiments

The seven NLUF experimental campaigns totaling 124 OMEGA target shots carried out in FY00 included the following:

High-Spatial-Resolution Imaging of Inertial Fusion Target Plasmas Using Bubble Neutron Detectors.
Principal Investigator: Raymond K. Fisher (General Atomics) and collaborators from the University of Rochester (LLE), CEA, and LLNL.

In this experiment, bubble neutron detectors were successfully used for the first time to record neutron images of ICF implosions in OMEGA experiments. The gel bubble detectors were attached to the back of a 10-in. manipulator (TIM) containing a neutron penumbral aperture designed and constructed by a team from the CEA. Figure 84.46(a) shows a photograph of the light transmitted through one of the detectors. Detailed analysis of the bubble density distribution yields the coded image shown in Fig. 84.46(b). The target plane neutron source distribution, obtained from a mathematical inversion of this image, is shown in Fig. 84.46(c). As expected, the counting statistics (resulting from the low neutron detection efficiency of the gel bubble detectors) limit the spatial resolution of this image to ~250 μm. There was no evidence of any background due to x rays or gamma rays. Development of a liquid bubble chamber detector should result in higher neutron detection efficiency and resolution of ~10 to 50 μm.

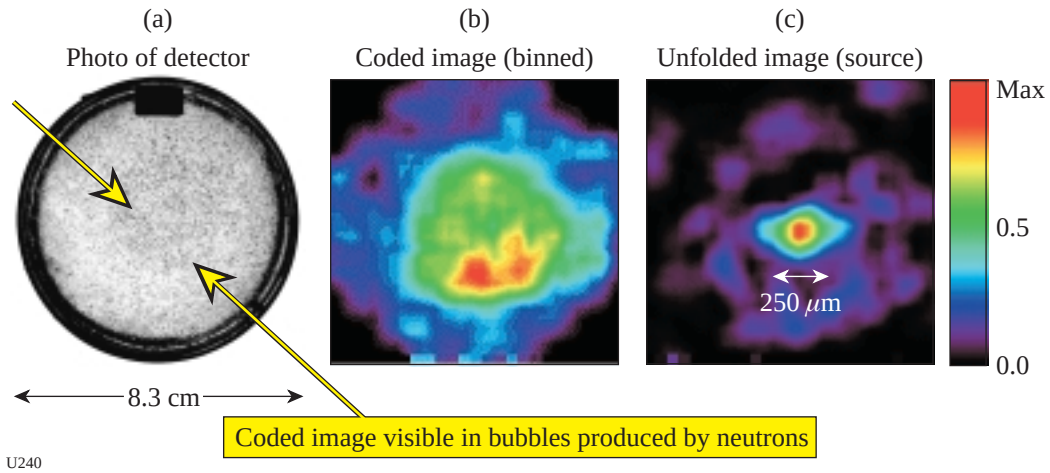

Figure 84.46
(a) Photograph of gel bubble detector after exposure to an OMEGA shot producing 6×10^{13} DT neutrons. The coded image is visible as a circular pattern of bubbles in the center of the detector. (b) Raw digitized coded image. (c) Unfolded neutron image.

Continuing Studies of Dynamic Properties of Shock-Compressed Solids by In-situ *Transient X-Ray Diffraction.* Principal Investigators: Marc Andre Meyers (University of California at San Diego) and Dan Kalantar (LLNL) and collaborators from LLNL, LLE, Oxford University, California Institute of Technology, and LANL.

This work continued a program of studies to investigate the response of crystals to shock compression in regions of strain rates previously unexplored. A series of experiments were conducted to demonstrate the time-dependent compression of a single-crystal Cu sample compressed by direct laser irradiation. Time-resolved streak records of the diffraction from two orthogonal lattice planes in Cu were obtained. Compressions of up to about 3% were observed in both directions at a shock pressure of approximately 200 kbar, confirming that the lattice responds plastically on a nanosecond time scale. A number of different thin-crystal target configurations were tested to identify and resolve issues of x-ray preheat due to the laser drive, and a mixed backlighter was tested to measure the compression of different parallel lattice planes. In addition, simultaneous shock compression and post-shock recovery experiments were conducted with single-crystal Cu to relate the residual damage to the *in-situ* diffraction measurements (Fig. 84.47). A series of nine 1-mm-thick Cu samples were shocked and recovered for post-shot TEM analysis.

Supernova Hydrodynamics on the OMEGA Laser. Principal Investigators: Paul Drake (University of Michigan) and Bruce Remington and Harry Robey (LLNL) and collaborators from LLNL, LLE, CEA, Osaka University, University of Arizona, University of Chicago, Eastern Michigan University, State University of New York–Stony Brook, and West Point Military Academy.

Supernovae are not well understood. Recent observations have clarified the depth of our ignorance by producing observed phenomena that current theory and computer simulations cannot reproduce. Such theories and simulations involve, however, a number of physical mechanisms that have never been studied in isolation. In this project, which this year involved 22 co-investigators from 11 institutions, well-scaled

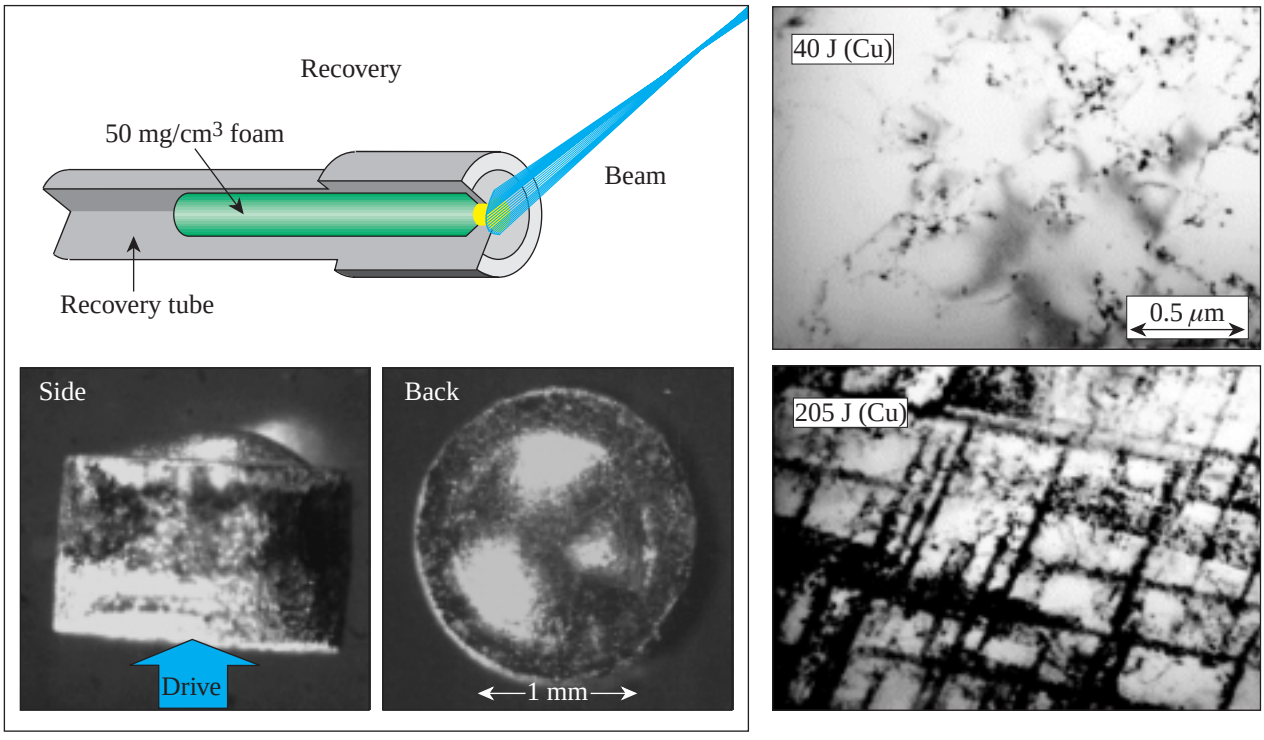

Figure 84.47
Illustration of crystal recovery experiments. Top left: the experimental configuration. Bottom left: photographs of a recovered Cu sample. Right: post-shot TEM photographs of shocked Cu samples shocked with a 40-J laser pulse (top) and a 205-J laser pulse (bottom). These samples were compressed at extreme strain rates, but they show similar residual dislocation and other microstructure as crystals shocked in lower-strain-rate gas-gun experiments.

experiments conducted on OMEGA investigated such mechanisms. Such experiments also provide clear tests of the codes used to simulate astrophysical phenomena. This past year's experiments were also used to observe interface coupling. In this case a shock wave was perturbed by structure at a Cu/plastic interface, and it in turn caused structure to evolve at a plastic/foam interface. Experiments were also conducted to study hydrodynamic instability growth at a spherically diverging interface (see Fig. 84.48). In addition, experiments were initiated to compare instability growth in 3-D versus 2-D, to examine the growth of multimode perturbations, and to produce and diagnose a radiative precursor shock.

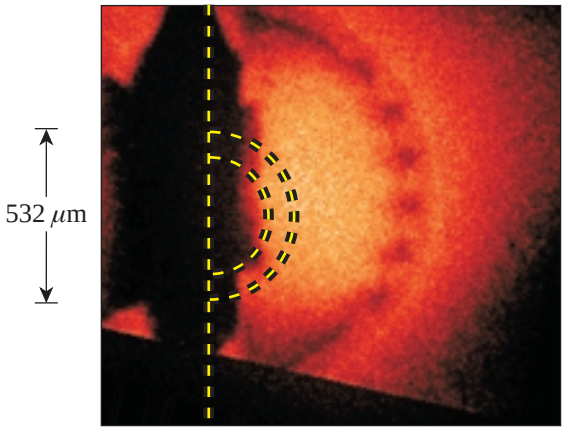

Figure 84.48
X-ray radiograph showing modulations on a spherical capsule that has expanded into resorcinol foam of density ~100 mg/cm^3. The initial outside diameter of the Br-doped CH capsule was 532 μm and the wall thickness was 97 μm. Initial perturbation wavelength and amplitude were 70 μm and 10 μm, respectively. Hydrodynamic instabilities, like those present in supernovae, caused the observed modulations to develop from the small initial perturbations.

Charged-Particle Spectroscopy on OMEGA: Recent Results, Next Steps.
Principal Investigator: Richard Petrasso (Massachusetts Institute of Technology) and collaborators from LLNL, LLE, and SUNY Geneseo.

The focus of this year's work has been the acquisition and interpretation of high-resolution secondary proton spectra [Fig. 84.49; see also LLE Review **83**, 130 (2000)]. These results are important not only for the information obtained for the current gas-filled capsule implosion experiments but also in demonstrating the potential to characterize cryogenic-target implosions. Secondary-proton spectroscopy may provide one of the best means for studying high-density cryogenic capsule implosions.

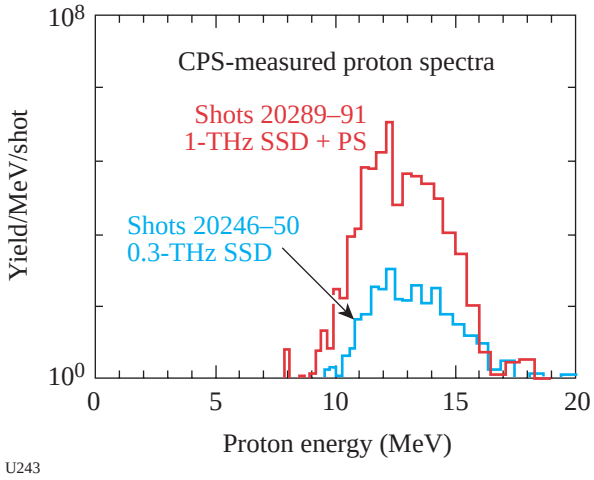

Figure 84.49
Comparison of multishot-averaged secondary proton spectra obtained with the CPS 2. Shots 20289 to 20291 were carried out with improved uniformity (1-THz, 2-D SSD and polarization smoothing), while shots 20246 to 20250 were carried out with 0.3-THz, 2-D SSD and no polarization smoothing. Note the higher secondary proton yields and increased energy downshift (indicating higher shell areal density) for the improved uniformity implosions.

Development of X-Ray Tracer Diagnostics for Radiatively Driven NIF Ignition Capsule Ablators.
Principal Investigator: David Cohen (Prism Computational Sciences) and collaborators from the University of Wisconsin, LLE, LANL, SNL, and LLNL.

This program continued a series of x-ray spectroscopic measurements to explore the physics of radiation-driven, NIF-type ablators. The FY00 campaign included two days of shots in which time-dependent backlit absorption spectra were measured from thin tracer layers buried inside capsule ablator samples that were mounted on halfraums (see Fig. 84.50). A significant signal was observed from NaCl tracers (Cl K_α) in both germanium-doped and undoped plastic ablator samples. The onset of the signal was seen to be delayed in the doped sample as compared to the undoped sample. Furthermore, especially in the doped sample, the progressive heating of the tracer can be seen as the dominant ionization state moves from Be-like to He-like over an interval of ~100 ps (Fig. 84.51). These data demonstrate the effects of ablator dopants on the radiation wave characteristics. Among other innovations in this year's campaign, we were able to construct targets and mount diagnostics in such a way as to do simultaneous spectroscopy of two samples on a single halfraum using two

different time-resolved spectrometers. These experiments are relevant for ablator characterization and target design efforts for NIF ICF targets.

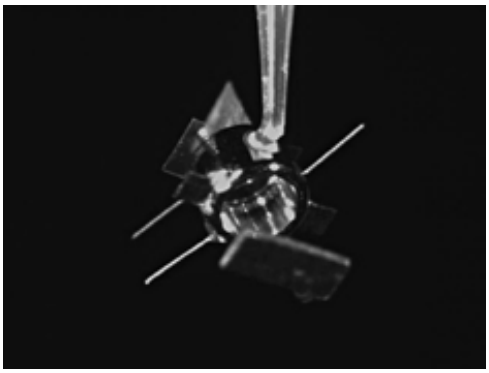

U244

Figure 84.50
A Powell-scope image of a halfraum target, seen from the laser entrance hole (LEH) side. The rectangular object in front of the LEH is a bismuth backlighter foil. The positioning stalk can be seen at the top of the barrel of the halfraum, and various positioning fibers and shields are also visible. The ablator sample (in the form of a witness plate) is on the back end of the cylinder.

Investigation of Solid-State Detection of Charged-Particle Spectrometry.
Principal Investigator: Kurtis Fletcher (State University of New York at Geneseo) and collaborators from MIT, LLE, and LLNL.

In this collaboration, electronic detection of charged particles was demonstrated using the charged-particle spectrometer (CPS1) on OMEGA. A 250-μm-thick pin diode was mounted in the spectrometer focal plane at the position corresponding to ~15-MeV protons. In a series of shots with D^3He-filled CH shells, high-energy protons passed through a collimator, an Al filter, and a CR-39 track detector before stopping in the diode. Each proton deposited about 3.5 MeV of energy in the diode. The resulting voltage signal of the diode was recorded on an oscilloscope [see Fig. 84.52(a)]. The CR-39 detector for each shot was later etched and the number of protons counted to provide a benchmark for the electronic detection system. As expected, the area of the proton peaks was proportional to the number of protons [see Fig. 84.52(b)]. This project demonstrated proof-of-principle that electronic detection of charged particles generated in the ICF environment is possible under appropriate conditions.

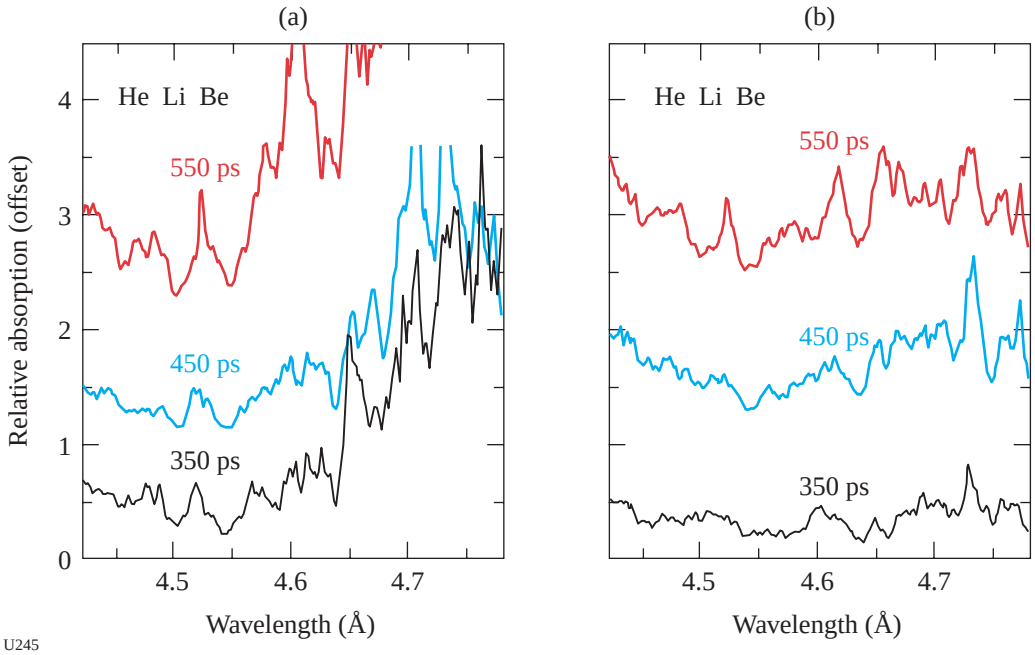

U245

Figure 84.51
Time-resolved absorption spectra of chlorine features from (a) an undoped sample and (b) a doped sample. The three prominent tracer absorption features are marked on each figure. The three lineouts shown in each figure are time-averaged over 100 ps.

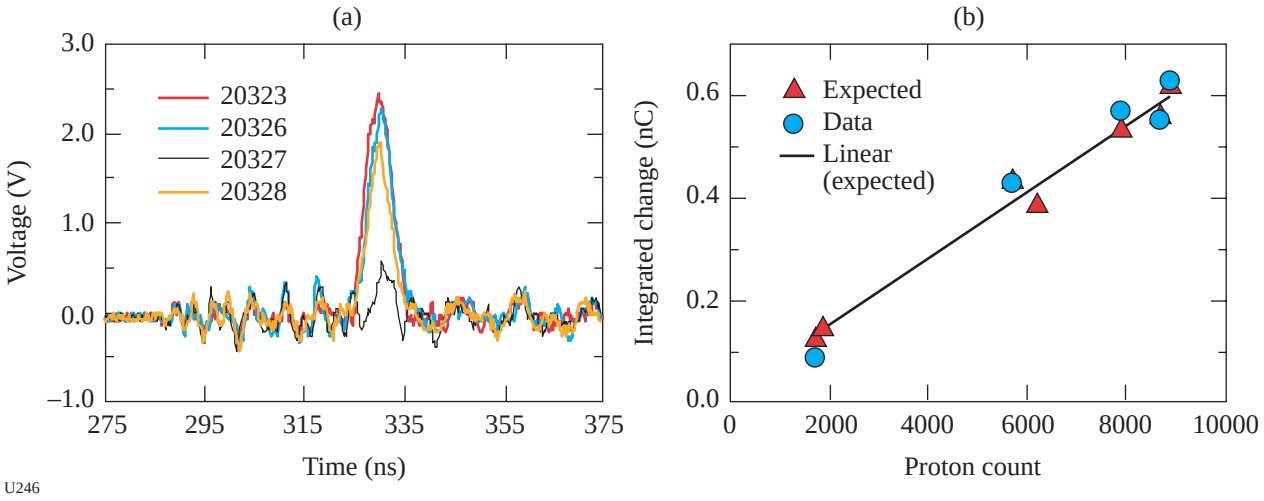

Figure 84.52
(a) Solid-state (PIN)-detector primary proton signals obtained on four shots (20323, 20326, 20327, and 20328) on D^3He-filled CH shells. (b) Integrated charge on solid-state detector versus the proton count as measured with a CR-39 track placed ahead of detector.

Optical Mixing of Controlled Stimulated Scattering Instabilities (OMC SSI) on OMEGA II.
Principal Investigator: Bedros Afeyan (Polymath Research Inc.) and collaborators from LLNL, LANL, and LLE.

In this collaboration, experiments continued to investigate optical-mixing-controlled stimulated scattering instabilities in NIF-like, long-scale-length plasmas. This year, the OMC SSI experiments concentrated on extending the previous results showing stimulated Raman scattering (SRS) backscattering reduction of an interaction or pump beam in the presence of an overlapping (probe) laser beam at the Mach = –1 surface. The interaction of the two beams is expected to produce a spatially localized, large-amplitude ion-acoustic wave (IAW). This IAW in turn dephases the SRS instability by producing IAW turbulence. The dependence of the nonlinear interaction processes on pump and probe beam intensity, probe beam spot size, and crossing region location were investigated in the FY00 experiments. Some of the results of these experiments are shown in Fig. 84.53.

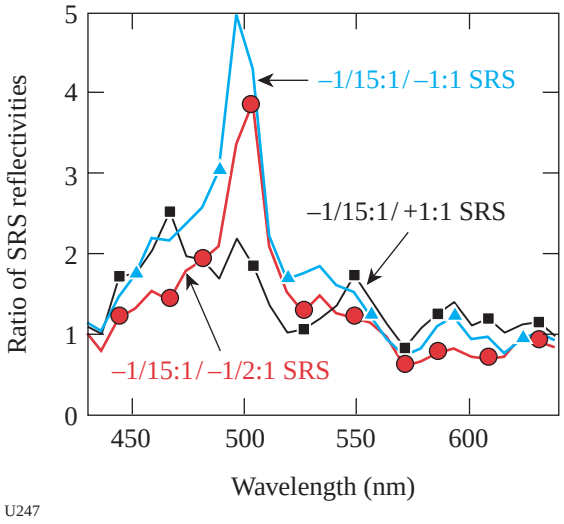

Figure 84.53
Ratio of stimulated Raman backscattering (SRBS) reflectivities plotted versus wavelength integrated over time. The plot shows weak-probe SRBS reflectivities where the intensity ratio between probe and pump beams is 15:1, divided by strong-probe SRBS reflectivities where the intensity ratio between probe and pump is 1:1 (blue curve) and 1/2:1 (red curve) and the probe beam is focused where the flow velocity is Mach = –1. The black curve is the control; the intensity ratio of pump to probe is 1:1 but the beams are focused where the flow is Mach = +1, where no resonant ion wave can be driven by the interaction of pump and probe. The black curve is not flat at M = +1 because even at that focus some of the light does get to Mach = –1, giving a slight reduction of the SRBS.

FY01 NLUF Proposals

A record 17 proposals with funding requests totaling $3,685,742 (total for FY01 and FY02) and with shot requests of 360 and 370 shots, respectively, in FY01 and FY02 were submitted to NLUF this year. For the first time, the successful proposals will be approved for a two-year period of performance (FY01 and FY02).

A DOE technical evaluation panel including Dr. David Bradley (LLNL), Dr. David Montgomery (LANL), Dr. Richard Olson (SNL), and Dr. Ned Sautoff (Princeton Plasma Physics Laboratory) reviewed the proposals on 19 May 2000. The NLUF Manager (non-voting) chaired the panel. The committee recommended approval of eight of the proposals (see Table 84.VII) with reduced funding and shot allocation to fit within the budget of $700,000 per year and NLUF shot allocation of 120 shots per year. A ninth proposal was conditionally approved pending additional funds from DOE.

FY00 National Laboratory, NWET, and CEA Programs

When Nova operations ended in FY99, national laboratory and other use of OMEGA continued to increase. Programs of the three national laboratories (LLNL, LANL, and SNL), NWET, and CEA accounted for over 38% of OMEGA use during this fiscal year. The following is a brief summary of some of the work carried out by the national laboratories, NWET, and CEA:

1. LLNL and NWET Campaigns

In FY00 LLNL had 320 shot opportunities at the OMEGA facility, divided as follows: 100 shots for target ignition physics (TIP), 200 shots for high-energy-density science (HEDS), and 20 shots for nuclear weapons effects testing (NWET). A total of 284 target shots were taken. These shots involved 15 Principal Investigators (including shots with collaborators from SNL and LANL) and spanned the 21 different mini-campaigns listed in Table 84.VIII.

Highlights of LLNL experiments include the following:

Conversion Efficiency: An initial OMEGA campaign was carried out to investigate the x-ray drive energetics in roughened hohlraums. Roughened hohlraums are required for infrared augmented β-layering on NIF, and the initial OMEGA results indicate that the rough hohlraums appear brighter than the smooth ones, contrary to expectations.

Cocktail Hohlraums: Experiments were initiated on OMEGA to investigate the soft x-ray emission of "cocktail" materials—i.e., mixtures of elements rather than the conventional Au-lined hohlraum. The initial results are in agreement with *LASNEX* simulations, and experiments will continue to confirm the expectations of higher drive with cocktail materials.

NIF Foot Symmetry: NIF-scale, 90-eV hohlraum symmetry experiments were carried out on OMEGA with a novel point-projection backlighting technique to assess the symmetry of drive in the foot of the NIF pulse. The results of these experiments indicate that the technique is capable of 1% accuracy in detecting asymmetry modes in NIF-scale targets.

Table 84.VII: Approved NLUF Proposals for FY01/02

Principal Investigator	Affiliation	Title of Proposal
C. F. Hooper, Jr.	University of Florida	Atomic Physics of Hot, Ultradense Plasmas
R. Mancini	University of Nevada, Reno	Determination of Temperature and Density Gradients in Imploded Cores of OMEGA Targets
R. Petrasso	Massachusetts Institute of Technology	Studies of Fundamental Properties of High-Energy-Density Plasmas
H. Baldis	University of California - Davis	Studies of Dynamic Properties of Shock-Compressed FCC Crystals
R. K. Fisher	General Atomics	High-Spatial-Resolution Neutron Imaging of Inertial Fusion Target Plasmas Using Bubble Neutron Detectors
R. B. Stephens	General Atomics	Asymmetric Fast Ignition Target Compression
P. Drake	University of Michigan	Supernova Hydrodynamics on the OMEGA Laser
B. B. Afeyan	Polymath Research, Inc.	Optical-Mixing-Controlled Stimulated Scattering Instability Experiments on OMEGA III and IV: Suppressing Backscattering Instabilities by the Externally Controlled Generation of Ion Acoustic Wave or Electron Plasma Wave Turbulence

High-Convergence Implosions: The multicone capability of OMEGA was used to conduct hohlraum-driven implosion experiments with an inferred convergence ratio up to 20. The resulting neutron yield on these implosions was significantly improved compared to the previous Nova results with a single cone of beams (see Fig. 84.54).

Shock Timing: Using a shock optical pyrometer (SOP), the UV emission of shock breakout was measured and used to infer shock velocity in radiation-driven ablators. Shock propagation data were obtained for Al, polyimide, and Be+0.9% Cu samples. These experiments were carried out in a collaboration involving SNL, LANL, LLNL, and UR/LLE.

Ablator Burnthrough: SNL led a team of LLNL, LANL, and LLE scientists in conducting an experiment to investigate burnthrough in a radiation-driven capsule. The experiment was designed to provide verification of ICF ablator burnthrough timing. Indirect-drive burnthrough data were obtained for polyimide and beryllium samples using the half-hohlraum (halfraum) geometry shown in Fig. 84.55(a). Spatially resolved streak camera imaging was used in conjunction with timing fiducials provided by two of OMEGA's beams to provide this data [see Fig. 84.55(b)].

Convergent Ablator Burnthrough: X-ray-backlit implosions were used to determine the ablation rate and payload trajectory in spherical geometry in the hohlraum drive. Some of the results from these experiments are shown in Fig. 84.56.

Planar RT: Polyimide ablator Rayleigh–Taylor growth measurements were conducted on radiation-driven planar targets on OMEGA. The initial OMEGA experiments show acceptable agreement with code predictions for all wavelengths (see Fig. 84.57).

Table 84.VIII: LLNL Campaigns on OMEGA in FY00.

Campaign	Sub-Element	Experiment	Target Shot Allocation
Target Ignition Physics	WBS 1 – Energetics	Conversion efficiency	15
		Laser–plasma interaction	10
		Cocktail hohlraums	5
	WBS 2 – Symmetry	NIF foot symmetry	20
		High-convergence implosions	5
	WBS 3 – Ablator Physics	Shock timing	15
		Ablator burnthrough	10
		Convergent ablator burnthrough	10
		Planar RT	10
High-Energy-Density Sciences	Solid-State Hydro		15
	Implosion Mix	Pushered shells	15
	Hydro I	Richtmyer–Meshkov	40
	Hydro II	Features	20
	Hydro III	Jets	20
	Radiation Transport	Low T_r drive	5
		Radiation transport in foams	30
	Equation of State (EOS)	Low- and high-Z EOS	35
	Capability Development	Backlighter development	15
		Fluorescence mix	5
Nuclear Weapons Effects Testing (NWET)	Source Development	Gas-filled-Be-can sources	10
		Hot-electron sources	10

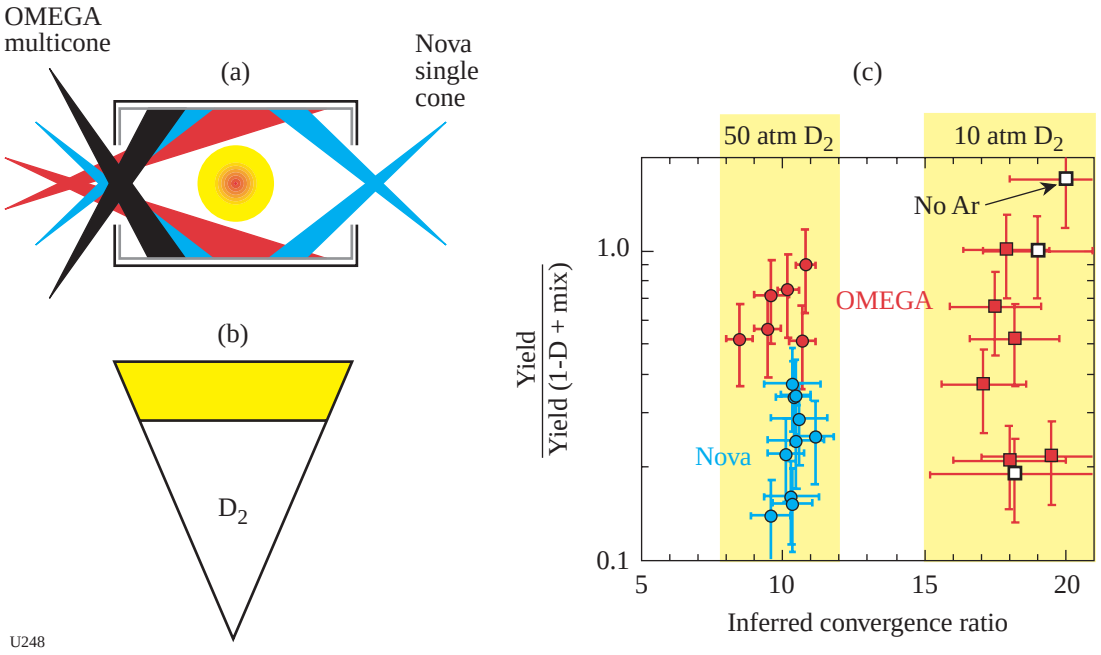

Figure 84.54
(a) Schematic illustrating the beam configuration for OMEGA compared to Nova. (b) Typical capsules used in these experiments were D_2-filled, Ge-doped CH shells. (c) Plot of the ratio of the measured neutron yield over the calculated 1-D yield including mix as a function of the inferred convergence ratio. The low-convergence-ratio targets contained 50 atm of deuterium (data points are circles), while the higher-convergence-ratio targets contained 10 atm (square data points). The open data points contained no Ar doping in the fuel. The Nova points are blue and the OMEGA data are red.

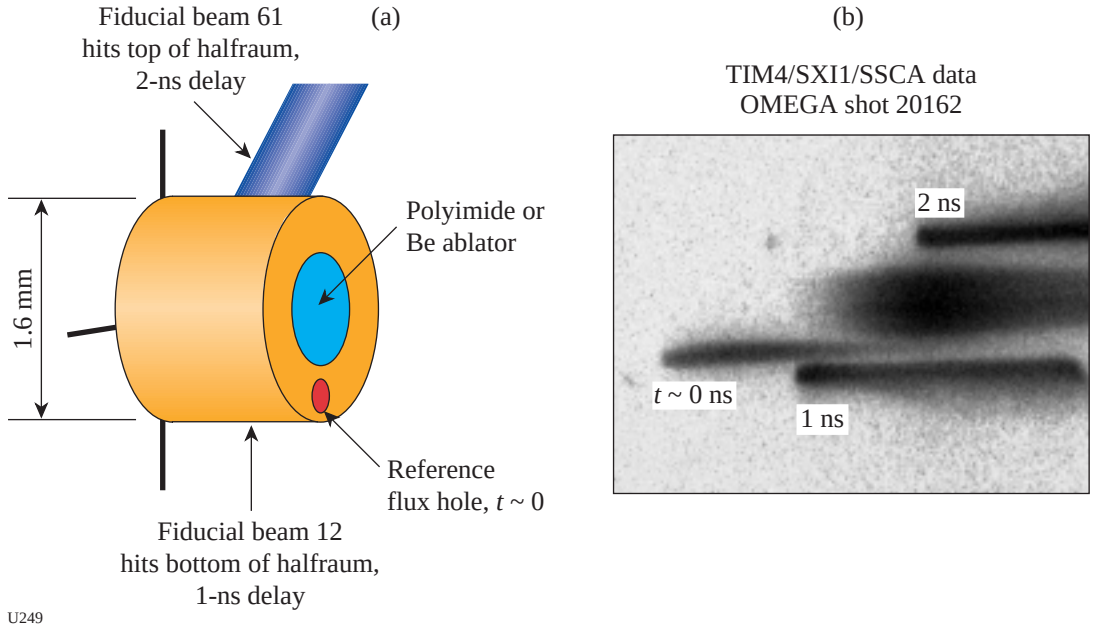

Figure 84.55
(a) Schematic of burnthrough experiment. Fifteen drive beams are brought into the halfraum in two cones, while two beams irradiate the top and bottom of the exterior of the halfraum to provide timing fiducials. A hole in the halfraum provides a time history of the x-ray flux in the halfraum. (b) Streak camera record of x-ray emission showing the reference flux hole emission ($t \sim 0$) and delays ($t \sim 1$ and 2 ns) along with the central delayed feature signaling burnthrough to the ablator being used in this experiment.

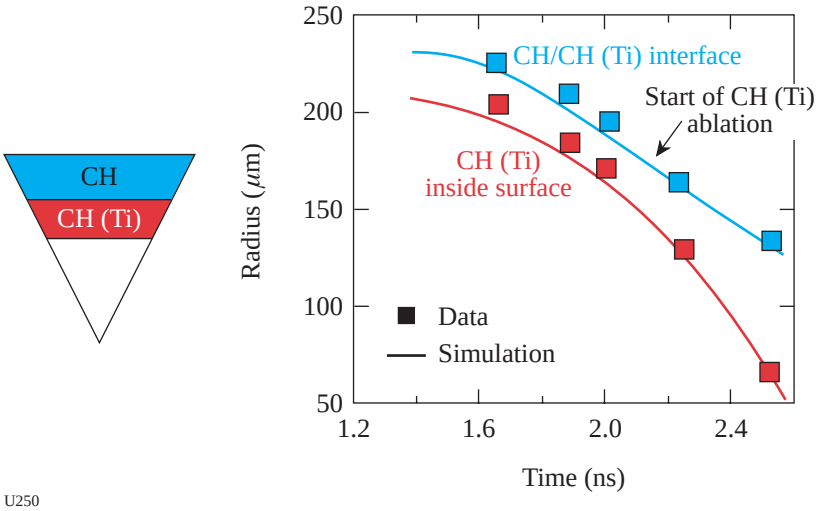

Figure 84.56
Measurement of ablation rate and payload trajectory in a hohlraum-driven spherical implosion experiment. The ablator for this experiment was CH, and an inner layer of Ti-doped CH served as the signature of ablator burn-through. Time-gated radiography with 5.2-keV x rays was used to make this measurement.

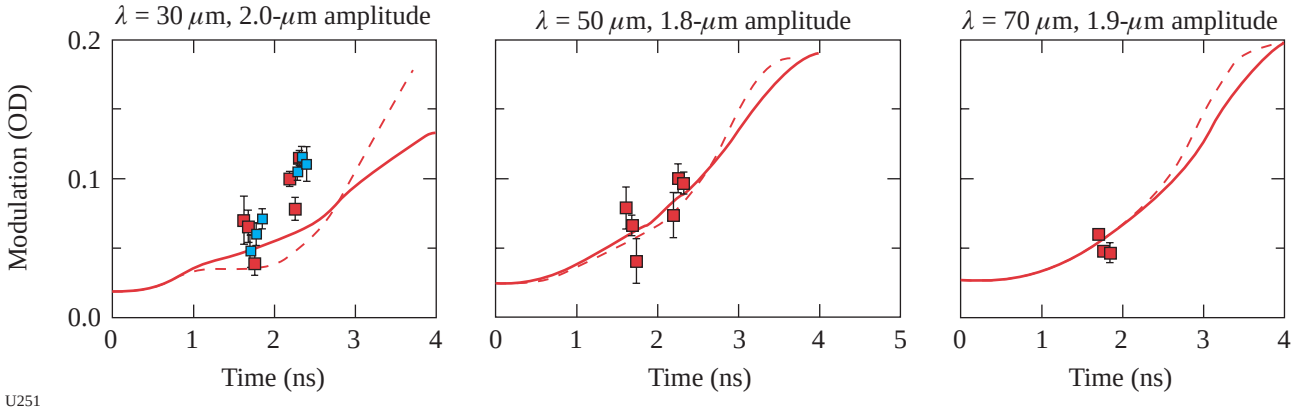

Figure 84.57
Results of Rayleigh–Taylor growth measurements on radiation-driven polyimide foils. These three plots show the measured modulation (OD) as a function of time for three radiation-driven planar targets with different initial wavelengths and amplitudes. The dashed lines represent simulations using a Planckian spectrum, while the solid lines represent the simulations using Dante-derived drive and calculated spectrum.

Pushered Shells: Experiments were conducted on a hohlraum-driven, single-shell target design consisting of a DT-filled glass shell overcoated with Ge-doped CH. The neutron burn history, neutron yield (20% of clean yield), radiation drive, and absorption imaging of the CH/SiO_2 trajectory were compared to hydrodynamics simulations.

Hydrodynamics: Several important hydrodynamics campaigns were carried out on OMEGA in FY00. A new shock-driven hydrodynamics geometry was successfully tested, and VISAR measurements of shock velocity were carried out. Simultaneous side-on and face-on data were obtained and 3-D features clearly observed on the interaction of a shock and a sphere. A collaborative experiment between the AWE (United Kingdom), LANL, and LLNL investigated the interaction of a supersonic jet with a counter-propagating shock. These experiments were simulated using the *RAGE* code at LANL, the *CALE* code at LLNL, and the *NYM-PETRA* code at AWE.

Long, Low T_r Drive: X-ray diffraction was used to measure melt and 1-D to 3-D lattice transitions on OMEGA. Simultaneous measurements of Bragg and Laue patterns on Cu showed 3-D compression of the crystal lattice.

Radiation Transport in Foams: The importance of wall structure and wall losses was demonstrated in experiments on foam-filled hohlraums.

Low- and High-Z EOS: Equation of state of relevant materials was measured at high pressures (1 to 50 Mbar) on OMEGA.

These experiments were conducted in both direct- and indirect-drive mode and showed that preheat is an issue for both approaches for these measurements.

Backlighter Development: A new backlighting capability was validated that will be used on NIF hydro experiments. This technique is pinhole-assisted point projection backlighting. Ultrahigh (100×)-magnification x-ray imaging was carried out to measure the core of OMEGA hohlraum-driven target implosions. This approach has the capability of providing 3-μm resolution at an x-ray energy of 6 keV.

Gas-Filled-Be-Can X-Ray Sources: Experiments were carried out on OMEGA to investigate the x-ray production of internally irradiated gas- and foam-filled Be cans. High conversion efficiency (~10%) to Ar *K*-shell and Xe *L*-shell radiation was measured for Ar- and Xe-filled Be cans. Foam-filled (6 mg/cm^2 SiO_2) cans demonstrated 30× enhancement of 50-keV x rays compared to previous measurements with 1% of critical density (n_c) C_6H_{12} gas-filled cans.

2. LANL Campaigns

Los Alamos National Laboratory conducted several experimental campaigns at OMEGA during FY00 as part of Campaign 10 Major Technical Efforts in Indirect-Drive Ignition and Support for Stockpile Stewardship. These campaigns included the following:

Double Shells: These experiments showed that the performance of the reduced M-band absorption (imaging) double-shell target exceeds that of all others at convergence ratio (CR) ~38 (see Fig. 84.58).

Classified Experiments: Classified experiments with important results were successfully hosted by LLE.

Direct-Drive Cylinder Experiments (DDCYL): DDCYLMIX experiments achieved good "low-mix/high-mix" comparison with well-characterized conditions for compressible plasmas in convergent geometry (see Fig. 84.59). Static targets better characterized the details of image analysis and careful comparison to theoretically simulated radiographs.

Backlighter Studies: Energy and intensity-dependent scaling for *K*-shell backlighters were determined for NIF-relevant backlighters. A series of experiments (Fig. 84.60) were carried out using Fe, Zn, and Ge backlighter targets driven at relatively high laser intensity (1×10^{16} W/cm^2).

High-Convergence Implosions: X-ray imaging of single-shell implosions showed transition from a limb-brightened image to a centrally peaked image at CR~23, indicative of mix.

Spike Dissipation: Laser-based experiments have shown that Rayleigh–Taylor growth in thin, perturbed copper foils leads to a phase dominated by narrow spikes between thin bubbles. These experiments are well modeled and measured until this "spike" phase, but not into the spike phase. Experiments were designed and carried out on OMEGA to explore the late-time spike phase. The OMEGA experiment used side-on radiography with a 6.7-keV Fe backlighter source. A gated x-ray imager time-resolved the x-ray transmission image from which the temporal development could be obtained (Fig. 84.61).

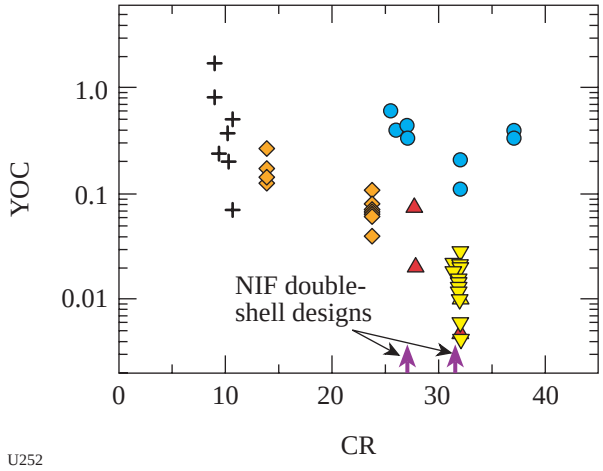

Figure 84.58
Ratio of measured neutron yield over the calculated clean yield (YOC) plotted as a function of calculated convergence ratio for indirect-drive Nova and OMEGA experiments. The diamonds indicate Nova cylindrical-hohlraum single-shell shots (1.4-ns square pulse shots). The crosses are data from tetrahedral-hohlraum single-shell-capsule experiments on OMEGA (1-ns square pulse). The inverted triangles represent standard double-shell data taken on OMEGA. The upright triangles represent suppressed M-band hohlraum double-shell-target data, and the solid circles represent reduced M-band absorption double-shell-capsule data taken on OMEGA. The arrows indicate NIF double-shell ignition designs with foams of 0.15 g/cc and 0.1 g/cc at convergence ratios 24 and 33, respectively.

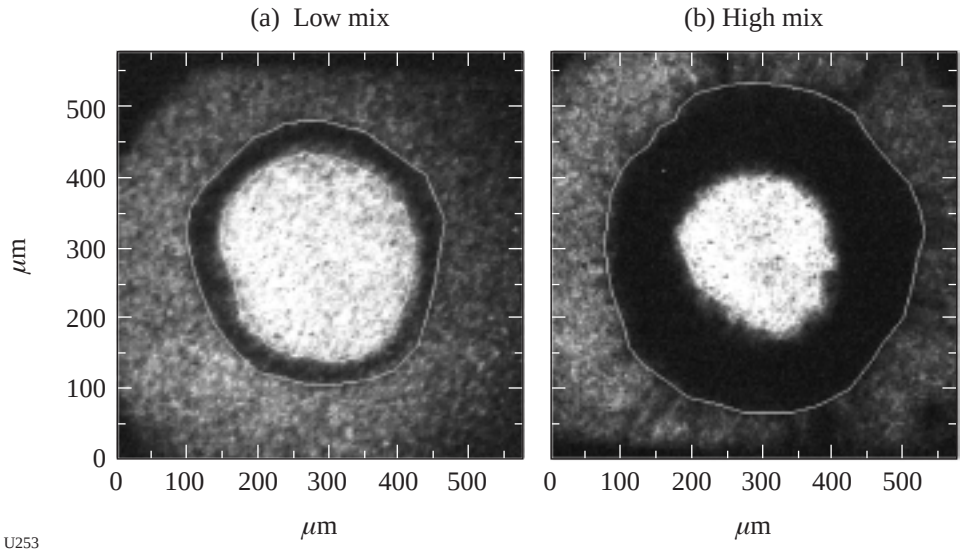

U253

Figure 84.59
X-ray radiographs taken along the cylinder axis of directly driven cylindrical target implosions. (a) Shot 18689 (19.1 kJ with Fe backlighter) low-mix target with dichloroprolystyrene marker layer (initial Atwood number = 0.15); (b) (Shot 18687 (19.9 kJ with Ti backlighter) high-mix target with Au marker layer (initial Atwood number = 0.95). Both images are taken 4.75 ns after t_0 in mass-matched implosions.

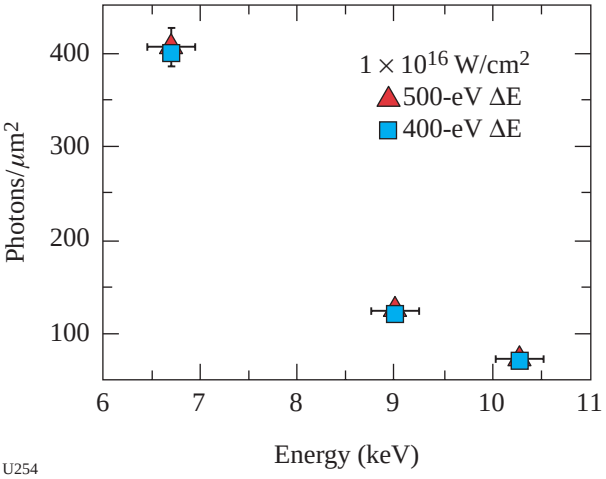

U254

Figure 84.60
X-ray fluence in photons per square micron plotted as a function of x-ray energy for Fe (6.7 keV), Zn (9.0 keV), and Ge (10.3 keV) *K*-shell x-ray emitters. The triangles represent 500-eV energy bandwidth, and squares represent 400-eV bandwidth. The experiments were carried out at an on-target intensity of 10^{16} W/cm^2.

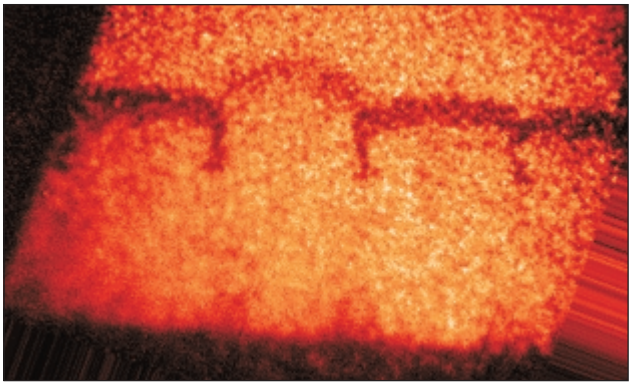

U255

Figure 84.61
Typical radiograph obtained on spike evolution experiment. The Cu target in this case was milled to generate a series of 10- to 20-μm-thin, 200-μm-long, 30-μm-high ridges 150 μm apart, leaving a thin, flat Cu backing. The target was placed on the side of a scale-1.2 OMEGA hohlraum with the ridges pointing into the hohlraum. A laser drive consisting of 1-ns square pulses heated the hohlraum to 190 eV to drive the target. The image shows the growth of the spikes and mushroom-like feet on the tips of the spikes.

High-Yield Neutron Shots for Diagnostic Development: NIF Phase 2 (Advanced) neutron diagnostics for burn history and neutron imaging were fielded, with first observations made of fusion gammas from an ICF target. The signal shown in Fig. 84.62 is from a Gas Cerenkov burn history diagnostic implemented on OMEGA.

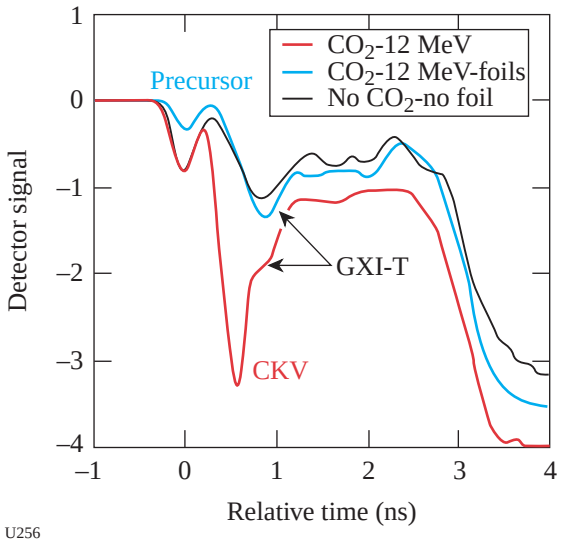

Figure 84.62
Typical Gas Cerenkov counter detector response for a high-neutron-yield, DT-filled-capsule shot (red line). The Cerenkov signal is the peak at ~0.6 ns (marked CKV). The plot also shows the signals from two other shots where the Cerenkov signal was blocked (black line) and where there was no CO_2 gas in the counter (blue line). The small hump in the back of the Cerenkov signal is apparently due to gamma rays generated by interaction of the neutrons generated in the implosion and the GXI diagnostic.

Los Alamos also supported several other campaigns at OMEGA:

Sandia WBS 3 ablator characterization, NLUF laser–plasma instability work, AWE Jet experiment, and transient x-ray diffraction materials work.

3. CEA Activities

In FY00, CEA (France) activities on OMEGA included the installation and activation of two diagnostics—a penumbral neutron imaging system (NIS) and an absolutely calibrated time-resolved broadband x-ray spectrometer (DMX)—and x-ray conversion efficiency experiments in spherical geometry.

Time-Resolved Broadband X-Ray Spectrometer (DMX): DMX (see Fig. 84.63) is a broad-bandwidth, absolutely calibrated x-ray spectrometer that uses new coaxial x-ray detectors (CXRD) to provide an overall ~100-ps temporal resolution in a compact 20-channel instrument. Spectral resolution is obtained by a combination of mirrors, filters, and detector spectral response. The current configuration covers a range of 50 eV to 20,000 eV. DMX was successfully activated and compared with a similar instrument (LLNL's Dante) on OMEGA shots in both direct and indirect drive. A satisfactory agreement was found between the two diagnostics on spectral shape and x-ray emission time history under various conditions (Fig 84.64), but a discrepancy was observed on absolute levels between the two diagnostics.[1] Further work is in progress to understand the origin of this discrepancy.

X-Ray Conversion Experiments: X-ray conversion experiments on disks are sensitive to 2-D effects. The OMEGA configuration delivers a very uniform laser irradiation pattern, enabling a quasi 1-D experiment in spherical geometry very suitable for the validation of numerical simulations. A set of experiments were carried out to study x-ray conversion on gold-coated, 950-μm-diam CH spheres (2.5 to 3 μm gold thickness) at laser intensities ranging from 3×10^{13} up to 8×10^{14} W/cm^{-2}. X-ray conversion history at different energies, x-ray imaging of plasma, and spectral measurements were used as benchmark simulations.

Neutron Imaging of an Imploding DT Target: Recently, CEA installed a new 14-MeV neutron imaging system (NIS) on OMEGA. This diagnostic measures the size of the neutron-emission area of a direct-drive implosion. A neutron image resolution better than 10 μm is required on future laser facilities such as LMJ and NIF. In June a prototype NIS was tested on OMEGA, using the technique of penumbral imaging, which has an ultimate resolution of 30 μm. The aperture is a massive cylinder (50 mm thick) of tungsten alloy, inside which an aperture with a biconical shape is drilled. The shape of this aperture is defined by entrance, middle, and output diameters of 600 μm, 760 μm, and 1070 μm, respectively. The entrance side of the aperture is set at 55 mm from the target with an aperture manipulator installed into a TIM. The aperture is positioned by a four-stage piezoelectric vacuum compatible actuator, which was tested in a high neutron flux environment. The image is recorded on a detector installed on the Target Bay floor at 8 m from the target chamber center (TCC). The detector is composed of 8000 plastic scintillating fibers. The light is generated mainly by the slowing of a proton produced by elastic scattering of a neutron on hydrogen. The resulting optical image is then amplified by a gated microchannel plate and recorded on the CCD. The CCD is protected from the direct interaction of the neutron by a shield made with polyethylene

and lead. The coded image [see Fig. 84.65(a)] is then unfolded by a filtered autocorrelation technique to produce the image shown in Fig. 84.65(b). The source is observed to be 120 μm in diameter on this shot and can be compared with the 3-keV x-ray image obtained on the same shot.

REFERENCES

1. See J. L. Bourgade *et al.*, "DMX: An Absolutely Calibrated Time-Resolved Broadband Soft X-Ray Spectrometer Designed for MJ Class Laser-Produced Plasmas," to be published in the Review of Scientific Instruments.

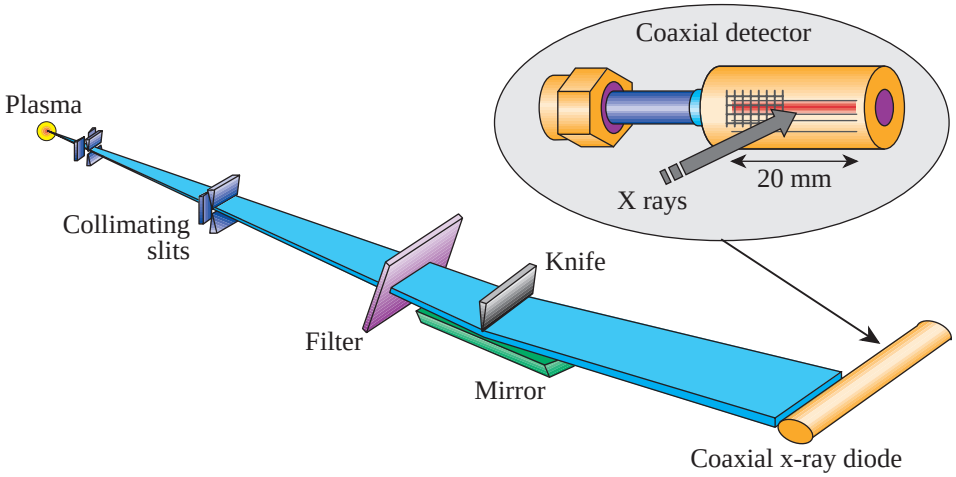

Figure 84.63
Illustration of a DMX diagnostic.

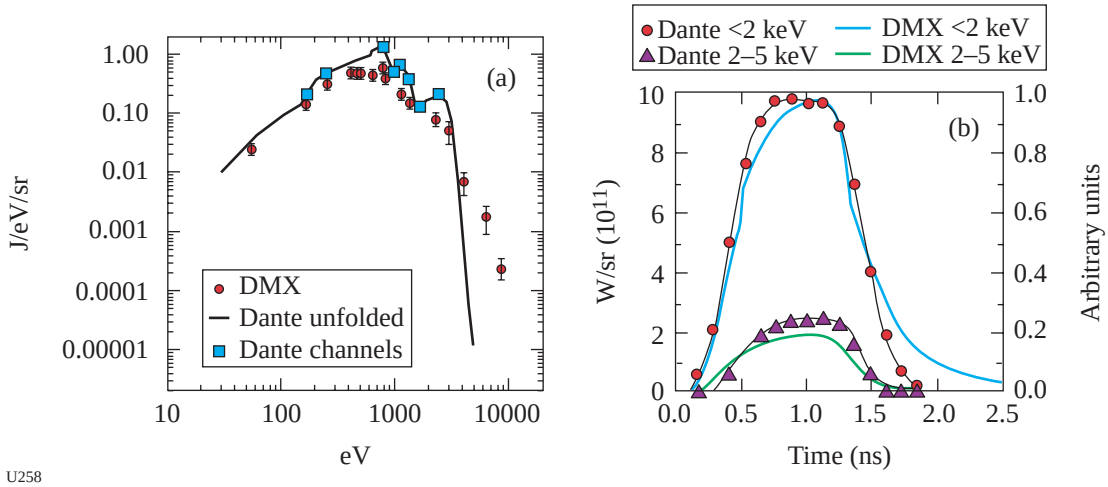

Figure 84.64
DMX/Dante experimental results comparison. (a) Time-integrated spectrum inferred from Dante (solid line and squares) and DMX (circles) on OMEGA Shot 18326. Symbols denote the mean energies of the channels for both diagnostics. (b) Spectrally integrated intensity as a function of time for $h\nu < 2$ keV and $2 < h\nu < 5$ keV. DMX data were rescaled with the same factor for both plots.

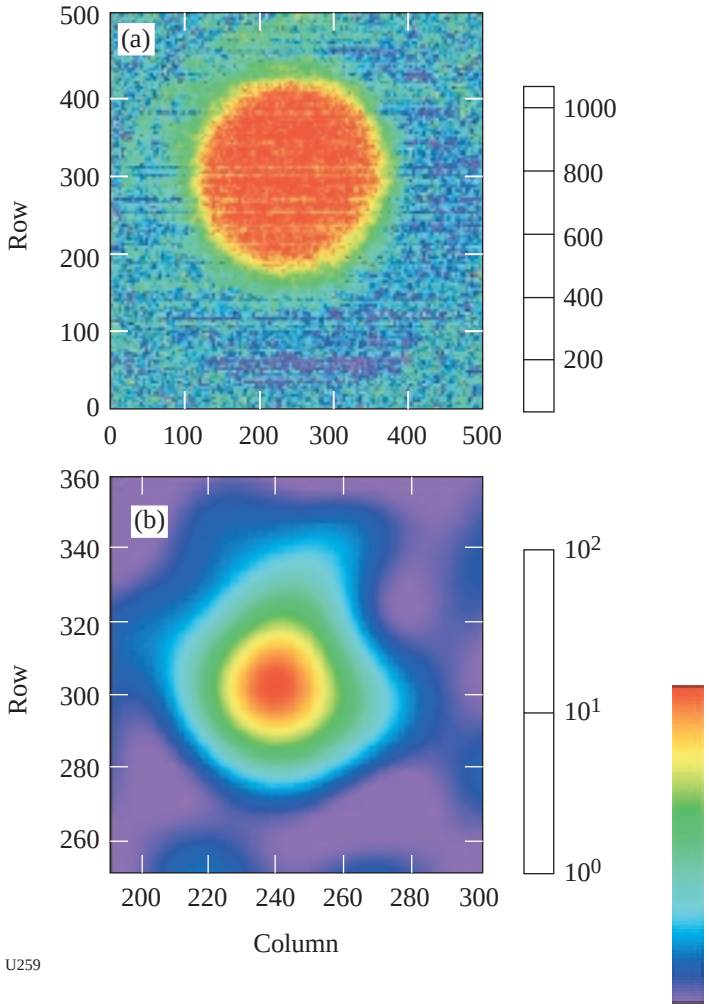

Figure 84.65
(a) Penumbral image of an imploded DT target. The central disk is the image of the neutrons passing through the entrance of the aperture. The neutron source size information is in the area surrounding the central disk. (b) Processed neutron image of a DT imploded target (Shot 20290). Ten pixels represent 28 μm on this image.

Publications and Conference Presentations

Publications

R. Adam, M. Currie, C. Williams, R. Sobolewski, O. Harnack, and M. Darula, "Direct Observation of Subpicosecond Single-Flux-Quantum Generation in Pulse-Driven Y-Ba-Cu-O Josephson Junctions," Appl. Phys. Lett. **76**, 469 (2000).

E. L. Alfonso, I. Anteby, and D. R. Harding, "Temperature Profiles and ℓ = 1 Nonuniformity Within Cryogenic ICF Targets," Fusion Technol. **38**, 149 (2000).

S. R. Arrasmith, I. A. Kozhinova, L. L. Gregg, H. J. Romanofsky, A. B. Shorey, S. D. Jacobs, D. Golini, W. I. Kordonski, P. Dumas, and S. Hogan, "Details of the Polishing Spot in Magnetorheological Finishing (MRF)," in *Optical Manufacturing and Testing III*, edited by H.Stahl (SPIE, Bellingham, WA, 1999), Vol. 3782, pp. 92–100.

A. Babushkin, M. J. Guardalben, R. S. Craxton, P. Adamson, H. Ammenheuser, R. L. Keck, and W. Seka, "Characterization of Frequency-Conversion Crystals for the Implementation of a 1-THz Bandwidth on the OMEGA Laser," in *Conference on Lasers and Electro-Optics*, 2000 Technical Digest Series (Optical Society of America, Washington, DC, 2000), pp. 290–291.

R. Betti and J. P. Freidberg, "Radial Discontinuities in Tokamak Magnetohydrodynamic Equilibria with Poloidal Flow," Phys. Plasmas **7**, 2439 (2000).

T. R. Boehly, D. D. Meyerhofer, Y. Fisher, W. Seka, and D. K. Bradley, "Measurements of the Optical Contrast on OMEGA: a 60-Beam, 30-kJ UV Fusion Laser," in *Conference on Lasers and Electro-Optics*, 2000 Technical Digest Series (Optical Society of America, Washington, DC, 2000), p. 539.

J. L. Chaloupka and D. D. Meyerhofer, "Characterization of a Tunable, Single-Beam Ponderomotive-Optical Trap," J. Opt. Soc. Am. B **17**, 713 (2000).

J. L. Chaloupka and D. D. Meyerhofer, "Observation of Electron Trapping in an Intense Laser Beam," Phys. Rev. Lett. **83**, 4538 (1999).

S. H. Chen, R. J. Jin, D. Katsis, J. C. Mastrangelo, S. Papernov, and A. W. Schmid, "Photoracemization Broadening of Selective Reflection and Polarization Band of Glassy Chiral-Nematic Films," Liq. Cryst. **27**, 201 (2000).

H. P. Chen, D. Katsis, J. C. Mastrangelo, S. H. Chen, S. D. Jacobs, and P. J. Hood, "Glassy Liquid-Crystal Films with Opposite Chirality as High-Performance Optical Notch Filters and Reflectors," Adv. Mat. **12**, 1283 (2000).

H. P. Chen, D. Katsis, J. C. Mastrangelo, K. L. Marshall, S. H. Chen, and T. H. Mourey, "Thermotropic Chiral–Nematic Poly(*p*-phenylene)s as a Paradigm of Helically Stacked π-Conjugated Systems," Chem. Mater. **12**, 2275 (2000).

S. H. Chen, J. C. Mastrangelo, and R. J. Jin, "Glassy Liquid-Crystal Films as Broadband Polarizers and Reflectors via Spatially Modulated Photoracemization," Adv. Mater. **11**, 1183 (1999).

T. J. B. Collins, H. L. Helfer, and H. M. VanHorn, "Oscillations of Accretion Disks and Boundary Layers in Cataclysmic Variables: I. Unperturbed, Steady-Flow Models," Astrophys. J. **534**, 934 (2000).

T. J. B. Collins, H. L. Helfer, and H. M. VanHorn, "Oscillations of Accretion Disks and Boundary Layers in Cataclysmic Variables: II. A Local, Linear Stability Analysis of Accretion Disk Boundary Layers," Astrophys. J. **534**, 944 (2000).

F. Dahmani, J. C. Lambropoulos, A. W. Schmid, S. Papernov, and S. J. Burns, "Crack Arrest and Stress Dependence of Laser-Induced Surface Damage in Fused-Silica and Borosilicate Glass," Appl. Opt. **38**, 6892 (1999).

F. Dahmani, A. W. Schmid, J. C. Lambropoulos, S. J. Burns, and S. Papernov, "Lifetime Prediction of Laser-Precracked Fused Silica Subjected to Subsequent Cyclic Laser Pulses," J. Mater. Res. **15**, 1182 (2000).

F. Y. Fan, J. C. Mastrangelo, D. Katsis, and S. H. Chen, "Novel Glass-Forming Liquid Crystals: V. Nematic and Chiral-Nematic Systems with an Elevated Glass Transition Temperature," Liq. Cryst. **27**, 1239 (2000).

V. N. Goncharov, S. Skupsky, T. R. Boehly, J. P. Knauer, P. W. McKenty, V. A. Smalyuk, R. P. J. Town, O. V. Gotchev, R. Betti, and D. D. Meyerhofer, "A Model of Laser Imprinting," Phys. Plasmas **7**, 2062 (2000) (invited).

V. N. Goncharov, S. Skupsky, P. W. McKenty, J. A. Delettrez, R. P. J. Town, and C. Cherfiles-Clérouin, "Stability Analysis of Directly Driven NIF Capsules," in *Inertial Fusion Sciences and Applications (IFSA 99): State of the Art 1999*, edited by C. Labaune, W. J. Hogan, and K. A. Tanaka (Elsevier, Paris, 2000), pp. 214–219.

S. R. Gorodkin, W. I. Kordonski, E. V. Medvedeva, Z. A. Novikova, A. B. Shorey, and S. D. Jacobs, "A Method and Device for Measurement of a Sedimentation Constant of Magnetorheological Fluids," Rev. Sci. Instrum. **71**, 2476 (2000).

M. J. Guardalben and N. Jain, "Phase-Shift Error as a Result of Molecular Alignment Distortions in a Liquid-Crystal Point-Diffraction Interferometer," Opt. Lett. **25**, 1171 (2000).

K. S. Il'in, M. Lindgren, M. Currie, A. D. Semenov, G. N. Gol'tsman, R. Sobolewski, S. I. Cherednichenko, and E. M. Gershenzon, "Picosecond Hot-Electron Energy Relaxation in NbN Superconducting Photodetectors," Appl. Phy. Lett. **76**, 2752 (2000).

S. D. Jacobs, "Take-Home Demo Excites Young People About Careers in Technology," Opt. Photonics News, 16 (July 2000).

S. D. Jacobs, S. A. Arrasmith, I. A. Kozhinova, L. L. Gregg, A. B. Shorey, H. J. Romanofsky, D.Golini, W. I. Kordonski, P. Dumas, and S. Hogan, "Magnetorheological Finishing (MRF): Computer-Controlled Optics Manufacturing," The American Ceramic Society Bulletin, December 1999, pp. 42–48.

S. D. Jacobs and A. B. Shorey, "Magnetorheological Finishing: New Fluids for New Materials," in *Optical Fabrication and Testing*, OSA Technical Digest (Optical Society of America, Washington, DC, 2000), pp. 142–144 (invited).

D. Katsis, P. H. M. Chen, J. C. Mastrangelo, S. H. Chen, and T. N. Blanton, "Vitrified Chiral-Nematic Liquid Crystalline Films for Selective Reflection and Circular Polarization," Chem. Mater. **11**, 1590 (1999).

J. P. Knauer, R. Betti, D. K. Bradley, T. R. Boehly, T. J. B. Collins, V. N. Goncharov, P. W. McKenty, D. D. Meyerhofer, V. A. Smalyuk, C. P. Verdon, S. G. Glendinning, D. H. Kalantar, and R. G. Watt, "Single-Mode Rayleigh–Taylor Growth-Rate Measurements on the OMEGA Laser System," Phys. Plasmas **7**, 338 (2000).

R. S. Knox, "Physical Aspects of the Greenhouse Effect and Global Warming," Am. J. Phys. **67**, 1227 (1999).

I. Kozhinova, S. Jacobs, S. Arrasmith, and L. Gregg, "Corrosion in Aqueous Cerium Oxide Magnetorheological Fluids," in *Optical Fabrication and Testing*, OSA Technical Digest (Optical Society of America, Washington, DC, 2000), pp. 151–153.

C. K. Li, D. G. Hicks, F. H. Séguin, J. A. Frenje, R. D. Petrasso, J. M. Soures, P. B. Radha, V. Yu. Glebov, C. Stoeckl, J. P. Knauer, R. Kremens, F. J. Marshall, D. D. Meyerhofer, S. Skupsky, S. Roberts, C. Sorce, T. C. Sangster, T. W. Phillips, M. D. Cable, and R. J. Leeper, "D-^{3}He Proton Spectra for Diagnosing Shell ρR and Fuel T_i of Imploded Capsules at OMEGA," Phys. Plasmas **7**, 2578 (2000).

F. J. Marshall, J. A. Delettrez, R. Epstein, V. Yu. Glebov, D. R. Harding, P. W. McKenty, D. D. Meyerhofer, P. B. Radha, W. Seka, S. Skupsky, V. A. Smalyuk, J. M. Soures, C. Stoeckl, R. P. J. Town, B. Yaakobi, C. K. Li, F. H. Séguin, D. G. Hicks, and R. D. Petrasso, "Direct-Drive, High-Convergence-Ratio Implosion Studies on the OMEGA Laser System," Phys. Plasmas **7**, 2108 (2000).

F. J. Marshall, J. A. Delettrez, V. Yu. Glebov, R. P. J. Town, B. Yaakobi, R. L. Kremens, and M. Cable, "Direct-Drive, Hollow-Shell Implosion Studies on the 60-Beam, UV OMEGA Laser System," Phys. Plasma **7**, 1006 (2000).

R. L. McCrory, R. E. Bahr, T. R. Boehly, T. J. B. Collins, R. S. Craxton, J. A. Delettrez, W. R. Donaldson, R. Epstein, V. N. Goncharov, R. Q. Gram, D. R. Harding, P. A. Jaanimagi, R. L. Keck, J. P. Knauer, S. J. Loucks, F. J. Marshall, P. W. McKenty, D. D. Meyerhofer, S. F. B. Morse, O. V. Gotchev, P. B. Radha, S. Regan, W. Seka, S. Skupsky, V. A. Smalyuk, J. M. Soures, C. Stoeckl, R. P. J. Town, M. D. Wittman, B. Yaakobi, J. D. Zuegel, R. D. Petrasso, D. G. Hicks, and C. K. Li, "OMEGA Experiments and Preparation for Moderate-Gain Direct-Drive Experiments on the NIF," in *Inertial Fusion Sciences and Applications (IFSA 99): State of the Art 1999*, edited by C. Labaune, W. J. Hogan, and K. A. Tanaka (Elsevier, Paris, 2000), pp. 43–53.

R. L. McCrory, J. M. Soures, A. Babushkin, R. E. Bahr, R. Betti, T. R. Boehly, R. Boni, D. K. Bradley, T. J. B. Collins, R. S. Craxton, J. A. Delettrez, W. R. Donaldson, R. Epstein, V. Yu. Glebov, V. N. Goncharov, R. Q. Gram, D. R. Harding, D. G. Hicks, B. Hughes, P. A. Jaanimagi, T. J. Kessler, J. P. Knauer, C. K. Li, S. J. Loucks, F. J. Marshall, P. W. McKenty, D. D. Meyerhofer, A. V. Okishev, S. Padalino, R. D. Petrasso, P. B. Radha, S. P. Regan, F. H. Séguin, W. Seka, R. W. Short, A. Simon, M. D. Skeldon, S. Skupsky, C. Stoeckl, R. P. J. Town, M. D. Wittman, B. Yaakobi, and J. D. Zuegel, "Recent Advances in Direct-Drive ICF Target Physics at the Laboratory for Laser Energetics," in *Fusion Energy 1998* (IAEA, Vienna, 1999), Vol. I, pp. 167–176.

P. W. McKenty, M. D. Wittman, and V. N. Goncharov, "Characterization of Thick Cryogenic Fuel Layers Using Convergent-Beam Interferometry: a Numerical Investigation," J. Appl. Phys. **88**, 2928 (2000).

C. J. McKinstrie and E. A. Startsev, "Forward and Backward Stimulated Brillouin Scattering of Crossed Laser Beams," Phys. Rev. E **60**, 5978 (1999).

A. V. Okishev, "The Oldest Higher-Educational Optical Institution in Russia Turns 100," Optics & Photonics News, March 2000, 17.

A. V. Okishev, R. Boni, M. Millecchia, B. Kubera, P. A. Jaanimagi, W. R. Donaldson, R. L. Keck, W. Seka, K. V. Dukelsky, M. A. Eronyan, G. A. Shevandin, and G. A. Ermolaev, "A Unique High-Bandwidth, Multimode UV Optical Fiber: Manufacturing, Testing, and Laser-Fusion Applications," in *Conference on Lasers and Electro-Optics*, 2000 Technical Digest Series (Optical Society of America, Washington, DC, 2000), pp. 292–293.

A. V. Okishev, M. D. Skeldon, R. L. Keck, and W. Seka, "All-Solid-State Optical Pulse Shaper for the OMEGA Laser Fusion Facility," in *Advanced Solid State Lasers*, edited by H. Injeyan, U. Keller, and C. Marshall, OSA Trends in Optics and Photonics, Vol. 34 (Optical Society of America, Washington, DC, 2000), pp. 30–32.

P. B. Radha, S. Skupsky, R. D. Petrasso, and J. M Soures, "A Novel Charged-Particle Diagnostic for Compression in ICF Targets," Phys. Plasmas **7**, 1531 (2000).

J. D. Schnittman and R. S. Craxton, "Three-Dimensional Modeling of Capsule Implosions in OMEGA Tetrahedral Hohlraums," Phys. Plasmas **7**, 2964 (2000).

A. B. Shorey, L. L. Gregg, H. J. Romanofsky, S. R. Arrasmith, I. Kozhinova, J. Jubregsen, and S. D. Jacobs, "Study of Material Removal During Magnetorheological Finishing (MRF)," in *Optical Manufacturing and Testing III*, edited by H. Stahl (SPIE, Bellingham, WA, 1999), Vol. 3782, pp. 101–111.

A. B. Shorey and S. D. Jacobs, "Nanohardness of Abrasive Particles Used in Magnetorheological Finishing (MRF)," in *Optical Fabrication and Testing*, OSA Technical Digest (Optical Society of America, Washington, DC, 2000), pp. 145–147.

A. B. Shorey, W. I. Kordonski, S. R. Gorodkin, S. D. Jacobs, R. F. Gans, K. M. Kwong, and C. H. Farny, "Design and Testing of a New Magnetorheometer," Rev. Sci. Instrum. **70**, 4200 (1999).

M. D. Skeldon, "A High-Bandwidth Electrical Waveform Generator Based on an Aperture-Coupled Stripline," Rev. Sci. Instrum. **71**, 3559 (2000).

R. Sobolewski, "Time-Resolved Nonequilibrium Phenomena in High-Temperature Superconductors," in *Superconductivity, Magneto-Resistive Materials, and Strongly Correlated Quantum Systems*, Recountres du Vietnam, edited by N. Van Hieu, T. Thanh Van, and G. Xiao, Hanoi (Vietnam National University Press, Hanoi, 2000), pp. 55–66 (invited).

F.-Y. Tsai, E. L. Alfonso, S. H. Chen, and D. R. Harding, "Mechanical Properties and Gas Permeability of Polyimide Shells Fabricated by the Vapor Deposition Method," Fusion Technol. **38**, 83 (2000).

D. L. Tubbs, C. W. Barnes, J. B. Beck, N. M. Hoffman, J. A. Oertel, R. G. Watt, T. Boehly, D. Bradley, P. Jaanimagi, and J. Knauer, "Cylindrical Implosion Experiments Using Laser Direct Drive," Phys. Plasmas **6**, 2095 (1999).

W. S. Varnum, N. D. Delamater, S. C. Evans, P. L. Gobby, J. E. Moore, J. M. Wallace, R. G. Watt, J. D. Colvin, R. Turner, V. Glebov, J. Soures, and C. Stoeckl, "Progress Toward Ignition with Noncryogenic Double-Shell Capsules," Phys. Rev. Lett. **84**, 5152 (2000).

B. Yaakobi, V. A. Smalyuk, J. A. Delettrez, F. J. Marshall, D. D. Meyerhofer, and W. Seka, "Measurement of Areal Density Modulation of Laser-Imploded Shells Through *K*-Edge Imaging," Phys. Plasmas **7**, 3727 (2000).

B. Yaakobi, V. A. Smalyuk, J. A. Delettrez, R. P. J. Town, F. J. Marshall, V. Yu. Glebov, R. D. Petrasso, J. M. Soures, D. D. Meyerhofer, and W. Seka, "Spherical Implosion Experiments on OMEGA: Measurements of the Cold, Compressed Shell," in *Inertial Fusion Sciences and Applications (IFSA 99): State of the Art 1999*, edited by C. Labaune, W. J. Hogan, and K. A. Tanaka (Elsevier, Paris, 2000), pp. 115–121.

B. Yaakobi, C. Stoeckl, T. Boehly, D. D. Meyerhofer, and W. Seka, "Measurement of Preheat Due to Fast Electrons in Laser Implosions," Phys. Plasmas **7**, 3714 (2000).

J. D. Zuegel, D. Jacobs-Perkins, J. A. Marozas, R. G. Roides, W. Bittle, E. M. R. Michaels, S. Regan, R. S. Craxton, J. H. Kelly, T. J. Kessler, W. Seka, and S. Skupsky, "Broadband Beam Smoothing on OMEGA with Two-Dimensional Smoothing by Spectral Dispersion," in *Inertial Fusion Sciences and Applications (IFSA 99): State of the Art 1999*, edited by C. Labaune, W. J. Hogan, and K. A. Tanaka (Elsevier, Paris, 2000), pp. 664–668.

Conference Presentations

J. L. Chaloupka and D. D. Meyerhofer, "Observation of Electron Trapping in an Intense Laser Beam," International Conference on Multiphoton Processes, Monterey, CA, 3–8 October 1999.

A. V. Okishev, M. D. Skeldon, J. H. Kelly, A. Babushkin, J. D. Zuegel, R. G. Roides, S. F. B. Morse, and W. Seka, "Front-End Laser System for the OMEGA Laser Fusion Facility," Optics '99, St. Petersburg, Russia, 19–21 October 1999.

The following presentations were made at the 13th Annual Target Fabrication Meeting, Catalina Island, CA, 8–11 November 1999:

E. L. Alfonso, I. Anteby, and D. R. Harding, "Temperature and Ice-Thickness Profiles Within Cryogenic ICF Targets."

M. Bonino, L. Elasky, R. Q. Gram, S. Noyes, and D. R. Harding, "Stress–Strain Performance of Spider Silk."

R. Q. Gram, J. Hobler, L. Lund, and D. R. Harding, "Initial Performance of the High-Pressure DT Filling Portion of the Cryogenic Target Handling System."

P. W. McKenty and M. D. Wittman, "Characterization of Thick Cryogenic Layers Using an Interferometric Imaging System and Legendre Mode Decomposition."

F.-Y. Tsai, E. L. Alfonso, S. H. Chen, and D. R. Harding, "Mechanical Properties and Gas Permeability of Polyimide Shells Fabricated by the Vapor Deposition Method."

The following presentations were made at the 41st Annual Meeting of the American Physical Society Division of Plasma Physics, Seattle, WA, 15–19 November 1999:

T. R. Boehly, O. Gotchev, V. N. Goncharov, J. P. Knauer, D. D. Meyerhofer, S. Skupsky, V. A. Smalyuk, R. P. J. Town, Y. Srebro, and D. Shvarts, "Measurements of Laser Imprinting on the OMEGA Laser System."

T. J. B. Collins and S. Skupsky, "The Effects of Pulse Shaping on Imprint."

R. S. Craxton and S. Skupsky, "Pulse Shapes and Beam Smoothing for OMEGA and the NIF."

J. A. Delettrez, V. Yu. Glebov, F. J. Marshall, C. Stoeckl, B. Yaakobi, and D. D. Meyerhofer, "Effect of Beam Smoothing and Pulse Shape on the Implosion of DD-Filled CH Shell Targets on OMEGA."

R. Epstein, J. A. Delettrez, V. N. Goncharov, P. W. McKenty, P. B. Radha, and S. Skupsky, "One-Dimensional Simulation of the Effects of Unstable Mix on Neutron and Charged-Particle Spectra from Laser-Driven Implosion Experiments."

V. Yu. Glebov, J. A. Delettrez, R. Epstein, P. W. McKenty, F. J. Marshall, D. D. Meyerhofer, P. B. Radha, V. A. Smalyuk, and C. Stoeckl, "Evidence for Fuel–Pusher Mixing in OMEGA Direct-Drive Implosions by Neutron Diagnostic."

V. N. Goncharov, S. Skupsky, P. W. McKenty, R. P. J. Town, T. R. Boehly, D. D. Meyerhofer, and O. V. Gotchev, "A Model of Laser Imprinting" (invited).

O. V. Gotchev, J. P. Knauer, D. D. Meyerhofer, and V. A. Smalyuk, "Characterization of an X-Ray Radiographic System for Measuring the Evolution of Broadband Imprint in Laser-Driven Planar Targets."

D. R. Harding, L. D. Lund, S. J. Loucks, D. J. Lonobile, R. Q. Gram, M. D. Wittman, M. J. Shoup III, G. Gerspacher, U. Kamal, L. Folnsbee, A. Nobile, G.Besenbruch, K. Schultz, and I. Anteby, "The OMEGA Cryogenic Target-Handling System."

D. G. Hicks, C. K. Li, F. H. Séguin, R. D. Petrasso, J. M. Soures, C. Stoeckl, J. P. Knauer, D. D. Meyerhofer, W. Seka, R. W. Short, A. Simon, T. W. Phillips, T. C. Sangster, and M. D. Cable, "Measurement of Accelerated Ions from OMEGA Targets."

P. A. Jaanimagi, R. Boni, and R. L. Keck, "Neutron-Induced Background in CCD Detectors."

A. V. Kanaev and C. J. McKinstrie, "Numerical Two-Dimensional Studies of Near-Forward Stimulated Brillouin Scattering of a Laser Beam in Plasmas."

D. Keller, T. J. B. Collins, J. A. Delettrez, P. W. McKenty, P. B. Radha, R. P. J. Town, B. Whitney, and G. A. Moses, "*DRACO*—A New Multidimensional Hydrocode."

J. P. Knauer, R. Betti, T. R. Boehly, V. N. Goncharov, D. D. Meyerhofer, and R. P. J. Town, "Feed-Out of Rear-Surface Perturbations to the Ablation Interface and Subsequent Growth."

M. V. Kozlov and C. J. McKinstrie, "Numerical Simulation of Sound-Wave Generation in Two-Ion Plasma."

C. K. Li, R. D. Petrasso, D. G. Hicks, F. H. Séguin, J. M. Soures, P. B. Radha, V. Yu. Glebov, J. P. Knauer, F. J. Marshall, S. Roberts, S. Skupsky, C. Sorce, C. Stoeckl, T. C. Sangster, T. W. Phillips, and M. D. Cable, "T-^{3}He Deuterons as a Diagnostic for Capsule Implosions on OMEGA."

V. Lobatchev and R. Betti, "Numerical Study of Feed-Out of Short-Wavelength Rear-Surface Perturbations in Planar Targets."

F. J. Marshall, J. A. Delettrez, R. Epstein, V. Yu. Glebov, D. R. Harding, P. W. McKenty, D. D. Meyerhofer, R. D. Petrasso, P. B. Radha, W. Seka, S. Skupsky, V. A. Smalyuk, J. M. Soures, C.Stoeckl, R. P . J. Town, B. Yaakobi, D. G. Hicks, C. K. Li, and F. H. Séguin, "Direct-Drive, High-Convergence-Ratio Implosion Studies on the OMEGA Laser System."

D. D. Meyerhofer, P. W. McKenty, V. N. Goncharov, J. A. Delettrez, V. Yu. Glebov, F. J. Marshall, P. B. Radha, S. P. Regan, V. A. Smalyuk, J. M. Soures, C.Stoeckl, R. P . J. Town, B.Y aakobi, and R. D. Petrasso, "Performance of Spherical Target Implosions on the OMEGA Laser System."

P. B. Radha, S. Cremer, J. A. Delettrez, R. Epstein, R. D. Petrasso, S. Skupsky, and J. M. Soures, "Charged-Particle Spectra Using Particle Tracking on a Two-Dimensional Grid."

S. P. Regan, J. A. Delettrez, D. K. Bradley, V. Yu. Glebov, D. D. Meyerhofer, and C. Stoeckl, "Burnthrough Experiments on OMEGA to Study Effects of Laser Irradiation Uniformity and Shinethrough Layers on Spherical Target Performance."

F. H. Séguin, R. D. Petrasso, C. K. Li, D. G. Hicks, J. M. Soures, P. B. Radha, V. Yu. Glebov, F. J. Marshall, D. D. Meyerhofer, C. Stoeckl, S. Roberts, C. Sorce, T. C. Sangster, T. W. Phillips, M. D. Cable, S. Padalino, and K. Fletcher, "Diagnostic Use of Secondary D-^{3}He Proton Spectra for DD OMEGA Targets."

W. Seka, D. D. Meyerhofer, S. P. Regan, B. Yaakobi, R. E. Bahr, R. S. Craxton, R. W. Short, and A. Simon, "Interaction Experiments Under Direct-Drive NIF Conditions."

R. W. Short, "Stability of Self-Focused Filaments in Laser-Produced Plasmas."

A. Simon, "Relativistic Electron Beams, Forward Thomson Scattering, and Raman Scattering."

V. A. Smalyuk, B. Yaakobi, V. N. Goncharov, J. A. Delettrez, F. J. Marshall, and D. D. Meyerhofer, "Imaging of Compressed Pure-CH Shells and CH Shells with Titanium-Doped Layers on OMEGA."

E. A. Startsev and C. J. McKinstrie, "Particle-in-Cell Simulations of Particle Acceleration."

C. Stoeckl, J. A. Delettrez, V. Yu. Glebov, D. D. Meyerhofer, W. Seka, V. A. Smalyuk, S. Sublett, and J. D. Zuegel, "Measurements of Hard X-Ray Emission from Laser–Plasma Instabilities on OMEGA."

R. P. J. Town, J. A. Delettrez, R. Epstein, V. N. Goncharov, P. W. McKenty, P.B. Radha, and S.Skupsky , "OMEGA Cryogenic Target Design."

J. D. Schnittman and R. S. Craxton, "Three-Dimensional Modeling of Capsule Implosions in OMEGA Tetrahedral Hohlraums," Israel Plasma Science Technology Association, Beer Sheva, Israel, 9 February 2000.

A. V. Okishev, M. D. Skeldon, R. L. Keck, and W. Seka, "All-Solid-State Optical Pulse Shaper for the OMEGA Laser Fusion Facility," Advanced Solid-State Lasers 15th Topical Meeting, Davos, Switzerland, 13–16 February 2000.

A. B. Shorey, K. M. Kwong, and S. D Jacobs, "Revealing Hardness Variations in Optical Polishing Abrasives," MTS Nano Instrument Users' Meeting, Albany, NY, 22 February 2000.

The following presentations were made at the 12th APS Topical Conference on Atomic Processes in Plasmas, Reno, NV, 19–23 March 2000:

S. P. Regan, J. A. Delettrez, B. Yaakobi, D. K. Bradley, R. E. Bahr, M. Millecchia, D. D. Meyerhofer, and W. Seka, "Spectroscopic Analysis of Electron Temperature in Laser-Driven Burnthrough Experiments."

V. A. Smalyuk, B. Yaakobi, F. J. Marshall, and D. D. Meyerhofer, "X-Ray Spectroscopic Measurements of Areal Density and Modulations in Areal Density of Cold Compressed Shells in Implosion Experiments on OMEGA."

J. P. Knauer, T. J. B. Collins, A. Frank, and E. Blackman, "Generation of Collimated Flows by Intense Irradiation with Applications to Astrophysical Phenomena," 3rd International Conference on Laboratory Astrophysics with Intense Lasers, Rice University, Houston, TX, 30 March–1 April 2000.

R. Adam, M. Darula, and R. Sobolewski, "Subpicosecond Dynamics of the Switching Process in Y-Ba-Cu-O Josephson Junctions," SPIE's 14th Annual International Symposium on Aerospace/Defense Sensing, Simulation, and Controls, Orlando, FL, 24–28 April 2000.

The following presentations were made at CLEO/QELS 2000, San Francisco, CA, 7–12 May 2000:

A. Babushkin, M. J. Guardalben, R. S. Craxton, P. Adamson, H. Ammenheuser, R. L. Keck, and W. Seka, "Characterization of Frequency-Conversion Crystals for the Implementation of a 1-THz Bandwidth on the OMEGA Laser."

T. R. Boehly, D. D. Meyerhofer, Y. Fisher, W. Seka, and D. K. Bradley, "Measurements of the Optical Contrast on OMEGA: a 60-Beam, 30-kJ UV Fusion Laser."

A. V. Okishev, R. Boni, M. Millecchia, B. Kubera, P. A. Jaanimagi, W. R. Donaldson, R. L. Keck, W. Seka, K. V. Dukelsky, M. A. Eronyan, G. A. Shevandin, and G. A. Ermolaev, "A Unique High-Bandwidth, Multimode UV Optical Fiber: Manufacturing, Testing, and Laser-Fusion Applications."

The following presentations were made at the 30th Annual Anomalous Absorption Conference, Ocean City, MD, 21–26 May 2000:

R. Betti, J. P. Knauer, V. Lobatchev, and M. Umanski, "Hydrodynamic Instabilities from the Beginning to the End."

R. S. Craxton, J. P. Knauer, and R. P. J. Town, "Two-Dimensional Simulations of Cryogenic Deuterium Foil Acceleration for NIF Instability Experiments."

J. A. Delettrez, V. Smalyuk, B. Yaakobi, and D. D. Meyerhofer, "Results of Two-Dimensional Simulations of Implosions of DD-Filled CH Shell Targets on the OMEGA Laser."

R. Epstein, J. A. Delettrez, V. Yu. Glebov, V. N. Goncharov, P. W. McKenty, P. B. Radha, and S. Skupsky, "One-Dimensional Simulation of the Effects of Unstable Mix on Neutron and Charged Particle Spectra from Laser-Driven Implosion Experiments."

A. V. Kanaev and C. J. McKinstrie, "Numerical Simulations of SSD-Smoothed Laser Beam Filamentation and Forward SBS in Plasmas."

V. Lobatchev, R. Betti, and M. Umanski, "Numerical Study of Deceleration-Phase Rayleigh–Taylor Instability."

P. B. Radha, T. J. B. Collins, J. A. Delettrez, D. Keller, P. W. McKenty, and R. P. J. Town, "*DRACO*—A Multidimensional Hydrocode for ICF."

S. P. Regan, J. A. Delettrez, B. Yaakobi, R. Epstein, D. K. Bradley, D. D. Meyerhofer, and W. Seka, "Laser-Driven Burnthrough Experiments on OMEGA."

R. W. Short, "The Effects of Beam Intensity Structure on Two-Plasmon Decay in Direct-Drive Fusion Targets."

C. Stoeckl, V. Yu. Glebov, D. D. Meyerhofer, W. Seka, B. Yaakobi, and J. D. Zuegel, "Optical and X-Ray Signatures from the Two-Plasmon-Decay Instability on OMEGA."

T. R. Boehly, B. Yaakobi, D. Hoarty, J. P. Knauer, D. D. Meyerhofer, R. P. J. Town, R. E. Bahr, and M. Millecchia, "Measurements of Shock Heating Using Al Absorption Spectroscopy in Planar Targets," International Workshop on Warm Dense Matter, Vancouver, B.C., Canada, 29–31 May 2000.

J. P. Knauer, T. J. B. Collins, A. Frank, and E. Blackman, "Generation of Collimated Flows by Intense Laser Irradiation with Applications to Astrophysical Phenomena," 196th Meeting of the American Astronomical Society, Rochester, NY, 4–8 June 2000.

The following presentations were made at the 26th European Conference on Laser Interaction with Matter, Prague, Czech Republic, 12–16 June 2000:

S. Skupsky, R. L. McCrory, R. E. Bahr, T. R. Boehly, T. J. B. Collins, R. S. Craxton, J. A. Delettrez, W. R. Donaldson, R. Epstein, V. N. Goncharov, R. Q. Gram, D. R. Harding, P. A. Jaanimagi, R. L. Keck, J. P. Knauer, S. J. Loucks, F. J. Marshall, P. W. McKenty, D. D. Meyerhofer, S. F. B. Morse, O. V. Gotchev, P. B. Radha, S. P. Regan, W. Seka, V. A. Smalyuk, J. M. Soures, C. Stoeckl, R. P. J. Town, M. D. Wittman, B. Yaakobi, J. D. Zuegel, R. D. Petrasso, D. G. Hicks, and C. K. Li, "Recent Progress in Direct-Drive ICF Research at the Laboratory for Laser Energetics."

B. Yaakobi, C. Stoeckl, T. R. Boehly, D. D. Meyerhofer, and W. Seka, "Measurement of Preheat due to Fast Electrons in Laser Implosions."

The following presentations were made at Optical Fabrication and Testing, Quebec City, Canada, 18–22 June 2000:

S. D. Jacobs and A. B. Shorey, "Magnetorheological Finishing: New Fluids for New Materials."

I. A. Kozhinova, S. D. Jacobs, S. R. Arrasmith, and L. L. Gregg, "Corrosion in Aqueous Cerium Oxide Magnetorheological Fluids."

A. B. Shorey and S. D. Jacobs, "Nanohardness of Abrasive Particles Used in Magnetorheological Finishing (MRF)."

The following presentations were made at the 13th Topical Conference on High-Temperature Plasma Diagnostics, Tucson, AZ, 18–22 June 2000:

T. R. Boehly, B. Yaakobi, D. Hoarty, J. P. Knauer, D. D. Meyerhofer, R. P. J. Town, R. E. Bahr, and M. Millecchia, "Measurements of Shock Heating Using Al Absorption Spectroscopy in Planar Targets."

J. A. Frenje, D. G. Hicks, C. K. Li, F. H. Séguin, R. D. Petrasso, K. Fletcher, H. Olliver, S. Padalino, S. Thompson, J. M. Soures, S. Roberts, C. Sorce, T. C. Sangster, and T. W. Phillips, "CR-39 Tract Detector Response to Charged Particles and Neutrons."

V. Yu. Glebov, D. D. Meyerhofer, C. Stoeckl, and J. D. Zuegel, "Secondary Neutron Yield Measurements by Current Mode Detectors."

P. A. Jaanimagi, R. Boni, and R. L. Keck, "Neutron-Induced Background in CCD Detectors."

C. K. Li, D. G. Hicks, F. H. Séguin, J. Frenje, R. D. Petrasso, J. M. Soures, P. B. Radha, V. Yu. Glebov, C. Stoeckl, J. P. Knauer, F. J. Marshall, D. D. Meyerhofer, S. Skupsky, S. Roberts, C. Sorce, T. C. Sangster, T. W. Phillips, and M. D. Cable, "Measuring Fusion Yields, Areal Densities, and Ion Temperatures of Imploded Capsules at OMEGA."

F. J. Marshall, T. A. Ohki, D. McInnis, Z. Ninkov, and J. Carbone, "Imaging of Laser–Plasma X-Ray Emission with Charge Injection Devices (CID)."

F. H. Séguin, C. K. Li, D. G. Hicks, J. A. Frenje, R. D. Petrasso, J. M. Soures, V. Yu. Glebov, P. B. Radha, D. D. Meyerhofer, S. Roberts, C. Sorce, T. C. Sangster, M. D. Cable, S. Padalino, and K. Fletcher, "Diagnostic Use of Secondary Proton Spectra for D-Filled ICF Targets."

V. A. Smalyuk, T. R. Boehly, L. S. Iwan, T. J. Kessler, J. P. Knauer, F. J. Marshall, D. D. Meyerhofer, C. Stoeckl, B. Yaakobi, and D. K. Bradley, "Fourier-Space Image Processing for Spherical Experiments on OMEGA."

C. Stoeckl, V. Yu. Glebov, D. D. Meyerhofer, W. Seka, B. Yaakobi, R. P. J. Town, and J. D. Zuegel, "Hard X-Ray Detectors for OMEGA and NIF."

The following presentations were made at Laser Optics 2000, St. Petersburg, Russia, 26–30 June 2000:

A. V. Okishev, R. Boni, M. Millechia, B. Kubera, P. A. Jaanimagi, W. R. Donaldson, R. L. Keck, K. V. Dukelsky, M. A. Eronyan, V. S. Shevandin, G. A. Ermolaeva, and G. Nikolaev, "A Unique High-Bandwidth, UV Fiber Delivery System for the OMEGA Diagnostics Applications."

A. V. Okishev, M. D. Skeldon, R. L. Keck, and W. Seka, "A New High-Bandwidth, All-Solid-State Pulse-Shaping System for the OMEGA Laser Facility."

R. Sobolewski, D. P. Butler, and Z. Celik-Butler, "Cooled and Uncooled Infrared Detectors Based on Yttrium Barium Copper Oxide," SPIE Baltic States Conference on Advanced Optical Materials (ADOM-2), Vilnius, Lithuania, 16–19 August 2000 (invited).

The following presentations were made at the Applied Superconductivity Conference (ASC), Virginia Beach, VA, 17–22 September 2000:

R. Adam, C. Williams, R. Sobolewski, J. Scherbel, M. Darula, and M. Siegel, "Experiments and Simulations of Subpicosecond SFQ Pulse Propagation in Y-Ba-Cu-O Josephson Transmission Lines."

G. Gol'tsman, O. Okunev, G. Chulkova, A. Lipatov, A. Dzardanov, K. Smirnov, A. Semenov, B. Voronov, C. Williams, and R. Sobolewski, "Fabrication and Properties of an Ultrafast NbN Hot-Electron Single-Photon Detector."

R. Sobolewski and J.-R. Park, "Magneto-Optical Modulator for Superconducting Digital Output Interface."

C. Williams, R. Adam, Y. Xu, R. Sobolewski, J. Scherbel, O. Harnack, M. Darula, and F. A. Hegmann, "Ultrafast Y-Ba-Cu-O Photodetector Based on the Nonequilibrium Kinetic Inductive Effect."

UNIVERSITY OF
ROCHESTER